Development of novel nanomedicines for the treatment of non-small cell lung cancer

Alexander Martyn Cryer

Lung Cell Biology Group

Airways Disease Section

National Heart and Lung Institute

Faculty of Medicine

Imperial College London

Sir Alexander Fleming Building

South Kensington Campus

Exhibition Road

London, United Kingdom

SW7 2AZ

Thesis submitted in accordance with the requirements of Imperial College London for the degree of Doctor of Philosophy

Abstract

Lung cancer stands as one of the deadliest diseases, responsible for the most cancer related deaths worldwide. The UK 5-year survival rate of non-small-cell lung cancer (NSCLC), the predominant subtype of lung cancer, stands at 9.5%, highlighting an unmet need for therapeutic intervention. A key issue is the lack of efficacy current chemotherapy regimens have in the clinic. These therapies often suffer from poor tumour targeting, resulting in dissemination throughout the body and inadequate concentrations in the tumour. This causes deleterious side effects contributing to a reduced patient quality of life and ultimately survival.

Nanomedicine may serve to overcome the current therapeutic hurdles in treating NSCLC; the use of nanoparticles (NPs) for the delivery of drugs can improve drug targeting to tumours, increasing efficacy and attenuating off-target side effects. NPs can be used to deliver multiple drugs and be made from varying materials such as gold (AuNPs) or polymers. Furthermore, the discovery of oncogenic mutations in genes like *EGFR* present druggable targets in patients harbouring the appropriate mutations. This can also be taken advantage of using NPs to more directly target tumours and increase therapeutic response. Therefore, the aim of this thesis was to develop novel NP formulations comprised of a chemically modified variant of the tyrosine kinase inhibitor afatinib and gold (Afb-AuNPs) or in combination with vinorelbine as a polymeric dual chemotherapy formulation (Dual-NPs).

Drug-bearing NPs were synthesised using a combination of organic chemistry and hydrophobic ion pairing, after which the NPs were extensively characterised to discern their physicochemical properties. We then sought to investigate the *in vitro* efficacy of NPs. Cell viability studies revealed Afb-AuNPs and Dual-NPs were significantly cytotoxic to various NSCLC cell lines and comparatively nontoxic to noncancerous cells. Moreover, NP formulations were found to significantly inhibit proliferation of A549, H226 and PC-9 cells

compared to clinical formulations as determined by electric cell-substrate impedance sensing. The mechanism of uptake in cancer cells was elucidated using fluorescent NPs as a model system and quantified using confocal microscopy. Finally, the *in vivo* activity of biocompatibility of Dual-NPs was investigated in a physiologically relevant murine model of NSCLC. Taken together, these results highlight the therapeutic potential for NP formulations of chemotherapy.

Declaration of Originality

The following work presented in this thesis has been performed by me, unless specific reference is otherwise made.

Synthesis and spectral assignment of afatinib analogues were done with the aid of Mr Richard Surgenor, Dr. Mahesh Mohan and Mr. Cheuk Chan (Department of Chemistry, Imperial College London). A patient-derived xenograft mouse model was established and monitored by Dr. Robert Hynds. Nanoparticle formulations were injected intravenously by Mr. Krishna Kolluri. The facilities and provision of the model were provided by Professor Sam Janes and Professor Charles Swanton as part of the Lungs for Living Research Centre at University College London. Ms Lorraine Lawrence (IRD Histology Service, Imperial College London) embedded and sectioned all organs and tumours, and subsequently stained sections with haematoxylin and eosin.

Copyright Declaration

The copyright of this thesis rests with the author. Unless otherwise indicated, its contents are licensed under a Creative Commons Attribution-Non Commercial 4.0 International Licence (CC BY-NC). Under this licence, you may copy and redistribute the material in any medium or format. You may also create and distribute modified versions of the work. This is on the condition that: you credit the author and do not use it, or any derivative works, for a commercial purpose. When reusing or sharing this work, ensure you make the licence terms clear to others by naming the licence and linking to the licence text. Where a work has been adapted, you should indicate that the work has been changed and describe those changes.

Acknowledgements

As is often the case with a PhD thesis and the work it entails, there are innumerable people to thank that have contributed in some way, shape or form to the scientific progression of the project, or to maintaining the sanity of the person behind it. To these people, I am grateful.

First, I would like to express my gratitude to my supervisors, Professor Terry Tetley, Dr. Andrew Thorley and Dr. Benjamin Almquist for allowing me to embark on this journey and guiding me throughout it. I am privileged I was able to entertain my passion for research under your dutiful supervision, participate in thought-provoking discussions (both scientifically and otherwise) and learn from your years of experience which has provided invaluable insight into both how to do good science and how to be a good scientist. Your tutelage has been instrumental throughout this chapter of my life and in preparation for the next.

Secondly, I am indebted to the colleagues and collaborators without whom this work would not have been possible. My thanks go to Professor Alan Spivey and his group, Professor Alexandra Porter, The Lungs for Living Group at UCL, particularly Dr. Robert Hynds, Professor Sam Janes and Professor Charles Swanton, Professor Michael Seckl, Dr. Andrew Rogers, the Lung Cell Biology group and several other groups within the NHLI for your energy, time and collaborative efforts. I would also like to acknowledge the masters students I was fortunate to supervise over the years, whose efforts comprise a significant portion of the gold nanoparticle work presented in this thesis.

Thirdly, I would like to thank my family, whose sacrifices and encouragement have allowed me to chart this course, and friends for their support. My gratitude extends especially to Peter Leafe, William St. Leger Moore, Rachele Invernizzi and each of their families. These individuals were deeply involved in my personal development over the years and were pillars of support without which I would have been lost.

Science is the art of elucidation through experimentation

Table of Contents

Abbreviations

3T3-J2 - Mouse embryonic fibroblast cells

A549 - adenocarcinoma human alveolar basal epithelial cells

ABCB1 - ATP-binding cassette sub-family B member 1

ACUPA - S,S-2-[3-(-amino-1- carboxypentyl)-ureido]-pentanedioic acid

ADC - adenocarcinoma

Afb - afatinib

Afb-A - alkyne afatinib (compound 17)

Afb-A - lipoic acid modified afatinib (compound 16)

Afb-AuNPs - gold nanoparticles with afatinib conjugated to the surface

ALK - anaplastic lymphoma kinase

ANOVA - analysis of variance

ATP - adenosine triphosphate

AuNP - gold nanoparticle

BALF - bronchoalveolar lavage fluid

Boc - *tert*-butyloxycarbonyl

BRAF - serine/threonine protein kinase B-raf

BSA - bovine serum albumin

CA - cholic acid

CavME - caveolae-mediated endocytosis

CD - cluster of differentiation

CHCl$_3$ - chloroform

CI - cell index

CLTC - clathrin heavy chain 1

CnME - clathrin-mediated endocytosis

COPD - chronic obstructive pulmonary disease

COSY - correlation spectroscopy

CRUK543 - primary patient derived non-small cell lung cancer cells

CT - computerised tomography

CTLA-4 - cytotoxic-T-cell lymphocyte-associated protein 4

DCC - dicyclohexylcarbodiimde

DCCM-1 - Defined Cell Culture Medium-1

DCM - dichloromethane

DIPEA - N,N-Diisopropylethylamine

DL - drug loading

DLS - dynamic light scattering

DLT - dose limiting toxicity

DMAP - 4-dimethylaminopyridine

DMEM - Dulbecco's Modified Eagle Medium

DMF - dimethylformamide

DMSO - dimethyl sulfoxide

DNA - deoxyribonucleic acid

Dual-NPs - polymeric nanoparticles containing vinorelbine and afatinib

(D)PBS - (Dulbecco's) Phosphate Buffered Saline

ECIS - electric cell-substrate impedance sensing

ECL - Enhanced chemiluminescence

EDC - 1-Ethyl-3-(3-dimethylaminopropyl)carbodiimide

EDTA - ethylenediaminotetraacetic acid

EE - encapsulation efficiency

EGF - recombinant human epidermal growth factor

EGFR - epidermal growth factor receptor

EIPA - 5-(N-Ethyl-N-isopropyl)amiloride

ELISA - enzyme-linked immunosorbent assay

EMA - European Medicines Agency

EPR - enhanced permeability and retention

ESE - emulsification solvent evaporation

Et_2O - diethyl ether

Et_3N - triethylamine

EtOAc - ethyl acetate

EtOH - ethanol

FBS - foetal bovine serum

FC - flash chromatography

FDA - Food and Drug Administration

FGFR - fibroblast growth factor receptor

Fli-1 - friend leukaemia integration 1 transcription factor

FTIR - Fourier transform infrared spectroscopy

GTP - guanosine triphosphate

H&E - haematoxylin and eosin

H226 - squamous cell carcinoma human lung epithelial cells

HBSS - Hank's Buffered Salt Solution

HCl - hydrochloric acid

HD - hydrodynamic diameter

HER2 - human epidermal growth factor receptor 2

HIP - hydrophobic ion pairing

HPLC - high performance liquid chromatography

HRMS - high resolution mass spectrometry

HRP - horseradish peroxidase

HSQC - heteronuclear single quantum coherence spectroscopy

HUVEC - Human umbilical cord vein endothelial cells

IASLC - International Association for the Study of Lung Cancer

IC_{50} - half maximal inhibitory concentration

ICP-MS - inductively coupled plasma-mass spectrometry

IgG - Immunoglobulin G

IHC - immunohistochemical/chemistry

IL - interleukin

KRAS - Kirsten rat sarcoma viral oncogene homolog

LAMP2 - lysosome-associated membrane protein 2

LCC - large-cell carcinoma

LDCT - low dose computerised tomography

LE - loading efficiency

LUAD - lung adenocarcinoma

LUSC - lung squamous cell carcinoma

MeCN - acetonitrile

MEF - mouse embryonic fibroblasts

MEK - mitogen activated protein kinase kinase

MeOH - methanol

MIRIBEL - minimum information reporting in bio-nano experimental literature

MMP - matrix metalloproteinase

MOMP - mechlorethamine, oncovin, methotrexate and prednisone

MOPS - (3-(N-morpholino)propanesulfonic acid)

MPM - malignant pleural mesothelioma

MPS - mononuclear phagocyte system

mRNA - messenger RNA

MTA - microtubule-targeting agent

MTD - maximum tolerated dose

mTOR - mammalian target of rapamycin

MTT - 3-(4,5-dimethylthiazol-2-yl)-2,5-diphenyltetrazolium bromide

MWCO - molecular weight cut off

NCS - newborn calf serum

NGS - next generation sequencing

NHS - N-hydroxysuccinimide

NIR - near-infrared

NK - natural killer

NMR - nuclear magnetic resonance

NP - nanoparticle

NSCLC - non-small cell lung cancer

NSG - nucleotide-binding oligomerisation domain (NOD).Cg-$Prkdc^{scid}IL2rg^{tm1Wjl}$/SzJ

O/W - oil-in-water

PARP - poly(adenosine diphosphate-ribose) polymerase

PC-9 - differentiated human lung adenocarcinoma cells

PCR - polymerase chain reaction

PD-1 - programmed cell death protein 1

PDGFR - platelet derived growth factor receptor

PDI - polydispersity index

PD-L1 - programmed death-ligand 1

PDX - patient derived xenograft

PEG - polyethylene glycol

PET - positron emission tomography

PFA - paraformaldehyde

PFS - progression free survival

PGA - poly(glycolic acid)

PLA - poly($_{D,L}$-lactic acid)

PLGA - poly($_{D,L}$-lactic-co-glycolic acid)

ppm - parts per million

PSG - penicillin/streptomycin/glutamine,

PTT - photothermal therapy

PVA - polyvinyl alcohol

RES - reticuloendothelial system

rhTNF- α - recombinant human tumour necrosis factor

RNA - ribonucleic acid

ROCK - Rho-associated, coiled coil containing protein kinase

ROS1 - ROS1 proto-oncogene receptor tyrosine kinase

rpm - revolutions per minute

RPMI-1640 - Roswell Park Memorial Institute (RPMI)-1640

RTK - receptor tyrosine kinase

SCC - squamous-cell carcinoma

SCLC - small cell lung cancer

SDS - sodium dodecyl sulfate

SEM - standard error of the mean

SERS - surface enhanced Raman scattering

siRNA - small interfering RNA

SPR - surface plasmon resonance

SRE stimulus responsive element

STAT - signal transducer and activator of transcription

TBST - Tween-20 in Tris buffered saline

TBTA - tris(1-benzyltriazolylmethyl)amine

TEM - transmission electron microscopy

TFA - trifluoroacetic acid

THF - tetrahydrofuran

THPTA - tris(3-hydroxypropyltriazolylmethyl)amine

TKI - tyrosine kinase inhibitor

TLC - thin layer chromatography

TMB - 3,3',5,5'-tetramethylbenzidine

TPGS - vitamin E D-α-tocopheryl PEG 1000 succinate

TT1 - Transformed type I-like human alveolar epithelial cell

UV - ultraviolet

UV-LC-MS - ultraviolet-liquid chromatography-mass spectrometry

VA - vinca alkaloid

VBL - vinblastine

VCR - vincristine

VEGFR - vascular endothelial growth factor receptor

VRL - vinorelbine

VRL-NPs - polymeric nanoparticles containing vinorelbine

W/O - water-in-oil

W/O/W - water-in-oil-in-water

WGA - wheat germ agglutinin

ZP - zeta potential

Figure Index

Table Index

Scheme Index

1. Introduction

This chapter establishes the central themes of the thesis which include the complexities of lung cancer, the current therapeutic landscape and associated challenges hence framing the problem, contextualised within a disease framework. The role of nanotechnology as a tool to address medical questions is outlined and the capacity of nanotechnology to influence the treatment of lung cancer is described including current clinical status, promises and pitfalls. Attention is given to gold nanoparticles (AuNPs) and polymeric NPs, their iterations, use in medicine and specifically as therapeutic drug delivery vehicles for cancer, in general and of the lung. Finally, the hypothesis and aims of this thesis are delineated.

1.1 Lung cancer

Lung cancer is an umbrella term for a heterogeneous set of diseases that arise due to a malignant metamorphosis of the epithelial cells, pluripotent epithelial stem cells or pleural mesothelium of the respiratory tract. Currently, lung cancer stands as the most common and most lethal malignancy worldwide, with approximately 2.1 million new cases annually, responsible for approximately 19% of total cancer deaths and 3% of all deaths across the globe which equates to around 1.76 million deaths a year[1]. Disquietingly, the burden of lung cancer is predicted to increase; the World Health Organisation projections suggest that by 2030, over 2 million people a year will succumb to lung cancer[2], reinforcing the lethality of these respiratory neoplasms. These statistics are echoed by the dismal 5-year survival rate of just 19%, second only to pancreatic as the cancer with the worst prognosis[3]. This is principally due to the advanced progression of disease upon diagnosis, predominantly stage III or IV, as well as evidence of metastasis, which eliminates the option of surgical resection and renders the current therapeutic arsenal impotent (see section 1.2.4. for further explanation). There are multiple aetiologies of lung cancer manifest as genetic, epigenetic, immunological and molecular

abnormalities that govern not only the progression of disease but also the optimal therapeutic course of action. This information combined with histopathological and clinical characteristics delineates the specific diagnosis, a vast preponderance of which are non-small cell lung cancer (NSCLC), the focus of this thesis. The other clinically significant diagnostic subtypes are small cell lung cancer (SCLC) and malignant pleural mesothelioma (MPM) which together comprise approximately 15% of lung cancers, and have their own unique diagnostic criteria, disease pathogenesis as well as molecular and biological architecture, however further exposition of these diseases is beyond the scope of this thesis, and further insight into SCLC[4-13] and MPM[14-24] can be sought by reference to the denoted excellent reviews and research articles.

1.1.1 Non-small cell lung cancer

NSCLC is the predominant form of lung cancer with approximately 85% of total lung cancer cases falling into the diagnostic remit of NSCLC[25] (Figure 1.1). Of these cases, it is estimated that 65% present with either metastatic or locally advanced disease[26]. Cigarette smoking is the most common risk factor, but other risk factors include second-hand cigarette smoke, alcohol, certain foods (cured and barbequed meats, deep-fried consumables), air pollutants, a sedentary lifestyle, and genetic susceptibility[27]. Indeed, in the era of next generation sequencing (NGS) technologies, genotyping of tumours has revealed particular oncogenic mutations in lung cancer that occur with varying regularity, and defining the mutational landscape has yielded some therapeutic targets, although not all are currently actionable. The most commonly occurring mutations in NSCLC occur in the following genes ("mutations" is used here to describe a wide variety of genetic alterations such as fusions, amplifications, deletions etc.) *TP53, EGFR, KRAS, HER2* (also known as *ERBB2*), *MET, EML4-ALK, TITF-1, LKB1, PIK3CA, BRAF, ROS1, STK11, KEAP1, CDKN2A, SMARCA4, SOX2, RET* and others[28,29], generally dependant on the stage at which the tumours are sequenced and the area of tumour, as intra-tumour heterogeneity varies between patients. The (heterogeneous) overexpression of

programmed death ligand 1 (PD-L1) on lung tumour cells and PD-1 on T-cells has led to a rise of prominence for immunotherapy in NSCLC (see section 1.2.), the success of which is partly due to the high nonsynonymous mutational burden witnessed in NSCLC[30]. However, even in an immunological context, the microenvironment of NSCLC displays high intra and inter heterogeneity and the immunoediting mechanisms that occur due to the selection pressure of the microenvironment sculpt NSCLC evolution and immune evasion[31].
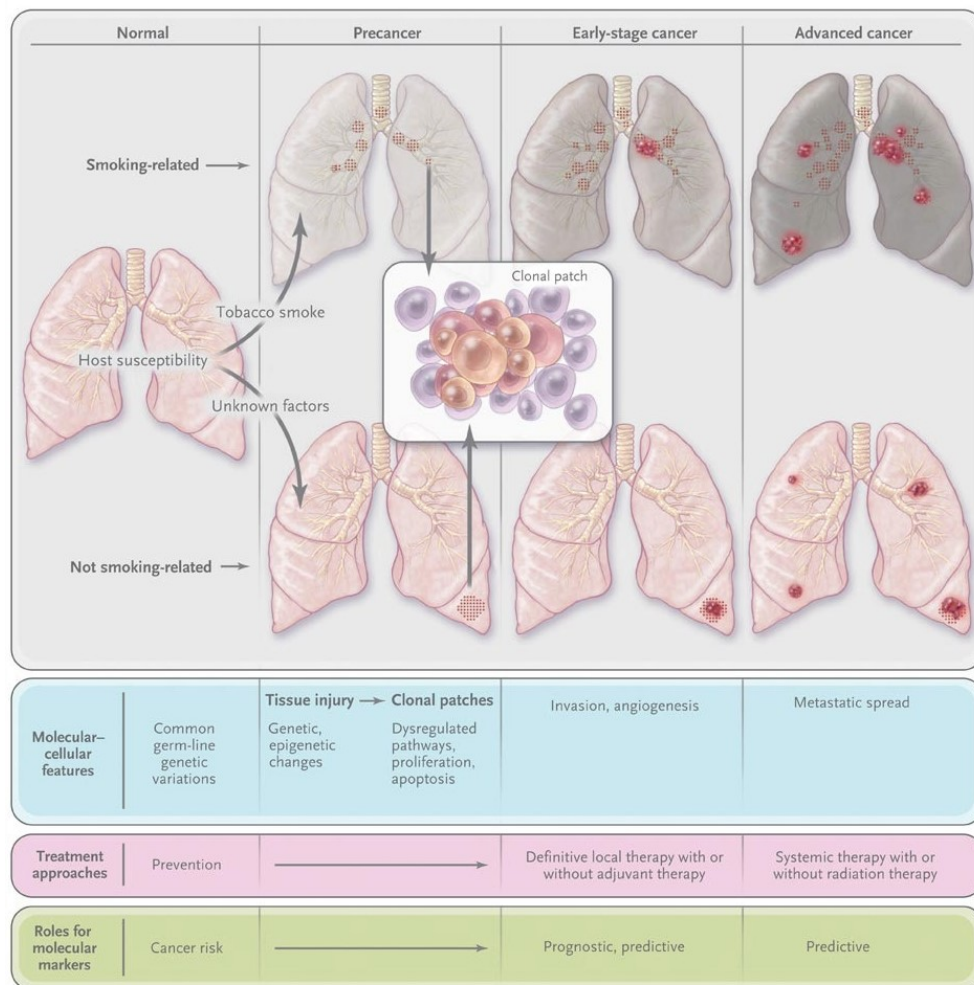
Figure 1.1. Evolution and development of NSCLC. The nature of the insult and the genetic susceptibility of the host dictates the initiation of the carcinogenic process. Smoking-induced carcinogenesis is a result of injury to the lungs that manifest as (epi)genetic and transcriptomic changes. Eventually, repeated insult over a prolonged period leads to dysregulation of cellular pathways involved in growth and proliferation, resulting in dysplasia and clonal patches. Further changes over time induce angiogenesis, invasive cell phenotypes and finally, metastasis. Despite a completely different molecular profile, non-smoking related carcinogenesis adopts a similar trajectory, harbouring mutations in key oncogenes or tumour-suppressor genes. Biomarkers can aid to stratify at-risk patients, prognosis and predicted sensitivity to therapy as well as track the disease from early to late stage. Adapted from Herbst *et al*. 2008[25].

Once symptomatic and a malignancy is suspected, a biopsy is obtained by thoracoscopy or bronchoscopy, with the aid of computerised tomography (CT) or positron emission tomography (PET) imaging if necessary[32]. Indeed, in the USA, annual low dose CT (LDCT) screenings are recommended in persons that are asymptomatic, aged 55-80, have equal to, or over 30 pack-years and currently smoke or have quit within the last 15 years[33]. Encouragingly in the UK, the SUMMIT study aims to enrol 50,000 participants, half of whom meet the above criteria and half, who are aged matched, that are not at high risk for lung cancer. The participants will undergo LDCT and blood tests to validate a genomic based method for early detection of lung cancer with return visits for the following two years (NCT03934866). Excitingly, machine learning platforms such as convolutional neural networks and other artificial intelligence systems can aid early diagnosis by interpreting radiographic images such as CT scans[34], and have even been shown to outperform radiologists in accurately diagnosing lung cancer when prior CT imaging was not available[35].

Upon successfully obtaining a biopsy of the suspected malignant tissue, NSCLC is diagnosed using pathological characteristics consisting of histological alterations, immunohistochemical (IHC) staining, mutational and molecular genetics analysis (e.g. fluorescence *in situ* hybridisation, Sanger sequencing, PCR and other genotyping methods[36]) and imaging techniques in order to ascertain the subtype of NSCLC, and saliently, the stage of disease progression[37,38]. Although not yet clinically utilised, NGS techniques can offer high throughput methodologies examining whole exomes or genomes and investigations into epigenetic modifications and transcriptomes. A recent study used autofluorescence bronchoscopy with biopsy to investigate the genetic, epigenetic and transcriptomic landscape of lung carcinoma *in situ*, which is the pre-invasive precursor to NSCLC, and were able to predict which carcinomas would progress based on a multi-omic picture[39]. There are several other screening modalities that may come to the fore to validate and quantify biomarkers in a variety of biofluids. From

the respiratory tract itself, sputum (micro)RNA or DNA and putative airway epithelial cell biomarkers can be examined[40,41], as well as exhaled breath condensate[42]. Analysis of bronchoalveolar lavage fluid (BALF) can also provide important diagnostic information such as tumour cells[43] and proteomic changes[44]. Increasing evidence also suggests the lung microbiome[45] and metabolome[46] can be used as diagnostic signatures of early lung cancer, the profiles of which can obtained either by biopsy, resection, sputum or BALF. A plethora of diagnostic markers can be obtained from the peripheral circulation too[47], such as metabolites, serum auto-antibodies, proteins, immunological markers, circulating tumour cells[48] and circulating tumour DNA, which can even be used to stratify patients to predict disease progression or therapeutic response[49]. Importantly, NSCLC is a clinical umbrella term used to designate a wide variety of malignancies that are categorised as adenocarcinoma (ADC), squamous-cell carcinoma (SCC), large-cell carcinoma (LCC) and other less differentiated variants[50]. Each possess cellular, genetic and epigenetic architecture heterogeneity that gives rise to unique tumour microenvironments in patients, significantly contributing to the difficulty of treating NSCLC[51,52].

1.1.1.1. Adenocarcinoma

Of the different histological variants of NSCLC, ADC (also known as lung adenocarcinoma – LUAD) is the most prevalent worldwide[53] and the incidence rate of ADC is increasing fastest in women[54]. Although smoking causes the majority of cases, decreases in smoking rates means that proportionally ADC is most prominent in never smokers. Due to the expansive heterogeneity that exists within ADC, the disease is notoriously difficult to accurately classify. The International Association for the Study of Lung Cancer (IASLC), American Thoracic Society and European Respiratory Society created a multidisciplinary consortium in order establish a more precise classification of ADC[55]. Recently, the IASLC guidelines for molecular testing in lung cancer have been updated with a focus of ADC due to the typically defining

mutational status present in ADC[56]. The majority of ADC cases can be distinguished from SCC by absence of SCC-specific morphological characteristics and concomitant positive expression of mucin, thyroid transcription factor-1 and cytokeratin-7[53,57]. Mutations in genes such as *EGFR, ELM4-ALK* (*ROS1* fusion)*, BRAF* and *KRAS* are almost exclusive to ADC[58,59] which, as well as other molecular biomarkers[60], may complement histological analysis in order to accurately grade the disease progression. Indeed, comprehensive molecular profiling of ADC corroborated the presence of these driver mutations but also identified further driver events in ADCs lacking canonical driver mutations; these included amplification of *MET* and *HER2* and mutations in *NF1* as well as reinforcing the importance of the MYC pathway in ADC[61]. Furthermore, the immune landscape of early lung ADC has been investigated using single cell time-of-flight mass cytometry which revealed changes in the cellular landscape were observed in as early as stage I ADC, towards a more tumour-promoting immunophenotype and hallmarks of this signature may function as therapeutic targets[62]. Indeed, these molecular aberrations combined with reformed ADC classification guidelines facilitate more specific ADC assignment and improved efficacious treatment regimens.

1.1.1.2. Squamous cell carcinoma

SCC (also known as lung squamous cell carcinoma – LUSC) is the second most common subtype of NSCLC, accounting for approximately 20-30% of all NSCLC cases, and is the most prevalent NSCLC lineage in men[63]. The biggest risk factor in the development of SCC is cigarette smoking (or tobacco use) but other specific risk factors include a familial predisposition and polymorphisms in certain genes involved in DNA repair, such as *MLH1*, and detoxification such as *CYP2A6* and *CYP1A2*[54]. Archetypically, SCC was designated as arising from the central airway, however the increasing frequency of peripheral tumours is beginning to rival cases presenting as a central airway tumour. From a histological standpoint, a well differentiated SCC presents with keratinisation and pearl formation with a dense

cytoplasm, and irregular hyperchromatic nuclei[63,64]. Although there are no SCC specific markers, typically SCC can be differentiated from ADC (and other forms of NSCLC) by positive expression of cytokeratin-5, p63, Δnp63, desmocollin-3 with the aid of miRNA profiles[65]. In depth analysis, spearheaded by The Cancer Genome Atlas Research Network, has illuminated the genetic landscape of SCC and identified distinguishing features from that of other NSCLC subtypes, particularly oncogenic driver mutations. After profiling 178 SCC cases, statistically recurrent mutations in 11 genes were found, including *TP53*, in almost all of the samples profiled, and a proportion had significantly altered pathways such as the *KEAP1*, *PI3K*, *RB1* and *CDKN2A* pathways. The study also revealed differences from that of ADC, such as altered mutational landscape of *EGFR*, *KRAS* and *FGFR*, in that highly recurrent tyrosine kinase mutations do not often occur in SCC[66,67]; these findings were affirmed in a separate cohort[68]. Further defining genomic features include amplification of chromosomal regions 3q, 7p11 and 8p12 that contain genes such as *SOX2*, *EGFR* and *FGFR1* respectively that are involved in cell proliferation, as well as alterations in genes that govern immunity including *HLA-A, B* and *C, ULBP1* and *2* amongst others[69]. Additional comparative studies have reinforced the notion that SCC possesses a distinct mutational identity, separate from other NSCLC subtypes[70,71], which may act as a diagnostic fingerprint when morphological differentiation is unclear. Moreover, artificial intelligence system have been developed that can accurate distinguish between healthy and cancerous lungs, and the subtype of NSCLC[72].

1.1.1.3. Large-cell carcinoma

LCC is the third most common NSCLC subtype and accounts for approximately 3-9% of diagnoses. LCC is the collective term for undifferentiated respiratory malignances that do not fall into the diagnostic criteria of SCC or ADC, are not of neuroendocrine origin (lung neuroendocrine tumours are distinct clinical entities) and have no other specific clinical traits. This designation is assigned to tumours from surgical resection that, when biopsied or

examined cytologically, have a lack of differentiating morphology under light microscopy, although the primary tumour mass may possess undetected alterations[73]. With the diagnostic hurdles associated with LCC, it is pertinent to differentiate tumours as accurately as possible using IHC analysis for the biomarkers mentioned above and/or genomic profiling of canonical driver mutations[74]. Analysis of 789 resected NSCLC tumours revealed that over half of LCC tumours examined did not contain recognisable mutational genetic linages but were found to have high expression of PD-L1, a key immune checkpoint molecule, and alterations in genes that play a regulatory role in the cell cycle[75]. Subunits of the switch/sucrose non-fermenting complex, which is involved in chromatin remodelling, were found to be reduced or lost more frequently in LCC than other NSCLC subtypes[76]. Despite these differentiating factors, traditional pathological and histological methods reveal inconclusive results in up to 70% of cases due to misrepresentative sampling of the tumour[77], highlighting the need to elucidate a more specific phenotype to guide which therapeutic avenues to pursue.

1.2. Current therapeutic landscape of NSCLC

At present, there are three principal categories of therapeutic intervention that can be explored in NSCLC: surgical resection, radiotherapy and molecular therapy encompassing chemotherapy, targeted therapy and immunotherapy. The applicability of a particular therapeutic option is dependent on the diagnostic information available, including stage, if metastasis has occurred, mutational status and the overall health of the patient (i.e. any comorbidities, age etc.). Surgical resection is the most effective modality, however resection is not a viable option of advanced or metastatic disease, which is the overwhelming presentation upon diagnosis. In an attempt to increase the viability of surgery, radiotherapy, neoadjuvant chemotherapy or both are often administered. Indeed, the use of these modalities is not restricted to a preoperative capacity and are implemented as outright treatment courses or can be given postoperatively. Stereotactic ablative radiotherapy, whereby high dose radiation is

administered directly to tumours, guided by advanced imaging modalities such CT, is recommended for patients where surgery is not possible (advanced disease, refusal, frail etc.) and has been shown to achieve reasonable control of primary tumours[78,79]. Chemotherapy (Table 1.1) comprises an integral part of the treatment regimen for respiratory malignancies, either as neoadjuvant or adjuvant therapy, the primary course, in combination with radiotherapy or other molecular therapies, as maintenance therapy or for palliation. Extensive clinical trial data accrued over decades has facilitated the creation of guidelines[80] as to the most appropriate scenario in which the particular (chemo)therapies are to be administered taking into account disease status and patient quality of life. The discovery that activating mutations in epidermal growth factor receptor (EGFR) sensitised lung cancers harbouring these mutations to treatment with EGFR inhibitors[81,82] ignited the development of small molecules and antibodies directed towards EGFR and other oncogenic driver mutations (in genes such as *ALK, ROS1, VEGFR*) in an attempt to treat an individual's tumour based on their specific mutational status, known as personalised medicine[83]. This form of therapy is commonly referred to as targeted therapy as particular (usually overexpressed) oncoproteins are the desired target of therapeutic molecules, as opposed to chemotherapy that are most efficacious in rapidly dividing cells such as cancer cells. The third class of molecular therapy is immunotherapy which saw a rise to prominence in lung cancer after two pivotal clinical trials demonstrated both anti-PD-1[84] and anti PD-L1[85] antibodies were able to induce objective responses in some advanced cancers, including NSCLC. Another trial showed improved progression free survival (PFS) in treatment-naïve patients with NSCLC who were treated with paclitaxel and carboplatin in combination with ipilimumab, an anti-cytotoxic-T-cell lymphocyte-4 (CTLA-4) monoclonal antibody as opposed to chemotherapy alone[86]. A further landmark trial that propelled immunotherapy to mainstream clinical approval and use in lung cancer reported that nivolumab, a fully human IgG4 anti PD-1 monoclonal antibody prolonged overall survival

Agent	Trade Name	Mechanism of Action
Cisplatin	Platinol	DNA crosslinking
Carboplatin	Paraplatin	DNA crosslinking
Mitomycin-C	Mitozytrex	DNA crosslinking
Paclitaxel	Taxol	Stabilises microtubules
Nab-paclitaxel	Abraxane	Stabilises microtubules
Docetaxel	Taxotere	Stabilises microtubules
Vincristine	Oncovin	Inhibits microtubule formation
Vinblastine	Velban	Inhibits microtubule formation
Vinorelbine	Navelbine	Inhibits microtubule formation
Topotecan	Hycamtin	Topoisomerase I inhibitor
Irinotecan	Camptosar	Topoisomerase I inhibitor
Etoposide	Etopophos	Topoisomerase II inhibitor
Doxorubicin	Adriamycin	Topoisomerase II inhibitor
Ifosfamide	Ifex	DNA alkylating agent
Cyclophosphamide	Cytoxan	DNA alkylating agent
Temozolomide	Temodar	DNA alkylating agent
Mechlorethamine	Mustargen	DNA alkylating agent
Pemetrexed	Alimta	Folate antimetabolite
Methotrexate	Trexall	Folate antimetabolite
Gemcitabine	Gemzar	Nucleoside analogue
Erlotinib	Tarceva	EGFR inhibitor
Gefitinib	Iressa	EGFR inhibitor
Afatinib	Gilotrif	EGFR/HER2 inhibitor
Cetuximab	Erbitux	EGFR inhibitor
Osimertinib	Tagrisso	EGFR inhibitor
Necitumumab	Portrazza	EGFR inhibitor
Crizotinib	Xalkori	ALK/ROS1 inhibitor
Entrectinib	Rozlytrek	ROS1 inhibitor
Ceritinib	Zykadia	ALK inhibitor
Alectinib	Alecensa	ALK inhibitor
Brigatinib	Alunbrig	ALK inhibitor
Bevacizumab	Avastin	VEGF-A inhibitor
Ramucirumab	Cyramza	VEGFR-2 inhibitor
Nintedanib	Vargatef	VEGFR/FGFR/PDGFR inhibitor
Everolimus	Afinitor	mTOR inhibitor
Nivolumab	Opdivo	PD-1 inhibitor
Pembrolizumab	Keytruda	PD-1 inhibitor
Atezolizumab	Tecentriq	PD-L1 inhibitor
Durvalumab	Imfinzi	PD-L1 inhibitor
Dabrafenib	Taflinlar	BRAF inhibitor
Trametinib	Mekinist	MEK inhibitor

Table 1.1 Current clinically approved therapies for NSCLC. ALK, anaplastic lymphoma kinase; BRAF, serine/threonine protein kinase B-raf; EGFR, epidermal growth factor receptor; FGFR, fibroblast growth factor receptor; HER2, human epidermal growth factor receptor 2; MEK, mitogen activated protein kinase kinase; mTOR, mammalian target of rapamycin; PDGFR, platelet derived growth factor receptor; PD-(L)1, programmed death receptor-(ligand)1; ROS1, ROS1 proto-oncogene receptor tyrosine kinase; VEGFR, vascular endothelial growth factor receptor. Adapted from Cryer and Thorley, 2019[87].

of patients with NSCLC that had progressed after platinum-based doublet chemotherapy when compared with docetaxel[88].Pembrolizumab is another anti-PD-1 monoclonal antibody that showed antitumour efficacy in patients with advanced NSCLC[89] and extended overall survival compared to docetaxel in previously treated NSCLC and validated PD-L1 expression as a biomarker for patients responsive to immunotherapy[90]. The current clinically approved arsenal of therapies for lung cancer is shown in Table 1.1; as our understanding of lung cancer biology and its mutational landscape and immune microenvironment increases, more targeted and immunological therapies are being tested in clinical trials and ultimately used in the clinic[91-93].

1.2.1 Vinca alkaloids

Traditional chemotherapy agents can be classified based either on their mechanism of action, origin or distinguishing molecular features. The main groups are alkylating agents, anthracyclines, topoisomerase inhibitors, antimetabolites, platinum-based agents and vinca alkaloids (VAs), all of which are used clinically. VAs are a collection of naturally occurring or semi-synthetic nitrogenous bases that are originally derived from the Madagascar periwinkle *Catharanthus roseus* (formerly known as *Vinca rosea*)[94]. Of approximately 130 monoterpenoid indole alkaloids produced by *C. roseus*[95], vinblastine (VBL) and vincristine (VCR) as well as the semi-synthetic derivatives vinorelbine (VRL) and vindesine are in clinical use, but only the first three are used in lung cancer. Vinflunine is a newer semi-synthetic analogue which is used as a salvage therapy in urothelial carcinoma and is in further clinical trials. The naturally occurring VAs VBL and VCR have been in clinical use since 1961 and 1963 respectively, whereas VRL was approved more recently in 1994. VAs are structurally characterised by the presence of an indole moiety (catharanthine) and a dihydroindole moiety (vindoline) linked together by a C-C bridge (Figure 1.2).
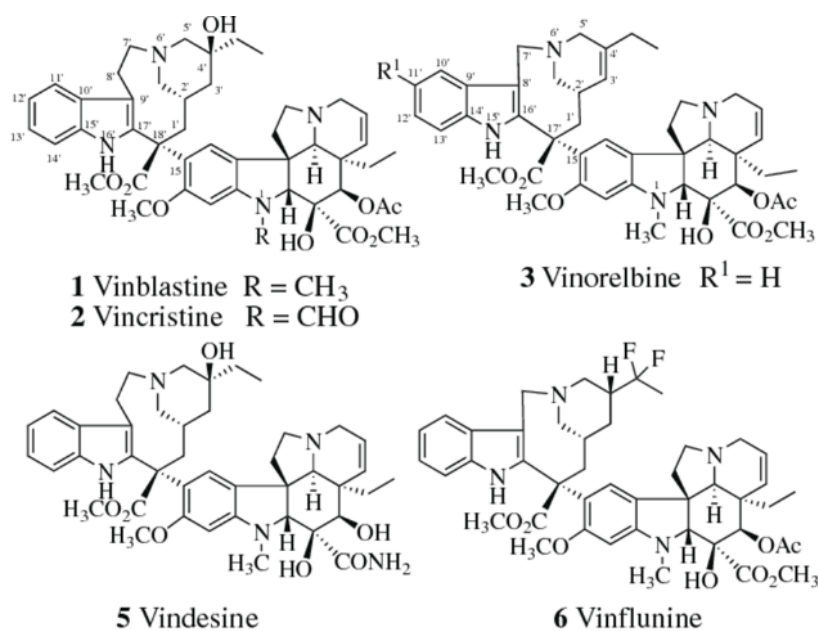
Figure 1.2. Chemical structures of clinically utilised vinca alkaloids. Adapted from Voss *et al.*, 2009[96].

Despite their natural occurrence, efforts in organic chemistry have resulted in using synthetic pathways to produce dimeric alkaloids or their monomeric precursors, vindoline and catharanthine, as the extraction processes from *C. roseus* is highly costly, time consuming and produces low yields[97]. VAs are microtubule-targeting agents (MTAs) which reflects their mechanism of action and consequent antitumour activity. VAs bind to the VA binding site (or vinca domain) which was first deciphered using a VBL complex and was found to be located at the interface between the α2-β1 tubulin heterodimers[98]. Further insight revealed that all VAs interact with tubulin at high affinity binding sites present at the ends of microtubules[99]. The biological ramifications of VA binding to tubulin is dependent on the concentration. Low concentrations of VA (sub-micromolar) restricts the elongation of microtubules by preventing GTP absorption. Whereas higher concentrations of VA promote the depolymerisation of microtubules; this is due increased occupation of VA binding sites that introduces a wedge between longitudinally aligned tubulin heterodimers, preventing the construction of a microtubule lattice due to the inability to of the dimers to transition from curved to straight[100]. This leads to aggregation into crystals, disintegration of the mitotic spindle and chromosomal

accumulation, hindering progression into anaphase of the cell cycle and culminating in apoptosis[101]. This mechanism is in contrast with other MTAs such as paclitaxel and other taxanes that binds to microtubules and encourages their polymerisation instead of destabilising them, as is the case with VAs.

1.2.1.1 Vinorelbine

Vinorelbine (VRL, also known as 5'-nor-anhydrovinblastine) is a semi-synthetic VA (Figure 1.2) which is used primarily as a treatment for NSCLC, and several other tumour types including soft tissue sarcoma and oesophageal cancer[102]. In NSCLC, VRL has been trialled and used as a first line therapy, in combination with other chemotherapies, with radiotherapy and for advanced, metastatic or unresectable disease[103]. The current clinical indication for VRL is as a first line single agent or in combination with cisplatin and/or radiotherapy in early stage NSCLC and for disease that has progressed after treatment with a tyrosine kinase inhibitor (UK) or advanced, unresectable NSCLC (US)[104]. VRL is also clinically indicated for treatment of metastatic or advanced breast cancer that has recurred after initial treatment either as a standalone therapy or in combination with non-cross-reactive chemotherapies/trastuzumab [monoclonal antibody directed against human epidermal growth factor receptor 2 (HER2)]. Structurally it differs from VBL, which is its molecular analogue, due to modifications on the catharanthine nucleus (the vindoline nucleus is identical) whereby an extra C=C is installed within the terminal ring with consequent loss of a hydroxyl group, substantially increasing lipophilicity. VRL has the highest lipophilicity of all clinically used VAs, resulting in sequestration into tissues and extensive tissue distribution throughout the body. Indeed, lung concentrations of VRL are 300-fold greater than that in the plasma, and significantly higher than lung concentrations achieved by other VAs. As VRL is an amphiphilic weak base with poor water solubility; it is clinically formulated as a tartrate or ditartrate salt known as Navelbine, which is suitable for oral or intravenous administration. However, VRL is a potent

vesicant and can cause significant venous and tissue damage if it extravasates from the venous lumen. Even after successful administration, phlebitis and venous sclerosis may occur, which requires further medical attention. The principal dose limiting toxicity associated with VRL is neutropenia and more mild toxicities include gastrointestinal dysfunction, thrombocytopenia, anaemia and pain[105].

1.2.2. Tyrosine kinase inhibitors

Tyrosine kinase inhibitors (TKIs) are a class of molecule designed to impede, disrupt or prevent the function and activation of receptor tyrosine kinases (RTKs). RTKs are a family of cell-surface transmembrane proteins that contain a large, glycosylated extracellular ligand binding domain and a cytoplasmic domain that contains a region for catalytic tyrosine kinase activity. RTKs act as activity regulators of a wealth of potent growth factors, hormones and cytokines that influence cellular processes such as growth, proliferation, differentiation and migration[106]. Therefore, it is unsurprising that when these regulatory mechanisms go awry due to overexpression of, or mutations in, these receptors, the propensity for cells to become malignant dramatically increases. This is evidenced by the widespread aberrant phenotype of different RTKs is observed in many cancers, principally the RTKs EGFR. HER2, vascular endothelial growth factor receptor (VEGFR), platelet derived growth factor receptor (PDGFR) and fibroblast growth factor receptor (FGFR), amongst others[107]. In response to oncogenic progression driven by hyper-activation of these receptors (and their downstream signalling pathways), an arsenal of TKIs have been developed. For brevity, only small molecules will be discussed, however the activity of TKIs can also be stymied using monoclonal antibodies that target the extracellular portion of RTKs and therefore prevent ligand binding; such entities are clinically utilised, e.g. trastuzumab (HER2), bevacizumab (VEGFR), necitumumab (EGFR)[108]. As the name suggests, in contrast to antibodies, TKIs exert their influence at the intracellular tyrosine kinase domain through different mechanisms. RTKs are dependent on ATP

recruitment and binding for downstream signals to be transduced effectively, therefore TKIs have been engineered to disrupt this process. TKIs can compete with ATP for the occupation of the ATP binding pocket within the active site; molecules of this class are known as type I inhibitors. Alternatively, TKIs can bind to an allosteric site and induce a conformational change such that the tyrosine kinase domain is less catalytically competent hindering binding of ATP and even the receptor substrate. This mode of inhibition is known as type II and is typified by a "DFG-out" conformation, whereby the aspartic acid residue of DFG (aspartic acid-phenylalanine-glycine), which is important for correct orientation of ATP within the activation loop, is rotated out of the active site[109]. Indeed, the selectivity of a TKI for its target is dependent on the conformation of the receptor and its own structural properties; however type II inhibitors appear to be more selective than type I inhibitors overall[110].

In lung cancer treatment, the most commonly used TKIs are targeted towards EGFR due to its relatively common overexpression, mutational status and the central role of EGFR signalling in the development of (lung) cancer[111]. The earliest EGFR TKIs, referred to as tyrphostins[112], where a hydroxy *cis*-cinnamonitrile moiety appeared to govern the potency of EGFR inhibition, based on a screen of several candidates. Further computational analysis, molecular docking studies and screening identified various core structures such as pyrrolopyrimidines, phenylpyrimidines, isoflavones, quinolones and anilinoquinazolines as well as designated areas within the ATP binding pocket that pharmacophores must satisfactorily occupy for efficient and selective EGFR inihibtion[113]. Indeed, the first generation of clinically approved EGFR inhibitors (Figure 1.3), gefitinib, erlotinib and lapatinib (not used for lung cancer) contain an anilinoquinazoline core. These TKIs bind reversibly to EGFR and initially showed promise, in part due to oncogenic activating mutations in EGFR. The most common primary mutations are a small in-frame deletion in exon 19 (glutamic acid-746 – alanine-750, del19) and a point mutation of leucine-858 to glycine (L858R) which confer sensitivity to TKIs due

to increased affinity of EGFR for the TKI and decreased affinity for ATP, against which the inhibitors are competing[114]. However, the emergence of secondary mutations is almost inevitable, rendering first generation therapies ineffective. The most prevalent is a substitution of threonine-790 to methionine (T790M, which introduces a bulkier amino acid in a key hydrophobic pocket of the ATP binding site thus sterically hindering reversible TKI binding and increasing the affinity for ATP[115]. Second generation TKIs such as afatinib and dacomitinib (both anilinoquinazolines) are still effective against T790M mutant EGFR, and mutant-specific third generation inhibitors such as osimertinib (monoanilinopyrimidine scaffold) have also been clinically employed.
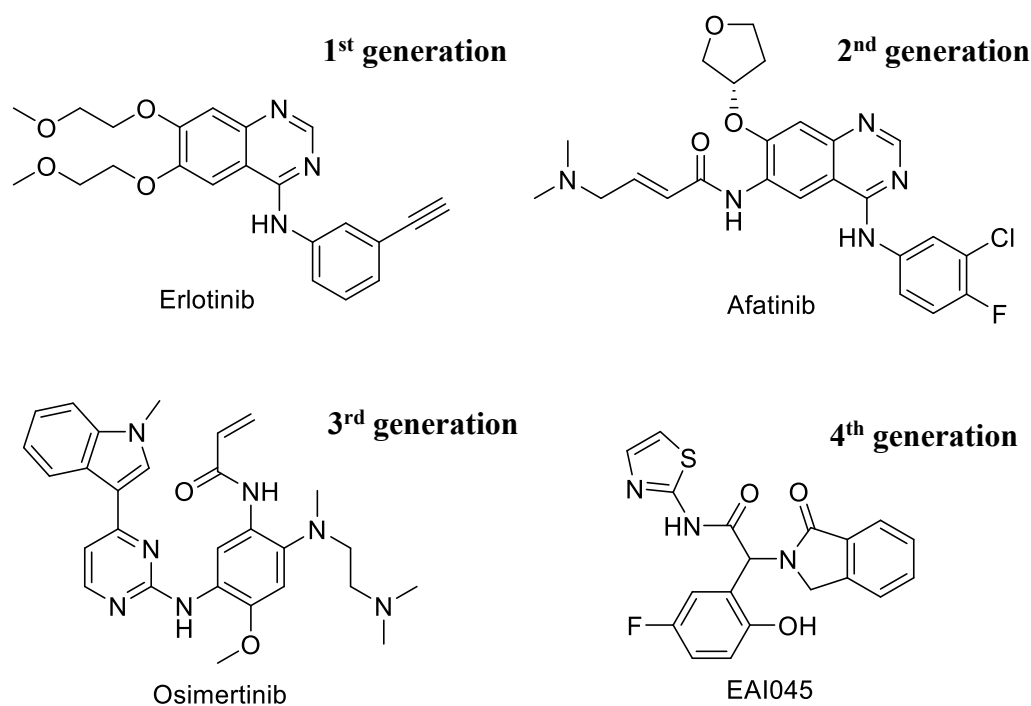
Figure 1.3. Chemical structures of generational iterations of EGFR specific TKIs. A representative molecule from each generation is presented, illustrating the structural differences as TKIs are modified to adapt and overcome resistance mechanisms.

However, the selection pressure exerted by these inhibitors brings about tertiary mutations in EGFR, the most common of which is the point mutations of cysteine-797 to serine (C797S). Second and third generation TKIs contain Michael acceptor moieties that covalently bind to Cys797; however, serine does not form covalent bonds with TKIs under physiological

conditions, therefore mitigating their efficacy. Attempts to overcome the mutational landscape of EGFR are being pursued by the construction of fourth generation, allosteric inhibitors based on 4-aminopyrazolopryrimidine and trisubstituted imidazole scaffolds, amongst others[116]. Indeed, there are other EGFR dependent and independent resistance pathways that can occur within the context of a solid tumour that require alternative therapeutic intervention.

1.2.2.1 Afatinib

Afatinib (Figure 1.3) is a second generation ATP-competitive TKI of the anilinoquinazoline family that is clinically indicated as a first-line therapy for locally advanced or metastatic EGFR (activating mutation) positive NSCLC or patients with NSCLC of squamous morphology that have progressed after platinum-based chemotherapy; this indication is consistent in the UK and the US[117]. The mechanism of action of afatinib centres on an electrophilic crotonamide group that can undergo a Michael addition with conserved cysteine residues in the ATP binding pocket within the tyrosine kinase domains of EFGR (Cys797), HER2 (Cys805) and ErB-4 (Cys803)[118]. The formation of covalent bonds means that afatinib is an irreversible inhibitor, which is in contrast to earlier generations of TKIs that bind reversibly to the ATP binding pocket. Indeed, computational molecular dynamic studies suggest that covalent bond formation aids in trapping water molecules within hydrophobic pockets of the tyrosine kinase domain, resulting in water-mediated strong hydrogen bond and halogen bond interactions, therefore enhancing the binding of afatinib to EGFR del19 in particular), increasing its potency[119]. The LUX-Lung series of clinical trials investigated and subsequently defined the role of afatinib in the treatment of NSCLC. The most significant findings from this trial series was that in patients with any classifiable activating EGFR mutation, median PFS was significantly longer in patients treated with afatinib compared to patients treated with pemetrexed and cisplatin, and patients who harboured the deletion mutation were found to live significantly longer (LUX-Lung 3). A similar outcome was seen

when afatinib was compared to patients receiving gemcitabine and cisplatin and notable improvements in side effects such as cough and pain were reported in the recipients of afatinib contrasted with chemotherapy treated patients (LUX-Lung 6). When afatinib was compared to gefitinib in patients who were positive for EGFR mutations del19 or L858R only, afatinib significantly reduced the likelihood of cancer progression and death, induced more clinical responses and increased the time to treatment failure (LUX-Lung 7)[120]. The aforementioned molecular simulations may provide some insight as to why afatinib was able to outperform conventional chemotherapy and first generation TKIs, especially in cohorts of patients who were del19 positive. Unfortunately, as with all chemotherapy, the promiscuous activity of afatinib towards all EGFR variants leads to side effects upon treatment, the most prominent of which include gastrointestinal disturbances (diarrhoea, nausea), rash, mucosal inflammation and folliculitis[121].

1.2.3. Clinical rationale for combination chemotherapy

The idea of using two or more pharmacological agents (not necessarily all chemotherapy) for the treatment of cancer is not a new one[122]. The first documented case of using combination chemotherapy was in 1958, which was the administration of folic acid (methotrexate) and purine antagonists for the treatment of a tumour of the placenta known as choriocarcinoma; this regimen proved to be curative[123], which was unprecedented and highly radical for the time. In the 1960s, emerging research on leukemic mouse models, discovery of new chemotherapies, combined with the notion of the "Cell Kill" hypothesis, predicated on work demonstrating a single, untreated leukaemia cell was fatal to mice[124], meant that more aggressive chemotherapy regimens were employed, in a defined schedule, to eliminate all malignant cells. The culmination of these efforts was the derivation and administration of the first combinatorial regimen, vincristine, amethopterin, 6-mercaptopurine and prednisone in children with leukaemia, which drastically improved the number and length of remissions[125]. Treatment of

advanced Hodgkin's disease followed a similar pattern whereby the development of mechlorethamine, oncovin (vincristine), methotrexate and prednisone (MOMP) and MOPP (procarbazine instead of methotrexate) programmes of chemotherapy dramatically increased the remission rate from almost zero to approximately 80%[126,127]. The combination of methotrexate and the alkylating agent thiotepa also demonstrated efficacy in the treatment of advanced breast cancer[128], however it took until the mid-1970s for combination chemotherapy to be used in an adjuvant setting. The 1970s also saw a huge expansion of funding for cancer research due to the National Cancer Act of 1971, which was influenced by the complete responses seen in the prior decade using combination chemotherapy. Consequently, more compounds and combinations were screened in mice, leading to the identification of entire families of chemotherapy such as the taxanes; this insurgence of funding incentivised industry to invest in drug discovery and development throughout the following decades, rapidly expanding the therapeutic arsenal available to oncologists. The discovery of oncogenes, tumour suppressor genes and cell signalling pathways essential for growth and development lead to identification of new drug targets (i.e. targeted therapies such as TKIs), combined with the advent of monoclonal antibodies designed to target overexpressed receptors amounted to a therapeutic landscape with many combinations[129]. These were eventually teased out with an iterative process of preclinical studies and clinical trials, much like today, to generate clinically useful combinatorial therapies. Indeed, the underpinning rationale for treating a malignancy with multiple therapies was initially predicated on the notion that a single dose given at any one time would only eradicate a fraction of cancer cells, therefore multiple therapies with different actions given at different times would be more effective. This theory has been expanded somewhat in the modern day and can be condensed into the idea that tumours are heterogeneous both in their genetic makeup and synchronicity of their cellular processes, and that chemotherapy imposes in a selection pressure that can directly influence, and add to, the

resistance mechanisms present within tumours. It is for these reasons that almost every clinically approved chemotherapy regimen involves multiple agents that impart cytotoxicity through different mechanisms, usually resulting in an additive or synergistic biological response. In lung cancer, common first line combination therapies are cis/carboplatin and pemetrexed (DNA crosslinker and antimetabolite), vinorelbine and cis/carboplatin (microtubule inhibitor and DNA crosslinker), and chemotherapy is often used in combination with targeted therapies and immunotherapy in patients harbouring the appropriate mutations[80]. Indeed, machine learning platforms have been developed to identify optimally synergistic chemotherapy combinations[130,131]. The combination of vinorelbine and afatinib has not been used clinically, however there have been several clinical trials examining this combination for treatment of HER2 positive breast cancer. Combined afatinib and vinorelbine therapy was demonstrated to bestow a clinical benefit in 20% of patients with inflammatory breast cancer who had progressed from afatinib monotherapy in a phase II trial[132]. This was encouraging after the results of the phase III trial LUX-Breast 1 whereby afatinib and vinorelbine was less tolerable and was associated with shorter overall survival than trastuzumab and vinorelbine in patients with HER2 positive metastatic breast cancer[133], although PFS was similar. A recent phase I trial examined oral and intravenous afatinib vinorelbine combination therapy in pre-treated solid tumours, including breast cancer and NSCLC. Of the tumour types examined, NSCLC responded the best with 7 patients achieving stable disease and 1 partial response, out of 14 patients recruited[134].

1.2.4. Problems with chemotherapy

The introduction of chemotherapy, targeted therapy and biological therapy into oncology has revolutionised the therapeutic landscape drastically over the past 50 years, as briefly discussed above. Notwithstanding the inherent biological and immunological complexity of lung cancer and its accompanying microenvironment, there are several issues associated with a

chemotherapeutic approach to treatment. Administration of chemotherapy, independent of the route (unless directly into the tumour) invariably results in systemic distribution throughout the body. This means that these cytotoxic agents encounter many different cells and tissues other than the tumour they are designated to treat. Chemotherapy is indiscriminate in that it cannot tell what is and what is not a cancer cell and the nature of these compounds is such that interaction with the healthy tissue, especially that with a high cell turnover rate, will cause result in damage and an injurious response. It is this promiscuity that is the principal origin of the side effects and dose limiting toxicities so often observed with chemotherapy[135]. Due to differing chemistry, pharmacokinetics and pharmacodynamics, each compound has an altered profile of side effects that must be managed by tempering the dose and additional palliative medications. It is these toxicities that dictate the dose that can be administered and consequentially the efficacy of the therapy. Furthermore, chemotherapy is rapidly metabolised, degraded and eliminated *in vivo*, which means it must be administered multiple times to maintain therapeutic concentrations in the body. As a result of the systemic dissemination, toxicity and rapid excretion, the intratumoural concentration of chemotherapy can be subtherapeutic, and is not homogenously distributed, leaving some regions, such as the necrotic core, untouched. The most pernicious trait of (lung) tumours is the intrinsic, adaptive and subsequently acquired, resistance mechanisms tumours display and develop over the course of therapy[136]. If chemotherapy fails to prevent recurrence by treatment resistant residual disease or metastasis, then prognosis is dismally poor.

1.3. Nanotechnology in medicine

Nanotechnology can be defined as the manipulation and engineering of matter on an atomic, molecular or supramolecular scale. This can be extended further to encompass the fabrication and application of materials, platforms and devices that fall within the region of 1-100 nm in at least one dimension, although falling outside of this size range does not disqualify a

particular application, especially when addressing unmet medical needs[137,138]. Indeed, the

designation of nanotechnology to answer medical questions is termed nanomedicine[139] and is

facilitated by the vast spectrum and innate physicochemical properties of materials at this

miniscule scale which can be leveraged for use in biological and medical systems, particularly

where macroscale technologies have fallen short.
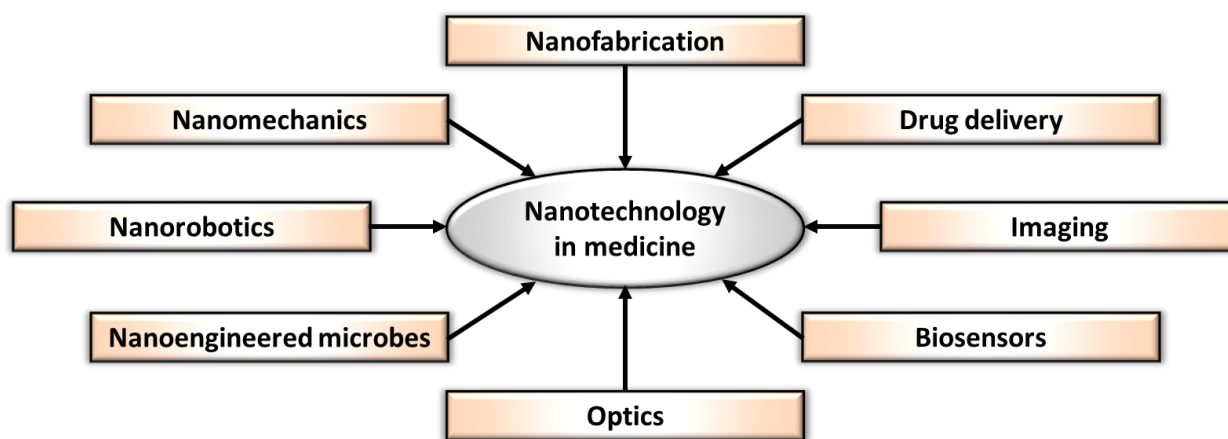
Figure 1.4. Facets of nanotechnology applied to medicine. The influence of nanotechnology
in medicine has been expansive and is now heavily studied research area, from drug delivery
and imaging to fabrication of nanochips as biosensors, computing and molecularly engineered
organisms.

As many diseases originate from aberrations or alterations on a molecular or nano scale, it

stands to reason that directed, deliberate and controlled intervention on this scale can

ameliorate dysregulated processes that culminate in disease[140]. The direct and controlled

manipulation of matter on a nanoscale has inevitably led to expansion of many sub-disciplines

of research under the umbrella of nanomedicine, including generation of nanoelectronic

biosensors, optical devices or imaging modalities for diagnosis (nanophotonics),

nanomechanics, nanofabrication, molecular nanotechnology which has applications in

genomics and proteomics, synthetic biology for the construction of nanoengineered microbes,

the creation of molecular machines and biomimetic structures and nanorobotics, to name just

a few applications of an ever-growing list of the use of nanotechnology in medicine[141-143]

(Figure 1.4). The interest in nanotechnology and output in terms of products is evidenced by

the increasing global market value which is projected to reach \$90 billion within the next two years and will continue to grow as further innovations become commercialised. Indeed, nanotechnology has a pivotal role to play in the diagnosis and treatment of diseases such as lung cancer[87], where alternative therapeutic modalities are desperately needed to improve patient survival and quality of life.

1.3.1 Nanoparticles as medicine

Currently, the cornerstone of nanomedicine is the development of drug delivery systems for the diagnosis and treatment of diseases such as cancer[144-147]. The term "drug" in this context is a broad term that can be used to describe a multitude of entities, such as small molecules, peptides, proteins, antibodies, hormones, aptamers and nucleic acids. The flagship drug delivery vehicle of nanotechnology is the nanoparticle (NP)[148-152], which is an umbrella term for a diverse range of nanovector shapes, sizes and structures, not just the spherical iteration (although these are the most common). There has been a surge of interest, and publications, over the past three decades in the use of NPs for a plethora of uses, primarily to function as drug delivery vectors to tumours, and have emerged as a promising alternative to traditional intravenous administration. NPs are afforded such potential due to the diverse molecular toolkit available using materials at the nanoscale. There are a multiplicity of different nanomaterials used to create NP based drug delivery systems (Figure 1.5) including lipids (liposomes, micelles and solid lipid NPs)[153], polymers (dendrimers, hydrogels, polymeric NPs)[154], carbon structures (nanotubes, fullerenes, nanodiamonds, graphene)[155,156] , proteins[157] and inorganic matter such as metals (gold, silver, iron)[158-160], silica[161], rare-earth elements[162], quantum dots[163], viral components[164] and others[165]. As mentioned above, NPs can be synthesised to encompass a wide variety of shapes and sizes, are either hollow or solid and have desirable chemical composition and surface chemistry such that the surface of NPs can be manipulated, coated or functionalised. NPs also have a high surface area to volume ratio compared with their

macromolecular counterparts, tuneable thermal, magnetic, optical and electrical properties. Due to these multifaceted characteristics, nanoparticles have the potential to overcome the biological and chemical barriers within the human body allowing for augmented therapeutic and diagnostic efficacy.
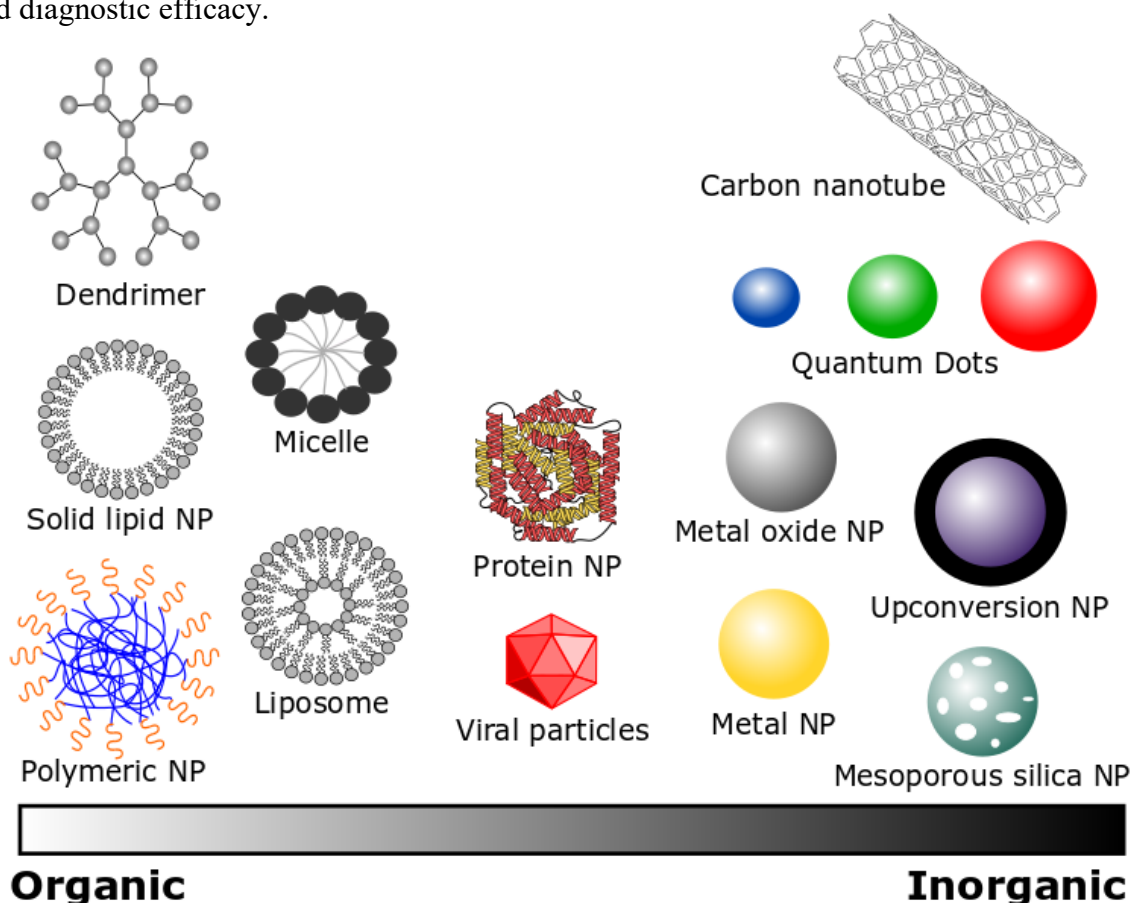
Figure 1.5. Spectrum of nanoparticles used to formulate anticancer medicines. Nanoparticle composition can be broadly defined as organic (polymers, lipids, dendrimers, proteins) or inorganic (metals, rare earth elements, carbonaceous). Protein-based or viral particles can be classed as either depending on their origin. Although spheres are primarily depicted (and used) nanoparticles can take the form of a variety of shapes such as rods, wires and other geometric structures (triangles, diamonds etc.). Adapted from Cryer and Thorley, 2019[87].

This is typically achieved as a result of multiple factors: improved aqueous solubility of hydrophobic drugs, prolongation of circulatory half-life by protecting cargo from the harsh, degradative external environment and reduction of immunogenicity, delivery of multiple agents with differing pharmacological properties (capacity for synergism or suppression/direction of drug resistance)[166] and controlled temporal release at the disease site

(tumour) either by the intrinsic properties of the NP or the incorporation of stimulus responsive elements (SREs)[167]. Release of therapeutic payload from NPs with SREs (Figure 1.6) can be triggered by either exogenous stimuli such as heat[168], light[169], ultrasound[170] or a magnetic field[171] as well as endogenous stimuli including pH[172], redox[173] or components of the physiological microenvironment[174], amongst other triggers[175,176].
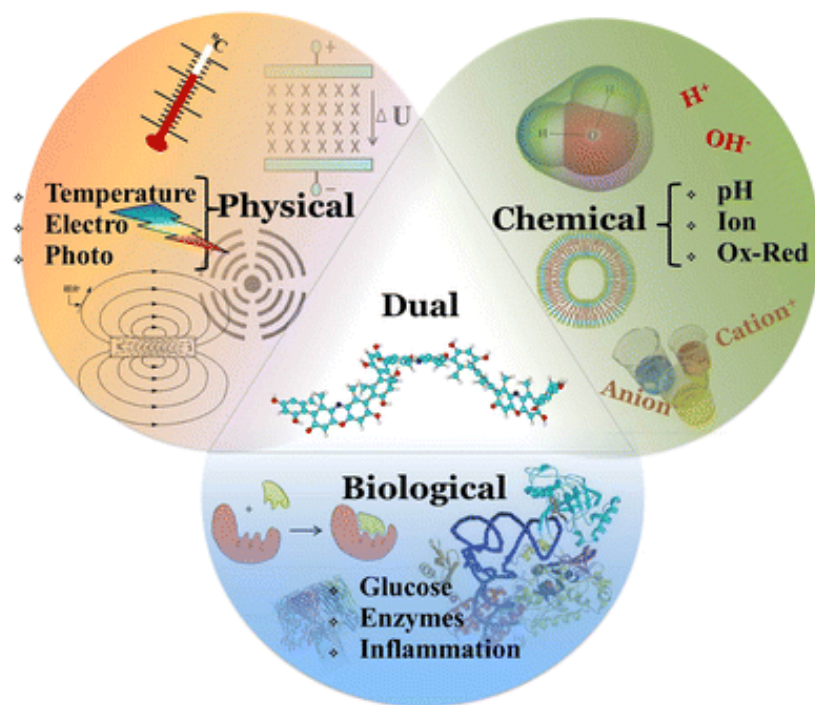
Figure 1.6. Various stimuli used for triggered drug release. The categories of stimuli used for deliberate drug release can be broadly classed into physical, chemical and biological. Indeed, some materials can be fabricated to take advantage of multiple facets of one category or facets from more than one category. Adapted from Cabane *et al*., 2012[177].

Indeed, the advantages of NP based drug delivery over conventional formulations has been translated to the clinic for treatment of a spectrum of diseases, including cancer; there are currently in excess of 50 clinically approved nanoformulations[178] and many more in preclinical development. However, there is a clear clinical bottleneck for the use of NPs to treat cancer, and lung cancer specifically which, along with the further explanation of the advantages of NPs for drug delivery, will be outlined in section 1.4. The work in this thesis focuses on the use of gold NPs and polymeric NPs and exploitation of their properties for drug delivery applications.

1.3.2. Gold nanoparticles

Gold NPs (AuNPs) are a class of inorganic, metallic NPs that have become increasingly popular vectors for use in diagnostic and therapeutic remediation of disease, including cancer[179]. Gold in its molecular form can be utilised in a variety of processes ranging from catalysis to anti-arthritic medication. Indeed, colloidal gold (NPs within the size range of 1-100 nm), unlike the macromolecular counterpart, can exhibit a range of vivid colours, a property that was used by the Romans in the construction of the famous Lycurgus Cup and throughout the proceeding centuries. The use of gold as a medicament can be dated back to 2500 BC China, and in the more recent past was prescribed for a variety of ailments such as fainting, epilepsy and as a diagnostic tool for syphilis. Colloidal gold was eventually formulated into a treatment for rheumatoid arthritis called auranofin in 1985, which is still used today[180].

1.3.2.1. Synthesis and intrinsic properties

The first synthesis of colloidal AuNPs undoubtedly predates the peer reviewed literature, however the first reported synthesis of AuNPs was in 1857 by Michael Faraday who demonstrated the reduction of aqueous chloroaurate by phosphorus in carbon disulfide[181]. However, it took until after the invention of the electron microscope for Turkevich *et al.* to report the first study of the structure of AuNPs under varying synthetic conditions in 1951[182]. This citrate-mediated growth method was further developed in a seminal paper, where it was shown that the relative proportion of reactants (amount of sodium citrate relative to a constant amount of tetrachloroaurate) would influence the nucleation and growth of NPs, resulting in monodisperse particles with different sizes, within the range of 15-150 nm[183]. The first synthesis of well-defined 1.4 nm phosphine stabilised gold clusters (in terms of size and molecular weight), as opposed to colloidal gold solutions, was demonstrated by Schmid *et al.* using diborane in benzene to reduce PPh_3AuCl[184], providing a reliable method to produce AuNPs under 5 nm in diameter. Following this, in 1994 the preparation of a dodecanethiol

stabilised AuNP was reported using a two-phase system whereby aqueous tetrachloroaurate was transferred to toluene using tetraoctylammonium bromide and subsequently reduced using sodium borohydride[185]. The use of thiols to functionalise AuNPs is now the most frequently employed stabilisation strategy and establishment of this chemistry and the formation of dative covalent Au-S bonds has led to an expansive diversification of the use of AuNPs (see 1.3.2.2.). These synthetic methods robustly and cheaply generate a homogenous population of spheres, but interest in synthesis of nanorods[186] and other shapes such as nanoshells, nanocages, nanostars, nanocubes has also increased throughout the decades (Figure 1.7).
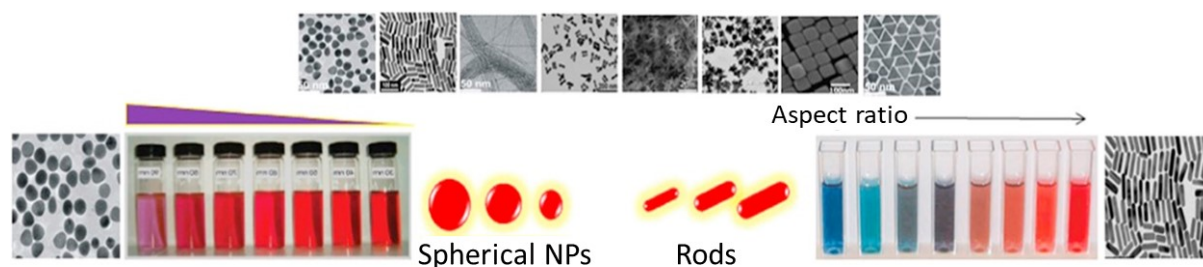
Figure 1.7. Geometric variations in gold nanoparticles. Gold nanoparticles are most commonly synthesised as spheres or rods for biomedical purposes which can have varying dimensions. Furthermore, depending on the reaction conditions, gold nanoparticles can be synthesised as many other different shapes. Adapted from Elahi *et al.*, 2018[187].

The synthesis and different morphologies of AuNPs has been reviewed extensively[188,189]. Indeed the size and shape of AuNP influence its properties, more specifically the optoelectronics of the particle[190]. The surface plasmon resonance (SPR) of AuNPs, which occurs due to oscillation of conduction electrons within an electromagnetic field, upon excitation by incident photons. The resonance frequency for AuNPs falls within the visible range of the electromagnetic spectrum (500-550 nm for spherical core sizes 1-100 nm), giving rise to the ruby-coloured solutions observed with smaller AuNPs. As the AuNP size increases, potentially due to particle aggregation or ligand binding/substitution, the SPR exhibits a red shift, which is detectable spectrophotometrically and accompanied by a colour change from red to purple/blue because of interparticle plasmon coupling[191]. AuNPs can also quench

fluorescence either due to the overlap of their SPR band with the emission wavelength of fluorophores (quenching by fluorescence resonance energy transfer) or by acting as an electron acceptor as a result of photoinduced electron transfer[192]. A further optoelectronic property of AuNPs is surface enhanced Raman scattering (SERS). Raman scattering occurs when photons scattered from a material are of a different energy level to that of the incident photons. AuNPs can be used to augment this scattering as, upon adsorption of a molecule to the particle surface, there is electromagnetic and chemical enhancement effects, caused by excitation of plasmons at the NPs surface and how amenable the surface molecules are to polarisation[193]. Other intrinsic properties of AuNPs include their biocompatibility, large surface area to volume ratio, surface reactivity and ability to participate in photothermal therapy (PTT). All these factors contribute to the potential of AuNPs as drug delivery vehicles, and their role will be outlined in the next section.

1.3.2.2. Drug delivery and photothermal therapy

In the context of anticancer therapeutics, there are predominantly two ways by which AuNPs can be utilised, and both modalities can be combined (using the appropriate AuNP). AuNPs can be used as multivalent drug delivery vehicles, achieved by attaching a therapeutic entity (small molecule, nucleic acid, antibody etc.) to the particle surface. Alternatively (or complimentarily), AuNPs, typically nanorods due to their optimal aspect ratios, can be used for PTT. As mentioned above, AuNPs above 10 nm are not intrinsically cytotoxic, as they are chemically inert, do not produce reactive ions as a result of dissolution and cannot enter the cell nucleus[194]. AuNPs also have high surface area to volume ratio (this is common to all NPs compared with their bulk material counterparts) which allows for precise attachment of many molecules on to the particle surface. Upon conjugation, AuNPs (and NPs in general) can deliver drugs or other therapeutic molecules to tumours by two overlapping mechanisms, passive targeting and active targeting. Passive targeting is based on the enhanced permeability and

retention (EPR) effect, whereby NPs and constructs under approximately 2000 nm have been demonstrated to traverse into solid tumours, after intravenous injection, as a result of fenestrations in the endothelium produced by rapid angiogenesis; these gaps are not typically present in healthy tissue. Lymphangiogensis is highly dysregulated in tumours and therefore there is insufficient lymphatic drainage, resulting in accumulation of molecules that have extravasated into the tumour, which include drug-bearing NPs. Active targeting refers to fuctionalisation of AuNPs with a construct such as an antibody, antibody fragment, aptamer or peptide directed towards an overexpressed or uniquely expressed protein within the tumour in an attempt to improve selective accumulation and uptake. These concepts have underpinned NP drug delivery since the discovery of the EPR effect[195], however these strategies have come under criticism over the past decade (see section 1.4 and Chapter 7). Indeed, the surface reactivity of AuNPs allows for a diverse toolkit of conjugation chemistries to be employed for robust and reproducible attachment of a spectrum of molecules with varying chemical properties. Two main strategies of surface loading are non-covalent (*via* electrostatic, ionic or hydrophobic interactions) or by covalent bonding, which can then be further modified or exchanged if necessary. The former strategy is employed in the minority of cases for drug delivery as the bonds formed are weaker than that of covalent bonds, therefore attached molecules can be easily displaced in biological media. The orientation of molecules on the surface is also random and a high concentration of molecules is required in order to achieve sufficient binding[196]. Covalent bonding (Figure 1.8) predominantly takes the form of an Au-S dative covalent bond[197] either with the sulfhydryl group of the biomolecule under investigation or, if that is absent then attachment of an adapter molecule that the biomolecule is subsequently linked to with further covalent coupling chemistries[198]. An elegant example of these differences can be illustrated when attempting to attach small molecules to the AuNP surface. Dhar *et al*. used a heterobifunctional oligonucleotide linker containing a terminal thiol and amine to

conjugate a platinum(IV) compound to AuNPs. The linker was first attached to the AuNP by the thiol, and well documented EDC/NHS cross coupling chemistry[199] was employed in an aqueous environment to form a peptide bond between the terminal amine groups of the linker and the carboxyl groups present on the platinum compound[200].
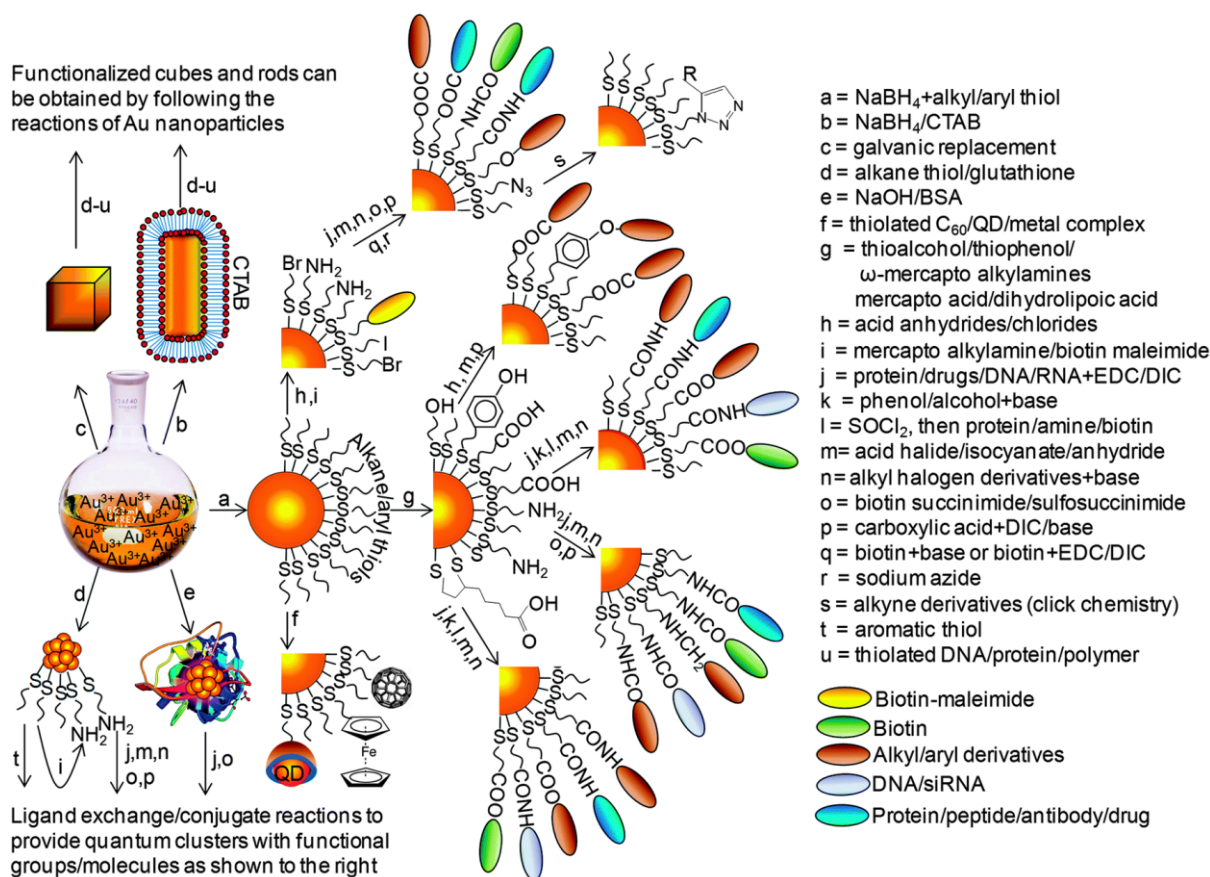
Figure 1.8. Conjugation of biomolecules to gold nanoparticles. The affinity of thiolated linkers for gold surfaces can facilitate either direct attachment or, by means of a secondary functional group, covalent attachment of native compounds including nucleic acids, small molecules or antibodies. Adapted from Biju, 2014[201].

AuNP constructs (and many other NPs) carrying therapeutic agents are typically coated with an antifouling polymer, the most common of which is polyethylene glycol (PEG)[202]. PEG is a clinically approved, biocompatible group of polymers that can improve circulatory half-life by reducing recognition by the mononuclear phagocyte system (MPS), therefore allowing NPs greater residence time in the body and ultimately the tumour (see section 1.4 for more detail). These linkers are modular in nature and can contain functional groups for conjugation or SREs.

Indeed, the release of these agents from the NP can be triggered by a variety of processes depending on the nature of the attachment and the linker. Common intracellular release mechanisms include low pH, such as that found in the lysosome, which can induce cleavage of acid labile bonds (Au-S, hydrazones, imines etc.) and reduction, and subsequent cleavage, of the Au-S bond (or other redox sensitive bonds) by antioxidants such as glutathione which is present at concentrations 1-3 orders of magnitude higher inside the cell compared to outside. Light can be used as a multifunctional tool; UV light can break photocleavable bonds[203] such as ortho-nitrobenzyl, esters present in coumarin/pyrene, azobenzenes, which can be present within the PEG linker, to release cargo on demand as a trigger extrinsic from the cellular environment. Near-infrared (NIR) light can also be used to induce drug release (typically materials doped with upconverting lanthanides) and has the advantage of greater tissue penetration compared with UV-light. This greater tissue penetration depth can be utilised for PTT (Figure 1.9); the localised SPR band of gold nanorods is split into traverse and longitudinal bands and the maximal absorbance wavelength depends on this aspect ratio. The structure of nanorods is such that the SPR falls within the NIR spectrum and therefore absorb large amounts of energy at these wavelengths. As these photons excite the conduction band electrons, they subsequently decay to the ground state and release this energy as heat to the surroundings[204]. Upon accumulation in tumour tissue (by the passive and/or active mechanisms outlined above), gold nanorods can be excited by NIR light, causing hyperthermia selectively in the tumour, ablating the tissue and inducing the elimination of malignant cells; this is the principle of PTT, a modality that can be combined with drug delivery. Indeed, AuroLase is a silica-coated gold nanoshell currently in clinical trials for use as a PTT agent.
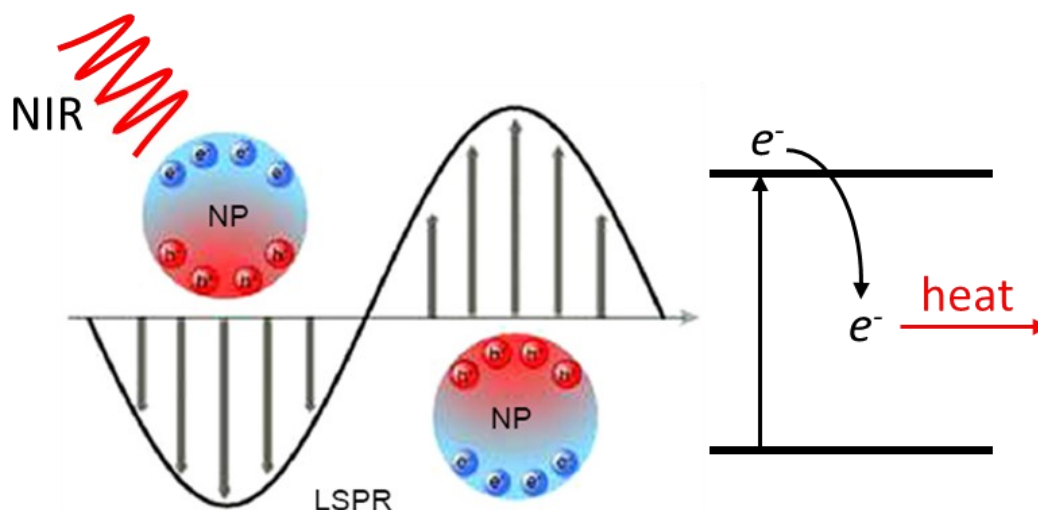
Figure 1.9. General principal of photothermal therapy. Upon exposure to near infrared (NIR) light, electrons are excited. The relaxation of these electrons releases large amounts of energy in the form of heat to the surrounding environment. Adapted from Hussein *et al.* 2018[205].

The therapeutic potential of AuNPs is starting to be realised as formulations begin to enter clinical trials. Aurimmune (CYT-6091) is a formulation of recombinant human tumour necrosis factor (rhTNF)-α, thiolated PEG and AuNPs[206] that was investigated in a phase I dose escalation trial, and was well tolerated at all examined doses with evidence of efficacy against solid tumours[207]; phase II trials are planned for the near future. Preclinical studies have been performed using a similar technology where thiolated paclitaxel derivatives were also attached to the Aurimmune formulation, which was termed CYT-21625, and demonstrated favourable pharmacokinetics[208] and reduction of tumour volume in several models as well as attenuation of side effects[209], suggesting the combination of paclitaxel and rhTNF-α delivered using AuNPs has clinical potential. Indeed, there is a plethora of preclinical studies illustrating the potential of AuNPs as drug carriers and intrinsic therapeutic agents (*via* PTT), however there are concerns regarding the toxicity of AuNPs (and NPs in general). The general consensus is that gold core of AuNPs is inert and non-toxic above 2 nm in size. AuNPs of this size have been noted to cause toxicity due to oxidative stress and mitochondrial damage[210], however almost all AuNP drug delivery vehicles are above 10 nm. Toxicity can stem from the use of

capping agents as opposed to the AuNPs themselves; the quaternary ammonium surfactant cetyltrimethylammonium bromide is a commonly used capping agent for gold nanorods, desorption of which from the nanorod surface can induce toxicity[211]. Indeed, the purity of the preparation and existence of other excipients in solution must be examined, as it may be these that are responsible for any observed toxic effects (applies for any NP preparation). *In vivo*, distribution and biopersistence are primary concerns. Most intravenously injected AuNPs accumulate in the liver and spleen, although antifouling agents and NP physicochemical properties can mitigate this and dictate distribution to some degree. AuNPs are not easily degraded and are ineffectively cleared, therefore accumulated AuNPs may cause direct damage to the cells of the liver/spleen or provoke an inflammatory response/the immune system. To date, most studies have not demonstrated overt *in vivo* AuNP toxicity, however few toxicological studies have been done compared to *in vitro* studies, and thus represents a future direction of study[212].

1.3.2.3. Imaging and sensing as diagnostic tools

As mentioned previously, AuNPs have unique and tuneable optical properties that have been investigated in a medical context, both as imaging agents and as biosensors (Figure 1.10); AuNPs are indefinitely photostable and do not blink, therefore aiding in the diagnostic process. This topic has been reviewed extensively[213,214], therefore a select few examples to illustrate the spectrum of usage will be outlined. In terms of imaging, AuNPs can act as contrast agents for CT scans and have been used to generate CT images of tumours in live animals[215]. Photoacoustic imaging relies on the generation of acoustic waves after laser-induced heating of AuNPs (due to their high extinction coefficients) and has been used to selectively image prostate cancer cells that had taken up anti-HER2 conjugated gold nanorods[216]. NIR excitation of nanorods also allows visualisation by two-photon luminescence. This effect arises due to the high quantum efficiency of gold nanorods under plasmon resonant conditions that increases

the detection of photons by several orders of magnitude due to the penetrance of NIR light, and can be used for *in vitro* and *in vivo* imaging at the single particle level[217]. The strong light scattering properties at their SPR make AuNPs suitable for imaging by dark-field microscopy and is typically used to image cancer cells by functionalising their surface with ligands that govern nanoparticle-receptor interactions. Differential interference contrast microscopy is a closely related technique that generates image contrasts based on the optical path length of the sample; AuNPs have a maximal contrast at their SPR, which is dependent on shape, size, dispersant etc. therefore multiplex imaging of different NPs on a cell surface can be undertaken[218]. As biosensors, AuNPs have been utilised in several applications geared towards detection of cancer cells, biomarkers, or analytes of interest in other disease contexts. SERS-based assays can be performed using AuNPs to differentiate cancer cells from normal cells due to the assembly of anti-EGFR gold nanorods on the cell surface and subsequently enhanced Raman signals[219]. Raman reporter particles have a molecule with a large Raman cross section (e.g. organic dye) attached to the surface and then a further moiety attached (e.g. ScFv region of antibody against overexpressed receptor) that is a distance away from the particle such that no Raman signal is detected. When unhealthy cells interact with these particles the Raman spectra from the dye are detected whereas this does not occur with healthy cells that interact with the particles far less; this strategy can be effectively employed to discern tumours *in vivo*[220]. This modular technology has also been used to detect pathogens[221] and other diseased tissues[222].

Localised SPR-based assays rely on the same principle, achieved through different methods. An increase in AuNP size (or technically refractive index) by adsorption of a protein, nucleic acid or other analyte to the NP surface for example, induces a red shift in the plasmon resonance wavelengths. Therefore, SPR can be used to detect perturbations in the local biochemical environment, and if the NP is functionalised appropriately, this shift can be molecule specific.

This label-free detection method has been comprehensively reviewed and is typically employed for biotin-streptavidin and antibody-antigen interactions[223].
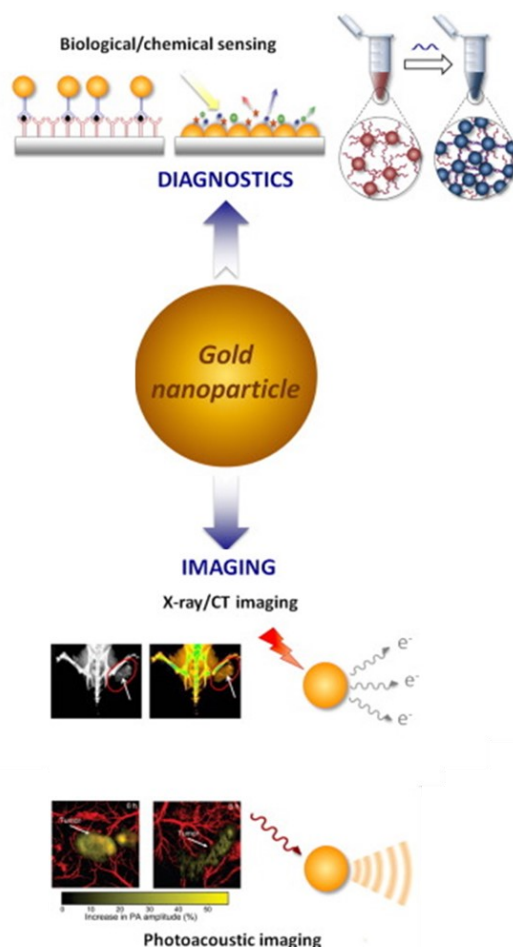
Figure 1.10. Diagnostic utility of gold nanoparticles. Attachment of nanoparticles to substrates or as substrates themselves can increase assay specificity and aggregation of nanoparticles provide sensitive colorimetric outputs. Gold nanoparticles can also be used as imaging agents due to their electron density or surface plasmon resonance. Adapted from Her *et al*., 2017[224].

Another form of localised SPR sensing is based on interparticle distance and the observation that assembly or aggregation of AuNPs also results in a red shift in SPR; furthermore, as the stability of the colloidal solution is compromised, a colour change is also visible. This technique has been employed for the detection of a plethora of molecules and has been reviewed extensively[225]. Examples include functionalisation of separate AuNP populations each with non-complimentary oligonucleotides that, upon addition of DNA complimentary to both strands, induced AuNP aggregation *via* hybridisation[226]. Phospholipase A_2 detection was

56

enabled due to hydrolysis of liposomes which contained the peptide JR2KC$_2$ that forms a complex with AuNP functionalised JR2EC peptide, thus leading to NP aggregation[227]. AuNPs decorated with specific substrates for matrix metalloproteinases (MMPs) were incubated in MMP-containing plasma, upon which MMPs digested their substrate, reducing AuNP colloidal stability and inducing aggregation[228]. The scope of molecules using this technology is versatile can be applied to many different systems, including lung cancer biomarkers, either from the blood, BAL or cell lysates.

1.3.3. Polymeric nanoparticles

Although the use of polymeric NPs does not predate that of AuNPs, the concept of biodegradable materials has a long history in medicine, dating back over 3000 years when natural materials such as plant and wool fibres were used as sutures by the ancient Egyptians[229]. Fast forwarding to the mid-20th century, the same principle is enacted, only this time with synthetic biodegradable polymers acting as a replacement for the commonly used, naturally derived catgut suture[230]. These polymers were polyesters, predominantly poly(glycolic acid) (PGA), poly($_{D,L}$-lactic acid) (PLA), and poly($_{D,L}$-lactic-*co*-glycolic acid) (PLGA) that ultimately proved to be safe and effective replacement materials to manufacture sutures from[231]. Around the same time, pioneering studies were undertaken using biodegradable polymers to control the release of drugs, proteins and other macromolecules; this was the birth of controlled release systems[232]. These systems were primarily macroscale drug depots, biocompatible implantation devices and sutures that, in the 1970s and 1980s, transitioned to fabrication of microscale particle controlled release systems[233]. At around the same time, the idea of polymer-drug conjugates was being developed, the first major successes of which were PEGylated iterations that showed enhanced circulation time and reduced immunogenicity. Other polymers such as poly(hydroxypropylmethylacrylamide) were utilised and conjugated to chemotherapy[234]. Further research incentive came in the form of the discovery of the EPR

effect and the idea of active targeting using antibodies, and in the late 1980s/early 1990s the first polymeric NP structures were developed. These were initially polymeric micelles constructed from a PEG block conjugated to a hydrophobic amino acid, poly(aspartic acid) block, to form block copolymers that spontaneously formed micelles in aqueous solutions above a very low critical micelle concentration. It was discovered that these micelles could carry small hydrophobic molecules (e.g. doxorubicin) by physical loading or conjugation, or could be functionalised with ligands specific for certain cells[235]. Simultaneously, PEGylated micelles based on poly(oxyethylene)-poly(oxypropylene)-poly(oxyethylene) triblock copolymers (PEO is PEG) were fabricated as drug carriers[236]. In the early 1990s, immense interest was generated by the concept of nucleic acid delivery where, amongst other formulations, polyethyleneimine was developed, which is a cationic polymer that complexes with anionic nucleic acids. PEGylated polycationic copolymers were synthesised as an extension of this concept to form PEGylated micelles with condensed nucleic acid-polycation complexes encapsulated in the core[237]. Around the same time, a landmark study demonstrated that NPs comprised of biodegradable diblock copolymers PLGA and PEG (PLGA-PEG NPs) exhibited long circulating half-lives and high encapsulation efficiency of the hydrophobic compounds lidocaine and prednisolone[238]. In the wake of this study, there has been a vast swathe of publications building on the concepts illustrated within and set a precedent for the use of biodegradable polymeric NPs, including polymersomes, polymeric micelles and dendrimers as drug delivery vehicles, which has been recently reviewed[154].

1.3.3.1. Common materials and fabrication methods of NPs

There is an arsenal of biodegradable polymers that have been utilised to govern the release of therapeutic agents, the full exposition of which is beyond the scope of this thesis. These polymers can be grouped according to their origin. Naturally occurring biodegradable polymers

can be categorised into two families, the polysaccharides (alginate, hyaluronic acid, chitosan, dextran, agarose, carrageenan and cyclodextrins) and proteinaceous polymers (gelatin, collagen and albumin). Synthetic polymers can be defined by their distinguishing functional moieties: poly(esters), poly(ortho esters), poly(amides), poly(ester amides), poly(phosphoesters) and poly(anhydrides). Poly(esters) can be further separated into polycaprolactones, poly(alkyl cyanoacrylates) and PLGA (co)polymers[154]. The majority of the polymeric NP literature focuses on fabrication methods for PLGA-based NPs and will therefore be delineated here, however these methods are likely to be applicable to other polymers too, under the appropriate conditions.

Polymeric NPs can be fabricated by a number of top-down methods, whereby NPs are generated by self-assembly of a preformed block copolymer consisting of two distinct polymer chains with different (and often contrasting) hydrophobicity (or water solubility). These techniques include nanoprecipitation (also referred to as solvent displacement/diffusion), salting out, and a variety of emulsification/solvent evaporation methods [including oil-in-water (O/W, single emulsion) and water-in-oil-in-water (W/O/W, double emulsion) emulsification-solvent evaporation, and emulsion diffusion]. Bottom-up methods involve polymerisation of monomers, typically classified as interfacial, microemulsion or precipitation polymerisation. As these methods have been established for decades, more contemporary NP fabrication methods have been constructed including spray-drying, electrospray, supercritical fluid technology, aerosol flow reactors and premix membrane emulsification. These bulk synthesis methods each have their own idiosyncrasies and fundamentally the suitability of a particular method and the subsequent characteristics of the produced NPs depends on many factors. This includes the chemical properties (particularly solubility/hydrophobicity) of the molecule to be encapsulated, as well as parameters like copolymer concentration, ratio and molecular weight, drug concentration, type and volume of solvent/aqueous phase/surfactant, method of mixing,

sonication source/power/time, method of evaporation and more. These methods have been reviewed in detail[239-241]; furthermore, microfluidic technology has facilitated the high-throughput production of homogenous polymeric NPs due to the precise control of the addition of reactants, rapid mixing, reproducible reaction conditions (temperature, pressure, reactant and solvent concentrations etc.), ease of post-synthesis processing (i.e. addition of cyroprotectants) and speed[242,243]. For brevity and relevance, the most common, top-down polymeric NP fabrication procedures will be described (Figure 1.11).
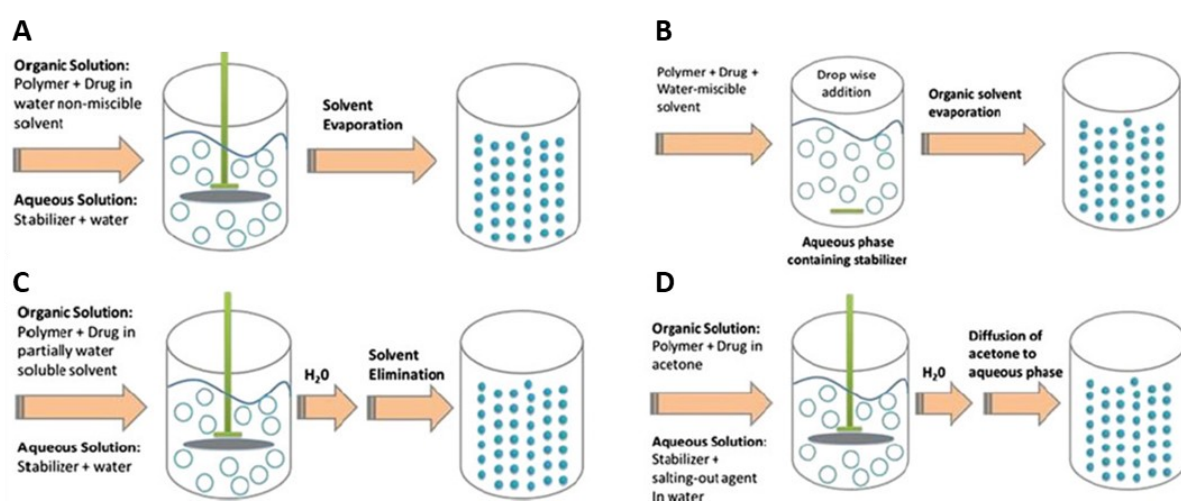
Figure 1.11. Common synthetic methods to produce polymeric nanoparticles. (A) emulsification-solvent evaporation, (B) nanoprecipitation, (C) emulsion diffusion and (D) salting-out technique. Adapted from Kunda *et al.*, 2013[244].

Nanoprecipitation is a popular method for the encapsulation of hydrophobic molecules. This method is predicated on interfacial polymeric deposition following contact with a polar solvent (aqueous phase) such as water. The polymer and drug cargo are dissolved in an organic phase (typically dichloromethane, ethanol or acetone) that is miscible with the aqueous phase, to which it is added under stirring. Upon addition of organic phase, a four step process of supersaturation, nucleation, growth and coagulation begins as the hydrophobic polymer and drug self-assemble into spherical structures[245]. The organic phase is then either evaporated at reduced pressure or at room temperature if the solvent is sufficiently volatile. The immediate formation of NPs is thought to be due to the principles of the Marangoni effect whereby

turbulence and tension is created at the interfacial boundary between two liquid phases[246]. This method was elegantly illustrated by Farokhzad *et al*. whereby a diblock copolymer consisting of PLGA and PEG were employed to encapsulate the hydrophobic chemotherapy docetaxel by nanoprecipitation. The resulting NPs were small, relatively homogenous by size and spherical in morphology, consisting of a hydrophobic PLGA core within which there was docetaxel, surrounded by a hydrophilic PEG layer[247]. The use of PEG in this synthesis eliminates the need for surfactants in the aqueous phase due to stabilisation of the dispersion by the PEG chains. Indeed, many different hydrophobic molecules have been encapsulated in NPs by nanoprecipitation and by adjusting the aqueous phase, the molecular repertoire can be extended to successfully encapsulate hydrophilic drugs. Nanoprecipitation produces small NPs in a facile and rapid fashion making it a suitable technology for large scale manufacturing. However, this process is not ideally suited for hydrophilic molecules as they are often retained in the more voluminous aqueous phase. Furthermore, encapsulation efficiencies are typically lower than emulsification based methods and it can be challenging to remove all organic solvent after the self-assembly process[248].

The emulsification-based methods (O/W, W/O/W) are the oldest methods used to create polymeric NPs from preformed polymers. All variants of these methods rely on the formation of an emulsion after the organic phase solution encounters an aqueous phase containing surfactant, followed by exposure to shear stress, then finally evaporation of organic solvent and self-assembly of NPs. Although traditionally used for the generation of microparticles, nano-emulsions can also be prepared[249].

The O/W method is used to encapsulate hydrophobic molecules within polymeric NPs and requires the compound and PLGA to be soluble in a solvent that is immiscible with water such as dichloromethane, chloroform or ethyl acetate. This organic phase is then poured into the aqueous phase (typically water with a surfactant such as sodium cholate, vitamin E D-α-

tocopheryl PEG 1000 succinate (TPGS) or polyvinyl alcohol (PVA). The resulting emulsion is then subjected to high shear stress either by homogenisation, sonication or microfluidisation, after which the organic solvent is evaporated either at room temperature or under reduced pressure depending on the volatility of the solvent. The self-assembled NPs are then collected by centrifugation or ultrafiltration and lyophilised.

The W/O/W method is used for the encapsulation of hydrophilic molecules or those with high water solubility such as proteins. The first step of this method is to generate a water-in-oil (W/O) emulsion whereby the aqueous phase contains the hydrophilic molecule and the organic phase contains PLGA (or polymer) and surfactant with a low hydrophilic-lipophilic balance (i.e. highly hydrophobic) such as Tween 80 or Pluronic F68. Emulsification occurs due to the input of high shear stress into the system. This W/O emulsion is then dispersed in an aqueous phase of a volume larger than that used for the initial W/O emulsion formation; this aqueous phase may or may not contain surfactant. The W/O/W emulsion is then sonicated or homogenised to reduce droplet size and finally the organic solvent is evaporated, promoting solidification of the NPs.

Both variants suffer from common drawbacks such as the need for intense shear stress that can destroy labile and fragile entities such as proteins. This can be exacerbated by toxic, chlorinated organic solvents. The locus of shear stress is such that it is not homogenously distributed throughout the emulsion, resulting in larger and more polydisperse particles compared with nanoprecipitation. The encapsulation of hydrophilic drugs using W/O/W is variable and moderate at best, and this method results in the largest NPs. Encouragingly however, W/O/W can still encapsulate water-soluble entities more efficiently than nanoprecipitation and O/W robustly produces NPs with a high encapsulation efficiency if the drug is sufficiently hydrophobic, higher than nanoprecipitation. The highly modular nature of these preparations necessitates the need for detailed comparisons of altered parameters, and indeed several studies

have endeavoured to elucidate the key factors involved in dictating resultant physicochemical properties of polymeric (PLGA-PEG) NPs. For example, Cheng *et al*. found that for NPs prepared by nanoprecipitation, an increase in organic-aqueous miscibility lead to a decrease in NP size, a linear relationship between the NP size and polymer concentration was described and drug loading was found to affect size[250]. Keum *et al*. found that the type of surfactant (Poloxamer 188, TPGS or PVA) and organic phase solvent altered the encapsulation efficiency of docetaxel. Amount of docetaxel initially added to the preparation, sonication time and power as well as evaporation method (reduced pressure, room temperature or under nitrogen) all influenced particle size and encapsulation efficiency[251]. Furthermore, Budhian *et al*. directly compared nanoprecipitation and O/W methods to encapsulate the hydrophobic drug haloperidol within PLGA NPs. Nanoprecipitation was found to produce the smallest NPs but suffered from low drug loading. The O/W method was split into two variants defined by the source of the sheer stress, homogenisation or sonication. Overall homogenisation appeared to produce NPs with higher loading efficiencies on average, however the NPs were larger and more polydisperse.

However, other factors such as initial drug concentration, volume of aqueous phase, polymer concentration to name a few also contributed to NP size and drug loading[252]. The take home message is that a variety of methods can be implemented to fabricate PLGA (polymeric) NPs, however the system is sensitive to change, in certain parameters more so than others, and therefore protocols must be optimised on a small and large scale to generate suitable NPs.

1.3.3.2. Clinical precedent as drug delivery vehicles

Although most clinically approved nanomedicines are liposomal formulations, the biocompatibility and modularity of polymers has also led to clinical success; some clinically approved degradable polymeric materials include PEG, PLGA, methacrylic acid copolymers

and ethylene vinyl polymers amongst others[253]. The diversity of synthesis methods, ease of fabricating NPs from polymers such as PLGA and PEG, ability to encapsulate a variety of cargo with differing chemical properties, co-delivery/active targeting potential (e.g. antibody or aptamer surface conjugation) and suitability for large scale manufacturing has resulted in several polymeric NP formulations reaching clinical trials. The following are some notable examples that illustrate the clinical potential of polymeric NPs.
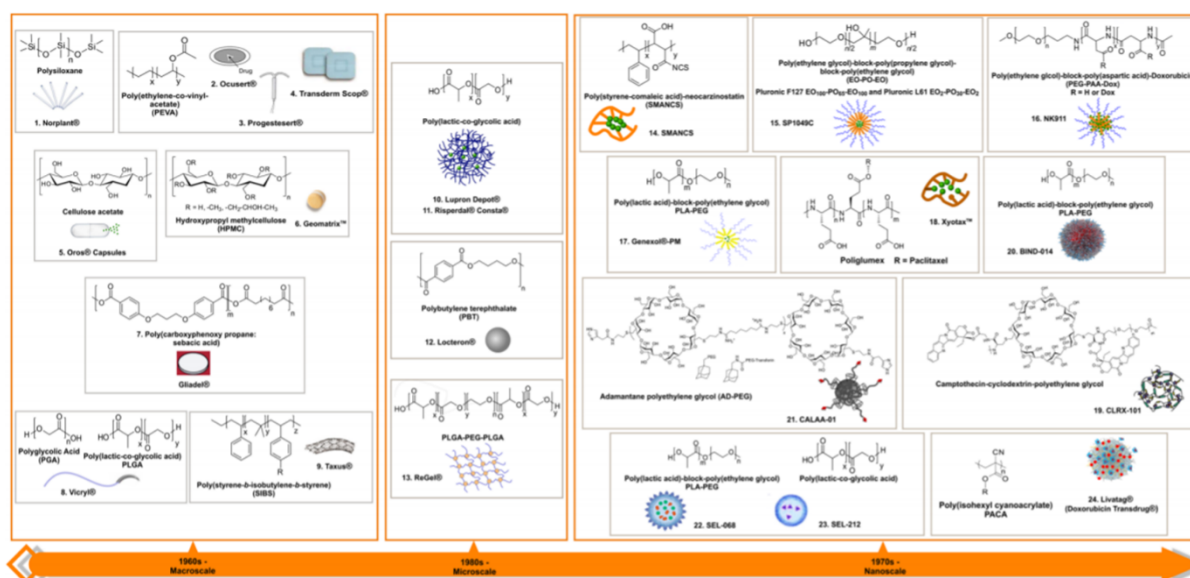
Figure 1.12. Evolution and development of polymeric drug delivery. The use of polymers for medical applications and drug delivery originated in the 1960's and took place on the macroscale. In the 1980's, miniaturisation techniques led to the fabrication of microscale polymeric delivery systems such as microparticles. The origination of nanoscale drug delivery systems for medical applications was the 1970's and made a significant impact on the formulation of clinically approved anticancer drugs. Indeed, several of the formulations depicted have either been clinically approved (e.g. Genexol-PM) or are currently in clinical trials (BIND-014, CLRX-101). It should be noted that these polymeric delivery systems have also been implemented in disease areas other than cancer including gout, smoking cessation and schizophrenia. Adapted from Kamaly *et al*., 2016[154].

BIND-014 is a PLGA-PEG NP containing docetaxel and has a S,S-2-[3-(-amino-1-carboxypentyl)-ureido]-pentanedioic acid (ACUPA) moiety conjugated to the surface. ACUPA is an inhibitor analogue of prostate-specific membrane antigen, the overexpression of which has been documented on tumour neovasculature, such as in NSCLC and SCLC. BIND-014 outperformed the clinical docetaxel formulation in NSCLC xenograft models and

displayed more favourable pharmacokinetics in nonhuman primates[254]. After a phase I trial[255] demonstrated prolonged release of docetaxel in humans with solid tumours and found the maximum tolerated dose (MTD) to be 60mg/m^2, phase II trials have commenced whereby BIND-014 is being investigated as therapeutic intervention for patients with advanced NSCLC (NCT01792479) or patients with KRAS positive squamous cell NSCLC (NCT02283320) which is based on results obtained from a previous phase II trial where some efficacy in KRAS mutated NSCLC was observed[256].

CRLX101 is a formulation constructed from a linear β-cyclodextrin-PEG copolymer conjugated to camptothecin that self-assembles to form NPs and has shown efficacy in multiple tumour models, including SCLC and NSCLC[257] leading to a phase I trial to determine the MTD[258] and further, a phase II trial. This trial showed CRLX101 had a favourable safety profile despite not reaching its primary endpoint of overall survival benefit (NCT01380769) and is now being investigated in further clinical trials in patients with lung cancer, amongst other solid tumours.

Another variety of NP that has reached clinical trials is polymeric micelles. NC-6004 is a formulation comprised of a coordination complex of cisplatin with poly(glutamic acid) which forms the inner core, surrounded by an outer shell of PEG. The resulting stable micellar structures are approximately 30 nm in diameter[259]. In patients with advanced solid tumours, a phase I trial demonstrated NC-6004 could prolong the circulatory half-life of cisplatin and delay its release. Furthermore, the formulation was well tolerated and there were no signs of ototoxicity or neurotoxicity which are common side effects of intravenous cisplatin administration[260]. NC-6004 is currently being investigated in a phase III trial in combination with gemcitabine for the treatment of pancreatic cancer (NCT02043288) and in a phase Ib/II trial for the treatment of stage IV NSCLC or other advanced solid tumours (NCT0224023). Indeed, this is a snapshot of the clinical utility of polymeric NPs and several other formulations

are being investigated as therapies for various malignancies. The track record of polymeric NPs in clinical trials combined with Food and Drug Administration (FDA) approval (Figure 1.12) of the starting materials and advantages of NPs as mentioned above reinforces the use of these materials for drug delivery. The increasing number of publications, both preclinical and clinical, utilising polymeric NPs for drug delivery is evidence of their expanding popularity and versatility.

1.4. Promises and pitfalls of nanoparticle drug delivery

Since the conceptualisation of NP drug delivery several decades ago, huge advancements have been made in this realm. As previously mentioned, some nanoformulations have been approved for clinical use due to increased circulatory retention time or alleviation of dose limiting toxicities, and there is an ever-growing number of formulations in the pipeline on the precipice of clinical translation[261]. Indeed, nanotherapies have uniquely appealing properties for drug delivery applications in that they can be used to ferry a large repertoire of biomolecules of different physical and chemical properties, which opens opportunities for, not only chemotherapy delivery, but also nucleic acid/protein modulation and immunotherapy[262]. The material used can be tailored to the property of the therapy such that efficient encapsulation or conjugation of the cargo can be achieved. For example, cationic polymers form complexes with anionic nucleotides or nucleic acids and more efficiently escape the endosome, which is essential for RNA delivery[263]. Lipid and polymeric NPs are suitable for hydrophobic cargo due to their hydrophobic cores while the surface chemistry of AuNPs allows facile conjugation of thiolated entities and combination therapy *via* the photothermal effect.

Many of these materials are highly biocompatible with defined structures and functional groups. Engineering materials to have SREs that are cleaved in response to pH (e.g. imine or hydrazone bonds), light (e.g. nitrobenzyl groups) or intracellular entities (such as cathepsin B

or glutathione) allows for spatiotemporal release of therapeutic cargo at defined locations. For instance, the altered physiological state of the tumour microenvironment (overexpression of markers such as CD44, MMPs, oncogenic proteins, hypoxic conditions, acidic pH) can also be used to trigger drug release on demand[264]. These processes can advantageously modify the pharmaceutical properties of biomolecules such as stability, reactivity, metabolism and tumour accumulation. This augmented accumulation is heavily predicated on the EPR effect (Figure 1.13), first described in 1986[265] as a physiological phenomenon of tumours that accounts for accumulation of NPs which are small enough to diffuse through the disordered vasculature and fenestrations in the endothelium but large enough to be retained and not diffuse back out into the circulation[266]. As previously mentioned, active targeting builds upon this concept by decorating the surface of NPs with antibodies, aptamers or other moieties that are designated towards an overexpressed or tumour-specific component, and has been another central focus of NP drug delivery in an attempt to increase the uptake of NPs by the tumour and specifically tumour cells.
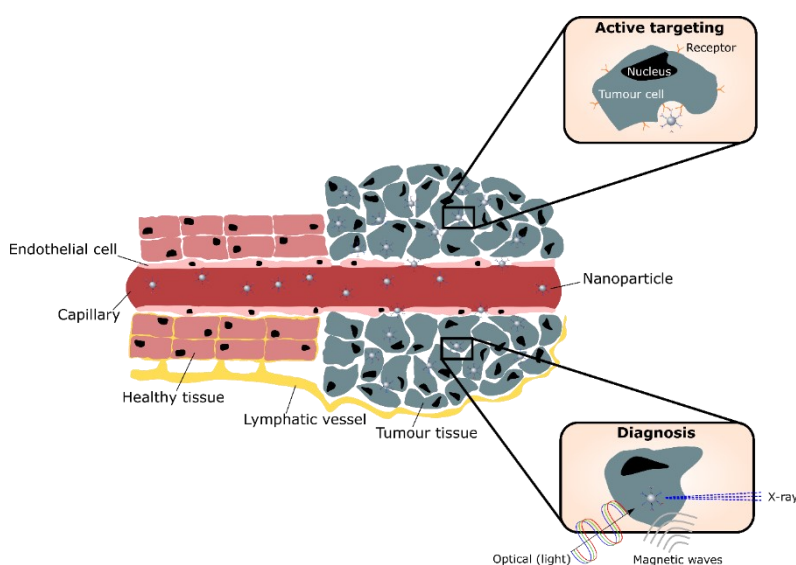
Figure 1.13. The enhanced permeability and retention (EPR) effect. A controversial premise that is predicated on the passive accumulation of NPs into tumours by virtue of gaps in the rapidly growing vasculature surrounding the tumour mass. This rapid growth also restricts lymphatic drainage in the tumour, leading to an accumulation of NPs at the tumour site. By functionalising NPs with targeting ligands, retention and internalisation within the tumour may be increased. The presence of NPs in the tumour, and the properties of the NP, can be leveraged for diagnostic purposes. The clinical utility and relevance of the EPR effect has been called into question and may better function as a biomarker for patient stratification as opposed to a veritable delivery mechanism. Adapted from Cryer and Thorley, 2019[87].

The modularity of molecules that can be delivered facilitates novel combinatorial therapies that would be difficult to achieve with conventional delivery, such as nucleic acids, antibodies and chemotherapy in the same formulation[267]. Traversal of the blood brain barrier, gastrointestinal tract or delivery to lymph nodes for example, provides accessibility to typically exclusionary zones of the body which can be capitalised on in order to treat diseases that arise in these areas[268]. Another additional benefit is that NPs can function effectively as imaging agents for a variety of modalities which can be further combined with therapy to provide a theranostic approach, whereby tumours are simultaneously visualised and treated[269], which can also provide real-time feedback on the efficacy of the delivered therapy[270]. NPs also have huge potential to enhance immunotherapeutic approaches due to the principals just outlined; for example, NPs carrying adjuvant and antigen can directly home to lymph nodes if under a certain size, or can target specific cells such as dendritic cells which are critical in mounting a robust antitumour response[271].

The advent of machine learning is coming to prominence in many avenues of medicine, including nanomedicine. The multifactorial nature of the field has led researchers to develop algorithms that can predict the fate of nanomaterials *in vivo* based on their protein adsorption profile[272], or to develop personalised dosing regimens and therapeutic compositions with minimal side effects based on large biological datasets and predictivity of how nanomaterials and therapeutics will help highly stratified patient populations[273]; this area will rapidly develop over the course of the coming decades.

However, despite the evident progress nanomedicine and NP drug delivery has made, the full clinical utility is still yet to be implemented. The challenges associated with NPs in drug delivery have been recently and elegantly reviewed[274-276], but in brief, fundamentally the design and engineering of NPs for drug delivery purposes is based on our understanding of the biological architecture of the body and how nanomaterials interact with chemical and

biological obstacles en route to their destination. Unfortunately, this space represents a large gap in knowledge, as we do not yet have a comprehensive understanding of how NPs act *in vivo*, both upon administration and arrival at the designated site, in particular the composition of the protein corona, the toxicological impact of nanomaterials or the underpinning biology of tumours. Moreover, there is a vast spectrum of nanomaterials and therapeutic combinations to evaluate, and although machine learning may expedite this process, the issue of large-scale manufacturing and good manufacturing processing standards may hinder high-throughput generation of efficacious nanomedicines.

The evaluable information we currently possess comes primarily from potentially misrepresentative animal models and therefore guides our thinking as such. A notable example is the controversy surrounding the clinical utility of the EPR effect, as this phenomenon may be replicated across animal models; accumulating evidence suggests that in humans the EPR effect is inconsistently observed and is even absent in some individuals[277]. There is a conscious effort to move to more representative animal models and/or use current ones for specific questions and not solely to prove a therapy can cure a mouse of a tumour. Indeed, current approval criteria for NPs to reach the clinic requires *in vivo* efficacy before being considered for clinical trials, but this criteria may be misaligned with what NPs can produce clinically and refinement of this criteria may see more approvals. The lack of clinical translation has prompted researchers to call for a standardisation approach to nanomedicine and documentation to this effect has recently been produced. Minimum information reporting in bio-nano experimental literature (MIRIBEL) proposed by Faria *et al*. seeks to create a robust reporting framework to encourage a transparent, open and reproducible body of literature involving nanomaterial and biological systems and their interactions[278]. MIRIBEL was generally well received by the community as described in a recent correspondence[279] and the consensus was that standardised reporting may enhance the quality and reproducibility of

literature produced and may help align the ever growing number of researchers in a similar direction, but it is not a panacea or a set of commandments that ought to be rigorously adhered to. The potential of NP drug delivery is clear but the path to progress is still very much being charted.

1.5. Hypothesis and aims

The overarching hypothesis of this thesis was that chemotherapeutic agents can be delivered to lung cancer cells using nanoparticles resulting in enhanced antitumourigenic activity compared to clinical formulations. In order to investigate this hypothesis, the aims of the thesis are as follows:

- Synthesis of modified afatinib analogues to enable conjugation to the surface of a nanoparticle.

- Fabrication and characterisation of inorganic (gold) and organic (polymeric) nanoparticles suitable for delivery of one or multiple chemotherapeutic agents to cells.

- *In vitro* evaluation of the cytotoxicity, antiproliferative and apoptotic capacity of nanoparticle formulations in lung cancer cells.

- *In vitro* evaluation of biocompatibility of nanoparticle formulations in noncancerous cells.

- Elucidation of the mechanism of nanoparticle uptake into lung cancer cells.

- *In vivo* appraisal of the safety and antitumour efficacy of chemotherapy-laden polymeric nanoparticles.

These aims will be achieved by a combination of organic and inorganic chemistry techniques followed by appropriate physicochemical characterisation of the end products. Conventional and contemporary *in vitro* assays will be utilised to assess cell viability, proliferation and apoptosis. Similarly, biocompatibility will be assessed by cell viability and release of

proinflammatory cytokines. In both cases the nanoformulations will be compared to the constituents of the formulations and equal doses of free drug. Fluorescence microscopy will be employed to investigate nanoparticle uptake. Finally, an original mouse model of lung cancer derived from the cells of a patient will be used for the *in vivo* studies, with endpoints assessed by measurement of tumours and the animals as well as by histology to give a holistic perspective.

2. Materials and methods

This chapter contains detailed information pertaining to the methods and materials used in order to carry out the research communicated in the subsequent chapters of this thesis. The materials listed include chemicals, solvents, reagents, cell lines, cell culture media, assay kits and other consumables. The methods encompass optimised protocols for the synthesis and characterisation of tyrosine kinase inhibitor analogues, polymeric and gold nanoparticles, as well as conjugation and encapsulation of drugs within nanoformulations. Moreover, techniques assessing the *in vitro* cytotoxicity, cellular entry mechanism, *in vivo* safety and efficacy of NPs is described.

2.1. Materials

Poly(D,L-lactide-*co*-glycolide) (PLGA, also known as Resomer RG 502 H), N-hydroxysuccinimide (NHS), dicyclohexylcarbodiimde (DCC), N,N-Diisopropylethylamine (DIPEA), pamoic acid, sodium phosphate monobasic, sodium phosphate dibasic, polyvinyl alcohol (PVA), sucrose, vinorelbine tartrate, coumarin-6, 30 nm gold nanoparticles (AuNPs), poly(ethylene glycol) 2-mercaptoethyl ether acetic acid (HS-PEG-COOH), copper sulfate, tris(3-hydroxypropyltriazolylmethyl)amine (THPTA), tris(1-benzyltriazolylmethyl)amine (TBTA), sodium ascorbate, Alexa Fluor 488-alkyne, ethylenediaminotetraacetic acid (EDTA), benzylazide, urea, Dulbecco's Phosphate Buffered Saline (PBS), newborn calf serum (NCS), [(penicillin/streptomycin)/glutamine] [(PS)/G], Roswell Park Memorial Institute (RPMI)-1640 medium, foetal bovine serum (FBS), trypsin/EDTA, mitomycin C, bovine serum albumin (BSA), Tween-20, polysorbate 80 hydrochloric acid (HCl), methanol, recombinant human epidermal growth factor (EGF), CelLytic M, phosphatase inhibitor cocktail 2 and 3, chlorpromazine, nocodazole, Hank's Buffered Salt Solution (HBSS) haematoxylin, eosin and T-25/T-75 tissue culture flasks were purchased from Sigma-Aldrich (Dorset, UK).

Vinorelbine tartrate, Dynasore, DRAQ5 and the following antibodies: rabbit anti human EGFR (ab52894), rabbit anti human EGFR (phosphor Y1068, ab5644), mouse anti human β-actin (ab8224), rabbit anti human clathrin heavy chain (ab21679), goat anti rabbit IgG HRP conjugate (ab6721) were purchased from Abcam (Cambridge, UK).

Paraformaldehyde (PFA), Restore Plus stripping buffer, Pierce protease inhibitor mini tablets anti-lysosome-associated membrane protein 2 (LAMP2)-Alexa Fluor 488 and wheat germ agglutinin (WGA)-Alexa Fluor 488 were purchased from Thermo Fisher Scientific (Loughborough, UK). Lipofectamine RNAiMAX, NuPAGE 4-12% Bis-Tris gels, NuPAGE MOPS SDS running buffer (20X) and Hoescht 33342 was purchased from Invitrogen (Paisley, UK). Organic solvents (e.g. ethanol) not used in the organic synthesis section and 3-(4,5-dimethylthiazol-2-yl)-2,5-diphenyltetrazolium bromide (MTT) were purchased from VWR (Lutterworth, UK). Endothelial Cell Growth Medium 2 and Growth Medium 2 SupplementMix were purchased from Promocell (Heidelberg, Germany). Dulbecco's Modified Eagle Medium (DMEM) and bovine serum was purchased from Gibco (Loughborough, UK). Amine PEG azide was purchased from Nanocs Inc. (NY, USA). Vinorelbine base was purchased from Santa Cruz Biotechnology, Inc. (TX, USA) or Enzo Life Sciences, Inc (Exeter, UK). Anhydrous ethyl acetate and benzyl alcohol was purchased from Acros Organics (NJ, USA). Dimethyl sulfoxide was purchased from Honeywell (Bucharest, Romania), 3-azido-7-hydroxycoumarin was purchased from Jena Biosciences (Thuringia, Germany) and phenylacetylene was purchased from Alfa Aesar (MA, USA). Phosphotungstic acid was purchased from Agar Scientific (Stanstead, UK). Defined Cell Culture Medium (DCCM)-1 was purchased from Geneflow (Lichfield, UK). Afatinib was purchased from LC Laboratories (MA, USA). TMB substrate reagent set was purchased from BD Biosciences (Berkshire, UK). Human standard ABTS ELISA development kits were purchased from PeproTech (London, UK). Rabbit anti human cleaved caspase 3-Alexa Fluor 488 and rabbit anti human cleaved poly (ADP-ribose)

polymerase (PARP)-Alexa Fluor 647 was purchased from New England BioLabs (Hertfordshire, UK). All siRNA oligonucleotides were purchased from Ambion (Loughborough, UK). AccuGENE 5M sodium chloride and 1M Tris-HCl (pH 8) were purchased from Lonza (Slough, UK). Goat anti mouse IgG HRP conjugate was purchased from Dako (Ely, UK). Enhanced chemiluminescence (ECL) western blotting detection reagent and illustra NAP-25 size exclusion chromatography columns were purchased from GE Healthcare (Buckinghamshire, UK). Genistein was purchased from Fluorochem Ltd (Hadfield, UK) and 5-(N-Ethyl-N-isopropyl)amiloride was purchased from Tocris Bioscience (Bristol, UK). Histo-Clear was purchased from Scientific Laboratory Supplies Ltd. (Nottingham, UK) and Distyrene Plasticiser Xylene was from Solmedia Ltd. (Shrewsbury, UK). All tissue culture treated plates were purchased from Corning Life Sciences (Amsterdam, Netherlands) unless otherwise stated.

Human alveolar epithelial type I-like (transformed type I, TT1) cells, adenocarcinoma human alveolar basal epithelial cells (A549) and squamous cell carcinoma human lung epithelial cells (H226) were used from in-house stocks. Differentiated human lung adenocarcinoma cells (PC-9, formerly known as PC-14) were kindly gifted by Professor Michael Seckl. Mouse embryonic fibroblast cells (3T3-J2), primary patient derived non-small cell lung cancer cells (CRUK543) and complete epithelial growth medium were kindly gifted by Professor Sam Janes and Professor Charles Swanton. Human umbilical cord vein endothelial cells (HUVECs) were kindly gifted by Dr. Charlotte Dean.

2.2. Organic synthesis

2.2.1. General directions

All reactions were performed in oven-dried glassware and under a nitrogen atmosphere unless otherwise stated. **Solvents and reagents:** Acetonitrile (MeCN), dichloromethane (DCM), *N,N*-dimethylformamide (DMF) and tetrahydrofuran (THF) were dried and deoxygenated with a Grubbs Pure-Solv 400 purification system (Innovative Inc., USA). The moisture content of the solvents was monitored by Karl Fischer coulometric titration (Mettler-Toledo DL39). All other solvents and reagents were obtained from commercial suppliers as were used as received unless otherwise stated. **Chromatography:** Thin layer chromatography (TLC) was performed on aluminium plates coated with 0.2 mm thickness of silica (Merck 60 F_{254}). TLC plates were visualised by staining with 10% (w/v) potassium permanganate in 1M sulphuric acid and examination under ultraviolet light ($\lambda = 254$ nm). Flash chromatography (FC) was performed on silica gel (230-400 mesh, Merck Kieselgel 60 F_{254}). **Proton nuclear magnetic resonance spectrometry (^{1}H NMR):** Spectra were recorded at 400 MHz using a Bruker AMX-400 spectrometer. All chemical shifts (δ_H) are given in parts per million (ppm) and are referenced to the appropriate residual solvent peak, with abbreviations s, d, t, q and m denoting singlet, doublet, triplet, quartet and multiplet respectively or derivatives thereof. **Carbon (^{13}C) NMR spectroscopy:** Spectra were recorded at 100 MHz using a Bruker AMX-400 spectrometer. All chemical shifts (δ_C) are given in ppm and are referenced to the appropriate residual solvent peak where the abbreviations s and d denotes a singlet or doublet respectively. Coupling constants (*J*) are given in Hz. Spectra were assigned using correlation spectroscopy (COSY) and heteronuclear single quantum coherence spectroscopy (HSQC) and interpreted using MestReNova software (Mestrelab Research, USA). **Infra-red spectroscopy:** Infra-red spectra were recorded as thin films or as solids using a Perkin Elmer Two Spectrum ATR-IR Spectrometer. Only selected absorbances (ν_{max}) are reported. **Mass spectrometry:** High-

resolution mass spectra (m/z) were recorded using a Micromass Autospec Premier mass spectrometer and measurements are valid to ± 5 ppm.

2.2.2. 4-(3-chloro-4-fluoro-phenylamino)-7-chloro-6-nitro-quinazoline (3)
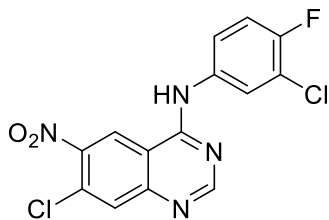
To a suspension of 7-chloro-6-nitro-4(3*H*)quinazolinone (1) (5.0 g, 22.16 mmol) in anhydrous MeCN (20 mL), a solution of freshly distilled Et_3N (3.72 mL, 26.68 mmol) was added dropwise at room temperature. The solution was stirred for 5 mins, followed by dropwise addition of phosphorous(V) oxychloride (2.5 mL, 26.90 mmol). The reaction mixture was heated to 80 °C and stirred for 5 h. Following this, a solution of 3-chloro-4-fluoroaniline (3.88 g, 26.60 mmol) in anhydrous dioxane (25 mL) was added dropwise to the reaction mixture and stirred for 1 h. The reaction was cooled to room temperature by the addition of H_2O (20 mL) before basifying with 50% (w/v) aqueous KOH (10 mL). The resulting solid was collected by filtration, then washed with cold H_2O and cold EtOH. The resulting orange-yellow solid **3** was dried at 40 °C *in vacuo* overnight and was used for the next step without further purification (7.83 g, 77 %). R_f (95:5 CHCl$_3$ / MeOH + 1 % NH$_4$OH) = 0.60; ^{1}H-NMR (400 MHz, d_6 DMSO) δ: 10.42 (bs, 1H), 9.41 (s, 1H), 8.75 (s, 1H), 8.14 (dd, *J* = 6.9, 2.6 Hz, 1H), 8.12 (s, 1H), 7.79 (ddd, *J* = 9.1, 4.4, 2.6 Hz, 1H), 7.49 (t, *J* = 9.1 Hz, 1H); ^{13}C-NMR (100 MHz, d_6 DMSO) δ: 158.1, 157.8, 155.0, 152.6, 151.7, 144.1, 135.6, 130.3, 129.0, 123.9, 122.9, 122.7 (d, *J* = 7.1 Hz), 119.0 (d, *J* = 18.3 Hz), 116.7 (d, *J* = 21.5 Hz), 113.3; IR (ATR) v_{max} 3418, 1692, 1566, 1498, 1424, 1319, 1082 cm^{-1}; HRMS (ES+): m/z calcd. for [M+H]$^+$ C$_{14}$H$_8$N$_4$O$_2$Cl$_2$F: 353.0008, found: 353.0010.

2.2.3. 4-(3-chloro-4-fluoro-phenylamino)-7-(phenylsulphonyl)-6-nitro-quinazoline (4)

To a mixture of **3** (6.0 g, 16.99 mmol) and benzenesulphinic acid (3.62 g, 22.08 mmol), anhydrous DMF (18 mL) was added at room temperature. The reaction mixture was heated to 90 °C and stirred for 6 h. The reaction was allowed to cool to room temperature, filtered, and the residue washed with ice cold MeOH (18 mL), H_2O (120 mL) and MeOH (6 mL). The resulting yellow solid **4** was dried at 50 °C *in vacuo* overnight and was used in the next step without further purification (6.78 g, 87 %). R_f (95:5 $CHCl_3$ / MeOH + 1 % NH_4OH) = 0.51; ^{1}H-NMR (400 MHz, d_6 DMSO) δ: 10.45 (bs, 1H), 9.32 (s, 1H), 8.88 (s, 1H), 8.64 (s, 1H), 8.14 (dd, J = 6.8, 2.6 Hz, 1H), 8.10-8.06 (m, 2H), 7.83-7.74 (m, 2H), 7.73-7.67 (m, 2H), 7.47 (t, J = 9.1 Hz, 1H); ^{13}C-NMR (100 MHz, d_6 DMSO) δ: 158.5, 157.9, 155.2, 152.8, 151.3, 143.3, 140.0, 137.0, 135.4, 134.5, 132.9, 129.6, 128.0, 124.2, 123.1, 122.9 (d, J = 7.1 Hz), 119.1 (d, J = 17.9 Hz), 116.9 (d, J = 21.9 Hz); IR (ATR) v_{max} 3405, 1658, 1498, 1359, 1319, 1152 cm^{-1}; HRMS (ES+): m/z calcd. for [M+H]$^+$ $C_{20}H_{13}N_4O_4SClF$: 459.0330, found: 459.0325.
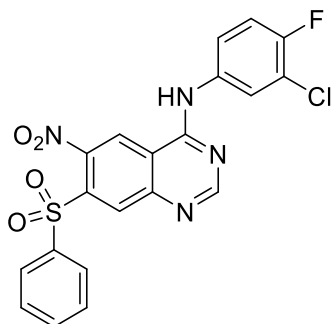
2.2.4. 4-(3-chloro-4-fluorophenyl)amino-6-nitro-7-[[(S)-tetrahydro-3-furanyl]oxy]-quinazoline (5)
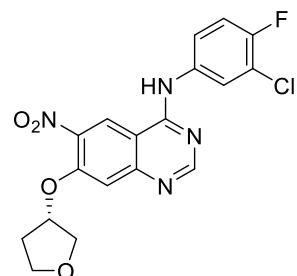
To a solution of potassium *tert*-butoxide (2.2 g, 19.60 mmol) in anhydrous THF (38 mL), (S)-(+)-tetrahydro-3-furanol (900 μL, 11.30 mmol) was added dropwise at room temperature and the mixture was stirred for 1 h. A solution of **4** (2.5 g, 5.45 mmol) in anhydrous THF (69 mL) was then added dropwise to the stirring reaction mixture using a dropping funnel over 30 min at room temperature. The reaction mixture was stirred at 25 °C for 4 h at which point complete consumption of **4** was observed by TLC. The solution was concentrated by rotary

evaporation and immediately "dry-loaded" onto the minimum amount of silica gel prior to purification by FC (CHCl$_3$/MeOH, 98:2) to give the product **5** as a yellow solid (1.46 g, 66 %). R$_f$ (95:5 CHCl$_3$ / MeOH + 1 % NH$_4$OH) = 0.27; ^{1}H-NMR (400 MHz, d$_6$ DMSO) δ: 10.11 (bs, 1H), 9.17 (s, 1H), 8.64 (s, 1H), 8.13 (dd, J = 6.7, 2.6 Hz, 1H), 7.77 (ddd, J = 7.0, 4.3, 2.2 Hz, 1H), 7.43 (s, 1H), 7.41 (t, J = 9.2 Hz, 1H), 5.56-5.32 (m, 1H), 4.00-3.93 (m, 1H), 3.92-3.75 (m, 3H), 2.40-2.27 (m, 1H), 2.10-2.00 (m, 1H); ^{13}C-NMR (100 MHz, d$_6$ DMSO) δ: 157.8, 157.4, 154.8, 153.1, 152.5, 139.3, 135.9, 123.8, 122.6 (d, J = 7.1 Hz), 122.0, 118.9 (d, J = 18.5 Hz), 116.7 (d, J = 21.8 Hz), 111.1, 108.0, 79.8, 72.0, 66.5, 32.3; IR (ATR) v_{max} 3325, 1624, 1573, 1538, 1496, 1422, 1339, 1253, 882 cm^{-1}; HRMS (ES+): m/z calcd. for [M+H]$^+$ C$_{18}$H$_{15}$N$_4$O$_4$ClF: 405.0766, found: 405.0786.

2.2.5. 4-(3-chloro-4-fluorophenyl)amino-6-amino-7-[[(S)-tetrahydro-3-furanyl]oxy]-quinazoline (6)
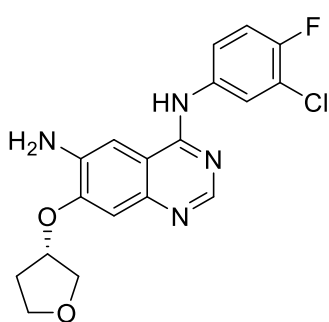
To a solution of **5** (1.34 g, 3.31 mmol) and NH$_4$Cl (496 mg, 9.27 mmol) in anhydrous DMF (22 mL), Raney nickel [, 1.5 mL, 50 % (w/v) in water] was added to the reaction mixture and stirred under a hydrogen atmosphere at 40 °C for 2 h. The reaction was then diluted with EtOH (10 mL), filtered through diatomaceous earth and washed with EtOH. The residue was concentrated by rotary evaporation and purified by FC (CHCl$_3$/MeOH, 95:5) to give **6** as a viscous brown oil (950 mg, 77 %). R$_f$ (95:5 CHCl$_3$ / MeOH + 1 % NH$_4$OH) = 0.13; ^{1}H-NMR (400 MHz, d_6 DMSO) δ: 9.40 (bs, 1H), 8.36 (s, 1H), 8.18 (dd, J = 6.9, 2.6 Hz, 1H), 7.80 (ddd, J = 9.1, 4.3, 2.6 Hz, 1H), 7.39 (t, J = 9.1 Hz, 1H), 7.38 (s, 1H), 7.04 (s, 1H), 5.40 (bs, 2H), 5.25-5.20 (m, 1H), 4.02-3.88 (m, 3H), 3.83-3.76 (m, 1H), 2.38-2.26 (m, 1H), 2.17-2.08 (m, 1H); ^{13}C-NMR (100 MHz, d_6 DMSO) δ: 155.0, 151.5, 150.5, 150.2, 144.5, 138.9, 137.5, 122.5, 121.5 (d, J = 6.4 Hz), 118.6 (d, J = 18.0 Hz), 116.4 (d, J = 21.7 Hz), 110.5, 107.3, 101.0, 78.0, 72.1, 66.6, 32.5; IR (ATR) v_{max} 3304, 1618, 1574,

1496, 1407, 1215, 1084, 838 cm^{-1}; HRMS (ES+): m/z calcd. for [M+H]$^{+}$ C$_{18}$H$_{17}$N$_{4}$O$_{2}$ClF: 375.1024, found: 375.1029.

2.2.6. Methyl-(*E*)-4-(*tert*-butoxycarbonyl-prop-2-ynyl-amino)but-2-enoate (9)
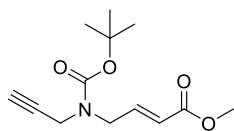
Initially, methyl 4-bromocrotonate was purified by FC (hexanes/Et$_2$O, 95:5) to give a colourless oil **7**, in order to obtain the *trans* isomer. Then, to a stirred solution of **7** (375 mg, 2.10 mmol) and K$_2$CO$_3$ (304 mg, 2.20 mmol) in anhydrous THF (25 mL), propargylamine (201 µL, 3.14 mmol) was added dropwise at room temperature. The reaction mixture was stirred for 56 h, after which the mixture was filtered and the residue washed with an excess of DCM. The resultant solution was concentrated under reduced pressure to afford **8** as a viscous orange oil. To a solution of the crude residue **8** and di-*tert*-butyl dicarbonate (695 mg, 3.14 mmol) in anhydrous DCM (5 mL), triethylamine (580 µL, 4.19 mmol) was added dropwise at room temperature and stirred for 16 h. After this time, the mixture was filtered and the white solid was washed with DCM (30 mL). The mother liqueur was then washed with H$_2$O (20 mL), 1M HCl (20 mL), H$_2$O (20 mL), saturated NaCl (20 mL), dried over MgSO$_4$ and concentrated *in vacuo*. The crude residue was purified by FC (hexanes/Et$_2$O, 4:1) to yield **9** as a colourless oil (270 mg, 48 %). R$_f$ (4:1 hexanes/ Et$_2$O) = 0.14; ^{1}H-NMR (400 MHz, CDCl$_3$) δ: 6.83 (dt, *J* = 15.7, 5.3 Hz, 1H), 5.86 (d, *J* = 15.7 Hz, 1H), 4.14-3.89 (m, 4H), 3.69 (s, 3H), 2.20 (t, *J* = 2.5 Hz, 1H), 1.42 (s, 9H); ^{13}C-NMR (100 MHz, CDCl$_3$) δ 166.5, 154.6, 143.6, 121.9, 81.0, 79.0, 72.3, 51.7, 47.1, 35.9, 28.3; IR (ATR) v_{max} 2976, 1722, 1697, 1455, 1403, 1366, 1273, 1246, 1162, 1125 cm^{-1}; HRMS (ES+): m/z calcd. for [M+Na]$^{+}$ C$_{13}$H$_{19}$NO$_{4}$Na: 276.1212, found: 276.1216.

2.2.7. 5-(1,2-dithiolan-3-yl)pentan-1-ol (11)
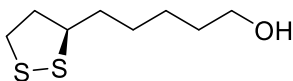
To a suspension of (±)-α-lipoic acid **10** (500 mg, 2.42 mmol) in anhydrous THF (30 mL), borane dimethylsulphide complex (1.8 mL,

2M in THF, 3.64 mmol) was added dropwise at 0 °C with stirring. The solution was gradually warmed to room temperature and after 3 hours the reaction was quenched with H_2O (20 mL). The phases were separated and the aqueous phase was extracted with EtOAc (3 x 30 mL). The combined organic extracts were washed with saturated $NaHCO_3$ (60 mL), dried over $MgSO_4$ and concentrated *in vacuo* to afford **12** as a yellow oil which was used in the next step without further purification (450 mg, 97 %). R_f (4:1 Hexane / EtOAc) = 0.80; ^{1}H-NMR (400 MHz, $CDCl_3$) δ: 3.64 (t, J = 6.5 Hz, 2H), 3.62-3.53 (dq, J = 8.4, 6.5 Hz, 1H), 3.23-3.07 (m, 2H), 2.51-2.42 (m, 1H), 1.97-1.86 (m, 1H), 1.75-1.34 (m, 9H); ^{13}C-NMR (100 MHz, $CDCl_3$) δ: 63.0, 56.8, 40.4, 38.6, 35.0, 32.7, 29.2, 25.7; IR (ATR) v_{max} 3367, 2930, 1646, 1635, 1557, 1540, 1506 cm^{-1}; HRMS (ES+): m/z calcd. for [M+H]$^+$ $C_8H_{17}OS_2$: 193.0721, found 193.0727.

2.2.8. 5-(1,2-dithiolan-3-yl)pentan-1-tosylate (12)
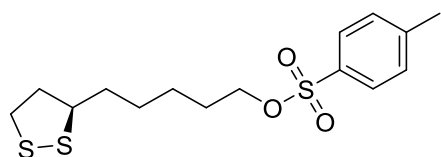
To a solution of **11** (170 mg, 0.88 mmol) in anhydrous DCM (13 mL), DMAP (143 µL, 1.77 mmol) and *p*-Toluenesulfonyl chloride (137 µL, 1.77 mmoL) were added sequentially in a dropwise manner at 0 °C with stirring. The reaction was slowly warmed to room temperature and was stirred for 16 h. The mixture was then extracted with DCM (3 x 15 mL) and the pooled organic phases were washed with saturated NaCl (25 mL), dried over Na_2SO_4 and concentrated *in vacuo*. The crude residue was purified by FC (hexanes/ EtOAc, 4:1) to give **12** as a yellow oil (150 mg, 62%). R_f (4:1 Hexane / EtOAc) = 0.29; ^{1}H-NMR (400 MHz, $CDCl_3$) δ: 7.79 (d, J = 8.3 Hz, 2H), 7.35 (d, J = 8.3 Hz, 2H), 4.02 (t, J = 6.4 Hz, 2H), 3.52 (dq, J = 8.6, 6.4 Hz, 1H), 3.21-3.06 (m, 2H), 2.52-2.39 (m, 1H), 2.45 (s, 3H), 1.88 (dq, J = 12.7, 6.9 Hz, 1H), 1.70-1.58 (m, 4H), 1.44-1.30 (m, 4H); ^{13}C-NMR (100 MHz, $CDCl_3$) δ:144.9, 130.0, 128.0, 125.4, 70.5, 56.6, 40.4, 38.6, 34.8, 28.8, 28.7, 25.3, 21.8; IR (ATR) v_{max}

2929, 2856, 1355, 1275, 1260, 1174, 1096, 948, 813 cm^{-1}; HRMS (ES+): m/z calcd. for

[M+H]$^+$ C$_{15}$H$_{23}$O$_4$S$_3$: 363.0753, found 363.0590.

2.2.9. 5-(1,2-dithiolan-3-yl)pentyl-1-azide (13)
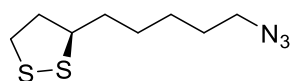
To a solution of **12** (150 mg, 0.55 mmol) in anhydrous DMF (8.2 mL), sodium azide (361 mg, 5.55 mmol) was added at room temperature. The mixture was heated to 60 °C and stirred for 16 h, after which H$_2$O was added and the mixture was extracted with EtOAc (3 x 10 mL). The organic phases were pooled and washed with saturated NaCl (5 x 5 mL), dried over Na$_2$SO$_4$ and concentrated *in vacuo* to afford **13** as a yellow oil which was used without further purification (71 mg, 76 %). R$_f$ (4:1 Hexane / EtOAc) = 0.73; ^{1}H-NMR (400 MHz, CDCl$_3$) δ: 3.57 (dq, J = 8.5, 6.4 Hz, 1H), 3.27 (t, J = 6.8 Hz, 2H), 3.22-3.08 (m, 2H), 2.52-2.42 (m, 1H), 1.91 (dq, J = 12.7, 7.0 Hz, 1H), 1.74-1.56 (m, 4H), 1.54-1.36 (m, 4H); ^{13}C-NMR (100 MHz, CDCl$_3$) δ: 56.6, 51.4, 40.4, 38.6, 34.9, 29.0, 28.8, 26.7; IR (ATR) v$_{max}$ 2929, 2855, 2092, 1290, 1245, 1162 cm^{-1}; HRMS (EI+): m/z calcd. for [M+H]$^+$ C$_8$H$_{15}$N$_3$S$_2$: 217.0705, found 217.0707.

2.2.10. *tert*-butyl-(*S,E*)-(4-((4-((3-chloro-4-fluorophenyl)amino)-7-((tetrahydrofuran-3-yl)oxy)quinazolin-6-yl)amino)-4-oxobut-2-en-1-yl)(prop-2-yn-1-yl)carbamate (14)
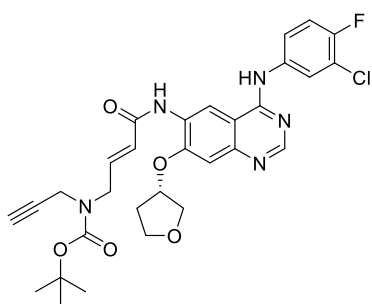
To **6** (261 mg, 0.69 mmol) a solution of **9** (250 mg, 1.04 mmol) in anhydrous DCM (12.5 mL) was added at room temperature and stirred. Trimethylaluminium (700 µL, 2M in hexane, 1.38 mmol) was added dropwise to the reaction mixture and stirred at room temperature until complete consumption of **6** was observed by TLC. The mixture was quenched with saturated NaHCO$_3$ and the phases were partitioned. The aqueous layer was extracted with DCM (3 x 15 mL) and the organic layers were combined, washed with saturated NaCl (20 mL), dried over Mg$_2$SO$_4$ and concentrated *in*

vacuo. The crude residue was purified by FC (CHCl₃/MeOH, 98:2) to give **14** as a colourless oil (400 mg, 95 %). R_f (95:5 CHCl₃ / MeOH + 1 % NH₄OH) = 0.29; ¹H-NMR (400 MHz, CDCl₃) δ: 9.06 (s, 1H), 8.60 (s, 1H), 8.07 (s, 1H), 7.83 (dd, J = 6.6, 2.7 Hz, 1H), 7.48 (ddd, J = 8.9, 4.1, 2.7 Hz, 1H), 7.16 (s, 1H), 7.06 (t, J = 8.8 Hz, 1H), 6.95 (dt, J = 15.2, 5.3 Hz, 1H), 5.17-5.11 (m, 1H), 4.20-3.98 (m, 8H), 3.96-3.89 (m, 1H), 2.73 (bs, 1H), 2.47-2.36 (m, 1H), 2.32 (t, J = 2.4 Hz, 1H), 2.28-2.18 (m, 1H), 1.49 (s, 9H); ¹³C-NMR (100 MHz, CDCl₃) δ: 163.7, 156.9, 156.0, 154.8, 154.5, 153.6, 150.6, 148.0, 142.0, 135.2, 128.1, 125.1, 124.6, 124.3, 121.8 (d, J = 6.7 Hz), 120.9 (d, J = 18.4 Hz), 116.5 (d, J = 22.2 Hz), 110.3, 109.5, 108.4, 81.3, 79.5, 79.3, 73.1, 67.3, 47.5, 32.8, 28.5; IR (ATR) v_{max} 2976, 1697, 1683, 1624, 1539, 1498, 1456, 1429, 1396, 1245, 1162 cm⁻¹ HRMS (ES+): m/z calcd. for [M+H]⁺ C₃₀H₃₂N₅O₅ClF: 596.2076, found 596.2068.

2.2.11. *tert*-butyl(((1-(5-((*R*)-1,2-dithiolan-3-yl)pentyl)-1*H*-1,2,3-triazol-4-yl)methyl)((*E*)-4-((4-((3-chloro-4-fluoro-phenyl)amino)-7-((((*S*)-tetrahydrofuran-3-yl)oxy)quinazolin-6-yl)amino)-4-oxobut-2-en-1-yl)carbamate (15)
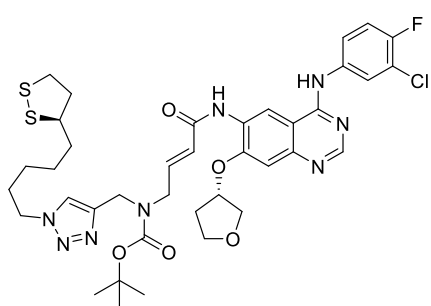
A solution of CuSO₄ (3.7 mg, 0.023 mmol) and (+)-sodium L-ascorbate (9.1 mg, 0.046 mmol) in distilled H₂O (0.6 mL) was added to a stirred solution of **13** (30 mg, 0.138 mmol), **14** (69 mg, 0.115 mmol), and Et₃N (19 μL, 0.138 mmol) in MeOH (0.6 mL) and DCM (1.2 mL). The resulting mixture was rapidly stirred for 5 h. The phases were separated and the aqueous phase was extracted with DCM (5 x 5 mL). The organic phases were collected, washed with saturated NH₄Cl (aq) (5 mL), dried over MgSO₄ and concentrated *in vacuo*. Purification of the residue by FC (CHCl₃/MeOH, 98:2) afforded the product **15** as a yellow oil (60 mg, 65 %). R_f (95:5 CHCl₃ / MeOH + 1 % NH₄OH) = 0.33; ¹H-NMR (400 MHz, CDCl₃) δ: 9.06 (s, 1H), 8.60 (s, 1H), 8.18 (s, 1H), 8.02 (bs, 1H), 7.84 (dd, *J* = 6.6, 2.7 Hz, 1H), 7.49 (ddd, *J* = 8.9, 4.2, 2.7 Hz, 1H), 7.14

(s, 1H), 7.06 (t, J = 8.8 Hz, 1H), 6.88 (dt, J = 15.2 Hz, 5.3 Hz, 1H), 6.16 (d, J = 15.2 Hz, 1H), 5.17-5.09 (m, 1H), 4.48 (s, 1H), 4.32-4.27 (m, 2H), 4.20-3.99 (m, 5H), 3.97-3.88 (m, 1H), 3.50 (dq, J = 8.7, 6.3 Hz, 1H), 3.19-3.03 (m, 2H), 2.92 (bs, 1H), 2.47-2.34 (m, 2H), 2.32-2.21 (m, 1H), 1.94-1.80 (m, 2H), 1.69-1.54 (m, 2H), 1.47 (s, 9H), 1.38-1.16 (m, 4H), 0.90-0.78 (m, 2H); ^{13}C-NMR (100 MHz, CDCl$_3$) δ: 163.8, 156.9, 155.9, 154.6, 153.5, 150.8, 148.2, 141.9, 135.3, 129.7, 128.1, 124.9, 124.2, 122.9, 121.8 (d, J = 6.7 Hz), 120.8 (d, J = 19.1 Hz), 116.4 (d, J = 21.8 Hz), 110.6, 109.5, 108.4, 80.8, 79.5, 77.4, 73.0, 67.3, 56.5, 50.3, 40.4, 38.6, 34.7, 32.9, 30.2, 29.8, 28.7, 28.5, 26.4; IR (ATR) v_{max} 1942, 1867, 1828, 1771, 1716, 1697, 1683, 1632, 1557, 1539, 1506, 1456, 1418 cm^{-1}; HRMS (EI+): m/z calcd. for [M+H]$^+$ C$_{38}$H$_{47}$N$_8$O$_5$ClFS$_2$: 813.2838, found 813.2783.

2.2.12. (*E*)-4-(((1-(5-((*R*)-1,2-dithiolan-3-yl)pentyl)-1H-1,2,3-triazol-4-yl)methyl)amino)-*N*-(4-((3-chloro-4-fluorophenyl)amino)-7-(((*S*)-tetrahydrofuran-3-yl)oxy)quinazolin-6-yl)but-2-enamide (16)
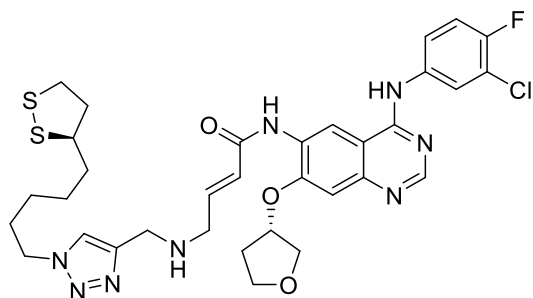
To a solution of **15** (20 mg, 0.025 mmol) in anhydrous dioxane (800 µL) was added concentrated HCl (50 µL, 37 %) at room temperature. After 45 mins, the reaction was quenched by the addition of saturated NaHCO$_3$ (aq).

The phases were separated and the product was extracted with DCM (5 x 3 mL), dried over Na$_2$SO$_4$ and concentrated *in vacuo* to afford the product **16** as a yellow oil with no further purification required (17 mg, 98 %). R$_f$ (95:5 CHCl$_3$ / MeOH + 1 % NH$_4$OH) = 0.28; ^{1}H-NMR (400 MHz, CDCl$_3$) δ: 9.09 (s, 1H), 8.62 (s, 1H), 8.17 (s, 1H), 7.90 (dd, J = 7.1 Hz, 3.1 Hz, 1H), 7.80 (bs, 1H), 7.53 (ddd, J = 9.1, 4.2, 2.7 Hz, 1H), 7.49 (s, 1H), 7.16 (s, 1H), 7.1 (t, J = 8.8 Hz, 1H), 7.07-7.01 (m, 2H), 6.30 (d, J = 15.3 Hz, 1H), 5.20-5.10 (m, 1H), 4.35 (t, J = 7.1 Hz, 2H), 4.20-3.99 (m, 5H), 3.95-3.81 (m, 1H), 3.58-3.38 (m, 2H), 3.21-3.02 (m, 2H), 2.50-2.34 (m,

2H), 2.31-2.21 (m, 1H), 1.97-1.83 (m, 2H), 1.71-1.58 (m, 2H), 1.53-1.26 (m, 4H), 0.91-0.87 (m, 2H); ^{13}C-NMR (100 MHz, CDCl$_3$) δ: 164.0, 157.0, 154.6, 148.2, 142.9, 130.0, 128.1, 126.4, 124.2, 122.5, 121.9 (d, J = 7.3 Hz), 116.5 (d, J = 20.7 Hz), 110.0, 109.5, 108.3, 90.1, 79.4, 73.1, 67.4, 67.2, 56.5, 50.4, 43.8, 40.4, 38.6, 34.8, 32.8, 32.1, 30.2, 29.8, 26.4, 22.8, 14.3; IR (ATR) v_{max} 2985, 2860, 1676, 1624, 1534, 1498, 1450, 1428, 1394, 1332, 1274, 1260, 1212 cm^{-1}; HRMS (EI+): m/z calcd. for [M+H]$^+$ C$_{33}$H$_{39}$N$_8$O$_3$ClFS$_2$: 713.2259, found 713.2272.

2.2.13.(*S*,*E*)-*N*-(4-((3-chloro-4-fluorophenyl)amino)-7-((tetrahydrofuran-3-yl)oxy)quinazolin-6-yl)-4-(prop-2-yn-1-ylamino)but-2-enamide
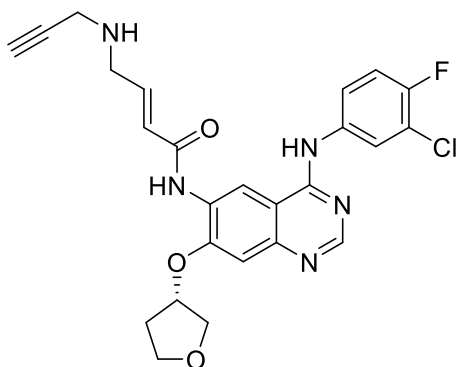
To a solution of **14** (10 mg, 0.017 mmol) in dry dioxane (600 μL) was added concentrated HCl (50 μL, 37 %) at room temperature with stirring. After 4 h, the reaction was quenched by the addition of saturated NaHCO$_3$ $_{(aq)}$. The product was extracted with DCM (5 x 3 mL), dried over Na$_2$SO$_4$ and concentrated at reduced pressure to afford the product as a light brown oil (8 mg, 96%). R$_f$ (95:5 CHCl$_3$ / MeOH + 1 % NH$_4$OH) = 0.29; ^{1}H-NMR (400 MHz, CDCl$_3$) δ: 9.10 (s, 1H), 8.63 (s, 1H), 8.07 (s, 1H), 7.92 (dd, J = 6.6, 2.6 Hz, 1H), 7.84 (s, 1H), 7.53 (ddd, J = 7.9, 5.0, 2.8 Hz, 1H), 7.18 (s, 1H), 7.16-7.05 (m, 2H), 6.26 (d, J = 15.2 Hz, 1H), 5.17 (t, J = 5.1 Hz, 1H), 4.20-4.00 (m, 4H), 3.94 (td, J = 8.5, 4.5 Hz, 1H), 3.62 (dd, J = 5.0, 1.7 Hz, 2H), 3.51 (d, J = 2.4 Hz, 2H), 2.48-2.36 (m, 1H), 2.31-2.20 (m, 2H); ^{13}C-NMR (100 MHz, CDCl$_3$) δ: 163.7, 156.6, 154.3, 150.3, 147.8, 144.3, 134.8, 128.1, 124.1, 123.9, 121.5 (d, J = 6.3 Hz), 120.7, 116.3 (d, J = 22.5 Hz), 109.7, 109.2, 108.2, 81.2, 79.3, 72.8, 72.0, 66.9, 48.5, 37.6, 32.6; HRMS (EI+): m/z calcd. for [M+H]$^+$ C$_{25}$H$_{24}$N$_5$O$_3$ClF: 496.1552, found 496.1550.

2.3. Synthesis of PLGA-*b*-PEG-N$_3$

To a solution of PLGA-OH (200 mg, 0.012 mmol, 7000-17000 MW, 50:50 lactide:glycolide, inherent viscosity 0.16-0.24 dL/g) and NHS (13.8 mg, 0.12 mmol) in anhydrous DCM (1.5 mL), a solution of DCC (24.8 mg, 0.12 mmol) in anhydrous DCM (0.5 mL) was added in a dropwise fashion at 0 °C. The reaction mixture was allowed to warm to room temperature and was stirred for 16 h. Subsequently, the solution was added dropwise into ice-cold Et_2O (30 mL) and the resultant precipitate was centrifuged at 3000 x g for 10 mins. The pellet was washed a further two times with Et_2O (10 mL), dried *in vacuo* for 4 h and then dissolved in $CHCl_3$ (1 mL). To this stirred solution was added NH_2-PEG-N_3 (48.8 mg, 0.014 mmol, 3400 MW) in $CHCl_3$ (0.5 mL) followed by dropwise addition of DIPEA (18.1 mg, 0.14 mmol) and the reaction was stirred for 16 h at room temperature. Following this, the reaction mixture was added dropwise to ice-cold Et_2O (30 mL) and centrifuged at 3000 x g for 5 mins. The pellet was washed a further two times with Et_2O (10 mL) and dried *in vacuo* to yield to block copolymer PLGA-PEG-N_3 (210 mg, 86%). ^{1}H-NMR (400 MHz, $CDCl_3$) δ: 5.22 (m, -O**CH**(CH_3)CONH-), 4.82 (m, -O**CH$_2$**COO-), 3.64 (s, -**CH$_2$CH$_2$**O-), 1.59 (d, -OCH(**CH$_3$**)CONH-). IR (ATR) v_{max} 3505, 2884, 2109, 1715, 1453, 1421, 1389, 1362, 1342, 1277, 1166, 1083 cm^{-1}.

2.4. Preparation of vinorelbine-encapsulated nanoparticles (VRL-NPs)

Optimised nanoparticles (NPs) were created *via* a nanoemulsion process based on a modified oil-in-water (o/w) emulsification solvent evaporation (ESE) method. An organic phase consisting of vinorelbine base (VRL), pamoic acid (PAM) and PLGA-PEG-N_3 in a solution of ethyl acetate/benzyl alcohol/DMSO (80:14:6 v/v/v) was added to a cooled, immiscible aqueous phase consisting of 1% (w/v) polyvinyl alcohol (PVA, 31000-50000 MW, 87-89% hydrolysed). This mixture was vortexed rapidly for 15 s prior to sonication on ice with a Branson 450 digital sonifier using 3 x 20 s pulses at an amplitude of 120W with 5 s intermissions between pulses. After sonication, the resulting emulsion was poured into a

stirring sodium phosphate buffer solution (0.25 M, pH 6.5) which was then stirred for 2 h to allow for evaporation of organic solvents and hardening of the NPs. Subsequently, the NPs were centrifuged at 9000 x g for 30 mins, the supernatant was decanted, and nanoparticles were resuspended in water. The nanoparticles were washed likewise a further two times and reconstituted either in water and lyophilised for further analysis or 10% (w/v) sucrose for storage at -20 °C. Empty (blank) NPs containing no VRL or PAM were fabricated in the same fashion as outlined above.

2.5. Pamoate salt formation

The formation of a hydrophobic ion pair between VRL and PAM was observed by ^{13}C NMR spectroscopy. The salt solution was composed of VRL base and PAM (0.5 M equivalent) suspended in benzyl alcohol/d_6-DMSO in a 1:1 (v/v) mixture and control solutions of base and acid were made using the same solvent. Spectra were acquired using a Bruker DRX-400 spectrometer at 100 MHz with 16384 scans and peaks were assigned using MestReNova software, with the guidance of the NMR prediction function in ChemDraw v18.0 (PerkinElmer, MA, USA).

2.6. Preparation of fluorescent nanoparticles

Fluorescent NPs were created based on an ESE method that was initially used for encapsulation of VRL. This method was found not to be suitable for encapsulation of amphiphilic weak bases such as VRL but the sufficient hydrophobicity of the fluorophores used in this work meant that encapsulation using the following method was feasible. An organic phase consisting of PLGA-PEG-N$_3$ and either VRL or coumarin-6 dissolved in DCM/acetone (4:1 v/v) was added to an aqueous phase consisting of a 1% PVA solution. This mixture was rapidly vortexed for 15 s and sonicated on ice with Branson 450 digital sonifier using 3 x 20 s pulses at an amplitude of 120W with 5 s intermissions between pulses. The emulsion was then poured into a stirred

solution of water and was further stirred for 4 h to allow the volatile organic solvents to completely evaporate. Subsequently, the NPs were centrifuged at 9000 x g for 30 mins, the supernatant was decanted and resuspended in water. The NPs were washed likewise a further two times and reconstituted either in water or 10% (w/v) sucrose, lyophilised and stored at - 20 °C.

2.7. Assembly of AFB-AuNPs

To a 1 mL solution of AuNPs, 70 µL of **16** (1 mM in DMSO) was added dropwise and stirred overnight in the dark at room temperature. Following this, the reaction mixture was purified using centrifugal filtration units (10kDa MWCO, Amicon Ultra-15, regenerated cellulose, Millipore, USA) at 2800 x g for 10 mins. AuNPs were washed with twice with water in this fashion, followed by the dropwise addition of 10 µL of 2 mM poly(ethylene glycol) 2-mercaptoethyl ether acetic acid (HS-PEG-COOH, MW 3400) to the AuNP solution. This was stirred overnight in the dark at room temperature and PEGylated AFB-AuNPs were purified using centrifugal filtration as described above and resuspended in water back to their original volume prior to conjugation.

2.8. Optimisation of click chemistry conditions

To optimise the reaction conditions for click chemistry to the surface of NPs, a fluorogenic coumarin assay[280] was implemented. The initial set of reactions were performed using conditions (0.25 mM CuSO$_4$, 1.25 mM THPTA ligand, 5 mM sodium ascorbate) known to give complete conversion of 3-azido-7-hydroxycoumarin to the fluorescent triazole derivative (λ_{ex} = 404 nm, λ_{em} = 477 nm)[281]. Phenylacetylene was used as a model aromatic alkyne. When these reaction conditions were applied to **14**, the product produced exhibited approximately 60% of the fluorescence emitted by the calibration triazole. Subsequent increases in Cu and ligand concentrations to five times that originally used were found to enable complete conversion of

alkyne bearing **14**. This reaction was then repeated with **17**, also exploring the use of a different ligand (TBTA).

To explore the efficacy of these reaction conditions the following experiments were performed using azide bearing NPs (PLGA-PEG-N$_3$ NPs) and Fluor 488-alkyne (λ_{ex} = 501 nm, λ_{em} = 525 nm) as a surrogate for **17**. PLGA-PEG-N$_3$ NPs (5 mg) were suspended in 790 µL PBS followed by addition of Alexa Fluor 488 alkyne (50 µL, 3.4 mM in DMSO). To this was added a premixed solution of CuSO$_4$ (10 µL, 50 mM) and THPTA (50 µL, 50 mM and sodium ascorbate (100 µL, 100 mM). The reaction was stirred overnight at room temperature, after which the reaction was quenched by exposure to air and addition of 5 µL saturated EDTA solution. The reaction mixture was purified using an illustra NAP-25 column where 1 mL fractions were collected. The fluorescence of each fraction was determined using a SpectraMax i3X (Molecular Devices, CA, USA) and quantified by reference to a calibration curve (0-100 µg/mL, R^2 = 0.9991). To ensure the measured fluorescence was due to Huisgen 1,3 dipolar cycloaddition, the above reaction was repeated after 3 h pre-incubation of a large excess of benzylazide in the presence of alkyne (quenching of the alkyne groups) and in the absence of the Cu/THPTA/sodium ascorbate (catalyst system).

2.9. Preparation of afatinib-vinorelbine nanoparticles

A typical preparation was created by diluting 200 µL of freshly made VRL-NPs (~30 mg/mL) with 590 µL of PBS. To this was added 50 µL of **17** (1 mM in DMSO) followed by 60 µL of a premixed solution of CuSO$_4$/THPTA (1:5, 50 mM). Finally, 100 µL of a freshly prepared solution of sodium ascorbate (100 mM) was added and the reaction vessel was immediately sealed, shaken and stirred overnight at room temperature in the dark. Subsequently, the reaction was quenched by exposure to air and addition of 5 µL saturated EDTA solution. The mixture was purified by centrifugal filtration (10 kDa MWCO) at 4000 x *g* for 10 mins at 4°C. The NPs

were washed twice with water and resuspended back to their original volume. NPs were used immediately or stored at 4°C for up to one week.

2.10. Characterisation of nanoparticles

Transmission electron microscopy (TEM) was performed using a JEOL 1400 Plus electron microscope (JEOL Ltd, Hertfordshire, UK) with an accelerating voltage of 120 keV. A 10 µL aliquot of the NP solution (20 µg/mL) was added to a Formvar carbon-coated, 300 mesh TEM copper grid (Agar Scientific, Essex, UK) and left to evaporate. Polymeric NPs were negatively stained with 2% (w/v) phosphotungstic acid prior to imaging whereas AuNPs were imaged without any modifications. Images were captured using an AMT XR16 camera and processed using AMT image capture software (Wolburn, MA, USA).

Dynamic light scattering and zeta potential measurements of NP formulations were obtained using a Zetasizer Nano ZS ZSP (Malvern Instruments Ltd, Worcestershire, UK). Samples were diluted to 20 µg/mL in water, injected into a DTS 1070 folded capillary cell (Malvern Instruments Ltd, UK) and analysed using a He-Ne laser ($\lambda = 633$ nm) with a scattering angle of 137°. Each sample was analysed in triplicate with each run consisting of ten measurements.

UV-visible spectroscopy was employed to further characterise AuNP formulations. AuNPs were diluted in water to 100µg/mL and 100 µL of this solution was added to a 96 well plate. The spectral profile was acquired using a SpectraMax i3X in the wavelength range from 350 to 700 nm, with a resolution of 1 nm.

2.11. Calculation of encapsulation efficiency and loading efficiency

Determination of the VRL content of NP formulations was achieved using ultraviolet-liquid chromatography-mass spectrometry (UV-LC-MS). A known quantity of NPs was dissolved in DMSO and sonicated for 2 mins to fully release encapsulated VRL. The solution was then analysed using an Agilent 1260 Infinity II LC System coupled with a variable wavelength

detector module and an Agilent 6130 quadrupole LC/MS (Agilent Technologies, CA, USA).

A Gemini C18 reverse-phase column (150 x 4.6 mm internal diameter, pore size 5 μm, Phenomenex, Macclesfield, UK) was utilised and the column temperature was maintained at 40 °C throughout the analysis. Gradient elution was employed with a mobile phase consisting of water with 0.1 % (v/v) formic acid (A) and acetonitrile with 0.1% (v/v) formic acid (B) with the sequence 10% B to 90% B to 10% B. The eluent absorbance was monitored by UV detection ($\lambda = 269$ nm). The flow rate was held at 1 mL/min and the injection volume used was 5 μL. Quantification was VRL was achieved by reference to a calibration curve (0-100 μg/mL, $R^2 = 0.9973$) and VRL detection was confirmed by electrospray ionisation mass spectrometry display of a molecular species with a *m/z* ratio of 778.9 corresponding to the molecular weight of VRL. Drug loading (DL) and encapsulation efficiency (EE) were calculated from the following formulae:

$$DL \left(\frac{drug\ (\mu g)}{NP\ (mg)}\right) = \frac{amount\ of\ VRL\ in\ NP\ (\mu g)}{total\ weight\ of\ NP\ (mg)}$$

$$EE\ (\%) = \frac{amount\ of\ VRL\ in\ NP\ (mg)}{initial\ amount\ of\ VRL\ added\ (mg)}\ x\ 100$$

Determination of AFB content of NPs was performed in a similar fashion whereby polymeric NPs were dissolved in DMSO and an aliquot of this solution was analysed by UV-vis spectroscopy ($\lambda = 345$ nm) using a SpectraMax Plus 384 spectrophotometer (Molecular Devices, UK). AFB content was quantified by reference to a calibration curve (0-500 μg/mL, $R^2 = 0.9942$). Similarly, the AFB content of AuNPs was determined spectrophotometrically, whereby AFB-AuNPs were directly analysed as well as the supernatant generated from the purification steps. The concentration of bound AFB was determined with reference to the above calibration curve and conjugation efficiency was calculated from the following equation:

$$CE\ (\%) = \frac{[amount\ of\ AFB\ on\ AuNPs\ (\mu g) - AFB\ in\ supernatant\ (\mu g)]}{initial\ amount\ of\ AFB\ added\ (\mu g)}\ x\ 100$$

2.12. *In vitro* drug release

Drug-containing polymeric NPs were diluted to a volume of 1 mL in PBS and placed inside a dialysis device (Float-A-Lyzer, MWCO 3500, SpectrumLabs, CA, USA). This was then suspended in 10 mM PBS (pH 7.4) containing 10% (w/v) urea and incubated at 37 °C with mild agitation (100 rpm). At predetermined time intervals, 1 mL aliquots were taken and stored at -80 °C for future analysis. The volume taken was replaced with fresh buffer to maintain the original volume and physiological sink conditions. At the end of the experiment, the NP solution was dissolved in DMSO and in order to determine released drug, the aliquots were analysed using the LC-MS method described above. The same method was applied for Afb-AuNPs except release of Afb-A was determined in PBS at pH 7.4 as above and in acetate buffer (10 mM, pH 5.5) both containing 0.5% (v/v) polysorbate 80. Absorbance measurements of release medium (λ = 345 nm) were acquired using a ND-1000 spectrophotometer (Thermo Fisher Scientific, DE, USA). The release kinetics were determined by comparing the drug concentration at each time point with the concentration of drug at the beginning of the experiment.

2.13. Cell culture

Human alveolar epithelial type I-like (TT1) cells were cultured to confluence in tissue culture plates or T-75 flasks using defined cell culture medium-1 (DCCM-1) supplemented with 10% (v/v) new-born calf serum (NCS) and 1% (v/v) penicillin/streptomycin/glutamine (PSG). Lung adenocarcinoma A549, PC-9 and squamous cell carcinoma H226 cells were cultured likewise using Roswell Park Memorial Institute (RPMI)-1640 medium without phenol red, supplemented with 10% foetal bovine serum (FBS) and 1% PSG. Human umbilical vein endothelial cells (HUVECs) were cultured using Endothelial Cell Growth Medium 2

supplemented with Growth Medium 2 SupplementMix. Throughout, cells were maintained in a humidified incubator at 37 °C, 5% CO_2.

Cells were passaged upon reaching confluency in T-75 tissue culture flasks. Medium was aspirated and cells were washed twice with PBS prior to the addition of 5 mL of trypsin-EDTA 1x solution. At this point, flasks were incubated at 37 °C, 5% CO_2 for 5 mins to facilitate detachment of the cells which could be observed by eye. Serum-containing medium was added to neutralise the trypsin and cells were centrifuged at 292 x g for 10 mins at room temperature. The supernatant was decanted, and the cell pellet was resuspended in an appropriate volume of complete medium. The cell suspensions were then counted using a haemocytometer and seeded at a density of $1x10^4$ cells/well in 96 well plates or $0.5x10^6$ cells/well in 6 well plates and confluence was achieved within 48 h. Approximately 200 µL of cells were added to new T-75 flasks where 15 mL of appropriate complete medium was added and flasks were then incubated at 37 °C, 5% CO_2.

Patient derived, primary human NSCLC ('543') cells were cultured in accordance with an established protocol[282,283]. Initially, 3T3-J2 mouse embryonic fibroblasts were cultured in Dulbecco's modified eagle medium (DMEM) containing 9% (v/v) bovine serum and 1% (v/v) penicillin/streptomycin (PS). When the cells reached 90% confluency, feeder layers were generated by the addition of mitomycin C to the fibroblast growth medium at a final concentration of 0.4 µg/mL. After 3 h incubation at 37 °C, 5% CO_2, mitotically inactivated fibroblasts were washed with PBS, trypsinised and re-plated at 20,000 cells/cm^2. The feeder cells were incubated overnight in fibroblast growth medium to allow adherence prior to the addition of tumour cells. The fibroblast medium was aspirated, tumour cells were added to the feeder layer and the co-culture was incubated with complete epithelial cell culture medium (DMEM/Ham's F12 nutrient mixture, 3:1 v/v, PS, 5% FBS, 5 µM Y-27632, 25 ng/mL hydrocortisone, 0.125 ng/mL rhEGF, 5 µg/mL insulin, 0.1 nM cholera toxin, 250 ng/mL

amphotericin B and 10 µg/mL gentamicin). Once the tumour cells reached a suitable confluency, cells were washed with PBS and the differential sensitivities of fibroblasts and epithelial (tumour) cells to trypsin was leveraged. The co-culture was initially incubated with 5 mL of 0.05% trypsin-EDTA at room temperature and the trypsin concentration was gradually increased until detachment of fibroblasts was observed using a microscope. The trypsin was aspirated and the remaining cells were washed with PBS and incubated with 1x (0.5%) trypsin-EDTA for 5 mins at 37 °C to facilitate detachment. At the point, the tumour cells were then treated in the same manner as all other cell types mentioned previously. Tumour cells were then re-seeded onto a fresh feeder layer for continued passage or plated in 96 well plates at a density of $1x10^4$ cells/well for future experiments.

2.14. Drug and nanoparticle exposure

Upon reaching confluency, cells were exposed to unmodified AuNPs, PEG-AuNPs and AFB-AuNPs in the AuNP studies and VRL, AFB, VRL-NPs, AFB-NPs, Dual-NPs or blank NPs for the polymeric NP studies. These treatments were dispersed in either DCCM-1 (TT1 cells), RPMI-1640 (A549, PC-9 and H226 cells) or epithelial cell culture medium (543 cells). Prior to exposure all solutions were sonicated for 30 s in a waterbath (VWR, PA, USA) and thoroughly vortexed to ensure full dissolution of the treatments. The dose range investigated in studies involving VRL was 1-0.003 µM and 10-0.03 µM for studies with AFB unless otherwise stated. The concentrations in the AuNP studies ranged from 0.03-30 µg/mL of AuNP. All exposures were performed in triplicate for all cell lines.

2.15. Cell viability assay

Cells were exposed to drug or NP formulations for 30 min, 2 h, 4 h or 8 h after which time the treatment-containing medium was removed. Cells were washed three times with PBS and fresh growth medium was added to the wells. The cells were then incubated for a total of 72 h.

Alternatively, cells were directly exposed to drug or NP formulations for 72 h without disturbance. After a 72 h exposure period, cell culture media were aspirated and cells were washed twice with PBS. Subsequently, 150 µL of 3-(4,5-dimethylthiazol-2-yl)-2,5-diphenyltetrazolium bromide (MTT) solution (0.5 mg/mL) was added to the cells, followed by incubation at 37 °C until insoluble formazan crystal formation could be observed. At this point, the MTT solution was removed, cells were lysed using 200 µL of DMSO and samples were analysed spectrophotometrically (λ_{abs} 570 nm) using a SpectraMax Plus 384 microplate reader (Molecular Devices, UK). Cells that had not been treated but had media changed in the same fashion as experimental cells were used as controls.

2.16. Electric cell-substrate impedance sensing (ECIS)

Real time analysis of cell proliferation was enabled using the RTCA iCelligence system (ACEA Biosciences, CA, USA). This system uses electrical resistance (impedance) as a measure of cell viability, which is translated as a cell index (CI), therefore allowing label-free, real time dynamic monitoring of cells and their behaviour. Drug or NP formulations (in the concentration ranges described in *Drug and nanoparticle exposure*) were prepared directly in cell suspensions in the appropriate complete growth medium. Cells were then seeded at a density of 0.375×10^4 cells/well on a L8 E-Plate (ACEA Biosciences, USA) in a volume of 400 µL/well. The plates were incubated at room temperature for 0.5-2 h to allow cellular equilibration and adhesion. Subsequently, the plates were placed in the impedance recorder, which was housed in a humidified environment at 37 °C, and impedance measurements were taken every hour for 72 h using RTCA Data Analysis Software 1.0 (ACEA Biosciences, USA). Cells grown in complete media and media alone were used as controls. Each treatment was assessed in triplicate or quadruplicate.

2.17. Measurement of inflammatory mediator release

To determine the concentration of pro-inflammatory cytokines interleukin (IL)-6, IL-8, IL-1β and tumour necrosis factor-α (TNF-α), the supernatant of HUVECs exposed to VRL-NPs or equivalent free drug for 24h was analysed using a sandwich enzyme-linked immunosorbent assay (ELISA). Briefly, high binding, half-area 96 well plates (Greiner Bio-One, Stonehouse, UK) were coated with the appropriate capture antibody at the recommended concentration. These were then sealed and incubated overnight at room temperature. Following this, the contents of the wells were discarded, and plates were washed three times with 0.05% (v/v) Tween-20 in PBS (wash buffer). A solution of 1% (v/v) bovine serum albumin (BSA) in PBS (block buffer) was added to each well and the plates were incubated for at least 1 h at room temperature. Plates were washed with wash buffer as before and conditioned medium was placed into the wells in triplicate, with the corresponding recombinant protein standard curve assayed in duplicate on each plate. After at least 2 h incubation at room temperature, plates were washed three times and incubated with appropriate biotinylated detection antibody at the recommended concentration for 2 h. Washed plates were then incubated with streptavidin-horseradish peroxidase at the recommended concentration for 20 mins. A final washing step was performed prior to addition of H_2O_2/3,3'5,5'-Tetramethylbenzidine (1:1 v/v). After 20 mins, further colour development was prevented using 1M HCl, resulting in a yellow solution that was then analysed spectrophotometrically (λ_{abs} 450 nm) using a SpectraMax Plus 384 microplate reader (Molecular Devices, UK). Cytokine concentrations were quantified with reference to a standard curve of known concentrations of the specific cytokine.

2.18. Flow cytometry

To evaluate the induction of apoptosis in lung cancer cells, flow cytometry was employed. A549, H226 and PC-9 cells were seeded at a density of 3×10^5 cells/well, incubated overnight (37 °C, 5% CO_2) and were treated with VRL-NPs or Dual-NPs (equivalent to approximately 10 μM VRL) for 12, 24 or 48 h. Following this, media were collected, and adherent cells were

washed with PBS, trypsinised then, along with conditioned media, centrifuged at 500 x g for 5 mins. The supernatant was aspirated, and the cell pellet was fixed with 4 % paraformaldehyde (PFA) at room temperature for 20 mins. The cells were then centrifuged at 500 x g for 5 mins at 4 °C, washed with PBS, centrifuged again then resuspended in 200 µL ice-cold methanol and permeabilised overnight at -20 °C. Subsequently, the cells were washed twice with PBS-Tween (0.1% v/v) *via* centrifugation and stained with fluorescently conjugated antibodies against cleaved caspase-3 (Alexa Fluor 488) and cleaved poly (ADP-ribose) polymerase (Alexa Fluor 647). Cells were analysed using a BD Accuri C6 Plus flow cytometer (BD Biosciences, CA, USA) and data was processed using FloJo software (FloJo LLC, OR, USA).

2.19. EGFR inhibition

To investigate whether the chemical modifications that were made to AFB (compound **17**) affected tyrosine kinase inhibitor activity, A549 cells were plated at a seeding density of $1x10^5$ cells/well in 6 well plates and incubated in a humidified environment (37 °C, 5% CO_2). Upon reaching ~80% confluency, cells were treated with AFB or **17** at concentrations ranging from 0-1000 nM for 3 h. Epidermal growth factor was added to the cells for the final 2.5 mins then the medium was aspirated and replaced with fresh medium for 30 mins. Cells were then processed as described in *Western blot analysis*.

2.20. siRNA knockdown

The Silencer Select Validated siRNA for clathrin heavy chain 1 (CLTC) oligonucleotide sequence was GGUUGCUCUUGUUACGGAUtt (sense) and AUCCGUAACAAGAGCAACCgt (antisense). A549 cells were seeded at a density of $1x10^5$ cells/well in 6 well plates and incubated overnight. Following this, cells were transfected using Lipofectamine RNAiMAX with a final siRNA concentration of 100 nM. A scrambled siRNA sequence was used as a control. Further controls included cells exposed to only Lipofectamine

and unexposed cells. Each treatment was applied for 24, 48 or 72 h, after which cells were processed as described in *Western blot analysis* to quantify protein knockdown.

2.21. Western blot analysis

To determine the extent of autophosphorylation of EGFR or knockdown of CLTC, western blotting of A549 cells treated as described in *EGFR inhibition* or *siRNA knockdown* was employed. After treatment, cells were washed twice with ice-cold PBS, scraped using a cell scraper with 500 µL PBS and transferred to a pre-chilled Eppendorf tube. The cell suspension was centrifuged at 500 x g for 5 mins at 4 °C, the supernatant was aspirated and the cell pellet was lysed on ice by the addition of 250 µL lysis buffer composed of CelLytic M, phosphatase inhibitor cocktail 2 and 3, and a protease inhibitor mini tablet. Lysates were either processed immediately or stored at -80 °C for future analysis. Cell lysates were centrifuged at 15,000 x g for 20 mins at 4 °C and the supernatants were transferred to a fresh pre-chilled Eppendorf tube. The protein concentration of each sample was measured using a NanoDrop ND-1000 UV-visible spectrophotometer (Thermo Fisher Scientific, MA, USA). Samples were normalised to contain approximately 30 µg of protein which was then denatured by heating at 90 °C for 5 mins. Subsequently, samples were loaded and resolved on 10-well pre-cast NuPAGE 4-12% Bis-Tris gels using NuPAGE MOPS SDS running buffer. Running conditions were 200 V, 120 mA for 50-65 mins. After this time, gels were transferred to polyvinylidene fluoride membranes using a semi-dry fast transfer iBlot system (Invitrogen, UK). Membranes were allowed to equilibrate in wash buffer (0.1% v/v Tween-20 in Tris Buffered Saline – TBST) for 15 mins prior to incubation in block buffer (5% BSA in TBST). Membranes were washed three times with wash buffer then incubated at 4 °C overnight with primary antibody against EGFR (1:1000), p-EGFR (Y1068, 1:500), CLTC (1:8000) or β-actin (1:1000) diluted in block buffer. Following this, membranes were washed three times with wash buffer and incubated for 1 h with the appropriate secondary antibody conjugated with horseradish peroxidase, diluted in

block buffer (1:2000 for EGFR studies, 1:5000 for siRNA studies). Membranes were washed a further three times, proteins were detected using enhanced chemiluminescence and visualised with an Odyssey Fc imaging system (Li-COR Biosciences, Cambridge UK). Quantification was performed using embedded Image Studio software (Li-COR Biosciences, UK). The EGFR studies required the membranes to be stripped, which was done by immersing the membrane in Restore Plus stripping buffer and incubating for 5-10 mins. The membranes were then washed for 10 mins three times with wash buffer, incubated with block buffer for 1 h then re-probed according to the procedure outlined above.

2.22. Assessment of nanoparticle uptake

A549 cells were seeded on a μ-Slide 8 well-chambered coverslip (Ibidi, Germany) at a density of 3×10^5 cells/well and incubated overnight to allow cellular attachment. The cells were then exposed to Afb-AuNPs (20 μg/mL) for 3 h, 6 h and 24 h. Afb-AuNP containing medium was removed and the cells were washed three times with PBS, fixed with 4% PFA and permeabilised with ice-cold methanol. Subsequently, cells were stained with anti-lysosomal-associated membrane protein (LAMP)-2-Alexa Fluor 488 and Hoescht 33342. AuNPs were visualised using a He-Ne laser, $\lambda = 543$ nm. Images were captured using a Leica TCS SP5 confocal microscope (Leica Microsystems, Germany) with a 63x objective lens and processed with ImageJ software

In order to elucidate the mechanism of uptake of polymeric NPs, a series of experimental conditions were implemented. The fluorophore coumarin-6 ($\lambda_{ex} = 458$ nm, $\lambda_{em} = 497$ nm in methanol) was encapsulated within the NPs to allow visualisation by confocal microscopy (with a Diode 405 laser, $\lambda = 405$ nm) and the NPs had Afb conjugated to the surface so as to more accurately mimic the *in vivo* encounters between Dual-NPs and cells. To examine the effect of temperature on uptake of NPs, A549 cells were seeded on a μ-Slide 8 well-chambered

coverslip at a density of $3x10^5$ cells/well and incubated overnight. Cells were then treated with 50 µL NPs (~1mg/mL) for 4, 8 or 24 h and maintained at 37 °C or incubated at 4 °C for 1 h prior to NP exposure and then kept at this temperature for the duration of the experiment. To discern the dominant endocytic pathway involved in NP uptake, cells were seeded likewise at a density of $3.3x10^4$ cells/well and incubated overnight. The cells were pre-incubated with five chemical inhibitors of endocytosis, chlorpromazine (22 µM), dynasore (70 µM), 5-(N-Ethyl-N-isopropyl)amiloride, (50 µM), genistein (150 µM) or nocodazole (20 µM) for 1 h prior to 2 h incubation with treatment with 50 µL NPs. To confirm the nature of endocytosis, A549 cells were seeded identically to the previous experiments and transfected with siRNA against *CLTC* as described in *siRNA knockdown* over a time course of 72 h. Cells transfected with scrambled siRNA and untreated cells were used as controls. After this time, cells were again treated with 50 µL NPs and incubated for 3 h. In all experiments, after the NP incubation period, the medium (containing NPs) was removed and cells were washed three times with PBS. The cells were then stained with wheat germ agglutinin-Alexa Fluor 488 (1:250 in Hank's Buffered Salt Solution) for 10 mins at 37 °C, washed three times with PBS, then fixed using 4% PFA for 20 mins at room temperature. Following this, the cells were washed three times with PBS and the nucleus was stained with DRAQ5 (1:1000 in PBS, λ_{ex} = 646 nm, λ_{em} = 697 nm) for 10 mins at room temperature. The cells were washed once with PBS prior to image capture with a Leica TCS SP5 confocal microscope (Leica Microsystems, Germany) with a 63x objective lens. Images were processed and fluorescence quantified with ImageJ software.

2.23. *In vivo* efficacy using a patient derived xenograft model of NSCLC

Male 6-8 week old nucleotide-binding oligomerisation domain (NOD).Cg-*Prkdc^scid^IL2rg^tm1Wjl^*/SzJ (NSG) mice were purchased from Charles River Laboratories (UK), housed in specific pathogen-free conditions and kept in individually ventilated cages with *ad libitum* access to autoclaved water and sterile food. All animal studies were approved by the

University College London Biological Services Ethical Review Committee and procedures were conducted in accordance with UK Home Office regulations and licence stipulations. Subcutaneous tumours were generated by anaesthetising mice using 2-4% isoflurane, shaving and cleaning the right flank prior to challenge with 0.5×10^6 patient derived lung cancer 543 cells in 200 µl growth-factor reduced Matrigel. These cells were of the F1 generation which originated from implantation of the fragments of the original lung tumour (F0 generation) into NSG mice followed by tumour growth, harvest and fragmentation (F1 generation). After 9 days of tumour growth, mice were randomised into four groups and treated with either PBS, 5 mg/kg VRL + 0.9 mg/kg AFB in PBS, 5 mg/kg Dual-NPs (based on VRL concentration) and 5mg/kg blank NPs (based on Dual-NP concentration). Each group contained 4 mice except the PBS-only group which contained 3 mice. Treatments were administered intravenously *via* tail vein injection on day 9, 11, 13 and 15 (where day 0 was initial tumour cell injection). Tumour dimensions were measured using callipers and were calculated using the formula L x W x H where L = length, W = width, H = height of the tumour, on separate orthogonal planes. Mouse body weight and tumour volume were regularly monitored throughout the study. Animals were euthanised if tumour volume exceeded 1500 mm^3 or 20% of body weight was lost (compared to that of the pre tumour-bearing state), however this did not occur at any point during the study. The sample sizes were determined such that the minimal number of animals could be used to discern statistically significant differences between groups.

2.24. Histological evaluation of NP safety

Upon study termination, mice were euthanised, the lungs, heart, liver, kidney and spleen were harvested and fixed in 10% neutral buffered formalin overnight at 4 °C. Following this, organs were transferred to 70% ethanol and stored likewise. Dehydrated tissues were then cleared with multiple incubations of xylene prior to embedding in paraffin wax. The wax was changed twice over several hours in order to permit full infiltration of the tissue. The embedded tissue was

placed into paraffin blocks and sections of 5 μm in thickness were prepared. Tissue sections were subsequently dewaxed using Histo-Clear, rehydrated with washes of 100%, 90% and 70% ethanol respectively and finally distilled water. Sections were stained with haematoxylin for 7 minutes and rinsed with water. The sections were differentiated in order to remove unbound haematoxylin from the tissue by successive dipping in 0.3% acid alcohol until only nuclear staining remained. After washing with water, sections were then stained with eosin for 2 minutes and washed once more with water. Stained sections were dehydrated using progressively concentrated ethanol washes, up to 100%, cleared with Histo-Clear and mounted using Distyrene Plasticiser Xylene. Images were captured using a Leica DM2500 Microscope (Leica Microsystems, Germany) and processed using Leica Application Suite v4.7 software.

2.25. Statistical analysis

Data are presented as the mean ± standard error, where $n = 3$ (whereby the experiment was replicated independently three times, within which each independent experiment contained a minimum of three technical replicates) unless otherwise stated or was not feasible. Treated groups were compared with an untreated control group that had experienced the same experimental conditions. Significant observations were statistically verified by Student's two-tailed t-test, one-way or two-way analysis of variance (ANOVA) with Bonferroni post-test correction for multiple comparisons. Prism v5 (GraphPad, CA, USA) was used for all statistical calculations and graph generation. In all analyses, a P value of <0.05 was considered significant.

3. Synthesis of afatinib analogues and development of gold and polymeric nanomedicines

This chapter describes the novel synthetic steps performed to create two afatinib (Afb) analogues, the development of gold or polymeric nanoparticles (NPs) and subsequent conjugation of Afb analogues to NPs. The synthesis and characterisation of the above constructs is outlined, and the resultant physicochemical properties of the NPs are discussed in a biological context. Conclusions are drawn regarding the suitability of the fabricated NPs as drug delivery carriers.

3.1. Introduction

There is currently a clinical unmet need for more effective therapies for treatment of diseases such as lung cancer. Due to the advanced or metastatic stage of diagnosis, therapeutic modalities for lung cancer are limited to chemotherapy and radiotherapy. The discovery of activating mutations in oncogenic driver genes such as *EGFR* and *ALK* paved the way for personalised medicine to become clinical reality, whereby patients can be stratified by their mutational status and treated with the most appropriate therapies[284]. Although the therapies targeted towards these mutations [e.g. tyrosine kinase inhibitors (TKIs)] are not curative, they can demonstrate encouraging efficacy in patients with sensitising mutations[285]. Unfortunately, these targeted therapies suffer from the same drawbacks as traditional chemotherapy including short circulatory half-life, rapid metabolism and excretion (poor bioavailability and pharmacokinetics) as well as poor tumour accumulation and distribution. The culmination of these factors is systemic dissemination of these molecules throughout the body, causing severe side effects such as neutropenia, hair loss, gastrointestinal disturbances and other toxicities. Intravenous administration is the most common method of delivery which intrinsically contributes to the systemic spread of these therapies throughout the body and to other organs.

Furthermore, some chemotherapies cause venous irritation and phlebitis upon injection, as well as other infusion-related reactions, inducing both local and systemic injury.

Despite these hindrances, chemotherapy is the mainstay treatment option for patients with lung cancer, at all stages of diagnosis. Indeed, the successful responses seen with chemotherapy and particularly targeted therapy in patients harbouring the appropriate mutations suggest this mode of treatment has efficacy, despite the side effects. Vinorelbine (VRL) is a semi-synthetic vinca alkaloid designated as a first line chemotherapy agent in the treatment of advanced NSCLC[286] and afatinib (Afb) is a second generation TKI approved as a therapy for epidermal growth factor receptor (EGFR) positive NSCLC[287]. As most chemotherapy regimens involve combinations of drugs as opposed to monotherapies, there is significant research interest focused on combinatorial chemotherapy, particularly in cohorts of patients with tumours suspected to be susceptible to a certain therapeutic regimen, such as those harbouring EGFR mutations. Indeed, the combination of VRL with chemotherapy[288], EGFR specific TKIs[289] and Afb[290] have all been trialled in humans, however VRL is a known vesicant and, along with Afb, can induce dose limiting toxicities such as febrile neutropenia, diarrhoea and skin rash. As such, there is a need for a safer and more sophisticated delivery mechanisms that may attenuate dose limiting toxicities and improve efficacy.

The use of NPs in medical applications has led to the emergence of the field of nanomedicine, which has received great research interest and attention over the past several decades. NPs of organic (polymers, lipids, dendrimers or proteins) or inorganic (metals or carbonaceous) origin have found utility as drug delivery vehicles, primarily in an oncological context[291] but also for other diseases[292], demonstrating the biological versatility of NPs. Gold (Au) NPs[293] and polymeric NPs, specifically poly(D,L-lactide-*co*-glycolide)-polyethylene glycol (PLGA-PEG) NPs[294] have shown promise as drug delivery vehicles for cancer therapy. Both types of NPs are biocompatible and easy to synthesise which facilitates scale-up to the pharmaceutical

manufacturing process. Moreover, these NPs possess multimodal functionalities; AuNPs have unique optical and thermal properties that can be exploited for use in CT scans or photothermal therapy[295] and polymeric NPs can accommodate a wide variety of cargo such as imaging contrast agents and therapeutic molecules simultaneously, a phenomenon termed theranostics[296]. NPs can also deliver combinations of therapies simultaneously, in a controlled fashion, which makes them an attractive choice for as vectors for drug delivery to tumours. This notion is reinforced by the progression of AuNP and PLGA-PEG based nanomedicines to clinical trials and the clinical approval of several other NP based therapies for the treatment of a variety of cancers[297].

Given the clinical precedent of both NPs and the combination of VRL and Afb, the overarching aim was to develop nanomedicine formulations incorporating VRL and Afb. The molecular structure of VRL does not permit conjugation to the surface of NPs or facile encapsulation within polymeric NPs. Moreover, Afb also does not possess any functional groups that permit conjugation to NPs. To circumvent these obstacles, herein is described a hydrophobic ion pairing methodology to permit encapsulation of VRL within polymeric NPs. Furthermore, the synthesis of Afb analogues with alkyne and disulfide functional groups that allow surface conjugation to polymeric and AuNPs respectively is outlined. The hypothesis of this chapter is that successful employment of synthetic methodology will lead to novel NP formulations, whose physicochemical properties are well suited for anticancer drug delivery purposes.

3.2. Aims

- Synthesis of afatinib analogues suitable for conjugation to NPs
- Development and characterisation of AuNP nanomedicine
- Synthesis of azide functionalised block co-polymer PLGA-PEG-N$_3$
- Development and characterisation of polymeric dual drug nanomedic

3.3. Results

3.3.1. *Synthesis of afatinib analogues for conjugation to NPs*

The construction of the final Afb analogues **16** and **17** can be divided into three synthetic phases (Scheme 1). The first phase was to synthesise a quinazoline core resembling that of Afb. This began with chlorination of the commercially available starting material, 7-chloro-6-nitro-4(3*H*)quinazolinone **1**, using phosphorus(V) oxychloride (Scheme 1A). This afforded 4-chloroquinazoline **2** which was not isolated but used in the subsequent nucleophilic aromatic substitution (S_NAr). The 4-Cl was substituted with the amine from 3-chloro-4-fluoroaniline to give derivative **3** (77%). Benzenesulfinic acid was then used to displace the 7-Cl substituent in another S_NAr reaction at high temperature to afford sulfone **4** (87%). This sulfone was then substituted by (*S*)-(+)-tetrahydro-3-furanol in the presence of potassium *tert*-butoxide to yield ether **5** (66%). The last reaction in this sequence was the reduction of the nitro group by hydrogenation using Raney-Ni as a catalyst to give the 6-amino quinazoline core **6** (77%). The second phase of the synthesis (Scheme 1B) comprised of making an appropriate linker that could both anchor to AuNPs and be easily appended to the quinazoline core whilst retaining the functional activity of Afb. The first step involved performing a nucleophilic substitution on methyl *trans* 4-bromocrotonate **7** using propargylamine in the presence of potassium carbonate to give amine **8**, which was not isolated. Amine **8** was protected *in situ* using di-*tert*-butyl dicarbonate to afford *tert*-butyloxycarbonyl (Boc) derivative **9** (48%). The part of the linker that contained a cyclic disulfide moiety was synthesised by borane dimethylsulfide complex mediated reduction of (±)-α-lipoic acid **10** to give alcohol **11** (97%) followed by tosylation using 4-dimethylaminopyridine as a nucleophilic catalyst yielding tosylate **12** (62%). Lastly, tosylate **12** was reacted with sodium azide in an S_N2 manner to give the azide **13** (76%). The final series of reactions (Scheme 1C) involved attaching the quinazoline core to the linker. Ester **9** was coupled with quinazoline **6** using trimethylaluminium mediated amidation to give
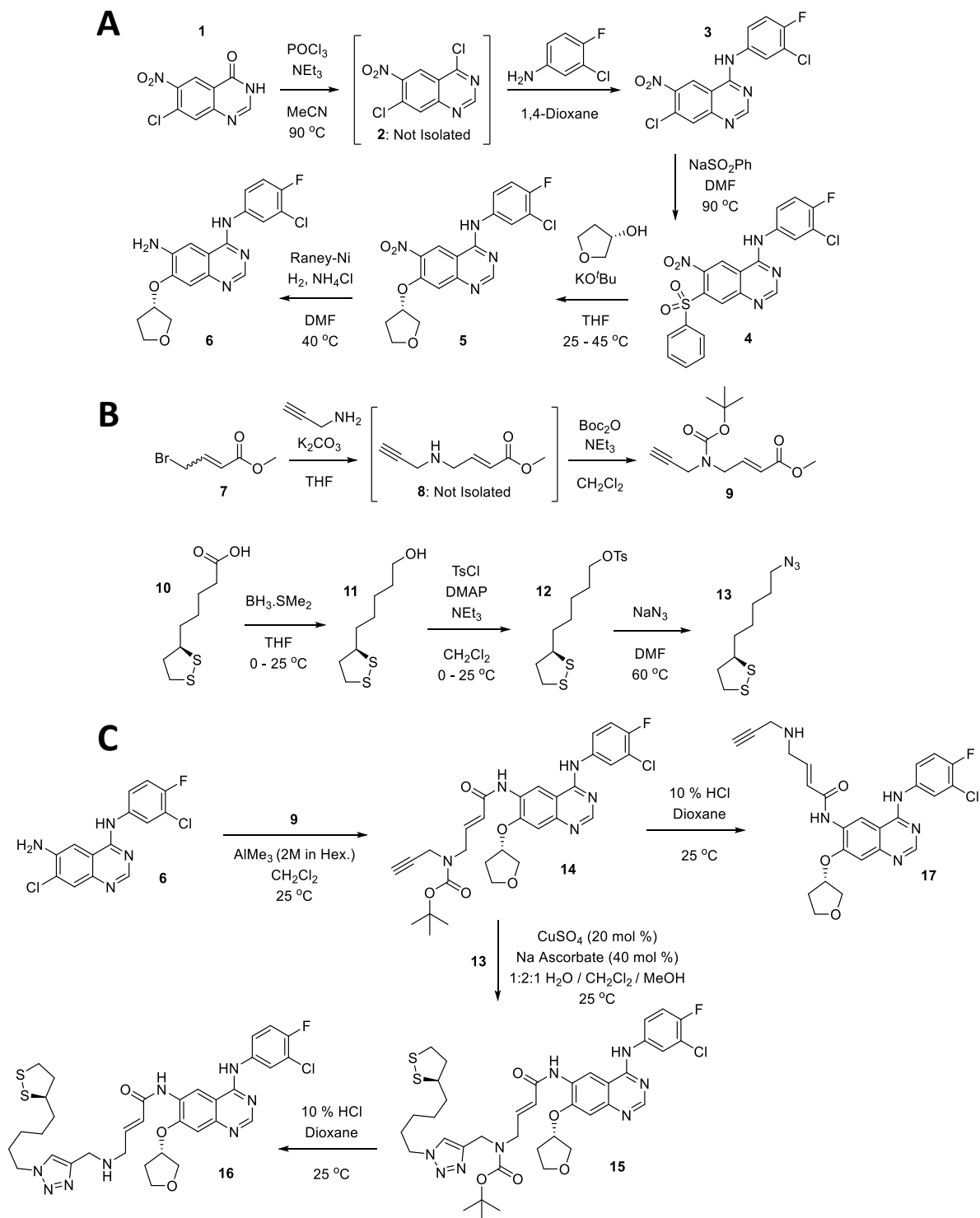
Scheme 1. Reaction series for the synthesis of afatinib analogues 16 and 17. (A) Beginning with starting material **1**, the quinazoline core (compound **6**) also found in afatinib was generated in 4 synthetic steps. (B) Synthesis of linker fragments whereby compound **9** contains an alkyne and 1**3** is bifunctional and has a cyclic disulfide group to allow attachment to AuNPs and an azide group for click chemistry with **9**. (C) Alkyne bearing **9** was attached to the quinazoline core and underwent a click reaction and deprotection to give the final compound **16**. Alternatively, **14** was directly deprotected to yield **17**.

amide **12** (95%). This molecule presents a terminal alkyne in place of the dimethylamino unit found in Afb, to facilitate a copper(I) catalysed Huisgen 1,3-dipolar cycloaddition (otherwise known as a 'click reaction')[298,299]. To attach the two components, azide **13** and alkyne **14** were reacted together in the presence of copper sulfate and sodium ascorbate to give triazole **15** (65%). Finally, Boc deprotection was achieved using 10% HCl in 1,4-dioxane to give **16** as the final product in a 98% yield. For use in the polymeric NP formulation, deprotection of alkyne **14** was achieved using the same conditions outlined above to give **17** as the final product in an 88% yield.

3.3.2. *Synthesis and characterisation of PLGA-PEG-N$_3$*

PLGA-PEG-N$_3$ was synthesised using a two-step procedure involving conventional carbodiimide crosslinker chemistry. The carboxyl end of acid terminated PLGA was activated using DCC in the presence of NHS to form the NHS ester of PLGA. The more active terminal esters were then coupled with the heterobifunctional NH$_2$-PEG-N$_3$ in the presence of DIPEA to form an amide bond between PLGA and PEG, leaving a terminal azide group free for surface chemistry modifications. When examined using ^{1}H NMR spectroscopy (Figure 3.1), the characteristic peak at 3.64 ppm generated by the methylene protons of PEG was observable in the co-polymer spectrum. Indeed, the corresponding PLGA peaks at 1.59, 4.82 and 5.22 ppm could also be identified in the co-polymer spectrum, implying successful linkage of the two polymeric components. The co-polymer was further characterised using IR spectroscopy; as shown in Figure 3.2 the co-polymer contained several distinct peaks. Most notably, peaks representing the characteristic N=N=N bond at 2109 cm^{-1}, C=O bond at 1750 cm^{-1} that denotes the ester bond in PLGA (also present in PLGA IR spectrum, Figure 3.2A) but may also incorporate C=O present in the newly formed amide bond. This was reinforced by the disappearance of the primary amine N-H peak at 1651 cm^{-1} seen only in the PEG IR spectrum (Figure 3.2B). The co-polymer spectrum (Figure 3.2C) also contained peaks denoting an alkane

C-H bond at 2884 cm^{-1}, derived from both the PLGA and PEG, as well as aliphatic ether C-O

bonds at 1085 cm^{-1} also present in both PLGA and PEG.
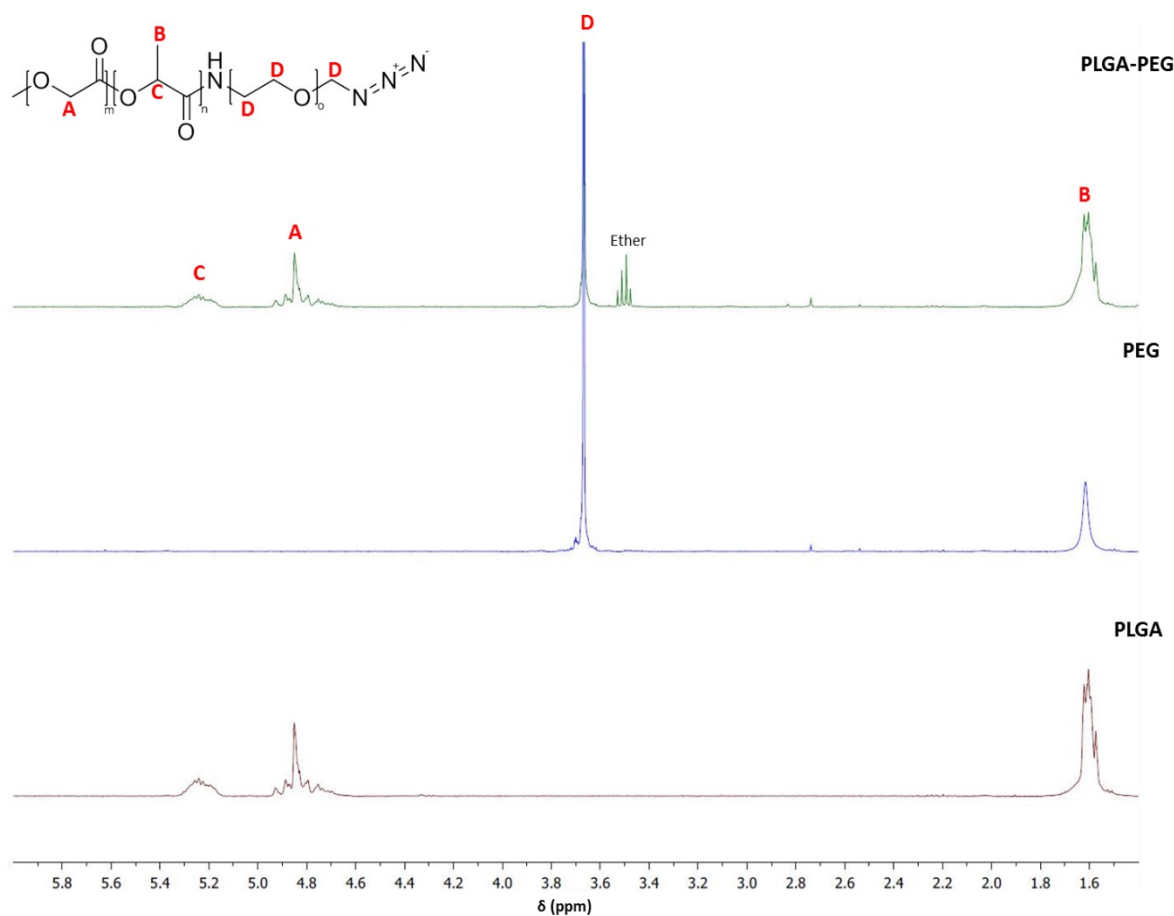
Figure 3.1. ^{1}H NMR spectrum (CDCl$_3$) of component polymers and copolymer PLGA-PEG-N$_3$. The spectra of PLGA (bottom) and PEG (middle) are displayed to show all peaks that were present in the copolymer spectrum (top). Letters denote the proton peaks with reference to the structure (inset).

3.3.3. Preparation of PLGA-PEG-N$_3$ NPs

Initial efforts to manufacture empty and VRL loaded polymeric NPs used the oil-in-water

emulsification solvent evaporation (OW-ESE) method. The first iterations of this method

reproducibly generated NPs in the size range of 200-250 nm as measured by DLS and negative

zeta potential values (approximately -22 mV), however, the success of this process was

hampered by very low encapsulation and loading efficiencies of vinorelbine tartrate (~8% EE,

1% LE). The parameters that governed this process such as polymer and drug concentrations,

organic and aqueous phase compositions and volume as well as sonication
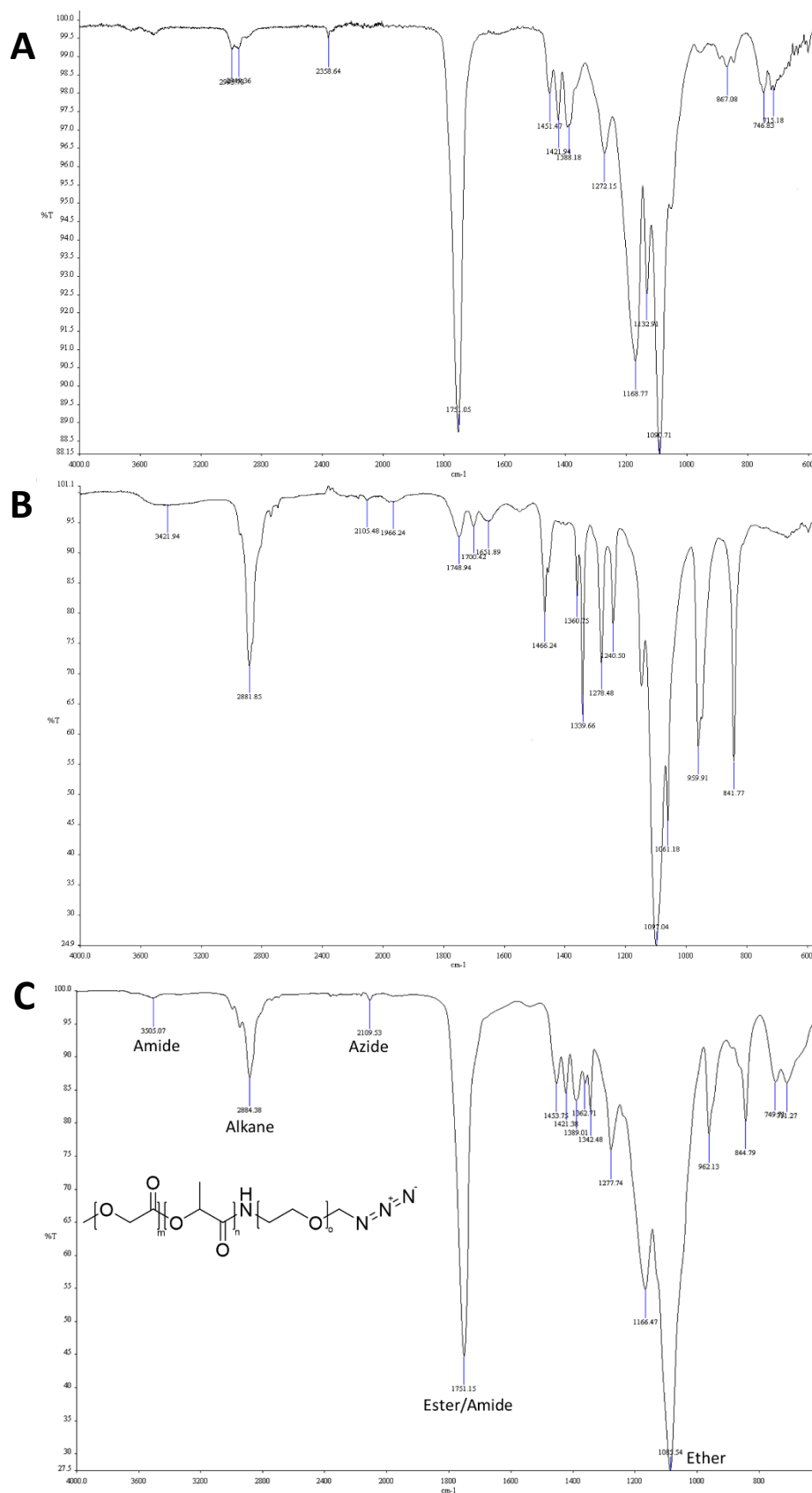
Figure 3.2. FTIR spectra of polymers. (A) PLGA, (B) NH_2-PEG-N_3 and (C) PLGA-PEG-N_3. Major functional groups of the polymer are labelled at their corresponding peak.

time/power were derived from the literature[300-302]. Despite the acceptable size and surface charge of these particles for drug delivery purposes, the EE/LE was deemed insufficient and optimisation steps were therefore implemented (Table 3.1). Altering the order of addition of components to the organic phase (i.e. dissolving either drug or polymer first) or increasing the sonication power from 20% to 40% (50W to 100W) did not appear to affect the drug loading kinetics (13% EE, 0.7% LE). To increase drug loading, the initial amount of vinorelbine tartrate used was increased (10 mg as opposed to usual 5 mg) and the pH of the aqueous phase (1% PVA in all formulations) was adjusted to 8.7. Despite these modifications, the drug loading remained largely unchanged. Further pH adjustments of the aqueous phase towards an acidic environment (3.6) resulted in even lower drug loadings which is to be expected as ionisation of a molecule increases its hydrophilicity. It was then hypothesised that the tartrate salt of vinorelbine was too hydrophilic for this method of encapsulation, therefore the freebase form of vinorelbine was utilised for further formulations. Incorporating the freebase into the NP

Formulation No.	Deviations from original synthesis	EE (%)	LE (%)
1	None	8	1
2	Order of addition of drug/polymer to organic phase, increased sonication power	13	0.7
3	Double initial VRL, pH of aqueous phase 8.7	16	1.1
4	pH of aqueous phase 3.6	8	0.6
5	VRL freebase instead of tartrate salt	15	0.7
6	Methanol instead of DCM in organic phase	13	0.7
7	pH of aqueous phase 9.5	22	1.2

Table 3.1. Modifications to initial NP synthesis. To increase EE and LE of VRL, different strategies were implemented into the synthesis protocol (annotated above) along with the calculated EE and LE after each NP fabrication.

fabrication process at this stage did not improve drug loading (15% EE, 0.7% LE). An alternative method of encapsulation was attempted based on methodology outlined by Betancourt *et al.* which was used to encapsulate the relatively hydrophilic chemotherapy doxorubicin (logP ~ 0.9, pKa 8.2)[303]. As such, the polymer was dissolved in acetone and vinorelbine was separately dissolved in methanol and then combined with acetone to form the

organic phase, as opposed to the conventionally used dichloromethane:acetone (4:1 v/v). This was followed by dropwise addition into the aqueous phase. However, these modifications failed to increase drug loading (13% EE, 0.7% LE), therefore a further alteration was made to the aqueous phase whereby the pH was adjusted to 9.5 to prevent ionisation of vinorelbine. Upon initial inspection the drug loading remained low (9% EE, 0.5% LE), however dissolving lyophilised NPs in DMSO prior to analysis led to apparent increases in drug loading (22% EE, 1.2 % LE).
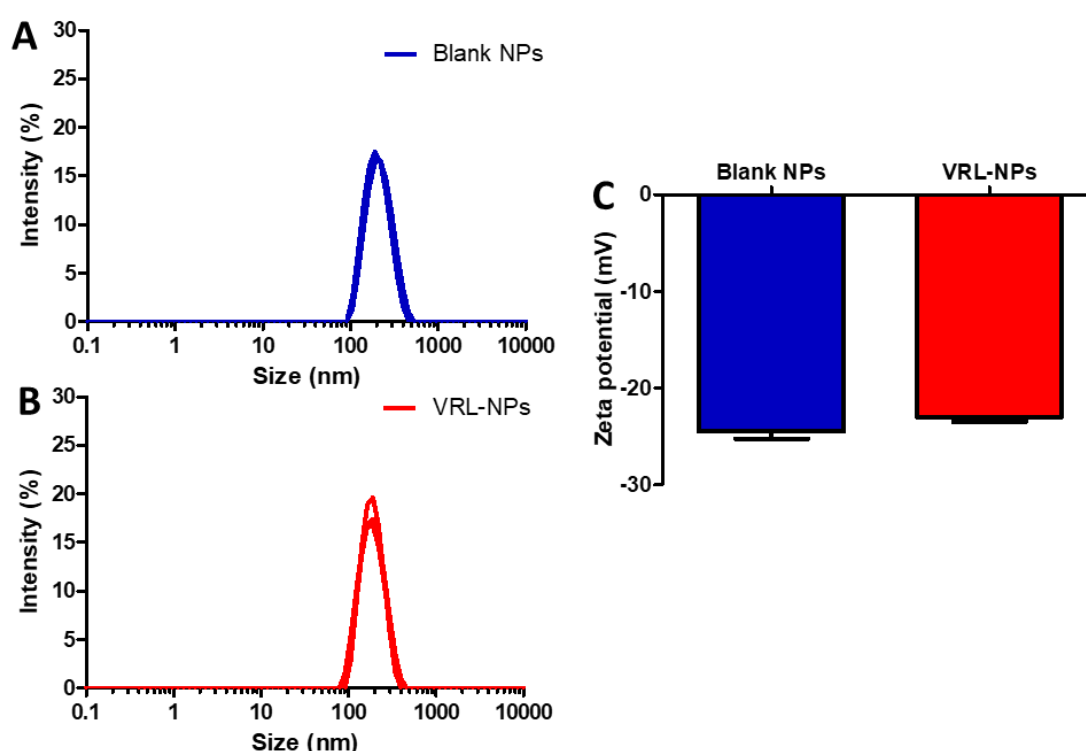
Figure 3.3. Characterisation of polymeric NPs fabricated using initial parameters. DLS measurements of (A) blank NPs and (B) NPs fabricated in the presence of VRL. (C) Zeta potential measurements of the NPs. Data are plotted as mean ± SD.

Despite the low drug loading, vinorelbine-loaded and blank NPs were produced using this iteration of the fabrication process and were found to exhibit desirable characteristics, suggesting the varying alterations made throughout did not negatively impact NP formation. Blank NPs were 203.2 nm and had a surface charge of -24.5 mV (Figure 3.3A and C). Similarly, drug-loaded NPs were 218.2 nm as measured by DLS and had a surface charge of -23 mV

(Figure 3.3B and C). Both formulations were also fairly homogenous, as evidenced by low polydispersity indexes (0.14 and 0.1 respectively). The amphiphilicity of vinorelbine was deemed to be the primary factor limiting the drug loading efficiency within polymeric NPs. This is reinforced by the successful encapsulation of the hydrophobic fluorophore coumarin-6 (logP 4.9).

3.3.4. *Hydrophobic ion pairing as a drug loading strategy*

Another method was sought that could improve the loading efficiency of amphiphatic weak bases such as VRL into polymeric NPs. Despite the acceptable size distribution, polydispersity index and zeta potential measurements of NPs prepared using OW-ESE, the low loading efficiency of VRL was sub-optimal for drug delivery applications. One such method, known as hydrophobic ion pairing (HIP) is a technique that results in ionic complexation of hydrophilic drug with another molecule of opposing charge, significantly altering the solubility properties of the drug by virtue of increased hydrophobicity[304]. This increase in hydrophobicity can be beneficial for loading amphipathic drugs into the hydrophobic core of polymeric NPs. Therefore, we chose to pair VRL base with a hydrophobic acid, as several studies have demonstrated successful entrapment of hydrophilic drugs into polymeric NPs using this technique[305,306]. With the OW-ESE protocol acting as a foundation for NP fabrication, we adapted the methodology of Song *et al.* and first explored pairing of VRL with cholic acid during the NP fabrication process (Table 3.2)[307]. It should be noted that all formulations contained sucrose when analysed by DLS as particles were lyophilised and resuspended prior to analysis. Sucrose acts as a cyroprotectant and analysis of particles without sucrose yielded large, aggregated particles which has been documented previously[250]. Results demonstrated that the loading and encapsulation efficiencies did improve slightly using cholic acid as an ion pair, however the NPs exhibited an enlarged average size of ~400 nm by DLS measurement and in the second iteration of NPs produced using this method (Chol 2), the NPs had a positive

zeta potential (+13 mV), which could be due to the influence of TFA in the formulation. Of note, the aqueous phase used in the synthesis of these particles did not contain PVA or any surfactant that could be contributing to the increased size of these particles compared with ones prepared by OW-ESE. Thus, when PVA was included again in the aqueous phase, the size of the NPs was significantly reduced (90-150 nm). NP formulations Chol 3 and Chol 4, despite showing improved loading efficiencies and smaller size than previous formulations, still exhibited an undesirable positive surface charge of + 21 mV and + 11 mV respectively.

Formulation No.	Counterion	Size* (nm)	ZP (mV)	EE (%)	LE (%)	Notes
Chol 1	CA	400	-25	24	1.9	
Chol 2	CA	539	13	35	2.7	TFA used in synthesis
Chol 3	CA	190	9	N/A	N/A	PVA in aqueous phase herein
Chol 4	CA	Agg	21	45	4.9	
5	PA	243	-24	80	27	Higher concentration of reactants, change of counterion

Table 3.2. Derivations of HIP fabrication of polymeric NPs. Using HIP, the EE and LE of VRL was found to increase, however other particles parameters needed further optimisation, ultimately the counterion pamoic acid (PA) yielded favourable particles. N/A – EE and LE not calculated due to unreliable NP weight. * Size measured by DLS. TFA – trifluoroacetic acid, PVA – polyvinyl alcohol, CA – cholic acid.

To further improve loading efficiency and restore the negative surface charge of polymeric NPs we employed the hydrophobic dicarboxylic acid, pamoic acid (PAM). When PAM was used as the hydrophobic ion pair there was a significant increase in the loading efficiency of VRL to 27% (w/w) coupled with a slight increase in NP size to 243.7 nm. The zeta potential was found to be -23.7 mV (Figure 3.4 A-B). TEM images of the polymeric NPs taken at various magnifications (Figure 3.4 C-E) revealed their spherical morphology, with reasonable homogeneity throughout the sample. These physicochemical properties align well with those required for effective drug delivery *in vivo* and as such PAM was used as the ion pair in all further polymeric NP preparations. There are several parameters that require optimisation for

efficient HIP. Song *et al*. identified key formulation variables using AZD2811 as a model drug such as acid:drug stoichiometry, quench buffer molarity and pH[307]. Given the extremely similar pKa values of AZD2811 and VRL (8.7 and 8.66 respectively) and the use of PAM as a hydrophobic counter ion, this information was used as a foundation for parameterisation of VRL-PAM ion pairing and subsequent polymeric NP formation. For VRL-PAM ion pairing a molar ratio 1:2 (acid:drug) was used, the sodium phosphate quench buffer pH was 6.5 and the molarity was 0.25M. The final fabrication process was optimised by increasing the amount of PAM in the organic phase and by increasing the volumes of the organic and aqueous phase as well as the volume of the quench buffer (maintaining the pH of 6.5 and molarity of 0.25M). These parameters enabled maximal VRL loading with maintenance of desired size and surface charge (Figure 3.4).
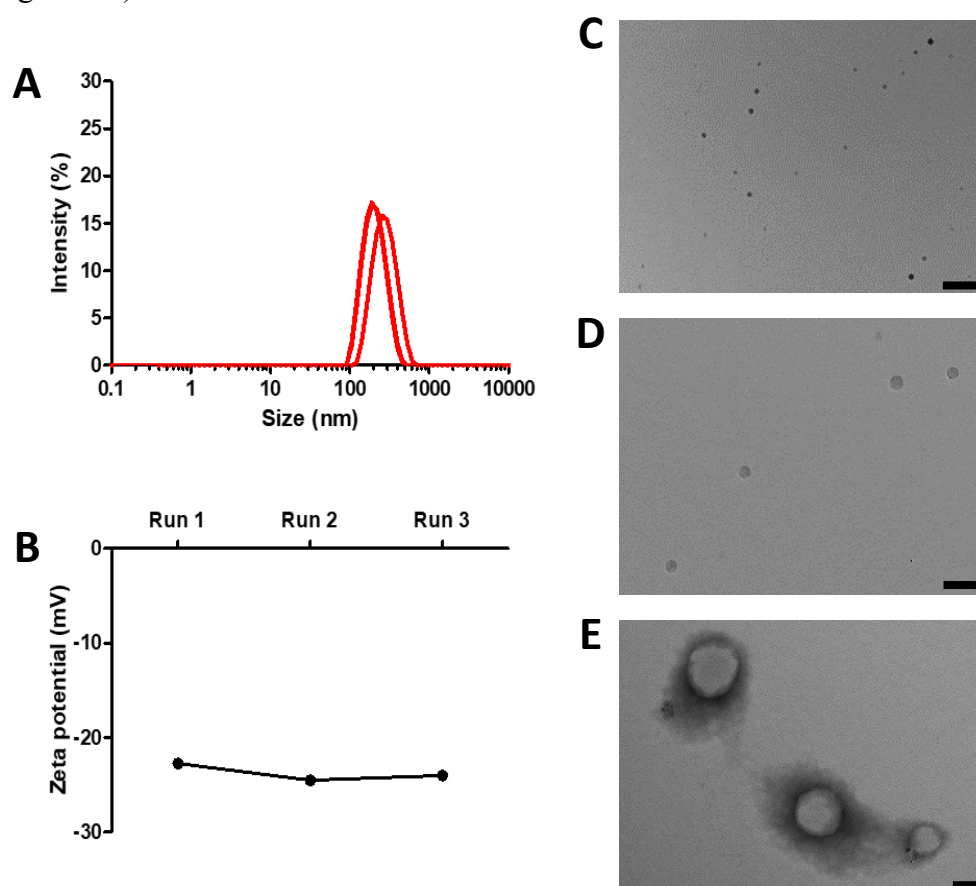
Figure 3.4. Characterisation of polymeric NPs fabricated using HIP. (A) DLS and (B) Zeta potential measurements of VRL-PAM NPs (each trace or point represents a separate run). NPs were stained and imaged by TEM (C) 10,000 x magnification, scale bar = 600 nm (D) 20,000 x magnification, scale bar = 200 nm (E) 100,000 x magnification, scale bar = 50 nm.

To confirm successful HIP between VRL and PAM via protonation of the amine functionality of VRL, ^{13}C NMR spectroscopy was employed. The control (unmodified) spectra of VRL freebase and PAM are shown in Figure 3.5A and B respectively and were acquired using 20 mg/mL solutions in a benzyl alcohol/DMSO (1:1 v/v) solution.
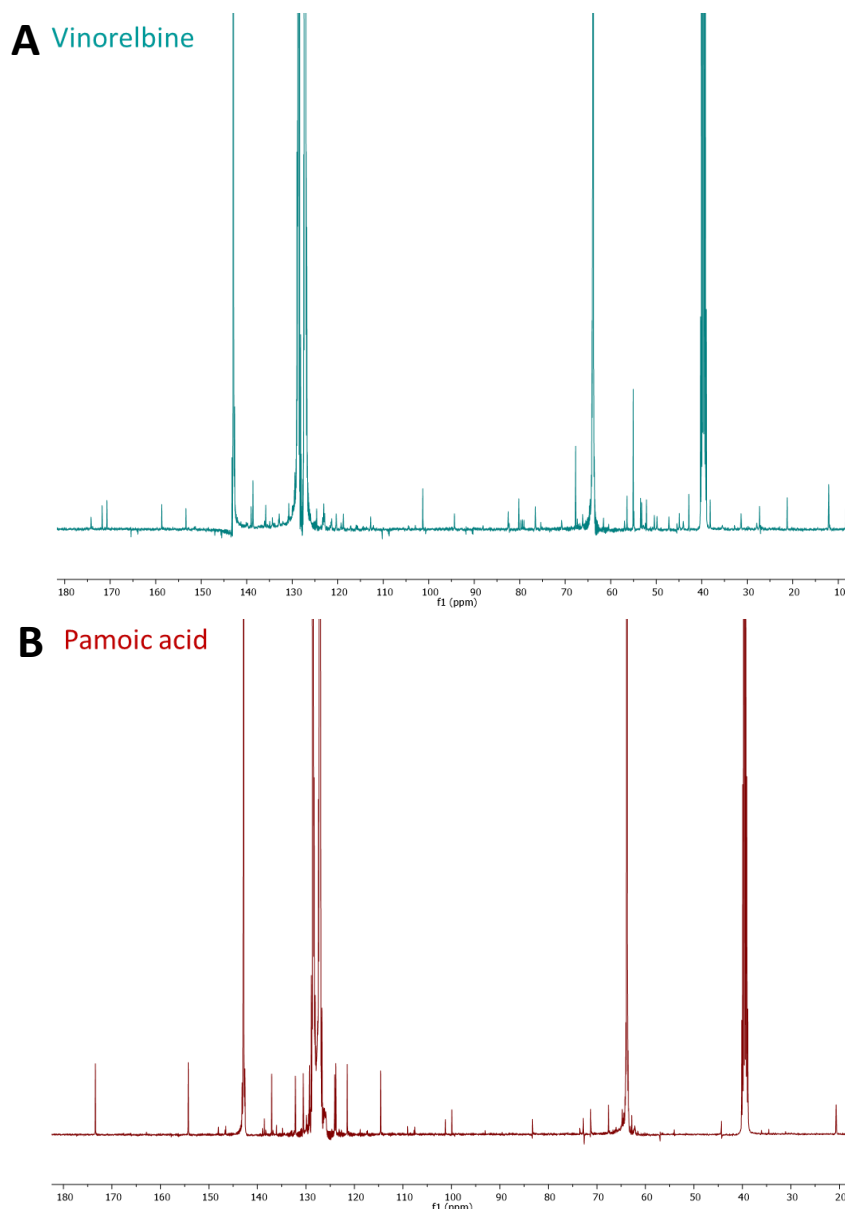
Figure 3.5. ^{13}C NMR spectra to confirm HIP. (A) VRL freebase and (B) pamoic acid. Spectra were obtained after 4096 scans. Note – the 10-180 ppm region is denoted for VRL and the 20-180 ppm region for pamoic acid. The largest peaks present in both spectra are solvent peaks.

Salt formation was then instigated by the presence of both acid and base (VRL) in solution, which was then subjected to NMR analysis as the separate solutions were previously. PAM

was added to the solution at 0.5M equivalent to account for the di-acidic nature of the molecule

and to ensure efficient ion pairing and protonation of the aminated free base VRL.
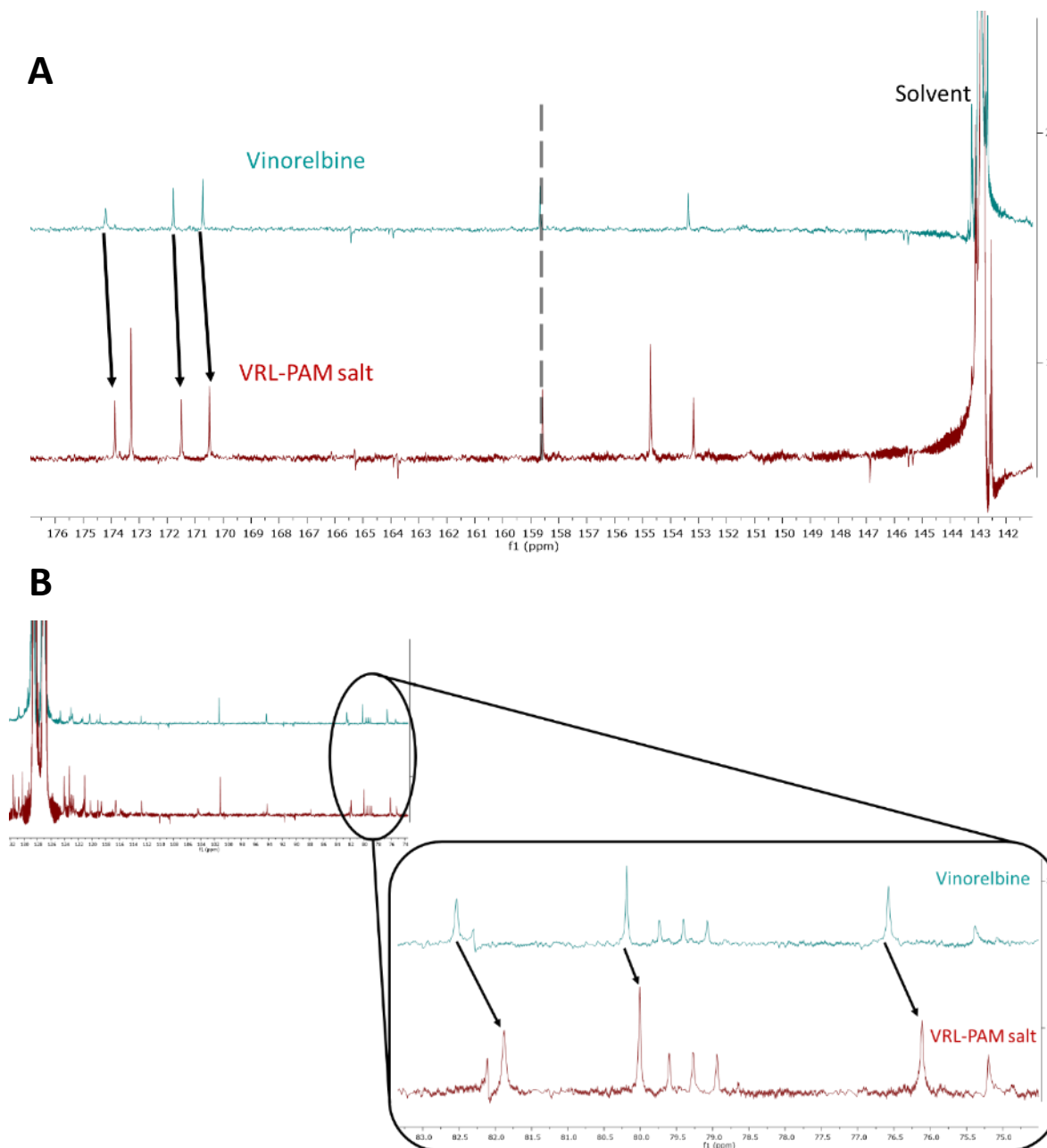
Figure 3.6. Upfield resonance shift of VRL upon HIP. ^{13}C NMR spectra of (A) VRL and VRL-PAM in with 140-180 ppm range with arrows denoting upfield resonance shifts. Dashed line represents peak in both spectra that is unmoved after alignment and solvent peaks are also labelled. (B) zoomed-in spectra within the 70-85 ppm range show further upfield shifts.

Spectral analysis of the salt solution revealed certain resonance shifts upfield in the spectrum

when compared to the freebase spectrum (Figure 3.6). In the 140-180 ppm region (Figure

3.6A), there were subtle but noticeable shifts of particular peaks (as denoted by the arrows),

reinforced by the unmoved position of the solvent peak and other peaks within the spectrum (dashed line). Similarly, in the 70-85 ppm region (Figure 3.6B), resonances were found to have shifted upfield. These upfield shifts are thought to be due to proximity to the carboxylate anion present in PAM, which is why not every peak is shifted to the same degree, if at all.

A further demonstration of successful HIP of VRL within polymeric NPs was achieved by examination of the release kinetics of VRL from NPs (Figure 3.7). When VRL was encapsulated without using a hydrophobic counterion as part of the fabrication process, VRL was found to be released in an initial burst accounting for over 60% of the encapsulated payload within the first 12 hours. A plateau was the reached whereby, of the remaining VRL encapsulated, a consistent amount of VRL was released for the duration of the experiment, culminating with ~80% of VRL released. In contrast, when VRL was paired with PAM and encapsulated, the released rate was significantly attenuated. At 12 hours, only approximately 20% of VRL had been released, which is markedly less than that observed with NPs lacking a hydrophobic excipient. At the final timepoint, a comparable amount of VRL had been released, however this was achieved over a prolonged period of approximately 4 days, as opposed to non-ion paired VRL that was predominantly released after 1 day.
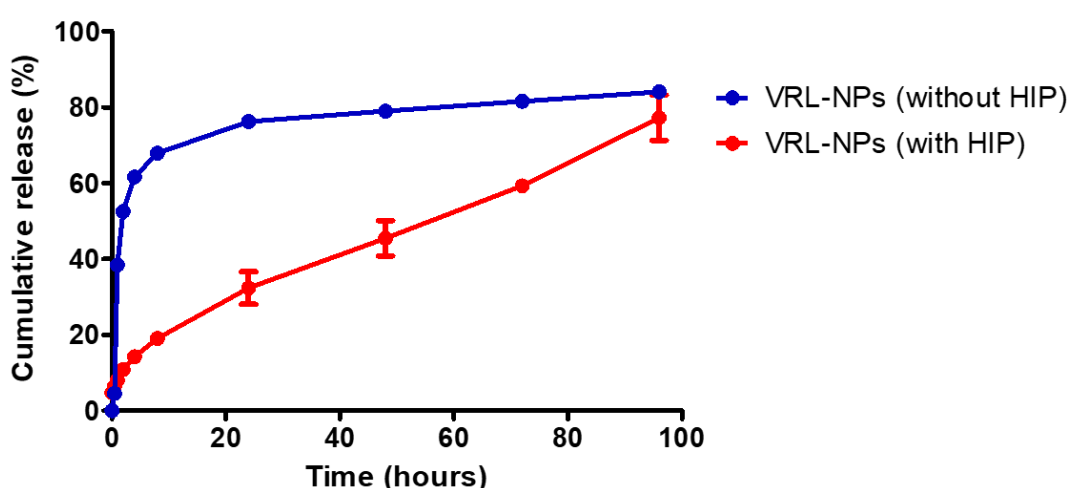
Figure 3.7. *In vitro* VRL release kinetics. VRL-NPs fabricated with or without a hydrophobic counterion were incubated in PBS (pH 7.4) at 37 ° C and drug release over time was determined by analysis of regularly sampled aliquots for VRL by HPLC. Data are presented as mean ± SEM, *n* = 3.

3.3.5. *Conjugation of afatinib analogues to nanoparticles - polymeric NPs*

To ensure that the structural modifications made to compound **17** that differ from afatinib were amenable to click chemistry, a fluorogenic coumarin assay was employed whereby successful reaction and creation of a triazole bearing product emitted fluorescence, whereas unreacted coumarin did not. The initial conditions involved reacting 3-azido-7-hydroxycoumarin with phenylacetylene (a surrogate aromatic alkyne) in the presence of a catalyst system known to give total conversion of non-fluorescent 3-azido-7-hydroxycoumarin to the fluorescent triazole derivative (0.25 mM CuSO$_4$, 1.25 mM THPTA ligand, 5 mM sodium ascorbate)[280]. The fluorescence generated from this reaction acted as a calibration for future reactions to discern whether the conditions were optimal for desired triazole product formation. The next reaction aimed to combine 3-azido-7-hydroxycoumarin with alkyne **14** using the same conditions as for the calibration reaction. The fluorescence generated from the product was approximately 60% than that of the calibration reaction (Figure 3.8A) implying the reaction conditions need to be altered in order to achieve complete product conversion and efficiency. It was speculated that increasing the concentration of copper and ligand (but maintaining the molar ratio) could act to enhance reaction efficiency. Indeed, this has proved successful in reacting azide bearing virus-like particles with polymeric alkynes[308]. When the copper and ligand concentrations were increased to five times that used in the calibration reaction and the concentration of all other reactants remained constant, a significant increase in fluorescence intensity was detected (Figure 3.8B). To test if these reaction conditions were applicable to the molecule of interest, alkyne **17** was reacted with 3-azido-7-hydroxycoumarin in the same fashion as with **14** and similar fluorescence intensity was detected, suggesting that the deprotected amine did not interfere with the azide-alkyne reaction dynamics and that the increased copper/ligand promoted more efficient product conversion with the alkynes used in this study. It has been noted that the type of ligand used can also influence the reaction efficiency, therefore another

ligand, TBTA, was utilised in the reaction of 3-azido-7-hydroxycoumarin and **17** (Figure 3.8C). The fluorescence generated from the product was equivalent to that of the previous reaction, however as TBTA has far less aqueous solubility and is reported to be a less efficient ligand[309], THPTA was used in all further click reactions.
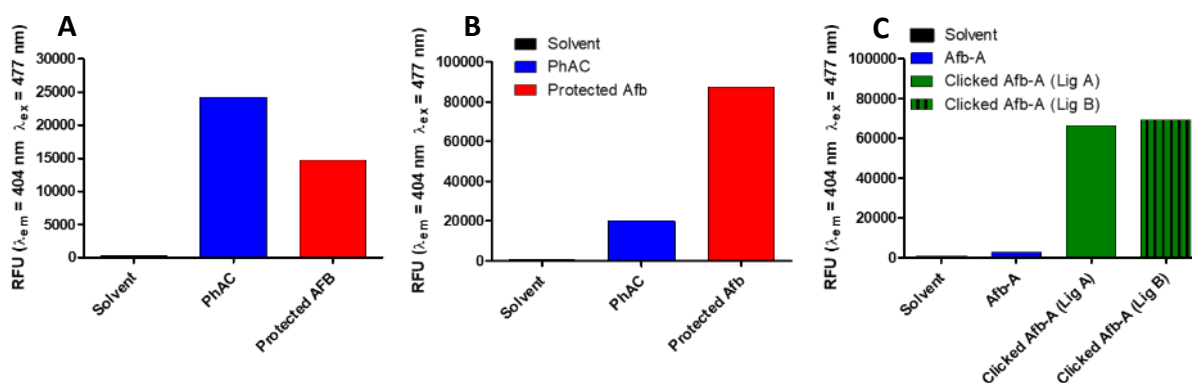
Figure 3.8. Optimisation of click reaction conditions. To acquire the optimal reaction conditions for click chemistry, a fluorogenic azide assay was performed. (A) using phenylacytelene as a model aryl alkyne (blue bar), conditions were not optimal for alkyne-bearing Afb coupling (red bar). (B) increasing the copper and ligand concentration was found to improve the reaction efficiency. (C) exploration of different ligands (THPTA and TBTA) based on their water solubility.

Once the appropriate reaction conditions had been established, the next step was to investigate the coupling efficiency of alkynes to azide bearing NPs. To achieve this, a fluorescent alkyne derivative of Alexa Fluor 488 was utilised as a surrogate for **17** and reacted with PLGA-PEG-N_3 NPs using the conditions described above. The reaction was allowed to proceed overnight to increase the probability of triazole product formation on the surface of NPs. After quenching the reaction, the mixture was purified using size exclusion chromatography to separate unreacted fluorescent alkyne from NP-conjugated fluorescent triazoles. The fluorescence intensity of each fraction was determined, and a typical elution profile is shown in Figure 3.9A. The fluorescent NPs are theorised to be contained in the earlier fractions due to a less hindered passage through the gel matrix. To confirm that the fluorescence detected in the earlier fractions was due to successful triazole formation and not unreacted fluorescent alkyne, two control experiments were performed; the reaction between azide bearing NPs and fluorescent alkyne

was repeated either in the absence of the copper/ligand/sodium ascorbate catalyst system which is a prerequisite for efficient azide-alkyne coupling[310], or repeated after the fluorescent alkyne was pre-incubated with a large excess of benzylazide prior to the reaction, in order to outcompete the azide groups present on NPs. Figures 3.9B and C show the elution profiles of these reactions.
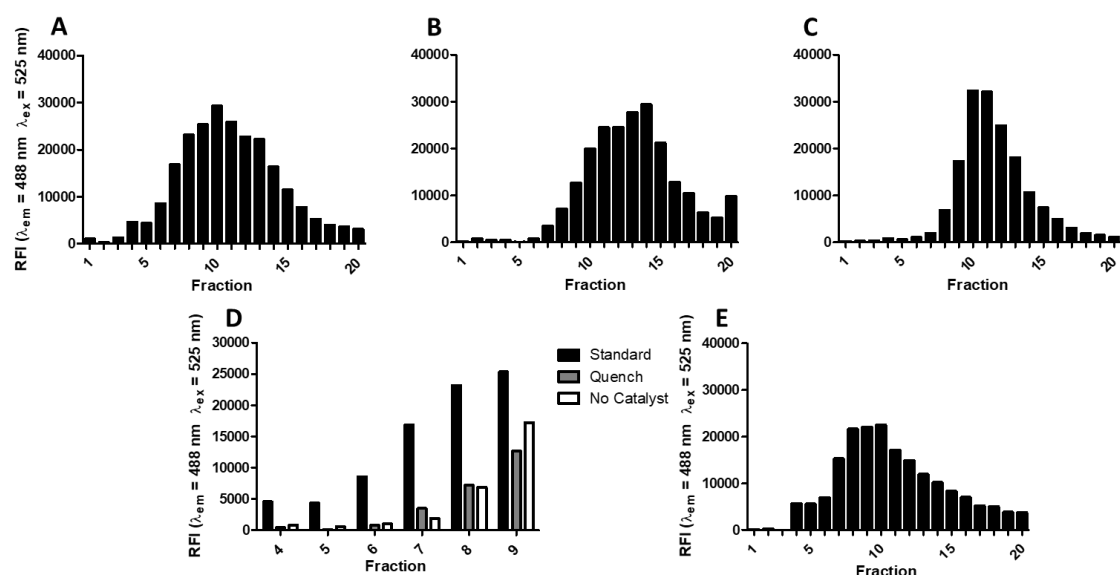
Figure 3.9. Determination of click chemistry efficiency to azide-functionalised NPs. Size exclusion chromatography elution profile of (A) azide NPs reacted with fluorescent alkyne under optimal conditions (B) reaction performed in the absence of catalyst system (C) reaction performed with "quenched" azides. (D) comparative fluorescence intensity of fractions 4-9 from the elution profiles of reactions A-C. (E) elution profile using optimal conditions but with double the initial NP concentration.

In both cases, there is a noticeable shift to the right in the elution curve, suggesting that the fluorescence intensity detected in the initial set of fractions collected is due to a successful reaction and product formation. Fractions 4-9 collected from the standard reaction exhibit significantly higher levels of fluorescence than in the corresponding fractions collected from the quenched alkyne and no catalyst reactions (Figure 3.9D). For instance, the fluorescence intensity in fraction 4 collected from the quenched alkyne and no catalyst reactions was only 9.6% and 17.7% respectively of that of the standard reaction. In fraction 7 the fluorescence intensity was 20.7% and 11.1 % of that of the standard reaction for quenched alkyne and no

catalyst reactions respectively. The majority of the unreacted fluorescent alkyne appeared to be eluted between fractions 10-15. Interestingly, increasing the initial concentration of NPs did not alter the elution profile compared to the standard reaction (Figure 3.9E). These results are in agreement with the underpinning theory of size exclusion chromatography and demonstrate that the proposed reaction conditions promote efficient click chemistry between azide decorated NPs and alkynes.

3.3.6. *Characterisation of dual NPs*

After identifying suitable conditions for click chemistry between biomolecule surrogates for the alkyne **17** and demonstrating the suitability of these conditions and azide functionalised NPs for click chemistry, the methodology of Pokorski *et al*. was adapted to facilitate conjugation of **17** to the surface of ion paired VRL azide bearing PLGA-PEG NPs[311]. Taking into account experimental considerations such as exposure to air, concentration of reactants and reaction time[280], **17** and PLGA-PEG-N$_3$ NPs were reacted in the presence of the optimised catalyst system and immediately sealed from air and left to react overnight in the dark. Approximately 1% (w/w) Afb-A was conjugated to NPs, as determined by UV-spectrometry with reference to a calibration curve (Figure 3.10A) and inference from conjugation of the fluorescent alkyne using the same conditions; this was possible due to a fluorescence calibration curve (Figure 3.10B). The conjugation of **17** to NPs did not drastically alter the physicochemical properties of the NPs compared to VRL-NPs and indirectly indicate successful conjugation to NPs by virtue of an increase in size and an increase in the surface charge to a more positive value, implying there have been surface modifications made to the NPs. NPs containing Afb and VRL (Dual-NPs) were found to be a monodisperse population of approximately 260 nm (as measured by DLS, Figure 3.10C) with a zeta potential of -16.4 mV.
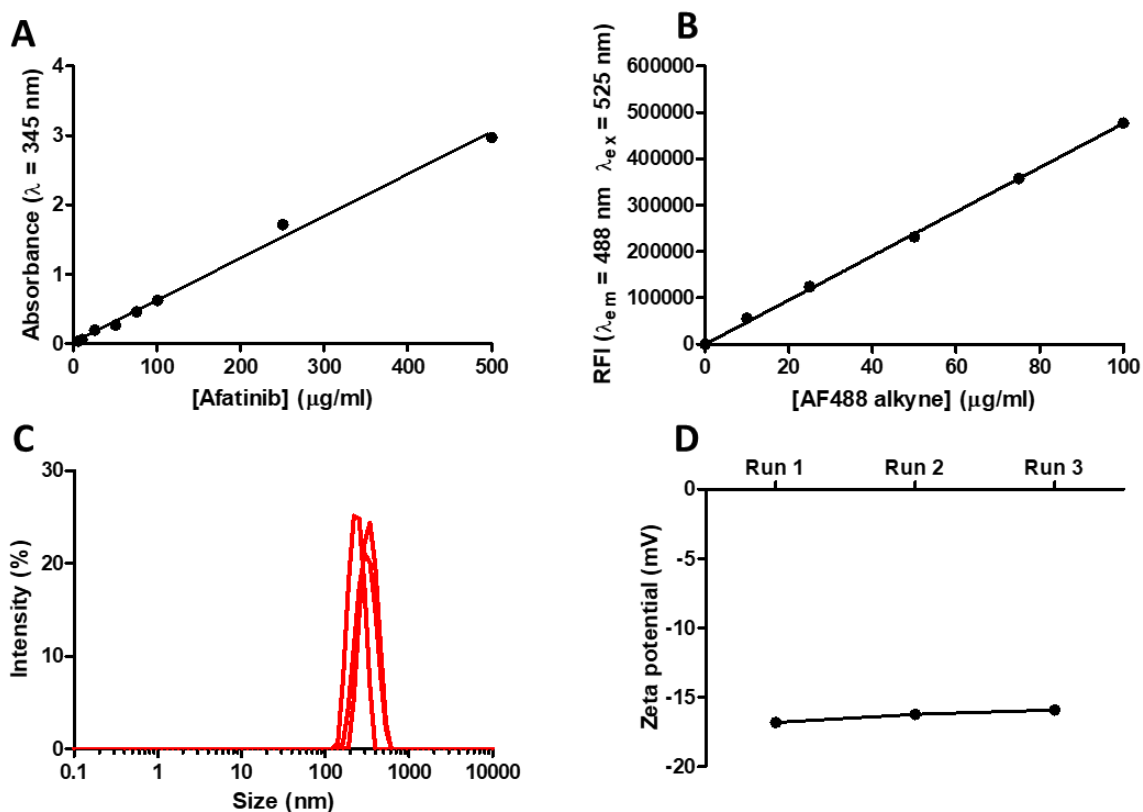
Figure 3.10. Characterisation of Dual-NPs. (A) Standard curve of Afb used for quantification of "clicked" Afb on to NPs. (B) Fluorescence standard curve used to quantify fluorescence intensity of "clicked" NPs using a fluorescent alkyne as a surrogate molecule. (C) DLS and (D) zeta potential measurements of post click reaction-purified polymeric NPs.

3.3.7. *Conjugation of afatinib analogues to nanoparticles - gold NPs*

Given the well-established chemistry of alkyl thiol- gold bond formation[185], the conjugation of afatinib analogue **16** to AuNPs required less optimisation. In order to maximise the amount of drug loaded to the surface of AuNPs without compromising colloidal stability, a solution of **16** was prepared and added to a 1 mL solution of AuNPs in 5 µL increments. It is known that when the colloidal stability of AuNPs is compromised, the colour of the solution changes due to agglomeration of AuNPs in solution as a result of larger particles. Using this qualitative metric, it was discovered that addition of volumes in excess of 70 µL of **16** caused the AuNP solution to change to a darker colour. Past the 70 µL threshold, any further addition of **16** to

the AuNP solution caused the intensity of the dark colour to increase, attributed to greater agglomeration of particles. As such, the optimal volume of **16**, (herein Afb-A) added to AuNPs was determined to be 70 µL to achieve ligand density saturation whilst maintaining AuNPs in solution. Following this, the remaining binding sites on drug bearing AuNPs were backfilled by incubating the conjugates in a solution of thiolated PEG. This is a well characterised procedure and contributes to the maintenance of colloidal stability of the AuNPs. After washing to remove unbound reactants, this process resulted in Afb-AuNPs which were subsequently characterised.

3.3.8. *Characterisation of gold NPs*

Using UV-vis spectroscopy and reference to a standard curve (Figure 3.10A), it was found that approximately 85% of Afb-A was conjugated to AuNPs which equated to 0.08 µg Afb-A per µg of AuNP. As with polymeric NPs, DLS and ZP measurements were obtained of AuNPs to discern the size and surface charge (Figure 3.11).
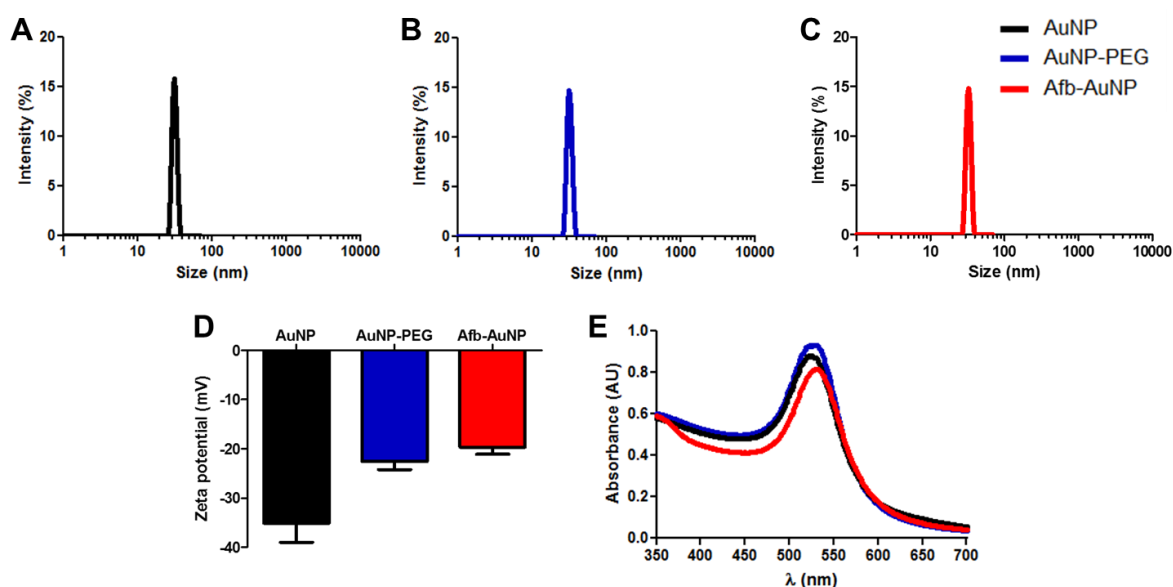
Figure 3.11. Characterisation of AuNPs. DLS measurements of (A) unmodified AuNPs, (B) PEGylated AuNPs and (C) Afb-AuNPs. (D) Zeta potential of AuNP variants; data represented as mean ± SD, $n = 3$. (E) UV-vis spectroscopy of AuNP formulations with surface plasmon resonance peaks depicted for each formulation.

DLS measurements (Figure 3.11A-C) revealed that unmodified AuNPs were 39.9 ± 0.22 nm, PEGylated AuNPs were 42.6 ± 2.70 nm and Afb-AuNPs were 46.1 ± 0.46. nm in diameter. This increase in the diameter of AuNPs as they were modified provides evidence of successful conjugation. Further indirect confirmation of conjugation was evidenced by the changes in surface charge, as measured by zeta potential. The zeta potential of unmodified AuNPs was -35.1 ± 3.85 mV, which became less negative as molecules were conjugated to the AuNP surface, owing to displacement of negatively charged citrate anions. Accordingly, AuNP-PEG had a zeta potential of -22.6 ± 1.64 mV and Afb-AuNPs had a zeta potential of -19.7 ± 1.46 mV (Figure 3.11D). UV-vis spectroscopy was also employed to determine AuNP size (Figure 3.11E) and, concordantly with DLS, there was an increase in size as AuNPs were modified. Unmodified AuNPs had a λ_{max} of 523 nm, which increased when AuNPs were PEGylated, to 525 nm and increased further to 530 nm when Afb-A and PEG were conjugated to AuNPs. The λ_{max} values agree with DLS measurements, affirming the size of AuNPs.
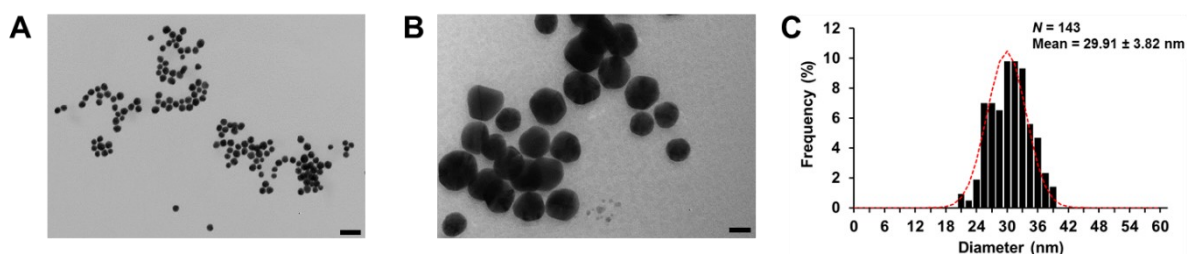
Figure 3.12. Transmission electron microscopy (TEM) images of Afb-AuNPs. TEM images were obtained of AuNPs after modifications with PEG and Afb and their spherical morphology and size was maintained. (A) 40,000 x magnification, scale bar = 100 nm. (B) 200,000 x magnification, scale bar = 20 nm. (C) Histogram of AuNP size distribution, data are represented as mean ± SD, $n = 143$.

TEM (Figure 3.12A-B) confirmed Afb-AuNPs had a spherical morphology and exhibited similar size as those measured using DLS and UV-vis. Computational analysis of TEM images produced a histogram (Figure 3.12C) confirming the homogeneity of the modified AuNPs, estimating the size to be approximately 30 nm, which is slightly smaller than measured by DLS, but is to be expected as AuNPs were completely dehydrated upon imaging by TEM.

Thus, AuNPs were successfully modified without drastically altering their physicochemical properties or compromising colloidal stability.
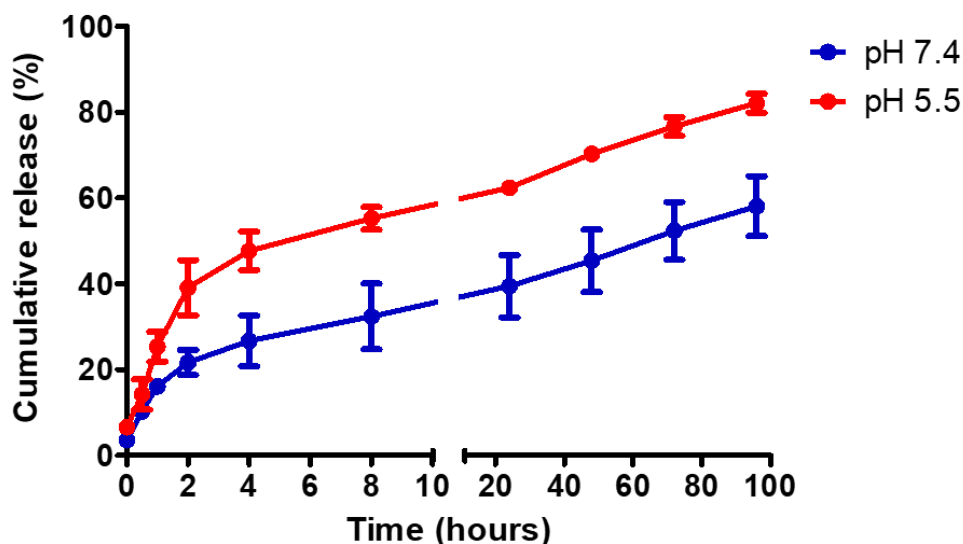
Figure 3.13. *In vitro* release kinetics of Afb from AuNPs. Afb-AuNPs were incubated at 37 °C and either pH 7.4 or pH 5.5 whereby aliquots were taken at predefined intervals. Drug release over time was determined by absorbance measurements of the sampled aliquots. Data are represented as mean ± SEM, *n* = 3.

The release of Afb from AuNPs (Figure 3.13) was also determined at both physiological and acidic pH (7.4 and 5.5 respectively). Differential rates of Afb liberation from AuNPs were observed between the two conditions, which became apparent after as early as 2 hours. At this timepoint, 41% of Afb had been released from AuNPs at pH 5.5, which was significantly more than at pH 7.4, whereby 23% had been released. Throughout the rest of the experiment, the cumulative release of Afb was consistently greater at pH 5.5 than at pH 7.4 and at the culmination of the experiment, approximately 23% more Afb had been released in acidic pH than in under physiological conditions.

3.4. Discussion

The work presented in this chapter describes the synthesis of Afb analogues and a block copolymer decorated with azide groups. The fabrication of NPs comprised of this copolymer as an attempt to encapsulate the chemotherapy VRL is outlined, as well as optimisation steps and full particle characterisation. Subsequently, dual chemotherapy-carrying particles were developed, incorporating VRL and an afatinib analogue, and characterised. Finally, an AuNP formulation was synthesised that contained another Afb analogue and PEG, the characterisation of which was also detailed.

The initial work of this chapter was focused on the development of Afb analogues (Scheme 1) that were envisioned to be conjugated to either polymeric or AuNPs. It was critical that the structural modifications made did not perturb the biological activity of the molecule and thus, the only functional group that differs from the original is the dimethylamino group. Preservation of the C-4 aniline and C-6 acrylamide that surround the quinazoline core is essential as these are critical function groups that dictate the selectivity of Afb for EGFR. The acrylamide group specifically is known to participate in irreversible covalent bonding (of Afb) to EGFR *via* Michael addition to cysteine 797 in the EGFR kinase domain[312]. Reinforcing this, X-ray crystallographic analysis of Afb bound to both wild type EGFR and the T790M EGFR mutant protein demonstrated the formation of covalent bond between cysteine 797 of EGFR and the acrylamide functionality of Afb[313], suggesting that the structure-activity relationship of Afb and EGFR is heavily influenced by the presence of the acrylamide group. This rationale governed the decision to modify the dimethylamino group with propargylamine; previous studies also opted to modify this site, suggesting this position has a good tolerance to substitution without dramatically affecting activity[314,315]. The introduction of propargylamine gave rise to quinazoline derivative **14** which contained a pendant alkynyl group to facilitate 1,3-dipolar cycloaddition with either azide bearing **13** or azide functionalised polymeric NPs.

Azide-bearing NPs originated from the block copolymer PLGA-PEG-N$_3$ which was synthesised using facile DCC/NHS chemistry to form an amide bond between the carboxylic acid of PLGA and the amine of the heterobifunctional PEG linker. This is a highly specific, well established and high yielding reaction that creates a stable linkage between the two polymers[247] such that the resultant product is amenable to further chemistries. The chemical connection of the two polymers was confirmed both by NMR and FTIR spectroscopy (Figure 3.1 and 3.2) that both demonstrated the presence of peaks belonging to both polymer components in the spectrum of the copolymer (more evident with NMR). Furthermore, the retention of the azide group after conjugation was achieved due to the specificity of the coupling reaction (as denoted by the azide peak at 2109 cm^{-1}), therefore leaving the azide functionality untouched.

After confirmation that the copolymer was synthesised with the desired properties (reactive azide intact, defined structure and molecular weight), polymeric NPs were then fabricated. The aim of using this polymer was to take advantage of its amphiphilicity to form a structure whereby, in an aqueous solution, the hydrophobic PLGA formed the core of the particles and the hydrophilic PEG component forms a shell-like structure surrounding the core[316], whereby the azide groups are orientated outwards from the surface and therefore available for reactions. The initial efforts to encapsulate VRL were predicated on an OW-ESE fabrication method whereby the organic phase, in which is dissolved the drug and copolymer, is emulsified in an aqueous phase, usually containing surfactant. After emulsification, the organic solvent is evaporated which contributes to hardening of the NPs. Indeed, there are several other methods that can be employed to synthesise polymeric NPs from preformed polymers (as opposed to monomeric polymerisation), including emulsification-solvent diffusion, salting out, dialysis, the use of supercritical fluid technology, the most common of which is nanoprecipitation or interfacial deposition[317]. ESE was chosen instead of the nanoprecipitation method for several

reasons: nanoprecipitation is only favourable for highly hydrophobic drugs (e.g. taxanes) limiting the scope of the formulations, the loading efficiencies are generally lower than that of ESE, large-scale syntheses are difficult, and finding an optimal drug/polymer/solvent/aqueous system is challenging as is thorough mixing of the components[318]. For example, Budhian *et al*. found that ESE produced unimodal polymeric NPs below 300 nm in diameter with high loading efficiency of haloperidol (hydrophobic, logP of approximately 4.3) compared to that when the nanoprecipitation method was employed[300]. Wang *et al*. observed that higher loading of salinomycin (hydrophobic, logP of approximately 7.5) was achieved using an emulsion-based method of polymeric NP synthesis as opposed to nanoprecipitation, however NPs made with emulsion were slightly larger and more polydisperse[319]. This is commonly witnessed as ESE is known to produce larger particles than nanoprecipitation, in part due to the need for external energy into the system, which may be heterogeneously distributed, that breaks up the microemulsions into nanoemulsions.

Indeed, within ESE itself there are many parameters and factors that can be considered in order to optimally encapsulate the drug of interest. Keum *et al* systematically investigated several of these parameters, solvent system, surfactant type and concentration, order of mixing, amount of initial drug, sonication time and power in order to optimally encapsulate docetaxel within PLGA NPs[302]. Ultimately however, a critical parameter is that of drug hydrophobicity; the reason why hydrophilic molecules are not efficiently encapsulated using these techniques is that they are more soluble in the aqueous phase and leach out from the organic phase during the formulation process. Even the double emulsion method of ESE[320], which can accommodate hydrophilic molecules somewhat, produces large NPs with moderate loading efficiencies. The initial preconception for using VRL was that it was hydrophobic enough for ESE based on its logP (4.3) and that it is formulated as a salt for use in the clinic which is usually a tactic employed to increase water solubility. ESE was able to produce NPs with good

physicochemical properties (Figure 3.3) such as a negative surface charge to prevent nonspecific adsorption of proteins and under 300 nm which is required for utilisation of the EPR effect (see Introduction and Chapter 4), but over 10 nm which is required to avoid glomerular filtration and excretion. However, as shown in Table 3.1, despite attempts to increase the loading of VRL by altering pH, drug amount and solvent system, VRL was deemed too hydrophilic for ESE in its original form, whereby VRL would freely diffuse into the aqueous phase upon NP preparation and was therefore not available for encapsulation in the more hydrophobic polymer core. This evidenced as the highest loadings were observed when the pH of the aqueous phase was above the pKa of VRL (8.7), therefore the amines are less protonated, decreasing water solubility, however inadequate buffering may have resulted in deleterious pH changes.

To increase the hydrophobicity of VRL, a strategy was implemented whereby the basicity of VRL was leveraged to create an ionic pairing with a hydrophobic acid. By successfully creating an ion pair, the hydrophobicity of the native molecule can increase dramatically thus making it more amenable for encapsulation into polymeric NPs[304]. HIP has been used to successfully encapsulate dexamethasone, topotecan, vincristine and other molecules into polymer NPs[305,306,321]. Moreover, a similar technique utilises salt gradients to encapsulate amphiphiles within liposomes; doxorubicin was efficiently loaded into liposomes using an ammonium sulfate gradient and VRL was subjected to transmembrane gradient loading into liposomes using triethylammonium sodium octasulfate, resulting in high loading which was thought to be due to strong ionic interactions and complexation leading to precipitation within the liposomes[322]. A notable study by Ashton *et al*. screened various hydrophobic ion pairing agents to efficiently encapsulate the aurora kinase B inhibitor AZD2811 within PLGA-PEG NPs; cholic acid (CA) was amongst the best performers in terms of formulation criteria and AZD2811-CA NPs demonstrated considerable antitumor efficacy *in vivo*[323]. Given that

AZD2811 and VRL have a similar pKa, initial HIP formulations were comprised using CA (Table 3.2) and whilst increased drug loadings were observed, parameters such as size and surface charge suffered. This was theorised to be due to the low solubility of CA in the organic phase and the use of trifluoroacetic acid which may have altered protonation states and pH of the aqueous phase.

PAM was used as a substitute counterion, as outlined in Song *et al.* and desirable properties were seen in terms of size, surface charge, morphology and drug loading (Figure 3.4 and Table 3.2). PAM is significantly more hydrophobic than CA and is a dicarboxylic acid; thus complexes could be formed comprised of two VRL molecules per PAM molecule. This means that more VRL could be driven into the core of the polymeric NP upon HIP complexation than with a monoacid which is also more hydrophilic. Vincristine, which is another vinca alkaloid with similar chemical properties, has been successfully encapsulated in PLGA-PEG NPs using PAM as a counterion suggesting that HIP is viable with vinca alkaloids[321]. Moreover, parameters delineated in Song *et al.* such as quench buffer type, molarity and pH (quench buffer is the solution the emulsion is poured into and where the organic phase evaporates from) were also accounted for[307].

HIP was confirmed using NMR spectroscopy (Figure 3.5 and 3.6) whereby VRL complexation with PAM caused upfield resonance shifts in specific peaks. This phenomenon can be attributed to increased electron density upon salt formation due to the proximity of the carboxylate anion, which would explain why certain peaks are affected more than others. Further evidence of salt formation can be seen in Figure 3.7 as the release of VRL is attenuated when complexed with PAM as opposed to conventional VRL. The hydrophobic salt has a greater affinity for the hydrophobic core of the polymeric NP than the aqueous surroundings, therefore slowing the release from the polymer matrix. This feature of HIP has been seen with other formulations and is considered a hallmark of successful salt formation. The formulation

parameters could be further optimised by screening with other counterions, optimising the volume and composition of the organic and aqueous phase, polymer and drug amounts and mixing. Indeed, formulations in clinical trials that rely on the same nanoemulsion synthesis as used here, such as BIND-014, utilise techniques such as tangential flow filtration to homogeneously mix the components and control particle size[324]. These formulations are generated on a larger scale where the HIP process may be more effective than repeated benchtop syntheses where parameters can vary.

After NP formation and VRL encapsulation, the next step was to covalently conjugate an Afb analogue to the surface of the NP. As previously mentioned, the polymeric NPs were decorated with azides that, under the appropriate conditions, can be coupled to alkynes, such as the one Afb analogue **17** possesses. Covalent conjugation was chosen as opposed to widely used noncovalent methods of ligand attachment (hydrophobic or electrostatic interactions) as upon *in vivo* administration, the surface of the construct is unlikely to remain stable, leading to loss of ligand and rapid elimination[325]. To attach the Afb analogue to polymeric NPs, well established click chemistry was employed and was optimised by reference to a series of papers published by the pioneering chemists behind the original click reaction between azides and alkynes[326].

The use of an azidocouramin derivative that became fluorescent upon successful reactions (i.e. formation of the triazole product) was employed to screen different reaction conditions, using phenylacetylene as a model aromatic alkyne. Phenylacetylene was reacted with 3-azido-7-hydroxycoumarin (Figure 3.8) using the conditions outlined in Presolski *et al.* to discern 100% conjugation efficiency[280], however when phenylacetylene was replaced with Afb alkyne **14** the reaction efficiency decreased. The popularity of azide-alkyne coupling has sparked thorough investigation into optimising conditions for an ever-increasing scope of azide or alkyne bearing substrates, which include peptides, proteins, nucleic acids, glycans, lipids, NPs and live cells[327].

Hong *et al.* explored a range of parameters that were found to effect click reaction efficiency including copper-to-ligand ratio (ligands are Cu-binding species, usually some derivation of tris(azolyl)amines, concentration of ascorbate, substrate concentration, Cu oxidation, solvent (buffer) suitability, reaction byproducts and contraindicated species such as thiols that are nucleophilic and can oxidise readily[281]. The practical and mechanistic implications of different ligands in relation to Cu concentration and solvent system were explored and it was found that the type of ligand can dramatically influence the reaction kinetics and therefore the ligand ought to be chosen based on the solvent system employed which ultimately is due to the biomolecules to be conjugated[328]; *in vivo* click chemistry optimisation has also demonstrated the need to tune the conjugation system to achieve successful labelling of *O*-linked glycans in zebrafish embryos with minimal toxicity[309].

In the current system, it was found that increasing the overall copper and ligand concentration by 5 (but maintaining the same molar ratio) increased reaction efficiency between alkyne **14** and the coumarin. Initial conditions may not have been optimal due to potential shielding of the alkyne or electronic interferences from the aryl systems present in the reaction. Two ligands were compared in this work based on their water solubilities and surprisingly there was no significant difference in the reaction efficacy using either ligand. The more hydrophilic variant was taken forward for further reactions as the solvent system was predominantly aqueous and has been used for bioconjugation reactions involving NPs. It is likely that this reaction could be further optimised given the scope of ligands and screening conditions (as mentioned above); however, this was beyond the remit of this thesis.

To confirm that the established reaction conditions could be taken forward and applied to a polymeric NP system, a fluorescent aromatic alkyne was reacted with azide-bearing polymeric NPs and the resultant NPs were purified using size exclusion chromatography (Figure 3.9). The principal of this technique relies on the more rapid elution of larger molecules (i.e. NPs)

compared with smaller ones, therefore NPs will be eluted in the earlier fractions and free dye in the later fractions[329]. Compared to controls (in this case NP-alkyne reactions with no catalyst or using a huge excess of another azide as a competitive inhibitor) more fluorescence was detected in the earlier fractions, indicating that eluted NPs had conjugated fluorescent alkyne. Interestingly, increasing the initial amount of NP did not appear to affect the conjugation efficiency, suggesting the alkyne was in excess with respect to the available azide binding sites. Such polymeric systems do not display every azide with complete fidelity and some may be buried within the polymeric network. The NPs themselves could also sequester copper reducing the amount available for catalysis of the reaction, or the alkynes themselves. Indeed, the versatility of this reaction has led others to conjugate various biomolecules to NPs using azide-alkyne chemistry, both with and without the use of a copper catalyst system. Such biomolecules include antibodies, peptides, gadolinium complexes, nucleic acids and small molecules[330,331].

The chemical toolkit available for bioconjugation "click" reactions is broad, the scope of which extends beyond this thesis, however there are many other functional groups that can be used to attach biomolecules to NPs or each other, such as thiols, maleimides, furans, N-hydroxysuccinimide esters, amines, acrylates, iodoacetamides, isothiocyanates and carboxyls to name several popular moieties (see ref. 332 for in-depth review). Nonetheless, alkyne was successfully conjugated to the NPs, and when fluorescent alkyne was replaced with alkyne **17** this surface modification did not appear to detrimentally affect the physicochemical properties of the NP (Figure 3.10). DLS and ZP measurements were consistent with fairly monodisperse and colloidally stable NPs; the slight increase in size compared to non-functionalised NPs can be attributed to conjugation of alkyne **17**. Similarly, the increased surface charge is due to a reduction in available charged azides as some were converted to triazoles by the click reaction. Unfortunately, it was difficult to quantify the exact number of conjugated molecules per NP as alkyne **17** is not intrinsically fluorescent, it cannot be quantified using techniques that are

applicable to peptides/proteins (e.g. BCA assay) and there have been no antibodies raised against it. However, using indirect quantification methods such as fluorescence of an analogous alkyne and UV-vis spectroscopy, an estimation of quantification was possible.

The synthesis of Afb-A facilitated attachment to AuNPs *via* a cyclic disulfide linker, the construction of which also relied on copper-catalysed click chemistry between an azido-lipoic acid moiety and alkyne **14**. A cyclic disulfide group was used to attach Afb-A to AuNPs as greater stability of Afb-A on the AuNP is achieved by virtue of providing two Au-S bonds per molecule; this also ensures robust drug loading and increased reaction efficiency. Indeed, molecules attached by single thiol-gold bonds are more labile and have been shown to be displaced by strong nucleophiles *in vivo*[333]. Moreover, previous methodology has been employed to link Afb to AuNPs using single thiol-gold bonds and a PEG linker[334], however the conjugation chemistry employed, EDC/NHS chemistry, is commonly used to create peptide bonds between carboxyl groups and nucleophilic primary amines[199]. Native Afb does not possess any amines that are accessible for this type of reaction, which may significantly limit conjugation and thus explains the higher conjugation efficacy achieved in this work.

Further capitalising on the reactivity of thiols, a PEG linker bearing free thiol groups was also attached to the AuNPs which is useful in NP drug delivery both from a chemical and biological perspective. PEGylation of NPs is achieved by ligand exchange at the AuNP surface[335] and is known to maintain colloidal stability upon conjugation of a biomolecule that otherwise disrupts the surface charge density and intensity of the NP[336]. There are varying degrees of PEGylation that can be achieved depending on the surface area of the NP, the amount of PEG added and the molecular weight of PEG. The less surface area there is, the less PEG added and the higher the molecular weight, the lower the number of PEG chains that are attached to a NP[337]. Typically defined by the number of PEG chains per $100nm^2$, PEGylation of a NP surface culminates in several regimes that can broadly be described as mushroom or brush

conformations[338]. Lower amounts of PEG/nm^2 usually give a mushroom-like structure whereas higher grafting densities give brush conformations which are favourable for *in vivo* applications due to the reduced proclivity of proteins to adsorb to the NP, translating to longer circulatory half-life[339]. The exact number of PEG chains/nm^2 attached to AuNPs was not calculated in this work, however recent work has shown that above a threshold value of 20 PEG chains/100 nm^2 circulatory half-life did not further increase[340]. Inductively coupled plasma-mass spectrometry (ICP-MS) can be used to quantify the varying elemental concentrations of a sample, for example the Au^+/S^+ content, which can then be used to infer the concentrations of PEG, Afb-A or any thiolated ligand to AuNPs. Given the initial amount of PEG added to the constructs, the threshold value is expected to have been reached. Indeed, after PEGylation the size of the AuNPs did increase, as did the surface charge (Figure 3.11), implying the surface had been modified and therefore successfully PEGylated or functionalised with Afb-A. The surface charge became more positive due to displacement of anionic citrate and replacement with thiolated PEG. The UV-vis spectra also hinted towards an increase in size once NPs were modified (either by PEG or both PEG and Afb-A). UV-vis spectroscopy can determine the size of AuNPs based on their surface plasmon resonance (SPR). Optical parameters such as the scattering efficiency and extinction coefficient of AuNPs are influenced by particle size. Therefore, based on their SPR, size can be predicted in excellent agreement with the mathematical theory that underpins the technique[341]. A red shift in SPR of modified AuNPs, indicative of increasing particle size, was further suggestive of successful conjugation of Afb-A to AuNPs. This red shift in the SPR was seen in both PEGylated AuNPs and Afb-AuNPs and can be attributed to the increase in dielectric constant around the surface of the AuNP upon conjugation with thiolated ligands[342].

Encouragingly, TEM (Figure 3.12) of modified AuNPs did not reveal any structural abnormalities after conjugation and the size measured aligned well with the other

characterisation techniques utilised, overall confirming the desirable properties of Afb-AuNPs. The expedited release of Afb from Afb-AuNPs in an acidic environment (Figure 3.13) was not unexpected despite this formulation not including any "acid-sensitive" bonds such as imines, oximes or hydrazones. The dative covalent thiol-gold bond is labile at acidic pH (6.5 and lower) due to protonation of the S atom[343,344] which results in bond cleavage and subsequent liberation of Afb-A from the AuNP. Fewer protons at neutral pH will therefore translate to attenuated release, which is precisely what was observed. The release kinetics of future formulations can be tuned by incorporating stimulus responsive elements (pH, heat, light, enzyme) to either increase or prolong the release of a biomolecule depending on the intracellular location of the target and required concentration for therapeutic effect.

3.5. Conclusion

In summary, the synthesis of novel afatinib analogues and their covalent attachment to polymeric and AuNPs is described. With respect to polymeric NPs, the development of hydrophobically paired VRL and its subsequent encapsulation is outlined. Despite initial unsuccessful efforts to encapsulate VRL, a methodology involving hydrophobic acids was devised to successfully accomplish this. The resulting NPs were a homogenous population found to exhibit physicochemical properties that are advantageous for drug delivery such as high drug loading, colloidal stability and diameter < 400 nm. Attachment of afatinib analogue **17** to the surface (using azide-alkyne click chemistry) did not adversely impact NP properties and thus a dual drug delivery system was created. Similarly, AuNPs functionalised with a separate afatinib analogue (by alkyl-thiol chemistry) resulted in a monodisperse and stable formulation as denoted by characterisation of NP properties. The methodologies and results presented in this chapter are versatile and may inform future attempts to encapsulate amphiphilic molecules or conjugate hydrophobic ones. Future studies would benefit from further optimisation of NP parameters such as conjugation efficiency, PEGylation density and

type (e.g. incorporation of environmentally responsive functionalities) and release kinetics. Incorporation of next generation therapies (immunotherapy, gene editing technology) will aid the future development of NP therapeutics.

4. Biological evaluation of afatinib analogue tethered gold nanoparticles *in vitro*

This chapter describes the biological assessment of optimised afatinib analogue tethered gold nanoparticles (Afb-AuNPs) in human lung cell lines of alveolar epithelial origin. The physicochemical properties of Afb-AuNP are summarised and the cytotoxicity and anti-proliferative effects are investigated in lung cancer cell lines. Cellular uptake of Afb-AuNPs is also examined as well as the biocompatibility of the nanoformulation, determined by cell viability and inflammatory cytokine release. The therapeutic utility of the non-traditional nanoconjugates compared to free drug are discussed in a biological context. The potential applicability of the conjugation method to other molecules and combination with other therapeutic modalities are considered.

4.1. Introduction

Gold nanoparticles (AuNPs) have received vast interest, especially over the past two decades, for their utility in medicine[158]. This is, in part, due to the ease, reproducibility and versatility of their synthesis[179,188]. The resulting AuNPs have unique optical and photothermal properties[345-347], a high surface area to volume ratio and surfaces that are readily amenable to modification by functional groups like thiols, amines and phosphines. Therapeutic or diagnostic molecules containing these functional groups can be anchored to the AuNP surface, increasing their functionality further[348,349]. AuNPs are also highly biocompatible and exhibit low intrinsic toxicity[350]. It is these characteristics that make them excellent candidates for drug delivery candidates[351,352].

Several different types of ligands have been functionalised to the surface of AuNPs, including oligonucleotides[353], peptides[354], antibodies[355] and small molecules such as chemotherapy[356].

The overarching goal of conjugation to the NP surface is to enable programmed release of payload in a site-specific manner. Surface conjugation also provides a means of targeting and protection of ligands from metabolism and excretion as well as prevention of side effects due to the reduction of systemic dissemination throughout the body mediated by the EPR effect or active targeting approaches[195]. This, combined with the proclivity of AuNPs to be endocytosed by design[357], is thought to improve the delivery and efficacy of therapeutic molecules. The attachment of chemotherapy to the NP surface is traditionally achieved using one of two main approaches. Non-covalent adsorption or covalent coupling, either with an adapter molecule or directly to the surface. Non-covalent adsorption relies on ionic and hydrophobic interactions between the molecule of choice and the AuNP[325], however the nature of these bonds increases the likelihood of displacement of chemotherapy from the surface in biological environments. As such, covalent conjugation is the most popular method of attachment and has been used for several chemotherapeutics such as paclitaxel, doxorubicin, cisplatin and others[198]. Typically, these molecules are attached to AuNPs that are coated with an adapter molecule that facilitates covalent conjugation with the native chemotherapy. The most common example of this is the use of varying polyethylene glycol (PEG) spacers; heterobifunctional PEG can be attached to the AuNP surface by virtue of thiol-gold dative covalent bond formation whilst the remaining functional group is free for subsequent reactions. This concept was illustrated by Brown *et al*. whereby AuNPs were first PEGylated prior to covalent conjugation of the active component of oxaliplatin to the free carboxylate groups of the PEG linker[358]. An alternative strategy is to PEGylate the chemotherapy directly prior to attachment, a tactic employed by Ding *et al*. for the attachment of paclitaxel to AuNPs[359].

As described in the previous chapter, a different approach was employed to conjugate afatinib to AuNPs (Figure 4.1). The creation of a novel nanoformulation (Afb-AuNPs) requires adequate biological interrogation, especially as the modification process outlined above

changes the physicochemical properties of AuNPs, directly influencing their biological impact. Initially, the cytotoxicity of AuNPs, PEGylated AuNPs and Afb-AuNPs was investigated using human lung adenocarcinoma cell lines A549 and PC-9 as well as human alveolar epithelial type I-like (TT1) cells[360].
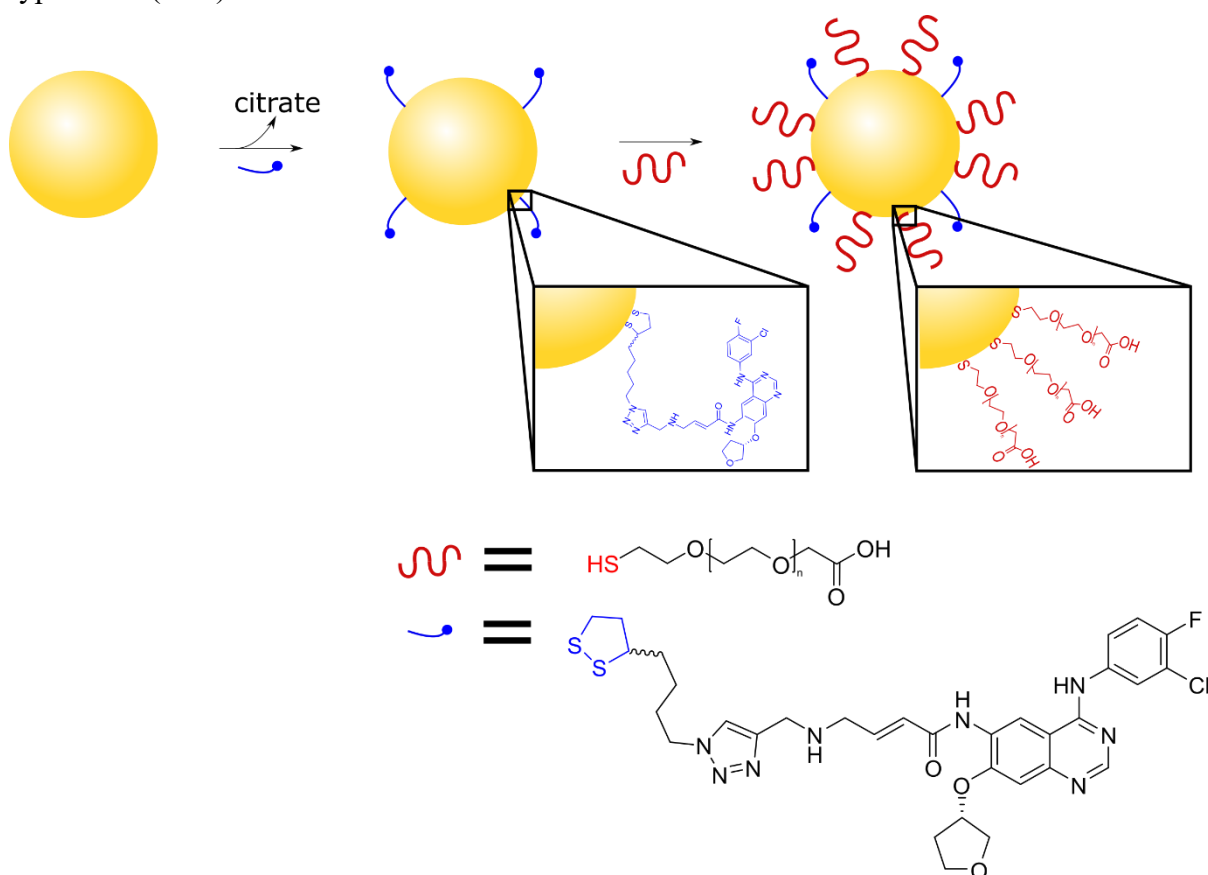
Figure 4.1. Schematic representation of the development of Afb-AuNPs. Citrate-capped AuNPs are first conjugated with thiolated afatinib analogues (blue) by virtue of a cyclic disulfide anchor. Subsequently, drug-bearing AuNPs are then PEGylated (red), enabled by further thiol-gold bond formation culminating in Afb-AuNPs. Reprinted with permission from Cryer AM, Chan C, Eftychidou A, et al. Tyrosine Kinase Inhibitor Gold Nanoconjugates for the Treatment of Non-Small Cell Lung Cancer. ACS Applied Materials & Interfaces 2019;11:16336-46[361] Copyright 2020 American Chemical Society.

The conventional MTT assay was employed for straightforward spectrophotometric quantification and as such represents the first study to examine the cytotoxic effects of AuNPs and AuNP conjugates on human carcinoma and non-carcinoma cells of alveolar epithelial origin. Despite the reputation of AuNPs as biocompatible, it is still imperative to ensure the safety of the drug delivery vehicle and to determine the efficacy of the attached

chemotherapeutic. Indeed, aberrant alveolar damage is involved in the pathogenesis of pulmonary fibrosis[362] and emphysema[363], which is to be avoided if a drug delivery system with a pulmonary target is to be safe and effective. To accompany traditional cytotoxicity studies, the effect of Afb-AuNPs on cancer cell proliferation was also examined in real time using a label-free technique that relies on electrical resistance to determine cellular health. As tumours cells proliferate more rapidly than the cells in the surrounding environment, it was considered appropriate to evaluate the efficacy of Afb-AuNPs in an actively proliferating system to more accurately mimic *in vivo* tumour cell dynamics.

As excessive inflammation is thought to exert a pro-tumourigenic effect[364], the release of the pro-inflammatory cytokines interleukin (IL)-6 and IL-8 from A549 cells was quantified upon exposure to Afb-AuNPs. In a similar vein to the cytotoxicity studies, the inflammatory profile of TT1 cells exposed to Afb-AuNPs and free drug was also investigated as increased inflammation induced by alveolar injury can contribute to and exacerbate lung disease[365] and NPs may serve to instigate an inflammatory response in the lung[366]. Therefore, biocompatibility in this context is as important as maintaining the viability of the healthy alveolar epithelium. Finally, the cellular uptake of Afb-AuNPs was studied using confocal microscopy. The endocytosis of AuNPs is dictated by their physicochemical properties and has been well documented[367], therefore it was important to ensure that functionalisation with chemotherapy and PEG did not negatively affect the propensity of AuNPs to be internalised by cancer cells. This is of particular relevance as the target of afatinib, the ATP binding pocket of epidermal growth factor receptor (EGFR), is intracellular. Therefore, the more drug that can enter and accumulate within the cell the greater the therapeutic effect. The hypothesis for this chapter is that Afb-AuNPs will display cytotoxicity in cancer cells by virtue of the tethered TKI and may exhibit reduced toxicity in non-cancerous cells. Modification of AuNPs with Ab is not predicted to prohibit the uptake of the AuNP constructs.

4.2. Aims

- Investigate the cytotoxicity of AuNP, AuNP-PEG and Afb-AuNPs in human lung carcinoma and non-carcinoma cells of alveolar epithelial origin.

- Determine the effect of AuNP, AuNP-PEG and Afb-AuNPs on proliferation of human lung carcinoma cells.

- Assess the inflammatory profile of Afb-AuNPs in a model of the healthy and cancerous alveolar epithelium.

- Evaluate cellular uptake of Afb-AuNPs .

4.3. Results

4.3.1. *Physicochemical properties of Afb-AuNPs*

Afb-AuNPs were synthesised and characterised as described in the previous chapter. Table 4.1 summarises the physicochemical properties of Afb-AuNPs, PEGylated AuNPs (AuNP-PEG) and unmodified AuNPs that were used throughout this work. These parameters were optimised to achieve maximal drug loading whilst maintaining colloidal stability, negative surface charge and appropriate size for endocytic uptake into cells.

Sample	HD (nm)	PDI	ZP (mV)	λ_{max} (nm)	Morphology (by TEM)	Afb-A (µg/ µg Au)
Unmodified AuNP	39.9 ± 0.22	0.19 ± 0.01	-35.1 ± 3.85	523	Spherical	N/A
AuNP-PEG	42.6 ± 2.70	0.20 ± 0.01	-22.6 ± 1.64	525	Spherical	N/A
Afb-AuNP	46.1 ± 0.46	0.26 ± 0.03	-19.7 ± 1.46	530	Spherical	0.08

Table 4.1. Physicochemical properties of AuNP formulations. Spectrum of parameters analysed in order to characterise AuNP formulations. Data are presented as mean ± standard deviation (*n* = 3). HD – hydrodynamic diameter, PDI – polydispersity index, ZP - zeta potential, λ_{max} – UV-vis maximum peak absorption, TEM – transmission electron microscopy

4.3.2. *Initial assessment of cytotoxicity of Afb-AuNPs*

After extensive characterisation of the Afb-A molecular structure and Afb-AuNPs, a proof of concept experiment was performed to investigate the cytotoxicity of Afb-AuNPs. A dose response to Afb-AuNP treatment was determined using confluent monolayers of the lung adenocarcinoma cell line PC-9, which harbours a deletion within exon 19 in EGFR[368], sensitising them to TKI therapies. Results demonstrated that exposure to both AuNPs (black bars) and AuNP-PEG (blue bars) did not cause any reduction in PC-9 cell viability at any of the doses investigated (0.03-10 µg/mL, Figure 4.2A) as determined using the MTT assay. This is in agreement with previous literature[369,370], further reinforcing the biocompatibility of

AuNPs, even when cells are exposed to significant amounts. There were no significant differences between AuNPs and AuNP-PEG at any of the concentrations investigated.
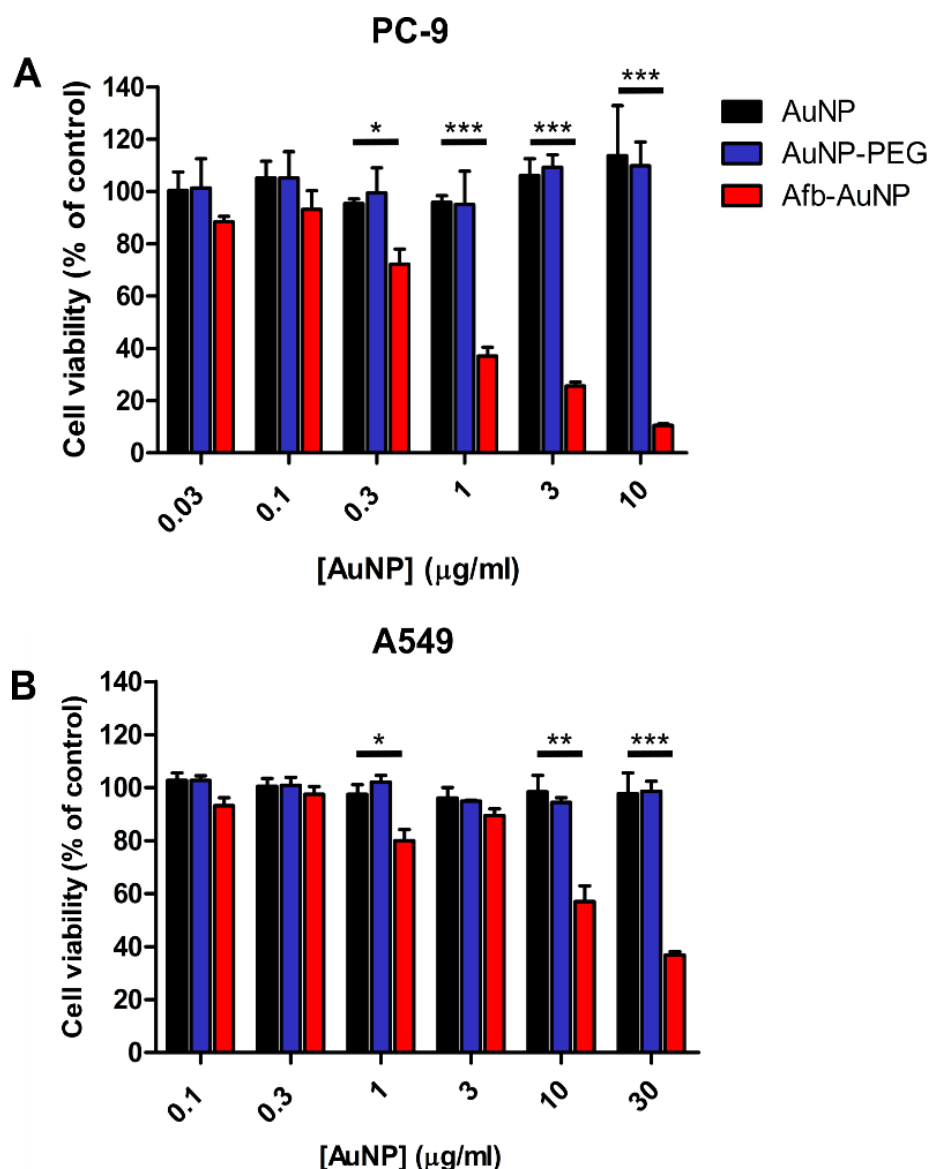
Figure 4.2. *In vitro* cytotoxicity of Afb-AuNPs. (A) The lung adenocarcinoma cell line PC-9 and (B) A549 were exposed to increasing concentrations (0.03 – 30 μg/mL) of AuNPs (black), AuNP-PEG (blue) or Afb-AuNPs (red) for 72 hours and cell viability was assessed by MTT assay. Data are expressed as mean ± SEM, $n = 3$, *, $P < 0.05$; **, $P < 0.01$; ***, $P < 0.001$. Reprinted with permission from Cryer AM, Chan C, Eftychidou A, et al. Tyrosine Kinase Inhibitor Gold Nanoconjugates for the Treatment of Non-Small Cell Lung Cancer. ACS Applied Materials & Interfaces 2019;11:16336-46. Copyright 2020 American Chemical Society.

Conversely, dose-dependent cytotoxicity was observed when PC-9 cells were exposed to Afb-AuNPs (red bars). There was a significant reduction in PC-9 cell viability (24% compared to AuNP, $P < 0.05$) observed at Afb-AuNPs amounts as low as 0.3 μg/mL (AuNP concentration,

equivalent to ~25 nM Afb-A). As the concentration of AuNPs, and therefore drug, increased, there were further reductions in cell viability. At a concentration of 1 µg/mL, Afb-AuNPs reduced cell viability by 59% compared to the equivalent quantity of AuNPs ($P < 0.001$). The differences between Afb-AuNPs and AuNPs were accentuated at AuNP concentrations of 3 µg/mL and 10 µg/mL; cell viability was reduced by 81% and 92% respectively, compared to AuNPs ($P < 0.001$). To explore the cytotoxic versatility of Afb-AuNPs, the conjugates were screened in a second lung adenocarcinoma cell line, A549, which are wild type for EGFR expression[371] and thus are not intrinsically sensitive to TKIs. As with PC-9 cells, AuNPs and AuNP-PEG did not induce any significant reductions in A549 cell viability across any of the concentrations examined (0.1-30 µg/mL, Figure 4.2B) and there were no differences in viability of A549 cells treated with either AuNPs or AuNP-PEG. Despite the decreased sensitivity to TKIs, Afb-AuNPs retained some efficacy, particularly at the higher doses examined. At an AuNP concentration of 10 µg/mL, Afb-AuNPs were found to reduce A549 cell viability by 42% compared to the equivalent dose of AuNPs ($P < 0.01$). A further decrease in cell viability was noted at an AuNP concentration of 30 µg/mL, where Afb-AuNPs elicited a 60% decrease in cell viability ($P < 0.001$). The juxtaposition between the cytotoxic effects of the unmodified AuNPs and Afb-AuNPs in both cell lines demonstrates both the biocompatibility of AuNPs and the therapeutic potential of Afb-AuNPs.

4.3.3. *Dose responses of Afb-A and Afb-AuNPs*

After observing Afb-AuNP induced cytotoxicity in human lung adenocarcinoma cells, it was important to elucidate the extent to which AuNPs were influencing the cytotoxic effect of Afb-A. In order to achieve this, the cytotoxic effect of free Afb-A and Afb-AuNPs at different doses was examined by MTT assay. In PC-9 cells (Figure 4.3A) Afb-AuNPs were significantly more cytotoxic than equimolar concentrations of free drug (Afb-A) at four of the six doses studied. At 0.03 µM, Afb-A decreased cell viability by 43%, whereas incubation with Afb-AuNPs (~0.4

µg/mL AuNP) at the same drug concentration further reduced cell viability by an additional 23% (66% total, $P < 0.05$). This observation was recapitulated at 0.1 µM whereby Afb-AuNPs induced an 87% loss of cell viability compared with 65% viability loss caused by Afb-A ($P < 0.01$). Treatment with the highest drug doses resulted in a flattening of the curve for Afb-AuNPs, which eventually caused ~91% cell death, whereas even at the highest doses of 0.3 µM and 1 µM Afb-A, cell death was significantly less than Afb-AuNPs greater significantly ($P < 0.001$) at ~73% and 81% respectively. When this dose response experiment was repeated in the less TKI sensitive A549 cells (Figure 4.3B), free Afb-A and Afb-AuNPs exhibited similar efficacy up to a concentration of 3 µM. At this concentration, Afb-AuNPs were found to be significantly more cytotoxic than equivalent free Afb-A (64% vs 40% reduction in viability, $P < 0.01$). This observation was also witnessed at 10 µM ($P < 0.01$). Reinforcing the increased potency of Afb-AuNPs, the half maximal inhibitory concentration (IC_{50}) value of free Afb-A in PC-9 cells was found to be 0.05 µM whereas Afb-AuNPs had an IC_{50} of 0.02 µM, representing a 2.5 fold increase in potency. Similarly, in A549 cells the Afb-A IC_{50} was 6.08 µM compared to 1.65 µM for Afb-AuNPs, translating to a 3.7 fold potency increase. As AuNPs were found to be non-cytotoxic in these cells lines, therefore not contributing to the loss in cell viability observed, the results indicate that conjugation to AuNPs enhances the efficacy of Afb-A.

The dose effect of free Afb-A and Afb-AuNPs on TT1 cells was also investigated (Figure. 4.3C); as these cells cover 95% of the alveolar epithelial surface[372], the implications of toxicity to these cells could be instrumental in determining choice of therapy and its success. At doses up to 1 µM, free Afb-A and Afb-AuNPs were not overtly cytotoxic (no less than 20% reduction in cell viability) and no significant differences were observed between the two treatments. At a dose of 3 µM, free Afb-A was more cytotoxic to TT1 cells than the equivalent concentration of drug conjugated to AuNPs ($P < 0.05$). This differential cytotoxicity was more pronounced

at the highest dose investigated (10 µM, *P* < 0.05) where 83% of cells exposed to Afb-AuNPs remained viable, only 64% were found to be viable when incubated with the equivalent dose of Afb-A. When TT1 cells were exposed to unmodified AuNPs, as in PC-9 and A549 cells, no appreciable loss in cell viability was seen at any of the doses examined (Figure 4.3D), affirming the biocompatibility of AuNPs and their suitability as drug carriers.
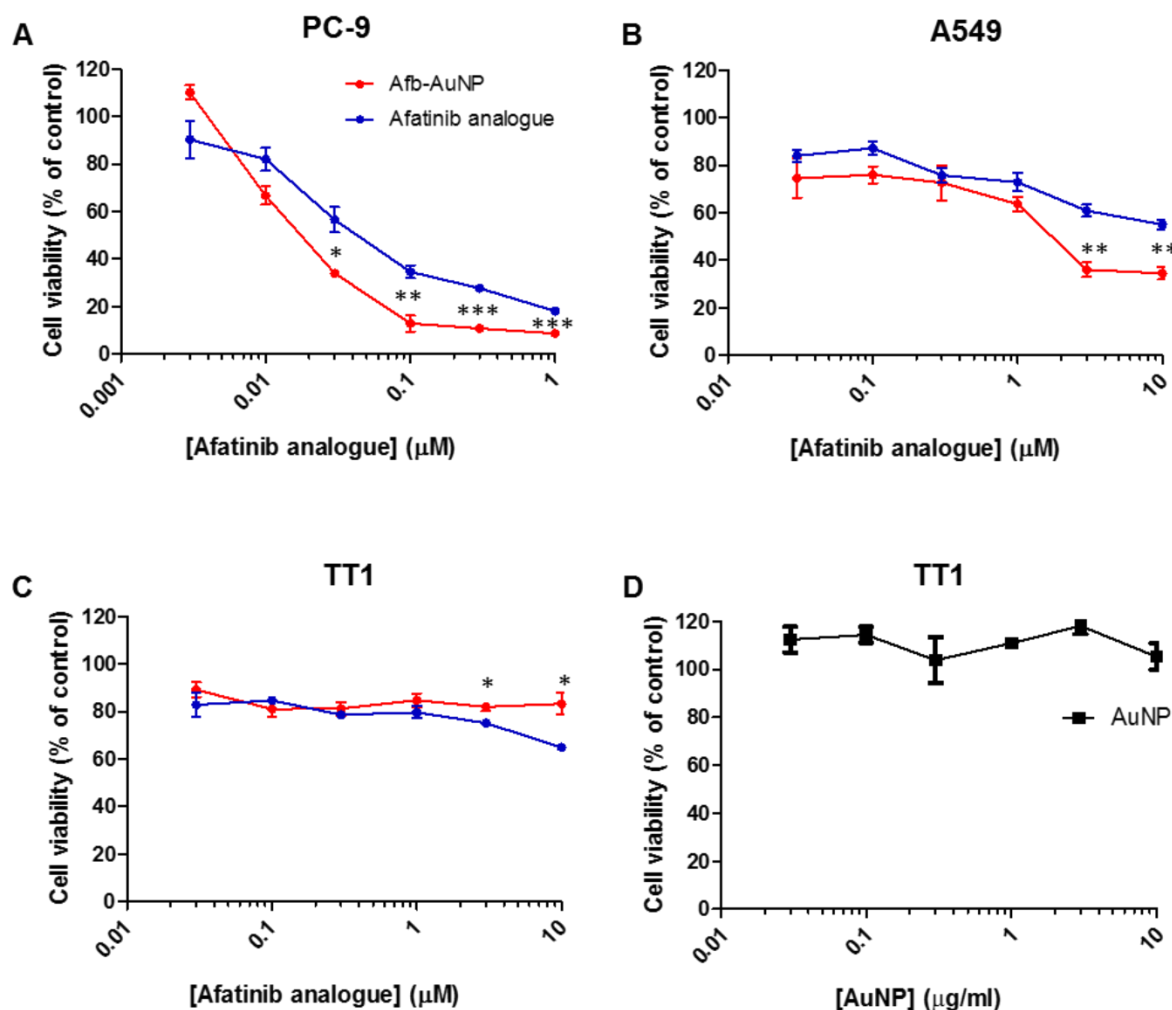
Figure 4.3. Dose response curves post Afb-AuNP and Afb-A treatment. (A) PC-9, (B) A549 and (C) alveolar epithelial TT1 cells were exposed to increasing concentrations (0.03 – 10 µM) of Afb-A or Afb-AuNPs. (D) TT1 cells exposed to unmodified AuNPs. In all treatment groups, cells were exposed for 72 hours and cell viability was assessed by MTT assay. Data are expressed as mean ± SEM, *n* = 3, *, *P* < 0.05; **, *P* < 0.01; ***, *P* < 0.001. Reprinted with permission from Cryer AM, Chan C, Eftychidou A, et al. Tyrosine Kinase Inhibitor Gold Nanoconjugates for the Treatment of Non-Small Cell Lung Cancer. ACS Applied Materials & Interfaces 2019;11:16336-46. Copyright 2020 American Chemical Society.

4.3.4. *Inhibition of NSCLC cell proliferation*

After profiling the effect of Afb-AuNPs on confluent monolayers, the effect of Afb-AuNPs on actively proliferating cells was investigated. This was accomplished using a technique known as electric cell-substrate impedance sensing (ECIS) that allows for label free, real-time study of cell proliferation by using electrical resistance as a measurement of cellular health, and this readout is given as a cell index (CI). Figure 4.4A illustrates a proliferation curve of PC-9 cells exposed to varying concentrations of Afb-AuNPs as well as AuNPs, AuNP-PEG and untreated cells (control). Consistent with results obtained from the cell viability experiments, AuNPs and AuNP-PEG appeared biocompatible and did not affect the proliferative capacity of PC-9 cells, however a dose-dependent response was observed when PC-9 cells were exposed to Afb-AuNPs with higher doses having a more profound anti-proliferative effect. At 72 h post-exposure, no significant differences between AuNP-PEG and 0.03 µM Afb-AuNP were observed when compared to AuNPs (7 µg/mL, which is same concentration as that used in the highest dose of Afb-AuNP, Figure 4.4B). However, 0.1 µM Afb-AuNPs inhibited cell proliferation to a significantly greater degree than AuNPs ($P < 0.01$), reflected by the 27% lower CI. This pattern was more prominent as the dose of Afb-AuNPs increased, resulting in enhanced inhibition of proliferation. Afb-AuNPs, at a dose of 0.3 µM, greatly inhibited PC-9 cell proliferation when compared with AuNPs ($P < 0.001$), denoted by a 75% reduction in CI. Similarly, at 1 µM, cell proliferation was inhibited by 78%, contrasted with AuNPs ($P < 0.001$). Figure 4.4C shows the proliferation curve for A549 cells exposed to varying concentrations of Afb-AuNPs, AuNPs, AuNP-PEG and untreated cells. A pattern reminiscent of the cell viability studies was also noted here as only the highest dose of Afb-AuNPs was able to inhibit cell proliferation. At a dose of 10 µM, Afb-AuNPs reduced the proliferative capacity of A549 cells by 33% ($P < 0.001$) when compared with equal concentrations of AuNPs that had no depreciative effect (Figure 4.4D). PEGylated AuNP, as in PC-9 cells, did not negatively affect

the ability of A549 cell to proliferate. Taken together, these results demonstrate that Afb-AuNPs can act not only on confluent monolayers of cells, but also actively proliferating cancer cells. Unmodified and PEGylated AuNPs were not observed to contribute to the anti-proliferative capacity of Afb-AuNPs, highlighting the utility of the AuNP drug carrier system.
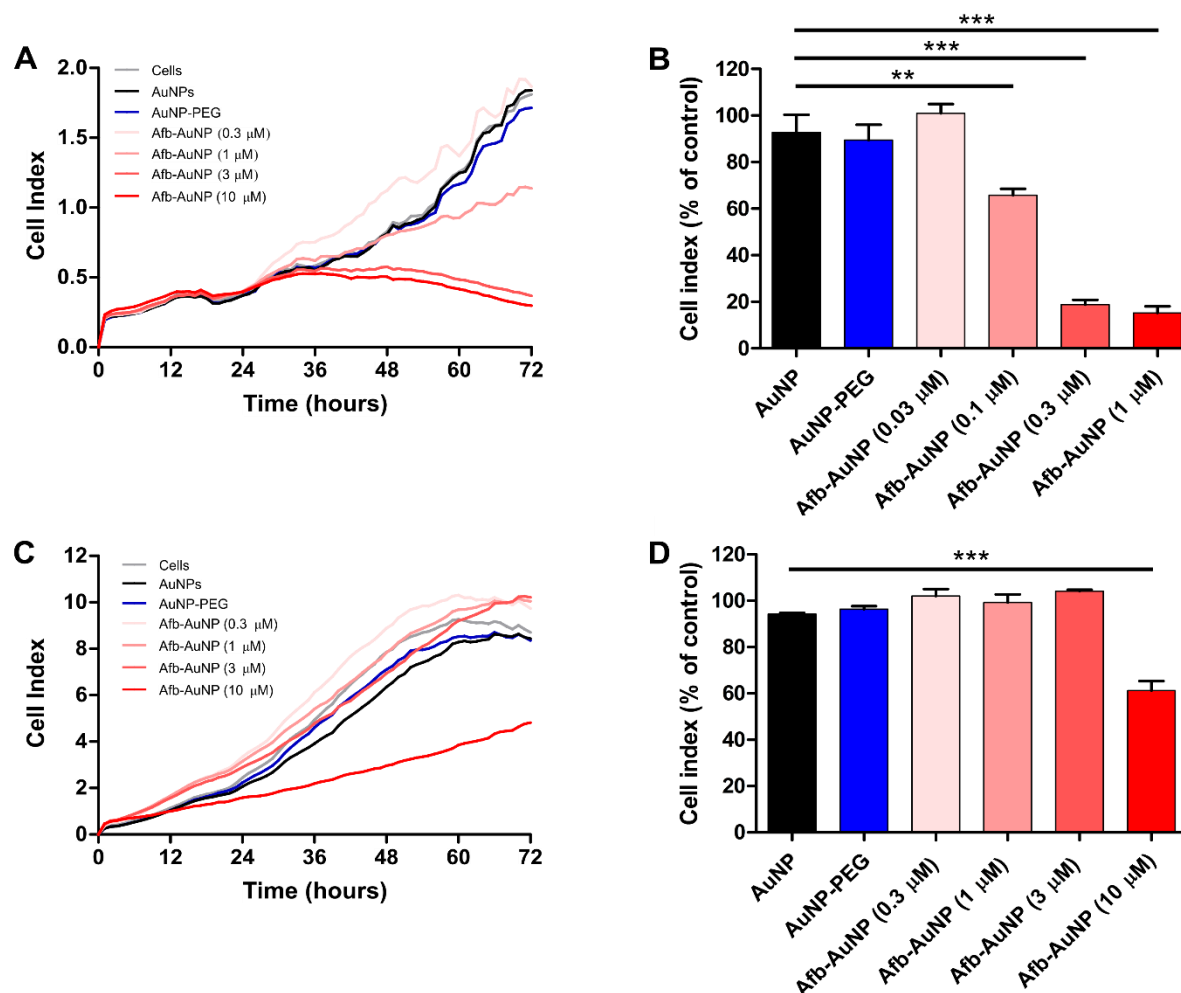
Figure 4.4. Inhibition of cell proliferation by Afb-AuNPs. (A) Representative proliferation curves of PC-9 cells upon exposure to AuNPs, AuNP-PEG (both 7 µg/mL) or increasing doses of Afb-AuNP (up to 1 µM Afb). (B) quantification of cell proliferation at 72 hours (untreated cells used as control). (C-D) as in (A-B) but cell proliferation assessed in A549 cells. Data are expressed as mean ± SEM, $n = 4$, **, $P < 0.01$; ***, $P < 0.001$. Reprinted with permission from Cryer AM, Chan C, Eftychidou A, et al. Tyrosine Kinase Inhibitor Gold Nanoconjugates for the Treatment of Non-Small Cell Lung Cancer. ACS Applied Materials & Interfaces 2019;11:16336-46. Copyright 2020 American Chemical Society.

4.3.5. *Inflammatory cytokine release*

After investigating the cytotoxicity and anti-proliferative effects of Afb-AuNPs on human lung adenocarcinoma cells, the inflammatory response of the healthy alveolar epithelium upon

exposure to Afb-AuNPs and the free drug equivalent was explored. When TT1 cells were exposed to Afb-AuNPs or Afb-A at doses equivalent to or below 3 µM, the release of the pro-inflammatory cytokine interleukin (IL)-6 was not significantly different between Afb-A and Afb-AuNPs (Figure 4.5A). A slight trend noted as there appeared to be increased IL-6 release from TT1 cells as the dose at exposure was increased. However, no more than 90 pg/mL was detected at any of these doses, suggesting a tolerability of Afb-AuNPs at the alveolar epithelial interface.
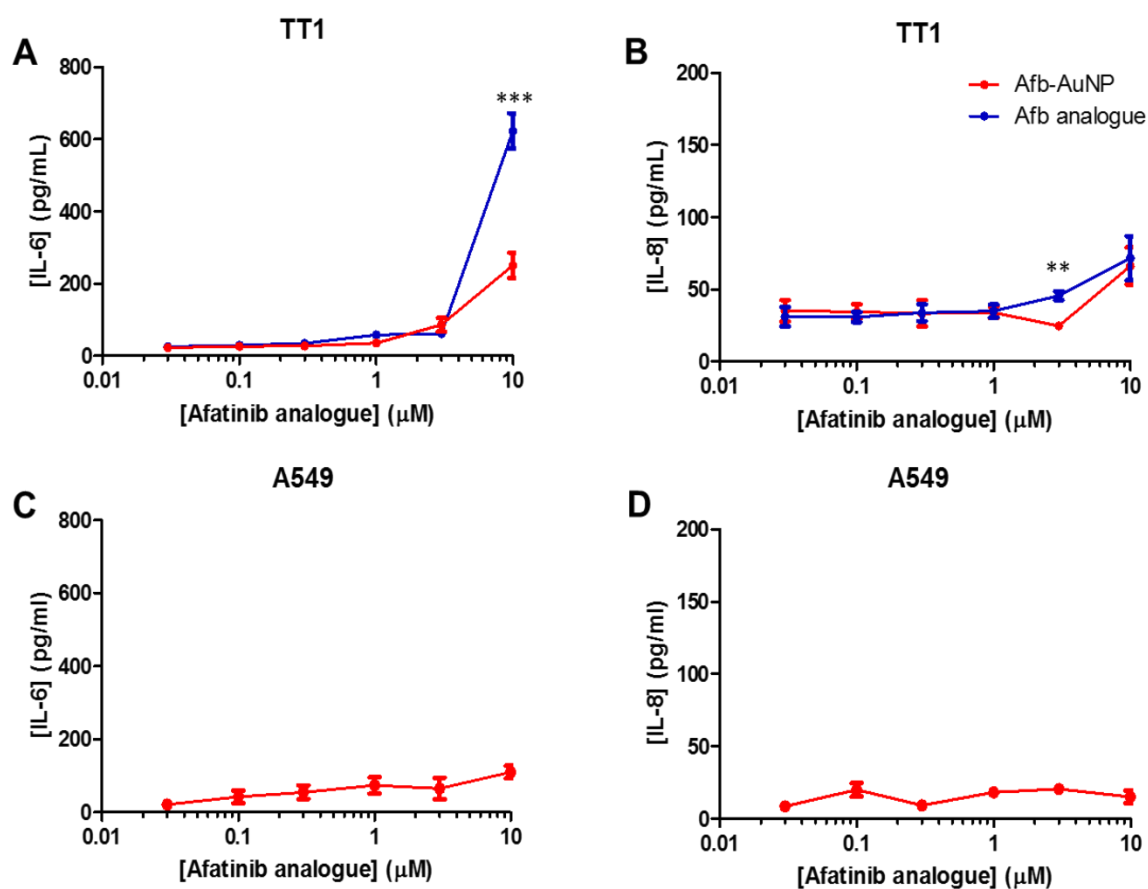
Figure 4.5. Inflammatory mediator release from alveolar epithelial cells. TT1 cells were exposed to increasing doses (0.03 – 10 µM) of Afb-A or Afb-AuNPs and the release of (A) IL-6 and (B) IL-8 from confluent monolayers was measured by ELISA. Similarly, A549 cells were exposed to Afb-AuNPs and both (C) IL-6 and (D) IL-8 production was quantified. Data are expressed as mean ± SEM, $n = 3$, **, $P < 0.01$; ***, $P < 0.001$. Reprinted with permission from Cryer AM, Chan C, Eftychidou A, et al. Tyrosine Kinase Inhibitor Gold Nanoconjugates for the Treatment of Non-Small Cell Lung Cancer. ACS Applied Materials & Interfaces 2019;11:16336-46. Copyright 2020 American Chemical Society.

At a dose of 10 µM, both Afb-AuNPs and Afb-A stimulated notably more IL-6 release than all lower doses studied, however Afb-A elicited a 2.5 fold increase in IL-6 production from TT1 cells compared to the equivalent dose of Afb-AuNPs ($P < 0.001$). The marked significant increase in IL-6 release at the highest concentration suggests that therapeutically there could be an important exposure threshold. The production of another pro-inflammatory cytokine, IL-8, was also determined and a similar pattern of IL-8 release from TT1 cells was observed (Figure 4.5B). Neither Afb-A nor Afb-AuNPs appeared to provoke significant production of IL-8 from TT1 cells. A 1.9 fold increase in the release of IL-8 at a dose of 3 µM Afb-A compared to Afb-AuNPs ($P < 0.01$) was noted however this difference was not observed at any other doses. Given the relatively low amounts of IL-6 and IL-8 from TT1 cells when exposed to Afb-AuNPs, the release of pro-inflammatory cytokines from A549 cells in response to Afb-AuNPs was also profiled to see if this pattern was also seen in other cell lines of alveolar epithelial carcinoma origin. Encouragingly, no obvious surge in cytokine release was observed. The release of IL-6 from A549 cells (Figure 4.5C) was generally higher as the exposure dose was increased. On average, no more than 110 pg/mL of IL-6 was detected at any of the treatment doses under examination. At the highest dose, less IL-6 was secreted by A549 cells than TT1 cells (250 pg/mL vs 110 pg/mL). With respect to A549 cell IL-8 release (Figure 4.5D), a pattern similar to TT1 cell release behaviour was observed whereby small quantities were detected at all doses examined. The overall inflammatory profile of Afb-AuNPs alludes to the lack of immunogenicity these molecules may possess.

4.3.6. *Cellular uptake of Afb-AuNPs*

Finally, in order gain an insight into the intracellular fate of Afb-AuNPs, the uptake of these particles by A549 cells was investigated using confocal microscopy (Figure 4.6). A549 cells were exposed to Afb-AuNPs for 3, 6 and 24 h to fully observe NP uptake dynamics. After 3 h, there was evidence of intracellular presence of AuNPs suggesting surface functionalisation

with Afb-A and PEG did not prevent internalisation. Although not shown, confirmatory z stacks were performed prior to image acquisition to ensure the NPs were inside of the cell. Visualised (in red) by virtue of their surface plasmon resonance, dispersed AuNPs were distributed throughout the cytoplasm and perinuclear region, and were not observed in the nucleus (blue) or co-localised with lysosomes (green), in agreement with previous studies using AuNPs of a similar size[373]. Small clusters of AuNPs appeared to localise near to endosomal structures (merge panel) implying an endosomal route may have been utilised by the cells to internalise the particles. At 6 h post AuNP exposure, the appearance of AuNP clustering in the cytoplasm was more apparent and there was no evidence of lysosomal co-localisation. This clustering effect may suggest that as time progresses, more AuNPs are internalised. When the cells were examined 24 hours post AuNP exposure, further coalescence of the AuNPs in the cytoplasm was evident, and although we did not observe signs of co-localisation, larger clusters of AuNPs were found to be close to the nucleus and proximal to lysosomes which could be due to lysosomal escape, allowing for cytoplasmic release of Afb and subsequent inhibition of EGFR.
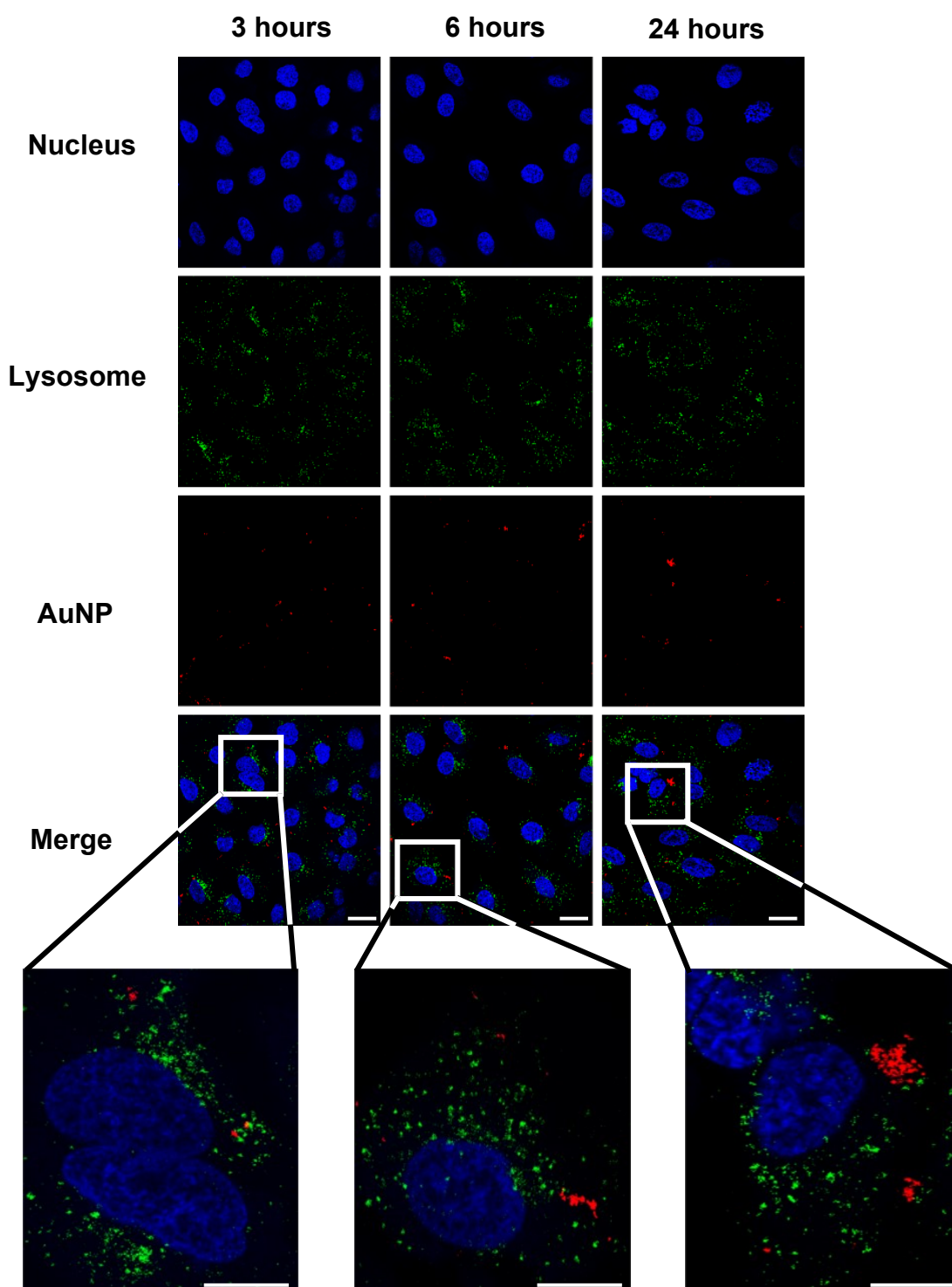
Figure 4.6. Intracellular uptake and distribution of Afb-AuNPs. A549 cells were exposed to Afb-AuNPs for 3, 6 or 24 hours prior to imaging by confocal microscopy. The nucleus is visualised in blue, lysosomes in green and AuNPs in red. Scale bar = 15 µm. Reprinted with permission from Cryer AM, Chan C, Eftychidou A, et al. Tyrosine Kinase Inhibitor Gold Nanoconjugates for the Treatment of Non-Small Cell Lung Cancer. ACS Applied Materials & Interfaces 2019;11:16336-46. Copyright 2020 American Chemical Society.

4.4. Discussion

The work presented in this chapter demonstrates the utility of AuNPs conjugated with a novel analogue of afatinib, Afb-AuNPs, as drug delivery vehicles for the treatment for NSCLC, the most predominant subtype of which, adenocarcinoma, was the focus of this study. As discussed in the previous chapter, the structural modifications that differentiate Afb-A from the clinically used afatinib were chosen by taking into account two key principals: maintenance of the structure-activity relationship of the molecule and ability to be conjugated to AuNPs. This was achieved by incorporation of an alkyne and disulfide group respectively into the molecular structure of Afb-A.

The construct was then PEGylated using a heterobifunctional PEG linker as is common practice when developing drug delivery systems. This principal is largely derived from the initial success of PEGylated liposomes ferrying doxorubicin (Doxil) that was approved by the FDA in 1995. Doxil dramatically improved the circulatory half-life of doxorubicin in patients compared to free drug, reflecting the "stealth" properties of PEGylation[374]. From a biological perspective, this stealth function is the creation of steric barrier to opsonisation due to increased surface hydrophilicity, thereby mitigating recognition by the reticuloendothelial system (RES)[202]. PEGylation has also been shown to reduce the haemolytic capacity of systemically injected NPs[375] and decrease the immunogenicity of intrinsically inflammatory nanomaterials such as carbon nanotubes thereby reducing potential toxicities, even though PEG itself is not invisible to the immune system and has been reported to induce the production of anti-PEG IgM antibodies[376]. The PEG used in this work was functionalised with terminal carboxyl groups that allow the AuNPs to retain a negative surface charge, despite displacement of citrate anions. The negative surface charge aids in preventing non-specific adsorption of proteins and other blood components to the surface of the NP. Furthermore, it has been shown the cationic NPs induce significantly more prominent inflammatory responses *in vivo* than neutrally

charged or anionic NPs, which could be due to initial activation of the innate immune system through Toll-like receptor 4 signalling[377]. As such, the negative surface charge provides another factor that can help evade immune recognition and potentially injurious responses. As highlighted in the previous chapter, Afb-AuNPs were found to be ~46 nm in diameter which is of a suitable size such that they avoid renal filtration and excess sequestration in the liver[378]. The fenestrated nature of these organs permits screening of circulating entities in the blood. Accordingly, NPs smaller than approximately 6 nm in diameter primarily undergo glomerular filtration by the kidneys[379] and as the NP size increases (from ~200 nm) so does the proclivity to become entrapped within the tortuous sinusoids of the liver[380] whereby the velocity of circulating nanomaterials is dramatically reduced, increasing the interactions with Kuppfer and other resident hepatic cells[381]. Therefore Afb-AuNPs fall within the range such that clearance by either the liver or kidneys is minimised. The culmination of these optimised properties (PEGylation, size, surface charge, shape) are known to increase the circulatory half-life of nanoparticles[382] improving the probability for drug-bearing NPs to accumulate in tumours in an *in vivo* setting. These physicochemical characteristics are well suited for delivery to solid tumours via the EPR effect and also reinforce the notion that the physicochemical properties of NPs dictate their biocompatibility, immunogenicity, *in vitro* efficacy, *in vivo* fate and site of action.

Although sole reliance on the EPR effect for nanoparticle delivery may not be optimal for all tumour types, strategies to augment this process can be implemented[383]. For example, localised hyperthermia can be used to promote vascular permeability in tumours[384]. This approach is of particular interest when using AuNPs as drug delivery vehicles; AuNPs such as hollow nanoshells and nanorods can transform photons in the form of near infra-red light into thermal energy, creating hyperthermic regions proximal to the NPs. This intrinsic property is leveraged in the process of photothermal therapy whereby AuNPs that have accumulated in tumours

thermally ablate the tissue[385]. This modality can increase the permeability of the tumour to chemotherapy and NPs acting as a dual therapy and EPR effect enhancer[386]. Moreover, terminal carboxyl groups on PEG chains can be used to attach tumour specific targeting moieties such as nucleic acids[387], antibodies[388] or peptides[389] in an attempt to more adroitly target tumours. Future iterations of the work presented in this chapter can be combined with these functionalities for multimodal chemo and thermal therapy.

The cytotoxic efficacy of Afb-AuNPs was evaluated using the MTT assay, which measures the metabolic activity of a cell that is inferred as an indicator of cell viability. In viable cells, mitochondrial nicotinamide adenine dinucleotide phosphate-dependant oxidoreductase enzymes convert the tetrazolium dye to a purple formazan product that is insoluble, allowing colorimetric determination of cell viability[390]. Using this technique in a proof of concept experiment, it was demonstrated that Afb-AuNPs induced dose-dependent cytotoxicity in PC-9 cells (Figure 4.2A), and to a lesser extent in A549 cells (Figure 4.2B). The difference in sensitivity between these two cells lines was expected as A549 express wild-type EGFR whereas PC-9 cells harbour the deletion mutation of amino acids 746-750 (Glu-Leu-Arg-Glu-Ala, ELREA) in exon 19 which is where the kinase domain resides. This deletion mutation activates EGFR, presumably due to conformational changes in the kinase domain that prolong an active dimer configuration[391] or destabilise the autoinhibited conformation found in the absence of ligand[392] but crystallographic characterisation remains elusive. The exact mechanism as to how these conformational changes lead to increased sensitivity is not known, however it is postulated that an oncogenic addiction to EGFR due to constitutive activation can develop. When this is established, subsequent deprivation of this pathway which the PC-9 cells are dependent on overrides any compensatory mechanism remaining for survival. Lending evidence to this is that phosphorylation of targets downstream of EGFR such as Akt and extracellular signal-regulated kinase 1/2 is attenuated upon treatment with a TKI[393,394]

culminating in cell death and tumour shrinkage *in vivo*. This is of clinical importance as a vast majority of patients with activating mutations in EGFR possess either this deletion or the point mutation L858R and stratification by mutation status impacts therapeutic response and progression free survival[395].

The biocompatibility of AuNPs was also evident as they did not induce cell death at any concentration tested; thus, we could attribute the cytotoxic effects observed to the conjugated Afb-A. These initial observations suggest that, in agreement with the literature[396], citrate-capped AuNPs are not intrinsically cytotoxic at the concentrations that were tested and that PEGylation did not negatively affect the biocompatibility of AuNPs, even after 72 hours exposure. Moreover, as the only difference between treatment groups was Afb-A, the modifications that were made to facilitate conjugation appeared not to completely compromise the cytotoxicity of the molecule. These observations were further extended when we directly compared free Afb-A and Afb-AuNPs at equivalent drug concentrations (Figure 4.3A and B). Although free Afb-A still retained cytotoxic potential, a significantly enhanced cytotoxic response was witnessed in the NSCLC cell lines when Afb-A was conjugated to AuNPs. As AuNPs and AuNP-PEG were deemed not to be cytotoxic at the doses investigated, it can be safely assumed that the loss in cell viability is derived from Afb-A, reinforcing the data from the initial cytotoxicity screen. Encouragingly, as PC-9 cells are sensitive to quinazoline-based TKIs in particular, it can be inferred that the structural modifications that differentiate Afb-A from afatinib maintained some semblance of its SAR and therefore Afb-A possesses TKI activity. The dose response observed with Afb-A would align with this notion, although further confirmation could be sought by performing an EGFR TKI assay or by western blot to measure phosphorylated EGFR levels upon exposure to Afb-A.

The IC_{50} values calculated for Afb-AuNPs were notably lower than for Afb-A in PC-9 cells. This pattern was also observed in A549 cells whereby the IC_{50} of Afb-AuNPs was significantly

lower than that reported previously for Afb[397] which was comparable to the IC_{50} of free Afb-A determined in this study. Although the mechanism underlying this increase in potency is not fully clear, one explanation could be increased intracellular concentration of Afb-A due to uptake of AuNPs[398]. As Afb has been shown to alter the efflux function of P-glycoprotein[399] (otherwise known as ATP-binding cassette sub-family B member 1, ABCB1), the enhanced intracellular levels of Afb-A may then serve to inhibit its own efflux over time, leading to greater or more sustained inhibition of EGFR; however, further studies would be needed to explore this.

The intrinsic sensitivity of distinct cell types to TKIs plays a role in the differential cytotoxicity of Afb-AuNPs, evidenced in the studies on confluent monolayers. This is further exemplified in the proliferation studies, whereby lower concentrations of Afb-AuNPs were required to inhibit PC-9 cell proliferation compared to A549 cells. These results demonstrated that Afb-AuNPs retained efficacy under different experimental conditions and corroborated those seen in the cytotoxicity studies whereby a dose-dependent response to Afb-AuNPs (notably less cell growth at the highest concentrations) was observed in PC-9 cells but only the highest dose of Afb-AuNPs significantly inhibited A549 cell proliferation. Further mirroring the cytotoxicity studies, unmodified AuNPs and AuNP-PEG were found not to impede proliferation of either cell type. From a technical standpoint, it was clear that the presence of AuNPs in the treatment groups did not interfere with impedance measurements. Also, cells were seeded at the same density and left to adhere prior to treatment, implying that the differential responses to Afb-AuNPs that were observed were not due to there being fewer cells at the initiation of the experiment. As the previous set of results had shown that Afb-A was less cytotoxic than the equivalent dose of Afb-AuNPs, the effect of free drug was not investigated in these set of experiments, although a dose response of A549 cells exposed to afatinib in presented in the next chapter and, particularly at higher doses, Afb-AuNPs show comparable efficacy. As

previously mentioned, the overall profile for the inhibitory effects seen in the cell proliferation results concurs with that seen in the cytotoxicity studies; however there is not a perfect overlap and these discrepancies may be explained by the different measurements produced by ECIS and the MTT assay. ECIS directly measures the electrical resistance of cells which takes place in real time, reflecting effect on cell proliferation/growth. Contrastingly, the MTT assay is an indirect measurement of viability that uses mitochondrial enzyme activity as a surrogate for cellular health of a confluent, fully formed monolayer of cells. Reduced MTT values could reflect overt cell death, for example induction, but not completion, of apoptotic cell death.

Having established that Afb-AuNPs displayed anticancer activity in NSCLC cells, the effect of applying these particles to the healthy alveolar epithelium was investigated, using TT1 cells as a surrogate. Examination of the normally functioning cells proximal to the disease area is a procedure which is often excluded from *in vitro* drug delivery studies even though there is potential for interaction with normal cells. This interaction between nanoparticles, especially those carrying a chemotherapeutic agent, and the surrounding healthy tissue can often be influential in dictating an individual's response to therapy[400], and side effects, therefore investigations of the possible undesirable toxicological aspects of nanomedicines and NPs in general are required. This is of particular importance in the lung as inhalation of NPs and their subsequent injurious effects on pulmonary health becomes increasingly clear[401]. Consistent with this line of reasoning, the vascularised architecture of the lung raises the chances of intravenously administered nanomedicines coming in to contact with healthy pulmonary epithelium. Encouragingly, Afb-AuNPs did not elicit significant TT1 cell death at any of the doses examined (Figure 4.3C) whereas at doses above 1 μM, Afb-A was comparatively more cytotoxic. The biocompatibility of AuNPs was again confirmed as there was no demonstrable evidence of loss of TT1 cell viability at any dose of AuNPs used (Figure 4.3D). This data suggests a selectivity of Afb-AuNPs towards cancerous cells, which could be predicated on

EGFR expression. Indeed, the distinction between TT1 cells and A549 cells has previously been shown and it was concluded that TT1 cells better represent the alveolar epithelial type I cell[402,403]. Therefore, although Afb-AuNPs are directed towards the three cell types used in this study, two of which originate from lung adenocarcinoma, the target mutant cells (PC-9) showed the most sensitivity to the Afb-AuNPs, producing the most desirable outcome and supporting the strategy employed.

As cytotoxicity is only one aspect of biocompatibility, the inflammatory profile of TT1 cells was explored. It was observed that there was an attenuation of pro-inflammatory cytokine release, particularly IL-6, from TT1 cells upon exposure to Afb-AuNPs compared to free Afb-A (Figure 4.5A and B). These differences could be due to the propensity for chemotherapies such as TKIs to induce an inflammatory response from cells of epithelial origin[404], which may be diminished upon association with a delivery vehicle such as AuNPs that are not intrinsically inflammatory. As IL-6 is a pleiotropic cytokine that has a role as a promoter of inflammation and in the pathogenesis of lung diseases such as asthma and chronic obstructive pulmonary disease (COPD)[405], therapies that elicit production above that of physiological levels are not ideally suited for pulmonary drug delivery. This is also the case for IL-8, which functions as a potent chemoattractant for neutrophils and is also implicated in the pathogenesis of a spectrum of lung diseases such as idiopathic pulmonary fibrosis and asthma[406]. It was also observed that low levels of IL-6 and IL-8 were released from A549 cells (Figure 4.5C and D). As IL-6 is heavily involved in driving pro-tumourigenic inflammation[407] this has led to its implication in the pathogenesis of lung cancer[408]. The underlying mechanism appears to centralise around an IL-6/STAT3 signalling axis whereby IL-6 fosters oncogenic signalling through activation of STAT3[409]. Moreover, activated EGFR prolongs this signalling cascade[410], providing a rationale for dual anti IL-6/EFGR therapy in lung cancer. Thus, in both health and disease, excess inflammation exacerbates pathological changes and may contribute to disease initiation or

progression. Afb-AuNPs appear to be quiescent from an inflammatory standpoint, which may be aided by the potential tolerance the alveolar epithelium has for NPs given the continuous exposure to particulate matter the lung is subjected to. However, insights into the generation of other canonical pro-inflammatory cytokines such as IL-1β and tumour necrosis factor-α as well as reactive oxygen species would provide a clearer view of this.

AuNPs are known to be internalised into cells by endocytosis, however their method of entry is largely dependent on their physicochemical properties as well as the type of cell and the culture conditions[411]. It was observed that Afb-AuNPs were taken up by A549 cells within 3 hours, with increased clustering observed in the perinuclear and cytoplasmic regions by 24 hours (Figure 4.6). Although 2-dimensional imaging does not confirm intracellular localisation, z stacking suggested that the NPs were inside of the cell as the NPs could be observed within multiple planes of focus and not just at the cell surface. These clustering dynamics are consistent with the intracellular trafficking of AuNPs of approximately 50 nm in diameter whereby AuNPs were previously found to accumulate and cluster in lysosomes over time[412]. This is the well-recognised process that NPs undergo after endocytosis whereby they are sorted from early to late endosomes and subsequently to lysosomes[413]. Although we did not see direct evidence of colocalisation with lysosomes at the 24-hour time point, Afb-AuNPs were found proximal to lysosomes suggesting Afb-AuNPs may be internalised by an endocytic mechanism. A more detailed time course analysis with corresponding endocytic markers such as early endosome antigen-1 would illuminate this mechanism. Indeed, it has been shown previously that AuNPs of this size are taken up into cells by endocytosis and subsequently located within lysosomes. Interestingly, in the same study, a portion of AuNPs were also observed by transmission electron microscopy (TEM) in the cytoplasm and as large agglomerates in endocytic vesicles determined not to be of endosomal or lysosomal origin[414]. TEM studies could provide further insight into the internalisation process of Afb-AuNPs and

fully determine their intracellular fate and ICP-MS can quantify the concentration of intracellular Au. Clustering of Afb-AuNPs via lysosomal processing could be due to increased agglomeration, as the Au-S bond is labile below pH 6 owing to protonation of the S atom[343,344]. This bond cleavage may then result in release of the drug cargo from the AuNPs into the cytoplasm where it can subsequently bind to and inhibit EGFR, providing a potential explanation for the increased potency demonstrated in the cytotoxicity studies.

4.5. Conclusion

In summary, a novel AuNP formulation was developed based on the clinically approved chemotherapy afatinib, Afb-AuNPs. Afb-AuNPs displayed evident cytotoxicity towards NSCLC cells and also attenuated their proliferation, which was measured in real time. Afb-AuNPs were found not to be cytotoxic to TT1 cells, a model cell of the healthy alveolar epithelium as assessed by cell viability studies, suggesting potential cancer cell specific cytotoxicity. Afb-AuNPs were also shown to be non-inflammatory in both healthy and other cancerous cells, and were effectively endocytosed, despite surface modifications; however, the mechanism is still to be fully elucidated. The results described in this chapter advocate that Afb-AuNPs would be promising candidates for future *in vivo* studies given their physicochemical properties and *in vitro* efficacy. Of further interest, the methodology outlined herein provides an avenue of exploration using other therapeutics not typically utilised for conjugation to NPs, expanding the molecular toolkit available for drug delivery.

5. *In vitro* assessment of chemotherapy-loaded polymeric nanoparticles as anticancer agents

This chapter describes the evaluation and suitability of polymeric nanoparticles (NPs) for delivery of combination chemotherapy to non-small cell lung cancer (NSCLC) cell lines. A summary of the physicochemical properties of polymeric NPs is first given. This is followed by examination of the cytotoxicity, apoptotic and anti-proliferative effects of polymeric NPs on a range of NSCLC cells. Detailed analysis of the mechanism of cellular uptake in lung cancer cells is presented. Furthermore, the biocompatibility of the NP system is examined by investigating inflammatory cytokine release from venous endothelial cells. The therapeutic efficacy of polymeric NPs compared to free drug is discussed in an oncological context as well as their aptness as drug delivery vehicles. The potential applicability of the encapsulation and conjugation methods to create drug-loaded polymeric NPs using other therapeutics and NP materials as well as future molecular combinations are considered.

5.1. Introduction

Polymeric NPs are the subject of increasing attention in the field of nanomedicine, particularly for their drug delivery applications[415]. Of particular interest is the ease by which polymer NP composition can be altered to encapsulate and deliver their cargo, ranging from chemotherapy, nucleic acids, proteins or hormones[416]. The therapeutic payload is therefore be protected from metabolism and degradation *in vivo* and can also be released in a controlled, defined fashion preferentially at the site of disease for a predetermined amount of time[417]. This exquisite spatiotemporal control can lead to increased concentrations of therapy at the disease site; within a tumour for instance. Furthermore, incorporation of particular moieties (functional groups within the polymer chain or the molecular structure of the polymer itself) can dictate the

responsiveness of NPs to specific physiological (e.g. pH, redox) or external (e.g. ultrasound, temperature) stimuli[418], conferring even greater release control.

Biodegradable polymers such as poly(D,L-lactide-*co*-glycolide) (PLGA) is approved by the FDA and the European Medicines Agency (EMA) for several biomedical applications[419-422]. PLGA has a rich history in clinical use, initially as a biomaterial for surgical sutures[423] followed by a transition as an excipient for the controlled release of parenteral drugs and molecules[424,425]. The composition of PLGA is such that, upon hydrolysis in the body, the harmless monomeric components, lactic acid and glycolic acid, are metabolised and excreted as carbon dioxide and water[426], thus reinforcing the biocompatibility and clinical use for the past five decades. Indeed, this biocompatibility combined with broad encapsulation potential of a multitude of molecules, including chemotherapy, make PLGA NPs an attractive choice for drug delivery[427-429]. Encapsulation within the PLGA core, much like conjugation described in the previous chapter, protects the cargo from rapid metabolism, degradation and excretion as well as from untoward spread throughout the body and to unintended locations in the viscera.

Recognition, opsonisation and subsequent clearance by the reticuloendothelial system (RES) is undesirable from a drug delivery perspective, therefore incorporation of another FDA/EMA approved polymer, polyethylene glycol (PEG) can serve to mitigate unfavourable pharmacokinetics and biodistribution. PEG is highly biocompatible and can bestow PLGA NPs with increased circulatory half-life and presence at the disease site due its "stealthing" properties[430,431]. PEG can also be modified with specific functional groups to modulate the surface charge or enable conjugation chemistries at the NP surface[432]. PLGA and PEG can be easily linked together to form a block co-polymer that is afforded the individuals advantages of PLGA and PEG and acts as an excellent nanomaterial with which to synthesise PLGA-PEG NPs to encapsulate chemotherapy[238,433].

There are a variety of methods that can be employed to encapsulate therapeutic entities within PLGA-PEG NPs[240,317], the most effective of which largely depend on the chemical properties of the molecule to be encapsulated and the resultant desired physicochemical properties of the NP. As the focus of this work is vinorelbine (VRL), a methodology was derived to enable sufficient amount of the amphiphilic drug to be encapsulated, known as hydrophobic ion pairing. This method was based on a nano-emulsification method and was found to be the optimal fabrication process (described in Chapter 3, section 3.3.4). Similar co-polymers have been used to synthesise NPs to encapsulate other chemotherapies such as cisplatin[434], docetaxel[247], gemcitabine[435] and vincristine[436], however the present work demonstrates, for the first time, the encapsulation of VRL within PLGA-PEG NPs using HIP. Indeed, VRL has been encapsulated within other types of NPs, primarily liposomes[437,438]. Despite the clinical success of liposomes there are a number of pitfalls associated with their use including low or no controlled release as liposomes have a tendency to release their cargo in one unloading event (known as the burst effect), low colloidal stability, poor shelf-life and a limited repertoire of therapeutics that can be successfully encapsulated[153,439].

Another novel aspect of this work is the conjugation of a second chemotherapy drug to the surface of VRL-loaded PLGA-PEG NPs (Figure 5.1). Previous work has focused on conjugation of "active targeting" moieties such as antibodies and aptamers to the surface of PLGA-PEG NPs[250,440] but combinatorial chemotherapy approaches are scant in the literature using these NPs. Dual therapy was enabled by conjugating an analogue of afatinib to free azide groups on PEG chains using copper catalysed click chemistry (described in Chapter 3, section 3.3.5). The rationale for this drug combination was based on the discovery that doxorubicin, a chemotherapy that exerts its effects in the nucleus, induces cancer cell apoptosis synergistically when combined with an EGFR specific tyrosine kinase inhibitor (TKI), in this case erlotinib, in a temporal fashion. Sustained inhibition of EGFR caused rewiring of cell signalling networks

that increased the susceptibility of cells to nuclear damage[441]. Consequently, this combination was incorporated into a liposomal NP formulation based on a lipid hydration technique which displayed efficacy *in vivo*[442]. As VRL also exerts its activity in the nucleus by binding to β-tubulin and destabilising microtubules[443] it was theorised that combining VRL with a TKI may produce similar effects. Afatinib was chosen as it is a more effective inhibitor of EGFR than the first generation TKIs erlotinib and gefitinib[444], and demonstrates greater efficacy than gefitinib[445] and cisplatin/pemetrexed[446] in patients with EGFR$^+$ lung cancer. Moreover, afatinib is more permissive to structural alterations that facilitate conjugation using click chemistry, while modification of the acetylene group of erlotinib is proposed to interfere with TKI activity[447].
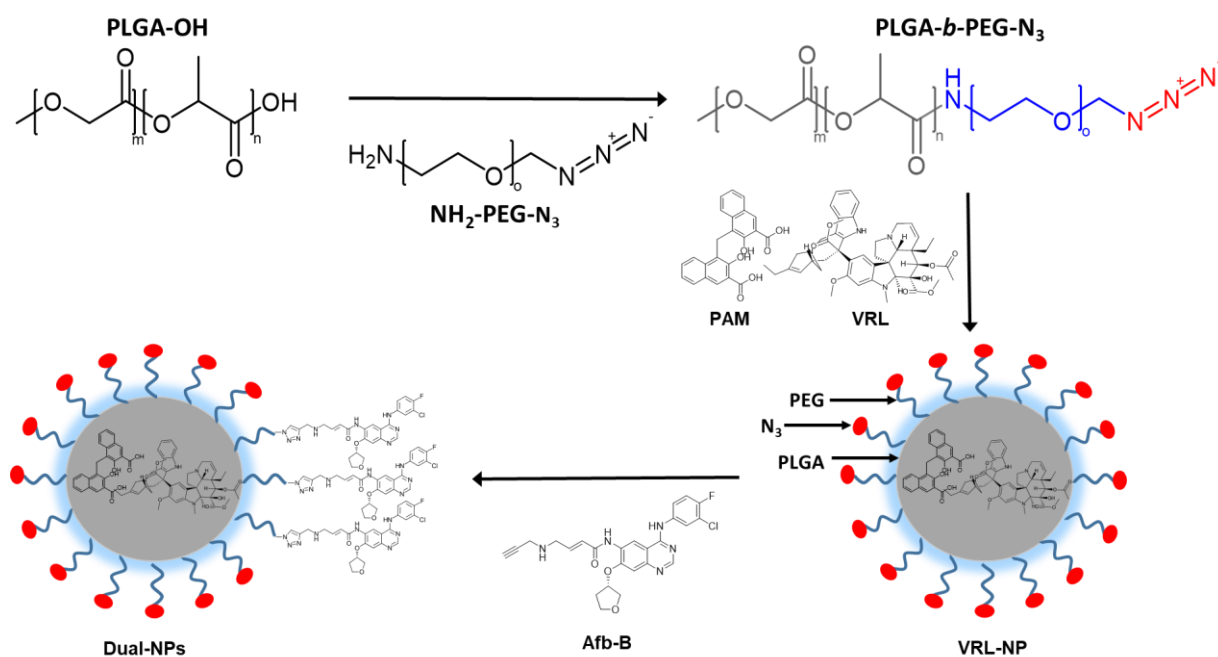
Figure 5.1. Schematic depiction of the formation of Dual-NPs. Biocompatible polymers PLGA and PEG are covalently linked to form a copolymer. This copolymer is used in the formation of NPs containing pamoic acid (PAM) paired vinorelbine (VRL), also bearing azide groups on the surface. These azides are used to attach the alkyne-modified afatinib analogue (Afb-B) to the surface of the particle, culminating in Dual-NPs.

As with any NP formulation, especially those ones involving novel molecular entities or encapsulation excipients, appropriate biological testing is needed to discern efficacy and

toxicity. Primarily, three NSCLC cell lines were used to investigate cytotoxicity and efficacy, the lung adenocarcinoma cell lines A549 and PC-9 as well as the lung squamous cell carcinoma cell line H226. As in the previous chapter, the MTT assay was used to assess cell viability and therefore cytotoxicity of chemotherapy and corresponding doses of nanomedicine. In tandem with these studies, the effect of drug-loaded NPs on the proliferation of NSCLC cells was determined in real time using electric cell-substrate impedance sensing (ECIS) which does not require labelling or addition of reagents to cells in order to examine cell viability. As mentioned previously, the physiological relevance of studies on actively proliferating cells as opposed to confluent monolayers is that *in vivo*, tumours proliferate at a rapid pace which may influence their response to therapy. Further insights into the mechanism of cell death (or loss of viability/proliferative capacity) was gained by assessing levels of apoptotic cells upon treatment with VRL-NPs or Dual-NPs by flow cytometry.

As VRL is a known vesicant and can cause venous irritation upon injection[448] the effect of VRL on the healthy endothelium was investigated. Thus, the release of canonical pro-inflammatory cytokines interleukin (IL)-6, IL-8, IL-1β and tumour necrosis factor (TNF)-α from human umbilical vein endothelial cells (HUVECs) upon exposure to VRL was measured. HUVECs were also exposed to equal concentrations of VRL loaded NPs (VRL-NPs) to discern if encapsulation within NPs attenuated or exacerbated the production of inflammatory cytokines from the endothelium. This is an important parameter that can affect the use of chemotherapies in the clinic and reduction of infusion related reactions is desirable where possible. The concluding work of this chapter is elucidation of the mechanism underlying cellular uptake of polymeric NPs. Using semi-quantitative confocal microscopy, the endocytic pathway dictating uptake of afatinib-coated NPs into A549 cells was identified, confirming that modifications to the surface of NPs did not appear to affect cellular uptake. As both VRL and afatinib have intracellular targets, their therapeutic effect is governed by the intracellular

concentrations of these molecules, and thus studies into particle uptake are hugely important. The hypothesis for this chapter is that NP formulations of chemotherapy will be cytotoxic, anti-proliferative and induce apoptosis across a panel of NSCLC lines; moreover, NPs will be internalised by cancer cells using an active endocytic process as opposed to passive diffusion alone.

5.2. Aims

- Profile the cytotoxicity of VRL-NPs, Dual-NPs, blank NPs and corresponding free drugs in human NSCLC cell lines.

- Examine the effect of nanomedicines and free drugs on proliferation of human lung carcinoma cells.

- Determine the inflammatory response of the human vascular endothelium upon exposure to VRL-NPs or equivalent free VRL

- Identify the uptake mechanism of surface modified polymeric NPs into lung cancer cells.

5.3. Results

5.3.1. *Physicochemical properties of polymeric NPs*

Polymeric NPs formulated with chemotherapy were synthesised and characterised as described in Chapter 3, section 3.3.5. Table 5.1 recapitulates the physicochemical properties of the NPs used in this work, blank NPs (NPs that do not contain any drug), VRL-NPs (NPs that have VRL encapsulated within the core) and Dual-NPs (VRL-NPs that have afatinib conjugated to the surface). The parameters outlined represent the cumulative attempts to fabricate NPs with optimal physicochemical characteristics (high drug loading, colloidal stability etc.) and sufficient size for avid endocytosis into cancer cells.

Sample	HD (nm)	PDI	ZP (mV)	Morphology (by TEM)	EE (%)	DL (µg drug /mg NP)
Blank NPs	203.2 ± 3.6	0.096 ± 0.005	-24.5 ± 0.8	Spherical	N/A	N/A
VRL-NPs	243.7 ± 2.70	0.136 ± 0.014	-23.7 ± 1.64	Spherical	77.47 ± 9.64	159.4 ± 1.98
Dual-NPs	260.1 ± 3.4	0.2 ± 0.010	-16.0 ± 0.5	Spherical	77.47 ± 9.64	159.4 ± 1.98, ~10

Table 5.1. Physicochemical properties of polymeric NPs. Key characteristics of polymeric NPs that dictate their biological impact. Data are presented as mean ± standard deviation ($n = 3$). HD – hydrodynamic diameter, PDI – polydispersity index, ZP - zeta potential, TEM – transmission electron microscopy, EE – encapsulation efficiency, DL – drug loading

5.3.2. *Determination of afatinib analogue activity*

Structural modifications to any clinically approved therapeutic molecule has the potential to significantly diminish its activity. Afatinib is a TKI with high specificity for epidermal growth factor receptor (EGFR) and human epidermal growth factor receptor (HER)2. Upon binding to activated EGFR, afatinib induces conformational changes in the receptor that restrict the phosphorylation of tyrosine residues Y1068, Y1148 and Y1173, therefore preventing EFGR mediated downstream signalling pathways[449]. In order to test if

A

Afatinib analogue

B

p-EGFR ◄ 175 kDa

EGFR ◄ 175 kDa

1000 500 250 100 50 10 2 0 0 (nM)

C

Afatinib

D

p-EGFR ◄ 175 kDa

EGFR ◄ 175 kDa

1000 500 250 100 50 10 2 0 0 (nM)

Figure 5.2. Effect of TKIs on EGF-induced autophosphorylation of EGFR. A549 cells were pre-treated with varying doses (0-1000 nM) of TKI for 3 hours prior to EGF stimulation for 2.5 minutes. Cell lysates were obtained and analysed by Western Blotting, probing for phosphorylated (p)-Y1068 and native EGFR. (A) Chemical structure of Afb-B. (B) Immunoblots of A549 cells exposd to Afb-B depicting levels of p-Y1068 and native EGFR. (C) Chemical structure of clincally approved TKI afatinib. (D) A549 cell immunoblots post afatinib treatment (as in B). Marker indicates molecular weight of EGFR (175 kDa). Blots are representative of at least three independent experiments.

the afatinib analogue (Afb-B) retained its inhibitory capacity, the levels of phosphorylated Y1068 were examined in A549 cells that were pre-treated with Afb-B at a range of concentrations prior to stimulation with epidermal growth factor (EGF). This same experimental design was applied to A549 cells pre-treated with afatinib as a comparison. As shown in Figure 5.2, the structural modifications performed in order to synthesise Afb-B (Figure 5.2A) did not detrimentally impact the its ability to inhibit EGFR autophosphorylation (Figure 5.2B). Afb-B was observed to markedly inhibit phosphorylation of Y1068 at concentrations as low as 50 nM. Even at doses as low as 2 nM, Afb-A was observed to inhibit phopshorylation. Levels of native EGFR appeared to be unaffected by Afb-B treatment. As the chemical structure of afatinib (Figure 5.2C) is designed as a TKI, it was unsurpirisng that at the concentrations examined, afatinib was also seen to inhibit EGFR phosphorylation (Figure 5.2D). Similarly to Afb-B, treatment with afatinib did not induce any changes in the levels of native EGFR detected. No ligand-independent autophosphorylation was detected, as evidenced by the absence of a band from the cells that were not treated with a TKI and not stimulated with EGF.
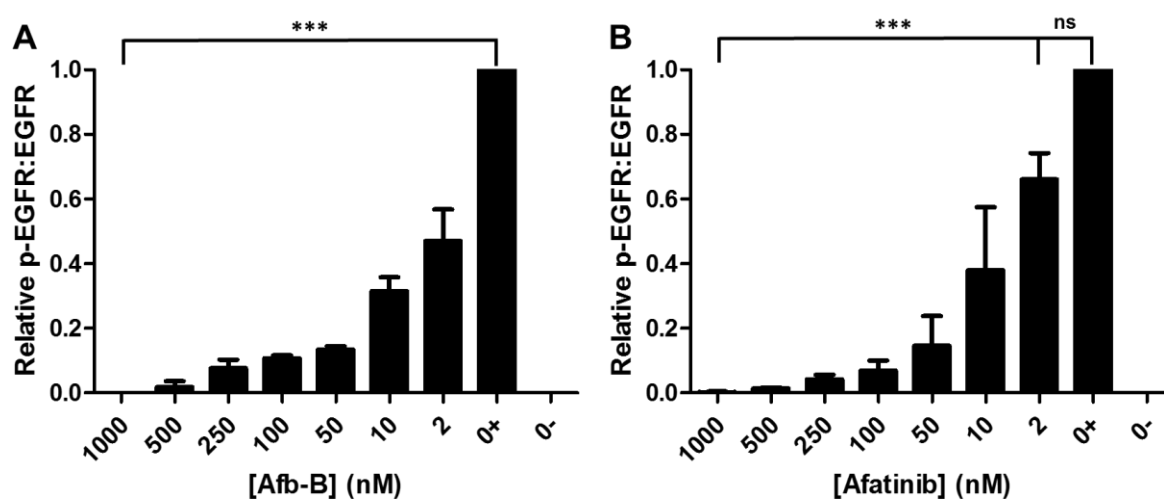
Figure 5.3. Dose dependant inhibition of tyrosine 1068 phosphorylation by TKIs. The band intensities of p-Y1068 and native EGFR for each dose of (A) Afb-A or (B) afatinib was measured and transformed to a ratio that was compared with the ratio of uninhibited EGF-stimulated phosphorylation (0+). Unstimulated EGFR is depicted as 0-. Data are expressed as mean ± SEM, $n = 3$, ***, $P < 0.001$; ns, not significant.

Quantification of phosphorylation inhibition (Figure 5.3) revealed a similar dose response pattern between Afb-A and afatinib whereby increasing does of either drug resulted in less phosphorylation of EGFR. As seen in Figure 5.3A, treatment with Afb-B at all of the doses examined signficantly inhibited EGF-stimulated phosphorylation compared with untreated cells ($P < 0.001$). At a dose of 1000 nM (1 µM), Afb-B completely inhibited the phosphoryation of Y1068, and recapitulating the immunoblot observations, potent inhibition was witnessed even at 50 nM (approximately 85% decrease in phosphorylation compared to untreated, stimulated cells). Treatment with the lowest dose tested, 2 nM, resulted in approximately 50% less Y1068 phosphorylation than would be expected from untreated cells. Similarly with afatinib (Figure 5.3B), all doses were seen to signfincantly attenuate phosphorylation of Y1068 ($P < 0.001$) except at a dose of 2 nM; as the dose of afatinib was increased, so was the degree of inhibition of phosphorylation. As with Afb-B, afatinib exposure at a dose of 1000 nM, no evidence of Y1068 phosphorylation was observed. At a dose of 50 nM, phosphorylation was inhibited by approximately 80%, matching levels incurred by equivlaent doses of Afb-A. These results suggest that the structural differences between Afb-B and afatinib did not detrimentally affect TKI activity.

5.3.3. *Dose responses of chemotherapy and NP formulations thereof*

Investigations into the cytotoxicty of the designated chemotherapeutic agents began by performing dose repsonses of A549 and H226 cells using the MTT assay. As A549 and H226 cells are wild type for EGFR expression, afatinib was expected to be significantly less cytotoxic than vinorelbine, which has broad spectrum antimitotic activity. As such, the range of concentrations explored with afatinib began at a higher dose to accommodate this. Recapitulating the repsonse observed when A549 were exposed to afatinib analogues in the previous chapter (section 4.3.3), only the highest dose of afatinib (10 µM) appeared to induce any significant decrease in cell viability (Figure 5.4A). This dose produced a 54% decrease in

cell viability whereas all other doses surveyed (0.03-3 µM) induced no more than a 29% loss in cell viabilty, however within these doses the range varied only by ~11% giving rise to the plateau of the curve before finally dipping at the highest concentration. Accordingly, the IC_{50} value for afatinib in these cells was calculated to be 9.04 µM, which is higher than that of previously published values[397]. Contrastingly, VRL was found to be more potent whereby the highest dose investigated (1 µM) induced a 67% decrease in cell viabilty. A more traditional dose response pattern was observed as decreasing doses of VRL translated to increased cell viability values. The IC_{50} value was calculated to be 0.1 µM, which is just under two orders of magnitude lower than afatinib. However, given their differential mechanisms of action and the phenotype of A549 cells, this result was expected. Indeed, a similar pattern emerged in H226 cells (Figure 5.4B) whereby VRL was decidedly more cytotoxic than afatinib at all doses examined. Only the highest dose of afatinib (10 µM) caused a decrease in cell viability (29%) whereas all other doses were found not to be cytotoxic (≥ 100% cell viability). With this particular dose repsonse the IC_{50} could not be calculated, however it can be noted that it is greater than 10 µM. The maximal dose of VRL examined (1 µM) was found to decrease cell viability by 68%, which is almost identical to the cytotoxicity observed in A549 cells. The IC_{50} was calculated to be 0.033 µM, in the region of that calculated for A549 cells.

Figure 5.4. Dose response curves post treatment with afatinib and VRL. (A) A549 cells or (B) H226 cells were treated with varying doses of afatinib (0.03 – 10 µM) or VRL (0.003 – 1 µM) for 72 hours, after which time cell viability was assessed by MTT assay. Data are expressed as mean ± SEM, $n = 3$.

After demonstrating that the modifications made to afatinib to generate Afb-B did not detrimentally impact the functionality of the molecule, the next step was to profile Afb-B in A549 and H226 cells compared to afatinib to determine any differences in cytotoxicity. In A549 cells (Figure 5.5A) viability values did not differ significantly at any of the doses examined and both treatments induced a dose responses whereby higher concentrations led to greater loss of cell viability. The calculated IC_{50} values for afatinib and Afb-B were 10.90 and 9.53 µM respectively, which reflects the similar nature of the dose response curves. Moreover, this pattern was recapitulated in H226 cells (Figure 5.5B) whereby the dose response curves for both treatment groups were almost identical. This was the case except for the at highest dose (10 µM) where afatinib was signficantly less cytotoxic than Afb-B (71% viable cells vs 57% viable cells respectively, $P < 0.01$). The IC_{50} values could not be calculated for either compound in H226 cells, which was also seen in the previous experiments described above and therefore this value was designated to be greater than 10 µM. These results reinforce the Western blot analysis presented previously and suggest that Afb-B is equally as efficacious as afatinib in inducing cytotoxicity in A549 and H226 cells, despite being of different malignant origin.
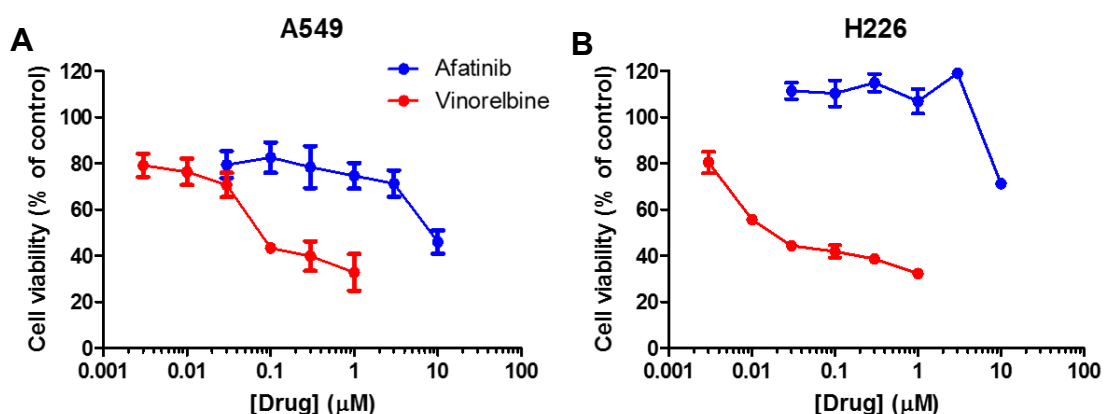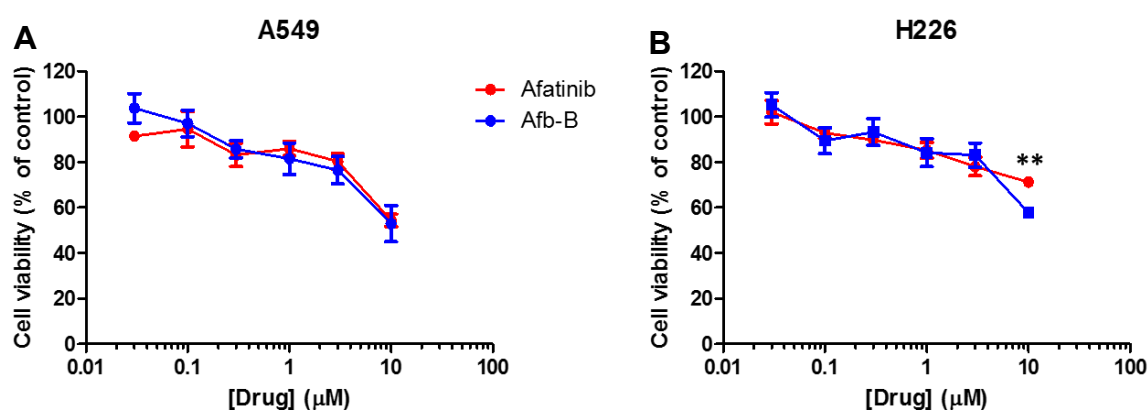

Figure 5.5. Dose response curves post treatment with TKIs afatinib or Afb-B. (A) A549 cells or (B) H226 cells were treated with varying doses of afatinib or Afb-B (0.03 – 10 µM) for 72 hours, after which time cell viability was assessed by MTT assay. Data are expressed as mean ± SEM, $n = 3$, **, $P < 0.01$.

The next set of experiments looked to determine the cytotoxic effects of VRL-NPs in comparison with equivalent concentrations of the free drug in both A549 and H226 cells. As expected, treatment of A549 cells with increasing concentrations of VRL-NPs corresponded with decreases in cell viability (Figure 5.6A, blue curve). As a comparison, A549 cells were also treated with the same doses of free drug (Figure 5.6A, red curve). At the highest doses studied, VRL and VRL-NPs were found to induce similar cell viability loss . However, as the concentration of VRL decrease, the dose response curves began to diverge. Despite not reaching statistical significance due to significant sample variability, VRL-NPs appeared to be more cytotoxic at the lower doses investigated, particularly at 0.03 µM and 0.01 µM. The mean cell viaibilty for VRL treated cells at these doses was 75% and 99% respectively whereas cell viability measurements for VRL-NP treated cells at these doses were 41% and 65% respectively. The calculated IC$_{50}$ for VRL-NPs was 0.06 µM and for VRL was 0.14 µM, in reasonable agreement with the previous dose response studies. To ensure the NPs themselves were not contributing to the cytotoxic effects observed, A549 cells were treated with blank NPs (identically synthesised NPs that do not contain any drug) at equivalent concentrations to the corresponding dose of VRL-NPs (Figure 5.6B). Blank NPs were found not to be overtly cytotoxic at any of the doses investigated. A minor loss of 12% cell viabilty was noted when cells were treated with the highest NP dose and no further losses in cell viability were observed at any other dose. In H226 cells (Figure 5.6C), a more differentiated dose response curve was witnessed when comparing VRL and VRL-NPs. At five of the six doses examined, VRL-NPs were significantly more cytotoxic than the equivalent concentration of VRL. Comparing the same doses as in A549 cells, only 23% of cells were viable when treated with 0.03 µM VRL-NPs opposed to 54% viable cells upon VRL treatment ($P < 0.01$). Simiarly at 0.01 µM, 28% of cells were viable after VRL-NP treatment, which is significantly less than the 69% of cells that remained viable after VRL dosing ($P < 0.01$). The IC$_{50}$ of VRL was calculated as 0.036

μM, which is excellent agreeement with the studies on H226 cells earlier in this chapter. However, the IC_{50} of VRL-NPs which was 0.008 μM is signficantly lower than VRL, affirming their increased potency against this cell line. Blank NPs were also found not to exert any cytotoxic influence in H226 cells (Figure 5.6D), even at the highest dose there was a marginal 7% loss in cell viability. Therefore the cytotoxicity of VRL-NPs is not governed by the NP itself as they are not intrinsically cytotoxic.
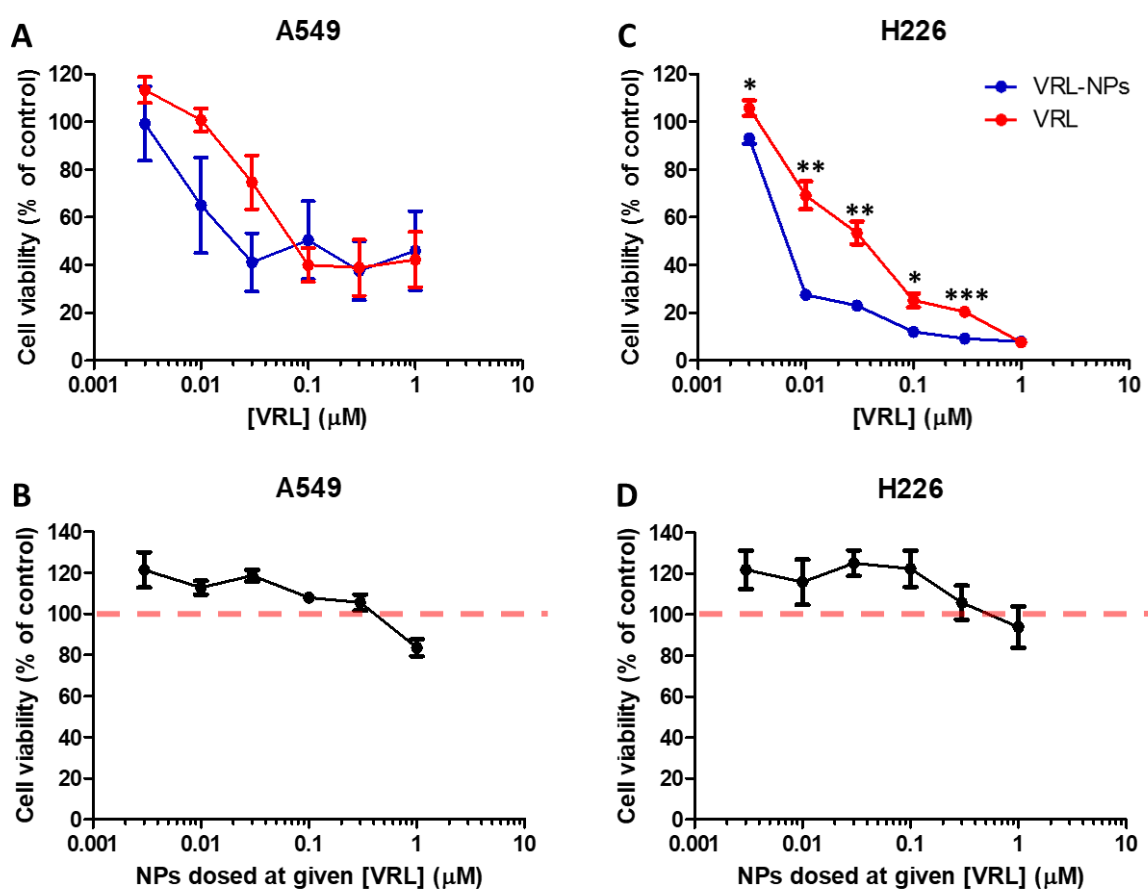
Figure 5.6. Dose responses of VRL, VRL-NPs and blank NPs. A549 cells were treated with varying doses (0.003 – 1 μM) of (A) VRL and VRL-NPs or (B) blank NPs. H226 cells were also exposed to (C) as in (A) and (D) as in (B) identically for 72 hours, after which time cell viability was assessed by MTT assay. Data are expressed as mean ± SEM, *n* = 3, *, $P < 0.05$; **, $P < 0.01$; ***, $P < 0.001$.

As in the previous chapter, studies were also performed on PC-9 cells to discern the cytotoxicity of drug-loaded polymeric NPs as well as gold NPs. Initially, a dose response to

VRL was performed whereby the concentrations previous used for A549 and H226 exposures were also investigated here. Figure 5.7A demonstrates that, as expected, increasing concentrations of VRL produced corresponding reductions in cell viability. Therefore PC-9 cells appear to be somewhat susceptible to the antimitotic effects of VRL. The IC_{50} was calculated to be 0.29 µM, which is higher than for both A549 and H226 cells. Following this, the PC-9 cells were exposed to the equivalent doses of VRL-NPs. In this case, as PC-9 cells are known to be sensitive to TKIs, the effect of VRL-NPs with conjugated Afb-B (Dual-NPs) was also investigated to determine whether combining the drugs would cause any further cytotoxicity (Figure 5.7B). Indeed, differential dose response profiles were observed as Dual-NPs were more cytotoxic at a majority of doses. Notably, significant differences were seen at 1 µM (23% Dual-NP treated viable cells vs 36% VRL-NP treated viable cells, $P < 0.05$), as well as at 0.1 µM (30% Dual-NP treated viable cells vs 68% viable cells, $P < 0.05$) and 0.01 µM (75% Dual-NP treated viable cells vs 93% viable cells, $P < 0.05$). The differential cytotoxicity was also evident in the IC_{50} values; VRL-NPs had an IC_{50} of 0.21 µM whereas the IC_{50} of Dual-NPs was 0.059 µM, which is 3.6 times lower than that of VRL-NPs. There was no evidence to suggest that blank NPs were contributing to the cytotoxic effects upon exposure to drug-loaded NPs (Figure 5.7C). PC-9 cell viability was not detrimentally affected by treatment with blank NPs at any of the concentrations investigated. Interestingly, when PC-9 cells were treated with NPs that only had afatinib conjugated to the surface, there was no demonstrable loss of cell viability (Figure 5.7D). This result was witnessed at all NP doses (i.e. the same dose of NPs and therefore afatinib that the cells would also be exposed to when treated with Dual-NPs) despite the fact that these NPs were prepared in precisely the same fashion as Dual-NPs but without the addition of VRL. These results suggest that a combination of the two agents (Afb-B and VRL) delivered by the same NP is more cytotoxic than when given independently.
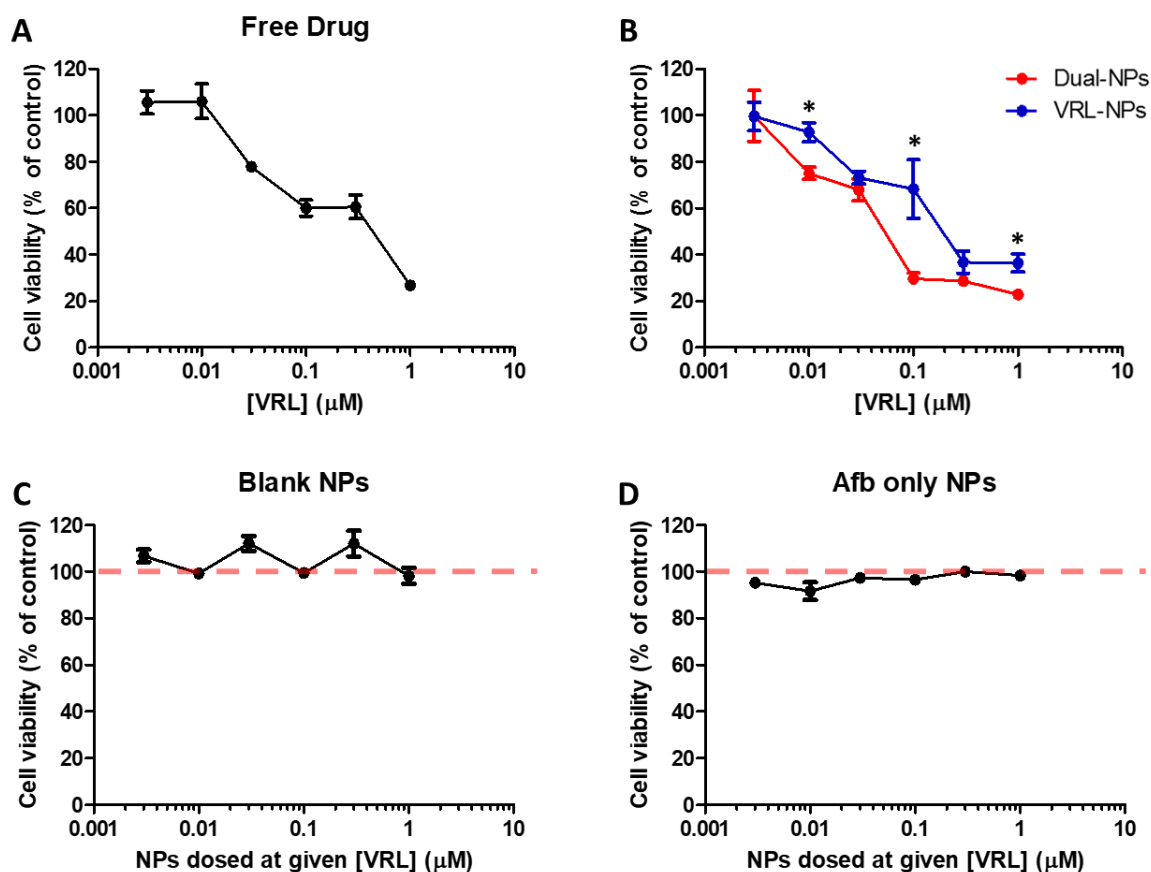
Figure 5.7. PC-9 dose responses upon treatment with chemotherapy and NP formulations thereof. PC-9 cells were treated with varying doses (0.003 – 1 µM) of (A) VRL (B) VRL-NPs or Dual-NPs (C) blank NPs and (D) Afb functionalised blank NPs. Cells were exposed identically for 72 hours, after which time cell viability was assessed by MTT assay. Data are expressed as mean ± SEM, $n = 3$, *, $P < 0.05$.

5.3.4. *In vitro cytotoxicity of polymeric chemotherapy nanoformulations*

After extensively profiling the dose responses of free drug and the respective components of each NP formulation, direct comparative cytoxicity studies were performed on each of the cell lines, looking at blank NPs, VRL-NPs and Dual-NPs. Using the MTT assay as before, the experimental design was altered in such a fashion that cytotoxicity was due to NP uptake and subsequent intracelluar release of VRL. As such, A549 and H226 cells were incubated with blank NPs, VRL-NPs or Dual-NPs for 2, 4 or 8 hours. PC-9 cells were incubated with the same NPs for 30 minutes, 2 or 4 hours. The particle containing medium was removed and then cells

were incubated for a total of 72 hours prior to assessment of cell viaiblty by MTT assay. This was to allow sufficient time for NP uptake, based on observations that polymeric NPs are avidly uptaken by cells within 2 hours[450,451]. In A549 cells (Figure 5.8A) there was a similar pattern of cytotoxicity noted at each of the time points examined. There was no signficant difference in cytotoxicty observed between VRL-NPs and Dual-NPs at any of the time points, however a trend can be noted whereby incubation with Dual-NPs appeared to induce slightly greater loss of cell viability when compared to VRL-NPs. Both VRL-NPs and Dual-NPs were significantly more cytotoxic than the equivalent dose of blank NPs at 2, 4 and 8 hours ($P < 0.001$) as expected, as blank NPs contain no drug and were not cytotoxic. For instance, 8 hours exposure to VRL-NPs and Dual-NPs caused a 36% and 48% loss in cell viabilty respectively when compared to blank NPs. In H226 cells (Figure 5.8B) a slightly different pattern was observed. After 2 hours of NP exposure, there were no signficant differences between any of the treatment groups. However, at 4 hours the differential cytotoxicity between NP formulations began to emerge, as VRL-NPs decreased cell viability by 17% compared to blank NPs ($P < 0.05$), while Dual-NPs decreased cell viaiblity by 29% ($P < 0.01$). This observation was also witnessed at 8 hours, whereby VRL-NPs produced only a 16% loss in cell viabilty, cells exposed to Dual-NPs were 39% less viable compared to blank NP treated cells ($P < 0.01$). Blank NPs were not overtly cytotoxic to H226 cells. In PC-9 cells (Figure 5.8C), as little as 30 minutes exposure to Dual NPs almost completely abrogated cell viability (89% loss of viability vs blank NPs, $P < 0.001$). In contrast to the previous cell lines, VRL-NPs were signficantly less cytotoxic. Compared to Dual-NPs, VRL-NPs were only able to elicit a 28% loss in viability resulting in a 61% difference ($P < 0.001$ vs Dual-NPs). The differential cytoxicity between VRL-NPS and Dual-NPs was also seen at the other time points examined where Dual-NPs were signficantly more cytotoxic than both blank NPs ($P < 0.001$) and VRL-NPs ($P < 0.001$) administered at equal doses. As with A549 and H226 cells, exposure to blank NPs did not result in significant

loss in cell viabilty, suggesting the cytotoxic effects discerned were due to intracellular release of VRL and Afb-B.
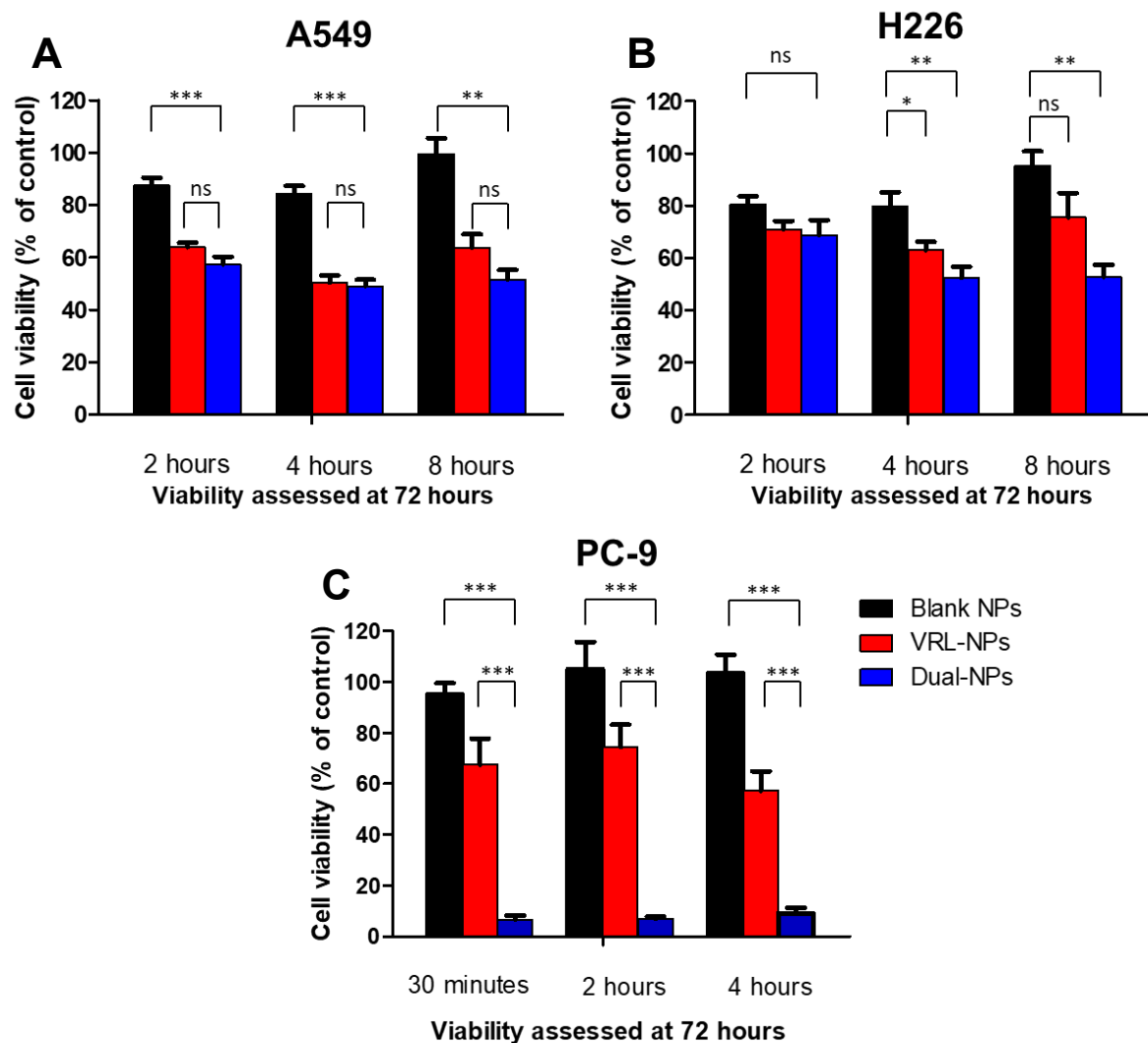
Figure 5.8. Cytotoxicity of polymeric NP formulations of chemotherapy. (A) A549 cells (B) H226 cells and (C) PC-9 cells were treated blank NPs, VRL-NPs or Dual-NPs for the designated timepoints, after which the particle-containing medium was removed and replaced. Cells were incubated for a total of 72 hours, after which time cell viability was assessed by MTT assay. Data are expressed as mean ± SEM, $n = 3$, *, $P < 0.05$; **, $P < 0.01$; ***, $P < 0.001$; ns, not significant.

5.3.5. *Assessment of inhibition of NSCLC cell proliferation*

The results above provide demonstrable evidence of the cytotoxicity of polymeric NP formulations on confluent lung cancer cell monolayers. The effect of the nanomedicines on actively proliferating cells is an important consideration as this more physiologically mimics

the *in vivo* environment. As such, the ECIS system was implemented that allows for real-time

montoring of cell proliferation in a non-invasive fashion. The first set of experiments were

designed to investigate the effect of drug dose on the proliferative capacity of lung cancer cells.

A549 cells were exposed to increasing doses of VRL and the effect on cell proliferation is

depicted in Figure 5.9A. For clarity, the black line represents untreated cells in standard cell

culture growth conditions and the grey line represents acellular complete growth medium to

ensure this was not influencing the proliferation curves. The overarching pattern is that

inhibition of cell proliferation was dose dependant, whereby higher doses of VRL induced

greater inhibition of cell proliferation. This can be most clearly seen at the terminal time point

of the experiment (72 hours) where all quantification for this series of experiments was

performed. At the highest dose investigated (1 µM), cell proliferation was decreased by 89%

compared to untreated cells. An intermediate dose of VRL, 0.03 µM, inhibited cell proliferation

by 42%, whereas the lowest dose investigated, 0.003 µM, was comparatively ineffective. A

similar pattern was witnessed when H226 cells were exposed to the same concentrations of

VRL (Figure 5.9B). A dose dependant decrease in cell proliferation was observed, although

the extent to which specific doses affected proliferation was slightly different to that of A549

cells. A dose of 1 µM VRL decreased H226 proliferation by 88% which was similar to that

seen in A549 cells, however a dose of 0.03 µM reduced proliferation by 53%, 11% more than

seen in A549 cells. The lowest dose investigate was still able to inhibit proliferation by 16%

when compared to untreated cells. The response of proliferating cells to afatinib was also

profiled in A549 and H226 cells (Figure 5.9C and D respectively). In A549 cells, no particular

dose was demonstably effective at halting cell proliferation. The difference in efficacy between

the highest dose examined (10 µM) and the lowest (0.03 µM) was 17 %, therefore it appears

there is signficantly less effect of dose than when compared to VRL. In H226 cells, 10 µM

afatinib was able to essentially prevent cell proliferation, however it was only this dose that

appeared to have a negative effect. All other proliferation curves, and therefore doses examined, were either comparable to untreated cells or had cell index values that were slightly higher. However, these data may be misleading as the proliferation curve for untreated cells was uncharacteristically lower than in all other experiments (e.g. comparison of untreated cells in Figure 5.9B). This can generate the impression that doses of afatinib lower than 1 µM are not only ineffectual at inhibiting cell proliferation but may actually promote it, which is likely a false interpretation.

Figure 5.9. Inhibition of cancer cell proliferation upon treatment with chemotherapy. (A) A549 cells or (B) H226 cells were treated with a range of VRL doses (1-0.003 µM) and cell proliferation was monitored on an hourly basis using electric cell-substrate impedence sensing up to 72 hours. (C-D) as in A-B except cells are treated with afatinib (10-0.3 µM). Each point of the proliferation curve is plotted as the mean ± SEM, n = 3-4 experiments.

Following this, the anti-proliferative capacity of VRL-NPs was investigated and compared to that of equivalent concentrations of free VRL using ECIS in order to corroborate the cytotoxicity observed when studying confluent monolayers. A549 cells were treated with VRL-NPs (equivalent VRL dose 1-0.003 µM) and the proliferation curves generated are depicted in Figure 5.10A. Indeed, increasing concentrations of VRL-NPs induced greater inhibition of

proliferaton and only the very lowest dose (0.003 µM) had negligable impact. The level of inhibition was quantified at the 72 hour time point as in the previous set of experiments. A dose of 1 µM almost halted cell proliferation (96% inhibition vs untreated cells) and at a dose of 0.03 µM there was a substantial 75% decrease in cell proliferation. The lowest dose examined (0.003 µM) did not invoke any significant loss in the ability of cells to proliferate. As both free VRL and VRL-NP cell indexes were quantified at 72 hours, the efficacy of both treatments was compared (Figure 5.10B). As the doses at the periphery of the range examined were similar in both treatment types, the intermediary doses were the focus of comparison. It was observed that at a dose of 0.03 µM, free VRL reduced proliferation by 42% compared to 72% when cells were treated with VRL-NPs ($P < 0.01$). At 0.1 µM, the difference in efficacy was even more pronounced, which stood at 32% (58% free VRL vs 90% VRL-NPs, $P < 0.001$). There was also a difference in inhibitory capacity noted at 0.3 µM of 15% (76% free VRL vs 91% VRL-NPs, $P < 0.05$). The proliferation curves of H226 cells exposed to VRL-NPs (Figure 5.10C) showed demonstrable evidence of inhibited cell proliferation, where the highest three doses inhibited over 90% of cell proliferation. Similarly to the previous experiments, the lowest examined dose was comparatively ineffective. As shown in Figure 5.10D, when investigated in more detail VRL-NPs were significantly more effective inhibitors of H226 cell proliferation. For consistency and comparative purposes, the same doses as examined in the A549 study were also examined here. At a dose of 0.03 µM, free VRL prevented cell proliferation by 52% whereas VRL-NPs equivalent to the same dose were more effective, responsible for a 94% decrease in cell proliferation ($P < 0.001$). At both 0.1 and 0.3 µM, VRL-NPs arrested cell proliferation by 95% and 96% respectively, which were clearly lethal doses. Comparative free VRL was able to reduce cell proliferation by 79% and 81% respectively ($P < 0.001$), less than VRL-NPs in both cases. Taken together, these data suggest that VRL-NPs are more effcacious inhibitors of cancer cell proliferation than equal concentrations of free VRL. Indeed, this

observation can only be gleaned within a specific concentration range and at the extremes of the dose range tested (i.e. highest and lowest).

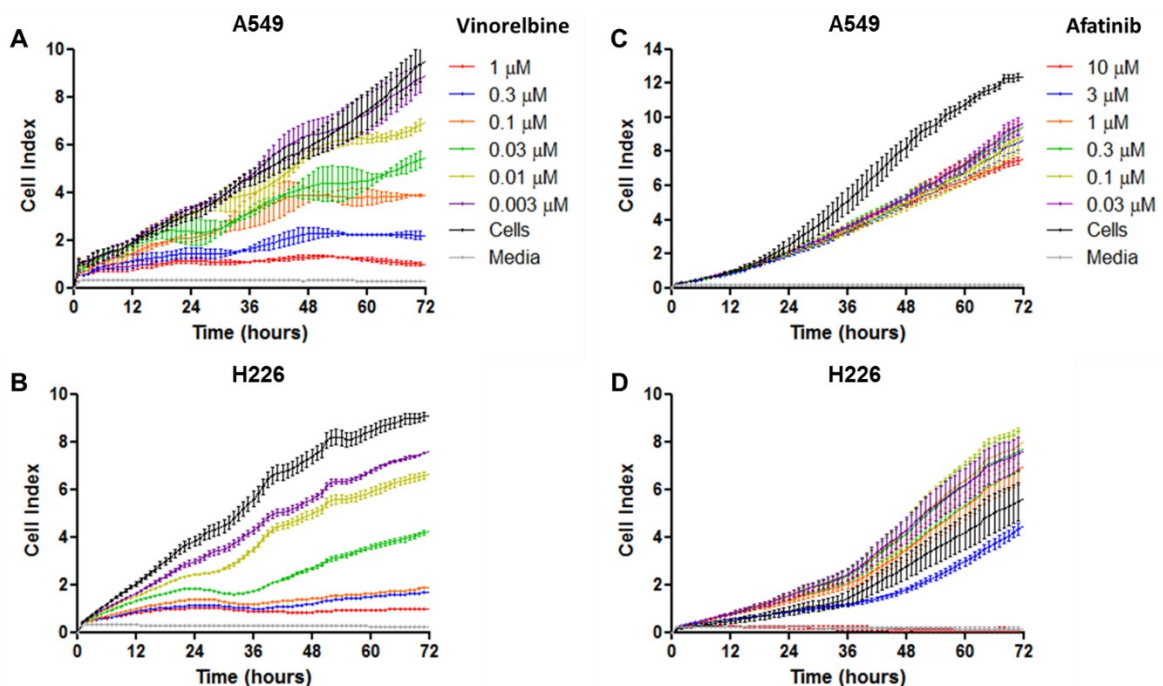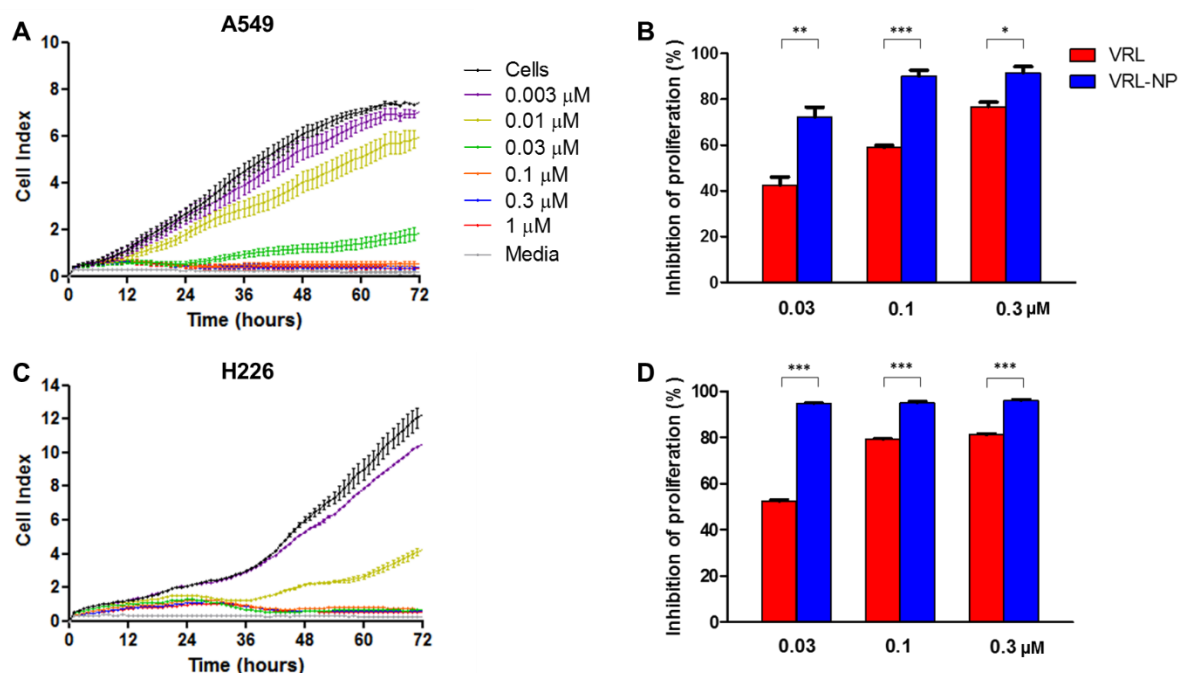**Figure 5.10. Inhibition of cancer cell proliferation upon treatment with VRL-NPs.** (A) A549 cells were treated with a range of VRL-NPs (1-0.003 µM) and cell proliferation was monitored on an hourly basis using electric cell-substrate impedence sensing. Each point of the proliferation curve is plotted as the mean ± SEM, $n = 3$ experiments. (B) Quantification of cell proliferation at 72 hours comparing equivalent concentrations of VRL and VRL-NPs. (C-D) as in A-B respectively except H226 cells were profiled. Data are expressed as mean ± SEM, $n = 3$, *, $P < 0.05$; **, $P < 0.01$; ***, $P < 0.001$.

To ascertain whether the anti-proliferative effects observed upon treatment with VRL-NPs could be attributed to the particles themselves, A549 cells were treated with blank NPs in the same dose repsonse fashion as in previous studies. The amount of particles administered to cells was approximately equal so that an appropriate comparison can be made. The proliferation curves when A549 cells were treated with blank NPs (Figure 5.11A) did not show any evidence of cytotoxicity even at the highest concentration (equivalent number of particles to that of 1 µM VRL-NP where molarity is in reference to the VRL content of the treatment). This observation was confirmed upon quantification of cell proliferation at 72 hours (Figure 5.11B) where no significant differences in cell index were observed when compared to

untreated cells, implying that the NPs themselves were not responsible for inhibition of proliferation. To test whether this was a cell specific effect, the same experiment was performed using TT1 cells as a non-cancerous model of the alveolar epithelium. Similarly to A549 cells, the proliferation curves (Figure 5.11C) revealed that incubaton with blank NPs did not induce any negative proliferative effects at any concentration investigated. Furthermore, quantification at 72 hours (Figure 5.11D) confirmed these results in that the cell index was not significantly different than that of untreated cells at any of the doses examined. Therefore, it can be concluded that blank NPs equal to the concentrations used in previous ECIS experiments were not anti-proliferative and do not contribute to the efficacy observed with VRL-NPs.
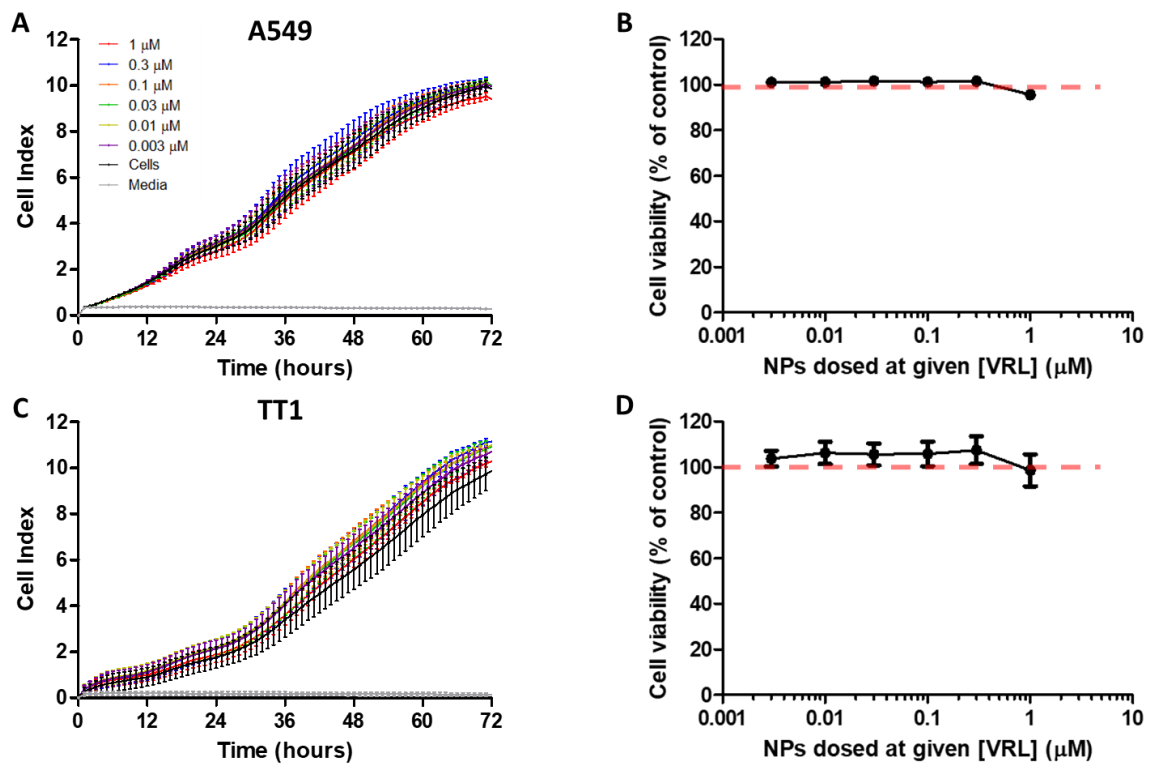
Figure 5.11. Proliferation profile of alveolar epithelial cells in response to blank NPs. (A) A549 cells were treated with blank NPs (equivalent to the concentrations of NPs present in the VRL-NP studies) and proliferation data was acquired using electric cell-substrate impedence sensing where measurements were taken every hour for 72 hours. (B) Quantification of proliferation at 72 hours comparing untreated cells with blank NP doses. (C-D) as in A-B respectively, except these studies were performed using TT1 cells. Data are expressed as mean ± SEM, $n = 3$.

After determination that the NP carriers themselves did not have intrinsic anti-proliferative capacity, the effect of Dual-NPs on the proliferation of PC-9 cells was studied. For comparative purposes, PC-9 cells were first exposed to free VRL in a dose response manner (as in the previous ECIS experiments, 1-0.003 µM) and cell index measurements were taken every hour.
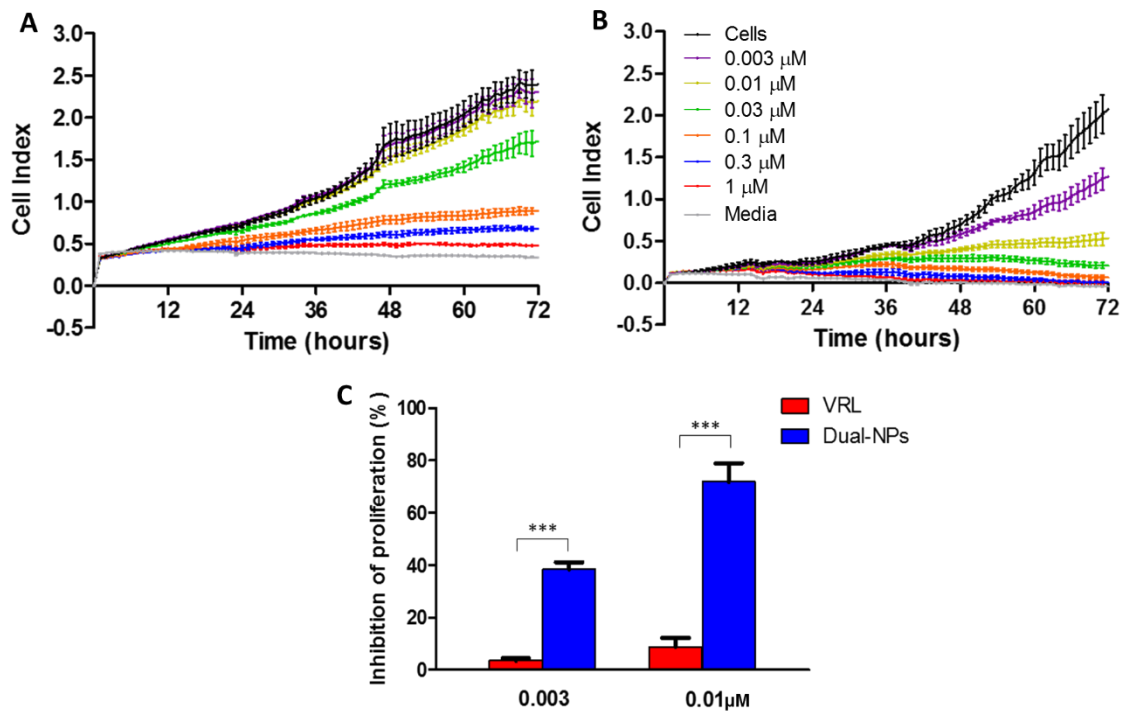
Figure 5.12. Comparative anti-proliferative capacity of VRL and Dual-NPs. PC-9 cells were treated with (A) free VRL (1-0.003 µM) or (B) Dual-NPs (equivalent VRL concentrations 1-0.003 µM) and cell proliferation measurements were obtained using electric cell-substrate impedence sensing. (C) Quantification of cell proliferation of 72 hours comparing the lowest doses of VRL and Dual-NPs used in this set of experiments. Data are expressed as mean ± SEM, $n = 3$, ***, $P < 0.001$.

The proliferation curve depicted in Figure 5.12A demonstrates the PC-9 cell proliferation is inhibited in a dose dependant fashion at medium and high doses. A VRL concentration of 0.1 µM or higher essentially stagnated cell proliferation whereas doses lower than 0.01 µM seemingly had little effect, while 0.03 µM had an intermediate effect. When PC-9 cells were treated with Dual-NPs (doses corresponding to that of free VRL. Figure 5.12B), a similar dose dependant effect was observed, although some differences were evident. For example, free

VRL at a dose of 0.03 µM was able to induce some inhibition of proliferation (~20%) at 36 hours, whereas the corresponding dose of Dual-NPs was able to essentially abrogate proliferation. Extending these observations further, when proliferation was quantified at 72 hours (Figure 5.12C) the lowest doses of free VRL had little effect on proliferation whereas Dual-NPs were found to be significantly more effective. A Dual-NP dose of 0.01 µM inibited proliferation by 72%, compared with 9% brought about by free VRL ($P < 0.001$), and the lowest dose, 0.003 µM Dual-NPs still caused 38% inhibition of proliferation, compared to only 4% upon treatment with free VRL.
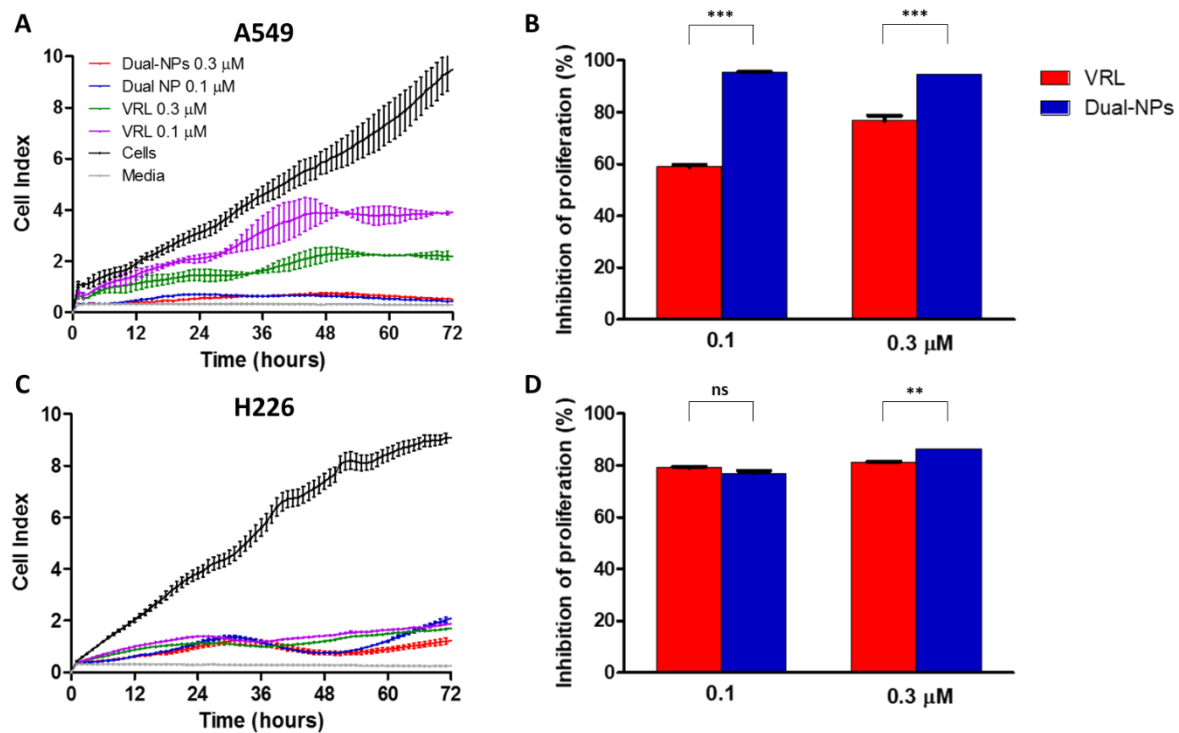
Figure 5.13. Inhibition of cancer cell proliferation upon treatment with Dual-NPs. (A) A549 cells were treated Dual-NPs and the equivalent dose of free VRL (0.3 and 0.1 µM), after which cell proliferation was monitored on an hourly basis using electric cell-substrate impedence sensing. Each point of the proliferation curve is plotted as the mean ± SEM, $n = 3$-4 experiments. (B) Quantification of cell proliferation at 72 hours comparing equivalent concentrations of VRL and VRL in Dual-NPs. (C-D) as in A-B respectively except H226 cells were profiled. Data are expressed as mean ± SEM, $n = 3$-4, **, $P < 0.01$; ***, $P < 0.001$; ns – not significant.

The antiproliferative effect of Dual-NPs was then investigated in A549 cells in comparison to equivalent doses of free VRL (Figure 5.13A). In a similar fashion to that seen with VRL-NPs,

Dual-NPs were able to more effectively inhibit proliferation than free VRL at 0.3 and 0.1 μM. At 72 hours post exposure (Figure 5.13B), a VRL dose of 0.1 μM as free drug attenuated proliferation by 59% compared with 96% when the same amount was given as Dual-NP ($P < 0.001$); a similar pattern was also seen with 0.3 μM VRL whereby free drug limited proliferation by 75% whereas Dual-NP-delivered VRL did so by 95% ($P < 0.001$). In H226 cells (Figure 5.13C), Dual-NPs were not significantly more effective than free VRL at a dose of 0.1 μM at the 72 hour timepoint, however at the higher dose of 0.3 μM, Dual-NPs were able to reduce cell proliferation by 85% compared to 80% when free VRL was administered. ($P < 0.01$). Therefore, Dual-NPs were comparatively more effective than free VRL in all cell lines examined.

5.3.6. *Mechanism of cell death upon NP treatment*

After elucidating the effects of VRL-NPs and Dual-NPs on confluent monolayers and actively proliferating NSCLC cells, a set of experiments were performed that were designed to examine the apoptotic response of NSCLC upon drug-loaded NP treatment. Measurement of levels of apoptosis can give a more accurate representation of the cytotoxicty of a given theapy and clarify the underlying mechanism of cell death. The NSCLC cell lines A549, H226 and PC-9 were treated with VRL-NPs or Dual-NPs for 12, 24 or 48 hours and levels of apoptosis were discerned using flow cytometry. Apoptotic cells were identified as positive for both cleaved caspase-3 and cleaved poly(adenosine diphosphate-ribose) polymerase (PARP). At the 12 and 24 hour timepoint, very little apoptosis was observed in A549 cells upon treatment with either VRL-NPs or Dual-NPs as evidenced by the low percentage of cells in the top right quadrant of the pseudocolour flow cytometry plots (Figure 5.14A). When apoptosis was quantified (Figure 5.14B) at these time points, indeed there was no significant difference between the treatments (0.96% vs 1.02 % at 12 hours, 0.57% vs 1.17% at 24 hours, VRL-NPs vs Dual-NPs). However, after 48 hours exposure, there was a significant increase in the amount of apoptotic cells

following treatment with VRL-NPs (0.57% to 16.3%) and Dual-NPs (1.17% to 21.9%). Notably, after 48 hours, more A549 cells treated with Dual-NPs were apoptotic than when treated with VRL-NPs, although this was not statistically significant at the 0.05 level ($P = 0.07$).

Figure 5.14. Apoptosis in A549 cells exposed to polymeric NP formulations. A549 cells were treated with VRL-NPs or Dual-NPs (1 µM VRL) for 12, 24 or 48 hours prior to assessment of apoptosis *via* flow cytometry. (A) Representative pseudocolour plots of NP treated cells. (B) Quantification of apoptosis whereby an apoptotic cell was classed as positive for both cleaved caspase 3 and cleaved PARP (double positive). Data are expressed as mean ± SEM, $n = 3$.

In H226 cells (Figure 5.15A), the overall pattern was comparable to that observed in A549 cells, whereby low levels of apoptotic cells were detected in both treatment groups at the 12 and 24 hour timepoint. At 12 hours post-treatment, 4.15% of VRL-NP treated cells were apoptotic compared to 2.25% treated with Dual-NPs. A similar amount was observed at 24 hours for both NP treatments (4.43% VRL-NPs vs 4.38% Dual-NPs). At 48 hours, there was a large rise in the amount of apoptotic cells detected that were exposed to VRL-NPs (4.43% to

32.1%) and Dual-NPs (4.38% to 30.3%). There was no statistically significant difference between either treatment group at any of the time points analysed (Figure 5.15B).
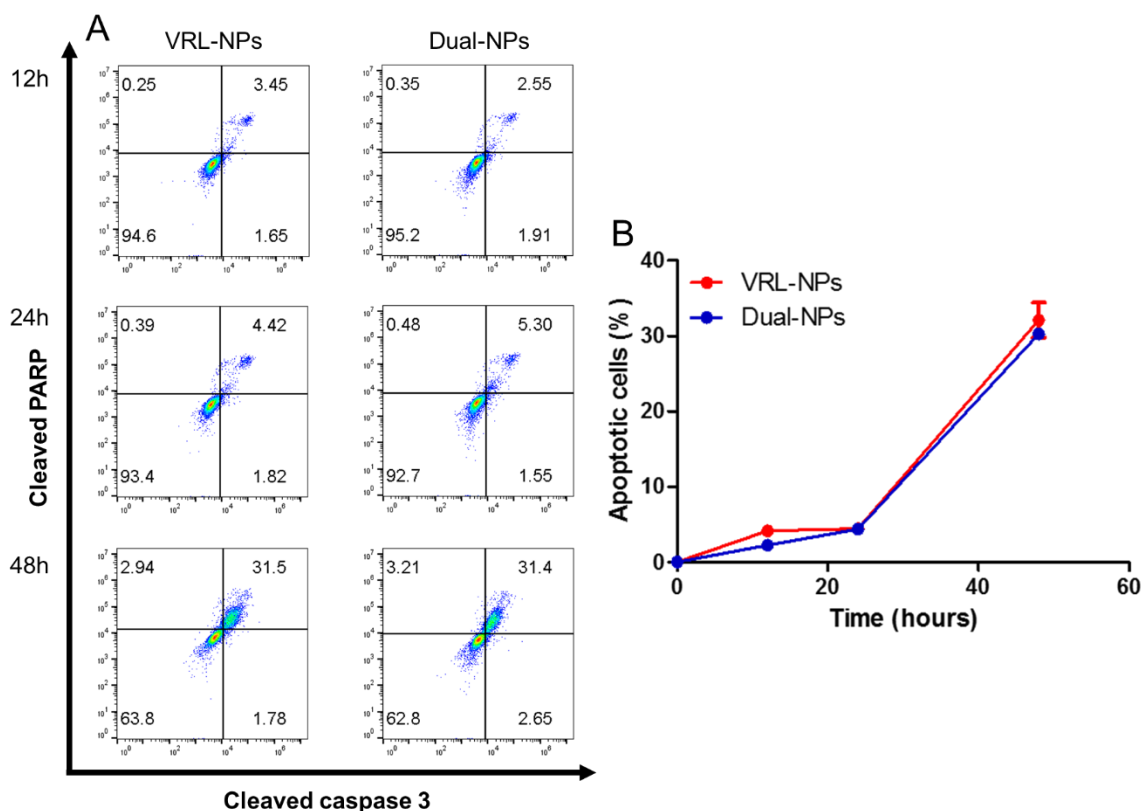
Figure 5.15. Apoptosis in H226 cells exposed to polymeric NP formulations. H226 cells were treated with VRL-NPs or Dual-NPs (1 µM VRL) for 12, 24 or 48 hours prior to assessment of apoptosis *via* flow cytometry. (A) Representative pseudocolour plots of NP treated cells. (B) Quantification of apoptosis whereby an apoptotic cell was classed as positive for both cleaved caspase 3 and cleaved PARP (double positive). Data are expressed as mean ± SEM, $n = 3$.

Corroborating the results from the cell viability and proliferation studies, PC-9 cells were susceptible to treatment with Dual-NPs. At all times points examined, Dual-NPs were significantly more effective inducers of apoptosis than VRL-NPs (Figure 5.16A). At 12 hours, exposure to VRL-NPs resulted in only 2.78% of cells undergoing apoptosis, whereas exposure to Dual-NPs instigated an increased apoptotic response in 28.3% of cells ($P < 0.01$). This pattern was also observed at 24 hours (VRL-NPs 7.20% vs Dual-NPs 35.1% apoptotic cells, $P < 0.01$). The difference between treatment groups widened further at 48 hours post exposure,

whereby VRL-NPs were responsible for inducing apoptosis in 13.1% of PC-9 cells, while Dual-NPs induced apoptosis in 61.9% of cells ($P < 0.001$, Fgure 5.16B). These results demonstrate the enhanced pro-apoptotic capacity of Dual-NPs in a range of NSCLC cell lines, reinforcing the findings of the cytotoxicity studies in the other cells.
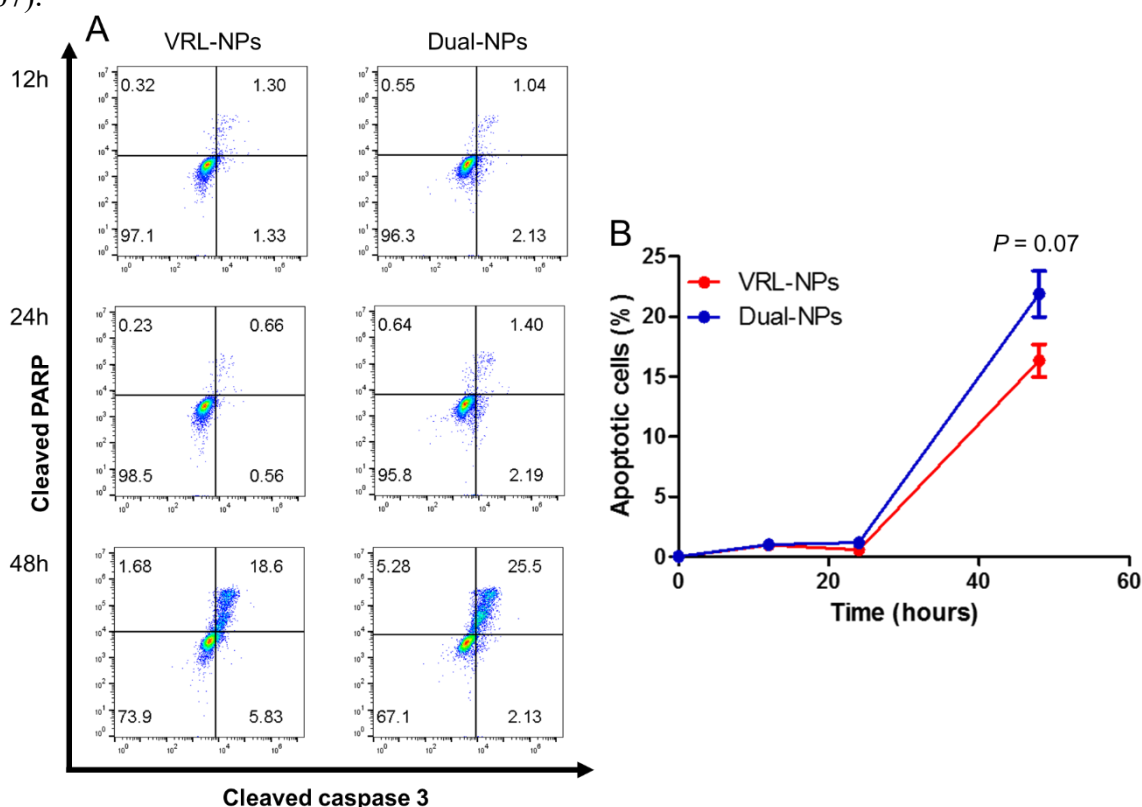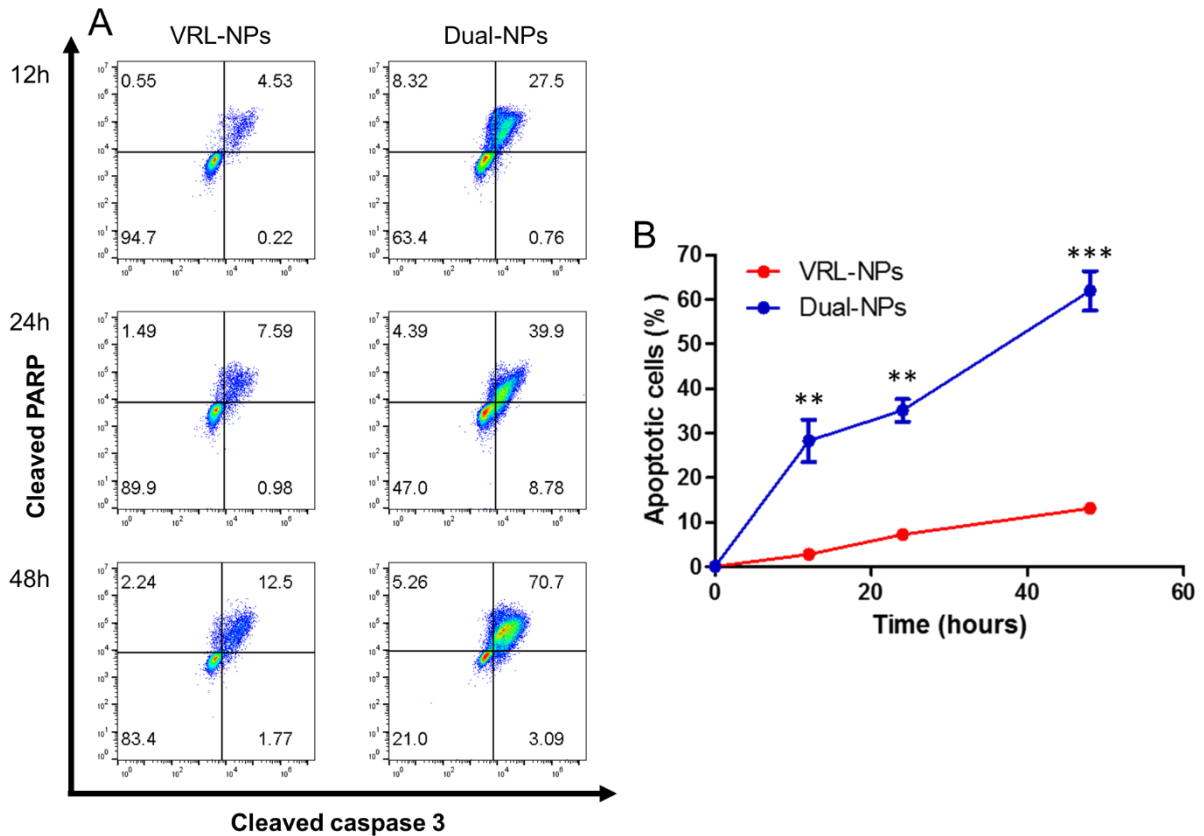

Figure 5.16. Apoptosis in PC-9 cells exposed to polymeric NP formulations. PC-9 cells were treated with VRL-NPs or Dual-NPs (1 μM) for 12, 24 or 48 hours prior to assessment of apoptosis *via* flow cytometry. (A) Representative pseudocolour plots of NP treated cells. (B) Quantification of apoptosis whereby an apoptotic cell was classed as positive for both cleaved caspase 3 and cleaved PARP (double positive). Data are expressed as mean ± SEM, $n = 3$, **, $P < 0.01$; ***, $P < 0.001$.

5.3.7. *Inflammatory cytokine release*

The traditional route of adminstration for VRL formulations is intravenous injection, whereby interaction with the venous endothelium is inevitable. As VRL is known to induce venous inflammation and injury after injection, the release of canonically inflammatory cytokines IL-6, IL-8, IL-1β and TNF-α was assessed, using HUVECs as a model for the venous endothelium.

Three different doses (3, 10 and 30 µM) of VRL or equivalent concentration of VRL-NPs and four time points (4, 8, 12 and 24 hours post initial 1 hour drug exposure) were examined. Figure 5.17 shows the cytokine release profile for HUVECs exposed to VRL at the aforementioned doses and time points.
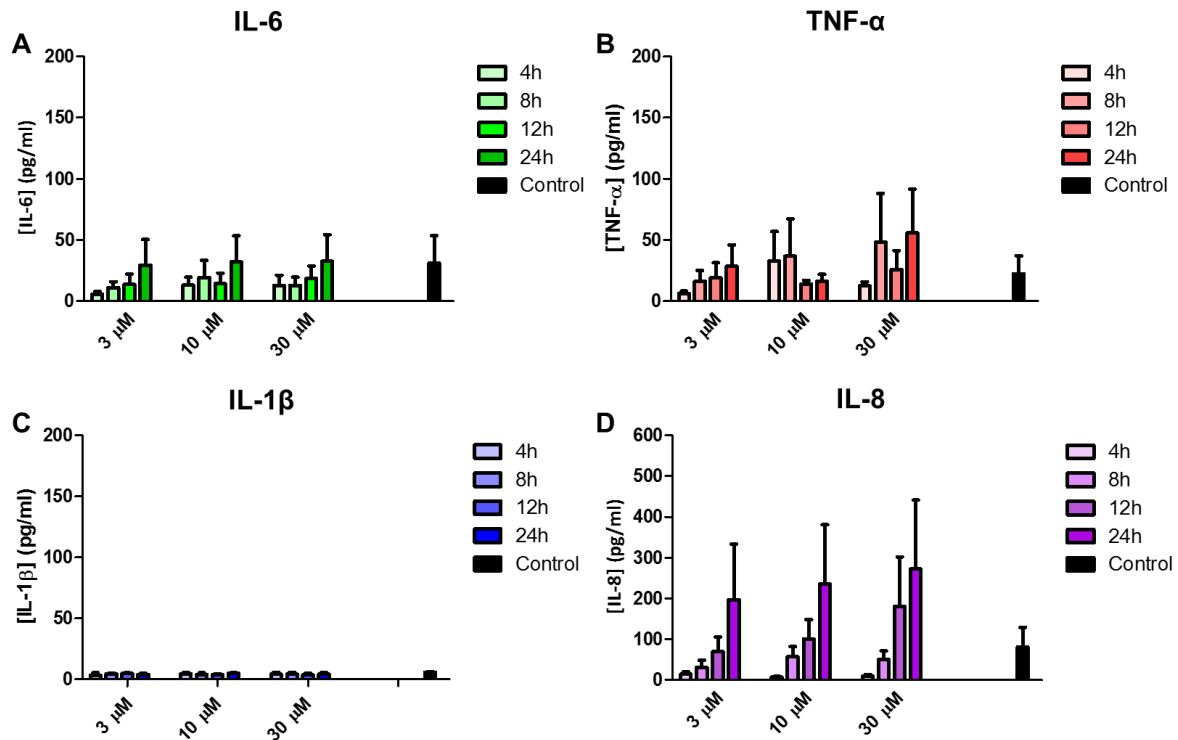
Figure 5.17. Inflammatory cytokine profile of HUVECs exposed to VRL. Primary HUVECs were incubated with 3, 10 or 30 µM VRL for 1 hour prior to media change and subsequent incubation for 4, 8, 12 or 24 hours. The release of pro-inflammatory cytokines (A) IL-6, (B) TNF-α, (C) IL-1β and (D) IL-8 was quantified by ELISA. Data are expressed as mean ± SEM, $n = 4$.

Somewhat surprisingly, there was little release of IL-6 from HUVECs at any of the doses or timepoints (Figure 5.17A). Increasing the time of exposure, but not the dose, elicited more cytokine release ($P = 0.0161$), and this can be seen across all three doses. At the 24 hour time point 29.6, 32.1 and 32.5 pg/mL IL-6 was detected at 3, 10 and 30 µM dose exposures respectively. Similar patterns were observed with TNF-α and IL-1β (Figure 5.17B and C). The levels of TNF-α detected varied based on time and dose, however overall there was no significant differences between treatment groups. Upon treatment of HUVECs with 3 µM VRL

a trend in time dependant increase in TNF-α production was observed, to a maximum of 28.5 pg/mL. This effect was not seen at 10 µM or 30 µM, however at the latter dose after 24 hours, the highest amount of TNF-α was noted (55.8 pg/mL). Negligable quantities of IL-1β were detected regardless of treatment dosage or time. The pattern of release of IL-8 (Figure 5.17D) upon treatment with VRL was in contrast to that of TNF-α and IL-1β. At each dose, a statstically significant time dependant increase in cytokine release was observed ($P = 0.0075$) with a maximal amount detected at the 24 hour timepoint. For example, 3 µM VRL induced 14.1 pg/mL IL-8 release at the 4 hour timepoint, whereas at 24 hours 197.5 pg/mL IL-8 was detected. This trend was reciprocated throughout for 10 and 30 µM VRL. Notably, as the dose increased so did the amount of IL-8 released at 12 and 24 hour timepoints. At the 12 and 24 hour timepoints, a dose of 10 µM generated 100.7 pg/mL and 235.2 pg/mL IL-8 respectively. When these same timepoints were inspected after a dose of 30 µM, 180.5 pg/mL and 272.4 pg/mL IL-8 was detected respectively, however differences in doses were not statistically significant.

To determine whether encapsulation within NPs affected the inflammatory response, HUVECs were treated as with VRL, except the equivalent dose was administrered as a NP formulation (VRL-NPs). Figure 5.18 shows the subsequent inflammatory cytokine release profile. The release pattern of IL-6 (Figure 5.18A) largely matched that of free VRL whereby increased exposure time leading to further cytokine release was observed ($P = 0.012$). A dose of 3 µM VRL (as VRL-NPs) at the earliest time point generated 10.4 pg/mL IL-6 which increased to 31.0 pg/mL at the 24 hour timepoint. At this timepoint, doses of 10 and 30 µM produced 29.2 pg/mL and 32.9 pg/mL of IL-6 respectively. Levels of TNF-α (Figure 5.18B) were found not to exceed 40 pg/mL regardless of dose or timepoint and there was no apparent trend evident in the release of TNF-α. In line with free VRL experiments, minute amounts of IL-1β were detected when exposed to VRL-NPs (Figure 5.18C). With respect to IL-8 release (Figure

5.18D), a time (P = 0.006) but not dose dependant response was witnessed, similarly to the profile of IL-6. At 3 µM the maximum IL-8 detected was at the 24 hour timepoint (68.3 pg/mL), which was the same for the other two doses (77.9 pg/mL and 85.3 pg/mL for 10 and 30 µM respectively).
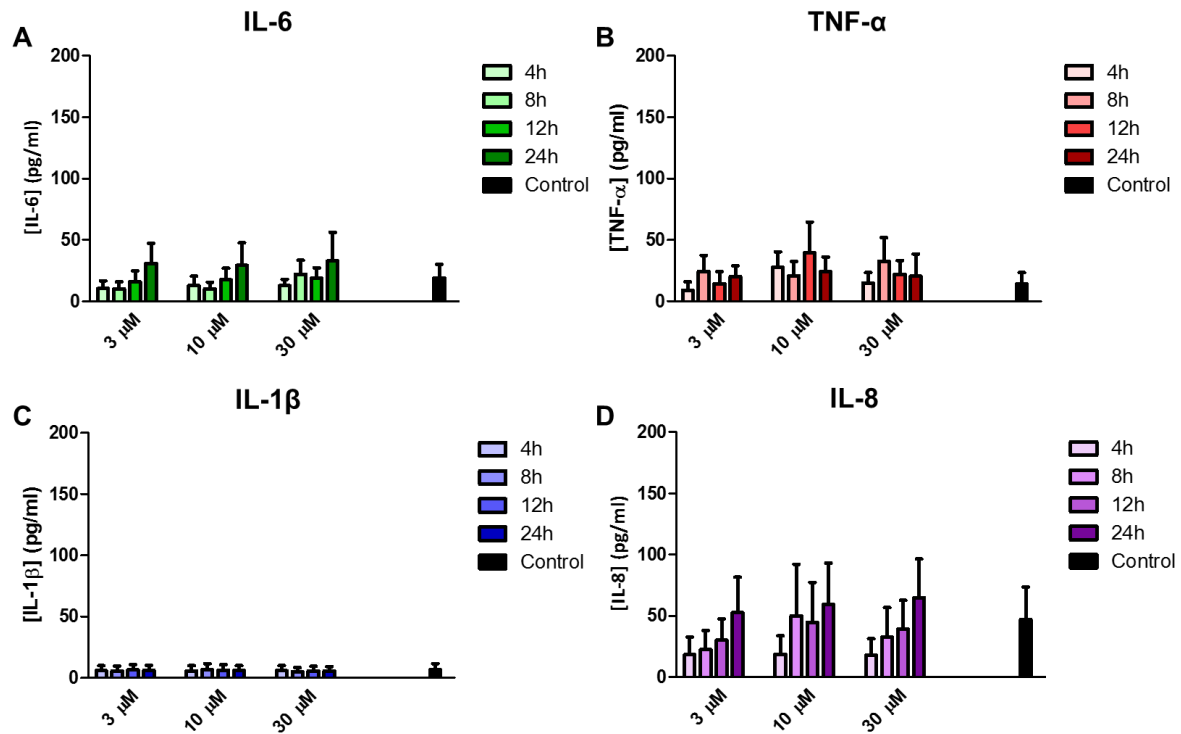
Figure 5.18. Inflammatory cytokine profile of HUVECs exposed to VRL-NPs. Primary HUVECs were incubated with VRL-NPs (3, 10 or 30 µM VRL equivalent) for 1 hour prior to media change and subsequent incubation for 4, 8, 12 or 24 hours. The release of pro-inflammatory cytokines (A) IL-6, (B) TNF-α, (C) IL-1β and (D) IL-8 was quantified by ELISA. Data are expressed as mean ± SEM, n = 4.

These results are in contrast to the IL-8 release profiles of VRL exposure, exemplified in Figure 5.19. which directly compares the IL-8 release generated following both treatment formulations across time and by dose. At 4 and 8 hour timepoints the amount of IL-8 produced did not differ dramatically between the type of treatment or dose. However at the 12 hour timepoint, each dose of VRL elicited higher levels of IL-8 from HUVECs than the corresponding dose of VRL-NPs. For instance, at a dose of 30 µM there is a mean difference of 129.4 pg/mL between VRL and VRL-NPs, which translates to 3.5 times less IL-8 generated upon exposure to VRL-NPs.

Moreover, this is more pronounced at the 24 hour timepoint; if the same dose is examined (30 µM) there is a 187.1 pg/mL difference in IL-8 release on average. This equates to production of approximately 3.2 times less IL-8 upon VRL-NP treatment. As previously observed, time was a signifcant factor in cytokine production ($P = 0.0004$). Unfortunately, the large variation of values obtained by ELISA meant that at each time point, the cytokine production from each type of treatment was not statistically different, however it can be gleaned that encapsualtion of VRL within NPs may attuenate the release of IL-8 from HUVECs which may have important physiological ramifications.
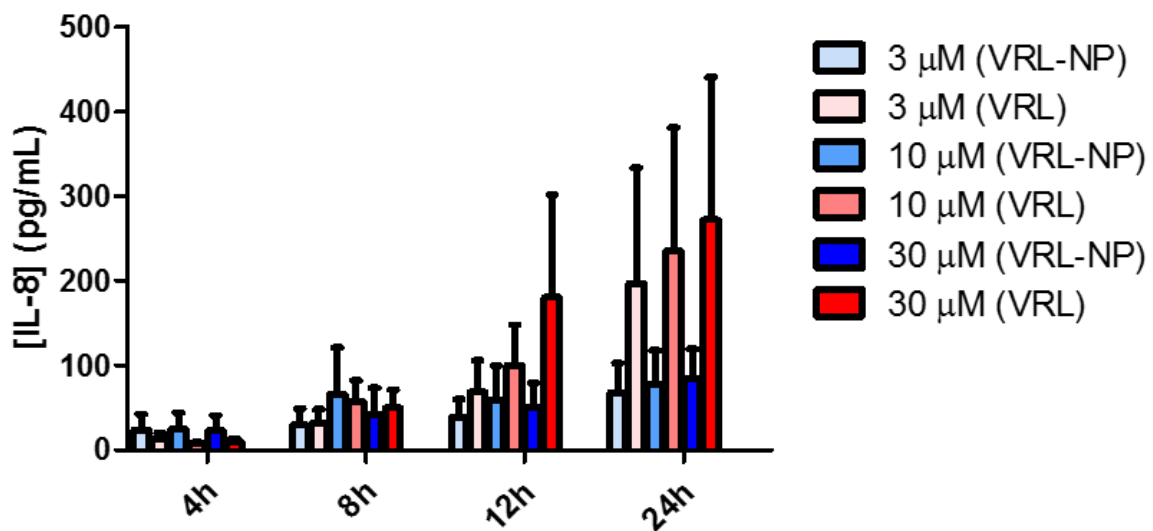
Figure 5.19. Comparative IL-8 release from HUVECs treated with VRL and VRL-NPs. HUVEC cells were treated with either VRL or VRL-NPs (3, 10 or 30 µM VRL) for 1 hour, drug containing medium removed and replaced with growth medium. IL-8 release was quantified by ELISA at the specified time points. Data are expressed as mean ± SEM, $n = 4$.

5.3.8. *Insights into mechanisms of cellular uptake of NPs – effect of temperature*

The uptake and intracellular fate of NPs is of critical importance, particularly from a therapeutic perspective. In order to discern the mechanism of uptake, a stepwise experimental approach was taken. To determine if energy dependant mechanisms of internalisation were responsible for NP uptake, the metabolic activity of cells was inhibited by cooling to 4 ºC. The uptake of fluorescent NPs functionalised with Afb (to more accurately mimic the complete NP

formulation) was then compared to uptake in cells incubated at 37 °C, where energy dependant processes are active. Figure 5.20A demonstrates the differential uptake of fluorescent NPs after a 4 hour incubation period. The NP fluorescence (blue) is due to the encapsulated hydrophobic fluorescent dye coumarin-6, which is impermeable and cannot cross the cell membrane, therefore the fluorescence observed can be attributed directly to the NP and not unencapsulated dye entering into the cell. Further evidence for this can be gleaned from the bright blue punctate spots distributed throughout the cells as opposed to diffuse cytoplasmic spread that would be expected if the dye crossed the cell membrane or there was signficant leakage from the NP. The nucleus is depicted in red and the plasma membrane is depicted in green for contrast. At this timepoint (4 hours) there is a clear distinction between the uptake of NPs taken up at 37 °C and at 4 °C. In this representative image, it can be seen that there is a significant decrease in the amount of NPs internalised at 4 °C compared to that at 37 °C, evidenced by the much clearer appearance and distrbution of NPs (in the blue channel). This uptake difference is not expected to be due to the number of cells present as this was relatively consistent throughout each experimental condition. Further time points were also investigated to see if this phenomenon persisted over time. Indeed, at 8 hours (Figure 5.20B) and 24 hours (Figure 5.20C) of incubation time with NPs, the observations at 4 hours were recapitulated whereby significantly more NPs were observed in cells kept at 37 °C compared with cells kept at 4 °C. Similarly to 4 hours incubation, the number of cells were not different between treatment groups and the morphology of the cells suggests that they are still viable. Numerous NPs were seen to coalesce at 8 hours and more so at 24 hours in the cells that were maintained at 37 °C compared to scant clustering and small patches of NPs in the cells kept at 4 °C (see merge panel for clearer distinctions). As an additional observation, there appeared to be an increase in NP uptake over time in both temperature conditions, however quantification of NP fluorescence showed that uptake had peaked before 4 hours (Figure 5.21) . The fluorescence intensity was

quantified at each time point and the relative decrease in fluorescence from NPs in cells treated at 4 °C was calculated (Figure 5.21). After 4 hours incubation there was a 66% decrease in NP fluorescence in cells treated at 4 °C compared with cells at 37 °C ($P < 0.01$). This discrepancy was maintained over time; at the 8 hour timepoint a 67% decrease in NP fluorescence was observed ($P < 0.01$) and after 24 hour incubation with NPs, a 59% decrease in fluorescence
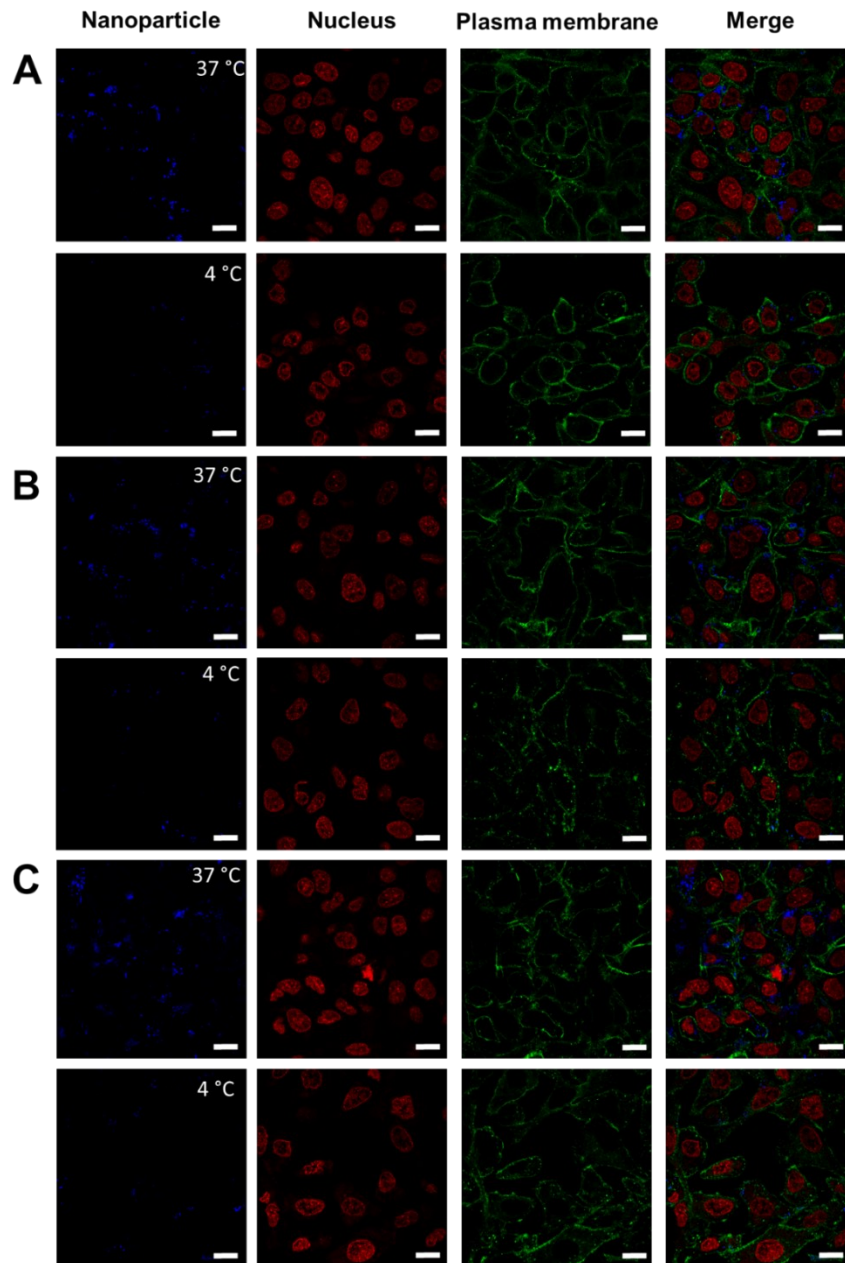
Figure 5.20. Effect of temperature on NP uptake. A549 cells were exposed to fluorescent NPs and incubated at either 37 °C or 4 °C for (A) 4 hours, (B) 8 hours or (C) 24 hours prior to preparation for and imaging by confocal microscopy. NPs are blue, nucleus is red and the plasma membrane is green. Scale bar = 15 μm.

was seen relative to cells housed at 37 °C for the duration of the experiment ($P < 0.01$). These observations suggest that NPs are rapidly internailsed into cancer cells primarily by an energy dependant mechanism although some uptake occurred due to passive diffusion across the cell membrane.
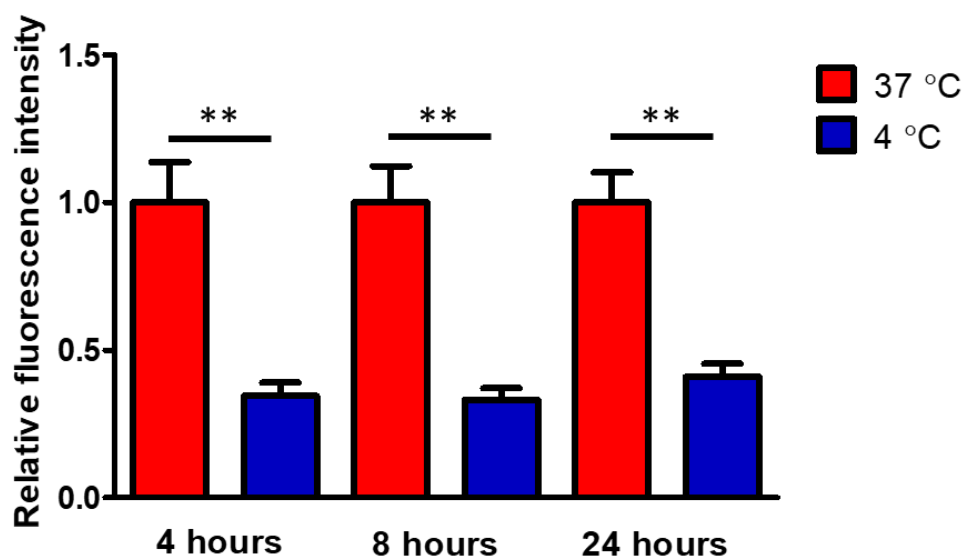
Figure 5.21. Quantification of internalised fluorescent NPs under different temperature conditions. A549 cells were imaged after incubation at 37 °C or 4 °C and NP uptake was quantified as fluorescence intensity relative that observed at 37 °C, at 4, 8 and 24 hour timepoints. Data are expressed as mean ± SEM, $n = 3$, **, $P < 0.01$.

5.3.9. *Insights into mechanisms of cellular uptake of NPs – effect of pharmacological inhibition*

Upon establishing that NPs were predominantly taken up by an energy dependant process (i.e. endocytosis), the next step was to determine which endocytic mechanism played the most dominant role in uptake of the particles. Inhibition of various endocytic pathways can be achieved using pharmacological modulators of endocytic processes. In this work, chlorpromazine and dynasore were implemented to inhibit clathrin-mediated endocytosis, genistein was used to inhibit caveolae-mediated endocytosis, and EIPA and nocodazole were employed to inhibit macropinocytosis.
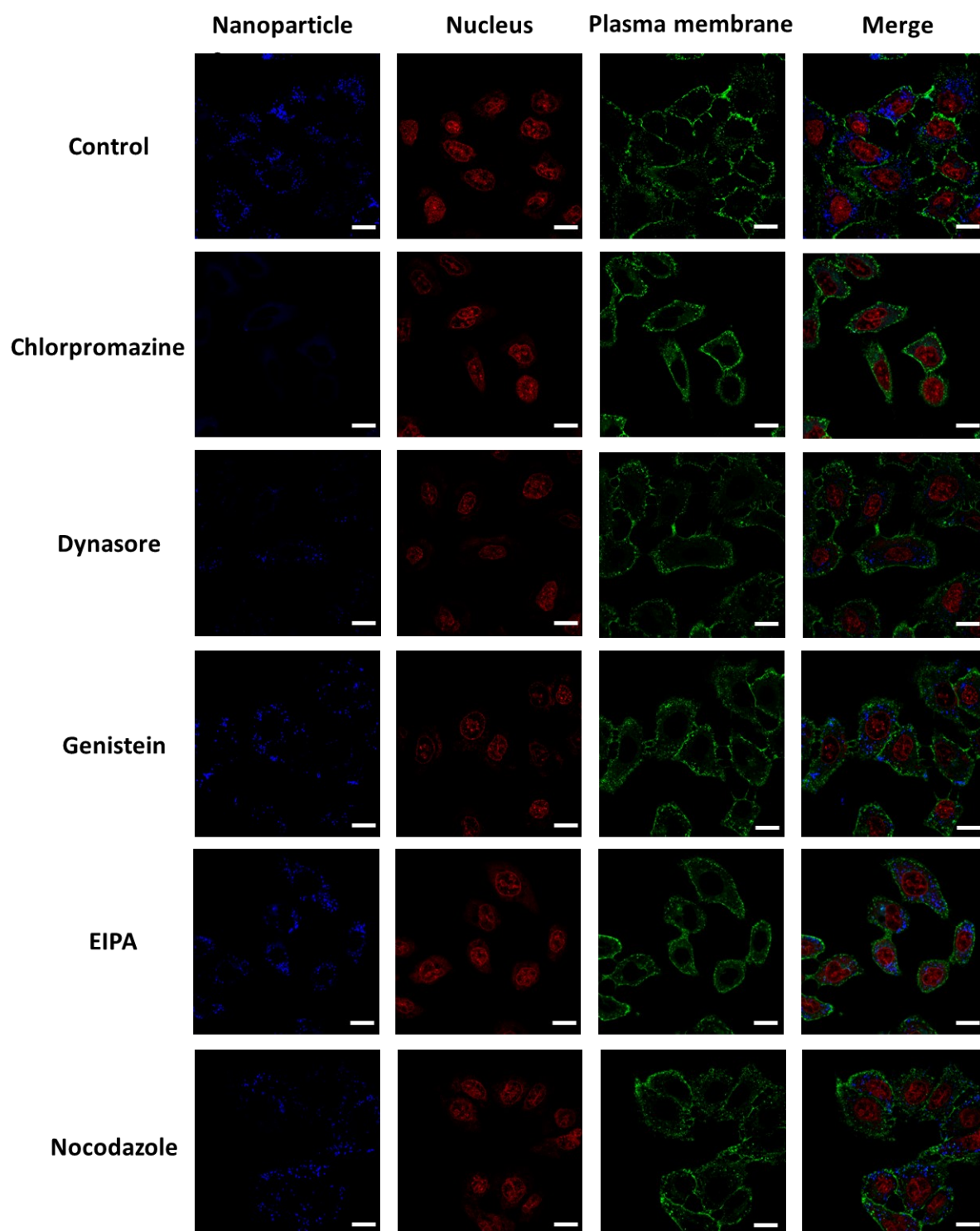
Figure 5.22. Effect of chemical inhibition of endocytosis on uptake of NPs. A549 cells were pre-incubated with a panel of inhibitors of endocytosis (chlorpromazine and dynasore – clathrin-mediated, genistein – caveolae-mediated, EIPA and nocodazole – macropinocytosis) for 1 hour prior to NP exposure for a further 2 hours. Cells were prepared for and imaged by confocal microscopy. NPs are blue, nucleus is red and the plasma membrane is green. Scale bar = 15 μm.

Figure 5.22 depicts the uptake of fluorescent NPs in untreated cells (control) and cells treated with the aforementioned endocytosis inhibitors. Observationally, NPs were avidly uptaken by untreated cells, as evidenced by widespread distribution of punctate NP clusters, matching the pattern seen in cells (although less confluent here) incubated at 37 °C for 4 hours or longer in the previous experiment, even though the cells were only incubated with NPs for 2 hours in this set of experiments (as saturation was observed at 4 hours in the previous experiment). Examination of the cells treated with either chlorpromazine or dynasore revealed little uptake of NPs compared to control cells, which is most apparent when comparing the nanoparticle only images (blue). Inhibition of caveolae-mediated endocytosis with genistein appeared to impair NP uptake by only a small degree, with many NPs still visibly taken up by cells, especially in comparison to chlorpromazine. Similar to treatment with genistein, cells pre-incubated with EIPA or nocodazole did not demonstrate any significant impairment of NP uptake and appeared visually comparable to control cells.
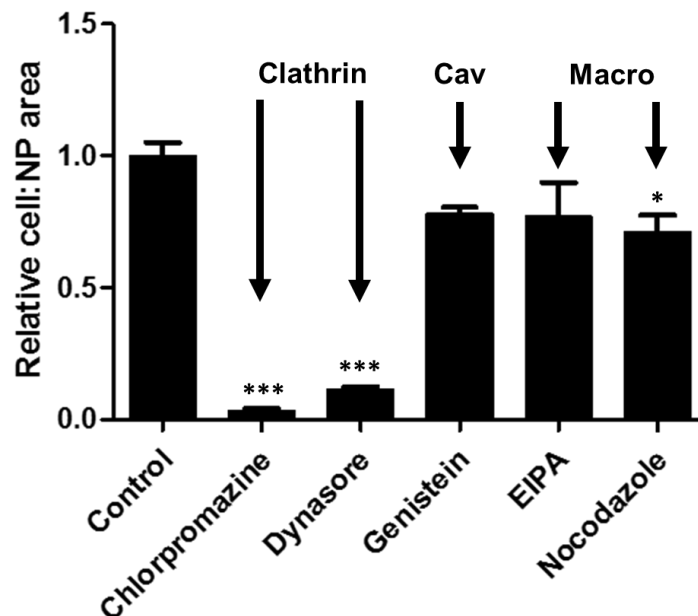
Figure 5.23. Quantification of NP uptake after chemical inhibition of endocytosis. A549 cells were pretreated with a panel of endocytosis inhibitors (chlorpromazine and dynasore – clathrin-mediated, genistein – caveolae-mediated, EIPA and nocodazole – macropinocytosis) for 1 hour. Cells were then treated with NPs for 2 hours after which they were imaged by confocal microscopy. Uptake was quantified relative to the untreated cells. Data are expressed as mean ± SEM, $n = 3$, *, $P < 0.05$; ***, $P < 0.001$.

Quantification of NP uptake (Figure 5.23) of differentially inhibited groups compared to control cells reinforced qualitative observations but also provided additional insight. Treatment with chlorpromazine or dynasore inhibited NP uptake by 98% and 89% respectively compared to control cells ($P < 0.001$). Genistein treatment impacted NP uptake by 21%, whereas EIPA treatment inhibited endocytosis of NPs by 23% (not significant) and nocodazole impaired uptake by 29% compared to control ($P < 0.05$). Taken together, these results point towards clathrin-mediated endocytosis as the dominant uptake pathway in cancer cells and other endocytic pathways such as caveolae-mediated endocytosis and macropinocytosis have more minor roles in dictating uptake of NPs.

5.3.10. *Insights into mechanisms of cellular uptake of NPs – effect of RNA interference*

Chemical inhibition of a variety of endocytic pathways highlighted clathrin-mediated endocytosis as the primary uptake pathway of fluorescent NPs. In order to confirm this observation. RNA interference was implemented. Delivery of siRNA targeting the clathrin heavy chain 1 (CLTC) gene, which codes for the CTLC protein that is a major structural component of clathrin pits, was achieved using Lipofectamine. Successful knockdown of this gene, and therefore absence of the protein, would cause structural perturbations in clathrin pits rendering them unable to effectively endocytose particles, or abolish their stucture completely. Prior to exposing cells to NPs, the conditions to achieve optimal knockdown of CLTC were determined. As shown in Figure 5.24A, A549 cells were treated with siRNA agaisnt CLTC (siCLTC) or equivalent concentrations of a scramble sequence for 48 or 72 hours, after which time the CLTC protein levels were quantified. The western blots show that CLTC levels were demonstrably lower in siCLTC treated cells compared to scramble treated cells at 48 hours and more notably at 72 hours, denoting successful gene knockdown. In all treatment groups, levels of the housekeeping gene β-actin were unaffected by knockdown of CLTC. Moreover, the effect of Lipofectamine alone was also investigated as well as examination of untreated cells

(Figure 5.24B). Indeed, at both 48 and 72 hour timepoints, Lipofectamine did not appear to have any detrimental effects with regards to expression levels of CLTC or β-actin, and the duration of study did not have any impact, as observed in the control treatment group. Quantification of knockdown efficiency (Figure 5.24C) confirmed visual observations whereby incubation for 72 hours produced the best knockdown efficiency. At 48 hours, CLTC protein levels were reduced by 51% ($P < 0.01$) compared to scramble treated cells, whereas at 72 hours, CLTC protein levels were 67% lower ($P < 0.001$). Therefore, as siRNA treatment for 72 hours produced the most efficient knockdown which can be attributued solely to delivery of siRNA and not the vector, this timepoint was chosen for future experiments.
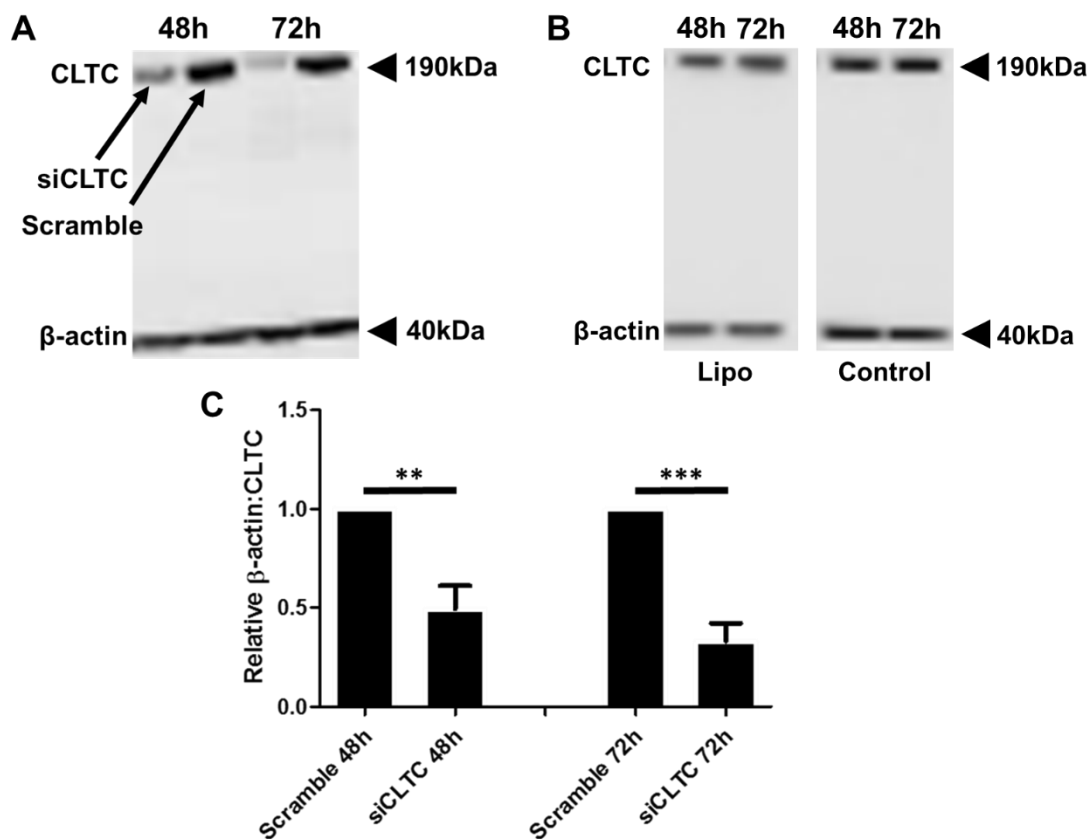
Figure 5.24. Knockdown of *CLTC* using RNA interference. (A) A549 cells were transfected with siRNA against *CLTC* or a scramble oligonucleotide sequence using Lipofectamine (Lipo) and expression of CLTC protein was measured after 48 and 72 hours. The loading control β-actin is shown for reference. (B) CLTC protein expression in A549 cells exposed to Lipo alone (not containing any oligonucleotide) as well as untreated cells. (C) Quantification of siRNA knockdown of *CLTC* at 48 or 72 hours post transfection. Data are expressed as mean ± SEM, $n = 3$, **, $P < 0.01$; ***, $P < 0.001$.

Following this, untreated A549 cells (control), cells treated with the scramble siRNA sequence (scramble) and siCLTC treated cells (generated as described above) were exposed to fluorescent NPs and uptake was once more evaluated by confocal microscopy. In agreement with the previous experiments (Figure 5.25), untreated cells displayed evidence of many punctate clusters of NPs in most cells, denoting avid uptake of NPs.
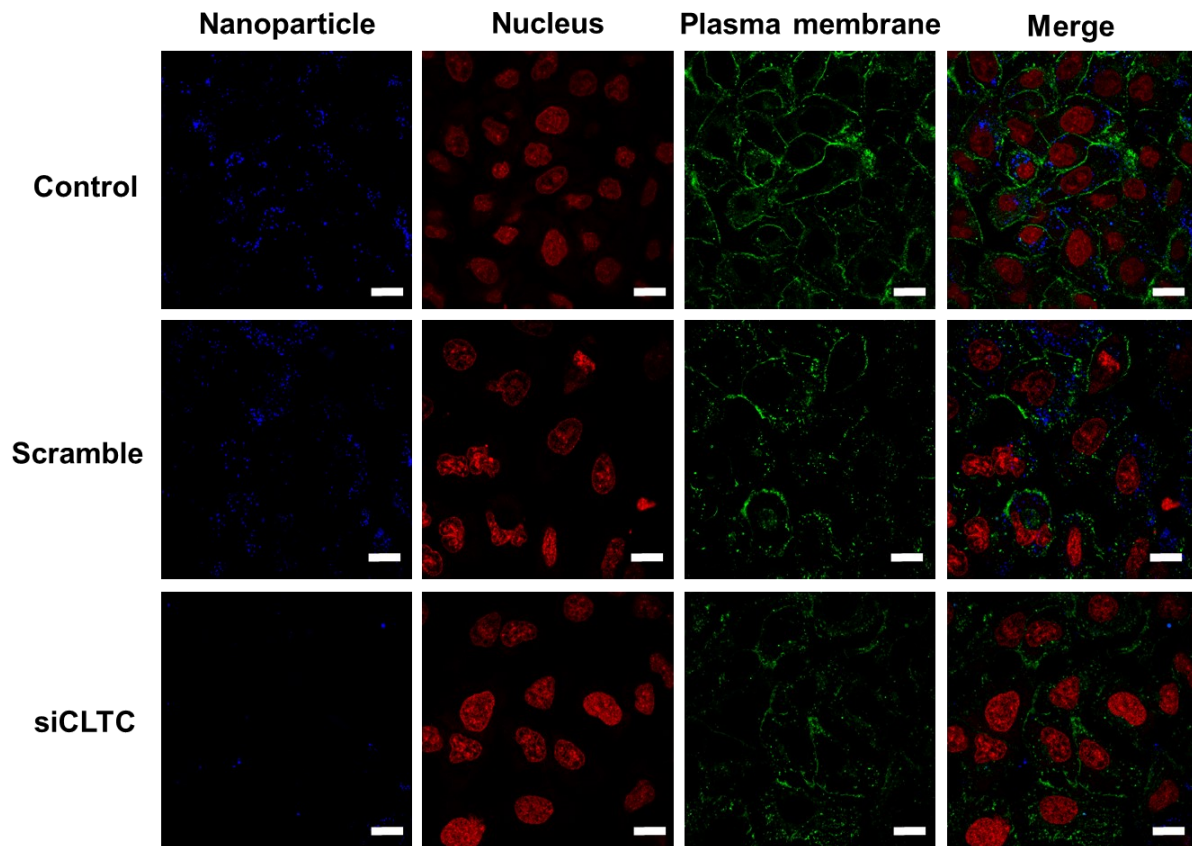
Figure 5.25. Effect of knockdown of *CLTC* on uptake of NPs. A549 cells previously transfected with siRNA against the heavy chain of clathrin (siCLTC), a scramble sequence (scramble) or untreated cells (control) were exposed to fluorescent NPs for 3 hours and imaged using confocal microscopy. NPs are blue, nucleus is red and the plasma membrane is green. Scale bar = 15 μm.

Similarly to control cells, scramble treated cells did not appear to display signs of reduced NP uptake as NP clusters were also present within the several cells. This suggests that treatment with Lipofectamine does not negatively impact the ability of cells to endocytose other types of NPs and reinforces that the scramble sequence did not have any unintended off-target effects

on endocytic machinery. Knockdown of CLTC was observed to significantly impact uptake of NPs, in line with inhibition of clathrin-mediated endocytosis by pharmacological agents. There were substantially fewer clusters of NPs visible in siCLTC cells when compared with control cells, implying that a majority of NPs could not be effectively endocytosed. Quantification of NP uptake (Figure 5.26) revealed that knockdown of CLTC attenuated NP internalisation by 62% compared to control ($P < 0.001$) whereas delivery of scramble siRNA did not result in signficantly less NP uptake. Taken together, these results lend credence to the notion that clathrin-mediated endocytosis is the primary method of NP entry into cancer cells, however other mechanisms of endocytosis cannot be completely discounted.
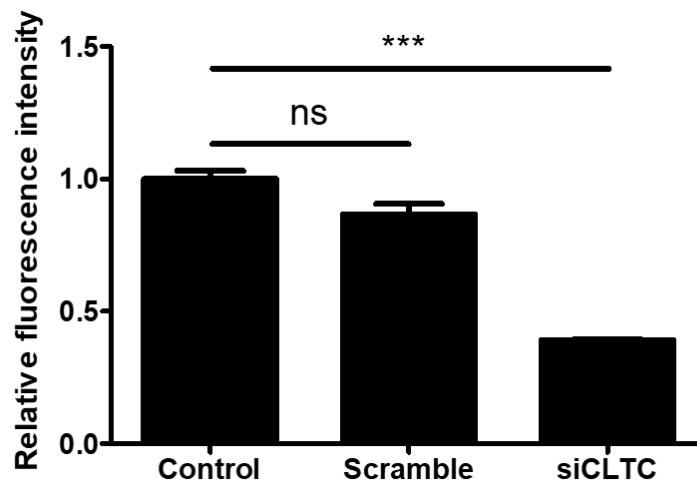
Figure 5.26. Quantification of NP uptake after *CLTC* knockdown. A549 cells transfected trasfected with siRNA against the heavy chain of clathrin (siCLTC), a scramble sequence (scramble) or untreated cells (control) were exposed to fluorescent NPs for 3 hours and NP uptake was visualised by confocal microscopy. Uptake (as fluorescence) was quantified relative to the untreated cells. Data are expressed as mean ± SEM, $n = 3$, ***, $P < 0.001$; ns, not significant.

5.4. Discussion

The work presented in this chapter demonstrates the cytotoxicity of polymeric NP formulations of chemotherapy, namely VRL-NPs and Dual-NPs, as well as providing insight into the mechanism of NP-mediated cell death, inflammatory cytokine release profile and uptake into cancer cells. The initial set of studies began by confirming that modification of afatinib to the its analogue Afb-B did not detrimentally effect its ability to act as a TKI (Figure 5.2 and 5.3). Encouragingly, Afb-B was able to prevent phosphorylation of EGFR in a dose dependant fashion and comparably to that of native afatinib, as determined by Western blot. This result furrher affirms the claims made in Chapter 4 whereby structural modification of the dimethylamino group did not appear to affect biological activity, which was also the case for Afb-B. The dimethylamino group was replaced by a propargylic alkyne in order to facilitate click chemisty to the NP surface, however the basicity of the nitrogen was maintained so that the afatinib derivative could still participate in the Michael addition with cysteine 797 in the ATP binding pocket of EGFR, thus preventing its phosphorylation (discussed in more detail in Chapter 3). Further confirmation of this finding could be obtained by investigating the differential phosophorylation of other tyrosine residues in EGFR apart from Y1068, including Y1148 and Y1173.

After confirming that the afatinib derivative did not lose TKI efficacy when compared with afatinib, the next set of experiments were designed to assess the cytotoxicity of free drugs (VRL, afatinib and Afb-B) and NP formulations of these drugs, using the NSCLC cell lines A549 and H226. Similarly to the investigations performed in the previous chapter, the MTT assay was utilised to determine the cytotoxicity of the aforementioned chemotherapy. VRL was decidedly more cytotoxic than afatinib, an observation that was consistent across NSCLC cell lines (Figure 5.4). This was an expected result given the promiscuous mechanism of action of VRL contrasted with the more conservative mechanism of action of afatinib. This difference

is biologically predicated as all nucleated cells contain the microtubular machinery that serve as the target for VRL; that target being the vinca binding domain of β-tubulin[443]. However most cells do not actively overexpress EGFR, including A549 and H226 cells, which is the target of afatinib. Moreover, cancer cells may not be dependant on EGFR for survival which serves to explain this cytotoxic discrepancy. Interestingly, when afatinib and Afb-B are directly compared in a dose response fashion (Figure 5.5), the cytotoxicity profile appears to be very similar in that a dose dependant decrease in cytotoxicity was observed for both TKIs and at the very highest doses, Afb-B was more cytotoxic than afatinib (in H226 cells). These observations affirm the earlier EGFR phosphorylation studies and suggest that in a biological system, the structural difference of Afb-B compared with that of afatinib did not hamper its activity.

These studies were then extended to investigate the comparative cytotoxicity of VRL and VRL-NPs (Figure 5.6) using A549 and H226 cells for consistency. In A549 cells, and to a greater extent in H226 cells, VRL-NPs were more cytotoxic, evidenced by dose dependant decreases in cell viabilty, especially at lower doses, and a reduced IC_{50} compared to that of VRL. Moreover, this increase in cytoxicity can not be attributed to the vehicle of VRL transport (i.e. the polymeric NP), as in both cells lines, blank NPs of equal concentration to that used when cells were treated with VRL-NPs, were not found to induce significant loss of cell viabilty. When PLGA NPs are degraded due to hydrolysis of the ester bonds, the result is generation of harmless byproducts lactic acid and glycolic acid, which are consequently excreted *in vivo*[452]. Build up of these byproducts *in vitro* due to NP degradation still did not adversly effect cancer cells. The increased cytotoxicity witnessed upon treatment with VRL-NPs could instead be a result of higher intracellular VRL concentrations, as free VRL may be effluxed from the cell by several mechanisms. Intracellular VRL concentrations have been shown the be depleted as a result of ATP-binding cassette sub-family B member 1 (ABCB1, commonly referred to as multidrug resistance 1 or P-glycoprotein) mediated efflux[453] as well as transporters such as

ABC subfamily C member 10 (also known as multidrug resistance-associated protein 7)[454] and the non-ABC binding drug transporter RLIP76[455]. As a consequence of gradual NP uptake and degradation, VRL intracelluar concentrations over time may remain higher than if free drug is adminstered, whereby more is initially available for cell entry but also for efflux or inactivation. This explanation could also account for the increased cytotoxicity observed in PC-9 cells (Figure 5.7) when they were treated with NP formulations, particularly at doses lower than 1 µM. When PC-9 cells were treated with Dual-NPs, they were more cytotoxic than equivalent concentrations of VRL-NPs, significantly so at 1, 0.1 and 0.01 µM (VRL concentration of the formulation). This could be attributed to the conugated Afb analogue to the surface of Dual-NPs, to which PC-9 cells are predicted to be vulnerable, due to the sensitising mutation these cells harbour which was outlined in the previous chapter. As with A549 and H226 cells, blank NPs were demonstrated to be biocompatible and thus did not contribute to the cytotoxicty of NP formulations observed in PC-9 cells. Interestingly, blank NPs that subsequently went through the same "click reaction" procedure as Dual-NPs but did not contain VRL (Afb only NPs) also did not have a negative effect on PC-9 cell viabilty. This was a surprising observation given the sensitivity of PC-9 cells to TKIs. A potential explanation for this result is that there was insufficient conjugation of the Afb analogue to the NPs, perhaps due to lack of available azides that may have been buried within the polymer matrix instead of presented on the surface[310]. Indeed, the concentration of Afb-B is expected to be several orders of magnitude lower than that of VRL and therefore may not be able to exert a therapeutic effect at very low doses. Somewhat contrastingly, increased cytotoxicity when both entites are combined suggests an element of additive therapeutic efficacy. This concept was explored with further cytotoxicity studies (Figure 5.8) whereby all three cell lines were exposed to a fixed dose of VRL-NPs or Dual-NPs (at the same VRL concentration) and blank NPs (the same NP concentration as drug-containing formulations) for varying periods of time, after which the

NPs were removed so that the observed effects were due to NPs that were either attached to the cell membrane or have been internalised, thus the effect of drug release into the culture medium was minimalised and the mechanism of action of NPs as drug delivery vehicles was maximised. Strikingly, PC-9 cell viabilty was essentially abrogated when treated with Dual-NPs as opposed to VRL-NPs, with this observation present but less pronounced in the other cell lines. The general trend across cell lines, that increased incubation time with NPs resulted in increased cytoxicity is consistent with the idea that intracellular NP concentrations (and therfore drug) increases over time[456], however the explanation as to why there are not large discrepancies between time points could be that a signficant proportion of NPs are taken up by a limited number of cells, acting almost as an NP sponge. Then gradually over time more NPs are taken up by remaining viable cells, which subsequently lose their viability due to intracellular release of drug.

Studies on actively proliferating cells corroborated the findings from experiments performed on confluent monolayers. VRL was demonstrably a more potent inhibitor of cell proliferation than afatinib in both A549 and H226 cells (Figure 5.9). Similarly to the explanation proffered for the observations recorded in confluent monolayers, the more promiscuous nature of VRL with respect to its anti-proliferative capacity suggests that in actively proliferating systems that require fully functional microtubules, VRL will outperform agents that target specific (and in this case not overexpressed) receptors that are not lethal to cells if such receptors are rendered inactive. It was also witnessed that VRL-NPs were able to inhibit cell proliferation to a greater extent than equivalent free VRL in both A549 and H226 cells (Figure 5.10). The gradual and prolonged intracellular accumulation of VRL delivered *via* NPs could be the determining factor driving the differences between formulations, which was also hypothesised for the confluent monolayer studies. The effect of NP degradation and release of VRL into the culture medium cannot be fully evaluated in this system but is expected to have contributed to the anti-

proliferative efficacy of VRL-NPs. The biocompatibilty of polymeric NPs as a delivery vehicle was further evidenced using ECIS as no concentration of NP was found to negatively affect proliferation of A549 cells or alveolar epithelial-like type 1 (TT1) cells (Figure 5.11), which were used as a model of the healthy alveolar epithelium[360]. Therefore, polymeric NPs and the byproducts of their degradation appear not to detrimentally impact the proliferation of cancerous or non-cancerous cells which is in agreement with the literature usage of these polymeric materials as NP components for drug delivery[457]. As with the cytotoxicity studies, Dual-NPs were also potent inhibitors of PC-9 cell proliferation, with as little as 3 nM (VRL concentration delivered by Dual-NPs, afatinib concentration at least 10 times less) causing significant antiproliferative effects (Figure 5.12). These observations can also be attributed to the increased sensitivity to TKIs that PC-9 cells possess, although the extremely low dose of afatinib that PC-9 cells are exposed to may lend evidence to the theory that inhibition of EGFR prior to nuclear disruption by chemotherapy may enhance therapeutic efficacy; the temporal nature of this system has been shown to be critical for increased cytotoxicity and apoptosis of some, but not all, cancer cells when using combination TKI and chemotherapy[441]. Dual-NPs were also effective inhibitors of A549 and H226 cell proliferation, much like VRL-NPs as discussed previously and were more potent than corresponding concentrations of free drug (Figure 5.13). The advantages of using ECIS to investigate the cellular response to (chemo)therapy over techniques such as the MTT assay (and tetrazolium reduction assays in general, as well as resazurin based assays) is the dynamic monitoring of changes in cell viability in real time, without the introduction of any reagents or labels that measure a particular biochemical parameter as a surrogate for cell viabilty and thus have limitied interpretability. ECIS relies on a physical parameter (i.e. cell adherence to the well translated to resistance) as a readout for cell viabilty and can monitor cell proliferation and the strength of intracellular junctions. However, ECIS is time consuming, expensive and cannot be used to investigate cells

that do not proliferate or grow in suspension. As the MTT assay is quick, inexpensive and useful for measuring viability of near confluent monolayers in a high throughput fashion, the work in this study utilises the strengths of both techniques to more adriotly examine cytotoxicity of the NP formulations.

Further to this point, to affirm the mechanism of cell death underpinning the previous set of results, flow cytometry analysis was employed. The markers used, cleaved caspase 3 (cC3) and cleaved PARP (cPARP), were used to exclusively distinguish apoptotic events. Cleavage of the central executioner caspase, caspase 3 is a feature of both the intrinsic and extrinisic apoptotic pathways and is therefore considered a hallmark of apoptosis[458]. Moreover, PARP is a substrate for caspase 3[459], therefore co-detection of this cleaved substrate (that is, cleaved PARP) is confirmation that caspase 3 had indeed been cleaved and apoptosis had occurred. When drug-bearing NP formulations were compared in A549 and H226 cells the levels of apoptosis were comparable across time and also signficantly rose at the 48 hour timepoint (Figures 5.14 and 5.15). This pattern is consistent with the kinetics of drug release (VRL) from NPs after internalisation and the subsequent kinetics of apoptosis upon stimulation with a chemotherapeutic agent that induces nuclear processes to induce cell death[460]. Indeed, the temporal facets of apoptosis are likely to be different depending on the stimulus and cell type; this pattern of apoptosis has been previously reported in A549 cells treated with NP formulations of TKIs and cisplatin. Notably, different combinations of TKI and cisplatin, or indeed of TKI and chemotherapy, as well as the cell line examined, produced markedly different apoptotic responses as measured by cC3/cPARP staining[442]. Treatment of PC-9 cells (Figure 5.16) with Dual-NPs produced a markedly increased apoptotic response compared to VRL-NPs which lends credence to the notion that the sensitivity these cells harbour (in this case inhibition of EGFR) is correlated with an apoptotic response. This also highlights that deprivation of oncogenic signals that cancer cells are reliant on can dramatically influence the

proclivity of that cell to survive. As with the other cell lines, as time progressed the amount of apoptotic cells detected increased, suggesting that some time is required for the apoptotic machinery to assemble in such a fashion that it was detectable in the system used and that prolonged exposure to an apoptotic stimulus (in the form of release of drug from NPs) incites further apoptosis. Cells grown in culture may undergo apoptosis, even in the absence of an extrinsic stimulus, however untreated cells left in the same culture conditions as treated cells but without NPs were found not to undergo apoptosis after 48 hours (data not shown) therefore the culture conditions did not contribute to the observed phenomenon of increased apoptosis over time. The most commonly used markers to detect apoptosis by flow cytometry are Annexin V co-staining with propidium iodide (PI), which can also aid in discerning cells in early apoptosis, late apoptosis or necrotic cells. Annexin V relies on the externalisation of phosphatidylserine residues on the cell membrane whereas incorporation of PI is predicated on loss of the exclusionary capacity of the cell membrane to cationic molecules. Though a verified technique, Annexin V/PI staining has a high false positive rate, requires millimolar concentrations of Ca^{2+} ions and needs additional staining to confirm the integrity of the cell membrane is lost and thus the cell is considered dead[461,462]. In this work, the aim was to exclusively and reliably define the apoptotic population of cells; with respect to tumours, an apoptotic response is more physiologically desirable than a necrotic response. Chemotherapy induced necrosis (or otherwise) of tumour cells is thought to contribute to tumour progression by elicitation of chronic inflammation combined with expulsion of cellular contents that contain metabolites and growth factors necessary for proliferation and angiogenesis, as well as modulation of the tumour microenvironment to support tumour growth[463,464]. As apoptosis is a much more orchestrated approach to cell death, cellular contents cannot be utilised and recycled by opportunistic cancer cells, therefore depriving the tumour of further nutrient sources. This line of reasoning is reflected in the literature as many *in vivo* studies focus on

immunohistochemical analysis of apoptosis (typically cC3) in treated tumours and not necrotic markers. Moreover, in patients, development of a necrotic core within tumours is associated with poor prognosis and more rapid disease progression[465,466]. This supports the notion that tumour cell necrosis, despite eliminating a portion of the tumour burden, can actually promote progression and therefore an apoptotic response is highly preferred from a therapeutic perspective, which was witnessed herein.

Another perspective that must be considered in drug delivery studies is that of toxicity or hallmarks thereof. Indeed, several approved nanomedicines were introduced into the clinic not for improved efficacy but for reduction of dose limiting, or fatal toxicities. As VRL is a known vesicant, it was proposed that encapsulation within polymeric NPs may attenuate its vesicant activity. Proinflammatory cytokine release was used as a surrogate for vesicant activity and using HUVECs as a model of the venous endothelium, somewhat similar repsonses were noted upon exposure to VRL-NPs compared to VRL. The doses examined were designed to encompass a range that is likely to be encountered at the injection site post adminstration and the initial time during the treatment cycle, but without killing the cells. Of the four canonical proinflammatory cytokines analysed, only significant amounts of IL-8 were produced upon treatment with VRL which was slightly unexpected. High doses of VRL have previously been shown to increase IL-8 mRNA levels in HUVECs[467] and physiologically, production of IL-8, which is a chemoattractant for neutrophils, is expected in the presence of an inflammogen such as VRL. This phenomenon may also contribute to the primary dose limiting toxicity of VRL which is neutropenia, as many mature neutrophils come into contact with VRL and further VRL-related mechanisms hinder their production and repopulation. The almost undectable levels of IL-1β can be explained by the fact that HUVECs do not produce IL-1β. IL-6 and TNF-α are cytokines released in the acute-phase inflammatory response, which is the intial cascade of signalling events that takes place after injury or other inflammatory insult. Exposure to VRL

induced very modest levels of release of these acute-phase proinflammatory cytokines suggesting VRL does not trigger an overt acute inflammatory reaction or injury in HUVECs. Indeed, IL-6, IL-8 and TNF-α, amongst other cytokines, are known to be produced by HUVECs in response to varying stimuli[468] and other proinflammatory mediators such as IL-1β[469] and IL-1α[470] but may not actively produce these cytokines in physiologically relevant quantities when treated with chemotherapy. In the circulation, during an acute-phase inflammatory response, typically macrophages and granulocytes such as neutrophils are the principal producers of proinflammatory cytokines[471]. Thus, it is not surprising that upon expsoure to a foreign substance, the cytokine that was found to be produced in the highest quantites by HUVECs, IL-8, is one that potently attracts neutrophils. Physiologically, it could be detrimental if the vascular endothelium as well as immune cells produced vast amounts of proinflammatory cytokines as this could lead to hyperpermeabilisation of the endothelium, vascular damage and a self-amplifying cytokine storm. Indeed, exposure to exogenously produced IL-1β can incite secretion of IL-6, IL-8 and modulate vascular pemeability[472]. Moreover, pulmonary endothelial cells were found to orchestrate both leucocyte recruitment and proinflammatory cytokine production leading to cytokine storm in a mouse model of human influenza virus infection[473], which supports the idea that the endothelium is an active participator in inflammation but not the initiator. A similar pattern of cytokine release was observed when HUVECs were treated with VRL-NPs, however a notable difference was that the amount of IL-8 released was attenuated compared to that released upon VRL exposure (Figure 5.17 and 5.18). This was thought to be due to less VRL exposure when delivered as an NP formulation. Internalisation of NPs by HUVECs has been shown to be partly dependant on NP composition, surface charge and hydrophobic interactions between the cell membrane and charged moities on the NP surface, such as polyelectrolytes[474] and as such the NPs used in this work may not have been avidly internalised, which would limit intracellular VRL exposure. Furthermore, polymeric

NPs are not overtly toxic to HUVECs[475] and therefore would not contribute to release of proinflammatory mediators through a cytotoxic mechanism of action.

Finally, the mechanism of NP uptake in lung cancer cells was examined to see which biological processes governed access to the intracellular compartments. To do this, fluorescent NPs were maunfactured from the same material and in the same manner as Dual-NPs with exclusion of VRL and replacement with the hydrophobic fluorophore coumarin-6. The surface also presented with conjugated afatinib so as to more closely match the finalised NP formulation and uptake kinetics thereof. Using these fluorescent NPs, it was initially determined that entry into cells was primarily achieved through an energy dependant mechanism, as incubation of cells with NPs at 4 °C significantly inhibited their uptake, regardless of the incubation time studied (Figure 5.20 and 5.21). As all forms of endocytosis are dependant on availability of ATP, cooling cells to a very low temperature serves to markedly reduce the synthesis and utilisation of ATP[476] and as a result many cellular processes cease to function. The reduction in fluorescence intensity observed when cells were incubated at 4 °C would therefore point to an endocytic mechanism of entry. However, there was not complete exclusion of NPs at this low temperature which can be attributed to passive diffusion of some NPs across the cell membrane, a process that does not require ATP and can therefore take place in a temperature-independent manner. Indeed, the passive diffusion of NPs across the cell membrane is primarily dictated by their physicochemical properties, namely size and surface charge[477,478], and as NP size is typically characterised as a distribution, it may well be the case that a proportion of fluorescent NPs are of the appropriate size to inflitrate cells passively. Taking the conclusion of these experiments forward, that is, NPs are predominantly internalised by endocytosis, a pharmacological inhibition screen was performed to elucidate which was the dominant endocytic pathway responsible for NP uptake. As such, cells were preincubated with a miscellany of small molecule inhibitors of endocytosis (chlorpromazine, dynasore, genistein,

EIPA and nocodazole) prior to NP exposure. It was observed that in cells which were pretreated with inhibitors of clathrin-mediated endocytosis (chlorpromazine and dynasore), NP uptake was drastically reduced, where pretreatment with an inhibitor of caveolae-mediated endocytosis (genistein) or macropinocytosis (EIPA or nocodazole) only mildly impacted NP uptake (Figure 5.22 and 5.23). These observations would suggest that clathrin-mediated endocytosis (CnME) is the major endocytic pathway involved in uptake of NP used in this study, with other pathways playing a minor role. CnME is typically involved with uptake of NPs between 50-200 nm in size[479]; polyester based NPs with an average size of approximately 150 nm were posited to be internalised by CnME[480]. As the predominant distribution of NPs used in this work fall within that size range, this would imply CnME could have the dominant endocytic role, although other physicochemical properties influence NP uptake[481]. However, this observation should be viewed in light of the caveats associated with studying NP uptake using pharmacological inhibition such as the small molecules used in this study. Compounds such as chlorpromazine, dynasore, EIPA and other endocytic inhibitors are toxic to cells, thus the treatment dose must be measured so as not to cause cytotoxicity but enough to inhibit the desired biological process. After several dose tritrations of the various inhibitors, suitable doses were found that did not appear to cause cytotoxicity and were used for subsequent experiments. Another limitation is that these molecules have promiscous biological activity *in vitro* and exhibit poor specificity for the proposed pathway they inhibit. For example, chlorpromazine may affect the biogenesis of intracellular vesicles and disrupt the formation of lipid structures, interfering with both caveolae-mediated endocytosis (CavME) and macropinocytosis[482]. Dynasore is known to interfere with actin structures[483] and similarly EIPA can reorganise actin filaments and modulate the intracellular distribution of endosomes[484]. These serve as just some examples of the unintended effects of using nonspecific molecules for rapid endocytosis screening. Furthermore, all mechanisms of endocytosis may not be captured using the panel

presented such as micropinocytosis, and other pinocytosis mechanisms such as Rho GTPase-dependant, Arf6 dependant, Flotillin dependant and lipid raft endocytosis[485]. Taken on its merits, a pharmacological screen highlighted that CnME was the predominant pathway involved in NP uptake. The caveats alluded to however permit further confirmatory experimentation which was undertaken by performing RNA interference experiments. The clathrin protein is composed of a light chain (two components A and B) and a heavy chain which cluster together as a trimer of three heavy chains and their associated light chains[486]. To investigate whether loss of clathrin did in fact negatively impact endocytosis of fluorescent NPs, transcription of the *CLTC* gene, which codes for the clathrin heavy chain protein CLTC was inhibited using targeted siRNA, delivered by Lipofectamine (Figure 5.24). It has been shown previously that elimination of the clathrin heavy chain abrogates CnME[487] and therefore reinforced *CLTC* as a valid knockdown target. Confirmation of CTLC knockdown was obtained by Western blot and it was observed that in A549 cells with reduced expression of CLTC, NP uptake was significantly attenuated (Figure 5.25 and 5.26). This was deemed to be due to reduction of CLTC expression as a scrambled oligonucleotide delivered with the same vector at the same concentration did not detrimentally impact NP uptake. Complete loss of NP uptake in cells with reduced CLTC expression was not observed which can be accounted for by the fact that total deletion of CTLC was not (and cannot) be achieved using siRNA, therefore some functional clathrin machinery still remained active in these cells. Furthermore, it is expected that other endocytic pathways such as CavME and macropinocytosis were active and could facilitate uptake of a portion of NPs in CnME deficient cells, as well as internalisation by passive diffusion, conclusions that can be drawn based on evidence from the previous two sets of uptake experiments. Taken together, NPs were internalised by an endocytic process that could primarily be ascribed to CnME, although the roles of CavME, macropinocytosis and other endocytic pathways cannot be discounted. It is also important to note that not only will

the physicochemical properties of NPs affect uptake dynamics, but also the type of cell is reported to influence the uptake pathway, such that the same NP can be endocytosed in different ways depending on the cell[488].

5.5. Conclusion

In summary, polymeric NP formulations loaded with the antimitotic agent VRL and functionalised with an analogue of the TKI afatinib were demonstrably cytotoxic across a range of NSCLC cell lines. This efficacy was retained in an actively proliferating system whereby VRL-NPs and Dual-NPs could credibly inhibit the proliferation of NSCLC cells. The polymeric NP itself (i.e. the vehicle to carry the chemotherapy) was not cytotoxic and did not possess any intrinsic antiproliferative potential. Chemotherapeutic NPs were also found to induce apoptosis in several NSCLC cell lines and attenuated the release of proinflammatory cytokines, primarily IL-8, from venous endothelial cells in comparison to free drug. The mechanism of NP uptake was revealed to be predominantly clathrin mediated, as determined by temperature, pharmacological and RNA interference studies, whilst other pathways of endocytosis played a minor role. Thus, the work presented in this chapter validates polymeric NPs as a suitable delivery vehicle for potent chemotherapy combinations, in line with the findings of many researchers that have previously used polymeric NPs and continue to utilise them for drug delivery and further biomedical applications.

6. *In vivo* evaluation of polymeric nanoparticles as chemotherapy delivery vehicles to lung tumours

This chapter describes the investigation and assessment of polymeric nanoparticles (NPs) carrying dual chemotherapy agents (Dual-NPs) for use as drug delivery carriers *in vivo*. The cytotoxicity profile of Dual-NPs screened in primary human lung cancer cells is described. Following this, appraisal of the efficacy and safety of Dual-NPs in mice harbouring tumours derived from primary human lung cancer cells is given, whereby these metrics are assessed based on tumour characteristics as well as organ and whole-body parameters. The efficacy and biocompatibility of Dual-NPs is discussed with a clinically translational focus, as well as the suitability of the model chosen to assess these criteria and animal models used in the wider literature.

6.1. Introduction

In the "bench-to-bedside" pipeline of translational research, the phases succeeding *in vitro* assessment using cell lines are classified as more physiologically relevant[489]. As such, cells derived from the tumours of patients can be employed as a model from which to further test the efficacy of therapeutics such as nanomedicines. After extensive *in vitro* profiling of Dual-NPs using a number of NSCLC cell lines, use of primary NSCLC cells obtained from surgical resection of the tumour would be progression towards physiological relevance and may act to provide a more informative picture of the efficacy of Dual-NPs. This is because cell lines are a predominantly homogenous population of cells that are only found in small proportions in human tumours and thus do not recapitulate the full heterogeneity of tumours[490]. Moreover, defining the molecular fingerprint of individual tumours is the central tenet to precision oncology, the outcome of which may be the ability to predict therapeutic outcome in clinical trials[491]. In this work, novel patient derived NSCLC cells with a defined mutational status

indicative of lung adenocarcinoma were initially utilised for *in vitro* and subsequently *in vivo* assessment of Dual-NPs. A protocol has been established whereby these primary cancer cells can be passaged in cell culture conditions which involves growing the cancer cells on feeder layers of mitotically inactivated mouse embryonic fibroblasts (MEFs) using a defined epithelial growth medium[282,492]. This facilitates *in vitro* screening and allows for generation of enough cells for *in vivo* engraftment. Interestingly, these primary cancer cells harbour, amongst other mutations, the canonical KRAS missense mutation at codon 12 whereby glycine is substituted with an aspartic acid (G12D) within switch I of KRAS. This interferes with binding of RAS effector proteins such as GTPase activating proteins and guanine nucleotide exchange factors which mediate the GTP-bound, active status of KRAS that culminates in activation of downstream tumourigenic signalling pathways[493]. Mutations in KRAS are notoriously difficult to target with any small molecule therapies[494] and the G12D variant has been clinically implicated with increased therapeutic resistance to EGFR inhibitors[495]. However, a recent study has revealed contrasting findings that demonstrate EFGR inhibitors, or more specifically the pan-ERBB inhibitor afatinib restrains KRAS driven lung tumourigenesis in cell line and patient derived xenograft models[496]. As Dual-NPs carry an afatinib analogue on their surface, this may provide a physiologically relevant target in primary cells that otherwise lack a targetable mutation. Following this reasoning, broad spectrum antimitotic agents such as VRL that do not require specific mutations for optimal efficacy may be well suited for treatment of proliferating tumours without targetable mutations.

The primary focus of this work was the *in vivo* evaluation of Dual-NPs using a patient derived xenograft model. The combination of VRL, specifically a hydrophobic ion paired NP formulation, and afatinib has not been investigated in a patient derived xenograft (PDX) model and thus represents a novel direction of anticancer therapeutic interrogation. Indeed, the caveats of using mouse models to study NP delivery to tumours such as tumour hypervascularisation,

insufficient recapitulation of the human tumour microenvironment and the lack of an immune system has been extensively outlined[497-500] and will be the subject of further discussion in Chapter 7. Nonetheless, transition from *in vitro* studies to *in vivo* studies is ultimately more informative by virtue of ascending the physiological relevance hierarchy. Moreover, *in vivo* assessment of nanomedicines is a prerequisite for entrance into clinical trials, and as a direct result of *in vivo* evaluation, polymeric NP therapies have reached this stage of the translational pipeline. Most notably, BIND-014, which is PLGA-PEG NP formulation carrying docetaxel also decorated with an aptamer for targeting overexpressed proteins, reached phase I clinical trials and was investigated in patients with advanced or metastatic solid tumours[255] or late stage NSCLC with defined mutational status in a phase II clinical trial[256]. CRLX101 is another polymeric NP composed of the topoisomerase I inhibitor campthothecin, β-cyclodextrin and PEG which was assessed in a phase IIa clinical trial as a therapy for patients with solid malignancies (including NSCLC)[258]. Unfortunately, these encouraging examples are rare and progression from clinical trials is almost unheard of, exemplified by the paucity of approved nanomedicines for lung cancer treatment, which stands at two, Abraxane and Genexol[274]. Clinical trials critically act as a bottleneck for translational progress, and one of the reasons that so few nanomedicines are approved for human use is that the preclinical models used to test them have physiological features not consistent with that of humans.

Despite these physiological inconsistencies, xenograft models, particularly patient derived ones, are still essential for studying nanoparticle-biological interactions and can give an insight into the therapeutic efficacy of a prospective anticancer nanotherapy. With these considerations in mind, the *in vitro* cytotoxicity of Dual-NPs was determined using primary NSCLC cells prior to efficacy and safety assessment of Dual-NPs using a novel, physiologically relevant PDX model of NSCLC. Therapeutic efficacy was evaluated by measurement of the tumour diameters over time as well as endpoint measurements of tumour volume and tumour weight.

To determine the safety of the nanomedicines, which is an important consideration within the translational research pipeline, the body weight of each mouse was monitored at regular intervals and upon termination of the study, the major organs were excised and examined histologically for tissue damage. Collectively, these parameters sought to provide a depiction of the therapeutic potential of Dual-NPs, building on preceding *in vitro* exploration, taking into account both the antitumour effect of the nanomedicine and its biocompatibility *in vivo*. Indeed, it is the balance between tumour cytotoxicity and safety that truly determines the clinical progression of not only nanomedicines, but any therapeutic intervention. The hypothesis of this chapter is that Dual-NPs are cytotoxic in patient-derived lung cancer cells and xenograft mouse models thereof, as well as demonstrable biocompatibility upon repeat dosing.

6.2. Aims

- Profile the cytotoxicity of Dual-NPs in a patient derived lung cancer cell line.
- Determine the efficacy of Dual-NPs in a xenograft model of lung cancer derived from primary human lung tumour cells.
- Assess safety and biocompatibility of the NP formulation in the aforementioned animal model.

6.3. Results

6.3.1. *Cytotoxicity of Dual-NPs in primary human lung cancer cells*

In the previous chapter, it was established that Dual-NPs were cytotoxic to NSCLC cell lines, as assessed by MTT assay amongst other techniques. As these cells do not recapitulate the true nature of human lung tumours, the effect of Dual-NPs on cells that originate from a patient who underwent surgical resection for NSCLC was investigated, as a more physiologically relevant model. Dual-NPs were compared to free VRL in a dose response fashion in order to better gauge efficacy. As blank NPs were shown not to be cytotoxic in the previous chapter, they were excluded from this portion of the study. The cytotoxicity of equal concentrations of Dual-NPs and free VRL was determined using the MTT assay as shown in Figure 6.1A. A dose range of 0.003-1 µM was used as in the previous studies. Results demonstrated that increasing doses of both free VRL and Dual-NPs induced greater decreases in viability, however the extent to which the formulations decreased cell viability differed. Looking from a dose comparison perspective, Dual-NPs were consistently more cytotoxic than the equivalent dose of VRL. For example, after treatment with 1 µM, 59% of cells remained viable, whereas after treatment with the equivalent dose of Dual-NPs only 35% of the cells were viable, translating to a 24% increase in cytotoxicity when Dual-NPs were used. For example, after treatment with 1 µM 41% of the cells were non-viable, whereas after treatment with the equivalent dose of dual-NPs saw this population rise to 65%, corresponding to an 85% increase in the cell death rate. Even at lower doses this differential cytotoxicity was maintained. After incubation with a VRL dose of 0.01 µM, there was 28% cytotoxicity which increased to 49% after Dual-NP treatment. Despite these demonstrable differences, statistical significance was not witnessed within each dose due to inter-experiment variation, which is a common issue encountered when using primary cells of human origin. However, comparing the dose response curves (Figure 6.1B) of free VRL and Dual-NPs revealed a statistically significant difference between them

(P = 0.0025). This reinforces the observation that there is higher cytotoxicity (or lower cell viability) when cells are treated with Dual-NPs. Interestingly, the calculated IC_{50} for Dual-NPs in these primary cancer cells was 0.35 µM whereas the IC_{50} for free VRL could not be calculated as no dose of VRL studied caused cell viability to fall below 50%, therefore it can be assumed that the IC_{50} for free VRL is in excess of 1 µM in these primary cancer cells, based on the data acquired.
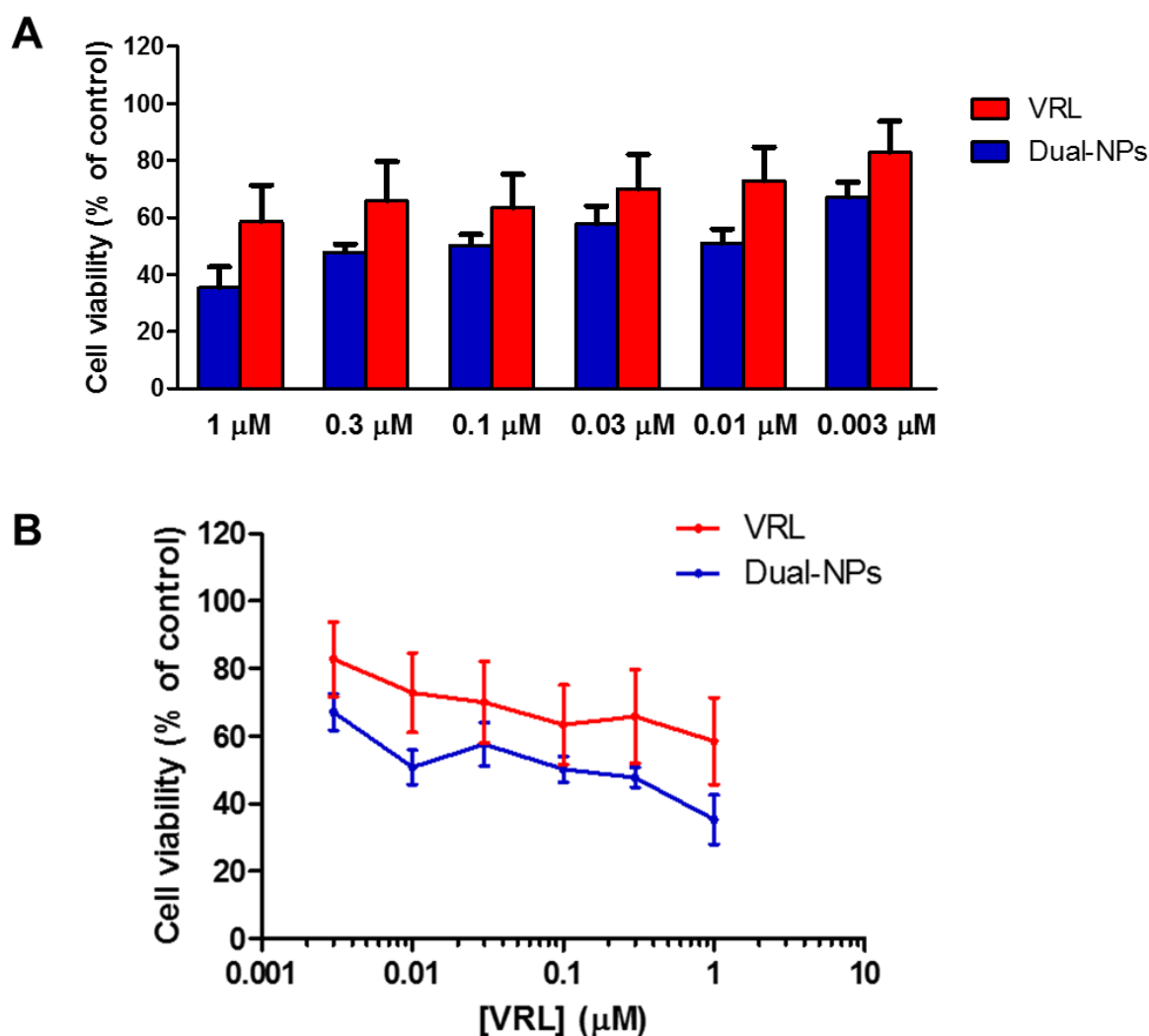
Figure 6.1 Comparative cytotoxicity of VRL and Dual-NPs in primary human lung cancer cells. Confluent monolayers of patient-derived lung adenocarcinoma cells were treated with serial dilution doses of free VRL (1-0.003 µM) and equivalent doses (with respect to VRL) of Dual-NPs for 72 hours after which time cell viability was assessed by MTT assay. (A) Dose comparison between free VRL and Dual-NPs. (B) Dose response curves of free VRL and Dual-NPs. Data are expressed as mean ± SEM, n = 5 and were analysed by two-way ANOVA with Bonferroni post tests for multiple comparisons.

6.3.2. *Assessment of in vivo safety and efficacy of nanodrug formulations – study design*

After extensive *in vitro* assessment of NP formulations of chemotherapy in traditional NSCLC cell lines and primary NSCLC cells, an *in vivo* study was designed in order to assess the efficacy of NPs in a more physiologically relevant system. The model involved subcutaneous implantation of primary human NSCLC cells to form xenograft tumours. Figure 6.2 represents the study design, outlining the study duration, treatment groups, dosing schedule and study endpoints. Further information regarding the *in vivo* studies can be found in the Materials and Methods chapter (Chapter 2, section 2.23).
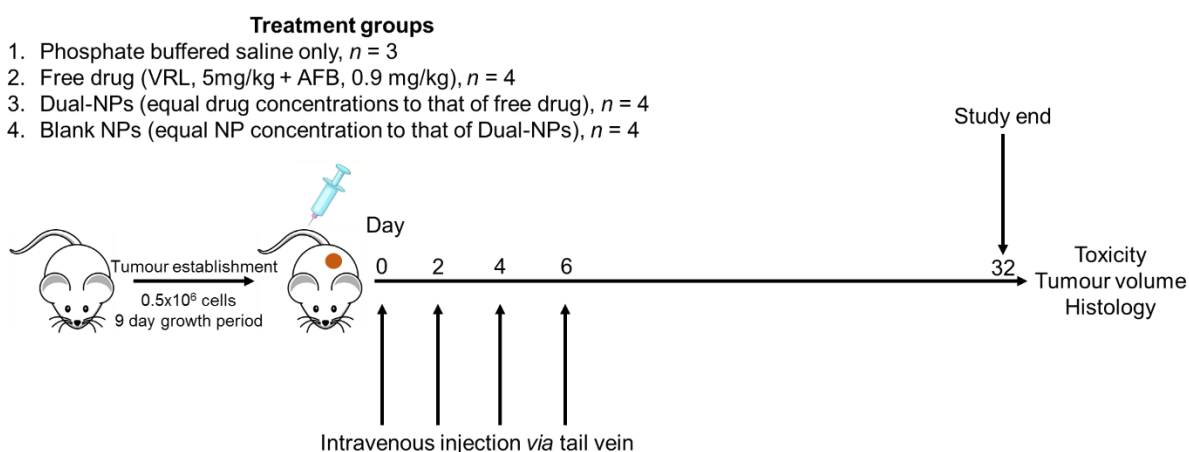
Figure 6.2. Design of *in vivo* study to assess NP safety and efficacy of Dual-NPs. Post tumour establishment (with inoculation of 0.5×10^6 cells and 9 day growth period), 4 doses of treatment were given to tumour bearing mice at the times indicated. 32 days from day 0, the study was terminated, mice sacrificed and criteria assessing safety and efficacy were evaluated.

6.3.3. *Assessment of in vivo efficacy of nanodrug formulations – tumour volume*

The principal parameter that is assessed in order to determine the efficacy of a formulation in mouse xenograft models, regardless of formulation (i.e. small molecule, NP, nucleic acid therapy etc.) is reduction in tumour volume. The tumours are monitored at regular intervals throughout the study duration and the dimensions (length, width, height) of palpable tumours are measured using callipers. At the culmination of the study, the tumours are excised, and the final set of dimension measurements are made. Disappointingly, we did not see any significant differences between the average tumour volume of treated mice (free drug, Dual-NPs or blank

NPs) compared to that of untreated mice (Figure 6.3A). The initial calculations for tumour volume were computed using the formula L x W x H (L = length, W = width, H = height of the tumour). Using these parameters, the mean tumour volume ($\pm$ SEM) for untreated mice was 629.3 ± 117.7 mm^3 whereas for free drug it was 422.6 ± 100.0 mm^3, for Dual-NPs 598.2 ± 176.6 mm^3 and blank NPs 444.5 ± 104.7 mm^3. Therefore, despite not achieving statistical significance due to large intra-group tumour volume variation, all treated groups had a mean tumour volume smaller than that of untreated mice. As expected, tumour bearing mice treated with free drug exhibited some decrease in tumour volume. Unexpectedly however, Dual-NPs treated mice did not exhibit a significant loss in tumour volume when compared to untreated controls. Even more surprisingly, blank NPs appeared to be more effective than Dual-NPs and were almost as effective as free drug. Using the volume calculations and average tumour volume for each group, free drug reduced tumour volume by 206.7 mm^3, blank NPs by 184.8 mm^3 and Dual-NPs only by 31.1 mm^3.

As tumours tend to be more spherical in shape, it was considered that the aforementioned volume formula may not be the most appropriate or most accurate for determining tumour volume. Indeed, there are two other formulae used in the literature that take the sphericity of a tumour into account. The first of these is (L x W^2) x 0.5; importantly, when the volumes are recalculated using this formula, there are numerical differences. The mean tumour volume for the untreated group was 432.0 ± 104.5 mm^3, for the free drug group 268.2 ± 76.7 mm^3, for Dual-NPs 454.7 ± 143.2 mm^3 and 359.5 ± 77.0 mm^3 for the blank NP group. Figure 6.3B shows a visual representation of these data and, as expected, the overarching result does not change in that there are still no statistically significant differences between untreated and treated groups. However, the calculated volume does change which may have implications for the experimental design and overall results of the study (see Discussion). Further to this point, the volumes were again recalculated using another commonly cited formula, (L x W x H) x (π/6).

The mean tumour volumes were again substantially different from those calculated with the previous two formulae. The untreated group mean tumour volume was 329.5 ± 61.6 mm^3, for the free drug group 209.7 ± 50.1 mm^3, for the Dual-NPs group 313.2 ± 92.5 mm^3 and for the blank NP group 232.7 ± 54.8 mm^3. A visual representation of these data can be seen in Figure 6.3C, which illustrates that even though the overall result does not change, there are large discrepancies between the average tumour volumes depending on the formula used. These data are summarised in Table 6.1.
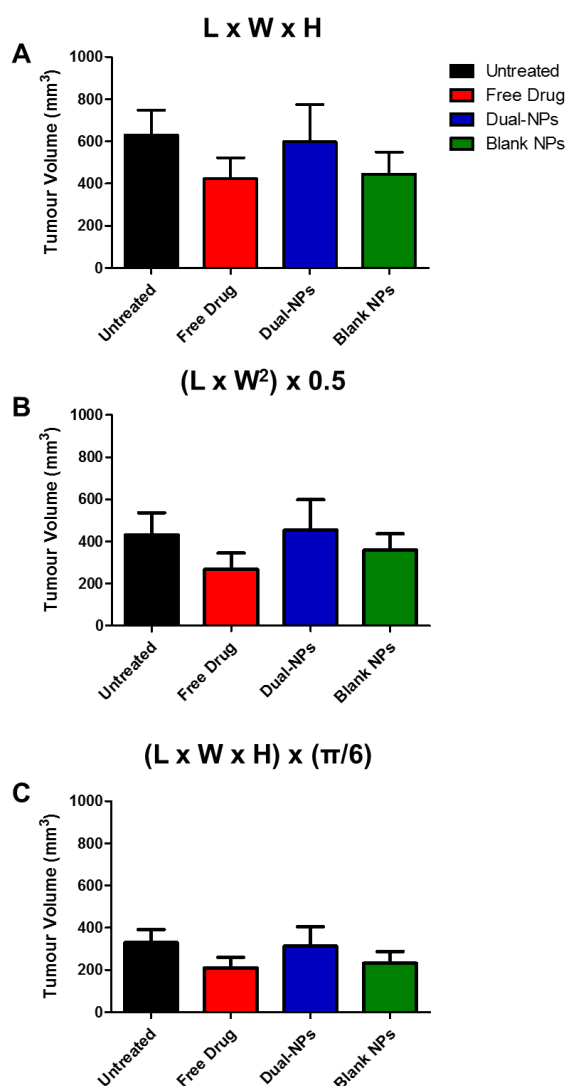
Figure 6.3. Comparison of tumour volumes and the effect of formula choice on estimation of tumour volume. At the termination of the study, patient derived xenograft tumour-bearing mice were humanely sacrificed and the volumetric dimensions (length – L, width – W and height – H) were ascertained by calliper measurement of excised tumours. Tumour volumes were subsequently calculated by (A) L x W x H, (B) (L x W^2) x 0.5 or (C) (L x W x H) x (π/6) and resulting values were compared. Data are expressed as mean $\pm$ SEM, n = 3-4.

	L x W x H	(L x W^2) x 0.5	(L x W x H) x (π/6)
PBS	629.3 ± 117.7	432.0 ± 104.5	329.5 ± 61.6
Free drug	422.6 ± 100.0	268.2 ± 76.7	209.7 ± 50.1
Dual-NPs	598.2 ± 176.6	454.7 ± 143.2	313.2 ± 92.5
Blank NPs	444.5 ± 104.7	359.5 ± 77.0	232.7 ± 54.8

Table 6.1. Numerical discrepancies in tumour volume estimates based on the use of different formulae. The length (L), width (W) and height (H) of excised tumours were obtained by calliper measurement as described in Figure 6.3. and values were computed by each formula to give a tumour volume (mm^3). Data for each group are presented as mean ± SEM, *n* = 3-4 animals.

6.3.4. *Assessment of in vivo efficacy of nanodrug formulations – tumour weight*

Another metric that can be used to determine therapeutic efficacy is the tumour weight, assuming that smaller tumours ought to be lighter than bigger tumours, this metric can act as a surrogate for efficacy. Assessment of tumour weight (Figure 6.4) revealed that, compared to untreated tumours, free drug-treated mice had the greatest reduction in tumour weight, followed by those treated with blank NPs. Dual-NPs appeared to have, on average, a slightly greater weight than untreated tumours. The average tumour weights were as follows: for untreated, 0.39 ± 0.06 g; for the free drug treated tumours, 0.30 ± 0.08 g; for Dual-NP tumours, 0.41 ± 0.12 g and blank NPs tumours weighed 0.37 ± 0.09 g. This translates to a tumour weight loss of 0.09 g when mice were treated with free drug, 0.02 g upon treatment with blank NPs and none observed when treated with Dual-NPs. As the tumour volume studies alluded to a lack of efficacy, it was expected that tumour weights would show similar patterns, however it was surprising that the mean tumour weight of Dual-NP treated tumours was marginally higher than those of untreated tumours. As with the tumour volume studies, statistical significance was not observed due to intra-group variation, however the general trend is the same, in that treatment of tumours did not significantly impact their size, and therefore volume and weight, and thus had limited therapeutic efficacy.
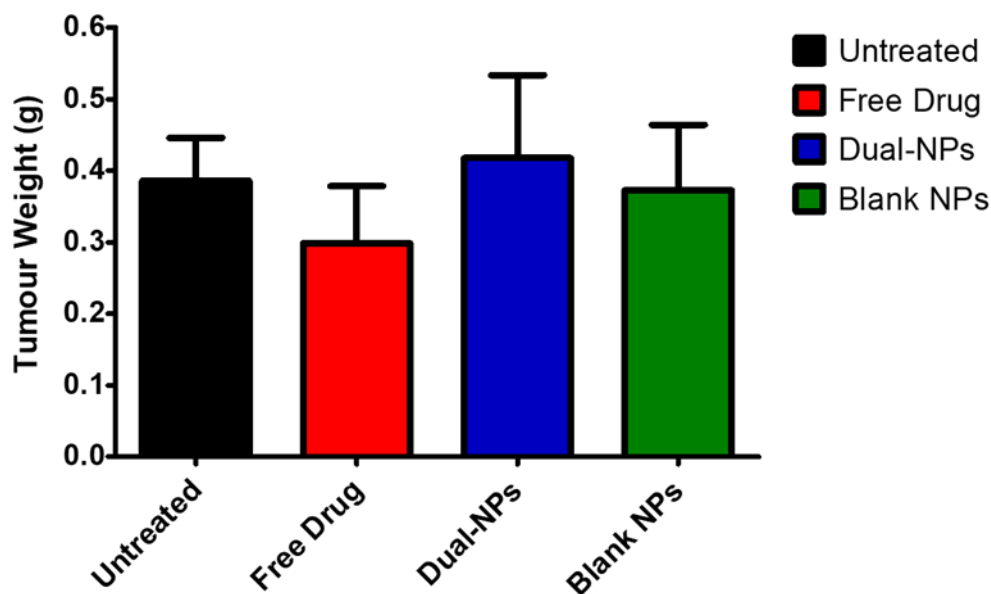
Figure 6.4. Post treatment tumour weight following treatment with free drug, Dual-NPs and blank NPs compared to untreated control. Upon study termination, tumours from each animal were excised, debrided of excess non-tumour tissue and weighed. The mean values of the tumour weight for each group were determined and are shown as a bar graph. Data are expressed as mean ± SEM, n = 3-4.

6.3.5. *Assessment of in vivo efficacy – tumour diameter over time*

A further indication of therapeutic efficacy is tumour diameter measurements made over time *in situ*, as these measurements can be made accurately with callipers despite still growing *in vivo* and do not require any formulaic calculation or assumption. Assuming a spherical shape, tumours with smaller diameters, especially as the study progresses, can be thought of as having a smaller volume and less cellular mass, therefore this metric can act as a surrogate for efficacy.

A total of 8 tumour diameter measurements were taken for each tumour over the course of the study, beginning when the tumours were only just palpable and ending one day before study termination. Figure 6.5 depicts the growth curves for the tumours in each treatment group over time. Commensurate with the other efficacy parameters explored above, measurements of tumour diameter did not reveal any statistically significant differences between any of the groups. A small trend can be observed whereby average tumour diameter measurements were

smallest in the free drug treated group compared to untreated tumours and other treatment groups. For example, the average tumour diameter for free drug treated tumours was 6.85 mm at the culmination of the study, whereas for untreated tumours it was 9.45 mm, Dual-NP treated mice 8.55 mm and blank NP 8.40 mm. This equates to an average tumour diameter reduction of 2.6 mm in free drug treated mice, and only 0.90 mm and 1.05 mm reductions in Dual-NP and blank NP treated mice respectively. Taken together, the data presented thus far suggest that no formulation was particularly efficacious from a therapeutic standpoint. Tumours treated with free drug appeared to be the most susceptible, whereas those treated with Dual-NPs or blank NPs were not overtly distinguishable from untreated tumours with respect to their physical properties (volume, weight, diameter).
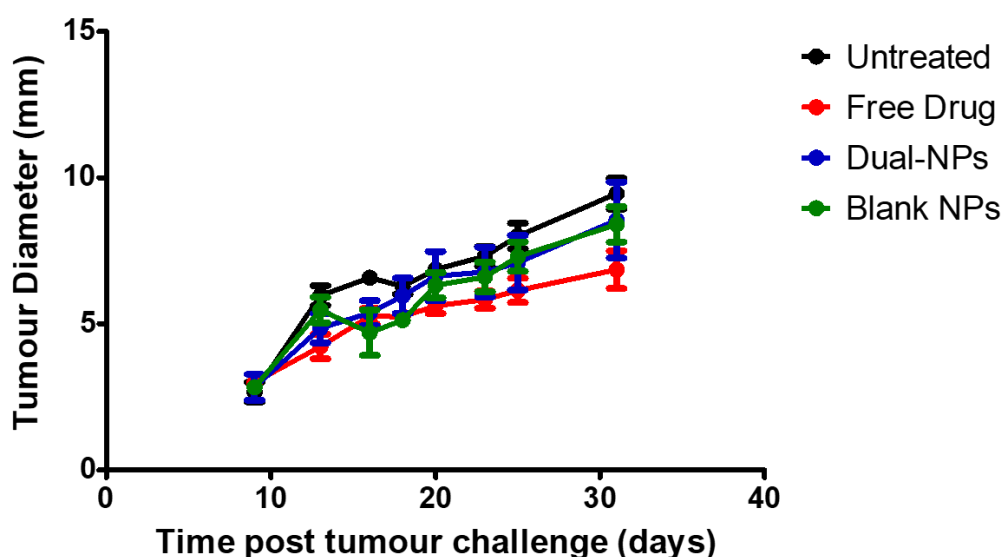
Figure 6.5. Progression of tumour growth over time. Tumour bearing mice were treated with free drug, Dual-NPs and blank NPs intravenously 4 times (Day 9, 11, 13 and 15 post tumour inoculation) after which no more treatment occurred. Once tumours became palpable, tumour diameters were obtained at regular intervals through the study by calliper measurement. Data are expressed as mean ± SEM, n = 3-4.

6.3.6. *Assessment of in vivo safety of nanodrug formulations – mouse body weight*
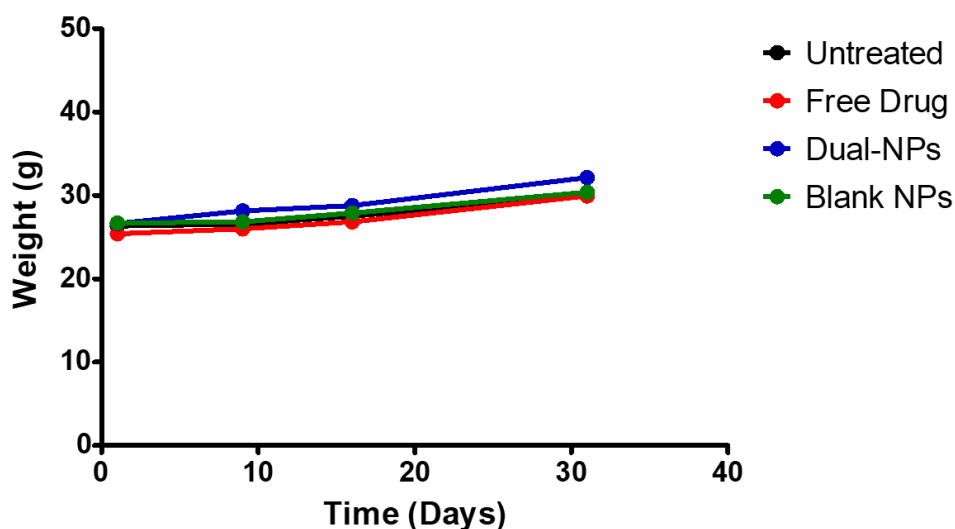
Figure 6.6. Mouse body weight change over time post tumour implantation. At regular intervals throughout the study, mice were weighed using a scale. The body weight changes of each mouse post tumour implantation and intravenous treatment was frequently monitored throughout the study and recorded. Data are expressed as mean $\pm$ SEM, $n = 3$-4.

The safety of any formulation is of paramount importance in terms of cancer therapy and drug delivery. Many therapeutic entities fail in clinical trials due to toxicity and safety concerns. In the context of *in vivo* drug delivery studies, the body weight of the animals is assessed regularly and acts as a marker for quality of life and safety of administered therapy. Reinforcing this notion, the humane intervention point for body weight loss in mice is usually 20% (i.e. if mice lose 20% of their pre-study body weight at any point during the study, they are euthanised). Indeed, this can be brought about by promiscuous cytotoxicity or immunogenicity of an experimental therapeutic formulation. Encouragingly, in this study, no loss in body weight in any mouse was observed at any point during the study (Figure 6.6). It was found that the average body weight of the mice increased slightly over the course of the study. Over the course of 32 days, untreated mice gained 3.83 g of body weight, free drug treated mice gained 4.55 g, Dual-NP treated mice gained 5.50 g and blank NP treated mice gained 3.70 g. This corresponds to a 14.6%, 17.9%, 20.6% and 13.9% increase in body weight for untreated, free drug, Dual-NP and blank NP treated mice respectively. This suggests that the mice tolerated tumour

establishment and growth, as well as the therapies themselves, both in terms of the dosage and formulation, reinforcing the biocompatibility demonstrated in the *in vitro* studies.

6.3.7. *Assessment of in vivo safety of nanodrug formulations – organ histology*

A further critical determinant in the safety profile of a therapeutic formulation is organ toxicity, a phenomenon that is extremely common upon intravenous administration of cytotoxic compounds such as chemotherapy. Indeed, each type of chemotherapy has a proclivity to cause toxicity to certain organs or organ systems, therefore histological analysis of these organs post treatment can give an indication of internal damage induced by these agents or their carriers. Typically, the organs examined in drug delivery studies are the heart, lungs, liver, spleen and kidney and it was the histology of these organs that were inspected in this study. Figure 6.7 shows the histology of the aforementioned organs for each of the groups used in the study. Microscopic examination of these tissue sections revealed that there were no obvious differences between the organs of untreated animals and those treated with any kind of therapeutic intervention, which bodes well from a safe drug delivery formulation perspective. Taking each organ in turn, in the heart there was retention of myofibril and heart striations and no sign of myocardial damage or fracture, when mice were treated with free drug, Dual-NPs or blank NPs suggesting a lack of cardiotoxicity. The lungs of untreated and treated groups displayed no evidence of injury, diffuse alveolar damage, inflammation or fibrosis. There was no evidence of interstitial thickening or pneumocyte hyperplasia and the airways were unobstructed and structurally normal. There were small collections of erythrocytes observed in the Dual-NP and blank-NP treated mouse tissue sections, however these were thought to be due to the method of animal sacrifice used and were not an indication of alveolar haemorrhage, which is uncommon in drug-induced lung injury, especially when the administered anticancer treatments are vinca alkaloids. There was also no indication of hepatotoxicity evidenced by lack of central vein (and general) necrosis, lack of liver degeneration, pigmentation or pigment

deposition. Similarly, there was no hyperplasia or evidence of enzyme induction and inflammation. The spleens of treated and untreated animals also did not exhibit any signs of toxicity, demonstrated by absence of necrosis and fibrosis around the germinal centre, marginal zone and red pulp, or in the parenchyma and subcapsular zone. There was also an absence of erythrocytes, indicating haemorrhage had not occurred. In line with examination of the other organs, nephrotoxicity was not observed histologically in either untreated or treated mice, as glomeruli were intact and there was no evidence of tubular necrosis or cellular degeneration.
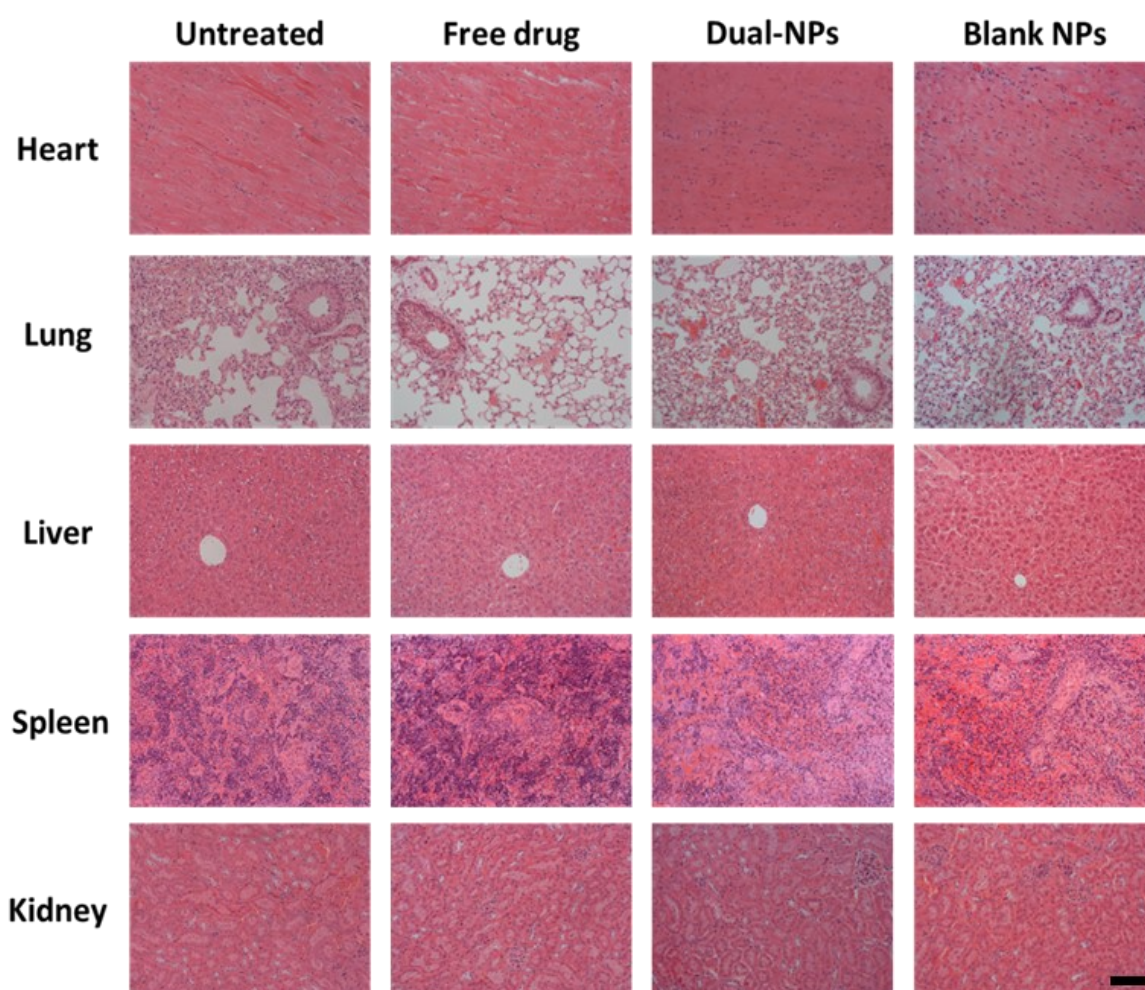
Figure 6.7. Representative histological images of major organs of untreated tumour bearing mice or following treatment with free VRL, Dual-NPs, or blank NPs. To assess any signs of organ damage or toxicity, histological analysis of major organs was performed. At the culmination of the study, major organs (heart, lungs, liver, spleen and kidney) were harvested and fixed in formalin overnight. Following this, samples were embedded in paraffin, dehydrated with varying ethanolic solutions and stained with haematoxylin and eosin. Stained samples were imaged by light microscopy and surveyed for histological signs of damage. Images taken at 20 x magnification. Scale bar = 50 μm

6.4. Discussion

The work presented in this chapter illustrates the potentials and pitfalls of *in vivo* experimentation, whereby the polymeric NP formulation Dual-NP was trialled as a therapeutic agent in a novel model of NSCLC. Continuing the theme from the previous chapter, the *in vitro* cytotoxicity of Dual-NPs (see Chapter 3 for characterisation) was investigated using primary human lung cancer cells and compared with free VRL. These primary cancer cells have a defined mutational status (P53, KRAS^{G12D}, FGFR 1) can be passaged in cell culture a limited number of times using a feeder layer of MEFs and defined epithelial culture medium containing a Rho-associated, coiled coil containing protein kinase (ROCK) inhibitor[492]. If the tumour cells are cultured directly from the lung tumour of the patient, the cells are lost due to competition from non-cancerous epithelium, as a pure population of tumour cells upon resection is extremely difficult to obtain in high enough numbers for culture. However, the mutational status of the cancer cells is maintained once the cells are isolated, form tumours successfully in a mouse and are then cultured as above[282]. Dual-NPs were demonstrated to be significantly more cytotoxic than free VRL when comparing dose response curves ($P = 0.0025$ by two-way ANOVA), which was observed as a trend within individual doses. (Figure 6.1). This was in line with the *in vitro* data presented in the previous chapter even though the potency demonstrated was less than that observed in cancer cell lines (A549, H226 and PC-9). The primary lung cancer cells used in this study harbour more oncogenic mutations than traditional lung cancer cell lines, two of which are classified as "undruggable" and thus may make them more resistant to apoptotic stimuli and prolong survival. Furthermore, the patient from which the tumour cells are derived was not chemotherapy-naïve thus the tumour has already been exposed to chemotherapy which can act as a selection pressure to generate tumour cells that have increased resistance mechanisms (genetic/epigenetic/metabolic alterations)[136]. Another consideration is that the cytotoxicity was only profiled using one technique, the MTT assay,

and further exploration of cytotoxicity by assessing parameters such as apoptosis/necrosis measurements will help to unveil a more precise picture of Dual-NPs cytotoxicity using primary human lung cancer cells.

In order to evaluate the efficacy and safety of Dual-NPs in a more physiologically relevant system, an *in vivo* study was designed. The patient derived xenograft (PDX) model was generated by implantation of primary human lung cancer cells subcutaneously into nucleotide-binding oligomerisation domain (NOD).Cg-*Prkdc^{scid}IL2rg^{tm1Wjl}*/SzJ (NSG) mice. After a short growth period the mice were subjected to an intravenous injection *via* the tail vein of either Dual-NPs, the equivalent dose of blank NPs or the equivalent dose of free drug (5 mg/kg VRL + 0.9 mg/kg AFB), followed by an injection every other day until a total of four injections were administered. The study ran for a period of 32 days after which the mice were sacrificed, and analysis could be performed (Figure 6.2). Judging from the parameters used to evaluate therapeutic efficacy in this study (endpoint tumour volume, endpoint tumour weight and tumour diameter over time), Dual-NPs were not effective anticancer agents. In this work, Dual-NPs were unable to reduce tumour volume or tumour weight, which was an unexpected finding. Administration of free drug was only able to induce small physical changes in the tumour and blank NPs also did not have a potent effect; the latter observations were anticipated and thus not entirely surprising. These results may be explained using several lines of reasoning. It could be concluded that Dual-NPs were merely ineffectual chemotherapeutic agents assuming that they managed to accumulate in the tumour and release drug over time. Indeed, as mentioned previously, this particular PDX model was generated from cells that were formerly exposed to chemotherapy, which may make the resulting tumour intrinsically more chemoresistant, therefore the dose of drug delivered in this study may not have been therapeutic even if a significant proportion of NP (or drug) arrived at the tumour site. Furthermore, it is possible that the NPs experienced significant degradation due to breakdown of the ester bonds that form the

polymer matrix of the NP, either in the circulation or organs, prior to arriving at the tumour site, which would dramatically decrease the intratumoral drug concentration. Although possible, this seems unlikely given the results *in vitro* presented in the previous chapter and the beginning of this one, therefore a more plausible explanation could be that the NPs did not accumulate in the tumour. To fully establish the xenograft model, a growth period is required after initial injection of tumour cells. In our study, a 9 day growth period was allowed after injection of half a million tumour cells which may have been too little time, both in terms of the growth period and also the amount of cells injected. In many *in vivo* studies, upwards of one million cells are initially injected and this can even reach 5 million cells[501]. Moreover, as PDX models are more difficult to establish than cell line generated xenograft models, because the conditions required for primary cells to proliferate are more stringent than for cell lines, it is more successful when small fragments of tumour are implanted into mice as opposed to solutions of suspended cells[502]. The sum total of cells that comprised these fragments likely number in the tens of millions. Therefore, injection of less than one million primary cells as described here may not be optimal for establishment of human lung cancer xenograft tumours. Predominantly in drug delivery studies, the parameter to begin the study is when tumour volume reaches 100 mm^3 and not "day" growth period. The reason for this number is that tumours have grown such that accurate calliper measurements can be obtained for future volume calculations and that tumours of this volume likely have developed a microenvironment within their host with established vasculature and nutrient supply. If the NP drug delivery strategy is predicated on the EPR effect (which a vast majority of NP chemotherapy drug delivery studies are), then rapidly growing tumours with disordered and permeable vasculature is essential, otherwise there is no biological or physiological cue for them to accumulate within the tumour[503,504], thus therapeutic efficacy is drastically reduced. Indeed, due to the paucity of cells initially injected and the alacrity with which the study was

commenced, this may explain why Dual-NPs seemingly had no therapeutic effect. To reinforce this notion, as shown in Figure 6.3A, tumour volumes were initially calculated using the formula L x W x H; however the spherical nature of the tumour must be taken into account with volume calculations and therefore the volumes were recalculated using the two most commonly used formulae in the literature, $(L \times W^2) \times 0.5$ (Figure 6.3B) or $(L \times W \times H) \times (\pi/6)$ (Figure 6.3C). Using the former formula, it was found the calculated volume was significantly lower than initially calculated; using the latter formulae the same pattern was observed, and even more markedly so. In all cases, application of a new formula decreased tumour volume and also decreased the SEM. Table 6.2 outlines the mean reductions in tumour volume when different formulaic inputs are used to calculate volume. Strikingly, when formula C is used, there is approximately a 50% reduction in calculated tumour volume based on the measurements obtained with callipers. Even though the overall pattern of the data and therefore the result does not change, this highlights the discrepancy between the perceived tumour volume and the actual tumour volume. This is important as tumour volume is sometimes used as a surrogate for how well the tumour is growing. Therefore, overestimating the tumour volume can provide ostensible information that the implantation conditions were appropriate, and the model is functioning such that the experimental questions posed can be thoroughly interrogated.

	MTV (mm³) using Formula A (LxWxH)	% reduction using Formula B (LxW²)x0.5	% reduction using Formula C (LxWxH)x(π/6)	% reduction from Formula B using Formula C
PBS	629.3	31.35	47.64	23.73
Free drug	422.6	36.54	50.38	21.81
Dual-NPs	598.2	23.99	47.64	31.12
Blank NPs	444.5	19.12	47.65	35.27

Table 6.2. Discrepancies in estimated tumour volume based on formula used. Tumour volumes were calculated using three different formulae and the values obtained using formula A are listed. The estimated reduction in tumour volumes (%) calculated for each group are also listed according to the formula used (either formula B or C). Thus, a 50% reduction in estimated tumour volume equates to a tumour volume half of that initially calculated. MTV = mean tumour volume.

Indeed, many untreated tumours in mice achieve tumour volumes in excess of 1500 mm^3, calculated using formula B or C[505], whereas in our study, using formula B or C, untreated tumours were only 329.5 mm^3 on average. This discrepancy suggests that the tumours themselves were not growing in a manner sufficient for NP drug delivery experiments where the EPR effect is a critical component. Further supporting this idea, administration of therapy began in our study when the tumours were barely palpable, after 9 days. Accurate measurements of the tumours are difficult to obtain at this stage, nevertheless diameter and length measurements were taken. If formula C is used to calculate the volume at this point (L = 4 mm, W = 5 mm, H = 3 mm as generous estimates) this gives 31.4 mm^3 and inputting these numbers into formula A gives 60 mm^3, in both cases a substantially lower volume than is traditionally used as a starting point for studies such as these. At this stage of tumour development and in the subsequent days when therapy was administered, it is highly plausible that the tumour had not fully integrated and lacked established vasculature, which is required both for rapid tumour growth and EPR effect-mediated NP delivery. The heterogeneity of the inoculate and injection variation, could affect the reproducibility of tumour growth. which could translate to improper tumour formation. Therefore, upon NP injection, instead of accumulating within the tumour, they accumulate in other regions of the body, most commonly the liver and spleen, or are expelled, which may explain the lack of therapeutic efficacy witnessed with Dual-NPs. Indeed, biodistribution studies using fluorescent NPs would inform as to where the NPs accumulate after intravenous administration. The overarching concept of tumour establishment is even more pronounced in these studies however, as tumours are often 200-600 mm^3 prior to imaging[506,507], ensuring NP accumulation is maximised. A further parameter that could be assessed is to examine markers for blood vessel formation such as CD31, CD34 and friend leukaemia integration 1 transcription factor (Fli-1) over time, by excising tumours at different time points. Tumours are excised at the end of these studies and

staining can also be performed at this time point, however tumours are likely to be at their largest (if untreated) so positive or strong expression of blood vessel formation at this stage may not capture the temporal nature of blood vessel formation at the initiation of the tumour formation and development.

When the tumour weights were assessed (Figure 6.4), these data corroborated with tumour volume in that the weights for Dual-NP treated tumours were very similar to that of untreated tumours, and free drug treated tumours appeared to weigh less. The relationship between tumour volume and tumour weight is well established whereby the greater the tumour volume the heavier the tumour. This relationship is affirmed by the assumption that tumour density approximates to $1mg/mm^3$. Using this metric and based of tumour weights, which are the most accurate endpoint tumour measurements, untreated mean tumour volume would be 390 mm^3, and 300 mm^3, 410 mm^3, and 370 mm^3 for free drug, Dual-NP and blank NP treated tumours respectively. The slight reduction in tumour volume witnessed in the free drug treated mice may stem from the intrinsic, albeit small, accumulation of drug in the tumour that occurs when therapies are administered intravenously. This is because small molecules do not rely on the EPR effect to reach the tumour site, and rather a vascular presence. These values are similar to those calculated using formula B which suggests that the volumes of the tumours were smaller than initially calculated and therefore may not have been growing efficiently *in vivo*. Supporting this notion of a weight-volume relationship, recent NP drug delivery studies that have published both tumour volumes and tumour weights demonstrate that larger tumours are heavier and that these metrics are roughly correlated. For example, tumours measured by Song *et al*. ranged in volume from 3000 mm^3 (untreated) to 150 mm^3 and correspondingly tumour weights ranged from 2000 mg to 100 mg. Of note, tumours that were approximately 750 mm^3 were also found to weigh around 750 mg and the smallest tumours also had the smallest volumes[508]. Similarly, Thambi *et al*. found that untreated tumours grew extremely quickly,

reaching 7000 mm^3 after 15 days, weighing over 5000 mg. Treated tumours had a volume of approximately 800 mm^3 and weighed roughly 800 mg[509]. Tumour volumes assessed by Wang *et al*. were found to range between 1400 mm^3 and 50 mm^3. Indeed, the largest tumours weighed around 1400 mg, tumours with a volume of 600-800 mm^3 weighed between 700-900 mg and smaller tumours around 200 mm^3 were 250 mg[510]. Another study carried out by Shen *et al*. determined that untreated tumour volume was in the region of 1000 mm^3 and these tumours weighed 1400 mg, whereas smaller, treated tumours that had a volume of nearly 700 mm^3 were found to weigh almost 800 mg[511]. To consolidate the idea gleaned from these data, tumours measured in a study by Tummala *et al*. were found to be no larger than 420 mm^3, the largest of which were untreated tumours. These tumours were found to weigh just over 700 mg on average, whereas tumours between 280-340 mm^3 where approximately 400-550 mg in weight[512]. These studies primarily highlight two points, that tumour volume and tumour weight are positively correlated, and that accurate determination of tumour weight can give an estimation of volume. Looking at the untreated tumours in the current work and their average weight of 390 mg, it can be reasonably estimated that the volume of these tumours would fall between 300-450 mm^3 after a 41-day *in vivo* growth period. The volume calculated using formula B and C would fall within this range and therefore suggests that the tumours produced by the *in vivo* model in this work were not as large as initially measured and therefore not proliferating at the expected rate. If these tumours were not proliferating rapidly and supplied by sufficient neovasculature then NP drug delivery therapy becomes extremely challenging. Comparing the terminal volume of the untreated tumours in this study with those seen in other studies using PDX models strongly suggests insufficient proliferation of the tumours in the work. Fragments of a SCLC explant SC61 were implanted into athymic mice and tumours were able to achieve an average volume of 2200 mm^3 from a starting volume (volume at the initiation of the study) of 200 mm^3 within 11 days[307]. A different study introduced 3x3x3 mm pieces

(14.1 mm^3) of lung tumour into nude BALB/c mice and these tumours reached approximately 1000 mm^3 after 24 days and 3800 mm^3 after 52 days from a volume of 80 mm^3 at the beginning of the study. Interestingly, treated tumours with terminal volumes of 350-400 mm^3 were found to weigh around 300-400 mg[513]. Pi *et al.* utilised a PDX model of colorectal cancer and tumours were observed to reach a volume of over 2200 mm^3 six weeks post tumour implantation, from a starting volume of around 300 mm^3, using NSG mice as the host[514]. The terminal volumes of tumours examined in these studies far exceeded the terminal volume recorded from this work, even using the volumes derived from formula A. This observation is not restricted to PDX models either; however as PDX tumours are more difficult to establish, this observation is more notable when contrasted with other PDX tumour models. The tumour diameter measurements (Figure 6.5) serve to confirm the overarching concept that tumours were proliferating insufficiently. For a tumour to achieve a volume of 2000 mm^3, calculated using formula B or C, two of the tumour dimensions (i.e. length and width) must be at least 16 mm and the third at least 15 mm. As shown in Figure 6.5, tumour diameter, by definition the longest dimension, measured throughout the study did not exceed 10 mm. The exact reason(s) the tumours did not reach the volumes expected are not known, however once the initial PDX model has been established, subsequent generations of tumours can be created more easily and quickly. The biological and practical advantages and limitations of PDX models has been extensively reviewed[515,516] and the utility of small animal models will undergo further exposition in Chapter 7. From a practical standpoint, the implantation conditions for PDX growth must be optimised, but most importantly a sufficient number of cells, whether a single cell suspension or fragments, must be used. It is possible that in this work, neither of these conditions were met. In terms of therapeutic efficacy inadequate tumour establishment is the biggest barrier, however intravenous administration of therapy is technically demanding and so it is not clear how much therapy was introduced in a venous capacity.

Despite disappointing results concerning therapeutic efficacy of Dual-NPs, the safety assessment of this therapy was more promising. Indeed, none of the therapies administered induced any negative body weight changes in any of the mice (Figure 6.6) which is a good indicator that the therapies were well tolerated, with no grievous adverse reactions. A lack of body weight change is suggestive that the dose chosen for the study was appropriate, although this could be disputed given the lack of therapeutic efficacy. The dose (5 mg/kg VRL) was chosen based on results presented in a study by Aston *et al.* that showed weekly dosing of VRL at a dose of 10 mg/kg caused significant body weight loss in both BALB/c and C57BL/6J mouse strains in the subsequent days after intravenous injection, after which the mice recovered before the next dose[517]. No body weight changes were witnessed at a dose of 5 mg/kg and as the frequency of dosing would be more than weekly in this study, the lower, safer dose was opted for. The effect of dose can differ depending on the background of the mouse, therefore it was assuring to see that repeated doses of 5 mg/kg VRL or Dual-NPs did not induce body weight loss. Supporting these claims, histology of major organs (Figure 6.7) did not reveal any obvious signs of toxicity. This is particularly notable as the liver is often the most prevalent site of NP accumulation, which would be even more pronounced in this work as the NP seemingly did not accumulate in the tumour to any therapeutic degree. Therefore, the probability that more NPs were sequestered into the liver is higher as there are less physiological NP depots (i.e. tumour). These encouraging results are somewhat unsurprising however, as the primary dose limiting toxicities (DLTs) of vinca alkaloids such as VRL are typically haematological, including granulocytopenia and leukopenia more broadly[518]. Due to the genetic background of NSG mice, they are severely immunocompromised and lack T, B and NK cells and also have defective macrophages and dendritic cells. Even though neutrophils and monocytes comprise most of the leukocytes detectable in the peripheral blood, neutropenia cannot be thoroughly assessed in isolation of a fully functioning immune system and as such

neutrophils were not examined in this study. Thus, assessment of the principal DLT of VRL could not be adequately investigated; however, of the safety parameters that were examined, Dual-NPs and other therapies trialled herein were well tolerated at the given dose.

6.5. Conclusion

In summary, the anticancer efficacy and biocompatibility of Dual-NPs was assessed *in vivo* using a physiologically relevant PDX model. Dual-NPs were investigated in tandem with equivalent free drug and blank NP formulations. Dual-NPs were found not to be particularly efficacious anticancer agents due to the absence of a reduction in tumour volume or weight compared to the tumours that developed in untreated mice. This was theorised to be due to the lack of tumour growth and insufficient vascularisation of the tumour, however the possibility that Dual-NPs were intrinsically ineffective cannot be ruled out. Dual-NPs, as well as other therapies tested, were not found to induce loss of mouse body weight or cause organ damage, suggesting that at the dose examined, Dual-NPs are well tolerated. Future studies ought to be conducted in a well characterised and rapidly growing *in vivo* model such that the EPR effect is more pronounced and the efficacy (or lack thereof) of Dual-NPs can be assessed. Immunohistochemistry of the tumours may give a clearer indication of its physiology and architecture. The use of further safety parameters, such as liver and kidney function as well as haematological assessment, would be useful to reinforce the safety assessment of these nanomedicines.

7. Summary discussion, future work and conclusions

This chapter highlights the novelty and key findings from each of the preceding research chapters and details their implications for the drug delivery field, particularly in an oncological context. The limitations of the study are outlined in combination with recommendations for future work based not only the findings presented within the thesis but also for the purpose of advancing the field of nanoparticle drug delivery to cancer as a whole. Lastly, concluding sentiments regarding thesis content and future directions are conveyed.

7.1. Thesis summary and implications

Lung cancer still presides as the most lethal malignancy worldwide, thus innovative therapeutic avenues must be explored in order to change the prognostic landscape, which is currently bleak. NPs have been thrust into the limelight over the past decades as a tool with which to better deliver chemotherapeutic agents to tumours, primarily driven by the EPR effect and the modular nature of NPs such that a combination of materials, therapies and other excipients (e.g. targeting ligands, PEG coatings) can be used to create anticancer NP formulations. Despite these advances, treatment of lung tumours is still of utmost clinical concern and given the breadth of available therapies, especially in the era of personalised medicine, reformulation of chemotherapy into NP formulations may represent a promising therapeutic direction. The development of novel NP formulations has been reported in this work was based around the understudied chemotherapy VRL and TKI AFB, both clinically approved, first line therapies for NSCLC. This was achieved by first synthesising AFB analogues that could be conjugated to the surface of NPs followed by creation of an acceptor block co-polymer PLGA-PEG. Methods were then developed to enable conjugation of AFB analogues to the surface of AuNPs or polymeric NPs whereby VRL had been previously encapsulated using a novel HIP technique, accompanied by appropriate characterisation. The *in vitro* cytotoxicity of Afb-

AuNPs was explored in a range of NSCLC cell lines as well as assessment of biocompatibility using the noncancerous alveolar epithelial cell line TT1. More in depth *in vitro* cytotoxicity studies were subsequently performed using NP formulations of either VRL or both VRL and AFB (Dual-NPs) as well as inflammatory cytokines release from a model of the venous endothelium and elucidation of the pathway responsible for internalisation of Dual-NPs. Finally, the *in vivo* efficacy and safety of Dual-NPs was investigated in a PDX model of NSCLC. The key findings and milestones of this study are detailed below along with their implications in NP-based drug delivery to solid tumours of the lung.

7.1.1. *Synthesis of AFB analogues, conjugation to NPs and HIP for VRL encapsulation in polymeric NPs*

The overarching aim of this work was the development of novel, effective nanomedicines that possessed therapeutic efficacy in NSCLC cells, centred around the molecules of interest, VRL and AFB, and NPs of interest which were polymeric and gold. Neither VRL nor AFB possess functional groups that permit covalent conjugation to the surface of NPs, however AFB is less structurally complex than VRL and more is known about its structure activity relationship and therefore was predicted to be more amenable to modification for conjugation to NPs without detrimental impact on efficacy[519]. As such, two novel AFB analogues were synthesised, Afb-A for conjugation to AuNPs by virtue of a terminal cyclic disulfide moiety and Afb-B for conjugation to azide functionalised polymeric NPs, facilitated by the terminal alkynyl group. Afb-A was then conjugated to AuNPs and subsequently PEGylated to afford colloidal stability. The novel construct was extensively characterised thus demonstrating that TKIs such as AFB can be structurally modified and successfully conjugated to AuNPs. In addition, an azide-bearing PEG was covalently linked to PLGA to form PLGA-PEG-N$_3$ from which polymeric NPs were generated. These NPs were designed to incorporate the amphiphilic base VRL using the HIP agent pamoic acid, which is the first report of VRL ion pairing for encapsulation within

polymeric NPs. Taking advantage of the azide groups orientated on the NP surface, Afb-B was conjugated to the surface using optimised click chemistry, resulting in Dual-NPs. The versatility of click chemistry means that others have adopted this reaction for conjugation of molecules to NPs[520,521], however this report is the first to do so with a self-synthesised TKI on to a NP with chemotherapy encapsulated within its core, specifically VRL, generating the novel formulation Dual-NPs. Indeed, the chemistry detailed within this thesis provides a methodology for modifying the structural architecture of molecules not intrinsically amenable to conjugation, such that they can be attached to NPs of organic or inorganic origin, and demonstration of their conjugation using facile chemistries. The NPs chosen in this work, gold and polymeric are, along with liposomes, the most commonly used NP vehicles for drug delivery to cancer, both preclinically and in clinical trials, therefore the pharmaceutical and chemical methodologies outlined in this thesis can be applied to materials at an advanced stage of the translational pipeline.

7.1.2. *Therapeutic utility of Afb-AuNPs*

The use of AuNPs as drug delivery vehicles has been extensively explored[522], and it is on these strong foundations that the generation of Afb-AuNPs was based. Conjugation of Afb-A to commercially available 30 nm AuNPs was successfully undertaken, however it was still to be determined if the structural modifications and conjugation itself negatively impacted therapeutic efficacy compared to that of the clinically used parent molecule AFB. As a proof of concept, the cytotoxicity of Afb-AuNPs was first demonstrated in NSCLC cells sensitive to treatment with TKIs and further expanded to another NSCLC cell line that does not display this sensitivity. When compared with free Afb-A and AFB, Afb-AuNPs were several times more cytotoxic at the equivalent AFB dose, with this increased efficacy attributed to higher intracellular concentrations of AFB when delivered using AuNPs although this was not directly quantified; AuNPs themselves did not cause toxicity which is also the prevailing view in the

literature. Conjugation of molecules to the surface of (Au)NPs not only may serve to attenuate their metabolism but can also act to reduce its systemic distribution and consequentially side effects. Using a unique alveolar epithelial cell line, TT1, contrasting cytotoxicity of AFB formulations at high doses was witnessed, whereby Afb-AuNPs did not induce any loss of cell viability compared to AFB. This observation was coupled with a reduction of proinflammatory cytokines when TT1 cells were exposed to conjugated AFB as opposed to the traditional formulation. The precise mechanism for this apparent cancer cell specific cytotoxicity was not fully elucidated, although EGFR expression and mutational status is known to dictate the efficacy of TKIs such as AFB. Furthermore, the rate of thiol exchange on the NP surface[335] may be different depending on the cell type, each with a unique intracellular environment and glutathione levels are known to be elevated in lung cancer[523]. The culmination of these factors is that noncancerous TT1 cells may be exposed to less active AFB than cancer cells, providing a potential explanation for the reduced cytotoxicity and cytokine release. As NPs are almost always internalised by endocytosis, escape from the endosome prior to endolysosomal fusion and subsequent degradation is a prerequisite for effective therapies. In the case of Afb-AuNPs however, it was theorised that upon protonation of the S atom, the pH labile Au-S bond is broken and hydrophobic Afb-A can freely diffuse across the lipid bilayer present in lysosomes[524] and into the cytoplasm before it is degraded, thus enabling its biological effect. Moreover, AuNPs have been observed in the cytoplasm of cells and not exclusively in the endosomes or lysosomes, implying AuNPs can either escape the endosome or be internalised without ever entering an endocytic compartment. In either case, Afb-A can accumulate in the cytoplasm, evidenced by the cytotoxicity displayed by Afb-AuNPs. Thus, the therapeutic efficacy of AFB was preserved and even enhanced by conjugation to AuNPs whilst biocompatibility was maintained, both of which are important aspects for NP-based drug delivery.

7.1.3. *Dual combination chemotherapy as a single polymeric NP formulation*

After demonstrating that AFB analogues can be conjugated to the surface of a NP and retention of efficacy thereafter, this principal was applied to a more complex nanoformulation, resulting in the development of Dual-NPs. Again, this proof of principle NP demonstrated that diverse conjugation chemistries can be employed to attach molecules of interest, in this case synthesised molecular derivatives of AFB, to functionalised polymeric NPs. Dual-NPs displayed evident cytotoxicity across a range of NSCLC cell lines as well as in patient derived NSCLC cells, which was a promising finding as this implies retention of therapeutic efficacy despite the incremental increase in physiological relevance (which often diminishes efficacy). Notably, single agent NPs (VRL-NPs) were more cytotoxic than equivalent concentrations of VRL and Dual-NPs were as cytotoxic or even more so than comparative doses of VRL-NPs. Encouragingly, blank NPs were not found to reduce cell viability at any dose tested, thus cytotoxicity can be fully attributed to the chemotherapeutic elements of the formulation. The anticancer efficacy of Dual-NPs was explored in further depth by investigating the antiproliferative response and apoptotic response, both of which were significantly pronounced in all cell lines, particularly to those sensitive to TKIs despite the low concentration of conjugated AFB compared to both the AuNP formulation and the encapsulated VRL. Venous endothelial cells exposed to VRL-NPs were found to produce less proinflammatory cytokines, particularly IL-8, than when treated with equivalent doses of free VRL; as VRL is known to exhibit vesicant activity in humans when administered intravenously[525], this finding could present an avenue for expedited clinical translation, provided efficacy is retained. The mechanism of Dual-NP internalisation into cancer cells was determined to be primarily mediated by clathrin-associated pathways, although other endocytic pathways were found to play a minor role. As the predominant size distribution of Dual-NPs falls below 200 nm, it was expected to some degree that clathrin-mediated uptake of Dual-NPs would act as the principal

entry mechanism[479]. Moreover, microscopy studies revealed that decoration of the NP surface with AFB did not affect its internalisation, which is promising from a drug delivery standpoint. Finally, the *in vivo* efficacy and safety of Dual-NPs was assessed using a PDX model. Dual-NPs were not found to induce significant loss of tumour volume or weight compared to untreated mice, however the biological and technical challenges associated with PDX models and such physiologically relevant models were highlighted, using this study as an example. Although antitumour efficacy was not observed in this work, Dual-NPs were found to be well tolerated and biocompatible, evidenced by retention of mouse body weight throughout the study and lack of discernible organ toxicity. The *in vitro* efficacy of Dual-NPs along with their biocompatibility *in vivo* would suggest that re-evaluation in a more established *in vivo* model would yield promising results, especially given the biological nuances associated with rapidly growing tumours in mice.

7.2. Limitations, future work and opportunities for progress

This work has demonstrated that rational modification of molecules can be performed to create "attachable" entities that could then be conjugated to a NP surface using facile benchtop chemistries. The NPs were either inorganic (gold) or organic (polymeric) in composition, and polymeric NPs contained an additional chemotherapy which required development of a HIP method to achieve suitable loading, resulting in the generation of a dual chemotherapy NP formulation. These formulations were characterised and the *in vitro* efficacy as well as *in vivo* safety was illustrated. Although comprehensive in scope, there were limitations of the work at each stage of the pipeline, from synthesis of particles to *in vivo* evaluation. These will be outlined and can act as the substrate from which future investigations can arise.

The traditional characterisation methods were employed for both sets of NPs such as DLS, zeta potential, TEM and more. However, more detailed characterisation may be useful to better

predict *in vivo* activity. For example, stability in serum over time was not assessed, although PEGylation is designed to confer colloidal stability in the presence of proteinaceous medium. Nanoparticle tracking analysis would act to confirm DLS results and provide an accurate measurement of NP concentration, which is difficult to discern otherwise. Due to novelty and time limitations, the absolute quantification of AFB on the surface of NPs was not obtained and was instead indirectly inferred by UV-vis spectroscopy with reference to a calibration curve at a designated wavelength. Quantification by HPLC could be achieved by dissolving AFB conjugated polymeric NPs in DMSO and directly analysing the supernatant or in the case of AuNPs, incubating Afb-AuNPs with a reducing agent such as dithiothreitol to break Au-S bonds and analysing the contents for the presence of AFB. It would also be useful to understand the amount of azides present on the surface of polymeric NPs so that the known maximal number of AFB molecules that can be attached could be discerned. With regards to HIP, this is difficult to prove experimentally, however further supporting spectra such as FTIR and Raman may confirm successful pairing, as well as logP determination to show the hydrophobicity of VRL increases when paired with pamoic acid.

With respect to the work presented on Afb-AuNPs, it would be interesting to determine if modification to the AuNP surface affected uptake of NPs, which can be quantified by ICP-MS. Moreover, TEM images of internalised AuNPs at different time points would provide a more informative view of their intracellular trafficking and ultimate cellular localisation. Indeed, both of these techniques have been extensively applied in the AuNP drug delivery literature, and it appears functionalisation with AuNPs does not decrease the amount of Au within cells and it is well established that AuNPs larger than approximately 10 nm do not penetrate the nucleus and, after 24 hours, are found in vesicles or the cytoplasm[357,358]. In this regard, investigating different PEG chain lengths and grafting densities that may influence cellular uptake would be insightful. Investigations into exocytosis of AuNPs from cells would also be

revealing, as reports vary as to the quantity of NPs exocytosed from cells[526-528]. This information could have a bearing on NP therapeutics in general, especially ones designed to deliver nucleic acids, whose escape from the endosome is a prerequisite for biological function. From a biological perspective, levels of EGFR inhibition upon treatment with Afb-AuNPs could be quantified by Western blot to determine that modified AFB is functional and that cytotoxicity stems from EGFR inhibition and not an indirect mechanism instigated by the intracellular presence of Afb-AuNPs. The concepts outlined in the Afb-AuNP chapter would be interesting to extend to gold nanorods, as these constructs can also be employed for photothermal therapy using tissue penetrating near infrared light, whereas spherical AuNPs do not possess this property. This modality has been shown to induce significant reductions in tumour volume[529] and this intrinsic property of gold nanorods can be rationally combined with chemotherapy or photosensitising molecules such as chlorin e6 to induce photodynamic damage via singlet oxygen production[530]. Another avenue of exploration is the use of diagnostic elements, either utilising the AuNP itself which can function as a contrast agent for CT scans[531], or attachment of fluorophores/chromophores. Indeed, the combination of therapeutic and diagnostic components in the same NP formulation, known as theranostics, is an attractive concept and one most easily accomplished using metallic NPs due to the large surface area for conjugation, versatile surface chemistries and intrinsic optical properties of elements such as Au, Fe and lanthanides.

Fabrication of a dual drug delivery system using polymeric NPs generated promising results *in vitro*, however a comprehensive understanding of the mechanisms underpinning the observed efficacy would be interesting. As this combination of chemotherapy was predicated on the reported synergistic activity of chemotherapy-induced nuclear damage and EGFR inhibition which centred on caspase 8 activation[441], examination of caspase 8 activation in this study would have suggested the same mechanism was governing cytotoxicity. It is worth considering

that this synergy may only be observed in certain cell lines and that EGFR is inhibited at least 4 hours prior to nuclear damage; the kinetics of EGFR inhibition and depletion of β-tubulin were not examined. Moreover, synergy may rely on direct DNA damage as agents that intercalate with DNA (doxorubicin) or form adducts (cisplatin) were amongst the most effective generators of a synergistic response. In the context of drug efficacy, synergy is currently defined by a Combination Index value of less than 1 which can be derived using models such as Chou-Talalay, Bliss and others[532] that incorporate a set of mathematical and pharmacological principals to evaluate drug combinations. It may be insightful to calculate the Combination Index for the drug combination used in this work and further interrogate VRL combinations to find potentially more effective therapies and the underpinning mechanisms. Cell cycle analysis may provide insights into the efficacy of VRL/AFB combinations as well as other iterations. As VRL acts on microtubules, one would expect an accumulation of cells in G_2/M phase and a reduction of cells in S phase to be the hallmark of efficacious therapy, as this would represent mitotic catastrophe and subsequent cell cycle arrest, leading to cell death.

Similarly to AuNPs, visualisation of the internalisation of Dual-NPs would provide useful information regarding their intracellular localisation. However, polymeric NPs are not intrinsically electron dense like metallic NPs and TEM preparations typically contain organic solvents and a hydrophobic resin that dissolves polymeric material such as PLGA. Hydrophilic resins have been employed that preserve polymeric NPs and cellular ultrastructure[533], however these images require significant optimisation and expertise to acquire. An alternative is confocal microscopy which was indeed performed in this work; however, images were only taken at one plane, albeit this plane was at a z depth consistently within a range of 2-3 μm. Despite this, it is still not conclusive evidence that the NPs were not just adsorbed to the cell surface, therefore z stacks ought to be acquired in future investigations to affirm internalisation. Confirmatory uptake studies by flow cytometry would also verify the findings from confocal

microscopy, even though this technique still does not exclude the possibility that cell membrane adherence of NPs is occurring.

In a broader context of advancing the NP drug delivery field, there are several areas of experimentation that can be explored. Often in the drug delivery literature, the *in vitro* biocompatibility of NP formulations is discounted in favour of *in vivo* safety analysis. Whilst *in vivo* safety is paramount, the advantage of *in vitro* toxicology is that it is quick, versatile and reproducible[534], therefore providing key insight into the behaviour of NPs prior to expensive and laborious *in vivo* studies. Indeed, the work presented in this thesis examined certain elements of *in vitro* toxicology using a noncancerous alveolar epithelial cell line and venous endothelial cells, principally cell viability and inflammatory cytokine release. This served to strengthen the case for the NP materials developed and used here as viable for further *in vivo* testing, which corroborated the *in vitro* findings of biocompatibility. Another hugely important factor to consider for intravenous and NP drug delivery in general is the formation of the corona. Often referred to as the protein corona (which is a misnomer as lipids and other molecules comprise the corona not just proteins), this biologically derived layer is created by adsorption of plasma proteins to the NP surface after intravenous administration and is dynamic based on the biological environments the NP encounters[535,536]. The corona has been theorised to heavily impact physiological responses to NPs such as immunogenicity, clearance, accumulation and bestows NPs with a new biological identity, altering their physicochemical properties[537,538]. Indeed, NPs are often engineered either to minimise protein corona formation[539,540], to utilise the formation of a corona to improve drug delivery[541], or pre-coated with a defined corona to minimise nonspecific interactions *in vivo*[542]. The identity of the corona is thought to be dependent on the physicochemical properties of the NP, such as size, shape, material and surface charge and not necessarily on the abundance of protein in the blood. For example, albumin, IgG and transferrin are the most abundant proteins in human plasma but the

most abundant proteins found adsorbed to silica NPs were apolipoprotein B 100 and complement factor H, regardless of surface charge, although differential composition of coronas was noted[543]. Important studies would seek to elucidate the identity of the corona and definitive parameters that affect NP uptake into tumours, recognition by the immune system or expedite elimination. This could be done using mass spectrometry after desorption of proteins from the NP surface that have been exposed to the human blood plasma environment, ideally *in vivo*.

A major limitation of almost every NP drug delivery study is the use of animal models that insufficiently recapitulate the human tumour microenvironment and physiology. It is imperative that the results obtained from mouse models are not extrapolated out of context and that they are used for the purpose with which they are designed. Mouse models are very poor predictors of clinical performance primarily due to the lack of heterogeneity which dramatically affects treatment efficacy and the relative size of their tumours. Tumours in mice can be up to 30% of their total body weight, compared with a human tumour that is usually less than 0.01% of body weight, thus the typical clinical scenario is not accurately mapped, especially when larger tumours in humans are resected or shrunk with chemotherapy or radiotherapy[544]. However, mouse models of cancer do provide valuable insight into fundamental bio-nano interactions, such as with tissue and organs, as well as the biodistribution of NPs under physiological conditions. One can also speculate with reasonable assurance that if a NP formulation fails to achieve a curative response in a murine tumour model then it is unlikely to do so in a human, therefore acting as a filter for therapies destined to fail in the clinic. Pharmacokinetic and pharmacodynamic measurements are often made but must be interpreted with caution and not in isolation as a predictor of how NPs would behave in humans. Studies in more physiologically relevant mouse models such as immunocompetent transgenic models or those with humanised immune systems that develop tumours spontaneously and that

metastasise, would act as the first step in the direction of progress. Investigations could also take place in animals that develop tumours naturally, such as dogs or cats, something that has been coined as comparative oncology[545]. At this point in the growth of the field of nanomedicine, it is not enough to simply demonstrate tumour shrinkage in an immunocompromised mouse with a hyper-vascularised, disproportioned and rapidly growing tumour. Building on this point, a significant portion of NP drug delivery strategies still heavily rely on the EPR effect. Over the past two decades, accumulating evidence has brought to light the "fallacy" of the EPR effect, in that sole reliance on this physiological phenomenon for delivery of NPs to human tumours is invariably a poor strategy. Critique of the EPR effect as the foundation for drug delivery has been extensively outlined[503,546-548] and predominantly centre around how viable it is for NPs to overcome extravasation, diffusion and convective barriers coupled with a lack of understanding of tumour biology and how NPs interact with the complex microenvironment. Illuminating the latter issue somewhat, a meta-analysis calculated that a median of 0.7% of the injected dose reaches the tumour in mouse models, taking into account the type of NP type, the method with which the cargo was delivered (conjugation or encapsulation), active or passive targeting and other physicochemical parameters[549]. This is insightful as it clearly demonstrates there is an issue with delivery of therapeutic NPs to tumours, although the ultimate goal should be to improve clinical outcomes not just the percentage of an injected dose of NPs to reach a tumour. A further study delved into these observations further and found that of the proportion of NPs that reach the tumour after intravenous administration, a vast majority are either taken up by tumour associated macrophages adjacent to the vasculature or are lodged in the acellular component of the tumour (extracellular matrix). This study calculated that of the injected dose, 0.0014% of particles interact with cancer cells within the tumour, reaffirming the notion that intravenously injected NPs appear to accumulate almost negligibly in tumours compared to the dose administered[550].

Moreover, from a histological perspective examination of xenograft, syngeneic, genetically engineered and PDX models, revealed that endothelial gaps were found to be extremely sparsely distributed, and this finding was corroborated in human tumours. However, NPs were still found to be internalised into tumours; the leading theory is that the endothelium itself is responsible for transcytosis of NPs or are permissive by another mechanism and it is not the (almost non-existent) fenestrations between adjacent cells[551]. Understanding how exactly NPs enter tumours and what parameters govern this process will lead to inform future researchers how best to engineer NP systems to infiltrate tumours and target the appropriate cells to achieve the best clinical response.

With respect to the lung more specifically, an extension of this work could be to develop an inhalation-based formulation to achieve more targeted delivery. Patel *et al.* recently developed an inhalable polymeric formulation to deliver mRNA to the lung epithelium. Using an ionisable, cationic poly(β-amino ester) nebulised NPs were delivered by inhalation and were able to reproducibly induce protein production through transfection of the epithelium[552]. Indeed, delivery of inhalable nanotherapeutics to ameliorate lung cancer and other pulmonary diseases is an extremely attractive prospect, and an area where progress is being made, but also one that is fraught with difficulties including optimisation of drug formulation and device for reproducible production of particles, the dosage that actually reaches the target site in the lung (aerodynamics of deposition, mucus penetration etc.) and the amount of the formulation that is cleared (mucocilliary clearance, metabolised etc.)[553]. Continuing developments in this area in combination with more sophisticated aerosolisation technologies will enable clinical breakthrough of therapies for lung cancer within the coming decades. Currently, intravenous delivery is the most studied and clinically utilised delivery avenue for pulmonary maladies. As such, the physicochemical properties of NPs that dictate lung-specific accumulation are beginning to be revealed. For example, cationic polymer-lipid NPs were shown to effectively

deliver mRNA to the lung endothelium after intravenous administration[554]. Indeed, optimisation of polymer and lipid properties such as molecular weight, pKa, tail length, geometry and more, using high-throughput screens and generation of libraries, can result in NP formulations that are highly effective delivery agents for nucleic acids[555]. Technologies such as DNA barcoded NPs can be used to screen for NPs with properties that bestow tissue specific delivery of nucleic acids and could be expanded to other molecules[556]. Moreover, high-throughput screening can be combined with machine learning algorithms to identify key properties of NPs that must be present in order to achieve maximal effect[557]. In this thesis, a dual chemotherapy combination was used, however there may be more optimal combinations of chemotherapy to be explored, both in terms of type, such as other first line therapies and inhibitors (i.e. fourth generation molecules such as EAI045.3), and in terms of number, as in clinical regimens in excess of three different drugs, are commonly used in an attempt to achieve a curative effect. Chemotherapies are not the only therapeutics that can be trialled in combination; exploration of nucleic acids, antibodies and non-chemotherapeutic small molecules (e.g. metabolic inhibitors, epigenetic therapies) should also be examined. Algorithmic pipelines and neural networks also have an important role to play here by identifying potent combinations or predicting more effective therapeutic entities[558]. Immunotherapy has clearly had a defining role on the therapeutic landscape of lung cancer, and nanoparticle formulations that attenuate the observed *in vivo* toxicity as well as potentiate the immune response are in development[271,559,560]. Increases in our understanding of how the lung immune microenvironment shapes tumour development, immune evasion mechanisms and the evolution of the mutational landscape of lung cancer[561,562] will lead to personalised therapies and treatment strategies that may leverage the advantages of NPs to maximise delivery and efficacy.

7.3. Overall conclusions

The results presented in this thesis can be divided into three main categories that together comprise the current experimental design framework for nanoparticle drug delivery to (lung) cancer. The first section is devoted to the synthesis of a novel TKI derivative, development of a novel HIP for VRL encapsulation within polymeric NPs, conjugation of TKIs to polymeric or gold NPs and subsequent characterisation. The second and most substantial section began with the *in vitro* evaluation of Afb-AuNP cytotoxicity and biocompatibility. This was further extended to assessment of anticancer activity of polymeric NP formulations, primarily Dual-NPs, *in vitro*, along with inferences into cytokine release profiles and mechanism of uptake in cancer cells. The final section focused on the appraisal of Dual-NPs *in vivo* as effective and safe cancer nanomedicines. Taken together, these findings demonstrated that novel NP formulations composed of organic or inorganic materials could be fabricated and were effective anticancer therapies *in vitro*. Furthermore, Dual-NPs were found to be biocompatible *in vivo*, and although there was not demonstrable *in vivo* anticancer activity, this was thought to be due, at least in part, to the model used. Future studies would seek to evaluate Dual-NPs in a more robust *in vivo* model, explore further combinatorial chemo and other therapies and examine immunotherapeutic avenues of treatment in translationally applicable models.

Bibliography

1.   Bray F, Ferlay J, Soerjomataram I, Siegel RL, Torre LA, Jemal A. Global Cancer Statistics 2018: GLOBOCAN Estimates Of Incidence And Mortality Worldwide For 36 Cancers In 185 Countries. CA: A Cancer Journal For Clinicians 2018;68:394-424.
2.   Projections Of Mortaility And Causes Of Death, 2016 To 2060. 2018. (Accessed 4 March, 2019, At Https://Www.Who.Int/Healthinfo/Global_Burden_Disease/Projections/En/.)
3.   Siegel RL, Miller KD, Jemal A. Cancer Statistics, 2019. CA: A Cancer Journal For Clinicians 2019;69:7-34.
4.   Van Meerbeeck JP, Fennell DA, De Ruysscher DK. Small-Cell Lung Cancer. The Lancet 2012;378:1741-55.
5.   Gregory PK, Wallace A, Paul B, Et Al. Small Cell Lung Cancer. Journal Of The National Comprehensive Cancer Network 2013;11:78-98.
6.   Byers LA, Rudin CM. Small Cell Lung Cancer: Where Do We Go From Here? Cancer 2015;121:664-72.
7.   Pietanza MC, Byers LA, Minna JD, Rudin CM. Small Cell Lung Cancer: Will Recent Progress Lead To Improved Outcomes? Clinical Cancer Research 2015;21:2244-55.
8.   George J, Lim JS, Jang SJ, Et Al. Comprehensive Genomic Profiles Of Small Cell Lung Cancer. Nature 2015;524:47.
9.   Kahnert K, Kauffmann-Guerrero D, Huber RM. SCLC-State Of The Art And What Coes The Future Have In Store? Clinical Lung Cancer 2016;17:325-33.
10.   Sabari JK, Lok BH, Laird JH, Poirier JT, Rudin CM. Unravelling The Biology Of SCLC: Implications For Therapy. Nature Reviews Clinical Oncology 2017;14:549-61.
11.   Gazdar AF, Bunn PA, Minna JD. Small-Cell Lung Cancer: What We Know, What We Need To Know And The Path Forward. Nature Reviews Cancer 2017;17:725.
12.   Tsoukalas N, Aravantinou-Fatorou E, Baxevanos P, Et Al. Advanced Small Cell Lung Cancer (SCLC): New Challenges And New Expectations. Annual Translational Medicine 2018;6:145-.
13.   Rudin CM, Poirier JT, Byers LA, Et Al. Molecular Subtypes Of Small Cell Lung Cancer: A Synthesis Of Human And Mouse Model Data. Nature Reviews Cancer 2019;19:289-97.
14.   Ismail-Khan R, Robinson LA, Williams CC, Jr., Garrett CR, Bepler G, Simon GR. Malignant Pleural Mesothelioma: A Comprehensive Review. Cancer Control : Journal Of The Moffitt Cancer Center 2006;13:255-63.
15.   Raja S, Murthy S, Mason D. Malignant Pleural Mesothelioma. Current Oncology Reports: Current Science Inc.; 2011:259-64.
16.   Mott FE. Mesothelioma: A Review. Ochsner Journal 2012;12:70-9.
17.   Porpodis K, Zarogoulidis P, Boutsikou E, Et Al. Malignant Pleural Mesothelioma: Current And Future Perspectives. Journal Of Thoracic Disease 2013:S397-S406.
18.   Van Zandwijk N, Clarke C, Henderson D, Et Al. Guidelines For The Diagnosis And Treatment Of Malignant Pleural Mesothelioma. Journal Of Thoracic Disease 2013;5:E254-E307.
19.   Bibby AC, Tsim S, Kanellakis N, Et Al. Malignant Pleural Mesothelioma: An Update On Investigation, Diagnosis And Treatment. European Respiratory Review 2016;25:472.
20.   Bueno R, Stawiski EW, Goldstein LD, Et Al. Comprehensive Genomic Analysis Of Malignant Pleural Mesothelioma Identifies Recurrent Mutations, Gene Fusions And Splicing Alterations. Nature Genetics 2016;48:407.
21.   Yap TA, Aerts JG, Popat S, Fennell DA. Novel Insights Into Mesothelioma Biology And Implications For Therapy. Nature Reviews Cancer 2017;17:475.
22.   Scherpereel A, Wallyn F, Albelda SM, Munck C. Novel Therapies For Malignant Pleural Mesothelioma. The Lancet Oncology 2018;19:E161-E72.
23.   Panou V, Gadiraju M, Wolin A, Et Al. Frequency Of Germline Mutations In Cancer Susceptibility Genes In Malignant Mesothelioma. Journal Of Clinical Oncology 2018;36:2863-71.
24.   Blum Y, Meiller C, Quetel L, Et Al. Dissecting Heterogeneity In Malignant Pleural Mesothelioma Through Histo-Molecular Gradients For Clinical Applications. Nature Communications 2019;10:1333.
25.   Herbst RS, Heymach JV, Lippman SM. Lung Cancer. New England Journal Of Medicine: Massachusetts Medical Society; 2008:1367-80.

26.   Reck M, Heigener DF, Mok T, Soria JC, Rabe KF. Management Of Non-Small-Cell Lung Cancer: Recent Developments. The Lancet 2013;382:709-19.

27.   Molina JR, Yang P, Cassivi SD, Schild SE, Adjei AA. Non-Small Cell Lung Cancer: Epidemiology, Risk Factors, Treatment, And Survivorship. Mayo Clinic Proceedings 2008;83:584-94.

28.   Carper MB, Claudio PP. Clinical Potential Of Gene Mutations In Lung Cancer. Clinical Translational Medicine 2015;4:33-.

29.   Forbes SA, Beare D, Boutselakis H, Et Al. COSMIC: Somatic Cancer Genetics At High-Resolution. Nucleic Acids Research 2016;45:D777-D83.

30.   Rizvi NA, Hellmann MD, Snyder A, Et Al. Cancer Immunology. Mutational Landscape Determines Sensitivity To PD-1 Blockade In Non-Small Cell Lung Cancer. Science 2015;348:124-8.

31.   Rosenthal R, Cadieux EL, Salgado R, Et Al. Neoantigen-Directed Immune Escape In Lung Cancer Evolution. Nature 2019;567:479-85.

32.   Dietel M, Bubendorf L, Dingemans A-MC, Et Al. Diagnostic Procedures For Non-Small-Cell Lung Cancer (NSCLC): Recommendations Of The European Expert Group. Thorax 2016;71:177.

33.   Moyer VA. Screening For Lung Cancer: U.S. Preventive Services Task Force Recommendation Statement. Annals Of Internal Medicine 2014;160:330-8.

34.   Bi WL, Hosny A, Schabath MB, Et Al. Artificial Intelligence In Cancer Imaging: Clinical Challenges And Applications. CA: A Cancer Journal For Clinicians 2019;69:127-57.

35.   Ardila D, Kiraly AP, Bharadwaj S, Et Al. End-To-End Lung Cancer Screening With Three-Dimensional Deep Learning On Low-Dose Chest Computed Tomography. Nature Medicine 2019.

36.   Salgia R. Diagnostic Challenges In Non-Small-Cell Lung Cancer: An Integrated Medicine Approach. Future Oncology: Future Medicine; 2015:489-500.

37.   Ettinger DS, Akerley W, Borghaei H, Et Al. Non-Small Cell Lung Cancer. Journal Of The National Comprehensive Cancer Network 2012;10:1236-71.

38.   Travis WD, Brambilla E, Nicholson AG, Et Al. The 2015 World Health Organization Classification Of Lung Tumors: Impact Of Genetic, Clinical And Radiologic Advances Since The 2004 Classification. Journal Of Thoracic Oncology 2015;10:1243-60.

39.   Teixeira VH, Pipinikas CP, Pennycuick A, Et Al. Deciphering The Genomic, Epigenomic, And Transcriptomic Landscapes Of Pre-Invasive Lung Cancer Lesions. Nature Medicine 2019;25:517-25.

40.   Hasan N, Kumar R, Kavuru M. Lung Cancer Screening Beyond Low-Dose Computed Tomography: The Role Of Novel Biomarkers. Lung: Springer US; 2014:639-48.

41.   Beane J, Campbell JD, Lel J, Vick J, Spira A. Genomic Approaches To Accelerate Cancer Interception. The Lancet Oncology 2017;18:E494-E502.

42.   Lopez-Sanchez LM, Jurado-Gamez B, Feu-Collado N, Et Al. Exhaled Breath Condensate Biomarkers For The Early Diagnosis Of Lung Cancer Using Proteomics. American Journal Of Physiology Lung Cellular And Molecular Physiology 2017;313:L664-L76.

43.   Ahrendt SA, Chow JT, Xu L-H, Et Al. Molecular Detection Of Tumor Cells In Bronchoalveolar Lavage Fluid From Patients With Early Stage Lung Cancer. JNCI: Journal Of The National Cancer Institute 1999;91:332-9.

44.   Carvalho AS, Cuco CM, Lavareda C, Et Al. Bronchoalveolar Lavage Proteomics In Patients With Suspected Lung Cancer. Scientific Reports 2017;7:42190.

45.   Lee SH, Sung JY, Yong D, Et Al. Characterization Of Microbiome In Bronchoalveolar Lavage Fluid Of Patients With Lung Cancer Comparing With Benign Mass Like Lesions. Lung Cancer (Amsterdam, Netherlands) 2016;102:89-95.

46.   Callejon-Leblic B, Garcia-Barrera T, Gravalos-Guzman J, Pereira-Vega A, Gomez-Ariza JL. Metabolic Profiling Of Potential Lung Cancer Biomarkers Using Bronchoalveolar Lavage Fluid And The Integrated Direct Infusion/ Gas Chromatography Mass Spectrometry Platform. Journal Of Proteomics 2016;145:197-206.

47.   Duffy MJ, O'Byrne K. Tissue And Blood Biomarkers In Lung Cancer: A Review. Advances In Clinical Chemistry 2018;86:1-21.

48.   Nagrath S, Sequist LV, Maheswaran S, Et Al. Isolation Of Rare Circulating Tumour Cells In Cancer Patients By Microchip Technology. Nature 2007;450:1235-9.

49.   Abbosh C, Birkbak NJ, Swanton C. Early Stage NSCLC — Challenges To Implementing Ctdna-Based Screening And MRD Detection. Nature Reviews Clinical Oncology 2018;15:577-86.

50. Goldstraw P, Ball D, Jett JR, Et Al. Non-Small-Cell Lung Cancer. The Lancet: Elsevier; 2011:1727-40.

51. Chen Z, Fillmore CM, Hammerman PS, Kim CF, Wong KK. Non-Small-Cell Lung Cancers: A Heterogeneous Set Of Diseases. Nature Reviews Cancer 2014;14:535-46.

52. Gridelli C, Rossi A, Carbone DP, Et Al. Non-Small-Cell Lung Cancer. Nature Reviews Disease Primers 2015.

53. Tang ER, Schreiner AM, Pua BB. Advances In Lung Adenocarcinoma Classification: A Summary Of The New International Multidisciplinary Classification System (IASLC/ATS/ERS). Journal Of Thoracic Disease 2014;6:S489-S501.

54. Sereno M, Esteban IR, Zambrana F, Et Al. Squamous-Cell Carcinoma Of The Lungs: Is It Really So Different? Critical Reviews In Oncology / Hematology: Elsevier; 2012:327-39.

55. Travis WD, Brambilla E, Noguchi M, Et Al. International Association For The Study Of Lung Cancer/American Thoracic Society/European Respiratory Society International Multidisciplinary Classification Of Lung Adenocarcinoma. Journal Of Thoracic Oncology 2011;6.

56. Lindeman NI, Cagle PT, Aisner DL, Et Al. Updated Molecular Testing Guideline For The Selection Of Lung Cancer Patients For Treatment With Targeted Tyrosine Kinase Inhibitors: Guideline From The College Of American Pathologists, The International Association For The Study Of Lung Cancer, And The Association For Molecular Pathology. Journal Of Thoracic Oncology 2018;13:323-58.

57. Rossi G, Marchioni A, Milani M, Et Al. TTF-1, Cytokeratin 7, 34βe12, And CD56/NCAM Immunostaining In The Subclassification Of Large Cell Carcinomas Of The Lung. American Journal Of Clinical Pathology 2004;122:884-93.

58. Bittner N, Ostoros G, Géczi L. New Treatment Options For Lung Adenocarcinoma - In View Of Molecular Background. Pathology Oncology Research 2014:11-25.

59. Yousem SA. Role Of Molecular Studies In The Diagnosis Of Lung Adenocarcinoma. Modern Pathology 2012;25:S11.

60. Calvayrac O, Pradines A, Pons E, Mazières J, Guibert N. Molecular Biomarkers For Lung Adenocarcinoma. European Respiratory Journal 2017;49:1601734.

61. The Cancer Genome Atlas Research N, Collisson EA, Campbell JD, Et Al. Comprehensive Molecular Profiling Of Lung Adenocarcinoma. Nature 2014;511:543.

62. Lavin Y, Kobayashi S, Leader A, Et Al. Innate Immune Landscape In Early Lung Adenocarcinoma By Paired Single-Cell Analyses. Cell 2017;169:750-65.E17.

63. Drilon A, Rekhtman N, Ladanyi M, Paik P. Squamous-Cell Carcinomas Of The Lung: Emerging Biology, Controversies, And The Promise Of Targeted Therapy. The Lancet Oncology: Elsevier; 2012:E418-E26.

64. Stinchcombe TE. Unmet Needs In Squamous Cell Carcinoma Of The Lung: Potential Role For Immunotherapy. Medical Oncology 2014;31:960.

65. Barbareschi M, Cantaloni C, Del Vescovo V, Et Al. Heterogeneity Of Large Cell Carcinoma Of The Lung: An Immunophenotypic And Mirna-Based Analysis. American Journal Of Clinical Pathology 2011;136:773-82.

66. The Cancer Genome Atlas Research N, Hammerman PS, Lawrence MS, Et Al. Comprehensive Genomic Characterization Of Squamous Cell Lung Cancers. Nature 2012;489:519.

67. Rooney M, Devarakonda S, Govindan R. Genomics Of Squamous Cell Lung Cancer. Oncologist 2013;18:707-16.

68. Choi M, Kadara H, Zhang J, Et Al. Mutation Profiles In Early-Stage Lung Squamous Cell Carcinoma With Clinical Follow-Up And Correlation With Markers Of Immune Function. Annals Of Oncology 2016;28:83-9.

69. Gandara DR, Hammerman PS, Sos ML, Lara PN, Jr., Hirsch FR. Squamous Cell Lung Cancer: From Tumor Genomics To Cancer Therapeutics. Clinical Cancer Research 2015;21:2236-43.

70. Campbell JD, Alexandrov A, Kim J, Et Al. Distinct Patterns Of Somatic Genome Alterations In Lung Adenocarcinomas And Squamous Cell Carcinomas. Nature Genetics 2016;48:607-16.

71. Yang Y, Wang M, Liu B. Exploring And Comparing Of The Gene Expression And Methylation Differences Between Lung Adenocarcinoma And Squamous Cell Carcinoma. Journal Of Cellular Physiology 2019;234:4454-9.

72.   Coudray N, Ocampo PS, Sakellaropoulos T, Et Al. Classification And Mutation Prediction From Non–Small Cell Lung Cancer Histopathology Images Using Deep Learning. Nature Medicine 2018;24:1559-67.

73.   Sholl LM. Large-Cell Carcinoma Of The Lung: A Diagnostic Category Redefined By Immunohistochemistry And Genomics. Current Opinion In Pulmonary Medicine 2014;20:324-31.

74.   Rekhtman N, Tafe LJ, Chaft JE, Et Al. Distinct Profile Of Driver Mutations And Clinical Features In Immunomarker-Defined Subsets Of Pulmonary Large-Cell Carcinoma. Modern Pathology 2013;26:511-22.

75.   Chan AW, Chau SL, Tong JH, Et Al. The Landscape Of Actionable Molecular Alterations In Immunomarker-Defined Large-Cell Carcinoma Of The Lung. Journal Of Thoracic Oncology 2019.

76.   Yoshimoto T, Matsubara D, Nakano T, Et Al. Frequent Loss Of The Expression Of Multiple Subunits Of The SWI/SNF Complex In Large Cell Carcinoma And Pleomorphic Carcinoma Of The Lung. Pathology International 2015;65:595-602.

77.   Pelosi G, Barbareschi M, Cavazza A, Graziano P, Rossi G, Papotti M. Large Cell Carcinoma Of The Lung: A Tumor In Search Of An Author. A Clinically Oriented Critical Reappraisal. Lung Cancer (Amsterdam, Netherlands) 2015;87:226-31.

78.   Timmerman R, Paulus R, Galvin J, Et Al. Stereotactic Body Radiation Therapy For Inoperable Early Stage Lung Cancer. Journal Of The American Medical Assoication 2010;303:1070-6.

79.   Onishi H, Shirato H, Nagata Y, Et Al. Stereotactic Body Radiotherapy (SBRT) For Operable Stage I Non-Small-Cell Lung Cancer: Can SBRT Be Comparable To Surgery? International Journal Of Radiation Oncology Physics 2011;81:1352-8.

80.   David SE, Dara LA, Douglas EW, Et Al. NCCN Guidelines Insights: Non–Small Cell Lung Cancer, Version 5.2018. Journal Of The National Comprehensive Cancer Network 2018;16:807-21.

81.   Paez JG, Jänne PA, Lee JC, Et Al. *EGFR* Mutations In Lung Cancer: Correlation With Clinical Response To Gefitinib Therapy. Science 2004;304:1497.

82.   Lynch TJ, Bell DW, Sordella R, Et Al. Activating Mutations In The Epidermal Growth Factor Receptor Underlying Responsiveness Of Non–Small-Cell Lung Cancer To Gefitinib. New England Journal Of Medicine 2004;350:2129-39.

83.   Mok TSK. Personalized Medicine In Lung Cancer: What We Need To Know. Nature Reviews Clinical Oncology 2011;8:661-8.

84.   Topalian SL, Hodi FS, Brahmer JR, Et Al. Safety, Activity, And Immune Correlates Of Anti–PD-1 Antibody In Cancer. New England Journal Of Medicine 2012;366:2443-54.

85.   Brahmer JR, Tykodi SS, Chow LQM, Et Al. Safety And Activity Of Anti–PD-L1 Antibody In Patients With Advanced Cancer. New England Journal Of Medicine 2012;366:2455-65.

86.   Lynch TJ, Bondarenko I, Luft A, Et Al. Ipilimumab In Combination With Paclitaxel And Carboplatin As First-Line Treatment In Stage IIIB/IV Non-Small-Cell Lung Cancer: Results From A Randomized, Double-Blind, Multicenter Phase II Study. Journal Of Clinical Oncology 2012;30:2046-54.

87.   Cryer AM, Thorley AJ. Nanotechnology In The Diagnosis And Treatment Of Lung Cancer. Pharmacology & Therapeutics 2019.

88.   Brahmer J, Reckamp KL, Baas P, Et Al. Nivolumab Versus Docetaxel In Advanced Squamous-Cell Non-Small-Cell Lung Cancer. New England Journal Of Medicine: Massachusetts Medical Society; 2015:123-35.

89.   Garon EB, Rizvi NA, Hui R, Et Al. Pembrolizumab For The Treatment Of Non-Small-Cell Lung Cancer. New England Journal Of Medicine: Massachusetts Medical Society; 2015:2018-28.

90.   Herbst RS, Baas P, Kim DW, Et Al. Pembrolizumab Versus Docetaxel For Previously Treated, PD-L1-Positive, Advanced Non-Small-Cell Lung Cancer (KEYNOTE-010): A Randomised Controlled Trial. The Lancet 2016;387:1540-50.

91.   Hirsch FR, Scagliotti GV, Mulshine JL, Et Al. Lung Cancer: Current Therapies And New Targeted Treatments. The Lancet 2017;389:299-311.

92.   Herbst RS, Morgensztern D, Boshoff C. The Biology And Management Of Non-Small Cell Lung Cancer. Nature 2018;553:446.

93.	Heigener DF, Kerr KM, Laing GM, Mok TSK, Moiseyenko FV, Reck M. Redefining Treatment Paradigms In First-Line Advanced Non–Small-Cell Lung Cancer. Clinical Cancer Research 2019.

94.	Moudi M, Go R, Yien CYS, Nazre M. Vinca Alkaloids. International Journal Of Preventative Medicine 2013;4:1231-5.

95.	Robert Van Der H, Denise IJ, Wim S, Didier H, Robert V. The Catharanthus Alkaloids:Pharmacognosy And Biotechnology. Current Medicinal Chemistry 2004;11:607-28.

96.	Voss ME, Ralph JM, Xie D, Et Al. Synthesis And SAR Of Vinca Alkaloid Analogues. Bioorganic & Medicinal Chemistry Letters 2009;19:1245-9.

97.	Roepke J, Salim V, Wu M, Et Al. Vinca Drug Components Accumulate Exclusively In Leaf Exudates Of Madagascar Periwinkle. Proceedings Of The National Academy Of Sciences 2010;107:15287.

98.	Gigant B, Wang C, Ravelli RB, Et Al. Structural Basis For The Regulation Of Tubulin By Vinblastine. Nature 2005;435:519-22.

99.	Cormier A, Knossow M, Wang C, Gigant B. Chapter 20 - The Binding Of Vinca Domain Agents To Tubulin: Structural And Biochemical Studies. In: Wilson L, Correia JJ, Eds. Methods In Cell Biology: Academic Press; 2010:373-90.

100.	Wieczorek M, Tcherkezian J, Bernier C, Et Al. The Synthetic Diazonamide DZ-2384 Has Distinct Effects On Microtubule Curvature And Dynamics Without Neurotoxicity. Science Translational Medicine 2016;8:365ra159.

101.	Martino E, Casamassima G, Castiglione S, Et Al. Vinca Alkaloids And Analogues As Anti-Cancer Agents: Looking Back, Peering Ahead. Bioorganic & Medicinal Chemistry Letters 2018;28:2816-26.

102.	Gregory RK, Smith IE. Vinorelbine--A Clinical Review. British Journal Of Cancer 2000;82:1907-13.

103.	Faller BA, Pandit TN. Safety And Efficacy Of Vinorelbine In The Treatment Of Non-Small Cell Lung Cancer. Clinical Medicine Insights In Oncology 2011;5:131-44.

104.	Piccirillo MC, Daniele G, Di Maio M, Et Al. Vinorelbine For Non-Small Cell Lung Cancer. Expert Opinion On Drug Safety 2010;9:493-510.

105.	Rowinsky E. The Vinca Alkaloids. In: Kufe DW PR, Weichselbaum RR, Et Al., Ed. Holland-Frei Cancer Medicine. 6th Ed. Hamilton (ON) BC Decker; 2003.

106.	Ullrich A, Schlessinger J. Signal Transduction By Receptors With Tyrosine Kinase Activity. Cell 1990;61:203-12.

107.	Regad T. Targeting RTK Signaling Pathways In Cancer. Cancers (Basel) 2015;7:1758-84.

108.	Fauvel B, Yasri A. Antibodies Directed Against Receptor Tyrosine Kinases: Current And Future Strategies To Fight Cancer. Mabs 2014;6:838-51.

109.	Garuti L, Roberti M, Bottegoni G. Non-ATP Competitive Protein Kinase Inhibitors. Current Medicinal Chemistry 2010;17:2804-21.

110.	Davis MI, Hunt JP, Herrgard S, Et Al. Comprehensive Analysis Of Kinase Inhibitor Selectivity. Nature Biotechnology 2011;29:1046.

111.	Hsu WH, Yang JCH, Mok TS, Loong HH. Overview Of Current Systemic Management Of EGFR-Mutant NSCLC. Annals Of Oncology 2018;29:I3-I9.

112.	Yaish P, Gazit A, Gilon C, Levitzki A. Blocking Of EGF-Dependent Cell Proliferation By EGF Receptor Kinase Inhibitors. Science 1988;242:933.

113.	Traxler P, Furet P. Strategies Toward The Design Of Novel And Selective Protein Tyrosine Kinase Inhibitors. Pharmacology & Therapeutics 1999;82:195-206.

114.	Kumar A, Petri ET, Halmos B, Boggon TJ. Structure And Clinical Relevance Of The Epidermal Growth Factor Receptor In Human Cancer. Journal Of Clinical Oncology 2008;26:1742-51.

115.	Yun C-H, Mengwasser KE, Toms AV, Et Al. The T790M Mutation In EGFR Kinase Causes Drug Resistance By Increasing The Affinity For ATP. P Proceedings Of The National Academy Of Sciences 2008;105:2070-5.

116.	Chen L, Fu W, Zheng L, Liu Z, Liang G. Recent Progress Of Small-Molecule Epidermal Growth Factor Receptor (EGFR) Inhibitors Against C797S Resistance In Non-Small-Cell Lung Cancer. Journal Of Medicinal Chemistry 2018;61:4290-300.

117.	Deeks ED, Keating GM. Afatinib In Advanced NSCLC: A Profile Of Its Use. Drugs & Therapy Perspectives 2018;34:89-98.

118.	Solca F, Dahl G, Zoephel A, Et Al. Target Binding Properties And Cellular Activity Of Afatinib (BIBW 2992), An Irreversible Erbb Family Blocker. Journal Of Pharmacology And Experimental Therapeutics 2012;343:342-50.

119.	Kannan S, Pradhan MR, Tiwari G, Et Al. Hydration Effects On The Efficacy Of The Epidermal Growth Factor Receptor Kinase Inhibitor Afatinib. Scientific Reports 2017;7:1540.

120.	Sharma N, Graziano S. Overview Of The LUX-Lung Clinical Trial Program Of Afatinib For Non-Small Cell Lung Cancer. Cancer Treatment Reviews 2018;69:143-51.

121.	Marshall J, Hwang J, Eskens FALM, Et Al. A Phase I, Open-Label, Dose Escalation Study Of Afatinib, In A 3-Week-On/1-Week-Off Schedule In Patients With Advanced Solid Tumors. Investigational New Drugs 2013;31:399-408.

122.	Bayat Mokhtari R, Homayouni TS, Baluch N, Et Al. Combination Therapy In Combating Cancer. Oncotarget 2017;8:38022-43.

123.	Li MC, Hertz R, Bergenstal DM. Therapy Of Choriocarcinoma And Related Trophoblastic Tumors With Folic Acid And Purine Antagonists. The New England Journal Of Medicine 1958;259:66-74.

124.	Furth J, Kahn MC, Breedis C. The Transmission Of Leukemia Of Mice With A Single Cell. The American Journal Of Cancer 1937;31:276.

125.	Freireich EJ, Karon M, Frei III E. Quadruple Combination Therapy (VAMP) For Acute Lymphocytic Leukemia Of Childhood. Proceedings Of The American Association For Cancer Research; 1964. P. 20.

126.	Devita VT, Moxley JH, Brace K, Frei III E. Intensive Combination Chemotherapy And X-Irradiation In The Treatment Of Hodgkin's Disease. Proceedings Of The American Association For Cancer Research; 1965. P. 881-95.

127.	Devita VT, Jr., Serpick AA, Carbone PP. Combination Chemotherapy In The Treatment Of Advanced Hodgkin's Disease. Annual Internal Medicine 1970;73:881-95.

128.	Greenspan E, Fieber M, Lesnick G, Edelman S. Response Of Advanced Breast Carcinoma To The Combination Of The Antimetabolite, Methotrexate, And The Alkylating Agent, Thio-TEPA. Journal Of The Mount Sinai Hospital, New York 1963;30:246-67.

129.	Devita VT, Chu E. A History Of Cancer Chemotherapy. Cancer Research 2008;68:8643.

130.	Preuer K, Lewis RPI, Hochreiter S, Bender A, Bulusu KC, Klambauer G. Deepsynergy: Predicting Anti-Cancer Drug Synergy With Deep Learning. Bioinformatics 2017;34:1538-46.

131.	Ding MQ, Chen L, Cooper GF, Young JD, Lu X. Precision Oncology Beyond Targeted Therapy: Combining Omics Data With Machine Learning Matches The Majority Of Cancer Cells To Effective Therapeutics. Molecular Cancer Research 2018;16:269.

132.	Goh G, Schmid R, Guiver K, Et Al. Clonal Evolutionary Analysis During HER2 Blockade In HER2-Positive Inflammatory Breast Cancer: A Phase II Open-Label Clinical Trial Of Afatinib +/- Vinorelbine. Plos Medicine 2016;13:E1002136-E.

133.	Harbeck N, Huang C-S, Hurvitz S, Et Al. Afatinib Plus Vinorelbine Versus Trastuzumab Plus Vinorelbine In Patients With HER2-Overexpressing Metastatic Breast Cancer Who Had Progressed On One Previous Trastuzumab Treatment (LUX-Breast 1): An Open-Label, Randomised, Phase 3 Trial. The Lancet Oncology 2016;17:357-66.

134.	Bahleda R, Varga A, Bergé Y, Et Al. Phase I Open-Label Study Of Afatinib Plus Vinorelbine In Patients With Solid Tumours Overexpressing EGFR And/Or HER2. British Journal Of Cancer 2018;118:344.

135.	Nurgali K, Jagoe RT, Abalo R. Editorial: Adverse Effects Of Cancer Chemotherapy: Anything New To Improve Tolerance And Reduce Sequelae? Frontiers In Pharmacology 2018;9:245-.

136.	Rotow J, Bivona TG. Understanding And Targeting Resistance Mechanisms In NSCLC. Nature Reviews Cancer 2017;17:637.

137.	Whitesides GM. The 'Right' Size In Nanobiotechnology. Nature Biotechechnology 2003;21:1161-5.

138.	Lavan DA, Mcguire T, Langer R. Small-Scale Systems For In Vivo Drug Delivery. Nature Biotechnology 2003;21:1184-91.

139.   Thorley AJ, Tetley TD. New Perspectives In Nanomedicine. Pharmacology & Therapeutics 2013;140:176-85.
140.   Kim BYS, Rutka JT, Chan WCW. Nanomedicine. New England Journal Of Medicine 2010;363:2434-43.
141.   Roco MC. Nanotechnology: Convergence With Modern Biology And Medicine. Current Opinion In Biotechnology 2003;14:337-46.
142.   Emerich DF, Thanos CG. Nanotechnology And Medicine. Expert Opinion On Biological Therapy 2003;3:655-63.
143.   Caruthers SD, Wickline SA, Lanza GM. Nanotechnological Applications In Medicine. Current Opinion In Biotechnology 2007;18:26-30.
144.   Ferrari M. Cancer Nanotechnology: Opportunities And Challenges. Nature Reviews Cancer 2005;5:161-71.
145.   Chow EK-H, Ho D. Cancer Nanomedicine: From Drug Delivery To Imaging. Science Translational Medicine 2013;5:216rv4-Rv4.
146.   Thakor AS, Gambhir SS. Nanooncology: The Future Of Cancer Diagnosis And Therapy. CA: A Cancer Journal For Clinicians 2013;63:395-418.
147.   Shi J, Kantoff PW, Wooster R, Farokhzad OC. Cancer Nanomedicine: Progress, Challenges And Opportunities. Nature Reviews Cancer 2017;17:20-37.
148.   Allen TM, Cullis PR. Drug Delivery Systems: Entering The Mainstream. Science 2004;303:1818-22.
149.   Peer D, Karp JM, Hong S, Farokhzad OC, Margalit R, Langer R. Nanocarriers As An Emerging Platform For Cancer Therapy. Nature Nanotechnology 2007;2:751-60.
150.   Davis ME, Chen Z, Shin DM. Nanoparticle Therapeutics: An Emerging Treatment Modality For Cancer. Nature Reviews Drug Discovery 2008;7:771-82.
151.   Wang AZ, Langer R, Farokhzad OC. Nanoparticle Delivery Of Cancer Drugs. Annual Review Of Medicine 2012;63:185-98.
152.   Doane TL, Burda C. The Unique Role Of Nanoparticles In Nanomedicine: Imaging, Drug Delivery And Therapy. Chemical Society Reviews 2012;41:2885-911.
153.   Allen TM, Cullis PR. Liposomal Drug Delivery Systems: From Concept To Clinical Applications. Advanced Drug Delivery Reviews 2013;65:36-48.
154.   Kamaly N, Yameen B, Wu J, Farokhzad OC. Degradable Controlled-Release Polymers And Polymeric Nanoparticles: Mechanisms Of Controlling Drug Release. Chemical Reviews 2016;116:2602-63.
155.   Chen D, Dougherty CA, Zhu K, Hong H. Theranostic Applications Of Carbon Nanomaterials In Cancer: Focus On Imaging And Cargo Delivery. Journal Of Controlled Release 2015;210:230-45.
156.   Yang K, Feng L, Liu Z. Stimuli Responsive Drug Delivery Systems Based On Nano-Graphene For Cancer Therapy. Advanced Drug Delivery Reviews 2016;105:228-41.
157.   Molino NM, Wang S-W. Caged Protein Nanoparticles For Drug Delivery. Current Opinion In Biotechnology 2014;0:75-82.
158.   Dreaden EC, Alkilany AM, Huang X, Murphy CJ, El-Sayed MA. The Golden Age: Gold Nanoparticles For Biomedicine. Chemical Society Reviews 2012;41:2740-79.
159.   Mahmoudi M, Sant S, Wang B, Laurent S, Sen T. Superparamagnetic Iron Oxide Nanoparticles (Spions): Development, Surface Modification And Applications In Chemotherapy. Advanced Drug Delivery Reviews 2011;63:24-46.
160.   Ge L, Li Q, Wang M, Ouyang J, Li X, Xing MMQ. Nanosilver Particles In Medical Applications: Synthesis, Performance, And Toxicity. International Journal Of Nanomedicine 2014;9:2399-407.
161.   Yang P, Gai S, Lin J. Functionalized Mesoporous Silica Materials For Controlled Drug Delivery. Chemical Society Reviews 2012;41:3679-98.
162.   Chen G, Qiu H, Prasad PN, Chen X. Upconversion Nanoparticles: Design, Nanochemistry, And Applications In Theranostics. Chemical Reviews 2014;114:5161-214.
163.   Zhang H, Yee D, Wang C. Quantum Dots For Cancer Diagnosis And Therapy: Biological And Clinical Perspectives. Nanomedicine 2008;3:83-91.
164.   Yildiz I, Shukla S, Steinmetz NF. Applications Of Viral Nanoparticles In Medicine. Current Opinion In Biotechnology 2011;22:901-8.

165.   Gultepe E, Nagesha D, Sridhar S, Amiji M. Nanoporous Inorganic Membranes Or Coatings For Sustained Drug Delivery In Implantable Devices. Advanced Drug Delivery Reviews 2010;62:305-15.

166.   Fan W, Yung B, Huang P, Chen X. Nanotechnology For Multimodal Synergistic Cancer Therapy. Chemical Reviews 2017;117:13566-638.

167.   Mura S, Nicolas J, Couvreur P. Stimuli-Responsive Nanocarriers For Drug Delivery. Nature Materials 2013;12:991-1003.

168.   Kneidl B, Peller M, Winter G, Lindner LH, Hossann M. Thermosensitive Liposomal Drug Delivery Systems: State Of The Art Review. International Journal Of Nanomedicine 2014;9:4387-98.

169.   Yue X, Zhang Q, Dai Z. Near-Infrared Light-Activatable Polymeric Nanoformulations For Combined Therapy And Imaging Of Cancer. Advanced Drug Delivery Reviews 2017;115:155-70.

170.   Zhang Y, Yu J, Bomba HN, Zhu Y, Gu Z. Mechanical Force-Triggered Drug Delivery. Chemical Reviews 2016;116:12536-63.

171.   Hoare T, Timko BP, Santamaria J, Et Al. Magnetically-Triggered Nanocomposite Membranes: A Versatile Platform For Triggered Drug Release. Nano Letters 2011;11:1395-400.

172.   Du J-Z, Du X-J, Mao C-Q, Wang J. Tailor-Made Dual Ph-Sensitive Polymer–Doxorubicin Nanoparticles For Efficient Anticancer Drug Delivery. Journal Of The American Chemical Society 2011;133:17560-3.

173.   Ryu J-H, Chacko RT, Jiwpanich S, Bickerton S, Babu RP, Thayumanavan S. Self-Cross-Linked Polymer Nanogels: A Versatile Nanoscopic Drug Delivery Platform. Journal Of The American Chemical Society 2010;132:17227-35.

174.   Huang S, Shao K, Kuang Y, Et Al. Tumor Targeting And Microenvironment-Responsive Nanoparticles For Gene Delivery. Biomaterials 2013;34:5294-302.

175.   Torchilin VP. Multifunctional, Stimuli-Sensitive Nanoparticulate Systems For Drug Delivery. Nature Reviews Drug Discovery 2014;13:813.

176.   Karimi M, Ghasemi A, Zangabad PS, Et Al. Smart Micro/Nanoparticles In Stimulus-Responsive Drug/Gene Delivery Systems. Chemical Society Reviews 2016;45:1457-501.

177.   Cabane E, Zhang X, Langowska K, Palivan CG, Meier W. Stimuli-Responsive Polymers And Their Applications In Nanomedicine. Biointerphases 2012;7:9.

178.   Farjadian F, Ghasemi A, Gohari O, Roointan A, Karimi M, Hamblin MR. Nanopharmaceuticals And Nanomedicines Currently On The Market: Challenges And Opportunities. Nanomedicine 2018;14:93-126.

179.   Daniel M-C, Astruc D. Gold Nanoparticles: Assembly, Supramolecular Chemistry, Quantum-Size-Related Properties, And Applications Toward Biology, Catalysis, And Nanotechnology. Chemical Reviews 2004;104:293-346.

180.   Pricker SP. Medical Uses Of Gold Compounds: Past, Present And Future. Gold Bulletin 1996;29:53-60.

181.   Faraday M. X. The Bakerian Lecture. —Experimental Relations Of Gold (And Other Metals) To Light. Philosophical Transactions Of The Royal Society Of London 1857;147:145-81.

182.   Turkevich J, Stevenson PC, Hillier J. A Study Of The Nucleation And Growth Processes In The Synthesis Of Colloidal Gold. Discussions Of The Faraday Society 1951;11:55-75.

183.   Frens G. Controlled Nucleation For The Regulation Of The Particle Size In Monodisperse Gold Suspensions. Nature Physical Science 1973;241:20-2.

184.   Schmid G, Pfeil R, Boese R, Et Al. Au55[P(C6H5)3]12CI6 — Ein Goldcluster Ungewöhnlicher Größe. Chemische Berichte 1981;114:3634-42.

185.   Brust M, Walker M, Bethell D, Schiffrin DJ, Whyman R. Synthesis Of Thiol-Derivatised Gold Nanoparticles In A Two-Phase Liquid–Liquid System. Journal Of The Chemical Society, Chemical Communications 1994:801-2.

186.   Nikoobakht B, El-Sayed MA. Preparation And Growth Mechanism Of Gold Nanorods (Nrs) Using Seed-Mediated Growth Method. Chemistry Of Materials 2003;15:1957-62.

187.   Elahi N, Kamali M, Baghersad MH. Recent Biomedical Applications Of Gold Nanoparticles: A Review. Talanta 2018;184:537-56.

188.   Grzelczak M, Pérez-Juste J, Mulvaney P, Liz-Marzán LM. Shape Control In Gold Nanoparticle Synthesis. Chemical Society Reviews 2008;37:1783-91.

189.   Cobley CM, Chen J, Cho EC, Wang LV, Xia Y. Gold Nanostructures: A Class Of Multifunctional Materials For Biomedical Applications. Chemical Society Reviews 2011;40:44-56.
190.   Hu M, Chen J, Li Z-Y, Et Al. Gold Nanostructures: Engineering Their Plasmonic Properties For Biomedical Applications. Chemical Society Reviews 2006;35:1084-94.
191.   Su K-H, Wei Q-H, Zhang X, Mock J, Smith DR, Schultz S. Interparticle Coupling Effects On Plasmon Resonances Of Nanogold Particles. Nano Letters 2003;3:1087-90.
192.   Doose S, Neuweiler H, Sauer M. Fluorescence Quenching By Photoinduced Electron Transfer: A Reporter For Conformational Dynamics Of Macromolecules. Chemphyschem 2009;10:1389-98.
193.   Tian F, Bonnier F, Casey A, Shanahan AE, Byrne HJ. Surface Enhanced Raman Scattering With Gold Nanoparticles: Effect Of Particle Shape. Analytical Methods 2014;6:9116-23.
194.   Khlebtsov N, Dykman L. Biodistribution And Toxicity Of Engineered Gold Nanoparticles: A Review Of In Vitro And In Vivo Studies. Chemical Society Reviews 2011;40:1647-71.
195.   Bertrand N, Wu J, Xu X, Kamaly N, Farokhzad OC. Cancer Nanotechnology: The Impact Of Passive And Active Targeting In The Era Of Modern Cancer Biology. Advanced Drug Delivery Reviews 2014;66:2-25.
196.   Jazayeri MH, Amani H, Pourfatollah AA, Pazoki-Toroudi H, Sedighimoghaddam B. Various Methods Of Gold Nanoparticles (Gnps) Conjugation To Antibodies. Sensing And Bio-Sensing Research 2016;9:17-22.
197.   Häkkinen H. The Gold–Sulfur Interface At The Nanoscale. Nature Chemistry 2012;4:443.
198.   Vigderman L, Zubarev ER. Therapeutic Platforms Based On Gold Nanoparticles And Their Covalent Conjugates With Drug Molecules. Advanced Drug Delivery Reviews 2013;65:663-76.
199.   Montalbetti CAGN, Falque V. Amide Bond Formation And Peptide Coupling. Tetrahedron 2005;61:10827-52.
200.   Dhar S, Daniel WL, Giljohann DA, Mirkin CA, Lippard SJ. Polyvalent Oligonucleotide Gold Nanoparticle Conjugates As Delivery Vehicles For Platinum(IV) Warheads. Journal Of The American Chemical Society 2009;131:14652-3.
201.   Biju V. Chemical Modifications And Bioconjugate Reactions Of Nanomaterials For Sensing, Imaging, Drug Delivery And Therapy. Chemical Society Reviews 2014;43:744-64.
202.   Suk JS, Xu Q, Kim N, Hanes J, Ensign LM. Pegylation As A Strategy For Improving Nanoparticle-Based Drug And Gene Delivery. Advanced Drug Delivery Reviews 2016;99:28-51.
203.   Linsley CS, Wu BM. Recent Advances In Light-Responsive On-Demand Drug-Delivery Systems. Therapeutic Delivery 2017;8:89-107.
204.   Alkilany AM, Thompson LB, Boulos SP, Sisco PN, Murphy CJ. Gold Nanorods: Their Potential For Photothermal Therapeutics And Drug Delivery, Tempered By The Complexity Of Their Biological Interactions. Advanced Drug Delivery Reviews 2012;64:190-9.
205.   Hussein EA, Zagho MM, Nasrallah GK, Elzatahry AA. Recent Advances In Functional Nanostructures As Cancer Photothermal Therapy. International Journal Of Nanomedicine 2018;13:2897-906.
206.   Paciotti GF, Myer L, Weinreich D, Et Al. Colloidal Gold: A Novel Nanoparticle Vector For Tumor Directed Drug Delivery. Drug Delivery 2004;11:169-83.
207.   Libutti SK, Paciotti GF, Byrnes AA, Et Al. Phase I And Pharmacokinetic Studies Of CYT-6091, A Novel Pegylated Colloidal Gold-Rhtnf Nanomedicine. Clinical Cancer Research 2010;16:6139-49.
208.   Paciotti GF, Zhao J, Cao S, Et Al. Synthesis And Evaluation Of Paclitaxel-Loaded Gold Nanoparticles For Tumor-Targeted Drug Delivery. Bioconjugate Chemistry 2016;27:2646-57.
209.   Nilubol N, Yuan Z, Paciotti GF, Et Al. Novel Dual-Action Targeted Nanomedicine In Mice With Metastatic Thyroid Cancer And Pancreatic Neuroendocrine Tumors. Journal Of The National Cancer Institute 2018;110:1019-29.
210.   Pan Y, Leifert A, Ruau D, Et Al. Gold Nanoparticles Of Diameter 1.4 Nm Trigger Necrosis By Oxidative Stress And Mitochondrial Damage. Small 2009;5:2067-76.
211.   Alkilany AM, Nagaria PK, Hexel CR, Shaw TJ, Murphy CJ, Wyatt MD. Cellular Uptake And Cytotoxicity Of Gold Nanorods: Molecular Origin Of Cytotoxicity And Surface Effects. Small 2009;5:701-8.

212. Fischer HC, Chan WCW. Nanotoxicity: The Growing Need For In Vivo Study. Current Opinion In Biotechnology 2007;18:565-71.

213. Rosi NL, Mirkin CA. Nanostructures In Biodiagnostics. Chemical Reviews 2005;105:1547-62.

214. Boisselier E, Astruc D. Gold Nanoparticles In Nanomedicine: Preparations, Imaging, Diagnostics, Therapies And Toxicity. Chemical Society Reviews 2009;38:1759-82.

215. Popovtzer R, Agrawal A, Kotov NA, Et Al. Targeted Gold Nanoparticles Enable Molecular CT Imaging Of Cancer. Nano Letters 2008;8:4593-6.

216. Agarwal A, Huang SW, O'Donnell M, Et Al. Targeted Gold Nanorod Contrast Agent For Prostate Cancer Detection By Photoacoustic Imaging. Journal Of Applied Physics 2007;102:064701.

217. Wang H, Huff TB, Zweifel DA, Et Al. *In Vitro* And *In Vivo* Two-Photon Luminescence Imaging Of Single Gold Nanorods. Proceedings Of The National Academy Of Sciences 2005;102:15752.

218. Luo Y, Sun W, Gu Y, Wang G, Fang N. Wavelength-Dependent Differential Interference Contrast Microscopy: Multiplexing Detection Using Nonfluorescent Nanoparticles. Analytical Chemistry 2010;82:6675-9.

219. Huang X, El-Sayed IH, Qian W, El-Sayed MA. Cancer Cells Assemble And Align Gold Nanorods Conjugated To Antibodies To Produce Highly Enhanced, Sharp, And Polarized Surface Raman Spectra: A Potential Cancer Diagnostic Marker. Nano Letters 2007;7:1591-7.

220. Qian X, Peng X-H, Ansari DO, Et Al. In Vivo Tumor Targeting And Spectroscopic Detection With Surface-Enhanced Raman Nanoparticle Tags. Nature Biotechnology 2007;26:83.

221. Porter MD, Lipert RJ, Siperko LM, Wang G, Narayanan R. SERS As A Bioassay Platform: Fundamentals, Design, And Applications. Chemical Society Reviews 2008;37:1001-11.

222. El-Said WA, Kim T-H, Yea C-H, Kim H, Choi J-W. Fabrication Of Gold Nanoparticle Modified ITO Substrate To Detect β-Amyloid Using Surface-Enhanced Raman Scattering. Journal Of Nanoscience And Nanotechnology 2011;11:768-72.

223. Mayer KM, Hafner JH. Localized Surface Plasmon Resonance Sensors. Chemical Reviews 2011;111:3828-57.

224. Her S, Jaffray DA, Allen C. Gold Nanoparticles For Applications In Cancer Radiotherapy: Mechanisms And Recent Advancements. Advanced Drug Delivery Reviews 2017;109:84-101.

225. Aldewachi H, Chalati T, Woodroofe MN, Bricklebank N, Sharrack B, Gardiner P. Gold Nanoparticle-Based Colorimetric Biosensors. Nanoscale 2018;10:18-33.

226. Elghanian R, Storhoff JJ, Mucic RC, Letsinger RL, Mirkin CA. Selective Colorimetric Detection Of Polynucleotides Based On The Distance-Dependent Optical Properties Of Gold Nanoparticles. Science 1997;277:1078.

227. Aili D, Mager M, Roche D, Stevens MM. Hybrid Nanoparticle−Liposome Detection Of Phospholipase Activity. Nano Letters 2011;11:1401-5.

228. Chuang Y-C, Huang W-T, Chiang P-H, Tang M-C, Lin C-S. Aqueous Zymography Screening Of Matrix Metalloproteinase Activity And Inhibition Based On Colorimetric Gold Nanoparticles. Biosensors And Bioelectronics 2012;32:24-31.

229. Muffly TM, Tizzano AP, Walters MD. The History And Evolution Of Sutures In Pelvic Surgery. Journal Of The Royal Society Of Medicine 2011;104:107-12.

230. Laufman H, Rubel T. Synthetic Absorable Sutures. Surgery, Gynecology & Obstetrics 1977;145:597-608.

231. Kulkarni RK, Moore EG, Hegyeli AF, Leonard F. Biodegradable Poly(Lactic Acid) Polymers. Journal Of Biomedical Materials Research 1971;5:169-81.

232. Hoffman AS. The Origins And Evolution Of "Controlled" Drug Delivery Systems. Journal Of Controlled Release 2008;132:153-63.

233. Davis SS, Illum L. Polymeric Microspheres As Drug Carriers. Biomaterials 1988;9:111-5.

234. Duncan R, Cable HC, Lloyd JB, Rejmanová P, Kopeček J. Polymers Containing Enzymatically Degradable Bonds, 7. Design Of Oligopeptide Side-Chains In Poly[N-(2-Hydroxypropyl)Methacrylamide] Copolymers To Promote Efficient Degradation By Lysosomal Enzymes. Die Makromolekulare Chemie 1983;184:1997-2008.

235.   Kwon G, Suwa S, Yokoyama M, Okano T, Sakurai Y, Kataoka K. Enhanced Tumor Accumulation And Prolonged Circulation Times Of Micelle-Forming Poly (Ethylene Oxide-Aspartate) Block Copolymer-Adriamycin Conjugates. Journal Of Controlled Release 1994;29:17-23.
236.   Kabanov AV, Chekhonin VP, Alakhov VY, Et Al. The Neuroleptic Activity Of Haloperidol Increases After Its Solubilization In Surfactant Micelles: Micelles As Microcontainers For Drug Targeting. FEBS Letters 1989;258:343-5.
237.   Harada A, Kataoka K. Chain Length Recognition: Core-Shell Supramolecular Assembly From Oppositely Charged Block Copolymers. Science 1999;283:65-7.
238.   Gref R, Minamitake Y, Peracchia MT, Trubetskoy V, Torchilin V, Langer R. Biodegradable Long-Circulating Polymeric Nanospheres. Science 1994;263:1600.
239.   Soppimath KS, Aminabhavi TM, Kulkarni AR, Rudzinski WE. Biodegradable Polymeric Nanoparticles As Drug Delivery Devices. Journal Of Controlled Release 2001;70:1-20.
240.   Avgoustakis K. Pegylated Poly(Lactide) And Poly(Lactide-Co-Glycolide) Nanoparticles: Preparation, Properties And Possible Applications In Drug Delivery. Current Drug Delivery 2004;1:321-33.
241.   Astete CE, Sabliov CM. Synthesis And Characterization Of PLGA Nanoparticles. Journal Of Biomaterials Science, Polymer Edition 2006;17:247-89.
242.   Karnik R, Gu F, Basto P, Et Al. Microfluidic Platform For Controlled Synthesis Of Polymeric Nanoparticles. Nano Letters 2008;8:2906-12.
243.   Wang H, Liu K, Chen K-J, Et Al. A Rapid Pathway Toward A Superb Gene Delivery System: Programming Structural And Functional Diversity Into A Supramolecular Nanoparticle Library. ACS Nano 2010;4:6235-43.
244.   Kunda NK, Somavarapu S, Gordon SB, Hutcheon GA, Saleem IY. Nanocarriers Targeting Dendritic Cells For Pulmonary Vaccine Delivery. Pharmaceutical Research 2013;30:325-41.
245.   Joye IJ, Mcclements DJ. Production Of Nanoparticles By Anti-Solvent Precipitation For Use In Food Systems. Trends In Food Science & Technology 2013;34:109-23.
246.   Fessi H, Puisieux F, Devissaguet JP, Ammoury N, Benita S. Nanocapsule Formation By Interfacial Polymer Deposition Following Solvent Displacement. International Journal Of Pharmaceutics 1989;55:R1-R4.
247.   Farokhzad OC, Cheng J, Teply BA, Et Al. Targeted Nanoparticle-Aptamer Bioconjugates For Cancer Chemotherapy. Proceedings Of The National Academy Of Sciences 2006;103:6315.
248.   Martínez Rivas CJ, Tarhini M, Badri W, Et Al. Nanoprecipitation Process: From Encapsulation To Drug Delivery. International Journal Of Pharmaceutics 2017;532:66-81.
249.   Anton N, Benoit J-P, Saulnier P. Design And Production Of Nanoparticles Formulated From Nano-Emulsion Templates—A Review. Journal Of Controlled Release 2008;128:185-99.
250.   Cheng J, Teply BA, Sherifi I, Et Al. Formulation Of Functionalized PLGA-PEG Nanoparticles For In Vivo Targeted Drug Delivery. Biomaterials 2007;28:869-76.
251.   Keum C-G, Noh Y-W, Baek J-S, Et Al. Practical Preparation Procedures For Docetaxel-Loaded Nanoparticles Using Polylactic Acid-Co-Glycolic Acid. International Journal Of Nanomedicine 2011;6:2225-34.
252.   Budhian A, Siegel SJ, Winey KI. Haloperidol-Loaded PLGA Nanoparticles: Systematic Study Of Particle Size And Drug Content. International Journal Of Pharmaceutics 2007;336:367-75.
253.   Marin E, Briceño MI, Caballero-George C. Critical Evaluation Of Biodegradable Polymers Used In Nanodrugs. International Journal Of Nanomedicine 2013;8:3071-90.
254.   Hrkach J, Von Hoff D, Ali MM, Et Al. Preclinical Development And Clinical Translation Of A PSMA-Targeted Docetaxel Nanoparticle With A Differentiated Pharmacological Profile. Science Translational Medicine 2012;4:128ra39-Ra39.
255.   Von Hoff D, Mita MM, Ramanathan RK, Et Al. Phase 1 Study Of PSMA-Targeted Docetaxel-Containing Nanoparticle BIND-014 In Patients With Advanced Solid Tumors. Clinical Cancer Research 2016.
256.   Natale R, Socinski M, Hart L, Et Al. Clinical Activity Of BIND-014 (Docetaxel Nanoparticles For Injectable Suspension) As Second-Line Therapy In Patients (Pts) With Stage III/IV Non-Small Cell Lung Cancer. European Journal Of Cancer 2014;50, Supplement 6:19.
257.   Schluep T, Hwang J, Cheng J, Et Al. Preclinical Efficacy Of The Camptothecin-Polymer Conjugate IT-101 In Multiple Cancer Models. Clinical Cancer Research 2006;12:1606-14.

258.   Weiss GJ, Chao J, Neidhart JD, Et Al. First-In-Human Phase 1/2a Trial Of CRLX101, A Cyclodextrin-Containing Polymer-Camptothecin Nanopharmaceutical In Patients With Advanced Solid Tumor Malignancies. Investigational New Drugs 2013;31:986-1000.
259.   Matsumura Y. Poly (Amino Acid) Micelle Nanocarriers In Preclinical And Clinical Studies. Advanced Drug Delivery Reviews 2008;60:899-914.
260.   Plummer R, Wilson RH, Calvert H, Et Al. A Phase I Clinical Study Of Cisplatin-Incorporated Polymeric Micelles (NC-6004) In Patients With Solid Tumours. British Journal Of Cancer 2011;104:593-8.
261.   Anselmo AC, Mitragotri S. Nanoparticles In The Clinic: An Update. Bioengineering & Translaltional Medicine 2019;4:E10143.
262.   Goldberg MS. Improving Cancer Immunotherapy Through Nanotechnology. Nature Reviews Cancer 2019;19:587-602.
263.   Samal SK, Dash M, Van Vlierberghe S, Et Al. Cationic Polymers And Their Therapeutic Potential. Chemical Society Reviews 2012;41:7147-94.
264.   Li L, Yang W-W, Xu D-G. Stimuli-Responsive Nanoscale Drug Delivery Systems For Cancer Therapy. Journal Of Drug Targeting 2019;27:423-33.
265.   Matsumura Y, Maeda H. A New Concept For Macromolecular Therapeutics In Cancer Chemotherapy: Mechanism Of Tumoritropic Accumulation Of Proteins And The Antitumor Agent Smancs. Cancer Research 1986;46:6387-92.
266.   Greish K. Enhanced Permeability And Retention (EPR) Effect For Anticancer Nanomedicine Drug Targeting. Methods In Molecular Biology (Clifton, NJ) 2010;624:25-37.
267.   Gurunathan S, Kang MH, Qasim M, Kim JH. Nanoparticle-Mediated Combination Therapy: Two-In-One Approach For Cancer. International Journal Of Molecular Sciences 2018;19.
268.   Blanco E, Shen H, Ferrari M. Principles Of Nanoparticle Design For Overcoming Biological Barriers To Drug Delivery. Nature Biotechnology 2015;33:941-51.
269.   Lammers T, Aime S, Hennink WE, Storm G, Kiessling F. Theranostic Nanomedicine. Accounts Of Chemical Research 2011;44:1029-38.
270.   Miller MA, Gadde S, Pfirschke C, Et Al. Predicting Therapeutic Nanomedicine Efficacy Using A Companion Magnetic Resonance Imaging Nanoparticle. Science Translational Medicine 2015;7:314ra183.
271.   Park W, Heo Y-J, Han DK. New Opportunities For Nanoparticles In Cancer Immunotherapy. Biomaterial Research 2018;22:24-.
272.   Lazarovits J, Sindhwani S, Tavares AJ, Et Al. Supervised Learning And Mass Spectrometry Predicts The In Vivo Fate Of Nanomaterials. ACS Nano 2019;13:8023-34.
273.   Yamankurt G, Berns EJ, Xue A, Et Al. Exploration Of The Nanomedicine-Design Space With High-Throughput Screening And Machine Learning. Nature Biomedical Engineering 2019;3:318-27.
274.   Hare JI, Lammers T, Ashford MB, Puri S, Storm G, Barry ST. Challenges And Strategies In Anti-Cancer Nanomedicine Development: An Industry Perspective. Advanced Drug Delivery Reviews 2017;108:25-38.
275.   Rosenblum D, Joshi N, Tao W, Karp JM, Peer D. Progress And Challenges Towards Targeted Delivery Of Cancer Therapeutics. Nature Communications 2018;9:1410.
276.   Hua S, De Matos MBC, Metselaar JM, Storm G. Current Trends And Challenges In The Clinical Translation Of Nanoparticulate Nanomedicines: Pathways For Translational Development And Commercialization. Frontiers In Pharmacology 2018;9:790.
277.   Golombek SK, May J-N, Theek B, Et Al. Tumor Targeting Via EPR: Strategies To Enhance Patient Responses. Advanced Drug Delivery Reviews 2018;130:17-38.
278.   Faria M, Björnmalm M, Thurecht KJ, Et Al. Minimum Information Reporting In Bio–Nano Experimental Literature. Nature Nanotechnology 2018;13:777-85.
279.   Leong HS, Butler KS, Brinker CJ, Et Al. On The Issue Of Transparency And Reproducibility In Nanomedicine. Nature Nanotechnology 2019;14:629-35.
280.   Presolski SI, Hong VP, Finn MG. Copper-Catalyzed Azide-Alkyne Click Chemistry For Bioconjugation. Curr Protoc Chem Biol 2011;3:153-62.

281.   Hong V, Presolski SI, Ma C, Finn MG. Analysis And Optimization Of Copper-Catalyzed Azide-Alkyne Cycloaddition For Bioconjugation. Angewandte Chemie International Edition 2009;48:9879-83.

282.   Hynds RE, Ben Aissa A, Gowers KHC, Et Al. Expansion Of Airway Basal Epithelial Cells From Primary Human Non-Small Cell Lung Cancer Tumors. International Journal Of Cancer 2018;143:160-6.

283.   Hynds RE, Butler CR, Janes SM, Giangreco A. Expansion Of Human Airway Basal Stem Cells And Their Differentiation As 3D Tracheospheres. Methods In Molecular Biology (Clifton, NJ) 2019;1576:43-53.

284.   Mascaux C, Tomasini P, Greillier L, Barlesi F. Personalised Medicine For Nonsmall Cell Lung Cancer. European Respiratory Review 2017;26:170066.

285.   Recondo G, Facchinetti F, Olaussen KA, Besse B, Friboulet L. Making The First Move In EGFR-Driven Or ALK-Driven NSCLC: First-Generation Or Next-Generation TKI? Nature Reviews Clinical Oncology 2018;15:694-708.

286.   Piccirillo MC, Daniele G, Di Maio M, Et Al. Vinorelbine For Non-Small Cell Lung Cancer. Expert Opinion On Drug Safety 2010;9:493-510.

287.   Park K, Wan-Teck Lim D, Okamoto I, Yang JC-H. First-Line Afatinib For The Treatment Of EGFR Mutation-Positive Non-Small-Cell Lung Cancer In The 'Real-World' Clinical Setting. Therapeutic Advances In Medical Oncology 2019;11:1758835919836374-.

288.   Minami S, Ogata Y, Yamamoto S, Komuta K. Combination Chemotherapy Of Gemcitabine And Vinorelbine For Pretreated Non-Small-Cell Lung Cancer: A Retrospective Study. Lung Cancer (Auckl) 2015;6:83-90.

289.   Sutiman N, Zhang Z, Tan EH, Et Al. Phase I Study Of Oral Vinorelbine In Combination With Erlotinib In Advanced Non-Small Cell Lung Cancer (NSCLC) Using Two Different Schedules. Plos One 2016;11:E0154316.

290.   Bahleda R, Varga A, Berge Y, Et Al. Phase I Open-Label Study Of Afatinib Plus Vinorelbine In Patients With Solid Tumours Overexpressing EGFR And/Or HER2. British Journal Of Cancer 2018;118:344-52.

291.   Tran S, Degiovanni P-J, Piel B, Rai P. Cancer Nanomedicine: A Review Of Recent Success In Drug Delivery. Clinical Translational Medicine 2017;6:44-.

292.   Singh AP, Biswas A, Shukla A, Maiti P. Targeted Therapy In Chronic Diseases Using Nanomaterial-Based Drug Delivery Vehicles. Signal Transduction And Targeted Therapy 2019;4:33.

293.   Fratoddi I, Venditti I, Cametti C, Russo MV. Gold Nanoparticles And Gold Nanoparticle-Conjugates For Delivery Of Therapeutic Molecules. Progress And Challenges. Journal Of Materials Chemistry B 2014;2:4204-20.

294.   Rezvantalab S, Drude NI, Moraveji MK, Et Al. PLGA-Based Nanoparticles In Cancer Treatment. Frontiers In Pharmacology 2018;9:1260.

295.   Huang X, El-Sayed IH, El-Sayed MA. Applications Of Gold Nanorods For Cancer Imaging And Photothermal Therapy. Methods In Molecular Biology (Clifton, NJ) 2010;624:343-57.

296.   Chen F, Ehlerding EB, Cai W. Theranostic Nanoparticles. Journal Of Nuclear Medicine 2014;55:1919-22.

297.   Wolfram J, Ferrari M. Clinical Cancer Nanomedicine. Nano Today 2019;25:85-98.

298.   Rostovtsev VV, Green LG, Fokin VV, Sharpless KB. A Stepwise Huisgen Cycloaddition Process: Copper(I)-Catalyzed Regioselective "Ligation" Of Azides And Terminal Alkynes. Angewandte Chemie International Edition 2002;41:2596-9.

299.   Liang L, Astruc D. The Copper(I)-Catalyzed Alkyne-Azide Cycloaddition (Cuaac) "Click" Reaction And Its Applications. An Overview. Coordination Chemistry Reviews 2011;255:2933-45.

300.   Budhian A, Siegel SJ, Winey KI. Haloperidol-Loaded PLGA Nanoparticles: Systematic Study Of Particle Size And Drug Content. International Journal Of Pharmaceutics 2007;336:367-75.

301.   Song X, Zhao Y, Wu W, Et Al. PLGA Nanoparticles Simultaneously Loaded With Vincristine Sulfate And Verapamil Hydrochloride: Systematic Study Of Particle Size And Drug Entrapment Efficiency. International Journal Of Pharmaceutics 2008;350:320-9.

302.   Keum CG, Noh YW, Baek JS, Et Al. Practical Preparation Procedures For Docetaxel-Loaded Nanoparticles Using Polylactic Acid-Co-Glycolic Acid. International Journal Of Nanomedicine 2011;6:2225-34.

303.   Betancourt T, Brown B, Brannon-Peppas L. Doxorubicin-Loaded PLGA Nanoparticles By Nanoprecipitation: Preparation, Characterization And In Vitro Evaluation. Nanomedicine (London, England) 2007;2:219-32.

304.   Meyer JD, Manning MC. Hydrophobic Ion Pairing: Altering The Solubility Properties Of Biomolecules. Pharmaceutical Research 1998;15:188-93.

305.   Gaudana R, Parenky A, Vaishya R, Samanta SK, Mitra AK. Development And Characterization Of Nanoparticulate Formulation Of A Water Soluble Prodrug Of Dexamethasone By HIP Complexation. Journal Of Microencapsulation 2011;28:10-20.

306.   Banala VT, Sharma S, Barnwal P, Et Al. Synchronized Ratiometric Codelivery Of Metformin And Topotecan Through Engineered Nanocarrier Facilitates In Vivo Synergistic Precision Levels At Tumor Site. Advanced Healthcare Materials 2018;7:E1800300.

307.   Song YH, Shin E, Wang H, Et Al. A Novel In Situ Hydrophobic Ion Pairing (HIP) Formulation Strategy For Clinical Product Selection Of A Nanoparticle Drug Delivery System. Journal Of Controlled Release 2016;229:106-19.

308.   Manzenrieder F, Luxenhofer R, Retzlaff M, Jordan R, Finn MG. Stabilization Of Virus-Like Particles With Poly(2-Oxazoline)S. Angewandte Chemie International Edition 2011;50:2601-5.

309.   Besanceney-Webler C, Jiang H, Zheng T, Et Al. Increasing The Efficacy Of Bioorthogonal Click Reactions For Bioconjugation: A Comparative Study. Angewandte Chemie International Edition 2011;50:8051-6.

310.   Lu J, Shi M, Shoichet MS. Click Chemistry Functionalized Polymeric Nanoparticles Target Corneal Epithelial Cells Through RGD-Cell Surface Receptors. Bioconjugate Chemistry 2009;20:87-94.

311.   Pokorski JK, Breitenkamp K, Liepold LO, Qazi S, Finn MG. Functional Virus-Based Polymer–Protein Nanoparticles By Atom Transfer Radical Polymerization. Journal Of The American Chemical Society 2011;133:9242-5.

312.   Wissner A, Overbeek E, Reich MF, Et Al. Synthesis And Structure-Activity Relationships Of 6,7-Disubstituted 4-Anilinoquinoline-3-Carbonitriles. The Design Of An Orally Active, Irreversible Inhibitor Of The Tyrosine Kinase Activity Of The Epidermal Growth Factor Receptor (EGFR) And The Human Epidermal Growth Factor Receptor-2 (HER-2). Journal Of Medicinal Chemistry 2003;46:49-63.

313.   Solca F, Dahl G, Zoephel A, Et Al. Target Binding Properties And Cellular Activity Of Afatinib (BIBW 2992), An Irreversible Erbb Family Blocker. The Journal Of Pharmacology And Experimental Therapeutics 2012;343:342-50.

314.   Tsou HR, Overbeek-Klumpers EG, Hallett WA, Et Al. Optimization Of 6,7-Disubstituted-4-(Arylamino)Quinoline-3-Carbonitriles As Orally Active, Irreversible Inhibitors Of Human Epidermal Growth Factor Receptor-2 Kinase Activity. Journal Of Medicinal Chemistry 2005;48:1107-31.

315.   Pisaneschi F, Nguyen QD, Shamsaei E, Et Al. Development Of A New Epidermal Growth Factor Receptor Positron Emission Tomography Imaging Agent Based On The 3-Cyanoquinoline Core: Synthesis And Biological Evaluation. Bioorganic & Medicinal Chemistry 2010;18:6634-45.

316.   Locatelli E, Comes Franchini M. Biodegradable PLGA-B-PEG Polymeric Nanoparticles: Synthesis, Properties, And Nanomedical Applications As Drug Delivery System. Journal Of Nanoparticle Research 2012;14:1316.

317.   Astete CE, Sabliov CM. Synthesis And Characterization Of PLGA Nanoparticles. Journal Of Biomaterials Science Polymer Edition 2006;17:247-89.

318.   Almoustafa HA, Alshawsh MA, Chik Z. Technical Aspects Of Preparing PEG-PLGA Nanoparticles As Carrier For Chemotherapeutic Agents By Nanoprecipitation Method. International Journal Of Pharmaceutics 2017;533:275-84.

319.   Wang Q, Wu P, Ren W, Et Al. Comparative Studies Of Salinomycin-Loaded Nanoparticles Prepared By Nanoprecipitation And Single Emulsion Method. Nanoscale Resesrch Letters 2014;9:351-.

320.   Liu J, Qiu Z, Wang S, Zhou L, Zhang S. A Modified Double-Emulsion Method For The Preparation Of Daunorubicin-Loaded Polymeric Nanoparticle With Enhanced In Vitro Anti-Tumor Activity. Biomedical Materials (Bristol, England) 2010;5:065002.

321.   Shalgunov V, Zaytseva-Zotova D, Zintchenko A, Et Al. Comprehensive Study Of The Drug Delivery Properties Of Poly(L-Lactide)-Poly(Ethylene Glycol) Nanoparticles In Rats And Tumor-Bearing Mice. Journal Of Controlled Release 2017;261:31-42.
322.   Drummond DC, Noble CO, Guo Z, Et Al. Improved Pharmacokinetics And Efficacy Of A Highly Stable Nanoliposomal Vinorelbine. The Journal Of Pharmacology And Experimental Therapeutics 2009;328:321-30.
323.   Ashton S, Song YH, Nolan J, Et Al. Aurora Kinase Inhibitor Nanoparticles Target Tumors With Favorable Therapeutic Index In Vivo. Science Translational Medicine 2016;8:325ra17.
324.   Hrkach J, Von Hoff D, Ali MM, Et Al. Preclinical Development And Clinical Translation Of A PSMA-Targeted Docetaxel Nanoparticle With A Differentiated Pharmacological Profile. Science Translational Medicine 2012;4:128ra39.
325.   Doane T, Burda C. Nanoparticle Mediated Non-Covalent Drug Delivery. Advanced Drug Delivery Reviews 2013;65:607-21.
326.   Kolb HC, Finn MG, Sharpless KB. Click Chemistry: Diverse Chemical Function From A Few Good Reactions. Angewandte Chemie International Edition 2001;40:2004-21.
327.   Hein CD, Liu X-M, Wang D. Click Chemistry, A Powerful Tool For Pharmaceutical Sciences. Pharmaceutical Research 2008;25:2216-30.
328.   Presolski SI, Hong V, Cho S-H, Finn MG. Tailored Ligand Acceleration Of The Cu-Catalyzed Azide−Alkyne Cycloaddition Reaction: Practical And Mechanistic Implications. Journal Of The American Chemical Society 2010;132:14570-6.
329.   Robertson JD, Rizzello L, Avila-Olias M, Et Al. Purification Of Nanoparticles By Size And Shape. Scientific Reports 2016;6:27494.
330.   Haldón E, Nicasio MC, Pérez PJ. Copper-Catalysed Azide–Alkyne Cycloadditions (Cuaac): An Update. Organic & Biomolecular Chemistry 2015;13:9528-50.
331.   Pickens CJ, Johnson SN, Pressnall MM, Leon MA, Berkland CJ. Practical Considerations, Challenges, And Limitations Of Bioconjugation Via Azide-Alkyne Cycloaddition. Bioconjugate Chemistry 2018;29:686-701.
332.   Kalia J, Raines RT. Advances In Bioconjugation. Current Organic Chemistry 2010;14:138-47.
333.   Zhang G, Yang Z, Lu W, Et Al. Influence Of Anchoring Ligands And Particle Size On The Colloidal Stability And In Vivo Biodistribution Of Polyethylene Glycol-Coated Gold Nanoparticles In Tumor-Xenografted Mice. Biomaterials 2009;30:1928-36.
334.   Coelho SC, Almeida GM, Pereira MC, Santos-Silva F, Coelho MA. Functionalized Gold Nanoparticles Improve Afatinib Delivery Into Cancer Cells. Expert Opinion On Drug Delivery 2016;13:133-41.
335.   Kluenker M, Mondeshki M, Nawaz Tahir M, Tremel W. Monitoring Thiol–Ligand Exchange On Au Nanoparticle Surfaces. Langmuir 2018;34:1700-10.
336.   Kalimuthu K, Lubin B-C, Bazylevich A, Et Al. Gold Nanoparticles Stabilize Peptide-Drug-Conjugates For Sustained Targeted Drug Delivery To Cancer Cells. Journal Of Nanobiotechnology 2018;16:34.
337.   Rahme K, Chen L, Hobbs RG, Morris MA, O'Driscoll C, Holmes JD. Pegylated Gold Nanoparticles: Polymer Quantification As A Function Of PEG Lengths And Nanoparticle Dimensions. RSC Advances 2013;3:6085-94.
338.   Brittain WJ, Minko S. A Structural Definition Of Polymer Brushes. Journal Of Polymer Science Part A: Polymer Chemistry 2007;45:3505-12.
339.   Jokerst JV, Lobovkina T, Zare RN, Gambhir SS. Nanoparticle Pegylation For Imaging And Therapy. Nanomedicine (London, England) 2011;6:715-28.
340.   Yang Q, Jones SW, Parker CL, Zamboni WC, Bear JE, Lai SK. Evading Immune Cell Uptake And Clearance Requires PEG Grafting At Densities Substantially Exceeding The Minimum For Brush Conformation. Molecular Pharmaceutics 2014;11:1250-8.
341.   Haiss W, Thanh NTK, Aveyard J, Fernig DG. Determination Of Size And Concentration Of Gold Nanoparticles From UV−Vis Spectra. Analytical Chemistry 2007;79:4215-21.
342.   Amendola V, Meneghetti M. Size Evaluation Of Gold Nanoparticles By UV−Vis Spectroscopy. The Journal Of Physical Chemistry C 2009;113:4277-85.

343. Xue Y, Li X, Li H, Zhang W. Quantifying Thiol–Gold Interactions Towards The Efficient Strength Control. Nature Communications 2014;5:4348.

344. Mani G, Kim S, Kim K. Development Of Folate-Thioglycolate-Gold Nanoconjugates By Using Citric Acid-PEG Branched Polymer For Inhibition Of MCF-7 Cancer Cell Proliferation. Biomacromolecules 2018;19:3257-67.

345. Huang X, Jain PK, El-Sayed IH, El-Sayed MA. Gold Nanoparticles: Interesting Optical Properties And Recent Applications In Cancer Diagnostics And Therapy. Nanomedicine 2007;2:681-93.

346. Huang X, El-Sayed MA. Gold Nanoparticles: Optical Properties And Implementations In Cancer Diagnosis And Photothermal Therapy. Journal Of Advanced Research 2010;1:13-28.

347. Riley RS, Day ES. Gold Nanoparticle-Mediated Photothermal Therapy: Applications And Opportunities For Multimodal Cancer Treatment. Nanomedicine And Nanobiotechnology 2017;9:10.1002/Wnan.449.

348. Love JC, Estroff LA, Kriebel JK, Nuzzo RG, Whitesides GM. Self-Assembled Monolayers Of Thiolates On Metals As A Form Of Nanotechnology. Chemical Reviews 2005;105:1103-70.

349. Tiwari PM, Vig K, Dennis VA, Singh SR. Functionalized Gold Nanoparticles And Their Biomedical Applications. Nanomaterials (Basel, Switzerland) 2011;1:31-63.

350. Shukla R, Bansal V, Chaudhary M, Basu A, Bhonde RR, Sastry M. Biocompatibility Of Gold Nanoparticles And Their Endocytotic Fate Inside The Cellular Compartment: A Microscopic Overview. Langmuir 2005;21:10644-54.

351. Giljohann DA, Seferos DS, Daniel WL, Massich MD, Patel PC, Mirkin CA. Gold Nanoparticles For Biology And Medicine. Angewandte Chemie International Edition 2010;49:3280-94.

352. Rana S, Bajaj A, Mout R, Rotello VM. Monolayer Coated Gold Nanoparticles For Delivery Applications. Advanced Drug Delivery Reviews 2012;64:200-16.

353. Giljohann DA, Seferos DS, Prigodich AE, Patel PC, Mirkin CA. Gene Regulation With Polyvalent Sirna-Nanoparticle Conjugates. Journal Of The American Chemical Society 2009;131:2072-3.

354. Tkachenko AG, Xie H, Coleman D, Et Al. Multifunctional Gold Nanoparticle−Peptide Complexes For Nuclear Targeting. Journal Of The American Chemical Society 2003;125:4700-1.

355. Kumar S, Aaron J, Sokolov K. Directional Conjugation Of Antibodies To Nanoparticles For Synthesis Of Multiplexed Optical Contrast Agents With Both Delivery And Targeting Moieties. Nature Protocols 2008;3:314.

356. Coluccia D, Figueiredo CA, Wu MY, Et Al. Enhancing Glioblastoma Treatment Using Cisplatin-Gold-Nanoparticle Conjugates And Targeted Delivery With Magnetic Resonance-Guided Focused Ultrasound. Nanomedicine: Nanotechnology, Biology And Medicine 2018;14:1137-48.

357. Chithrani BD, Ghazani AA, Chan WCW. Determining The Size And Shape Dependence Of Gold Nanoparticle Uptake Into Mammalian Cells. Nano Letters 2006;6:662-8.

358. Brown SD, Nativo P, Smith J-A, Et Al. Gold Nanoparticles For The Improved Anticancer Drug Delivery Of The Active Component Of Oxaliplatin. Journal Of The American Chemical Society 2010;132:4678-84.

359. Ding Y, Zhou Y-Y, Chen H, Et Al. The Performance Of Thiol-Terminated PEG-Paclitaxel-Conjugated Gold Nanoparticles. Biomaterials 2013;34:10217-27.

360. Kemp SJ, Thorley AJ, Gorelik J, Et Al. Immortalization Of Human Alveolar Epithelial Cells To Investigate Nanoparticle Uptake. American Journal Of Respiratory Cell And Molecular Biology 2008;39:591-7.

361. Cryer AM, Chan C, Eftychidou A, Et Al. Tyrosine Kinase Inhibitor Gold Nanoconjugates For The Treatment Of Non-Small Cell Lung Cancer. ACS Applied Materials & Interfaces 2019;11:16336-46.

362. Wuyts WA, Agostini C, Antoniou KM, Et Al. The Pathogenesis Of Pulmonary Fibrosis: A Moving Target. European Respiratory Journal 2013;41:1207.

363. Sharafkhaneh A, Hanania NA, Kim V. Pathogenesis Of Emphysema: From The Bench To The Bedside. Proceedings Of The American Thoracic Society 2008;5:475-7.

364. Mantovani A, Allavena P, Sica A, Balkwill F. Cancer-Related Inflammation. Nature 2008;454:436.

365.   Moldoveanu B, Otmishi P, Jani P, Et Al. Inflammatory Mechanisms In The Lung. Journal Of Inflammation Research 2008;2:1-11.

366.   Li Jje, Muralikrishnan S, Ng C-T, Yung L-YL, Bay B-H. Nanoparticle-Induced Pulmonary Toxicity. Experimental Biology And Medicine 2010;235:1025-33.

367.   Zhang S, Gao H, Bao G. Physical Principles Of Nanoparticle Cellular Endocytosis. ACS Nano 2015;9:8655-71.

368.   Han H-S, Lim S-N, An JY, Et Al. Detection Of EGFR Mutation Status In Lung Adenocarcinoma Specimens With Different Proportions Of Tumor Cells Using Two Methods Of Differential Sensitivity. Journal Of Thoracic Oncology 2012;7:355-64.

369.   Tkachenko AG, Xie H, Liu Y, Et Al. Cellular Trajectories Of Peptide-Modified Gold Particle Complexes: Comparison Of Nuclear Localization Signals And Peptide Transduction Domains. Bioconjugate Chemistry 2004;15:482-90.

370.   Kim D, Park S, Lee JH, Jeong YY, Jon S. Antibiofouling Polymer-Coated Gold Nanoparticles As A Contrast Agent For In Vivo X-Ray Computed Tomography Imaging. Journal Of The American Chemical Society 2007;129:7661-5.

371.   Li N, Li H, Su F, Li J, Ma X, Gong P. Relationship Between Epidermal Growth Factor Receptor (EGFR) Mutation And Serum Cyclooxygenase-2 Level, And The Synergistic Effect Of Celecoxib And Gefitinib On EGFR Expression In Non-Small Cell Lung Cancer Cells. International Journal Of Clinical And Experimental Pathology 2015;8:9010-20.

372.   Crapo JD, Barry BE, Gehr P, Bachofen M, Weibel ER. Cell Number And Cell Characteristics Of The Normal Human Lung. American Review Of Respiratory Disease 1982;126:332-7.

373.   Klein S, Petersen S, Taylor U, Rath D, Barcikowski S. Quantitative Visualization Of Colloidal And Intracellular Gold Nanoparticles By Confocal Microscopy. Society Of Photo-Optical Instrumentation Engineers 2010.

374.   Barenholz Y. Doxil® — The First FDA-Approved Nano-Drug: Lessons Learned. Journal Of Controlled Release 2012;160:117-34.

375.   Qi R, Gao Y, Tang Y, Et Al. PEG-Conjugated PAMAM Dendrimers Mediate Efficient Intramuscular Gene Expression. The AAPS Journal 2009;11:395-405.

376.   Ishida T, Ichihara M, Wang X, Et Al. Injection Of Pegylated Liposomes In Rats Elicits PEG-Specific Igm, Which Is Responsible For Rapid Elimination Of A Second Dose Of Pegylated Liposomes. Journal Of Controlled Release 2006;112:15-25.

377.   Kedmi R, Ben-Arie N, Peer D. The Systemic Toxicity Of Positively Charged Lipid Nanoparticles And The Role Of Toll-Like Receptor 4 In Immune Activation. Biomaterials 2010;31:6867-75.

378.   Longmire MR, Ogawa M, Choyke PL, Kobayashi H. Biologically Optimized Nanosized Molecules And Particles: More Than Just Size. Bioconjugate Chemistry 2011;22:993-1000.

379.   Choi HS, Liu W, Misra P, Et Al. Renal Clearance Of Quantum Dots. Nature Biotechnology 2007;25:1165-70.

380.   Sykes EA, Chen J, Zheng G, Chan WCW. Investigating The Impact Of Nanoparticle Size On Active And Passive Tumor Targeting Efficiency. ACS Nano 2014;8:5696-706.

381.   Tsoi KM, Macparland SA, Ma X-Z, Et Al. Mechanism Of Hard-Nanomaterial Clearance By The Liver. Nature Materials 2016;15:1212.

382.   Alexis F, Pridgen E, Molnar LK, Farokhzad OC. Factors Affecting The Clearance And Biodistribution Of Polymeric Nanoparticles. Molecular Pharmaceutics 2008;5:505-15.

383.   Kobayashi H, Watanabe R, Choyke PL. Improving Conventional Enhanced Permeability And Retention (EPR) Effects; What Is The Appropriate Target? Theranostics 2013;4:81-9.

384.   Kong G, Braun RD, Dewhirst MW. Hyperthermia Enables Tumor-Specific Nanoparticle Delivery: Effect Of Particle Size. Cancer Research 2000;60:4440-5.

385.   Abadeer NS, Murphy CJ. Recent Progress In Cancer Thermal Therapy Using Gold Nanoparticles. The Journal Of Physical Chemistry C 2016;120:4691-716.

386.   Von Maltzahn G, Park J-H, Lin KY, Et Al. Nanoparticles That Communicate In Vivo To Amplify Tumour Targeting. Nature Materials 2011;10:545.

387.   Conde J, Ambrosone A, Sanz V, Et Al. Design Of Multifunctional Gold Nanoparticles For In Vitro And In Vivo Gene Silencing. ACS Nano 2012;6:8316-24.

388.   Mustafaoglu N, Kiziltepe T, Bilgicer B. Site-Specific Conjugation Of An Antibody On A Gold Nanoparticle Surface For One-Step Diagnosis Of Prostate Specific Antigen With Dynamic Light Scattering. Nanoscale 2017;9:8684-94.

389.   Bartczak D, Kanaras AG. Preparation Of Peptide-Functionalized Gold Nanoparticles Using One Pot EDC/Sulfo-NHS Coupling. Langmuir 2011;27:10119-23.

390.   Stockert JC, Horobin RW, Colombo LL, Blázquez-Castro A. Tetrazolium Salts And Formazan Products In Cell Biology: Viability Assessment, Fluorescence Imaging, And Labeling Perspectives. Acta Histochemica 2018;120:159-67.

391.   Tsigelny IF, Wheler JJ, Greenberg JP, Et Al. Molecular Determinants Of Drug-Specific Sensitivity For Epidermal Growth Factor Receptor (EGFR) Exon 19 And 20 Mutants In Non-Small Cell Lung Cancer. Oncotarget 2015;6:6029-39.

392.   Zhang X, Gureasko J, Shen K, Cole PA, Kuriyan J. An Allosteric Mechanism For Activation Of The Kinase Domain Of Epidermal Growth Factor Receptor. Cell 2006;125:1137-49.

393.   Ono M, Hirata A, Kometani T, Et Al. Sensitivity To Gefitinib (Iressa, ZD1839) In Non-Small Cell Lung Cancer Cell Lines Correlates With Dependence On The Epidermal Growth Factor (EGF) Receptor/Extracellular Signal-Regulated Kinase 1/2 And EGF Receptor/Akt Pathway For Proliferation. Molecular Cancer Therapeutics 2004;3:465.

394.   Ninomiya T, Takigawa N, Ichihara E, Et Al. Afatinib Prolongs Survival Compared With Gefitinib In An Epidermal Growth Factor Receptor-Driven Lung Cancer Model. Molecular Cancer Therapeutics 2013;12:589.

395.   Gazdar AF. Activating And Resistance Mutations Of EGFR In Non-Small-Cell Lung Cancer: Role In Clinical Response To EGFR Tyrosine Kinase Inhibitors. Oncogene 2009;28 Suppl 1:S24-S31.

396.   Alkilany AM, Murphy CJ. Toxicity And Cellular Uptake Of Gold Nanoparticles: What We Have Learned So Far? Journal Of Nanoparticle Research 2010;12:2313-33.

397.   Suzawa K, Toyooka S, Sakaguchi M, Et Al. Antitumor Effect Of Afatinib, As A Human Epidermal Growth Factor Receptor 2-Targeted Therapy, In Lung Cancers Harboring HER2 Oncogene Alterations. Cancer Science 2016;107:45-52.

398.   Dreaden EC, Mwakwari SC, Sodji QH, Oyelere AK, El-Sayed MA. Tamoxifen-Poly(Ethylene Glycol)-Thiol Gold Nanoparticle Conjugates: Enhanced Potency And Selective Delivery For Breast Cancer Treatment. Bioconjugate Chemistry 2009;20:2247-53.

399.   Wang S-Q, Liu S-T, Zhao B-X, Et Al. Afatinib Reverses Multidrug Resistance In Ovarian Cancer Via Dually Inhibiting ATP Binding Cassette Subfamily B Member 1. Oncotarget 2015;6:26142-60.

400.   Elsaesser A, Howard CV. Toxicology Of Nanoparticles. Advanced Drug Delivery Reviews 2012;64:129-37.

401.   Hayes A, Dechsakulthorn F. Nanoparticles: A Review Of Particle Toxicology Following Inhalation Exposure AU - Bakand, Shahnaz. Inhalation Toxicology 2012;24:125-35.

402.   Swain RJ, Kemp SJ, Goldstraw P, Tetley TD, Stevens MM. Assessment Of Cell Line Models Of Primary Human Cells By Raman Spectral Phenotyping. Biophysical Journal 2010;98:1703-11.

403.   Thorley AJ, Grandolfo D, Lim E, Goldstraw P, Young A, Tetley TD. Innate Immune Responses To Bacterial Ligands In The Peripheral Human Lung--Role Of Alveolar Epithelial TLR Expression And Signalling. Plos One 2011;6:E21827-E.

404.   Gurule NJ, Heasley LE. Linking Tyrosine Kinase Inhibitor-Mediated Inflammation With Normal Epithelial Cell Homeostasis And Tumor Therapeutic Responses. Cancer Drug Resistance (Alhambra, Calif) 2018;1:118-25.

405.   Rincon M, Irvin CG. Role Of IL-6 In Asthma And Other Inflammatory Pulmonary Diseases. International Journal Of Biological Sciences 2012;8:1281-90.

406.   Mukaida N. Pathophysiological Roles Of Interleukin-8/CXCL8 In Pulmonary Diseases. American Journal Of Physiology-Lung Cellular And Molecular Physiology 2003;284:L566-L77.

407.   Sansone P, Bromberg J. Targeting The Interleukin-6/Jak/Stat Pathway In Human Malignancies. Journal Of Clinical Oncology 2012;30:1005-14.

408.   Qu Z, Sun F, Zhou J, Li L, Shapiro SD, Xiao G. Interleukin-6 Prevents The Initiation But Enhances The Progression Of Lung Cancer. Cancer Research 2015;75:3209-15.

409.   Harada D, Takigawa N, Kiura K. The Role Of STAT3 In Non-Small Cell Lung Cancer. Cancers (Basel) 2014;6:708-22.

410.   Wang Y, Van Boxel-Dezaire AHH, Cheon H, Yang J, Stark GR. STAT3 Activation In Response To IL-6 Is Prolonged By The Binding Of IL-6 Receptor To EGF Receptor. Proceedings Of The National Academy Of Sciences 2013;110:16975-80.

411.   Levy R, Shaheen U, Cesbron Y, See V. Gold Nanoparticles Delivery In Mammalian Live Cells: A Critical Review. Nano Reviews 2010;1.

412.   Liu M, Li Q, Liang L, Et Al. Real-Time Visualization Of Clustering And Intracellular Transport Of Gold Nanoparticles By Correlative Imaging. Nature Communications 2017;8:15646-.

413.   Canton I, Battaglia G. Endocytosis At The Nanoscale. Chemical Society Reviews 2012;41:2718-39.

414.   Yue J, Feliciano TJ, Li W, Lee A, Odom TW. Gold Nanoparticle Size And Shape Effects On Cellular Uptake And Intracellular Distribution Of Sirna Nanoconstructs. Bioconjugate Chemistry 2017;28:1791-800.

415.   Kumari A, Yadav SK, Yadav SC. Biodegradable Polymeric Nanoparticles Based Drug Delivery Systems. Colloids And Surfaces B: Biointerfaces 2010;75:1-18.

416.   Elsabahy M, Wooley KL. Design Of Polymeric Nanoparticles For Biomedical Delivery Applications. Chemical Society Reviews 2012;41:2545-61.

417.   Dinarvand R, Sepehri N, Manoochehri S, Rouhani H, Atyabi F. Polylactide-Co-Glycolide Nanoparticles For Controlled Delivery Of Anticancer Agents. International Journal Of Nanomedicine 2011;6:877-95.

418.   Liu X, Yang Y, Urban MW. Stimuli-Responsive Polymeric Nanoparticles. Macromolecular Rapid Communications 2017;38:1700030.

419.   Betancourt T, Brown B, Brannon-Peppas L. Doxorubicin-Loaded PLGA Nanoparticles By Nanoprecipitation: Preparation, Characterization And In Vitro Evaluation. Nanomedicine 2007;2:219-32.

420.   Simpson RL, Wiria FE, Amis AA, Et Al. Development Of A 95/5 Poly(L-Lactide-Co-Glycolide)/Hydroxylapatite And B-Tricalcium Phosphate Scaffold As Bone Replacement Material Via Selective Laser Sintering. Journal Of Biomedical Materials Research Part B: Applied Biomaterials 2008;84B:17-25.

421.   Kumbar SG, Nukavarapu SP, James R, Nair LS, Laurencin CT. Electrospun Poly(Lactic Acid-Co-Glycolic Acid) Scaffolds For Skin Tissue Engineering. Biomaterials 2008;29:4100-7.

422.   Lee M, Wu BM, Dunn JCY. Effect Of Scaffold Architecture And Pore Size On Smooth Muscle Cell Growth. Journal Of Biomedical Materials Research Part A 2008;87A:1010-6.

423.   Conn J, Oyasu R, Welsh M, Beal JM. Vicryl (Polyglactin 910) Synthetic Absorbable Sutures. The American Journal Of Surgery 1974;128:19-23.

424.   Kitchell JP, Wise DL. Poly(Lactic/Glycolic Acid) Biodegradable Drug-Polymer Matrix Systems. Methods In Enzymology 1985;112:436-48.

425.   Guerin C, Olivi A, Weingart JD, Lawson HC, Brem H. Recent Advances In Brain Tumor Therapy: Local Intracerebral Drug Delivery By Polymers. Investigational New Drugs 2004;22:27-37.

426.   Nixon JR. Biodegradable Poly(Lactic Acid) And Poly(Lactide-Co-Glycolide) Microcapsules: Problems Associated With Preparative Techniques And Release Properties AU - Jalil, R. Journal Of Microencapsulation 1990;7:297-325.

427.   Jain RA. The Manufacturing Techniques Of Various Drug Loaded Biodegradable Poly(Lactide-Co-Glycolide) (PLGA) Devices. Biomaterials 2000;21:2475-90.

428.   Bala I, Hariharan S, Kumar MN. PLGA Nanoparticles In Drug Delivery: The State Of The Art. Critical Reviews In Therapeutic Drug Carrier Systems 2004;21:387-422.

429.   Acharya S, Sahoo SK. PLGA Nanoparticles Containing Various Anticancer Agents And Tumour Delivery By EPR Effect. Advanced Drug Delivery Reviews 2011;63:170-83.

430.   Jokerst JV, Lobovkina T, Zare RN, Gambhir SS. Nanoparticle Pegylation For Imaging And Therapy. Nanomedicine 2011;6:715-28.

431.   Pasut G, Veronese FM. State Of The Art In Pegylation: The Great Versatility Achieved After Forty Years Of Research. Journal Of Controlled Release 2012;161:461-72.

432.   Kolate A, Baradia D, Patil S, Vhora I, Kore G, Misra A. PEG — A Versatile Conjugating Ligand For Drugs And Drug Delivery Systems. Journal Of Controlled Release 2014;192:67-81.

433.   Zhang K, Tang X, Zhang J, Et Al. PEG–PLGA Copolymers: Their Structure And Structure-Influenced Drug Delivery Applications. Journal Of Controlled Release 2014;183:77-86.

434.   Dhar S, Kolishetti N, Lippard SJ, Farokhzad OC. Targeted Delivery Of A Cisplatin Prodrug For Safer And More Effective Prostate Cancer Therapy In Vivo. Proceedings Of The Natational Academy Of Sciences 2011;108:1850-5.

435.   Aggarwal S, Gupta S, Pabla D, Murthy RS. Gemcitabine-Loaded PLGA-PEG Immunonanoparticles For Targeted Chemotherapy Of Pancreatic Cancer. Cancer Nanotechnology 2013;4:145-57.

436.   Li S, Shen Q, He H, Zhang Y. Enhanced Cellular Uptake Of Folic Acid–Conjugated PLGA–PEG Nanoparticles Loaded With Vincristine Sulfate In Human Breast Cancer AU - Chen, Jianian. Drug Development And Industrial Pharmacy 2011;37:1339-46.

437.   You J, Wan F, De Cui F, Sun Y, Du YZ, Hu FQ. Preparation And Characteristic Of Vinorelbine Bitartrate-Loaded Solid Lipid Nanoparticles. International Journal Of Pharmaceutics 2007;343:270-6.

438.   Zhang H, Wang ZY, Gong W, Li ZP, Mei XG, Lv WL. Development And Characteristics Of Temperature-Sensitive Liposomes For Vinorelbine Bitartrate. International Journal Of Pharmaceutics 2011;414:56-62.

439.   Drummond DC, Meyer O, Hong K, Kirpotin DB, Papahadjopoulos D. Optimizing Liposomes For Delivery Of Chemotherapeutic Agents To Solid Tumors. Pharmacological Reviews 1999;51:691-743.

440.   Amrutiya J, Bhatt P, Javia A, Jain M, Misra A. Targeted Delivery Of Monoclonal Antibody Conjugated Docetaxel Loaded PLGA Nanoparticles Into EGFR Overexpressed Lung Tumour Cells AU - Patel, Jitendrakumar. Journal Of Microencapsulation 2018;35:204-17.

441.   Lee MJ, Ye AS, Gardino AK, Et Al. Sequential Application Of Anticancer Drugs Enhances Cell Death By Rewiring Apoptotic Signaling Networks. Cell 2012;149:780-94.

442.   Morton SW, Lee MJ, Deng ZJ, Et Al. A Nanoparticle-Based Combination Chemotherapy Delivery System For Enhanced Tumor Killing By Dynamic Rewiring Of Signaling Pathways. Science Signaling 2014;7:Ra44.

443.   Capasso A. Vinorelbine In Cancer Therapy. Current Drug Targets 2012;13:1065-71.

444.   Chen G, Kronenberger P, Teugels E, Umelo IA, De Grève J. Targeting The Epidermal Growth Factor Receptor In Non-Small Cell Lung Cancer Cells: The Effect Of Combining RNA Interference With Tyrosine Kinase Inhibitors Or Cetuximab. BMC Medicine 2012;10:28.

445.   Park K, Tan EH, O'Byrne K, Et Al. Afatinib Versus Gefitinib As First-Line Treatment Of Patients With EGFR Mutation-Positive Non-Small-Cell Lung Cancer (LUX-Lung 7): A Phase 2B, Open-Label, Randomised Controlled Trial. The Lancet Oncology 2016;17:577-89.

446.   Sequist LV, Yang JC, Yamamoto N, Et Al. Phase III Study Of Afatinib Or Cisplatin Plus Pemetrexed In Patients With Metastatic Lung Adenocarcinoma With EGFR Mutations. Journal Of Clinical Oncology 2013;31:3327-34.

447.   Stamos J, Sliwkowski MX, Eigenbrot C. Structure Of The Epidermal Growth Factor Receptor Kinase Domain Alone And In Complex With A 4-Anilinoquinazoline Inhibitor. Journal Of Biological Chemistry 2002;277:46265-72.

448.   Rittenberg CN, Gralla RJ, Rehmeyer TA. Assessing And Managing Venous Irritation Associated With Vinorelbine Tartrate (Navelbine). Oncology Nursing Forum 1995;22:707-10.

449.   Lemmon MA, Schlessinger J, Ferguson KM. The EGFR Family: Not So Prototypical Receptor Tyrosine Kinases. Cold Spring Harbor Perspectives In Biology 2014;6:A020768.

450.   Lunov O, Syrovets T, Loos C, Et Al. Differential Uptake Of Functionalized Polystyrene Nanoparticles By Human Macrophages And A Monocytic Cell Line. ACS Nano 2011;5:1657-69.

451.   Lee J, Twomey M, Machado C, Et Al. Caveolae-Mediated Endocytosis Of Conjugated Polymer Nanoparticles. Macromolecular Bioscience 2013;13:913-20.

452.   Gentile P, Chiono V, Carmagnola I, Hatton PV. An Overview Of Poly(Lactic-Co-Glycolic) Acid (PLGA)-Based Biomaterials For Bone Tissue Engineering. International Journal Of Molecular Sciences 2014;15:3640-59.

453.   Nakanishi T, Menju T, Nishikawa S, Et Al. The Synergistic Role Of ATP-Dependent Drug Efflux Pump And Focal Adhesion Signaling Pathways In Vinorelbine Resistance In Lung Cancer. Cancer Medicine 2018;7:408-19.

454.   Bessho Y, Oguri T, Ozasa H, Et Al. ABCC10/MRP7 Is Associated With Vinorelbine Resistance In Non-Small Cell Lung Cancer. Oncology Reports 2009;21:263-8.

455. Stuckler D, Singhal J, Singhal SS, Yadav S, Awasthi YC, Awasthi S. RLIP76 Transports Vinorelbine And Mediates Drug Resistance In Non–Small Cell Lung Cancer. Cancer Research 2005;65:991-8.

456. Cartiera MS, Johnson KM, Rajendran V, Caplan MJ, Saltzman WM. The Uptake And Intracellular Fate Of PLGA Nanoparticles In Epithelial Cells. Biomaterials 2009;30:2790-8.

457. Calzoni E, Cesaretti A, Polchi A, Di Michele A, Tancini B, Emiliani C. Biocompatible Polymer Nanoparticles For Drug Delivery Applications In Cancer And Neurodegenerative Disorder Therapies. Journal Of Functional Biomaterials 2019;10.

458. Porter AG, Janicke RU. Emerging Roles Of Caspase-3 In Apoptosis. Cell Death And Differentiation 1999;6:99-104.

459. Rhun YL, Kirkland JB, Shah GM. Cellular Responses To DNA Damage In The Absence Of Poly(ADP-Ribose) Polymerase. Biochemical And Biophysical Research Communications 1998;245:1-10.

460. Jordan MA, Kamath K. How Do Microtubule-Targeted Drugs Work? An Overview. Current Cancer Drug Targets 2007;7:730-42.

461. Rieger AM, Hall BE, Luong Le T, Schang LM, Barreda DR. Conventional Apoptosis Assays Using Propidium Iodide Generate A Significant Number Of False Positives That Prevent Accurate Assessment Of Cell Death. Journal Of Immunological Methods 2010;358:81-92.

462. Demchenko AP. Beyond Annexin V: Fluorescence Response Of Cellular Membranes To Apoptosis. Cytotechnology 2013;65:157-72.

463. Vakkila J, Lotze MT. Inflammation And Necrosis Promote Tumour Growth. Nature Reviews Immunology 2004;4:641.

464. Karsch-Bluman A, Feiglin A, Arbib E, Et Al. Tissue Necrosis And Its Role In Cancer Progression. Oncogene 2019;38:1920-35.

465. Pflanz S, Brookman-Amissah S, Roigas J, Kendel F, Hoschke B, May M. Impact Of Macroscopic Tumour Necrosis To Predict Survival Of Patients With Surgically Resected Renal Cell Carcinoma. Scandinavian Journal Of Urology And Nephrology 2008;42:507-13.

466. Pichler M, Hutterer GC, Chromecki TF, Et Al. Histologic Tumor Necrosis Is An Independent Prognostic Indicator For Clear Cell And Papillary Renal Cell Carcinoma. American Journal Of Clinical Pathology 2012;137:283-9.

467. Biziota E, Briasoulis E, Mavroeidis L, Marselos M, Harris AL, Pappas P. Cellular And Molecular Effects Of Metronomic Vinorelbine And 4-O-Deacetylvinorelbine On Human Umbilical Vein Endothelial Cells. Anti-Cancer Drugs 2016;27:216-24.

468. Mai J, Virtue A, Shen J, Wang H, Yang X-F. An Evolving New Paradigm: Endothelial Cells – Conditional Innate Immune Cells. Journal Of Hematology & Oncology 2013;6:61.

469. Makó V, Czúcz J, Weiszhár Z, Et Al. Proinflammatory Activation Pattern Of Human Umbilical Vein Endothelial Cells Induced By IL-1β, TNF-A, And LPS. Cytometry Part A 2010;77A:962-70.

470. Kaplanski G, Teysseire N, Farnarier C, Et Al. IL-6 And IL-8 Production From Cultured Human Endothelial Cells Stimulated By Infection With Rickettsia Conorii Via A Cell-Associated IL-1 Alpha-Dependent Pathway. The Journal Of Clinical Investigation 1995;96:2839-44.

471. Gruys E, Toussaint MJM, Niewold TA, Koopmans SJ. Acute Phase Reaction And Acute Phase Proteins. Journal Of Zhejiang University Science B 2005;6:1045-56.

472. Puhlmann M, Weinreich DM, Farma JM, Carroll NM, Turner EM, Alexander HR, Jr. Interleukin-1beta Induced Vascular Permeability Is Dependent On Induction Of Endothelial Tissue Factor (TF) Activity. Journal Of Translational Medicine 2005;3:37.

473. Teijaro JR, Walsh KB, Cahalan S, Et Al. Endothelial Cells Are Central Orchestrators Of Cytokine Amplification During Influenza Virus Infection. Cell 2011;146:980-91.

474. Voigt J, Christensen J, Shastri VP. Differential Uptake Of Nanoparticles By Endothelial Cells Through Polyelectrolytes With Affinity For Caveolae. Proceedings Of The National Academy Of Sciences 2014;111:2942.

475. Cao Y, Gong Y, Liu L, Et Al. The Use Of Human Umbilical Vein Endothelial Cells (Huvecs) As An In Vitro Model To Assess The Toxicity Of Nanoparticles To Endothelium: A Review. Journal Of Applied Toxicology 2017;37:1359-69.
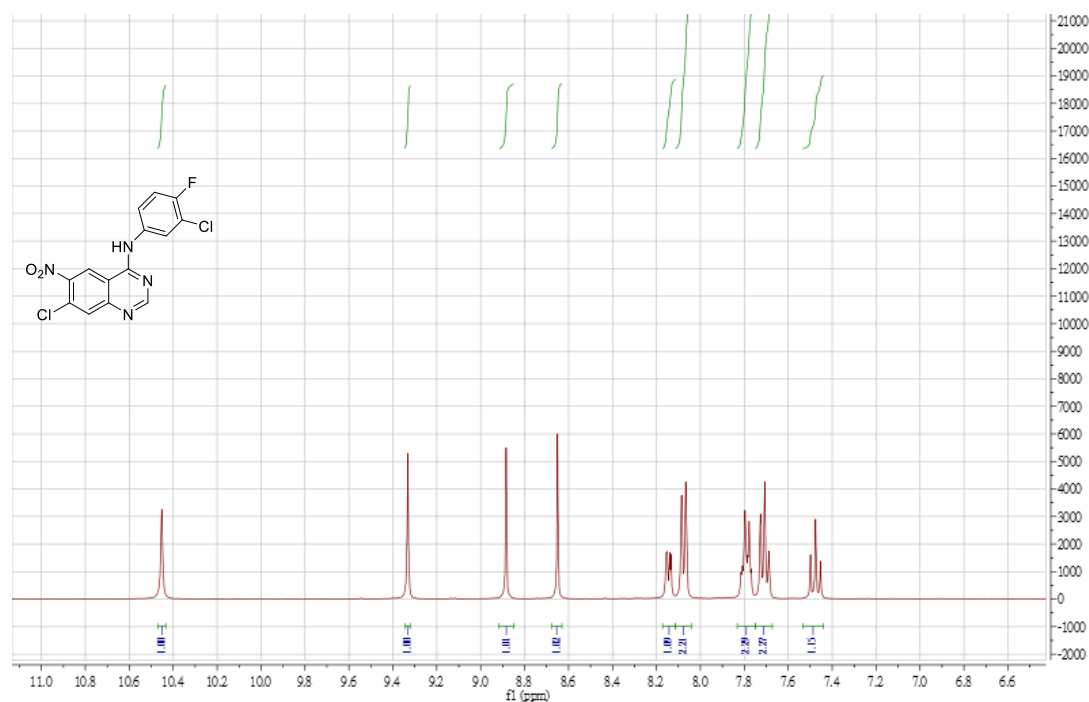
476.	Negendank W, Shaller C. Temperature-Dependence Of ATP Level, Organic Phosphate Production And Na,K-Atpase In Human Lymphocytes. Physiological Chemistry And Physics 1982;14:513-8.

477.	Roiter Y, Ornatska M, Rammohan AR, Balakrishnan J, Heine DR, Minko S. Interaction Of Nanoparticles With Lipid Membrane. Nano Letters 2008;8:941-4.

478.	Wang T, Bai J, Jiang X, Nienhaus GU. Cellular Uptake Of Nanoparticles By Membrane Penetration: A Study Combining Confocal Microscopy With FTIR Spectroelectrochemistry. ACS Nano 2012;6:1251-9.

479.	Rejman J, Oberle V, Zuhorn IS, Hoekstra D. Size-Dependent Internalization Of Particles Via The Pathways Of Clathrin- And Caveolae-Mediated Endocytosis. The Biochemical Journal 2004;377:159-69.

480.	Yan Y, Liu L, Xiong H, Et Al. Functional Polyesters Enable Selective Sirna Delivery To Lung Cancer Over Matched Normal Cells. Proceedings Of The National Academy Of Sciences 2016;113:E5702-E10.

481.	Zhu M, Nie G, Meng H, Xia T, Nel A, Zhao Y. Physicochemical Properties Determine Nanomaterial Cellular Uptake, Transport, And Fate. Accounts Of Chemical Research 2013;46:622-31.

482.	Ogiso T, Iwaki M, Mori K. Fluidity Of Human Erythrocyte Membrane And Effect Of Chlorpromazine On Fluidity And Phase Separation Of Membrane. Biochimica Et Biophysica Acta 1981;649:325-35.

483.	Gu C, Yaddanapudi S, Weins A, Et Al. Direct Dynamin-Actin Interactions Regulate The Actin Cytoskeleton. The EMBO Journal 2010;29:3593-606.

484.	Fretz M, Jin J, Conibere R, Et Al. Effects Of Na+/H+ Exchanger Inhibitors On Subcellular Localisation Of Endocytic Organelles And Intracellular Dynamics Of Protein Transduction Domains HIV-TAT Peptide And Octaarginine. Journal Of Controlled Release 2006;116:247-54.

485.	Morteza Hasanzadeh K, Frances JH, Nicolas HV. Insights Into Cellular Uptake Of Nanoparticles. Current Drug Delivery 2015;12:63-77.

486.	Royle SJ. The Cellular Functions Of Clathrin. Cellular And Molecular Life Sciences 2006;63:1823-32.

487.	Wettey FR, Hawkins SFC, Stewart A, Luzio JP, Howard JC, Jackson AP. Controlled Elimination Of Clathrin Heavy-Chain Expression In DT40 Lymphocytes. Science 2002;297:1521.

488.	Kettler K, Veltman K, Van De Meent D, Van Wezel A, Hendriks AJ. Cellular Uptake Of Nanoparticles As Determined By Particle Properties, Experimental Conditions, And Cell Type. Environmental Toxicology And Chemistry 2014;33:481-92.

489.	Kodack DP, Farago AF, Dastur A, Et Al. Primary Patient-Derived Cancer Cells And Their Potential For Personalized Cancer Patient Care. Cell Reports 2017;21:3298-309.

490.	Kim K-T, Lee HW, Lee H-O, Et Al. Single-Cell Mrna Sequencing Identifies Subclonal Heterogeneity In Anti-Cancer Drug Responses Of Lung Adenocarcinoma Cells. Genome Biology 2015;16:127-.

491.	Lee J-K, Liu Z, Sa JK, Et Al. Pharmacogenomic Landscape Of Patient-Derived Tumor Cells Informs Precision Oncology Therapy. Nature Genetics 2018;50:1399-411.

492.	Hynds RE, Butler CR, Janes SM, Giangreco A. Expansion Of Human Airway Basal Stem Cells And Their Differentiation As 3D Tracheospheres. Methods In Molecular Biology (Clifton, NJ) 2016.

493.	Welsch ME, Kaplan A, Chambers JM, Et Al. Multivalent Small-Molecule Pan-RAS Inhibitors. Cell 2017;168:878-89.E29.

494.	Cox AD, Fesik SW, Kimmelman AC, Luo J, Der CJ. Drugging The Undruggable RAS: Mission Possible? Nature Reviews Drug Discovery 2014;13:828-51.

495.	Mao C, Qiu LX, Liao RY, Et Al. KRAS Mutations And Resistance To EGFR-Tkis Treatment In Patients With Non-Small Cell Lung Cancer: A Meta-Analysis Of 22 Studies. Lung Cancer (Amsterdam, Netherlands) 2010;69:272-8.

496.	Moll HP, Pranz K, Musteanu M, Et Al. Afatinib Restrains K-RAS–Driven Lung Tumorigenesis. Science Translational Medicine 2018;10:Eaao2301.

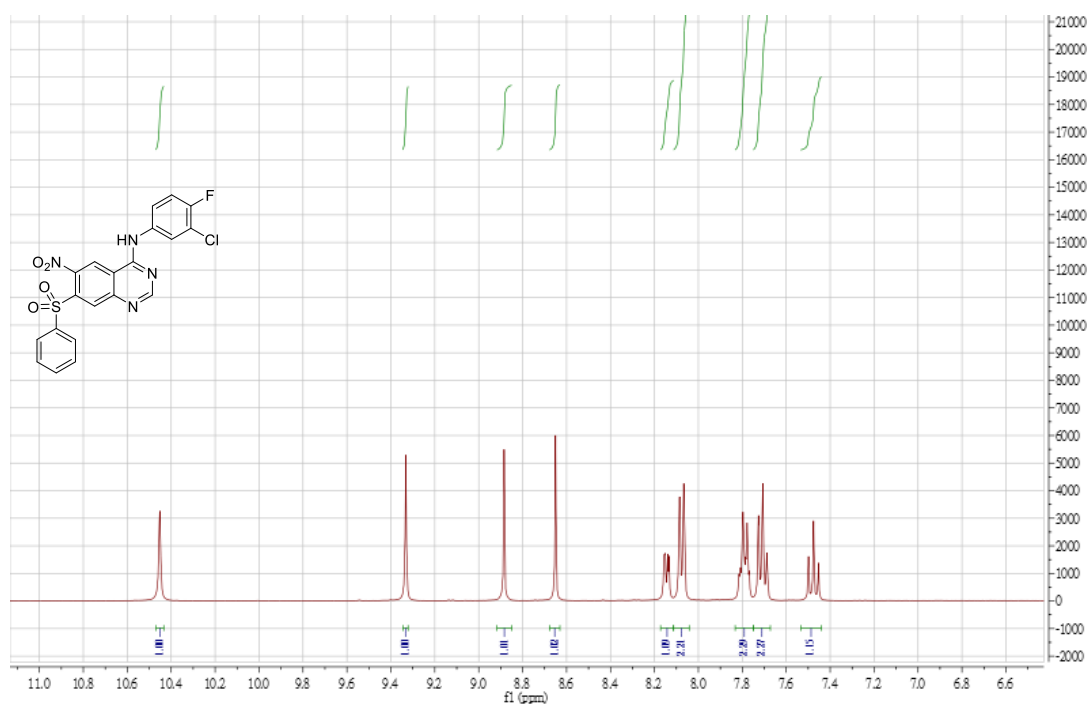497.	Cheon DJ, Orsulic S. Mouse Models Of Cancer. Annual Review Of Pathology 2011;6:95-119.

498. Cekanova M, Rathore K. Animal Models And Therapeutic Molecular Targets Of Cancer: Utility And Limitations. Drug Design, Development And Therapy 2014;8:1911-21.

499. Mak IW, Evaniew N, Ghert M. Lost In Translation: Animal Models And Clinical Trials In Cancer Treatment. American Journal Of Translational Research 2014;6:114-8.

500. Jackson SJ, Thomas GJ. Human Tissue Models In Cancer Research: Looking Beyond The Mouse. Diseasemmodels & Mechanisms 2017;10:939-42.

501. Hassan MS, Awasthi N, Li J, Schwarz MA, Schwarz RE, Von Holzen U. A Novel Intraperitoneal Metastatic Xenograft Mouse Model For Survival Outcome Assessment Of Esophageal Adenocarcinoma. Plos One 2017;12:E0171824-E.

502. Ji X, Chen S, Guo Y, Et Al. Establishment And Evaluation Of Four Different Types Of Patient-Derived Xenograft Models. Cancer Cell International 2017;17:122-.

503. Danhier F. To Exploit The Tumor Microenvironment: Since The EPR Effect Fails In The Clinic, What Is The Future Of Nanomedicine? Journal Of Controlled Release 2016;244:108-21.

504. Perry JL, Reuter KG, Luft JC, Pecot CV, Zamboni W, Desimone JM. Mediating Passive Tumor Accumulation Through Particle Size, Tumor Type, And Location. Nano Letters 2017;17:2879-86.

505. Sahu A, Choi WI, Tae G. Recent Progress In The Design Of Hypoxia-Specific Nano Drug Delivery Systems For Cancer Therapy. Advanced Therapeutics 2018;1:1800026.

506. Ebeid K, Meng X, Thiel KW, Et Al. Synthetically Lethal Nanoparticles For Treatment Of Endometrial Cancer. Nature Nanotechnology 2018;13:72-81.

507. Meng F, Wang J, Ping Q, Yeo Y. Quantitative Assessment Of Nanoparticle Biodistribution By Fluorescence Imaging, Revisited. ACS Nano 2018;12:6458-68.

508. Song W, Tang Z, Zhang D, Li M, Gu J, Chen X. A Cooperative Polymeric Platform For Tumor-Targeted Drug Delivery. Chemical Science 2016;7:728-36.

509. Thambi T, Deepagan VG, Yoon HY, Et Al. Hypoxia-Responsive Polymeric Nanoparticles For Tumor-Targeted Drug Delivery. Biomaterials 2014;35:1735-43.

510. Wang Y, Xie Y, Li J, Et Al. Tumor-Penetrating Nanoparticles For Enhanced Anticancer Activity Of Combined Photodynamic And Hypoxia-Activated Therapy. ACS Nano 2017;11:2227-38.

511. Shen S, Wu Y, Li K, Et Al. Versatile Hyaluronic Acid Modified AQ4N-Cu(II)-Gossypol Infinite Coordination Polymer Nanoparticles: Multiple Tumor Targeting, Highly Efficient Synergistic Chemotherapy, And Real-Time Self-Monitoring. Biomaterials 2018;154:197-212.

512. Tummala S, Gowthamarajan K, Satish Kumar MN, Wadhwani A. Oxaliplatin Immuno Hybrid Nanoparticles For Active Targeting: An Approach For Enhanced Apoptotic Activity And Drug Delivery To Colorectal Tumors. Drug Delivery 2016;23:1773-87.

513. Cong Y, Xiao H, Xiong H, Et Al. Dual Drug Backboned Shattering Polymeric Theranostic Nanomedicine For Synergistic Eradication Of Patient-Derived Lung Cancer. Advanced Materials 2018;30:1706220.

514. Pi F, Binzel DW, Lee TJ, Et Al. Nanoparticle Orientation To Control RNA Loading And Ligand Display On Extracellular Vesicles For Cancer Regression. Nature Nanotechnology 2018;13:82-9.

515. Dobrolecki LE, Airhart SD, Alferez DG, Et Al. Patient-Derived Xenograft (PDX) Models In Basic And Translational Breast Cancer Research. Cancer Metastasis Reviews 2016;35:547-73.

516. Jung J, Seol HS, Chang S. The Generation And Application Of Patient-Derived Xenograft Model For Cancer Research. Cancer Research And Treatment 2018;50:1-10.

517. Aston WJ, Hope DE, Nowak AK, Robinson BW, Lake RA, Lesterhuis WJ. A Systematic Investigation Of The Maximum Tolerated Dose Of Cytotoxic Chemotherapy With And Without Supportive Care In Mice. BMC Cancer 2017;17:684.

518. Serin D, Verrill M, Jones A, Et Al. Vinorelbine Alternating Oral And Intravenous Plus Epirubicin In First-Line Therapy Of Metastatic Breast Cancer: Results Of A Multicentre Phase II Study. British Journal Of Cancer 2005;92:1989-96.

519. Tu Y, Ouyang Y, Xu S, Et Al. Design, Synthesis, And Docking Studies Of Afatinib Analogs Bearing Cinnamamide Moiety As Potent EGFR Inhibitors. Bioorganic & Medicinal Chemistry 2016;24:1495-503.

520. Von Maltzahn G, Ren Y, Park JH, Et Al. In Vivo Tumor Cell Targeting With "Click" Nanoparticles. Bioconjugate Chemistry 2008;19:1570-8.
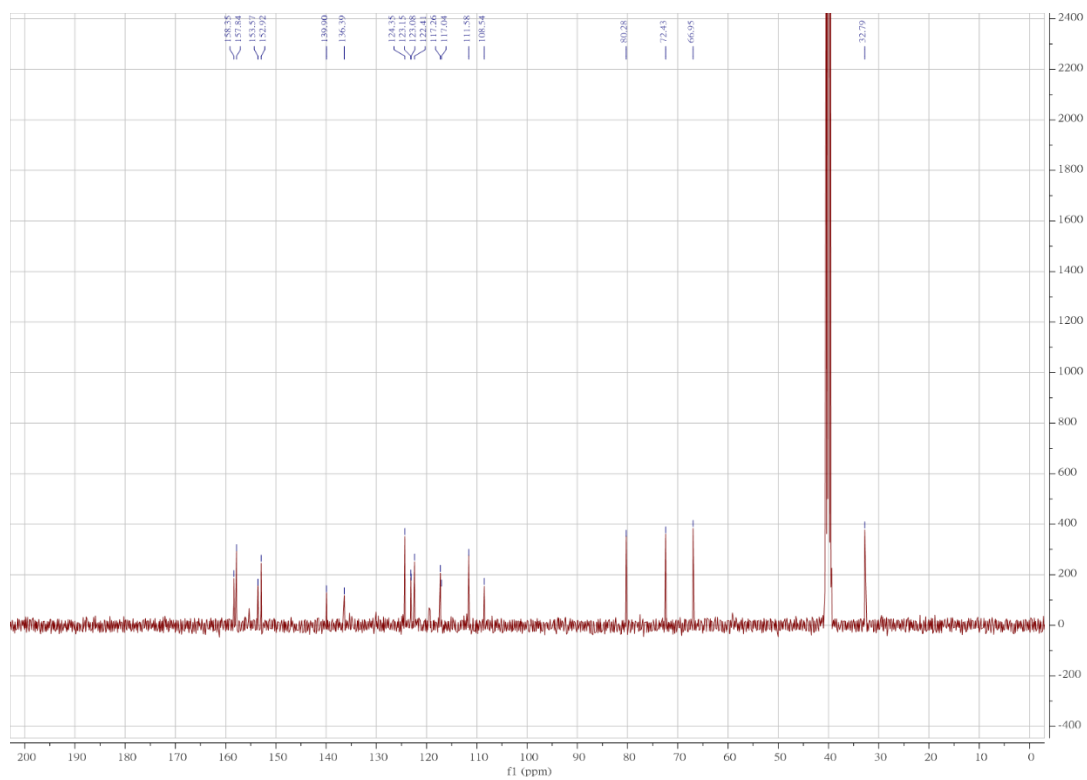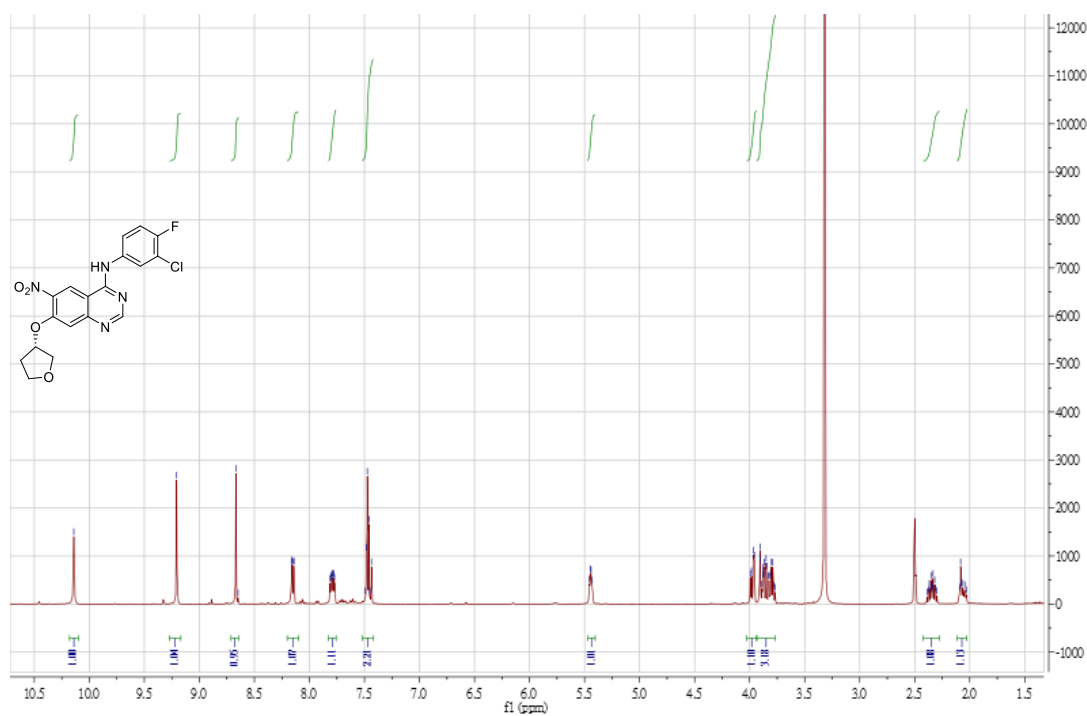
521.   Yi G, Son J, Yoo J, Park C, Koo H. Application Of Click Chemistry In Nanoparticle Modification And Its Targeted Delivery. Biomaterial Research 2018;22:13-.

522.   Dreaden EC, Austin LA, Mackey MA, El-Sayed MA. Size Matters: Gold Nanoparticles In Targeted Cancer Drug Delivery. Therapeutic Delivery 2012;3:457-78.

523.   Gamcsik MP, Kasibhatla MS, Teeter SD, Colvin OM. Glutathione Levels In Human Tumors. Biomarkers : Biochemical Indicators Of Exposure, Response, And Susceptibility To Chemicals 2012;17:671-91.

524.   Lloyd JB. Lysosome Membrane Permeability: Implications For Drug Delivery. Advanced Drug Delivery Reviews 2000;41:189-200.

525.   Kreidieh FY, Moukadem HA, El Saghir NS. Overview, Prevention And Management Of Chemotherapy Extravasation. World Journal Of Clinical Oncology 2016;7:87-97.

526.   Oh N, Park JH. Surface Chemistry Of Gold Nanoparticles Mediates Their Exocytosis In Macrophages. ACS Nano 2014;8:6232-41.

527.   Oh N, Park JH. Endocytosis And Exocytosis Of Nanoparticles In Mammalian Cells. International Journal Of Nanomedicine 2014;9 Suppl 1:51-63.

528.   Kim CS, Le NDB, Xing Y, Et Al. The Role Of Surface Functionality In Nanoparticle Exocytosis. Advanced Healthcare Materials 2014;3:1200-2.

529.   Huang X, Jain PK, El-Sayed IH, El-Sayed MA. Plasmonic Photothermal Therapy (PPTT) Using Gold Nanoparticles. Lasers In Medical Science 2008;23:217-28.

530.   Huang X, Tian XJ, Yang WL, Ehrenberg B, Chen JY. The Conjugates Of Gold Nanorods And Chlorin E6 For Enhancing The Fluorescence Detection And Photodynamic Therapy Of Cancers. Physical Chemistry Chemical Physics 2013;15:15727-33.

531.   Xi D, Dong S, Meng X, Lu Q, Meng L, Ye J. Gold Nanoparticles As Computerized Tomography (CT) Contrast Agents. RSC Advances 2012;2:12515-24.

532.   Foucquier J, Guedj M. Analysis Of Drug Combinations: Current Methodological Landscape. Pharmacology Reseearch Perspectives 2015;3:E00149-E.

533.   Ellis T, Chiappi M, García-Trenco A, Et Al. Multimetallic Microparticles Increase The Potency Of Rifampicin Against Intracellular Mycobacterium Tuberculosis. ACS Nano 2018;12:5228-40.

534.   Savage DT, Hilt JZ, Dziubla TD. In Vitro Methods For Assessing Nanoparticle Toxicity. Methods In Molecular Biology (Clifton, NJ) 2019;1894:1-29.

535.   Lundqvist M, Stigler J, Cedervall T, Et Al. The Evolution Of The Protein Corona Around Nanoparticles: A Test Study. ACS Nano 2011;5:7503-9.

536.   Lara S, Perez-Potti A, Herda LM, Adumeau L, Dawson KA, Yan Y. Differential Recognition Of Nanoparticle Protein Corona And Modified Low-Density Lipoprotein By Macrophage Receptor With Collagenous Structure. ACS Nano 2018;12:4930-7.

537.   Monopoli MP, Aberg C, Salvati A, Dawson KA. Biomolecular Coronas Provide The Biological Identity Of Nanosized Materials. Nature Nanotechnology 2012;7:779-86.

538.   Glancy D, Zhang Y, Wu JLY, Ouyang B, Ohta S, Chan WCW. Characterizing The Protein Corona Of Sub-10 Nm Nanoparticles. Journal Of Controlled Release 2019;304:102-10.

539.   Bertrand N, Grenier P, Mahmoudi M, Et Al. Mechanistic Understanding Of In Vivo Protein Corona Formation On Polymeric Nanoparticles And Impact On Pharmacokinetics. Nature Communications 2017;8:777.

540.   Mosquera J, García I, Henriksen-Lacey M, González-Rubio G, Liz-Marzán LM. Reducing Protein Corona Formation And Enhancing Colloidal Stability Of Gold Nanoparticles By Capping With Silica Monolayers. Chemistry Of Materials 2019;31:57-61.

541.   Yeo ELL, Thong PSP, Soo KC, Kah JCY. Protein Corona In Drug Delivery For Multimodal Cancer Therapy In Vivo. Nanoscale 2018;10:2461-72.

542.   Oh JY, Kim HS, Palanikumar L, Et Al. Cloaking Nanoparticles With Protein Corona Shield For Targeted Drug Delivery. Nature Communications 2018;9:4548.

543.   Tenzer S, Docter D, Kuharev J, Et Al. Rapid Formation Of Plasma Protein Corona Critically Affects Nanoparticle Pathophysiology. Nature Nanotechnology 2013;8:772-81.

544.   Björnmalm M, Thurecht KJ, Michael M, Scott AM, Caruso F. Bridging Bio–Nano Science And Cancer Nanomedicine. ACS Nano 2017;11:9594-613.

545.   Leblanc AK, Breen M, Choyke P, Et Al. Perspectives From Man's Best Friend: National Academy Of Medicine's Workshop On Comparative Oncology. Science Translational Medicine 2016;8:324ps5.

546.   Prabhakar U, Maeda H, Jain RK, Et Al. Challenges And Key Considerations Of The Enhanced Permeability And Retention Effect For Nanomedicine Drug Delivery In Oncology. Cancer Research 2013;73:2412-7.

547.   Nichols JW, Bae YH. EPR: Evidence And Fallacy. Journal Of Controlled Release 2014;190:451-64.

548.   Nakamura Y, Mochida A, Choyke PL, Kobayashi H. Nanodrug Delivery: Is The Enhanced Permeability And Retention Effect Sufficient For Curing Cancer? Bioconjugate Chemistry 2016;27:2225-38.

549.   Wilhelm S, Tavares AJ, Dai Q, Et Al. Analysis Of Nanoparticle Delivery To Tumours. Nature Reviews Materials 2016;1:16014.

550.   Dai Q, Wilhelm S, Ding D, Et Al. Quantifying The Ligand-Coated Nanoparticle Delivery To Cancer Cells In Solid Tumors. ACS Nano 2018;12:8423-35.

551.   Sindhwani S. How Do Nanoparticles Enter Solid Tumours? Keystone Symposia: Delivering Therapeutics Across Biological Barriers; 2019; Dublin.

552.   Patel AK, Kaczmarek JC, Bose S, Et Al. Inhaled Nanoformulated Mrna Polyplexes For Protein Production In Lung Epithelium. Advanced Materials 2019;31:1805116.

553.   Hickey AJ. Controlled Delivery Of Inhaled Therapeutic Agents. Journal Of Controlled Release 2014;190:182-8.

554.   Kaczmarek JC, Kauffman KJ, Fenton OS, Et Al. Optimization Of A Degradable Polymer–Lipid Nanoparticle For Potent Systemic Delivery Of Mrna To The Lung Endothelium And Immune Cells. Nano Letters 2018;18:6449-54.

555.   Fenton OS, Kauffman KJ, Mcclellan RL, Et Al. Customizable Lipid Nanoparticle Materials For The Delivery Of Sirnas And Mrnas. Angewandte Chemie International Edition 2018;57:13582-6.

556.   Dahlman JE, Kauffman KJ, Xing Y, Et Al. Barcoded Nanoparticles For High Throughput In Vivo Discovery Of Targeted Therapeutics. Proceedings Of The Natational Academy Of Sciences 2017;114:2060-5.

557.   Yamankurt G, Berns EJ, Xue A, Et Al. Exploration Of The Nanomedicine-Design Space With High-Throughput Screening And Machine Learning. Nature Biomedical Engineering 2019;3:318-27.

558.   Ekins S, Puhl AC, Zorn KM, Et Al. Exploiting Machine Learning For End-To-End Drug Discovery And Development. Nature Materials 2019;18:435-41.

559.   Irvine DJ, Hanson MC, Rakhra K, Tokatlian T. Synthetic Nanoparticles For Vaccines And Immunotherapy. Chemical Reviews 2015;115:11109-46

560.   Yoon HY, Selvan ST, Yang Y, Et Al. Engineering Nanoparticle Strategies For Effective Cancer Immunotherapy. Biomaterials 2018;178:597-607.

561.   Rosenthal R, Cadieux EL, Salgado R, Et Al. Neoantigen-Directed Immune Escape In Lung Cancer Evolution. Nature 2019;567:479-85.

562.   Turajlic S, Sottoriva A, Graham T, Swanton C. Resolving Genetic Heterogeneity In Cancer. Nature Reviews Genetics 2019.

Appendix A – NMR and mass spectra

Figure A1. ^{1}H NMR(400 MHz, DMSO-d$_6$) of **3**

Figure A2. ^{13}C NMR(400 MHz, DMSO-d$_6$) of **3**

Figure A3. ^{1}H NMR(400 MHz, DMSO-d$_6$) of **4**

Figure A4. ^{13}C NMR(400 MHz, DMSO-d$_6$) of **4**

Figure A5. ^{1}H NMR(400 MHz, DMSO-d$_6$) of **5**

Figure A6. ^{13}C NMR(400 MHz, DMSO-d$_6$) of **5**
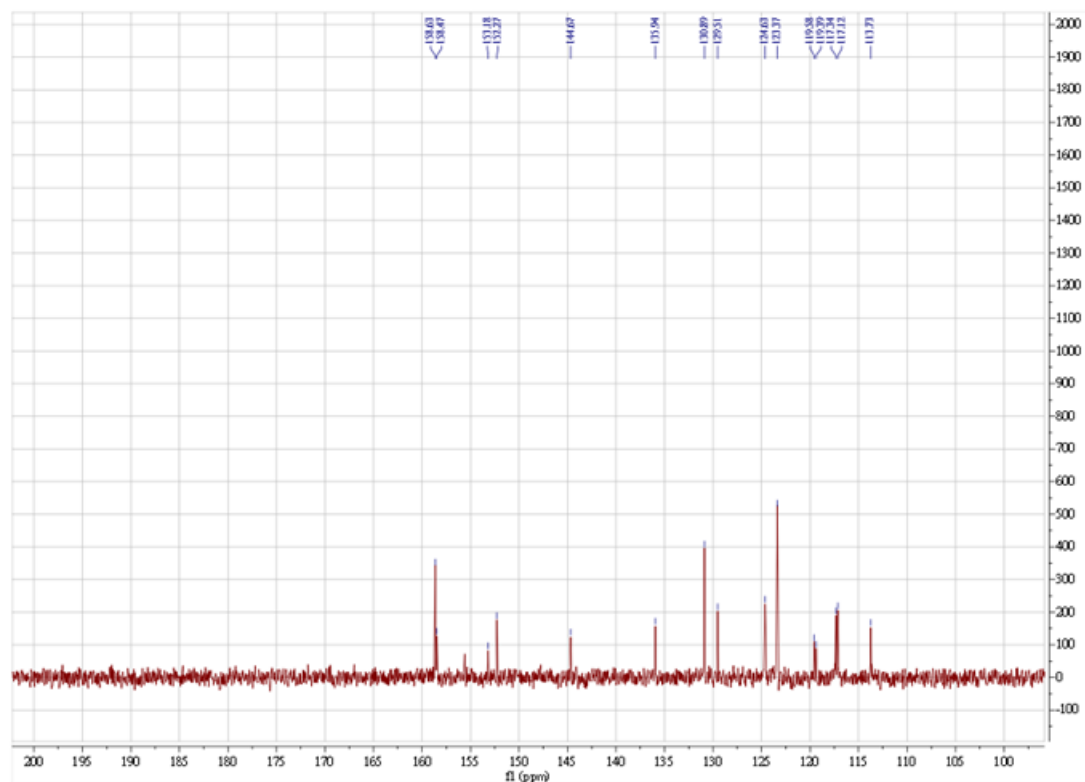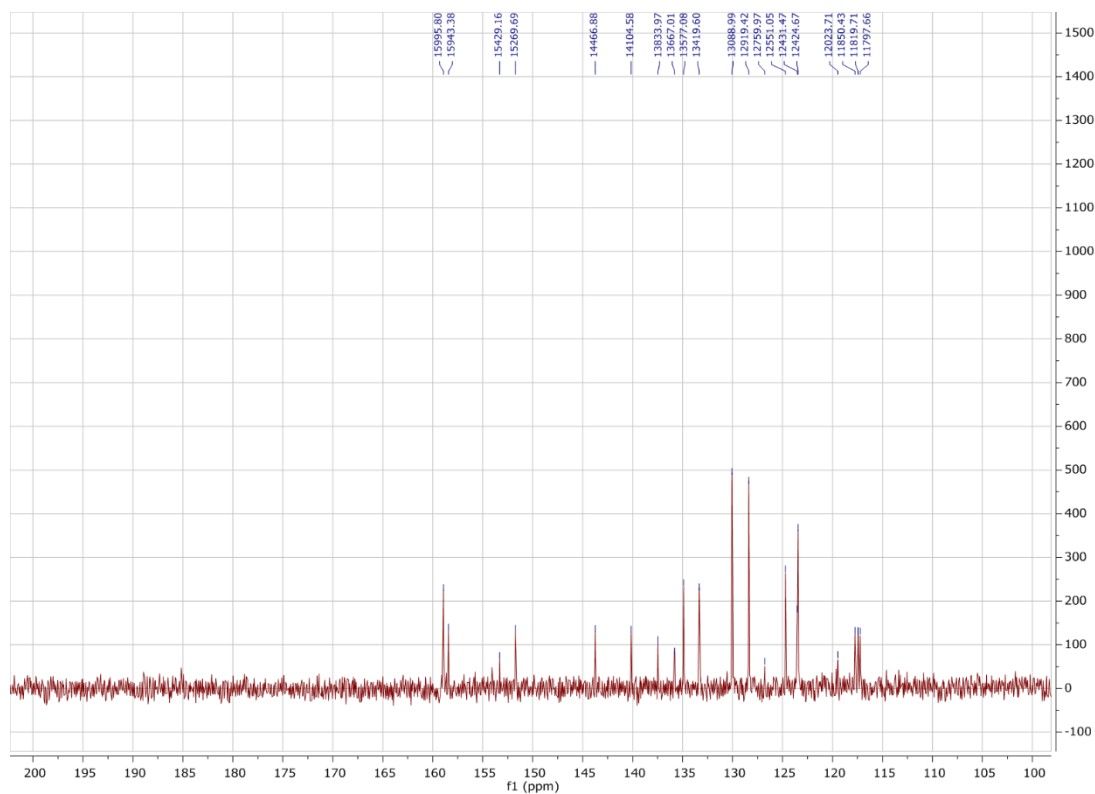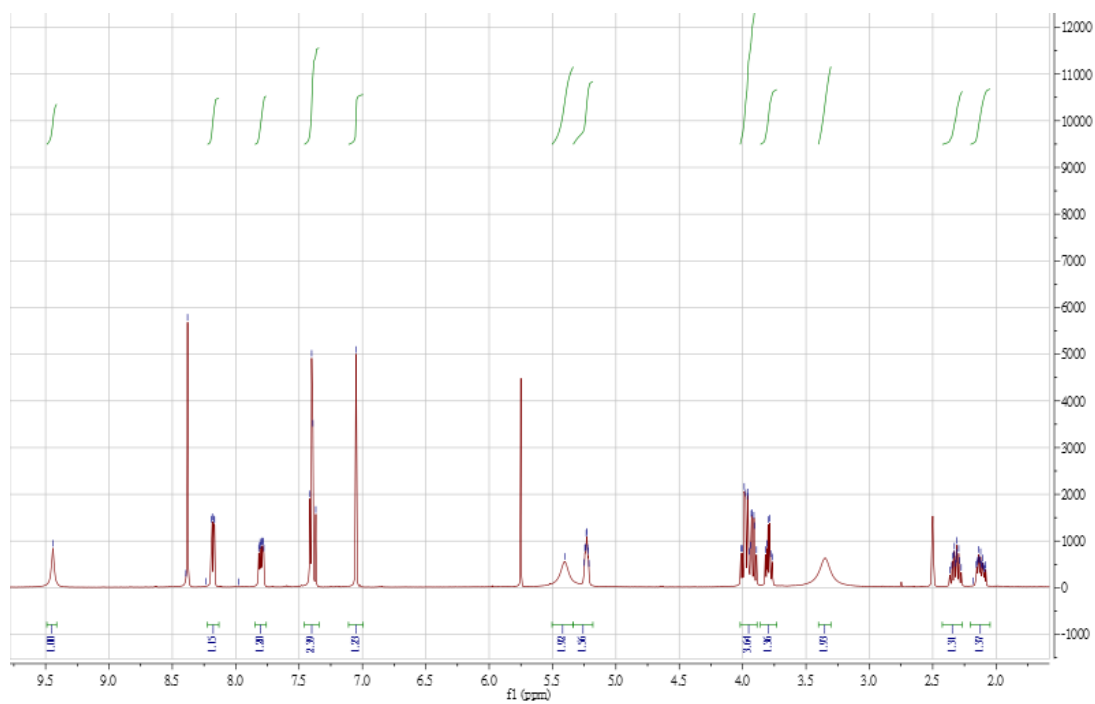
Figure A7. ^{1}H NMR(400 MHz, DMSO-d$_6$) of **6**
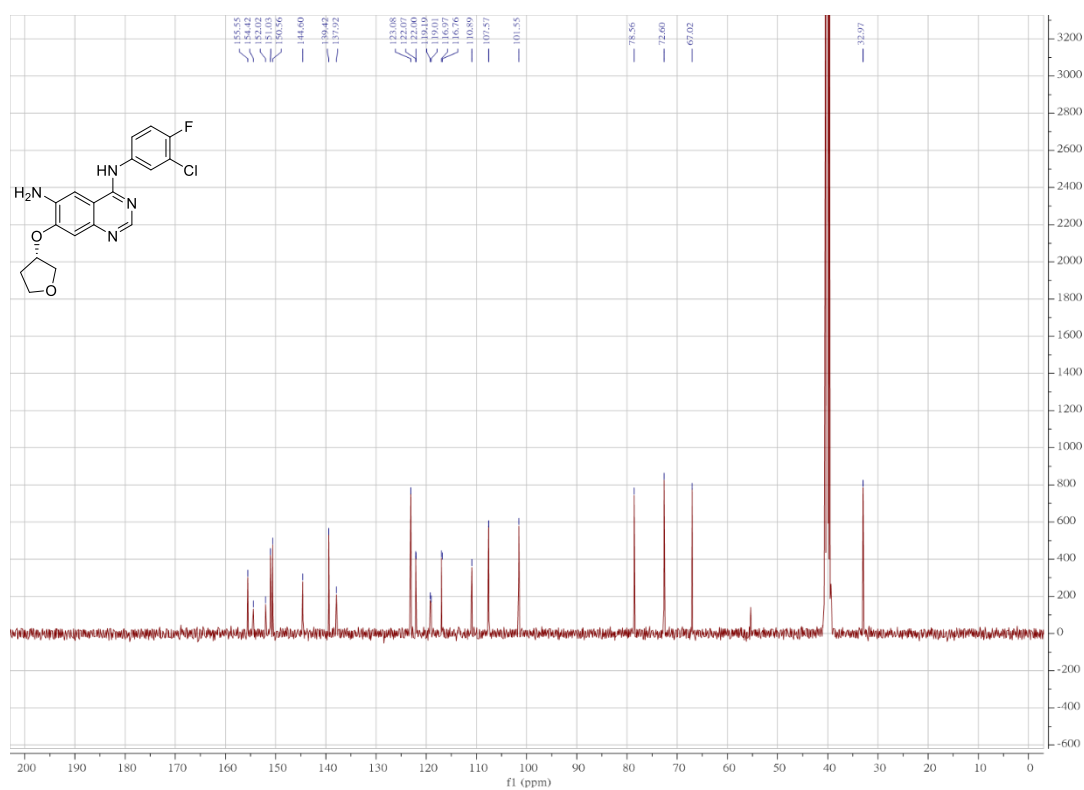
Figure A8. ^{13}C NMR(400 MHz, DMSO-d$_6$) of **6**
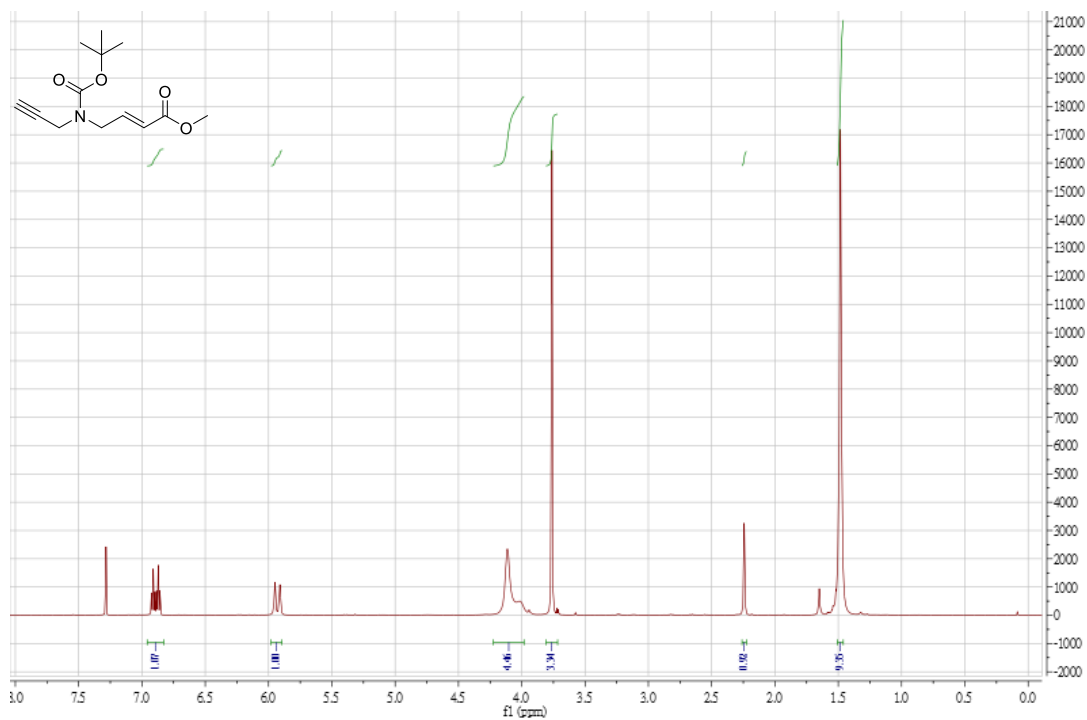
Figure A9. ^{1}H NMR(400 MHz, CDCl$_3$) of **9**
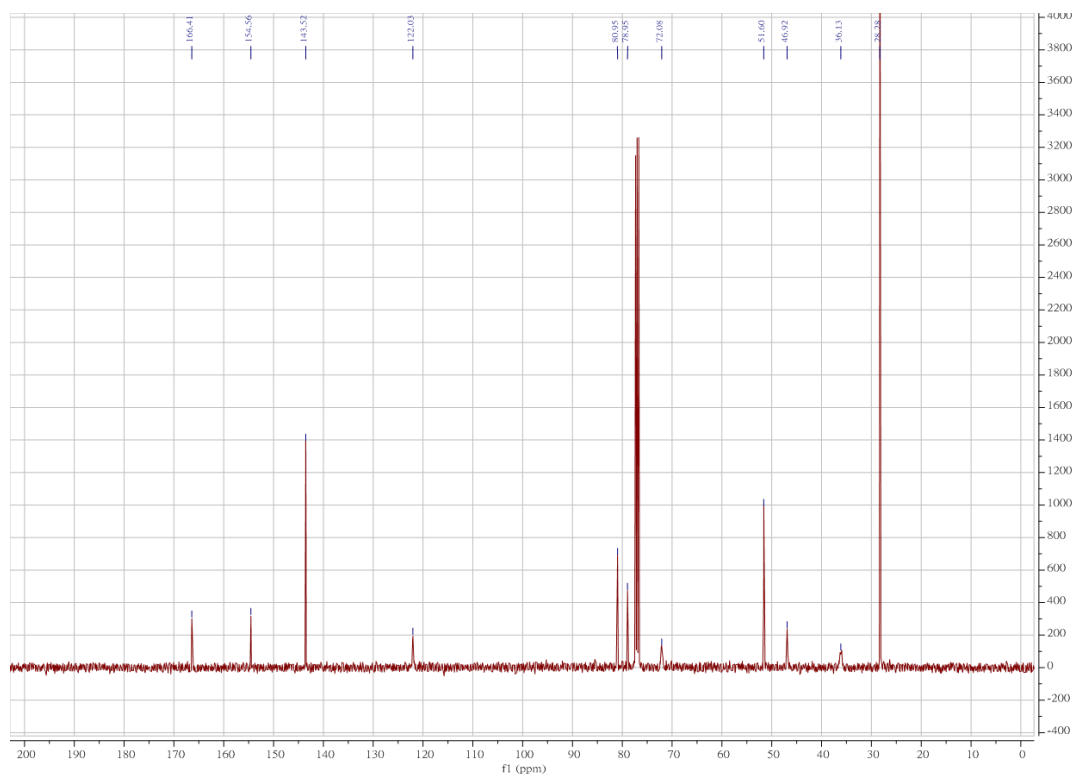
Figure A10. ^{13}C NMR(400 MHz, CDCl$_3$) of **9**

Figure A11. ^{1}H NMR(400 MHz, CDCl$_3$) of **11**

Figure A12. ^{13}C NMR(400 MHz, CDCl$_3$) of **11**
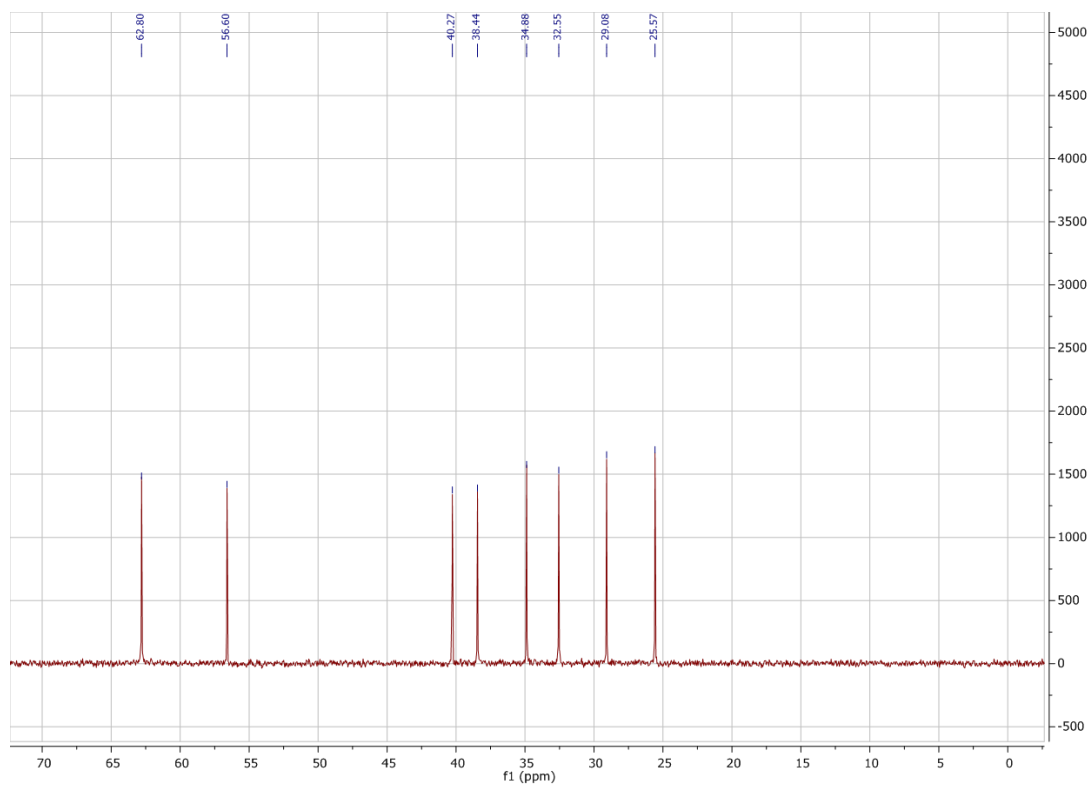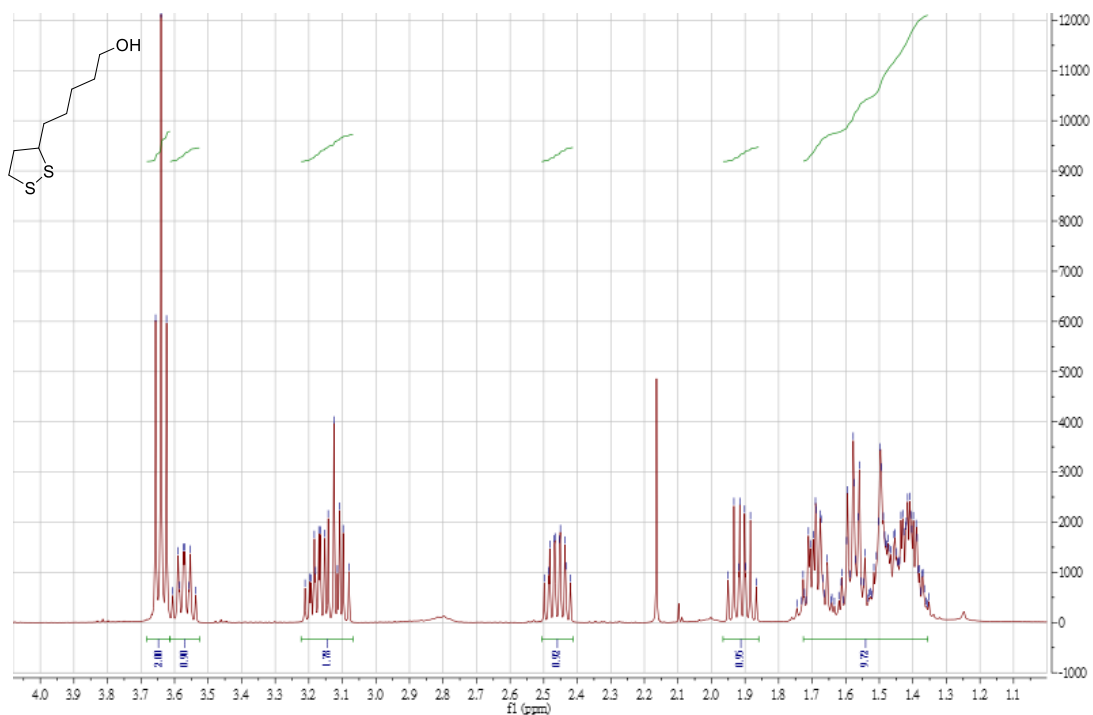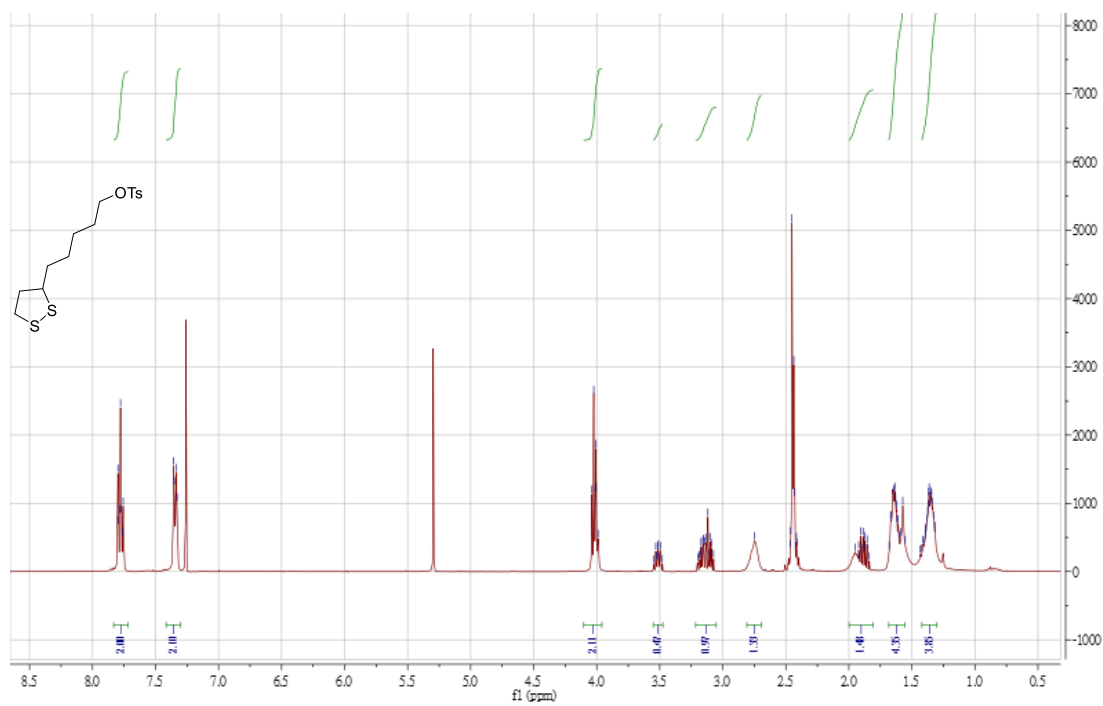
Figure A13. ^{1}H NMR(400 MHz, CDCl$_3$) of **12**
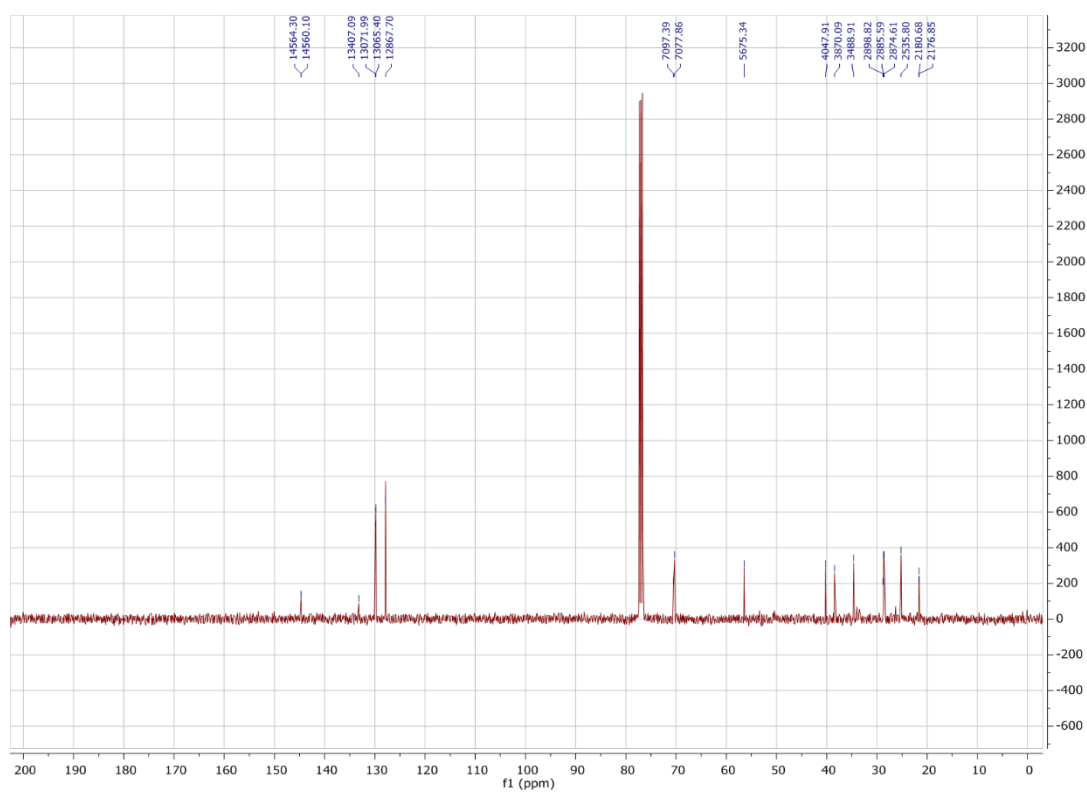
Figure A14. ^{13}C NMR(400 MHz, CDCl$_3$) of **12**
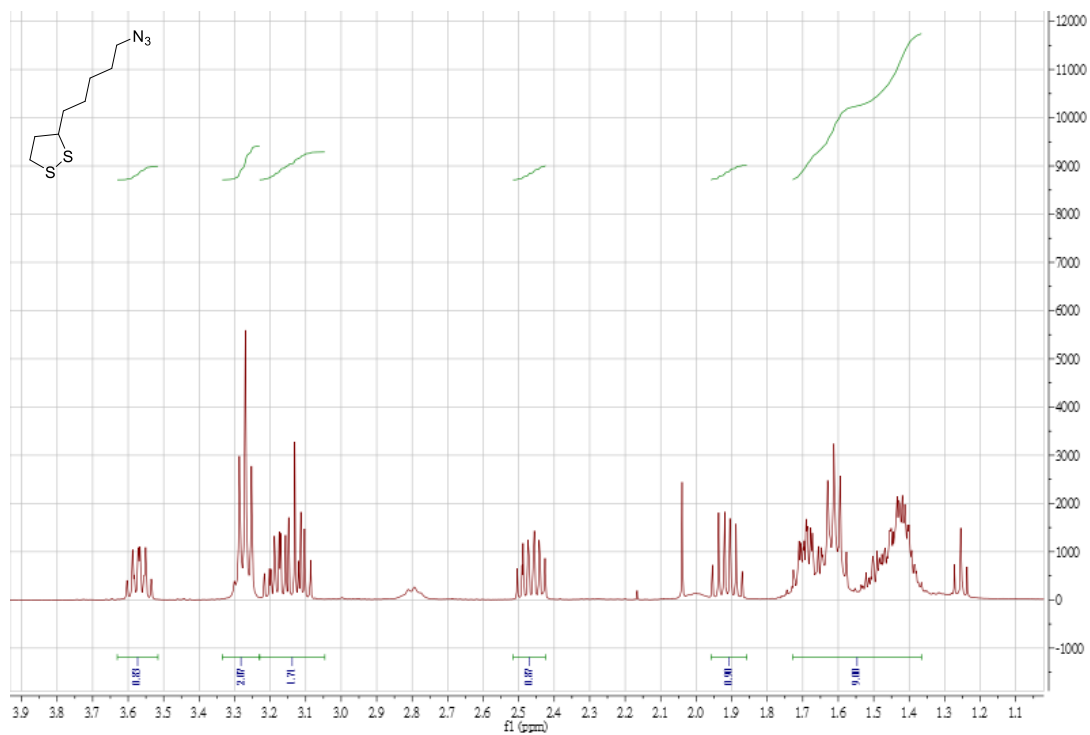
Figure A15. ^{1}H NMR(400 MHz, CDCl$_3$) of **13**
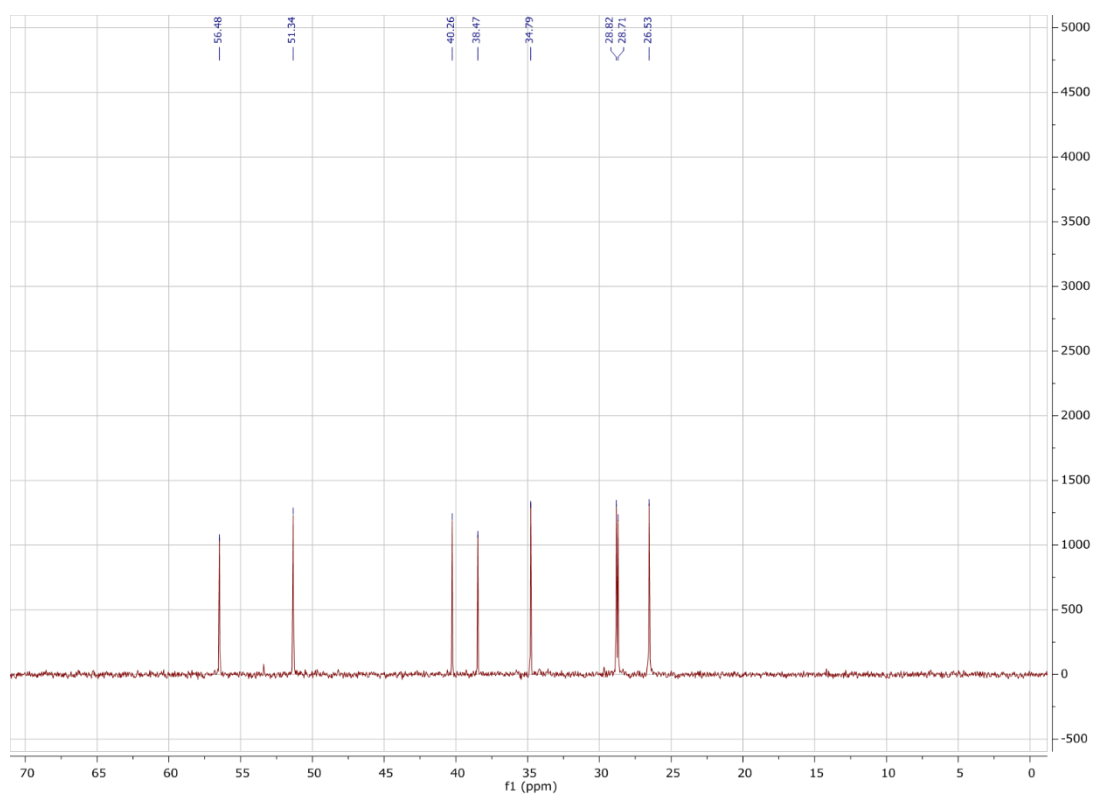
Figure A16. ^{13}C NMR(400 MHz, CDCl$_3$) of **13**

Figure A17. ^{1}H NMR(400 MHz, CDCl$_3$) of **14**

Figure A18. ^{13}C NMR(400 MHz, CDCl$_3$) of **14**
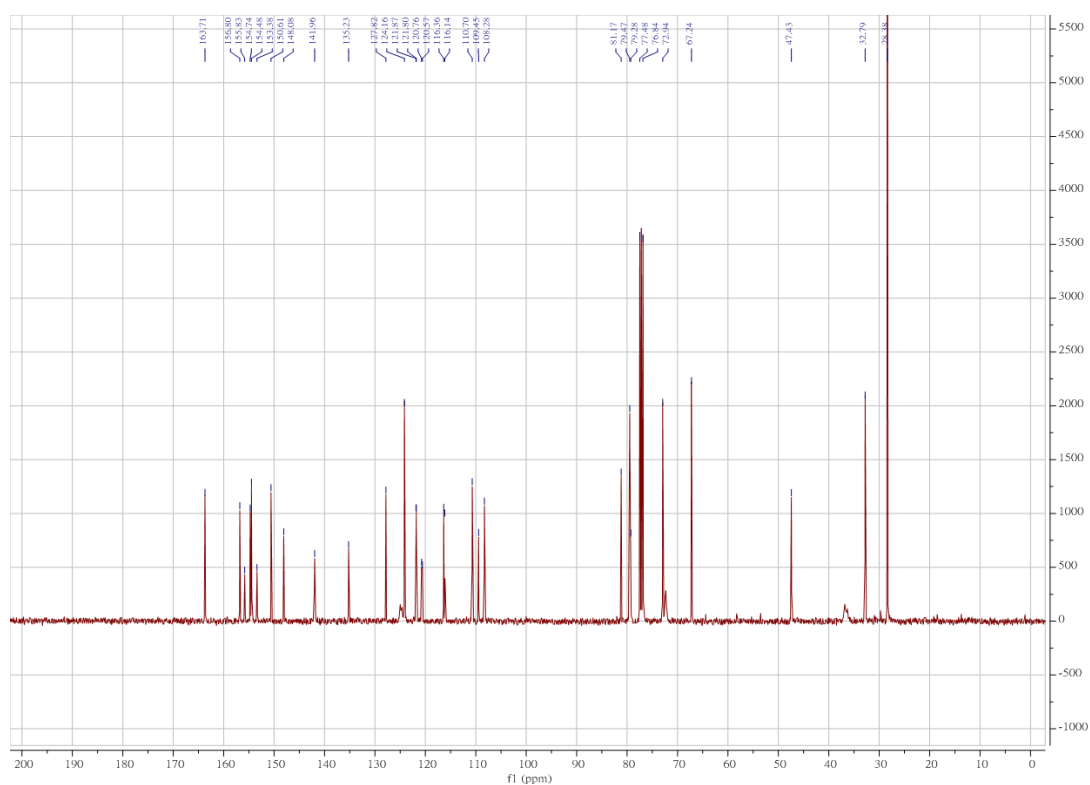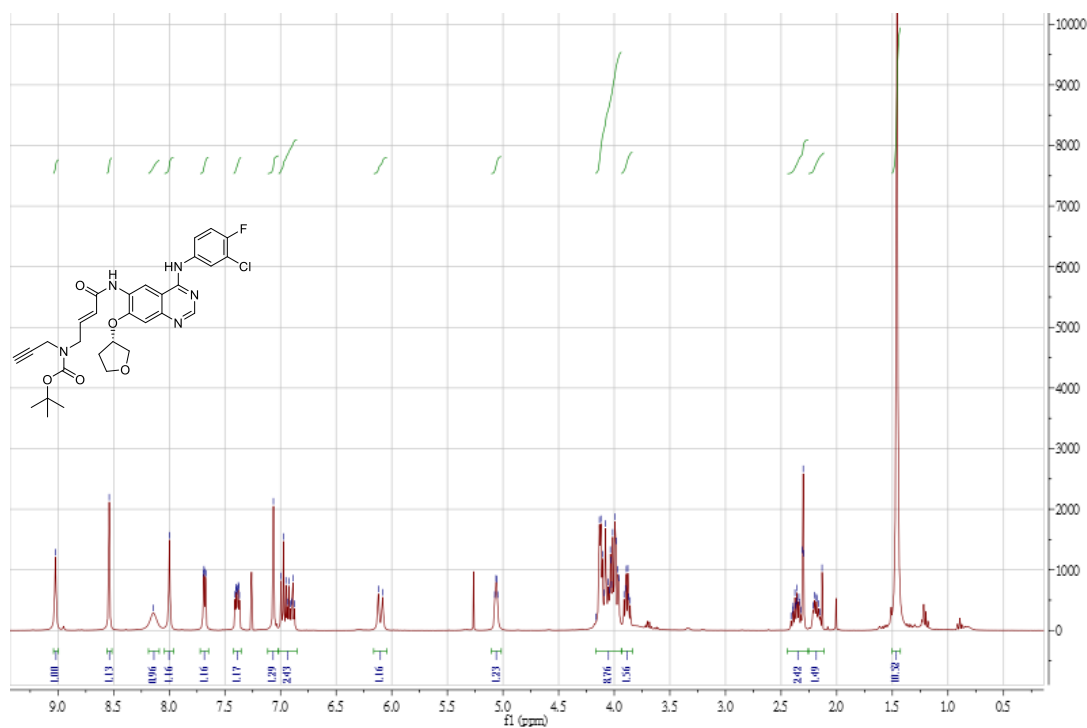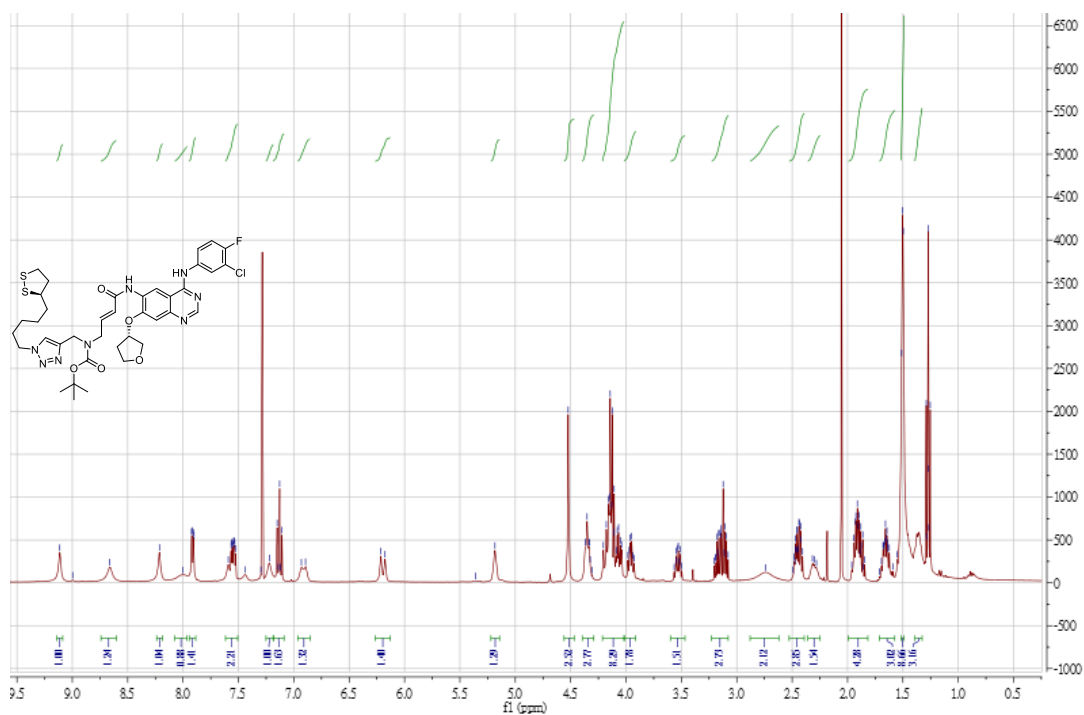
Figure A19. ^{1}H NMR(400 MHz, CDCl$_3$) of **15**
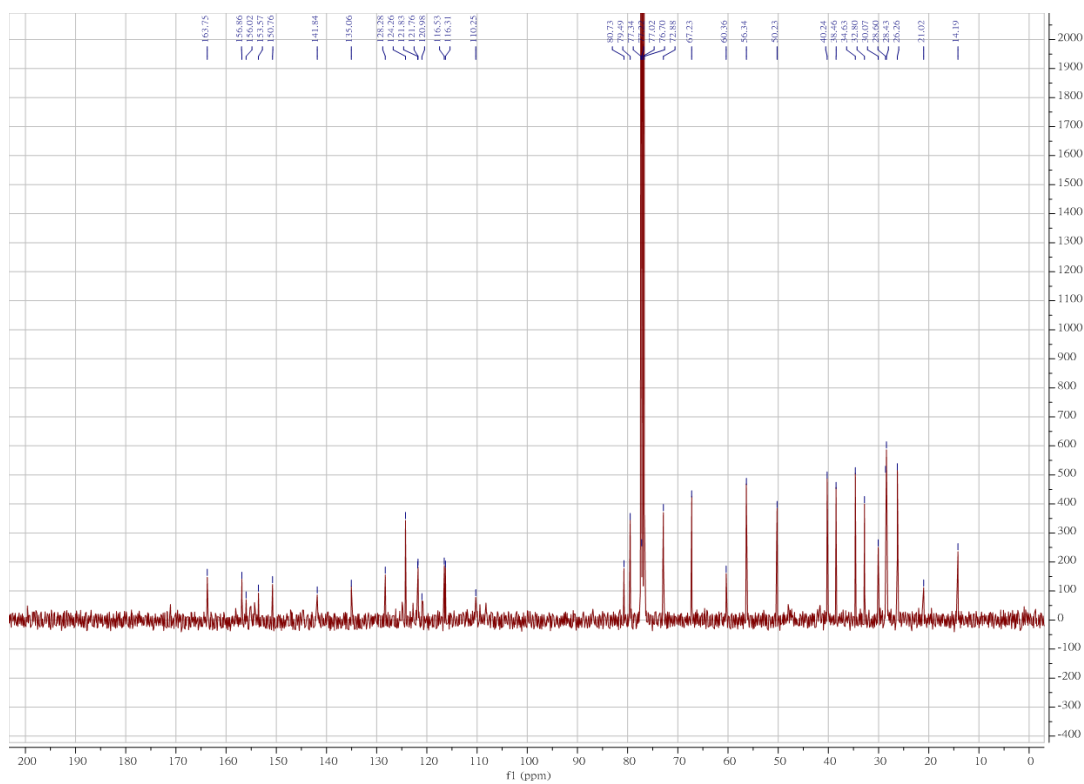
Figure A20. ^{13}C NMR(400 MHz, CDCl$_3$) of **15**
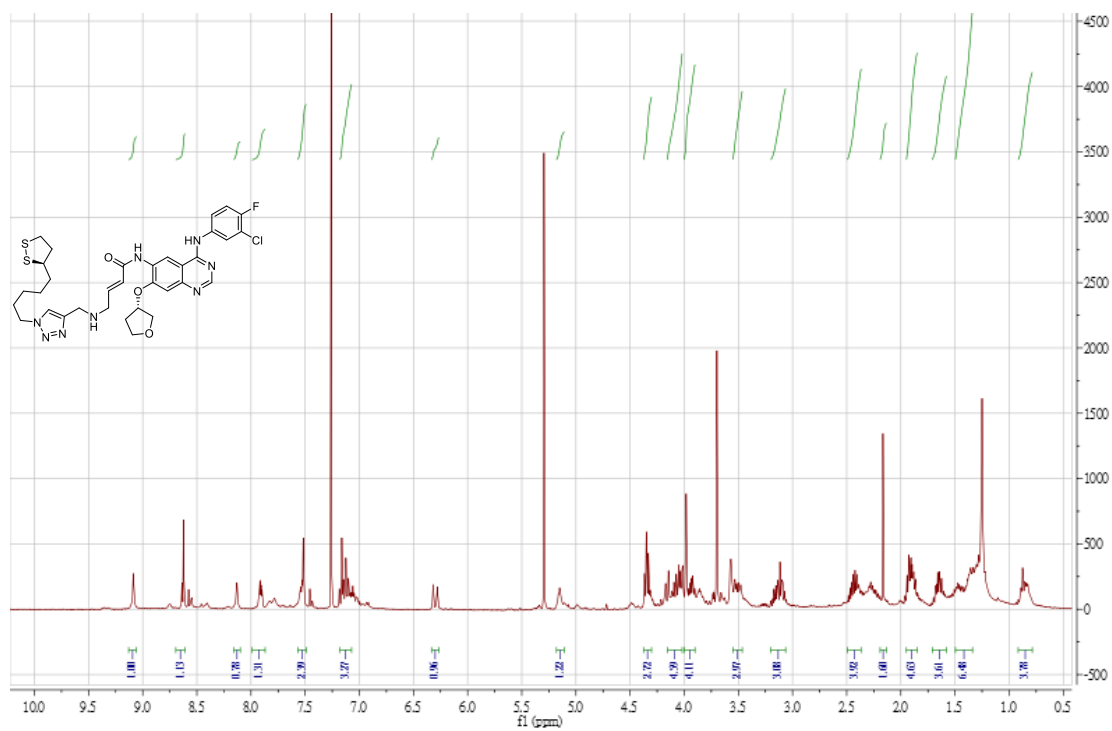
Figure A21. ^{1}H NMR(400 MHz, CDCl$_3$) of **16**
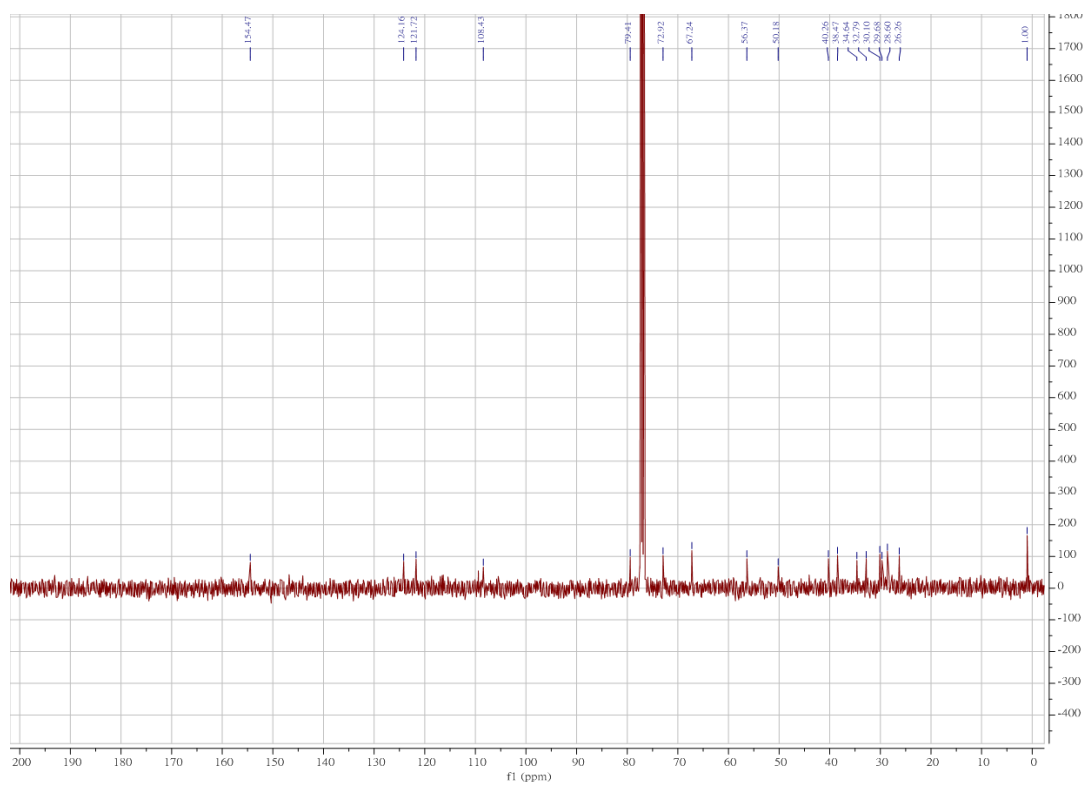
Figure A22. ^{13}C NMR(400 MHz, CDCl$_3$) of **16**
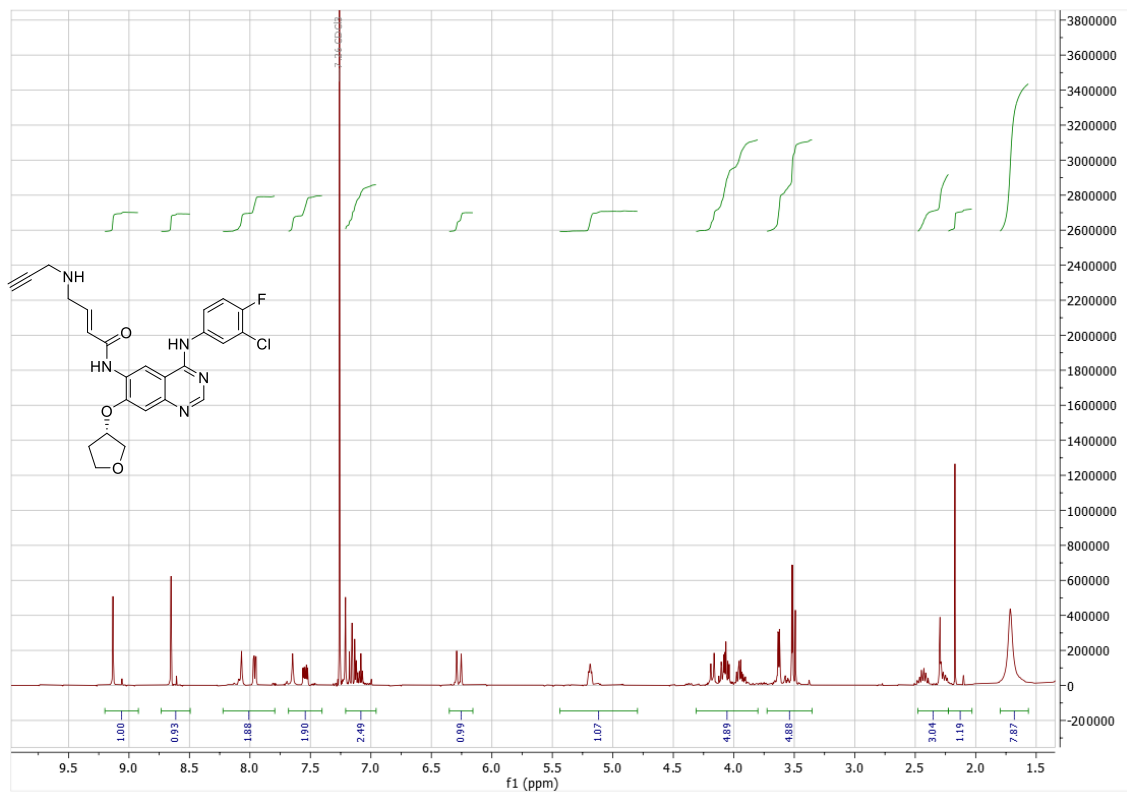
Figure A23. ^{1}H NMR(400 MHz, CDCl$_3$) of **17**
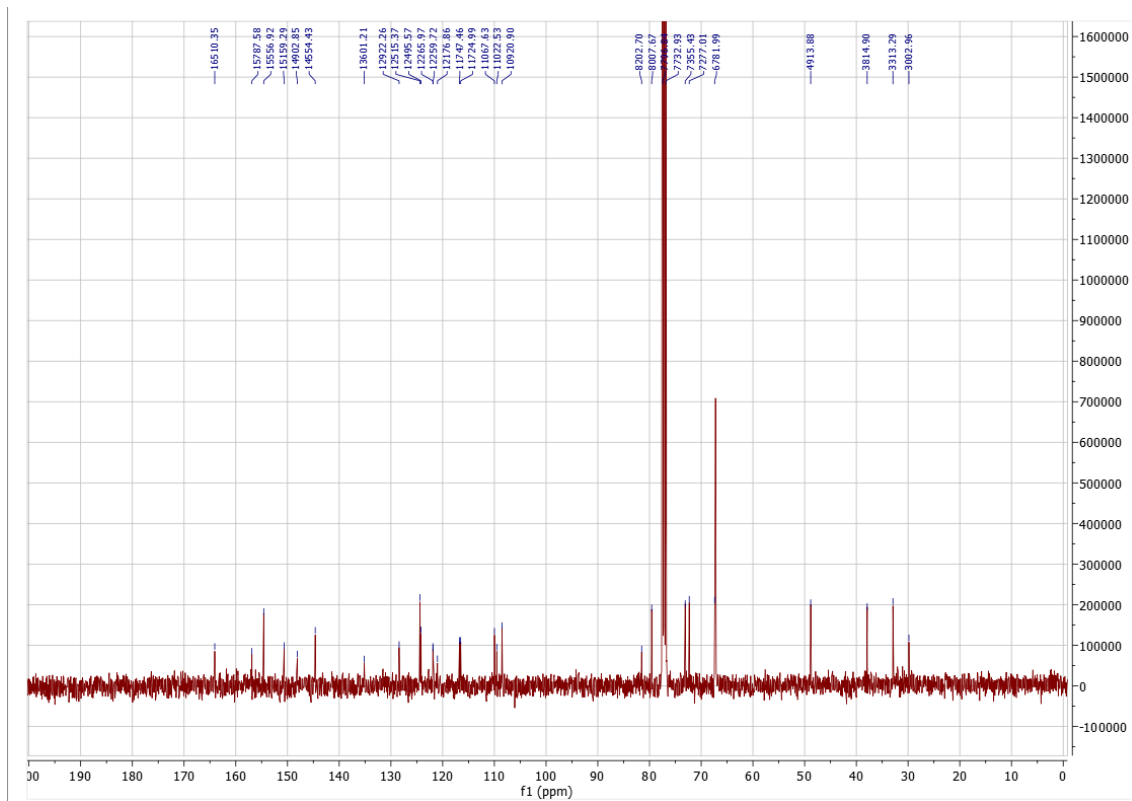
Figure A24. ^{13}C NMR(400 MHz, CDCl$_3$) of **17**

100

%

635.2409 641.2300   670.4127 686.3784   711.2316   713.2258
715.2264
729.2258
731.2211 745.1973
732.2250 746.2014
752.1694 773.2127
787.2659

m/z

630 640 650 660 670 680 690 700 710 720 730 740 750 760 770 780 790 800

Minimum:				-1.5			
Maximum:		5.0	10.0	50.0			
Mass	Calc. Mass	mDa	PPM	DBE	i-FIT		Formula
713.2258	713.2259	-0.1	-0.1	17.5	0.6		C33 H39 N8 O3 S2 Cl F
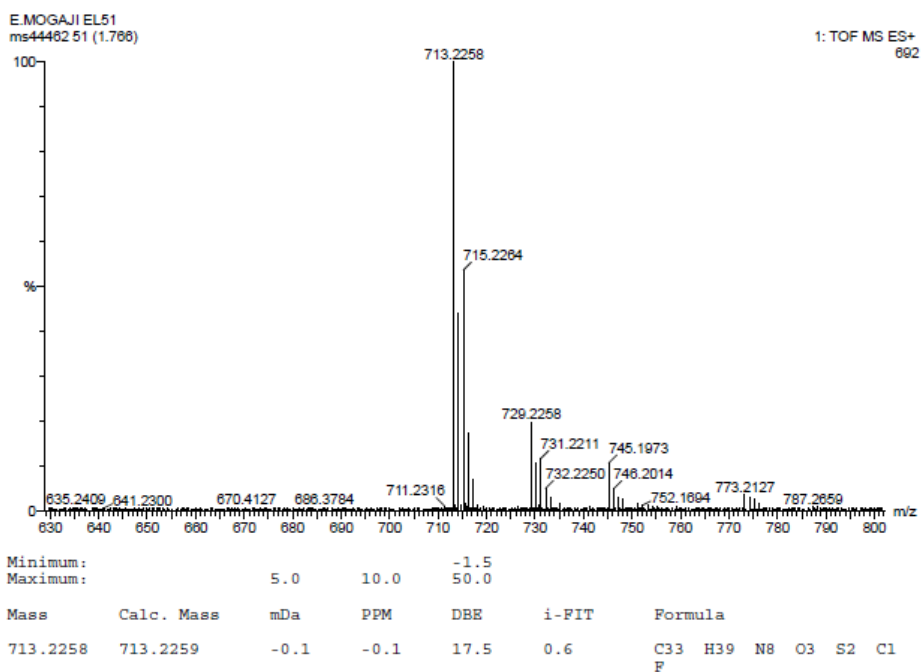
Figure A25. Mass spectrum of **16** confirming the molecular identity and retention of the disulfide bond throughout the synthetic process.

C.TRAN AMC001
MS37806 6 (0.199)
ES-ToF
12-May-2017
1: TOF MS ES+
1.27e3

100

177.1133

352.2475

285.1333

496.1566

269.0887

172.1349

393.2743

347.2924 355.1750
339.1822
389.3380
320.2565
301.1579
242.2867
372.3488
400.3820
498.1568 520.1177
178.1161
152.0679
210.1118 239.1246 251.1275
408.2941443.2295 454.2862
471.2370
499.1523 522.1109
541.2958 568.1982

m/z

150 160 170 180 190 200 210 220 230 240 250 260 270 280 290 300 310 320 330 340 350 360 370 380 390 400 410 420 430 440 450 460 470 480 490 500 510 520 530 540 550 560 570 580 590 600

Minimum:				-1.5				
Maximum:		5.0	10.0	80.0				
Mass	Calc. Mass	mDa	PPM	DBE	i-FIT	i-FIT (Norm)		Formula
496.1566	496.1552		1.4	2.8	15.5	82.9	0.0	C25 H24 N5 O3 Cl F

Figure A26. Mass spectrum of **17.**

ACS **APPLIED** MATERIALS &INTERFACES

Tyrosine Kinase Inhibitor Gold Nanoconjugates for the Treatment of Nonsmall Cell Lung Cancer

Alexander M. Cryer,*,[†] Cheuk Chan,[†,‡] Anastasia Eftychidou,[†,‡] Christy Maksoudian,[†,‡] Mohan Mahesh,[‡] Teresa D. Tetley,[†] Alan C. Spivey,[‡] and Andrew J. Thorley[†]

[†]National Heart and Lung Institute and [‡]Department of Chemistry, Imperial College London, London SW7 2AZ, United Kingdom

Ⓢ *Supporting Information*

ABSTRACT: Gold nanoparticles (AuNPs) have emerged as promising drug delivery candidates that can be leveraged for cancer therapy. Lung cancer (LC) is a heterogeneous disease that imposes a significant burden on society, with an unmet need for new therapies. Chemotherapeutic drugs such as afatinib (Afb), which is clinically approved for the treatment of epidermal growth factor receptor positive LC, is hydrophobic and has low bioavailability leading to spread around the body, causing severe side effects. Herein, we present a novel afatinib-AuNP formulation termed Afb-AuNPs, with the aim of improving drug efficacy and biocompatibility. This was achieved by synthesis of an alkyne-bearing Afb derivative and reaction with azide-functionalized lipoic acid using copper-catalyzed click chemistry, then conjugation to AuNPs via alkylthiol—gold bond formation. The Afb-AuNPs were found to possess up to 3.7-fold increased potency when administered to LC cells *in vitro* and were capable of significantly inhibiting cancer cell proliferation, as assessed by MTT assay and electric cell—substrate impedance sensing, respectively. Furthermore, when exposed to Afb-AuNPs, human alveolar epithelial type I-like cells, a model of the healthy lung epithelium, maintained viability and were found to release less pro-inflammatory cytokines when compared to free drug, demonstrating the biocompatibility of our formulation. This study provides a new platform for the development of nontraditional AuNP conjugates which can be applied to other molecules of therapeutic or diagnostic utility, with potential to be combined with photothermal therapy in other cancers.

KEYWORDS: *gold nanoparticles, drug delivery, lung cancer, nanomedicine, afatinib*
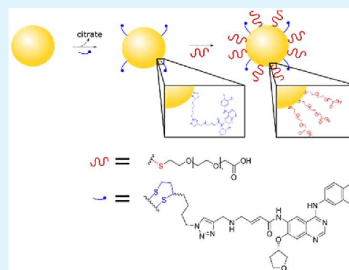
1. INTRODUCTION

Nonsmall cell lung cancer (NSCLC), the predominant subtype of LC, is responsible for the most cancer-related deaths worldwide.[1] A variety of chemotherapeutic drugs are employed to achieve disease control; however, the heterogeneity of NSCLC[2] coupled with resistance mechanisms[3] largely prevents curative outcomes. The discovery of activating (oncogenic) mutations in the tyrosine kinase domain of epidermal growth factor receptor (EGFR) in patients that responded to the tyrosine kinase inhibitor (TKI) gefitinib[4,5] laid the foundations for personalized medicine approaches in NSCLC. This form of therapy whereby specific oncogenic mutations are targeted improved survival for patients harboring such alterations.[6] Activating mutations in EGFR are the most common mutations in NSCLC;[7] therefore, inhibition of EGFR represents an attractive therapeutic strategy. However, as with chemotherapy, these TKIs suffer from poor accumulation in the tumor and induce dose limiting toxicities due to systemic distribution around the body, limiting clinical efficacy. This is reflected in the 5-year survival rate of NSCLC, which stands at 19%,[8] highlighting an unmet need for more efficacious therapeutic options.

Nanomedicine involves the application of nanotechnology to address medical questions and has the potential to greatly enhance cancer diagnosis and therapy.[9,10] Of particular interest is the use of nanoparticles (NPs) for drug delivery applications.[11] The enhanced permeability and retention (EPR) effect[12] can permit augmented accumulation of NPs at the tumor site, a phenomenon that has been documented *in vivo*.[13] Additionally, the decoration of NPs with poly(ethylene glycol) (PEG) facilitates a prolonged circulatory half-life,[14] reduces opsonization and clearance by the mononuclear phagocyte system,[15] and decreases nonspecific protein adsorption,[16] culminating in more time for NPs to accumulate in tumors. Although reliance on the EPR effect is not optimal *in vivo*,[17] these factors predicate most NP-based drug delivery strategies to solid tumors. Gold nanoparticles (AuNPs)[18] are excellent candidates for drug delivery vehicles[19,20] based on their biocompatibility,[21] ease of functionalization,[22] optical and photothermal properties,[23,24] and potential for pharmaceutical scale-up.[25] The clinical utility of AuNP conjugates is evidenced by the success of CYT-6091, a formulation of recombinant human tumor necrosis factor-α, thiolated PEG, and AuNPs, in phase I trials[26] as well as other preclinical studies.[27]
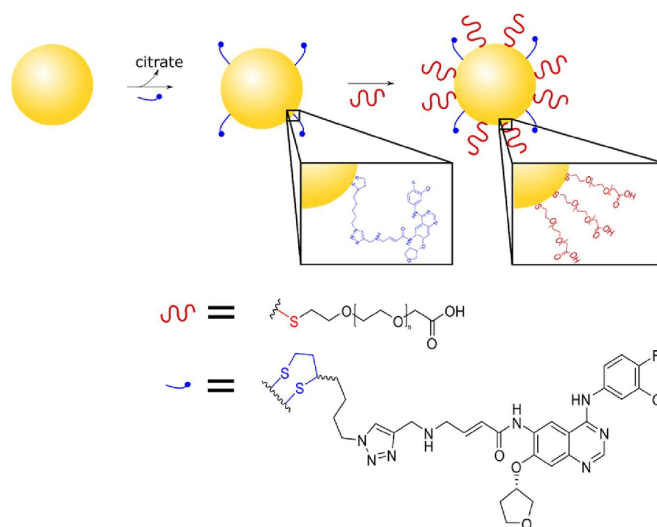
A

Figure 1. Schematic representation of the development of Afb-AuNPs. Citrate-capped AuNPs are first conjugated with thiolated afatinib analogues (blue) by virtue of a cyclic disulfide anchor. Subsequently, drug-bearing AuNPs are then PEGylated (red), enabled by further thiol–gold bond formation culminating in Afb-AuNPs.

We sought to develop an AuNP-conjugate platform using afatinib (Afb), a second-generation TKI that has demonstrated enhanced efficacy in EGFR mutated LC over first line platinum-based chemotherapy[28] and TKIs such as gefitinib.[29] The native structure of Afb does not permit direct conjugation to AuNPs; therefore, we synthesized a novel Afb analogue containing a pedant alkynyl which was coupled to an azide-functionalized lipoic acid moiety using a copper(I)-catalyzed Huisgen 1,3-dipolar cycloaddition (otherwise known as a "click reaction").[30] The cyclic disulfide group of lipoic acid enabled covalent attachment of the Afb analogue to the surface of AuNPs. The AuNPs were then PEGylated for biocompatibility and colloidal stability using a heterobifunctional PEG containing sulfhydryl (−SH) and carboxyl (−COOH) groups. The resulting formulation, termed Afb-AuNPs (Figure 1), comprises of both the active component of Afb and PEG as independent entities, as opposed to the conventional strategy to PEGylate AuNPs prior to drug linkage, or via noncovalent attachment, which can affect drug loading.[31,32]

The conjugates were fully characterized prior to assessment of *in vitro* cytotoxicity in LC cells and human alveolar epithelial type I-like cells (TT1) cells, a unique model of the healthy lung epithelium derived from primary human alveolar type II cells,[33] that we previously used to demonstrate pulmonary uptake and translocation of NPs.[34] The real time effect on proliferation and uptake in LC cells was also evaluated. Furthermore, we examined cytokine release from LC cells and TT1 cells to gain insight into the inflammatory response upon AuNP exposure. We hypothesize that Afb-AuNPs possess enhanced anticancer activity in LC cells, particularly in cells with EGFR mutations. In this report, we demonstrate the novel synthesis and development of Afb-AuNPs, highlighting the anticancer potential of such a system and applicability to other small molecules and therapeutics.

2. EXPERIMENTAL SECTION

2.1. Organic Synthesis. The syntheses of compounds **2−6** were performed by adaptation of a published method[35] from the commercially available starting material **1** (7-chloro-6-nitro-4(3*H*)-quinazolinone). The full synthetic details and characterization of these and all other compounds (**9−16**) can be found in the Supporting Information (Figures S1−S23).

2.2. Assembly of Afb-AuNPs. To a 1 mL solution of unmodified AuNPs (Sigma-Aldrich, UK, 500 μg/mL), 70 μL of disulfide **16** (50 μg, 1 mM in DMSO) was added dropwise and stirred for 2 h in the dark at room temperature. The reaction mixture was subjected to centrifugal filtration at 2800g for 10 min (10 kDa MWCO, Amicon Ultra-15, regenerated cellulose, Millipore, MA), washed twice with water, and resuspended back to their original volume. This was then followed by the dropwise addition of 10 μL of 2 mM poly(ethylene glycol) 2-mercaptoethyl ether acetic acid (HS-PEG-COOH, MW 3400; Sigma-Aldrich, UK) to the AuNPs. This was stirred overnight in the dark at room temperature. Subsequently, Afb-AuNPs were purified using centrifugal filtration as described above, resuspended in water, and stored at 4 °C.

2.3. Characterization of Afb-AuNPs. Transmission electron microscopy was performed using a JEOL 1400 Plus electron microscope (JEOL Ltd., Hertfordshire, UK) with an accelerating voltage of 120 keV. Images were captured using an AMT XR16 camera and processed using AMT image capture software (Woburn, MA). Dynamic light scattering and zeta-potential measurements were determined in water using a Zetasizer Nano ZS ZSP (Malvern Instruments Ltd., Worcestershire, UK) in triplicate. UV−vis spectra were obtained using 100 μL of appropriately diluted sample per well in a 96-well plate and acquired using a SpectraMax i3X (Molecular Devices, San Jose, CA).

2.4. Calculation of Drug Conjugation Efficiency. To determine the amount of Afb-A bound to AuNPs, a solution of Afb-AuNPs (100 μL, 100 μg/mL) and supernatant after conjugation (100 μL) was analyzed using UV−vis spectroscopy (λ_{abs} = 345 nm). The concentration of Afb-A bound to AuNPs was calculated with reference to a calibration curve (0−500 μg/mL, R^2 = 0.9942).

297

Scheme 1. Synthesis of Afatinib Analogue[a]
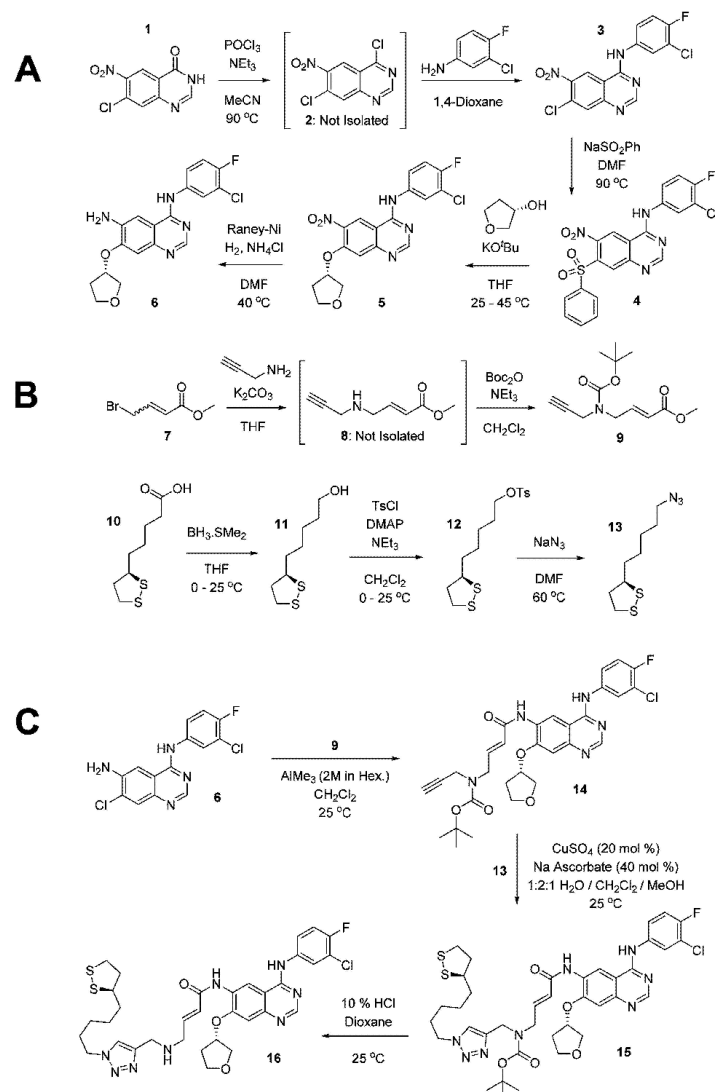
[a](A) Beginning with starting material **1**, we generated the quinazoline core (compound **6**) also found in afatinib, in four synthetic steps. (B) Synthesis of linker fragments and completion of the molecule. Compound **9** contains an alkyne, and **13** has a cyclic disulfide group to allow attachment to AuNPs and an azide group for click chemistry with **9**. (C) Attachment of the alkyne bearing group to the quinazoline core and subsequent click reaction and deprotection to give the final compound **16**.

2.5. In Vitro Drug Release. A 1 mL solution of Afb-AuNPs was placed into a Float-A-Lyzer dialysis device (3.5 kDa MWCO, Spectrum Laboratories Inc., Rancho Dominguez, CA) and incubated in either phosphate buffer (10 mM, pH 7.4) or acetate buffer (10 mM, pH 5.5) containing 0.5% (v/v) polysorbate 80 with mild agitation (100 rpm) at 37 °C. At predetermined time points, 1 mL of sample was taken, and the removed volume was immediately replaced with fresh buffer. Absorbance measurements (λ_{abs} = 345 nm) of the release medium were acquired using a ND-1000 spectrophotometer (Thermo Fisher Scientific, Waltham, MA).

2.6. Cell Culture and Nanoparticle Exposure. TT1 cells were cultured to confluence in 96-well tissue culture plates using DCCM-1

298

152 medium (Geneflow, Lichfield, UK) supplemented with 10% (v/v)
153 newborn calf serum (NCS, Invitrogen, Paisley, UK) and 1% (v/v)
154 penicillin/streptomycin/glutamine (PSG; Invitrogen, UK). AS49 (lung
155 adenocarcinoma) and PC-9 (lung adenocarcinoma, kindly gifted by
156 Professor Michael Seckl, Imperial College London) were cultured in
157 RPMI-1640 medium (Sigma-Aldrich, UK) supplemented with 10% (v/
158 v) fetal bovine serum (FBS; Invitrogen, UK) and 1% (v/v) PSG. Cells
159 were plated at 0.25×10^5 per well, and confluence was achieved within
160 48 h. Throughout, cells were maintained in a humidified incubator at 37
161 °C and 5% CO_2. Confluent monolayers were treated with AuNPs, PEG-
162 AuNPs, and Afb-AuNPs dispersed in appropriate medium at
163 concentrations ranging from 0.03 to 30 μg/mL of AuNP, and exposures
164 were performed in triplicate for all cell lines.

165 　　**2.7. Cell Viability.** Following exposure to nanoparticles for 72 h,
166 growth media containing AuNPs was removed, and cells were washed
167 twice with sterile Dulbecco's phosphate buffered saline (DPBS; Sigma-
168 Aldrich, UK). Cells were then incubated in a solution of 3-(4,5-
169 dimethylthiazol-2-yl)-2,5-diphenyltetrazolium bromide (MTT, VWR,
170 UK), placed at 37 °C, and left until formazan crystal formation could be
171 observed. The MTT solution was aspirated, cells were lysed, and
172 samples were analyzed spectrophotometrically (λ_{abs} = 570 nm) using a
173 SpectraMax Plus 384 spectrophotometer (Molecular Devices, UK).

174 　　**2.8. Electric Cell–Substrate Impedance Sensing (ECIS).** Live
175 cell proliferation studies were performed using the RTCA iCELLigence
176 system with RTCA Data Analysis Software 1.0 (ACEA Biosciences, San
177 Diego, CA). This system allows for label-free, real-time, dynamic
178 monitoring of cells using impedance as a readout of cell viability and
179 proliferation. AuNPs, PEG-AuNPs, and AFB-AuNPs were mixed with
180 the cell suspensions at equivalent concentrations, seeded on a L8 E-
181 plate (ACEA Biosciences), and incubated for 0.5–2 h at room
182 temperature to allow cellular equilibration and adhesion. The plates
183 were then placed in the impedance recorder in a humidified incubator at
184 37 °C and 5% CO_2, and measurements were taken every hour for 72 h.
185 A cell concentration of 0.25×10^5 cells per well was used for all
186 experiments. Cells grown in complete medium and medium alone were
187 used as controls. Each treatment was assessed in triplicate or
188 quadruplicate.

189 　　**2.9. Inflammatory Mediator Release.** Following exposure of cells
190 to NPs for 72 h, conditioned media was collected, and release of IL-6
191 and IL-8 was quantified using enzyme-linked immunosorbent assays
192 (ELISA). Samples were analyzed in accordance with the manufacturer's
193 instructions (PeproTech, USA). Data were collected spectrophoto-
194 metrically (λ_{abs} = 450 nm) using a SpectraMax Plus 384
195 spectrophotometer (Molecular Devices, UK). Results were generated
196 from three separate experiments with three readouts per experiment.

197 　　**2.10. Nanoparticle Uptake.** A549 cells were plated on a μ-Slide 8
198 well-chambered coverslip (Ibidi, Germany) at a density of 3×10^5 cells
199 per well and incubated overnight to allow cellular attachment. The cells
200 were then exposed to Afb-AuNPs (20 μg/mL) prepared in the
201 complete growth medium used for initial cell plating. After 3, 6, and 24
202 h, Afb-AuNPs were removed, and the cells were washed three times
203 with PBS, fixed with 4% (v/v) paraformaldehyde, and permeabilized
204 with ice-cold methanol. Subsequently, cells were stained with
205 antilysosomal-associated membrane protein (LAMP)-2-Alexa Fluor
206 488 (Thermo Fisher Scientific, UK) and Hoescht 33342 (Thermo
207 Fisher Scientific, UK). AuNPs were visualized using a He–Ne laser (λ =
208 543 nm). Images were captured using a Leica TCS SP5 confocal
209 microscope (Leica Microsystems, Germany) with a 63× objective lens
210 and processed with ImageJ software.

211 　　**2.11. Statistical Analysis.** Data are presented as the mean ±
212 standard error, where $n = 3$ (three independent experiments performed
213 with three different cell generations) unless otherwise stated. Statistical
214 comparisons were selected *a priori*; therefore, significant observations
215 were verified by t test or one-way analysis of variance (ANOVA) with
216 Bonferroni post-test. Prism v5 (GraphPad, USA) was used for all
217 statistical calculations. In all analyses, a P value of <0.05 was considered
218 significant.

3. RESULTS AND DISCUSSION

3.1. Synthesis of an Afatinib Analogue for Conjugation to AuNPs.
219 The first step was to synthesize an analogue of
221 Afb that retained its activity and was amenable to conjugation to
222 AuNPs. The construction of the Afb model **16** (Scheme 1) s1
223 required the synthesis of an afatinib precursor **6** and the
224 synthesis of alkyne- and azide-containing units **9** and **13** which
225 would combine via a "click" reaction to form the linker portion
226 of the construct. In brief, chlorination of commercially available
227 7-chloro-6-nitro-4(3*H*)quinazolinone (**1**) using $POCl_3$ afforded
228 4-chloroquinazoline (**2**) which was not isolated but used in the
229 subsequent nucleophilic aromatic substitution (S_NAr) reaction
230 at C-4 with 3-chloro-4-fluoroaniline to give 4-aminoquinazoline
231 (**3**) (77%). Two sequential further S_NAr reactions at C-7 with
232 benzenesulfinic acid (→ **4**, 87%) and then (*S*)-(+)-tetrahydro-3-
233 furanol gave ether **5** (66%). Reduction of the C-6 nitro group
234 using Raney Ni then gave the 6-aminoquinazoline core **6** (77%,
235 Scheme 1A). Ensuring the preservation of the C-4 aniline and C-
236 6 acrylamide groups surrounding the quinazoline core was
237 important, as they have been shown to be critical motifs that
238 dictate selectivity for EGFR and irreversible covalent binding via
239 Michael addition to cysteine 797 in the EGFR kinase domain,[36]
240 respectively. Indeed, X-ray crystallography of Afb bound to both
241 wild-type EGFR and the $EGFR^{T790M}$ mutant demonstrated
242 covalent bond formation between the acrylamide group of Afb
243 and cysteine 797,[37] confirming the structure–activity relation-
244 ship is governed by the acrylamide group in particular.

245 　　Synthesis of the alkyne- and azide-containing units **9** and **13**,
246 which were designed to combine to form the linker between the
247 AuNPs and the 6-aminoquinazoline **6**, required just two steps
248 and three steps, respectively, from commercial materials. Thus,
249 the alkyne **9** was prepared by reaction of methyl *trans* 4-
250 bromocrotonate (**7**) with propargylamine to give amine **8**,
251 which was not isolated but protected as its *N*-Boc derivative
252 (48%). The azide **13**, which contains the aurophilic cyclic
253 disulfide moiety, was synthesized by reduction of (±)-α-lipoic
254 acid (**10**) to give alcohol **11** (97%), tosylation to give sulfonate
255 **12** (62%), and then azide displacement (76%). The assembly of
256 compounds **6**, **9**, and **13** was orchestrated as shown in Scheme
257 1B. Ester **9** was coupled with quinazoline **6** by trimethyl-
258 aluminum mediated amidation to give amide **12** (95%). This
259 molecule presents a terminal alkyne in place of the
260 dimethylamino unit found in Afb to facilitate the click reaction.
261 We chose to replace the dimethylamino group with propargyl-
262 amine, as previous studies have shown good tolerance to
263 substitution at this position.[38,39] The introduction of propargyl-
264 amine gave quinazoline derivative **14** which contains an alkyne
265 functionality to facilitate the click reaction with azide **13**. To
266 attach the two components, we therefore reacted azide **13** and
267 alkyne **14** together in the presence of copper sulfate and sodium
268 ascorbate to give triazole **15** (65%). Finally, Boc deprotection
269 was achieved using 10% HCl in 1,4-dioxane to give **16** as the
270 final product in a 98% yield (Scheme 1C).

3.2. Development and Characterization of Afb-AuNPs.
271 The construction of Afb-AuNPs began by taking commercially
272 available citrate-capped AuNPs and tethering the Afb analogue
274 **16** (termed Afb-A) to them, followed by addition of a thiolated
275 PEG linker, utilizing well-established alkyl thiol–gold chem-
276 istry.[40] The cyclic disulfide group was used to attach Afb-A to
277 AuNPs; by providing two Au–S bonds per molecule, greater
278 stability is achieved, thereby ensuring efficient drug loading, as
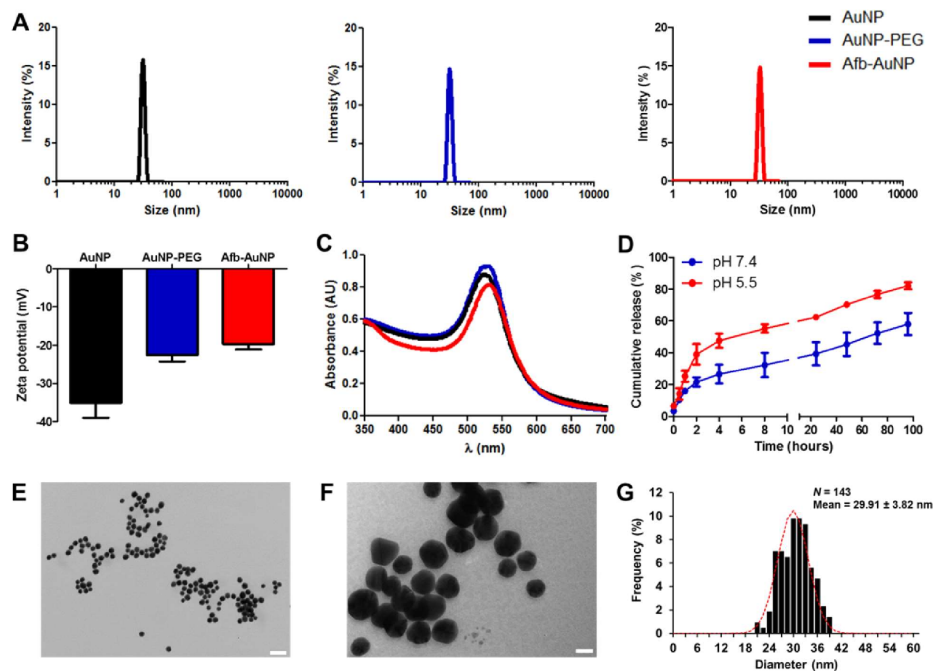279 single Au–S bonds have been shown to be displaced by strong

Figure 2. Characterization of Afb-AuNPs. (A) Hydrodynamic diameter measurements of AuNPs (black), AuNP-PEG (blue), and Afb-AuNPs (red) obtained by dynamic light scattering. (B) Zeta-potential measurements of the AuNPs mentioned above (mean ± SD, $n = 3$). (C) UV−vis spectra of AuNPs discerning the λ_{max} and corresponding red-shifts as AuNPs are functionalized. (D) *In vitro* release profile of Afb-A from AuNPs at pH 7.4 or pH 5.5 (mean ± SD, $n = 3$). (E) transmission electron micrograph of Afb-AuNPs (40000× magnification, scale bar = 100 nm). (F) Further magnified image of Afb-AuNPs (200000× magnification, scale bar = 20 nm). (G) Histogram of Afb-AuNP sizes as measured by TEM (distribution presented as mean ± SD).

nucleophiles.[41] One previous study that used single Au−S linkages to PEGylate AuNPs also aimed to conjugate Afb.[42] However, the conjugation yields were significantly less than presented here, potentially due to the method of coupling. EDC/NHS chemistry is well suited for nucleophilic primary amines;[43] as Afb does not possess any, this may have prevented conjugation.

Conjugation of Afb-A was confirmed by UV−vis spectrometry. We found that 80% of Afb-A was bound to AuNPs, equivalent to 0.08 μg of Afb-A per μg of AuNP (0.4 mol of Afb-A per AuNP). Dynamic light scattering (DLS) measurements (Figure 2A) revealed an increase in the diameter of AuNPs, confirming conjugation. Unmodified AuNPs were 40 nm, PEGylated AuNPs were ∼43 nm, and Afb-AuNPs were ∼46 nm in diameter (Table S1). Further indirect confirmation of conjugation was evidenced by the changes in surface charge, as measured by zeta potential (Figure 2B). The zeta potential of unmodified AuNPs was −35 mV, which became less negative as molecules were conjugated to the AuNP surface because of displacement of negatively charged citrate anions. The construct was PEGylated to afford increased biocompatibility and retention of a negative surface charge by virtue of free, terminal carboxyl groups. The negative surface charge also aids in preventing nonspecific adsorption of proteins to the surface of the NP. Accordingly, Afb-AuNPs had a zeta potential of −19.7

mV (Table S1). Optical parameters such as the extinction and scattering efficiencies of AuNPs are influenced by particle size. As such, UV−vis spectroscopy can determine the size of AuNPs based on their surface plasmon resonance (SPR), in excellent agreement with the mathematical theory that underpins the technique.[44] Concordantly with DLS, UV−vis spectroscopy (Figure 2C) revealed an increase in size as AuNPs were modified. We observed a red-shift in SPR of modified AuNPs, indicative of increasing particle size, further suggesting successful conjugation of Afb-A to AuNPs. The red-shift in the SPR can be attributed to the increase in dielectric constant around the surface of the AuNP upon conjugation with thiolated ligands.[45] Unmodified AuNPs had a λ_{max} of 523 nm, which increased when AuNPs were PEGylated to 525 nm and increased further to 530 nm when Afb-A and PEG were conjugated to AuNPs. The release of Afb-A from AuNPs (Figure 2D) was examined at physiological and acidic pH (7.4 and 5.5, respectively). Differential rates of liberation from AuNPs were observed after as early as 2 h, whereby 41% of Afb-A had been released at pH 5.5 compared with 23% at pH 7.4. At all further time points assessed the cumulative release of Afb-A was consistently greater at pH 5.5 than that at pH 7.4. The Au−S bond is labile below pH 6 due to protonation of the S atom;[46,47] therefore, the acidic environment may act to expedite release from the AuNP. Transmission electron microscopy (TEM)

300

confirmed Afb-AuNPs had a spherical morphology (Figure 2E,F) and exhibited size measurements in agreement with those obtained using alternative methods (Figure 2G). Thus, AuNPs were successfully modified without drastically altering their physicochemical properties or compromising colloidal stability.

These physicochemical characteristics are well suited for delivery to solid tumors via the EPR effect. Afb-AuNPs are of a suitable size (~46 nm) such that they avoid renal filtration (NPs with a diameter <6 nm are filtered by the kidneys) and excess sequestration in the liver as larger NPs become entrapped within hepatic sinusoids.[48] Moreover, a PEG sheath increases hydrophilicity which provides a steric barrier to opsonization, thereby further mitigating recognition by the RES.[49] These properties are known to increase the circulatory half-life of nanoparticles *in vivo*,[50] improving the probability for drug-bearing NPs to accumulate in tumors. Although dependence on the EPR effect for nanoparticle delivery may not be optimal for all tumor types, strategies to augment this process can be implemented.[51] For example, localized hyperthermia can be used to promote vascular permeability in tumors.[52]

This approach is of particular interest when using AuNPs as drug delivery vehicles; AuNPs such as hollow nanoshells and nanorods can transform photons in the form of near-infrared light into thermal energy, creating hyperthermic regions proximal to the NPs. This intrinsic property is leveraged in the process of photothermal therapy whereby AuNPs that have accumulated in tumors thermally ablate the tissue.[53] This modality can increase the permeability of the tumor to chemotherapy and NPs acting as a dual therapy and EPR effect enhancer.[54] Moreover, terminal carboxyl groups on PEG chains can be used to attach tumor specific targeting moieties such as nucleic acids[55] or peptides[56] in an attempt to more adroitly target tumors. The work presented in this study can be combined with these functionalities for multimodal chemotherapy and thermal therapy

3.3. Afb-AuNPs Cause NSCLC Cell Cytotoxicity. As a proof of concept, a dose response to Afb-AuNP treatment was determined using confluent monolayers of the lung adenocarcinoma cell line PC-9, which harbors a deletion within exon 19 in EGFR,[57] sensitizing them to TKI therapies. AuNPs and PEGylated AuNPs were not cytotoxic at any of the doses investigated, in agreement with previous literature,[58] whereas dose-dependent cytotoxicity was observed when cells were exposed to Afb-AuNPs (Figure 3A).

Significant reductions in cell viability (24% compared to AuNP, $P < 0.05$) were seen at doses as low as 0.3 μg/mL AuNP. There were further reductions in cell viability with increasing concentrations of Afb-AuNPs; at 3 μg/mL, Afb-AuNPs reduced cell viability by 81% compared to the equivalent concentration of AuNPs ($P < 0.001$), demonstrating both the biocompatibility of AuNPs and the therapeutic potential of Afb-AuNPs. The versatility of the system was shown by screening Afb-AuNPs in the lung adenocarcinoma cell line A549 (Figure 3B) which are wild type for EGFR expression and are not sensitive to TKIs. Despite this, Afb-AuNPs retained some efficacy, particularly at the higher doses examined. At an AuNP concentration of 10 μg/mL, Afb-AuNPs induced a 42% reduction in cell viability compared to the equivalent dose of AuNPs ($P < 0.01$). A further decrease in cell viability was noted at an AuNP dose of 30 μg/mL, where Afb-AuNPs elicited a 60% decrease in cell viability ($P < 0.001$).

To elucidate the extent to which AuNPs were influencing the cytotoxic effect of Afb-A, the effect of free Afb-A and Afb-AuNPs
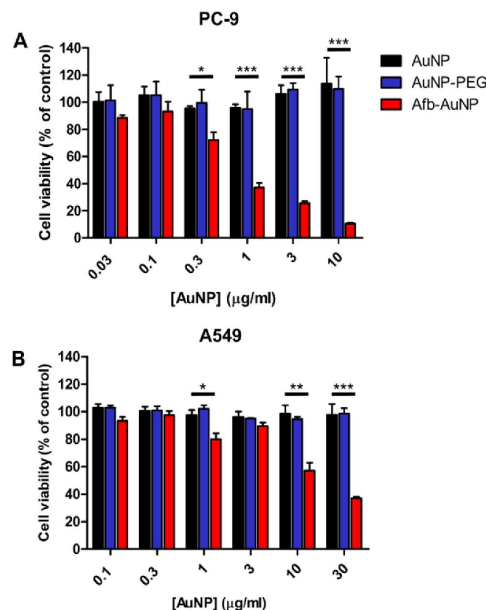

Figure 3. *In vitro* cytotoxicity of Afb-AuNPs. (A) The lung adenocarcinoma cell line PC-9 and (B) A549 were exposed to increasing concentrations of AuNPs (black), AuNP-PEG (blue), or Afb-AuNPs (red) for 72 h, and cell viability was assessed by MTT assay. Data are expressed as mean ± SEM, $n = 3$. *$P < 0.05$; **$P < 0.01$; ***$P < 0.001$.

at different doses was examined. In PC-9 cells (Figure 4A) Afb-AuNPs were significantly more cytotoxic than equimolar concentrations of free drug at a majority of doses studied. At 0.03 μM, Afb-A decreased cell viability by 43%, whereas Afb-AuNPs at the same drug concentration caused significantly more cell viability loss (66%, $P < 0.05$). This observation was recapitulated at 0.1 μM ($P < 0.01$) and further increased doses ($P < 0.001$) where Afb-AuNPs induced almost complete loss of cell viability (~91%). In the less sensitive A549 cells (Figure 4B) free Afb-A and Afb-AuNPs exhibited similar efficacy up to a concentration of 3 μM where Afb-AuNPs were significantly more cytotoxic than equivalent free Afb-A (64% vs 40% reduction in viability, $P < 0.01$), a result that was also observed at 10 μM ($P < 0.01$). Similar observations were also witnessed when Afb-AuNPs were compared to free Afb in a dose response fashion (Figure S24). Furthermore, the IC$_{50}$ of free Afb-A in PC-9 cells was found to be 0.05 μM, whereas Afb-AuNPs had an IC$_{50}$ of 0.02 μM, representing a 2.5-fold increase in potency. Similarly, in A549 cells the Afb-A IC$_{50}$ was 6.08 μM compared to 1.65 μM for Afb-AuNPs, translating to a 3.7-fold potency increase; thus, we could attribute the cytotoxic effects observed to the conjugated Afb-A. Indeed, in A549 cells the IC$_{50}$ of Afb-AuNPs was significantly lower than that reported previously for Afb[59] which was comparable to free Afb-A. Although the mechanism underlying this increase in potency is not fully clear, one explanation could be increased intracellular concentration of Afb-A due to uptake of AuNPs.[60] As Afb has been shown to alter the efflux function of P-glycoprotein[61] (otherwise known as
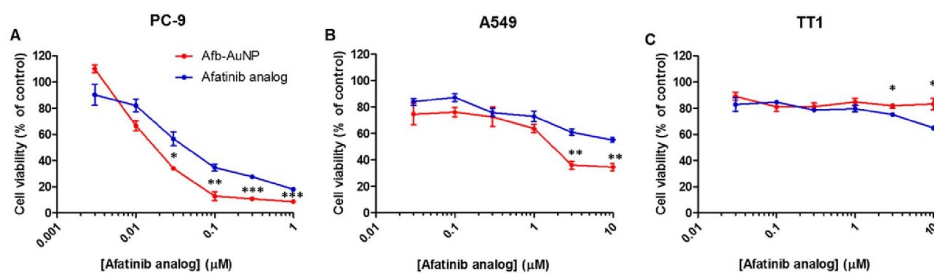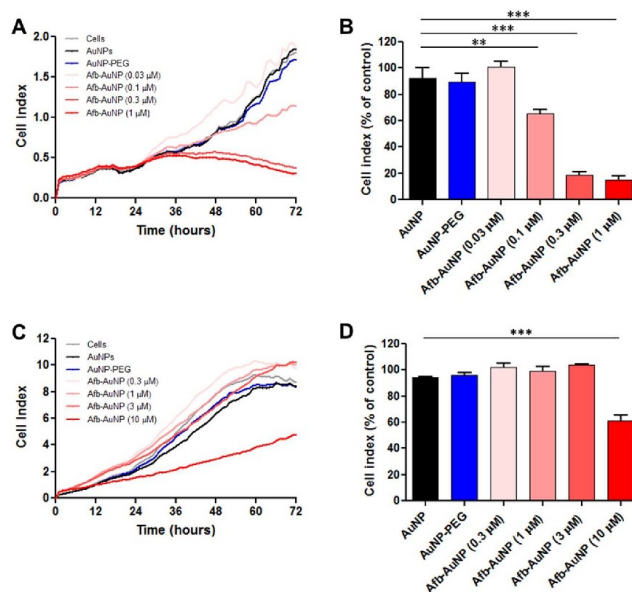
Figure 4. Dose response curves post Afb-AuNP and Afb-A treatment. (A) PC-9, (B) A549, and (C) alveolar epithelial TT1 cells were exposed to increasing concentrations of Afb-A or Afb-AuNPs for 72 h, and cell viability was assessed by MTT assay. Data are expressed as mean ± SEM, $n = 3$. *$P <$ 0.05; **$P < 0.01$; ***$P < 0.001$.

Figure 5. Inhibition of cell proliferation by Afb-AuNPs. (A) Representative proliferation curves of PC-9 cells upon exposure to AuNPs, AuNP-PEG, or increasing doses of Afb-AuNP. (B) Quantification of cell proliferation at 72 h (untreated cells used as control) . (C, D) as in (A, B) but cell proliferation assessed in A549 cells. Data are expressed as mean ± SEM, $n = 4$. **$P < 0.01$; ***$P < 0.001$.

ATP-binding cassette subfamily B member 1, ABCB1), the enhanced intracellular levels of Afb-A may then serve to inhibit its own efflux over time, leading to greater or more sustained inhibition of EGFR; however, further studies would be needed to explore this.

We also investigated the effect of free Afb-A and Afb-AuNPs on TT1 cells (Figure 4C); as these cells cover 95% of the alveolar epithelial surface,[62] the implications of toxicity to these cells could be instrumental in determining choice of therapy and its success. Moreover, examination of the normally functioning cells proximal to the disease area of interest is a procedure which is often excluded from *in vitro* drug delivery studies even though there is potential for drug interaction with normal cells. Afb-AuNPs and unmodified AuNPs (Figure S25) were not overtly cytotoxic at any of the doses studied; however, free Afb-A was

found to be significantly more cytotoxic at 3 and 10 μM ($P <$ 0.05). This data may suggest a selectivity of Afb-AuNPs toward cancerous cells, which could be predicated on EGFR expression. Indeed, we have previously shown the distinction between TT1 cells and A549 cells and that TT1 cells better represent the alveolar epithelial type I cell[63] and therefore serves to more accurately reflect the differential *in vivo* interactions of Afb-AuNPs in the alveolar region where lung adenocarcinomas are most prevalent.

3.4. Afb-AuNPs Inhibit NSCLC Cell Proliferation. After profiling the effect of Afb-AuNPs on confluent monolayers, we next investigated the effect of Afb-AuNPs on actively proliferating cells, using a cell-impedance based system that allows for label-free, real-time study of cell proliferation. A dose-dependent response to Afb-AuNPs was observed in PC-9 cells
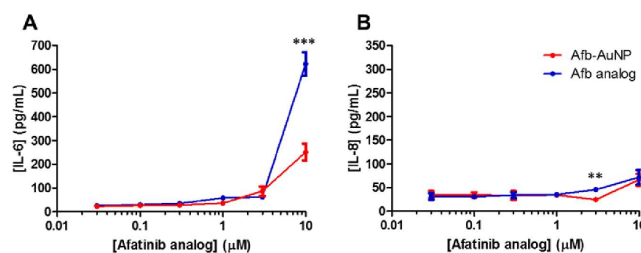
G

Figure 6. Inflammatory mediator release from TT1 cells. Alveolar epithelial cells were exposed to increasing doses of Afb-A or Afb-AuNPs, and the release of (A) IL-6 and (B) IL-8 from confluent monolayers was measured by ELISA. Data are expressed as mean ± SEM, $n = 3$. **$P < 0.01$; ***$P < 0.001$.

(Figure 5A), whereas AuNPs and PEGylated AuNPs did not have antiproliferative effects (AuNP concentration was equal to the AuNP concentration in the highest dose of Afb-AuNPs), consistent with cell viability results. No significant difference was noted when cells were treated with Afb-AuNPs at a dose of 0.03 μM (Figure 5B); however, 0.1 μM Afb-AuNPs significantly inhibited cell proliferation compared to AuNPs ($P < 0.01$). As the dose of Afb-AuNPs increased, the inhibition of proliferation was greater; 0.3 and 1 μM Afb-AuNPs inhibited cell proliferation by 74% and 78%, respectively, compared to AuNPs ($P < 0.001$). In A549 cells (Figure 5C), a pattern somewhat similar to cell viability studies was observed whereby only the highest dose of Afb-AuNPs was able to inhibit cell proliferation. This dose of free Afb (10 μM) was also able to inhibit cell proliferation to the same degree (Figure S26), suggesting maintenance of therapeutic efficacy using Afb-AuNPs. The biocompatibility of AuNPs and PEGylated AuNPs was again confirmed in A549 cells as no inhibitory effect was noted (Figure 5D), whereas Afb-AuNPs at a dose of 10 μM reduced the proliferative capacity of the cells by 33% ($P < 0.001$).

The intrinsic sensitivity to TKIs plays a role in the differential cytotoxicity of Afb-AuNPs, which is exemplified by these proliferation studies, whereby lower concentrations of Afb-AuNPs were required to inhibit PC-9 cell proliferation compared to A549 cells. These results corroborated those observed in the cytotoxicity studies but also demonstrated that Afb-AuNPs retained efficacy under different experimental conditions, as unmodified AuNPs were not found to significantly reduce the proliferation of either cell type. Taken together, these results demonstrate that Afb-AuNPs can not only act on confluent monolayers of cells but also actively proliferate cancer cells, highlighting the utility of the AuNP system.

3.5. Conjugation of Afb to AuNPs Attenuates Inflammatory Cytokine Release. After investigating the anticancer capacity of Afb-AuNPs, we next explored the inflammatory response of the healthy alveolar epithelium upon exposure to Afb-AuNPs and the free drug equivalent. At a majority of the doses investigated, the release of interleukin (IL)-6 from TT1 cells was not significantly different between Afb-A and Afb-AuNPs (Figure 6A). A slight trend toward increased IL-6 release as the dose increased was noted, with no more than 90 pg/mL detected, suggesting a tolerability of Afb-AuNPs at the alveolar epithelial interface. At a dose of 10 μM, both Afb-AuNPs and Afb-A stimulated IL-6 release; however, Afb-A elicited a 2.5-fold increase in IL-6 production compared to the equivalent dose of Afb-AuNPs ($P < 0.001$). We observed a similar pattern with IL-8 release from TT1 cells (Figure 6B); we

noted a 1.9-fold increase in the release of IL-8 at a dose of 3 μM Afb-A compared to Afb-AuNPs ($P < 0.01$); however, this difference was not observed at any other doses. Moreover, we did not see significant release of IL-6 or IL-8 by A549 cells when exposed to Afb-AuNPs (Figure S27), indicating the lack of immunogenicity these molecules possess. As IL-6 is heavily involved in driving pro-tumorigenic inflammation,[64] this has led to its implication in the pathogenesis of LC.[65] The underlying mechanism appears to centralize around an IL-6/STAT3 signaling axis, whereby IL-6 fosters oncogenic signaling through activation of STAT3.[66] Moreover, activated EGFR prolongs this signaling cascade,[67] providing a rationale for dual anti IL-6/EGFR therapy in LC. Indeed, attenuation of proinflammatory cytokine release, particularly IL-6, from TT1 cells upon exposure to Afb-AuNPs compared to free Afb-A provides supporting evidence for the biocompatibility of our system.

3.6. Cellular Uptake of Afb-AuNPs. Finally, to better understand the intracellular fate of Afb-AuNPs, the uptake of these particles by A549 cells was investigated using confocal microscopy (Figure 7). After 3 h, there was evidence of intracellular accumulation of AuNPs, suggesting surface functionalization did not prevent internalization. Visualized (in red) by virtue of their SPR, dispersed AuNPs were distributed throughout the cytoplasm and perinuclear region and were not observed in the nucleus (blue), in agreement with previous studies using AuNPs of a similar size.[68] Small clusters of AuNPs appeared to localize near endosomal structures (merge panel), implying an endosomal route may have been utilized by the cells to internalize the particles. At 6 h post AuNP exposure, the appearance of AuNP clustering in the cytoplasm was more apparent, and there was no evidence of lysosomal colocalization. When we examined the cells 24 h post AuNP exposure, further coalescence of the AuNPs in the cytoplasm was evident, and although we did not observe signs of colocalization, larger clusters of AuNPs were found to be close to the nucleus and proximal to lysosomes which could be due to lysosomal escape, allowing for cytoplasmic release of Afb and subsequent inhibition of EGFR. AuNPs are known to be internalized into cells by endocytosis; however, their method of entry is largely dependent on their physicochemical properties. The clustering dynamics we observed are consistent with the intracellular trafficking of AuNPs of ~50 nm in diameter, whereby AuNPs were found to accumulate and cluster in lysosomes over time.[69] Although we did not see direct evidence of colocalization at the 24 h time point, Afb-AuNPs appeared to coalesce proximally to lysosomes, suggesting Afb-AuNPs may be internalized by an endocytic mechanism. It has been shown previously that AuNPs
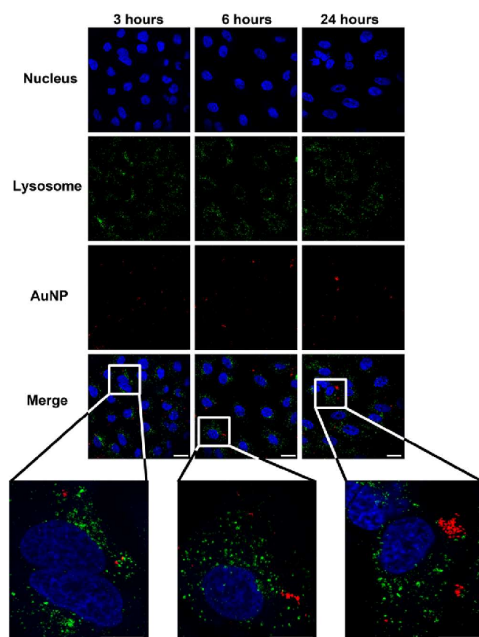
303

Figure 7. Intracellular uptake and distribution of Afb-AuNPs. A549 cells were exposed to Afb-AuNPs for 3, 6, or 24 h prior to imaging by confocal microscopy. The nucleus is visualized in blue, lysosomes in green, and AuNPs in red. Scale bar = 15 μm.

of this size are taken up into cells by endocytosis,[70] although future studies would be needed to fully outline the internalization process. Clustering of Afb-AuNPs via lysosomal processing could be due to increased agglomeration, as the cleavage of Afb-A and PEG from AuNPs may impact colloidal stability. Similar to the tumor microenvironment, lysosomes have an acidic pH which can lead to increased Afb-A release from AuNPs due to Au–S bond breakage. This bond cleavage results in release of the drug cargo from the AuNPs into the cytoplasm where it can subsequently bind to EGFR. A majority of Afb-A is released from AuNPs after 48 h and may continue to be released from AuNP depots within the cell, whereas free Afb-A initially traverses the plasma membrane. Tt may be effluxed or inactivated as previously postulated; therefore, more Afb-A becomes available over time if delivered using AuNPs, providing a potential explanation for the increased potency demonstrated in the cytotoxicity studies.

4. CONCLUSION

In summary, a novel AuNP formulation was developed based on the clinically approved chemotherapeutic agent Afb. To achieve this, a molecular analogue of Afb was synthesized that permitted conjugation to AuNPs to create Afb-AuNPs. Afb-AuNPs were shown to exhibit cytotoxicity toward and inhibit proliferation of NSCLC cells while maintaining biocompatibility in TT1 cells, a model cell of the healthy alveolar epithelium. Afb-AuNPs were also shown to be noninflammatory in both healthy and cancerous cells and were internalized despite surface mod-

ifications; however, the mechanism is still to be fully elucidated. Results presented here suggest Afb-AuNPs would be promising candidates for future *in vivo* studies given their physicochemical properties and *in vitro* efficacy. Furthermore, the methodology outlined provides an avenue of exploration using other therapeutics not typically utilized for conjugation to NPs, expanding the molecular toolkit available for drug delivery.

■ ASSOCIATED CONTENT

ⓢ Supporting Information

The Supporting Information is available free of charge on the ACS Publications website at DOI: 10.1021/acsami.9b02986.

> Experimental details for synthesis of all compounds, ^{1}H and ^{13}C NMR spectra of all compounds, ESI mass spectrum of compound **16**, afatinib dose responses, TT1 cell viability, inhibition of cancer cell proliferation by TKIs, A549 cytokine release, and table listing additional information about AuNP formulations (PDF)

■ AUTHOR INFORMATION

Corresponding Author

*E-mail: a.cryer14@imperial.ac.uk (A.M.C.).

ORCID ⓞ

Alexander M. Cryer: 0000-0002-3954-2179
Alan C. Spivey: 0000-0001-5114-490X

Author Contributions

C.C. and A.E. contributed equally to this work

Notes

The authors declare no competing financial interest.

■ REFERENCES

(1) Torre, L. A.; Bray, F.; Siegel, R. L.; Ferlay, J.; Lortet-Tieulent, J.; Jemal, A. Global Cancer Statistics, 2012. *Ca-Cancer J. Clin.* **2015**, *65*, 87−108.

(2) Chen, Z.; Fillmore, C. M.; Hammerman, P. S.; Kim, C. F.; Wong, K. K. Non-Small-Cell Lung Cancers: A Heterogeneous Set of Diseases. *Nat. Rev. Cancer* **2014**, *14*, 535−546.

(3) Rotow, J.; Bivona, T. G. Understanding and Targeting Resistance Mechanisms in NSCLC. *Nat. Rev. Cancer* **2017**, *17*, 637−658.

(4) Lynch, T. J.; Bell, D. W.; Sordella, R.; Gurubhagavatula, S.; Okimoto, R. A.; Brannigan, B. W.; Harris, P. L.; Haserlat, S. M.; Supko, J. G.; Haluska, F. G.; Louis, D. N.; Christiani, D. C.; Settleman, J.; Haber, D. A. Activating Mutations in the Epidermal Growth Factor Receptor Underlying Responsiveness of Non-Small-Cell Lung Cancer to Gefitinib. *N. Engl. J. Med.* **2004**, *350*, 2129−2139.

(5) Paez, J. G.; Janne, P. A.; Lee, J. C.; Tracy, S.; Greulich, H.; Gabriel, S.; Herman, P.; Kaye, F. J.; Lindeman, N.; Boggon, T. J.; Naoki, K.; Sasaki, H.; Fujii, Y.; Eck, M. J.; Sellers, W. R.; Johnson, B. E.; Meyerson, M. EGFR Mutations in Lung Cancer: Correlation with Clinical Response to Gefitinib Therapy. *Science* **2004**, *304*, 1497−1500.

(6) Mok, T. S. K. Personalized Medicine in Lung Cancer: What We Need To Know. *Nat. Rev. Clin. Oncol.* **2011**, *8*, 661−668.

(7) Herbst, R. S.; Morgensztern, D.; Boshoff, C. The Biology and Management of Non-Small Cell Lung Cancer. *Nature* **2018**, *553*, 446−454.

(8) Siegel, R. L.; Miller, K. D.; Jemal, A. Cancer Statistics, 2019. *CA-Cancer J. Clin.* **2019**, *69*, 7−34.

(9) Chow, E. K.; Ho, D. Cancer Nanomedicine: From Drug Delivery to Imaging. *Sci. Transl. Med.* **2013**, *5*, 216rv4.

(10) Shi, J.; Kantoff, P. W.; Wooster, R.; Farokhzad, O. C. Cancer Nanomedicine: Progress, Challenges and Opportunities. *Nat. Rev. Cancer* **2017**, *17*, 20−37.

(11) Peer, D.; Karp, J. M.; Hong, S.; Farokhzad, O. C.; Margalit, R.; Langer, R. Nanocarriers as an Emerging Platform for Cancer Therapy. *Nat. Nanotechnol.* **2007**, *2*, 751−760.

(12) Maeda, H.; Nakamura, H.; Fang, J. The EPR Effect for Macromolecular Drug Delivery to Solid Tumors: Improvement of Tumor Uptake, Lowering of Systemic Toxicity, and Distinct Tumor Imaging In Vivo. *Adv. Drug Delivery Rev.* **2013**, *65*, 71−79.

(13) Miller, M. A.; Gadde, S.; Pfirschke, C.; Engblom, C.; Sprachman, M. M.; Kohler, R. H.; Yang, K. S.; Laughney, A. M.; Wojtkiewicz, G.; Kamaly, N.; Bhonagiri, S.; Pittet, M. J.; Farokhzad, O. C.; Weissleder, R. Predicting Therapeutic Nanomedicine Efficacy Using a Companion Magnetic Resonance Imaging Nanoparticle. *Sci. Transl. Med.* **2015**, *7*, 314ra183.

(14) Gref, R.; Minamitake, Y.; Peracchia, M. T.; Trubetskoy, V.; Torchilin, V.; Langer, R. Biodegradable Long-Circulating Polymeric Nanospheres. *Science* **1994**, *263*, 1600−1603.

(15) Owens, D. E., III; Peppas, N. A. Opsonization, Biodistribution, and Pharmacokinetics of Polymeric Nanoparticles. *Int. J. Pharm.* **2006**, *307*, 93−102.

(16) Otsuka, H.; Nagasaki, Y.; Kataoka, K. PEGylated Nanoparticles for Biological and Pharmaceutical Applications. *Adv. Drug Delivery Rev.* **2003**, *55*, 403−419.

(17) Maeda, H. Toward a Full Understanding of the EPR Effect in Primary and Metastatic Tumors as well as Issues Related to its Heterogeneity. *Adv. Drug Delivery Rev.* **2015**, *91*, 3−6.

(18) Dreaden, E. C.; Alkilany, A. M.; Huang, X.; Murphy, C. J.; El-Sayed, M. A. The Golden Age: Gold Nanoparticles for Biomedicine. *Chem. Soc. Rev.* **2012**, *41*, 2740−2779.

(19) Ghosh, P.; Han, G.; De, M.; Kim, C. K.; Rotello, V. M. Gold Nanoparticles in Delivery Applications. *Adv. Drug Delivery Rev.* **2008**, *60*, 1307−1315.

(20) Giljohann, D. A.; Seferos, D. S.; Daniel, W. L.; Massich, M. D.; Patel, P. C.; Mirkin, C. A. Gold Nanoparticles for Biology and Medicine. *Angew. Chem., Int. Ed.* **2010**, *49*, 3280−3294.

(21) Alkilany, A.; Murphy, C. Toxicity and Cellular Uptake of Gold Nanoparticles: What We Have Learned So Far? *J. Nanopart. Res.* **2010**, *12*, 2313−2333.

(22) Vigderman, L.; Zubarev, E. R. Therapeutic Platforms Based on Gold Nanoparticles and Their Covalent Conjugates with Drug Molecules. *Adv. Drug Delivery Rev.* **2013**, *65*, 663−676.

(23) Huang, X.; El-Sayed, I. H.; Qian, W.; El-Sayed, M. A. Cancer Cell Imaging and Photothermal Therapy in the Near-Infrared Region by Using Gold Nanorods. *J. Am. Chem. Soc.* **2006**, *128*, 2115−2120.

(24) Koo, M.; Oh, K. T.; Noh, G.; Lee, E. S. Gold Nanoparticles Bearing a pH-Sensitive Cyclodextrin Cap. *ACS Appl. Mater. Interfaces* **2018**, *10*, 24450−24458.

(25) Paciotti, G. F.; Myer, L.; Weinreich, D.; Goia, D.; Pavel, N.; McLaughlin, R. E.; Tamarkin, L. Colloidal Gold: A Novel Nanoparticle Vector for Tumor Directed Drug Delivery. *Drug Delivery* **2004**, *11*, 169−183.

(26) Libutti, S. K.; Paciotti, G. F.; Byrnes, A. A.; Alexander, H. R.; Gannon, W. E.; Walker, M.; Seidel, G. D.; Yuldasheva, N.; Tamarkin, L. Phase I and Pharmacokinetic Studies of CYT-6091, a Novel PEGylated Colloidal Gold-rhTNF Nanomedicine. *Clin. Cancer Res.* **2010**, *16*, 6139−6149.

(27) Paciotti, G. F.; Zhao, J.; Cao, S.; Brodie, P. J.; Tamarkin, L.; Huhta, M.; Myer, L. D.; Friedman, J.; Kingston, D. G. I. Synthesis and Evaluation of Paclitaxel-Loaded Gold Nanoparticles for Tumor-Targeted Drug Delivery. *Bioconjugate Chem.* **2016**, *27*, 2646−2657.

(28) Sequist, L. V.; Yang, J. C.-H.; Yamamoto, N.; O'Byrne, K.; Hirsh, V.; Mok, T.; Geater, S. L.; Orlov, S.; Tsai, C.-M.; Boyer, M.; Su, W.-C.; Bennouna, J.; Kato, T.; Gorbunova, V.; Lee, K. H.; Shah, R.; Massey, D.; Zazulina, V.; Shahidi, M.; Schuler, M. Phase III Study of Afatinib or Cisplatin Plus Pemetrexed in Patients With Metastatic Lung Adenocarcinoma With EGFR Mutations. *J. Clin. Oncol.* **2013**, *31*, 3327−3334.

(29) Park, K.; Tan, E.-H.; O'Byrne, K.; Zhang, L.; Boyer, M.; Mok, T.; Hirsh, V.; Yang, J. C.-H.; Lee, K. H.; Lu, S.; Shi, Y.; Kim, S.-W.; Laskin, J.; Kim, D.-W.; Arvis, C. D.; Kölbeck, K.; Laurie, S. A.; Tsai, C.-M.; Shahidi, M.; Kim, M.; Massey, D.; Zazulina, V.; Paz-Ares, L. Afatinib Versus Gefitinib as First-Line Treatment of Patients with EGFR Mutation-Positive Non-Small-Cell Lung Cancer (LUX-Lung 7): A Phase 2B, Open-Label, Randomised Controlled Trial. *Lancet Oncol.* **2016**, *17*, 577−589.

(30) Liang, L.; Astruc, D. The Copper(I)-Catalyzed Alkyne-Azide Cycloaddition (CuAAC) "Click" Reaction and its Applications. An Overview. *Coord. Chem. Rev.* **2011**, *255*, 2933−2945.

(31) Du, Y.; Xia, L.; Jo, A.; Davis, R. M.; Bissel, P.; Ehrich, M. F.; Kingston, D. G. I. Synthesis and Evaluation of Doxorubicin-Loaded Gold Nanoparticles for Tumor-Targeted Drug Delivery. *Bioconjugate Chem.* **2018**, *29*, 420−430.

(32) Doane, T.; Burda, C. Nanoparticle Mediated Non-Covalent Drug Delivery. *Adv. Drug Delivery Rev.* **2013**, *65*, 607−621.

(33) Kemp, S. J.; Thorley, A. J.; Gorelik, J.; Seckl, M. J.; O'Hare, M. J.; Arcaro, A.; Korchev, Y.; Goldstraw, P.; Tetley, T. D. Immortalization of Human Alveolar Epithelial Cells to Investigate Nanoparticle Uptake. *Am. J. Respir. Cell Mol. Biol.* **2008**, *39*, 591−597.

(34) Thorley, A. J.; Ruenraroengsak, P.; Potter, T. E.; Tetley, T. D. Critical Determinants of Uptake and Translocation of Nanoparticles by the Human Pulmonary Alveolar Epithelium. *ACS Nano* **2014**, *8*, 11778−89.

(35) Schroeder, J.; Dziewas, G.; Fachinger, T.; Jaeger, B.; Reichel, C.; Renner, S. Process for Preparing Aminocrotonylamino-Substituted Quinazoline Derivatives. Google Patents, 2008.

(36) Wissner, A.; Overbeek, E.; Reich, M. F.; Floyd, M. B.; Johnson, B. D.; Mamuya, N.; Rosfjord, E. C.; Discafani, C.; Davis, R.; Shi, X.; Rabindran, S. K.; Gruber, B. C.; Ye, F.; Hallett, W. A.; Nilakantan, R.; Shen, R.; Wang, Y.-F.; Greenberger, L. M.; Tsou, H.-R. Synthesis and Structure−Activity Relationships of 6,7-Disubstituted 4-Anilinoquinoline-3-carbonitriles. The Design of an Orally Active, Irreversible Inhibitor of the Tyrosine Kinase Activity of the Epidermal Growth Factor Receptor (EGFR) and the Human Epidermal Growth Factor Receptor-2 (HER-2). *J. Med. Chem.* **2003**, *46*, 49−63.

(37) Solca, F.; Dahl, G.; Zoephel, A.; Bader, G.; Sanderson, M.; Klein, C.; Kraemer, O.; Himmelsbach, F.; Haaksma, E.; Adolf, G. R. Target Binding Properties and Cellular Activity of Afatinib (BIBW 2992), an Irreversible ErbB Family Blocker. *J. Pharmacol. Exp. Ther.* **2012**, *343*, 342−350.

(38) Tsou, H.-R.; Overbeek-Klumpers, E. G.; Hallett, W. A.; Reich, M. F.; Floyd, M. B.; Johnson, B. D.; Michalak, R. S.; Nilakantan, R.; Discafani, C.; Golas, J.; Rabindran, S. K.; Shen, R.; Shi, X.; Wang, Y.-F.; Upeslacis, J.; Wissner, A. Optimization of 6,7-Disubstituted-4-(arylamino)quinoline-3-carbonitriles as Orally Active, Irreversible Inhibitors of Human Epidermal Growth Factor Receptor-2 Kinase Activity. *J. Med. Chem.* **2005**, *48*, 1107−1131.

(39) Pisaneschi, F.; Nguyen, Q.-D.; Shamsaei, E.; Glaser, M.; Robins, E.; Kaliszczak, M.; Smith, G.; Spivey, A. C.; Aboagye, E. O. Development of a New Epidermal Growth Factor Receptor Positron Emission Tomography Imaging Agent Based on the 3-Cyanoquinoline Core: Synthesis and Biological Evaluation. *Bioorg. Med. Chem.* **2010**, *18*, 6634−6645.

(40) Brust, M.; Walker, M.; Bethell, D.; Schiffrin, D. J.; Whyman, R. Synthesis of Thiol-Derivatised Gold Nanoparticles in a Two-Phase Liquid−Liquid System. *J. Chem. Soc., Chem. Commun.* **1994**, *7*, 801−802.

(41) Zhang, G.; Yang, Z.; Lu, W.; Zhang, R.; Huang, Q.; Tian, M.; Li, L.; Liang, D.; Li, C. Influence of Anchoring Ligands and Particle Size on the Colloidal Stability and In Vivo Biodistribution of Polyethylene Glycol-Coated Gold Nanoparticles in Tumor-Xenografted Mice. *Biomaterials* **2009**, *30*, 1928−1936.

(42) Coelho, S. C.; Almeida, G. M.; Pereira, M. C.; Santos-Silva, F.; Coelho, M. A. N. Functionalized Gold Nanoparticles Improve Afatinib Delivery into Cancer Cells. *Expert Opin. Drug Delivery* **2016**, *13*, 133−141.

(43) Montalbetti, C. A. G. N.; Falque, V. Amide Bond Formation and Peptide Coupling. *Tetrahedron* **2005**, *61*, 10827−10852.

(44) Haiss, W.; Thanh, N. T. K.; Aveyard, J.; Fernig, D. G. Determination of Size and Concentration of Gold Nanoparticles from UV−Vis Spectra. *Anal. Chem.* **2007**, *79*, 4215−4221.

(45) Amendola, V.; Meneghetti, M. Size Evaluation of Gold Nanoparticles by UV−vis Spectroscopy. *J. Phys. Chem. C* **2009**, *113*, 4277−4285.

(46) Xue, Y.; Li, X.; Li, H.; Zhang, W. Quantifying Thiol−Gold Interactions Towards the Efficient Strength Control. *Nat. Commun.* **2014**, *5*, 4348.

(47) Mani, G.; Kim, S.; Kim, K. Development of Folate-Thioglycolate-Gold Nanoconjugates by Using Citric Acid-PEG Branched Polymer for Inhibition of MCF-7 Cancer Cell Proliferation. *Biomacromolecules* **2018**, *19*, 3257−3267.

(48) Longmire, M. R.; Ogawa, M.; Choyke, P. L.; Kobayashi, H. Biologically Optimized Nanosized Molecules and Particles: More Than Just Size. *Bioconjugate Chem.* **2011**, *22*, 993−1000.

(49) Suk, J. S.; Xu, Q.; Kim, N.; Hanes, J.; Ensign, L. M. PEGylation as a Strategy for Improving Nanoparticle-Based Drug and Gene Delivery. *Adv. Drug Delivery Rev.* **2016**, *99*, 28−51.

(50) Alexis, F.; Pridgen, E.; Molnar, L. K.; Farokhzad, O. C. Factors Affecting the Clearance and Biodistribution of Polymeric Nanoparticles. *Mol. Pharmaceutics* **2008**, *5*, 505−515.

(51) Kobayashi, H.; Watanabe, R.; Choyke, P. L. Improving Conventional Enhanced Permeability and Retention (EPR) Effects; What is the Appropriate Target? *Theranostics* **2014**, *4*, 81−89.

(52) Kong, G.; Braun, R. D.; Dewhirst, M. W. Hyperthermia Enables Tumor-specific Nanoparticle Delivery: Effect of Particle Size. *Cancer Res.* **2000**, *60*, 4440−4445.

(53) Huang, X.; Jain, P. K.; El-Sayed, I. H.; El-Sayed, M. A. Gold Nanoparticles: Interesting Optical Properties and Recent Applications in Cancer Diagnostics and Therapy. *Nanomedicine* **2007**, *2*, 681−693.

(54) von Maltzahn, G.; Park, J.-H.; Lin, K. Y.; Singh, N.; Schwöppe, C.; Mesters, R.; Berdel, W. E.; Ruoslahti, E.; Sailor, M. J.; Bhatia, S. N. Nanoparticles That Communicate In Vivo to Amplify Tumour Targeting. *Nat. Mater.* **2011**, *10*, 545−552.

(55) Conde, J.; Ambrosone, A.; Sanz, V.; Hernandez, Y.; Marchesano, V.; Tian, F.; Child, H.; Berry, C. C.; Ibarra, M. R.; Baptista, P. V.; Tortiglione, C.; de la Fuente, J. M. Design of Multifunctional Gold Nanoparticles for In Vitro and In Vivo Gene Silencing. *ACS Nano* **2012**, *6*, 8316−8324.

(56) Bartczak, D.; Kanaras, A. G. Preparation of Peptide-Functionalized Gold Nanoparticles Using One Pot EDC/Sulfo-NHS Coupling. *Langmuir* **2011**, *27*, 10119−10123.

(57) Han, H.-S.; Lim, S.-N.; An, J. Y.; Lee, K. M.; Choe, K. H.; Lee, K. H.; Kim, S. T.; Son, S.-M.; Choi, S.-Y.; Lee, H.-C.; Lee, O.-J. Detection of EGFR Mutation Status in Lung Adenocarcinoma Specimens with Different Proportions of Tumor Cells Using Two Methods of Differential Sensitivity. *J. Thorac. Oncol.* **2012**, *7*, 355−364.

(58) Kim, D.; Park, S.; Lee, J. H.; Jeong, Y. Y.; Jon, S. Antibiofouling Polymer-Coated Gold Nanoparticles as a Contrast Agent for in Vivo X-ray Computed Tomography Imaging. *J. Am. Chem. Soc.* **2007**, *129*, 7661−7665.

(59) Suzawa, K.; Toyooka, S.; Sakaguchi, M.; Morita, M.; Yamamoto, H.; Tomida, S.; Ohtsuka, T.; Watanabe, M.; Hashida, S.; Maki, Y.; Soh, J.; Asano, H.; Tsukuda, K.; Miyoshi, S. Antitumor Effect of Afatinib, as a Human Epidermal Growth Factor Receptor 2-Targeted Therapy, in Lung Cancers Harboring HER2 Oncogene Alterations. *Cancer Sci.* **2016**, *107*, 45−52.

(60) Dreaden, E. C.; Mwakwari, S. C.; Sodji, Q. H.; Oyelere, A. K.; El-Sayed, M. A. Tamoxifen-Poly(ethylene glycol)-Thiol Gold Nanoparticle Conjugates: Enhanced Potency and Selective Delivery for Breast Cancer Treatment. *Bioconjugate Chem.* **2009**, *20*, 2247−2253.

(61) Wang, S.-Q.; Liu, S.-T.; Zhao, B.-X.; Yang, F.-H.; Wang, Y.-T.; Liang, Q.-Y.; Sun, Y.-B.; Liu, Y.; Song, Z.-H.; Cai, Y.; Li, G.-F. Afatinib Reverses Multidrug Resistance in Ovarian Cancer via Dually Inhibiting ATP Binding Cassette Subfamily B Member 1. *Oncotarget* **2015**, *6*, 26142−26160.

(62) Crapo, J. D.; Barry, B. E.; Gehr, P.; Bachofen, M.; Weibel, E. R. Cell Number and Cell Characteristics of the Normal Human Lung. *Am. Rev. Respir. Dis.* **1982**, *126*, 332−337.

(63) Swain, R. J.; Kemp, S. J.; Goldstraw, P.; Tetley, T. D.; Stevens, M. M. Assessment of Cell Line Models of Primary Human Cells by Raman Spectral Phenotyping. *Biophys. J.* **2010**, *98*, 1703−1711.

(64) Sansone, P.; Bromberg, J. Targeting the Interleukin-6/Jak/Stat Pathway in Human Malignancies. *J. Clin. Oncol.* **2012**, *30*, 1005−1014.

(65) Qu, Z.; Sun, F.; Zhou, J.; Li, L.; Shapiro, S. D.; Xiao, G. Interleukin-6 Prevents the Initiation but Enhances the Progression of Lung Cancer. *Cancer Res.* **2015**, *75*, 3209−3215.

(66) Harada, D.; Takigawa, N.; Kiura, K. The Role of STAT3 in Non-Small Cell Lung Cancer. *Cancers* **2014**, *6*, 708−722.

(67) Wang, Y.; van Boxel-Dezaire, A. H. H.; Cheon, H.; Yang, J.; Stark, G. R. STAT3 Activation in Response to IL-6 is Prolonged by the Binding of IL-6 Receptor to EGF Receptor. *Proc. Natl. Acad. Sci. U. S. A.* **2013**, *110*, 16975−16980.

(68) Klein, S.; Petersen, S.; Taylor, U.; Rath, D.; Barcikowski, S. Quantitative Visualization of Colloidal and Intracellular Gold Nanoparticles by Confocal Microscopy. *J. Biomed. Opt.* **2010**, *15*, 036015.

(69) Liu, M.; Li, Q.; Liang, L.; Li, J.; Wang, K.; Li, J.; Lv, M.; Chen, N.; Song, H.; Lee, J.; Shi, J.; Wang, L.; Lal, R.; Fan, C. Real-Time Visualization of Clustering and Intracellular Transport of Gold Nanoparticles by Correlative Imaging. *Nat. Commun.* **2017**, *8*, 15646−15646.

(70) Chithrani, B. D.; Ghazani, A. A.; Chan, W. C. W. Determining the Size and Shape Dependence of Gold Nanoparticle Uptake into Mammalian Cells. *Nano Lett.* **2006**, *6*, 662−668.

Appendix C – Permissions

RightsLink®

Home | Help | Email Support | Sign in | Create Account

ACS Publications
Most Trusted. Most Cited. Most Read.

Tyrosine Kinase Inhibitor Gold Nanoconjugates for the Treatment of Non-Small Cell Lung Cancer

Author: Alexander M. Cryer, Cheuk Chan, Anastasia Eftychidou, et al
Publication: Applied Materials
Publisher: American Chemical Society
Date: May 1, 2019

Copyright © 2019, American Chemical Society

PERMISSION/LICENSE IS GRANTED FOR YOUR ORDER AT NO CHARGE

This type of permission/license, instead of the standard Terms & Conditions, is sent to you because no fee is being charged for your order. Please note the following:

- Permission is granted for your request in both print and electronic formats, and translations.
- If figures and/or tables were requested, they may be adapted or used in part.
- Please print this page for your records and send a copy of it to your publisher/graduate school.
- Appropriate credit for the requested material should be given as follows: "Reprinted (adapted) with permission from (COMPLETE REFERENCE CITATION). Copyright (YEAR) American Chemical Society." Insert appropriate information in place of the capitalized words.
- One-time permission is granted only for the use specified in your request. No additional uses are granted (such as derivative works or other editions). For any other uses, please submit a new request.
If credit is given to another source for the material you requested, permission must be obtained from that source.

BACK | CLOSE WINDOW

.